

Imaging Techniques for the Assessment of Coronary Atherosclerosis, Intracoronary Devices and Vessel Response after Metallic or Polymeric Scaffolds Implantation

Salvatore Brugaletta

Financial support by Abbott Vascular, Cardialysis B.V, InfraReDx, and Volcano Corporation for the publication of this thesis is gratefully acknowledged

Layout and printing: Optima Grafische Communicatie, Rotterdam, The Netherlands

ISBN: 978-94-6169-261-0

**Imaging Techniques for the Assessment of Coronary Atherosclerosis,
Intracoronary Devices and Vessel Response after Metallic or Polymeric
Scaffolds Implantation**

Beeldvormende technieken voor de beoordeling van coronaire atherosclerose,
intracoronaire stents en de reactie van de vaatwand na de implantatie van een metalen
of een oplosbare stent

Thesis

to obtain the degree of Doctor from the
Erasmus University Rotterdam
by command of the
rector magnificus

Prof.dr. H.G. Schmidt

and in accordance with the decision of the Doctorate Board.

The public defence shall be held on
Tuesday the 22nd of May, 2012 at 9:30 o'clock

by

Salvatore Brugaletta
born in Ragusa, Italy



DOCTORAL COMMITTEE

Promotor

Prof.dr. P.W.J.C. Serruys

Co-promotor:

Dr. H.M. Garcia-Garcia

Other members

Prof.dr. P.J. de Feyter

Prof.dr. F. Zijlstra

Prof.dr. E. Boersma

Prof.dr. H.Reiber

Prof.dr M. Sabaté

Dr. Nico Bruining

To my parents and my sister

TABLE OF CONTENTS

	Introduction	9
Chapter 1.	Basic principles and internal validation of IVUS-based techniques	13
1.1	Tissue characterization using virtual histology and iMAP: current status and potential clinical applications.	15
1.2	Reproducibility of intravascular ultrasound iMAP for radiofrequency data analysis: implications for design of longitudinal studies.	37
Chapter 2.	Coronary plaque characterization through near infra-red spectroscopy	51
2.1	Assessment of Coronary Plaque Composition with Near Infrared Spectroscopy.	53
2.2	In vivo distribution of lipid core containing plaque according to distance from the ostium by near infrared spectroscopy in non-culprit coronary arteries.	71
Chapter 3.	Combined imaging and functional approaches for coronary atherosclerosis evaluation.	77
3.1	NIRS and IVUS for characterization of atherosclerosis in patients undergoing coronary angiography.	79
3.2	Assessment of Coronary Atherosclerosis Progression and Regression at Bifurcations Using Combined IVUS and OCT.	89
3.3	Comprehensive Assessment of Atherosclerotic Plaques at Coronary Bifurcations with Multislice Computed Tomography Angiography and Intravascular Ultrasound –Virtual Histology.	97
3.4	Morphology of coronary artery lesions assessed by virtual histology intravascular ultrasound tissue characterization and fractional flow reserve.	113
3.5	Relationship between palpography and virtual histology in patients with acute coronary syndromes: a sub-analysis from the PROSPECT trial.	123
Chapter 4.	Assessment of findings after coronary metallic stent implantation	133
4.1	Evaluation of in-stent restenosis in the APPROACH trial (assessment on the prevention of progression by Rosiglitazone on atherosclerosis in diabetes patients with cardiovascular history).	135
4.2	Poor Agreement Of Qualitative Assessment of Stent Struts Coverage By Optical Coherence Tomography.	147
Chapter 5.	Use of imaging techniques for the assessment of bioresorbable vascular scaffolds.	155
5.1	Comparison between the first and second generation bioresorbable vascular scaffolds: a six month virtual histology study.	157
5.2	A comparative assessment by optical coherence tomography of the performance of the first and second generation of the everolimus-eluting bioresorbable vascular scaffolds.	165
5.3	Agreement and reproducibility of grey-scale intravascular ultrasound and optical coherence tomography for the analysis of the bioresorbable vascular scaffold.	179
Chapter 6.	Evaluation of mechanical properties of bioresorbable vascular scaffolds.	197

6.1	Angiographic geometric changes of the lumen arterial wall after bioresorbable vascular scaffolds and metallic platform stents at 1-year follow-up.	199
6.2	Comparison of in vivo eccentricity and symmetry indices between metallic stents and bioresorbable vascular scaffolds: Insights from the ABSORB and SPIRIT trials.	211
6.3	Vascular distensibility of the treated and adjacent coronary segments after bioresorbable vascular scaffold implantation.	223
Chapter 7.	Assessment of changes in the structure of bioresorbable vascular scaffolds overtime.	233
7.1	Serial in vivo IVUS-based echogenicity changes of everolimus-eluting bioresorbable vascular scaffold during the first 12 months after implantation. Insights from ABSORB B trial.	235
7.2	Serial analysis of the malapposed and uncovered struts of the new generation of everolimus-eluting bioresorbable scaffold using optical coherence tomography.	245
7.3	Head to head comparison of optical coherence tomography, intravascular ultrasound echogenicity and virtual histology for the detection of changes in polymeric struts over time. Insights from the ABSORB trial.	257
Chapter 8.	Assessment of morphological and functional modifications in the coronary artery after bioresorbable vascular scaffolds implantation.	265
8.1	Temporal changes of coronary artery plaque located behind the struts of the everolimus eluting bioresorbable vascular scaffold.	267
8.2	Analysis of one-year virtual histology changes in coronary plaque located behind the struts of the everolimus eluting bioresorbable vascular scaffold.	277
8.3	Endothelial-dependent vasomotion in coronary segment treated by ABSORB everolimus-eluting bioresorbable vascular scaffold system is related to plaque composition at the time of bioresorption of the polymer: indirect finding of vascular reparative therapy?	287
8.4	Circumferential evaluation of the neointima by optical coherence tomography after ABSORB bioresorbable vascular scaffold implantation: can the scaffold cap the plaque?	297
	Summary and Conclusions	305
	Acknowledgments	317
	Curriculum Vitae	321
	List of Publications	323
	Color section	333

INTRODUCTION

The recognition of the ubiquity of substantial but non-flow limiting lesions that may be at high risk for subsequent plaque rupture and cannot be identified by coronary angiography has resulted in a paradigm shift in thinking about the pathophysiology of coronary artery disease, with the focus no longer solely on the degree of arterial luminal narrowing. (1,2) This growing need for more information about coronary atherosclerosis in order to identify patients and lesions at risk for complications during PCI and for future adverse cardiac events has been the primary impetus for the development of novel intra-coronary imaging methods, able to detect plaque composition.

The introduction of intravascular ultrasound (IVUS) initially allowed a detailed evaluation of coronary atherosclerosis, but its limited resolution (axial 100-200 μm) precluded the visualization of certain microstructure and its capability to characterize coronary plaques, based on their greyscale-IVUS appearance, is limited. For these reasons, some other ultrasound and light based intra-coronary imaging techniques have been developed in order to provide tissue characterization of the coronary plaques. (3)

Chapter 1 analyses the various ultrasound-based intracoronary imaging techniques, used for tissue characterization, highlighting their potential clinical applications, and explores the inter- and intra-observer, intra-catheter and inter-catheter variabilities of one of these techniques (iMAP). IVUS iMAP characterizes necrotic core content of coronary plaque, its reproducibility was evaluated in a longitudinal study simulation.

A new imaging technique, based on the near infra-red light to detect lipid coronary plaques, and its ability to assess the in vivo lipid core plaque longitudinal distribution is analyzed in Chapter 2.

It is important to note that all these imaging modalities can detect different compositional,

functional or mechanical properties of a coronary plaque. The various information which are derived can be therefore variously combined for atherosclerosis evaluation, in order to enhance the identification of vulnerable plaques. (Chapter 3)

It is important to consider that these imaging techniques can be used not only for assessment of coronary atherosclerosis, but also for characterizing the vessel response after metallic or polymeric scaffolds implantation. In chapter 4, IVUS was, for example, applied to determine the restenosis parameters (plaque behind stent, intra-stent intima hyperplasia) and the effect of anti-diabetic drugs on intra-stent neointima after metallic stent implantation. We also revised the qualitative OCT approach for the assessment of metallic strut coverage by measuring the inter- and intra-observer agreement and evaluating the influence of various zoom settings.

An important part of this thesis is about the use of imaging modalities for the evaluation of the completely bioresorbable vascular scaffolds, which have been recently introduced in interventional cardiology with the aim to allow a normal healing process eliminating the permanent caging of a metallic stent. (4-6) Intracoronary imaging techniques can be therefore used either to analyze the in vivo changes of these devices overtime during the bioresorption process or to characterize the vessel reparative process after polymeric scaffold implantation, once the scaffold is bioresorbed.

In chapter 5 we described the information that can be obtained by IVUS, IVUS-VH and OCT in order to characterize the bioresorbable vascular scaffolds.

In chapter 6, the changes in bioresorbable vascular scaffolds overtime were evaluated by IVUS-based echogenicity and OCT. A comparison between these imaging modalities was also performed.

Chapter 7 evaluated the mechanical properties of bioresorbable vascular scaffolds, such as conformability, eccentricity and symmetry, and

analyzes the changes in vascular distensibility after its implantation in coronary arteries.

Finally, in chapter 8 we assessed the morphological and functional modifications in the coronary artery after bioresorbable vascular scaffold implantation.

To conclude, the aim of this thesis was therefore:

1) to explore the potential usefulness of single or combined intra-coronary imaging techniques in detecting plaque vulnerability as well as to find

a role for them in the clinical setting or in future trial design; 2) to assess in vivo the mechanical and structural properties of the bioresorbable vascular scaffolds, used for the treatment of coronary atherosclerosis; 3) to evaluate the interaction of these bioresorbable vascular scaffolds and the vessel wall, providing some surrogate imaging endpoints, which can be applied in the preparation of future trials.

REFERENCES

1. Topol EJ, Nissen SE. Our preoccupation with coronary luminology. The dissociation between clinical and angiographic findings in ischemic heart disease. *Circulation* 1995;92:2333-42.
2. Stone GW, Maehara A, Lansky AJ, et al. A prospective natural-history study of coronary atherosclerosis. *N Engl J Med* 2011;364:226-35.
3. Garcia-Garcia HM, Costa MA, Serruys PW. Imaging of coronary atherosclerosis: intravascular ultrasound. *Eur Heart J*;31:2456-69.
4. Serruys PW, Ormiston JA, Onuma Y, et al. A bioabsorbable everolimus-eluting coronary stent system (ABSORB): 2-year outcomes and results from multiple imaging methods. *Lancet* 2009;373:897-910.
5. Serruys PW, Onuma Y, Ormiston JA, et al. Evaluation of the second generation of a bioresorbable everolimus drug-eluting vascular scaffold for treatment of de novo coronary artery stenosis: six-month clinical and imaging outcomes. *Circulation* 2010;122:2301-12.
6. Serruys PW, Onuma Y, Dudek D, et al. Evaluation of the second generation of a bioresorbable everolimus-eluting vascular scaffold for the treatment of de novo coronary artery stenosis 12-month clinical and imaging outcomes. *J Am Coll Cardiol* 2011;58:1578-88.

Chapter 1

Basic principles and internal validation of IVUS-based techniques

1.1

Tissue characterization using virtual histology and iMAP:
current status and potential clinical applications.

Brugaletta S, Garcia-Garcia HM.

Coronary Atherosclerosis: Current management and treatment, In press

INTRODUCTION

Coronary angiography depicts arteries as a planar silhouette of the contrast-filled lumen. Importantly, angiography does not provide visualization of the vessel wall and is not suitable for complete assessment of atherosclerosis. Angiographic disease assessment is based on the comparison of the stenotic segment with the adjacent, “normal-appearing” coronary, which is often an incorrect assumption due to the diffuse nature of atherosclerosis, as shown by pathological and intravascular ultrasound (IVUS) studies.¹

Grayscale IVUS is the modality that has been established as the gold standard for *in vivo* imaging of the vessel wall of the coronary arteries.^{2,3} However, the grayscale representation of the coronary vessel wall and plaque morphology in combination with the limited resolution of the current IVUS catheters makes difficult, if not impossible, to identify qualitatively (e.g. visually) the plaque morphology similar as that of histopathology, the gold standard to characterize and quantify coronary plaque tissue components.⁴

Meanwhile, this limitation has been partially overcome by new innovative IVUS-based methods such as: virtual histology IVUS⁵⁻⁷ (VH-IVUS, Volcano Therapeutics, Rancho Cordova, CA, USA) and iMAP-IVUS^{8,9} (Boston Scientific, Santa Clara, CA, USA), based on interpretation of the raw radiofrequency analysis.

Tissue characterization using virtual histology IVUS (VH-IVUS)

The first commercial available RadioFrequency (RF) signal based tissue composition analysis tool was the so-called virtual histology (VH-IVUS, Volcano Therapeutics) software. It uses in-depth analysis of the backscattered RF-signal in order to provide a more detailed description of the atheromatous plaque composition and is performed with either a 20 MHz, 2.9F phased array transducer catheter (Eagle Eye™ Gold, Volcano Therapeutics) or 45 MHz 3.2F rotational catheter (Revolution, Volcano Therapeutics) that acquires IVUS data electrocardiogram gated.⁷ The main principle of this technique is that it uses not only the envelope amplitude of the reflected RF signals (as gray-scale IVUS does), but also the underlying frequency content to analyze the tissue components present in coronary plaques. **(Figure 1)** This combined information is processed using autoregressive models and thereafter in a classification tree that determines four basic plaque tissue components⁵: (1) Fibrous tissue (dark green), (2) Fibrofatty tissue (light green), (3) Necrotic core (red) and (4) Dense calcium (white). The current software version assumes the presence of a media layer, which is artificially added, positioned just at the inside of the outer vessel contour. This technique has been compared in several studies against histology in humans and other species (table 1).

FOCUS BOX

1. Angiography is limited to evaluate coronary plaque. It does only provide information on the lumen.
2. IVUS and IVUS-based modalities can help us not only to fully assess the coronary vessel wall but also to characterize plaque tissue components.

Table 1.

		VH IWUS		
Nair (Circulation 2002;106:2200-2206)	Ex vivo	2002	Coronary plaque classification with intravascular ultrasound radiofrequency data analysis	Autoregressive classification schemes performed better than those from classic Fourier spectra with accuracies of 90.4% for fibrous, 92.8% for fibrolipidic, 90.9% for calcified, and 89.5% for calcified-necrotic regions in the training data set and 79.7%, 81.2%, 92.8%, and 85.5% in the test data, respectively.
Nasu (JACC 2005;47:2405-12)	In vivo	2006	Accuracy of In Vivo Coronary Plaque Morphology Assessment: A Validation Study of In Vivo Virtual Histology Compared With In Vitro Histopathology	Predictive accuracy from all patients data: 87.1% for fibrous, 87.1% for fibro-fatty, 88.3% for necrotic core, and 96.5% for dense calcium regions, respectively Sensitivities: NC:67.3%, FT:86%, FF:79.3%, DC:50%. Specificities: NC:92.9%, FT:90.5%, FF:100%, DC:99%
Nair (Eurointervention 2007;3:113-20)	Ex vivo	2007	Automated coronary plaque characterisation with intravascular ultrasound backscatter: ex vivo validation	The overall predictive accuracies were 93.5% for FT, 94.1% for FF, 95.8% for NC, and 96.7% for DC. Sensitivities: NC: 91.7%, FT:95.7%, FF:72.3%, DC:86.5%. Specificities: NC:96.6%, FT:90.9%, FF:97.9%, DC:98.9%
Granada (ATVB 2007;27:387-93)	Ex vivo	2007	In vivo plaque characterization using intravascular ultrasound-virtual histology in a porcine model of complex coronary lesions	Compared with histology, IWUS-VH correctly identified the presence of fibrous, fibro-fatty, and necrotic tissue in 58.33%, 38.33%, and 38.33% of lesions, respectively. Sensitivities: fibrous 76.1%, fibro-fatty 46%, and necrotic core 41.1%
Van Herk (Eurointervention 2009;5:149-56)	Ex vivo	2009	Validation of in vivo plaque characterisation by virtual histology in a rabbit model of atherosclerosis	VH-IWUS had a high sensitivity, specificity and positive predictive value for the detection of non-calcified thin cap fibroatheroma (88%, 96%, 87%, respectively) and calcified thin cap fibroatheroma (95%, 99%, 93%, respectively). These values were respectively 82%, 94%, 85% for non-calcified fibroatheroma and 78%, 98%, 84% for calcified fibroatheroma. The lowest values were obtained for pathological intimal thickening (74%, 92%, 70%, respectively). For all plaque types, VH-IWUS had a kappa-value of 0.79.
Thim (Circ Cardiovasc Imaging 2010;3:384-91)	Ex vivo	2010	Unreliable Assessment of Necrotic Core by VH-TM IWUS in Porcine Coronary Artery Disease	No correlations were found between the size of the necrotic core determined by VH IWUS and histology. VH IWUS displayed necrotic cores in lesions lacking cores by histology.

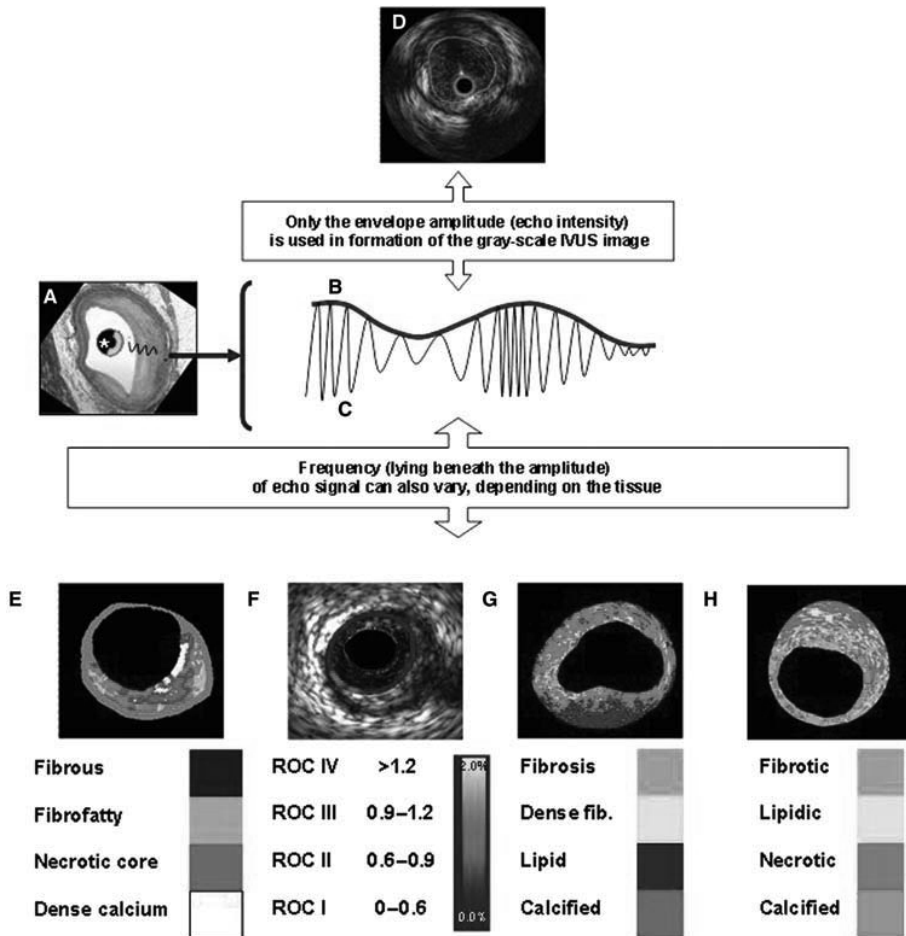


Figure 1. Intravascular ultrasound signal is obtained from the vessel wall (A). Grayscale intravascular ultrasound imaging is formed by the envelope (amplitude) (B) of the radiofrequency signal (C). By grayscale, atherosclerotic plaque can be classified into four categories: soft, fibrotic, calcified and mixed plaques. (D) shows a cross-sectional view of a grayscale image. The blue lines limit the actual atheroma. The frequency and power of the signal commonly differ between tissues, regardless of similarities in the amplitude. From the backscatter radiofrequency data different types of information can be retrieved: virtual histology (E), palpography (F), integrated backscattered intravascular ultrasound (G) and iMAP (H). Virtual histology is able to detect four tissue types: necrotic core, fibrous, fibrofatty and dense calcium. Plaque deformability at palpography is reported in strain values, which are subsequently categorized into four grades according to the Rotterdam Classification (ROC). The tissues characterized by integrated backscattered intravascular ultrasound are lipidic, fibrous and calcified; iMAP detects fibrotic, lipidic, necrotic and calcified. (from *Eur Heart J* 2010;31:2456-69). See color figure on page 335

FOCUS BOX

IVUS-VH, based on backscattering signal interpretation, enables characterization of fibrous and fibrofatty tissues, necrotic core and dense calcium in coronary plaques.

Natural history of Atherosclerosis

Acute coronary syndromes are often the first manifestation of coronary atherosclerosis, making the identification of plaques at high-risk of complication an important component of strategies to reduce casualties associated with atherosclerosis. Our current understanding of plaque biology suggests that ~60% of clinically evident plaque rupture originates within an inflamed thin-capped fibroatheroma.^{10,11} Pathological studies demonstrated that ruptured plaques are mainly located in the proximal portions of the left anterior descending and circumflex arteries, and are more dispersed in the right coronary artery.¹² This tendency of advanced plaques to develop preferentially in these locations has been explained by the low shear stress conditions generated in areas with tortuosity or many branches. Low shear stress may induce the migration of lipid and monocytes into the vessel wall leading to the progression of the lesion towards a plaque with high risk of rupture.¹³

Although a detailed description of atherosclerosis development and composition is beyond the scope of this chapter, some concepts are important to support the use of tissue characterization imaging modalities for plaque characterization. In brief, an atheroma is formed by an intricate sequence of events, not necessarily in a linear chronological order, that involves extracellular lipid accumulation, endothelial dysfunction, leucocyte recruitment, intracellular lipid accumulation (foam cells), smooth muscle cell migration and proliferation, expansion of extracellular matrix, neo-angiogenesis, tissue necrosis and mineralization at later stages.^{14,15} The ultimate characteristic of an atherosclerotic

plaque at any given time depends on the relative contribution of each of these features.¹⁴ Thus, in histological cross-sections, the pathologic intimal thickening is rich in proteoglycans and lipid pools, but no trace of necrotic core is seen. Conversely, the necrotic core appears in the fibroatheroma (FA), that is the precursor lesion of symptomatic heart disease. Thin-capped fibroatheroma (TCFA) is a lesion characterized by a large necrotic core containing numerous cholesterol clefts, cellular debris and microcalcifications. The overlying fibrous cap is thin and rich in inflammatory cells, macrophages and T lymphocytes with a few smooth muscle cells.

Plaque type characterization by IVUS-VH

Using IVUS-VH, it is possible to define the various stages of atherosclerosis. (**Figure 2**) The definition of an IVUS-derived thin capped fibro-atheroma (TCFA), for example, is a lesion fulfilling the following criteria in at least 3 consecutive frames: (1) plaque burden $\geq 40\%$; (2) confluent necrotic core $\geq 10\%$ in direct contact with the lumen (i.e. no visible overlying tissue).¹⁶ Using this definition of IVUS-derived TCFA, in patients with ACS who underwent IVUS of all three epicardial coronaries there were, on average, two IVUS-derived TCFA per patient with half of them showing outward remodelling.¹⁶

Hong et al., reported the frequency and distribution of TCFA identified by IVUS-VH in ACS (105 pts) and SAP (107 pts) in a 3-vessel IVUS-VH study.¹⁷ There were 2.5 ± 1.5 in ACS and 1.7 ± 1.1 in SAP TCFA per patient ($p < 0.001$). Presentation of ACS was the only independent predictor for multiple virtual histology derived TCFA (VH-TCFA) ($p = 0.011$).

Lesion Type	
<p>Adaptative Intimal Thickening (AIT) <600 μm of intima thickness for <20% of the circumference</p>	
<p>Pathological Intimal Thickening (PIT) $\geq 600 \mu\text{m}$ thickness for >20% of the circumference with FF >15%, and no confluent NC or DC</p>	
<p>Fibrotic Plaque (FT) Dominant FT and no confluent NC or DC</p>	
<p>Fibrocalcific Plaque (FC) >10% Confluent DC with no confluent NC</p>	
<p>Fibroatheroma (FA) >10% Confluent NC not at the lumen on three consecutive frames</p>	
<p>Thin Cap Fibroatheroma (TCFA) >10% Confluent NC at the lumen on three consecutive frames</p>	

Figure 2. Virtual histology plaque types. (from Eur Heart J 2010;31:2456-69). See color figure on page 336

Eighty-three percent of VH-TCFAs were located within 40 mm of the coronary.

The potential value of these IVUS-VH derived plaque types in the prediction of adverse coronary events was evaluated in an international multicentre prospective study, the Providing Regional Observations to Study Predictors of Events in the Coronary Tree study (PROSPECT study).¹⁸ The PROSPECT trial was a multi-center, natural history study of acute coronary syndrome patients. All patients underwent PCI in their culprit lesion at baseline, followed by an angiogram and IVUS virtual histology of the three major coronary arteries. A TCFA with a minimum lumen area of $\leq 4\text{mm}^2$ and a large plaque burden ($\geq 70\%$) had a 17.2% likelihood of causing an event within three years. Interestingly,

compared with fibrotic and fibrocalcific plaques in terms of increase of plaque area and decrease in lumen.²⁰ At the site of coronary bifurcation, using a combined approach VH/OCT, we previously showed that most necrotic core rich plaques remained unchanged.²¹ (**Figure 3**)

Although plaque characteristics (i.e. tissue characterization) do not yet influence current therapeutic guidelines, the available clinical imaging modalities, IVUS and IVUS-based tissue characterization techniques such as virtual histology and iMAP have the ability to identify some of the pathological atheroma features described above and could help us to advance further our understanding on atherosclerosis.

FOCUS BOX

IVUS-VH TCFA has been found to be associated with long term clinical event in the PROSPECT trial.

the anticipated high frequency of acute thrombotic cardiovascular events did not occur, with only a 1% rate of myocardial infarction and no deaths directly attributable to non-culprit vessels over 3 years of follow-up. These results suggest that non-culprit, yet obstructive coronary plaques are most likely to be associated with increasing symptoms rather than thrombotic acute events, with 8.5% of patients presenting with worsening angina and 3.3% with unstable angina. The PROSPECT findings were recently confirmed by the VIVA study.¹⁹

By use of IVUS-VH, the serial changes in VH plaque type have been also investigated. In particular Kubo et al. showed that most of VH-TCFA healed during 12 months follow-up. However, during this time new VH-TCFA developed and in general PIT and necrotic core plaques had a significant progression

Tissue characterization using iMAP-IVUS

Recently, another RF-based processing method has become commercially available for coronary plaque tissue characterization and it is called iMAP-IVUS (Boston Scientific).⁸ In principle this software is comparable, from methodological point of view, to the IVUS-VH or other IVUS-based technique for tissue characterization. (Table 2) However, by design, these two IVUS catheters have different capabilities for tissue characterization. Unlike VH, iMap uses a 40MHz single rotational transducer on a drive shaft and can acquire radiofrequency data continuously, while VH uses similar catheter and additionally is also available in the electronic catheter (20 MHz). Virtual histology acquired only ECG gated data. In addition, VH feeds the spectra that are obtained

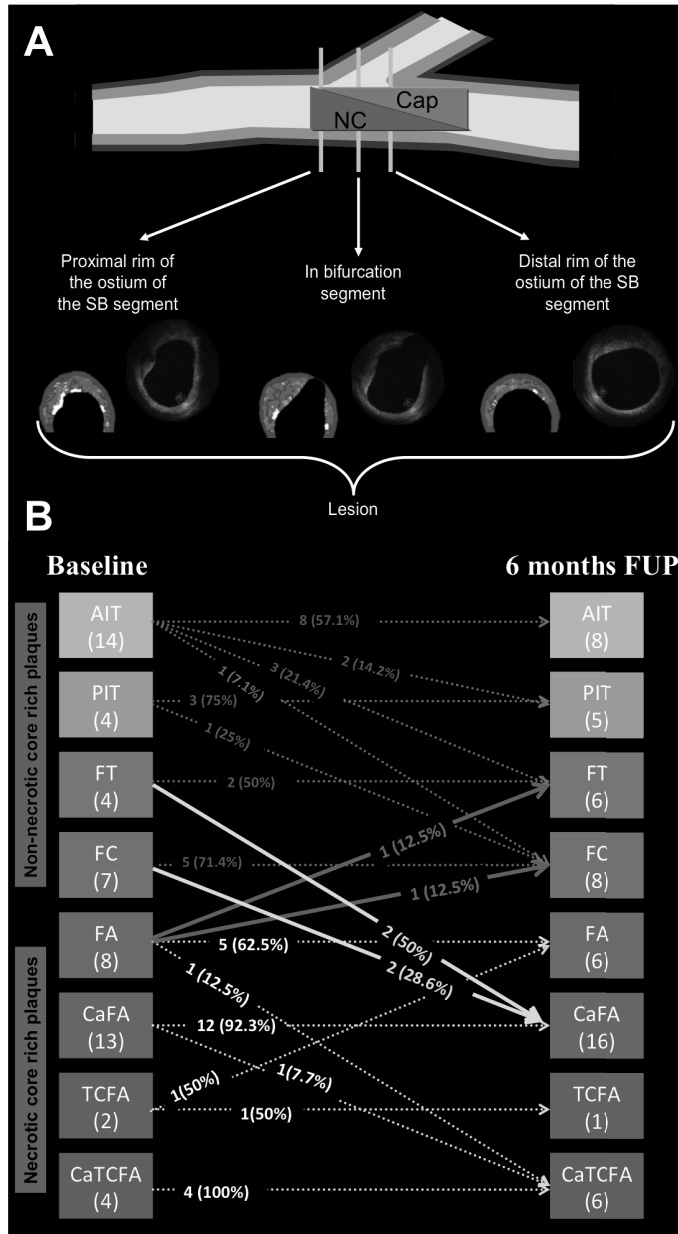


Figure 3. Panel A: At bifurcations, plaque were analyzed only in the main coronary arteries at the proximal rim of the ostium of the side branch (the first frame proximal to the takeoff of the side branch), at the in-bifurcation site (the frame with the largest ostial diameter of the side branch) and at the distal rim of the ostium of the side branch (the first frame distal to the takeoff of the side branch). VH and OCT frames were selected. **Panel B:** Changes in bifurcation plaque type at 6-month follow-up. For each plaque type, the number and percent of changes are reported. AIT = adaptive intimal thickening; CaFA = calcified fibroatheroma; CaTCFA = calcified thin-cap fibroatheroma; FA = fibroatheroma; FC = fibrocalcific plaque; FT = fibrotic plaque; PIT = pathological intimal thickening.

Table 2. Similarities and differences of IVUS and IVUS-based imaging modalities

	IVUS	VH	i-MAP	Integrated Backscatter	Echogenicity
Type of device	Mechanical & electrical	Mechanical and Electrical	Mechanical	Mechanical	Mechanical and electrical
Transducer Frequency	20-40 MHz	20-45 MHz	40MHz	40 MHz	20-40 MHz
Color code	Gray-scale	Fibrous: Green	Fibrous: Light green	Fibrous: Green	Red for hyperechogenic areas and green for hypoechogenic areas
		Necrotic Core: Red	Necrotic Core: Pink	Necrotic Core: Blue	
		Calcium: White	Calcium: Blue	Calcium: Red	
		Fibrofatty: Light green	Fibrofatty: Yellow	Fibrofatty: Yellow	
Backscatter Radiofrequency signal analysis	Amplitude (dB)	Autoregressive model	Fast Fourier Transformation	Fast Fourier Transformation	It does not use backscatter radiofrequency but the amplitude of the signal

from the radiofrequency data using autoregressive models into a classification tree that has reported diagnostic accuracies of over 90% each plaque components as compared to histology.⁶ iMap uses a pattern recognition algorithm on the spectra that were obtained from a fast Fourier transformation and a histology-derived database.⁸ Taken together, it is possible that these distinctive features may lead to differences in the tissue characteristics of the images of coronary plaque obtained. iMap and VH (40 MHz vs. 45/20 MHz) have relative advantages and disadvantages in displaying greyscale images. iMap has higher resolution, but displays specific artifacts such as non-uniform rotational distortion, because it is a rotational catheter. In addition, far-

field imaging can be more problematic with high frequency catheters due to amplified attenuation and enhanced blood backscatter.

The colour code for tissue types is different. iMap depicts fibrotic (light green), lipidic (yellow), necrotic (pink) and calcified tissue (blue), while VH depicts fibrous (green), fibrofatty (yellow green), necrotic core (red) and dense calcium (white), respectively.

Shin et al. compared in vivo the findings of this two IVUS-based tissue characterization system, showing a significant and systematic variability in plaque composition estimates.⁹ iMap classified plaque as necrotic tissue in poor signal areas, such as guidewire artifact or acoustic shadowing, while VH displays fibrofatty. (**Figure 4**) VH showed external

FOCUS BOX

iMAP is an IVUS-based technology that helps to characterize tissue composition of coronary plaques. Although the principle of the technique is similar to that of IVUS-VH, it presents some important differences as compared to VH.

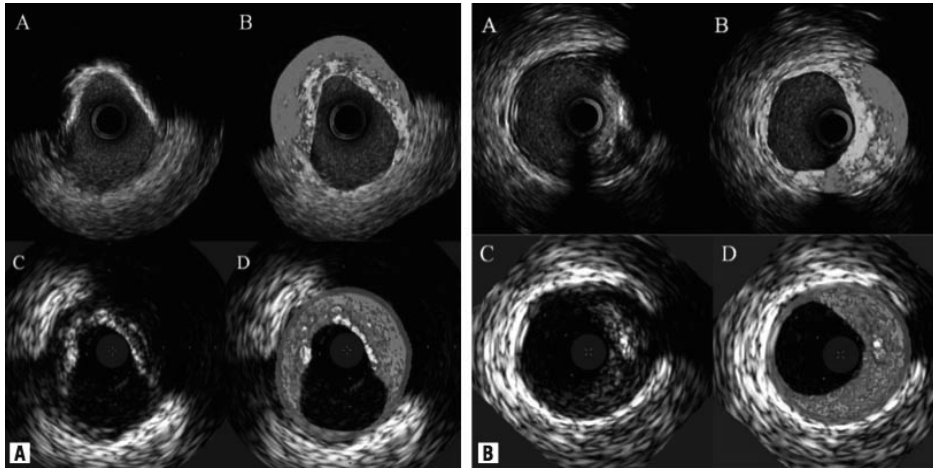


Figure 4. Corresponding cross-section of iMap (top) and VH images (bottom). iMap shows large amounts of necrotic tissue behind calcium, while with VH the same area is reported as fibrous or fibrofatty tissue. In panel B, iMAP shows necrotic tissue because also of the wire artifact. (from *Eurointervention* 2011;6:1017-1019). See color figure on page 337

elastic membrane as a grey medial stripe, while iMap always provided plaque composition results even for very thin plaques. VH tended to overestimate metallic stent struts, and iMap showed thinner stent thickness than VH. Also, there was peri-stent and calcium necrotic core halo in VH that was not seen in iMap.

Taken all together, these findings warrant further exploration of these imaging techniques in a large population to find particular areas of clinical usefulness.

Assessment of drug effect on atherosclerosis by IVUS-VH (Table 3)

IVUS-VH has been so far used in various studies in order to show serial changes of plaque composition in patients treated with various statin treatments.

In one of them, patients with stable angina pectoris (n=80) treated with fluvastatin for 1 year had significant regression of the plaque volume, and changes in the atherosclerotic plaque composition with a significant reduction of the fibrofatty volume ($p < 0.0001$). These changes in the fibrofatty volume had a significant correlation with changes in the LDL-cholesterol level ($r = 0.703$, $p < 0.0001$) and in the hs-C reactive protein level ($r = 0.357$, $p = 0.006$).²² Of note, the necrotic core did not change significantly.

In a second study, Hong et al. randomized 100 patients with stable angina and ACS to either rosuvastatin 10 mg or simvastatin 20 mg for 1 year. The overall necrotic core volume significantly decreased ($p = 0.010$) and the fibrofatty plaque volume increased ($p = 0.006$) after statin treatments. Particularly, there was a significant decrease in the necrotic

FOCUS BOX

IVUS-VH has been used to monitor the effect of new treatments, such as statins or Lp PLA2-inhibitors, on plaque composition.

Table 3.

IVUS-based tissue characterization studies							
Yokoyama(41)	RCT	2005	atorvastatin	25	6 months	Overall plaque size and tissue characterization by IB IVUS	Atorvastatin reduced plaque size and changed plaque composition
			control	25			
Kawasaki(42)	RCT	2005	pravastatin,	17	6 months	Overall tissue characterization by IB IVUS	Statins reduced lipid without changes in plaque size
			atorvastatin	18			
			diet	17			
IBIS 2(14)	RCT	2008	darapladib	175	12 months	Necrotic core volume by IVUS VH	Darapladib significantly reduced necrotic core
			placebo	155			
Nasu(5)	Observational	2009	fluvastatin	40	12 months	Overall tissue characterization by IVUS-VH	Fluvastatin reduced plaque and fibro-fatty volume
			control	40			
Hong(6)	RCT	2009	simvastatin	50	12 months	Overall tissue characterization by IVUS-VH	Both reduced necrotic core and increased fibro-fatty volume
			rosuvastatin	50			
Toi(43)	RCT	2009	atorvastatin	80	2-3 weeks	Overall tissue characterization by IVUS-VH	Pitavastatin reduced plaque volume and fibro-fatty
			pivastatin	80			
Miyagi(44)	Observational	2009	statin (pravastatin, pitavastatin, atorvastatin, fluvastatin, simvastatin)	44	6 months	Overall tissue characterization by IB IVUS	Statins reduced lipid and increased fibrous
			non statin	56			

RCT, randomised controlled trial; PAV, percent atheroma volume; IVUS, intravascular ultrasound; IB, integrated backscatter; VH, virtual histology.

core volume ($p=0.015$) in the rosuvastatin-treated subgroup. By multiple stepwise logistic regression analysis, they showed that the only independent clinical predictor of decrease in the necrotic core volume was the baseline HDL-cholesterol level ($p=0.040$, OR: 1.044, 95% CI 1.002-1089).²³

The IBIS 2 study compared the effects of 12 months of treatment with darapladib (oral Lp-PLA2 inhibitor, 160 mg daily) or placebo in 330 patients.²⁴ Endpoints included changes in necrotic core size (IVUS-VH), and atheroma size (IVUS-grayscale). Background therapy was comparable between groups, with no difference in LDL-cholesterol at 12 months (placebo: 88 ± 34 and darapladib: 84 ± 31 mg/dL, $p=0.37$). In the placebo-treated group, however, necrotic core volume increased significantly, whereas darapladib halted this increase, resulting

in a significant treatment difference of -5.2 mm^3 ($p=0.012$). These intra-plaque compositional changes occurred without a significant treatment difference in total atheroma volume.

Despite all these studies, there is no a single report describing a clear direct association between reduction in the plaque size and/or the plaque composition with reduction in clinical events. The best attempt was a pooled analysis of 4,137 patients from 6 clinical trials that used serial IVUS: the relationship between baseline and change in percent atheroma volume (PAV) with incident major adverse cardiovascular events (MACE) was investigated. Each standard deviation increase in PAV was associated with a 1.32-fold (95% CI: 1.22 to 1.42; $p < 0.001$) greater likelihood of experiencing a MACE.²⁵

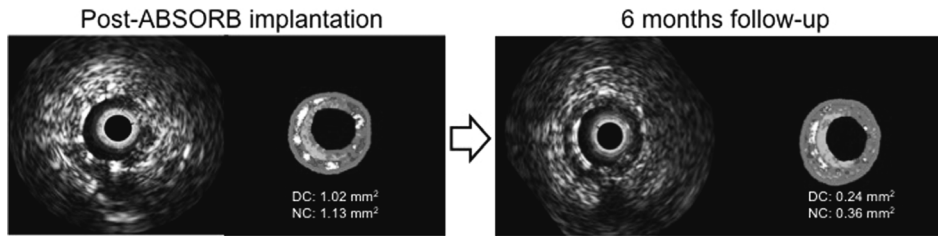


Figure 5. IVUS-VH recognizes the polymeric struts of the ABSORB scaffold as dense calcium (DC), surrounded by a read halo of necrotic core (NC). At follow-up, a reduction in DC and NC can be appreciated. In order to pick up all the struts, the lumen contour has been drawn surrounding the catheter, according to the Shin's method. See color figure on page 337

ASSESSMENT OF STENT BY IVUS-VH

Polymeric scaffolds

Kim et al. have previously shown that metallic stents eluting sirolimus and paclitaxel introduce artifacts in IVUS-VH images, that interfere with the classification of plaque behind the struts.²⁶ Normally struts of drug-eluting stents appear as dense calcium, surrounded by a red halo. Although the ABSORB scaffold is made of non-metallic materials, it is also recognized by IVUS-VH software as dense calcium and necrotic core. Moreover the presence of "pseudo" dense calcium and necrotic core could be used as quantitative surrogate for the presence of the polymeric material of the scaffold and may help to evaluate the bioresorption process during follow-up.²⁷⁻³⁰ Garcia-Garcia et al. have already shown in a sub-study of ABSORB cohort A trial that polymeric struts are identified with radiofrequency backscattering signal as calcific structures and that the ability of IVUS-VH to recognize polymeric struts is important not only to study imaging of the ABSORB post-implantation, but also to potentially follow the mechanical support or bioresorption process.²⁸ (Figure 5) The absence of validation to recognize polymeric material by VH should be, however, acknowledged.

Analysis of changes in scaffolded plaque composition

IVUS-VH can be also used to analyze the changes in composition of the plaque scaffolded by a metallic or a bioresorbable scaffold. Kubo et al., analyzing the long-term effects of DES and of BMS on coronary arterial wall morphology by IVUS-VH, have shown that DES-treated lesions had a greater frequency of unstable lesion morphometry at follow-up compared to BMS.³¹ In particular assessing the total amount of the four color-VH components including also the contribution of the stent, they found that DES-treated lesions showed at follow-up a significantly higher incidence of necrotic core abutting the lumen compared to BMS-treated lesions, although there was not a significant difference in necrotic core mean area between the two groups. This was due to a suppression of the protective neointimal hyperplasia layer in DES compared with BMS.

Aoki et al. have demonstrated in vivo that plaque volume behind the metallic stent eluting sirolimus increases slightly at 4 months follow-up and then significantly decreases at 4 years follow-up compared to post-implantation and that change in echogenicity is suggestive of a change in plaque composition.³² He also documented a significantly increase of plaque area outside metallic stent eluting paclitaxel at 6 months, with its regression at 2 years.³³ In these situations, it would be interesting

to know what type of tissue contributed to this process and, from a quantitative point, to develop a third (stent) contour in the VH software in order to characterize selectively intimal hyperplasia and peri-stent tissue. The potential lack of validation of VH in the assessment of in-stent restenosis should be, however, acknowledged.

Sarno et al. analyzing IVUS-VH plaque characterization behind the first generation ABSORB scaffold found a reduction in necrotic core component between 6-month and two years follow-up, probably related to a synergistic effect of the bioresorption process and the anti-inflammatory action of everolimus.³⁴

Nevertheless, it should be kept in mind that, since the stent's struts are recognized by IVUS-VH as dense calcium and necrotic core, careful evaluation of exclusively the plaque behind the stent should be done to avoid any misclassification of the actual tissue.^{26,29} Recently a customized software has been developed and used to introduce in a semi-automatic way a third contour behind the stent, allowing then to focus the analysis on only the plaque behind the struts.³⁵

Stent thrombosis

Another possible application of IVUS-VH for stent evaluation is about stent thrombosis mechanisms. It is known that one of the proposed pathological mechanisms of coronary stent thrombosis is stenting of necrotic core rich plaques with extensive tissue prolapse and plaque disruption in the proximity of the stented arterial segment.³⁶⁻³⁸ Thus, pre-stenting imaging using IVUS-VH can give us an insight not only into the extent of plaque, but also on the extent of necrotic core within and beyond the intended stenting segment. In this context, studying 24 patients in whom 26 stented segments using IVUS-VH were assessed, no stent thrombosis was observed, where necrotic core rich areas were left unstented.³⁸ Ramcharitar et al. presented a first clinical case of a patient with a culprit IVUS-VH

derived thin cap fibroatheroma, successfully treated with PCI, with a good 6-month angiographic follow-up.³⁹ A large trial in which patients are randomized to IVUS-VH or angiography guided optimal coronary stenting is required to draw firm conclusions.

Edge effects assessed by IVUS-VH

Based on previous pathological studies, we hypothesized that the tissue associated with increase of plaque at the edges of the paclitaxel stent is mainly fibro-fatty tissue as assessed by IVUS-VH. Fibro-fatty, in IVUS-VH, has been described as loosely packed bundles of collagen fibers with regions of lipid deposition and extracellular matrix without necrotic areas³⁷.

In the BETAX study⁴⁰, 24 patients (26 paclitaxel eluting stents) were studied. Serial expansive vascular remodeling was observed at the proximal and distal edges of the stent to accommodate fibro-fatty and fibrous tissue growth. More specifically, proximal and distal segments were divided into 5 sub-segments of 1-mm. In the first 2 sub-segments adjacent to the proximal edge of the stent, the vessel wall grew to compensate the plaque growth without affecting the lumen size. In the following 3 sub-segments, overcompensation (vessel wall increased more than plaque size) was observed. Consequently, the lumen size increased. At the distal edge, overcompensation was observed in all 5 sub-segments, followed by an increase in lumen size. In summary, proximal and distal growth patterns were characterized by an increase in fibrofatty tissue ($p < 0.001$ and $p < 0.001$, respectively), decrease in necrotic core ($p = 0.014$ and $p < 0.001$, respectively), and decrease in dense calcium content ($p < 0.001$ and $p < 0.001$ respectively).

Combined assessment of coronary atherosclerosis by using VH and other imaging modalities

In the future, integration of multiple image technologies in a single catheter is likely to provide a

FOCUS BOX

1. IVUS-VH can be applied for the evaluation of metallic/polymeric scaffolds. In case of polymeric scaffolds, it can be used to monitor the bioresorption or the changes in composition of the plaque behind.
2. For the metallic stents, IVUS-VH can study not only the compositional changes of the plaque scaffolded, but also the geographical miss (necrotic core remained uncovered) that is the basis for stent thrombosis or edge effect.

more comprehensive assessment of the coronary vasculature. The combined use of IVUS-VH analysis and OCT seems to improve the accuracy for TCFA detection.^{41,42} IVUS-VH has a limited axial resolution (100-200 μm) not allowing a precise measurement of the fibrous thin cap; on the contrary OCT is a high-resolution imaging technique (10-20 μm) that can be used in the assessment of microstructure, but only using OCT in plaque-type characterization can be a source of misclassification. The OCT signals has in fact a low penetration, limited to 1-2 mm, and could not detect lipid pools or calcium behind thick fibrous caps, thus producing inaccurate detection of signal-poor areas.⁴³ The combined use of IVUS-VH analysis and OCT seems to improve the accuracy for TCFA detection.^{41,42} Recently, the combined use of IVUS-VH and an index of physiological significance of a coronary lesion, such as fractional flow reserve (FFR) has been also explored: no differences were found in terms of plaque composition and virtual histology plaque types in coronary lesions with FFR more or less than 0.80.⁴⁴ (**Figure 6**)

IVUS-VH has been compared with near infrared spectroscopy (NIRS) for the detection of lipid/

necrotic core rich-plaques: although large plaques were more often associated with either elevated VH-NC and NIRS-lipid core, the correlation between the detection of lipid core by NIRS and necrotic core by VH was weak (**figure 7**).⁴⁵

Furthermore, several lines of investigation have validated plaque imaging by coronary computed tomography angiography against other imaging modalities, such as IVUS-VH or optical coherence tomography.⁴⁶ In particular low-density non-calcified plaques correlated with the sum of necrotic core and fibrofatty tissue by IVUS-VH.⁴⁷

PERSONAL PERSPECTIVE

During the last 10 years, IVUS-VH has been widely applied to study the natural history of coronary plaques "in vivo" and to assess the efficacy of new drug or new devices. A lot of achievements have been reached: 1) VH-derived TCFA were strongly correlated to future coronary events; 2) VH showed the pharmacological or mechanical treatment of coronary atherosclerosis may positively modify

FOCUS BOX

A combined approach between IVUS-VH and other imaging modalities should be considered for a complete evaluation of coronary plaque.

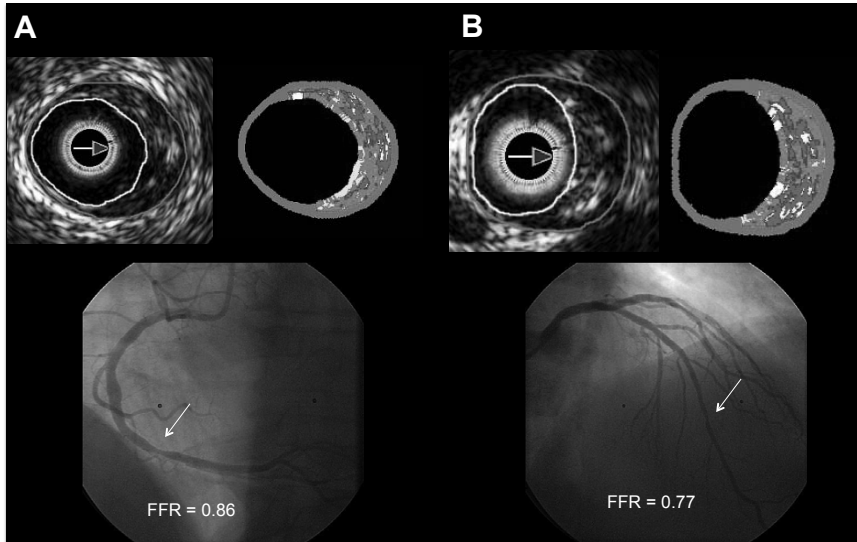


Figure 6. Example of two fibroatheromas at the level of two different lesions (white arrows) with a FFR >0.80 (Panel A) and ≤ 0.80 (Panel B). Red and yellow contours in the IVUS images indicate vessel and lumen contours, respectively. (adapted by Brugaletta et al. Int J Cardiovasc Imaging 2011 Febr 19, epub ahead of print)

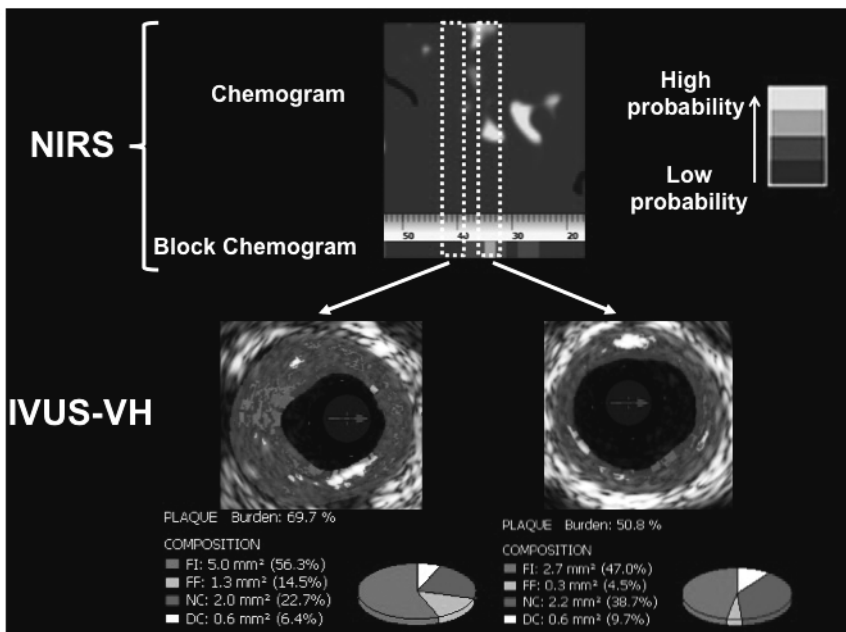


Figure 7. Near infra-red spectroscopy displays the probability of lipid core plaque in a false color scale from red (low probability) to yellow (high probability). In this example, two VH-necrotic core rich plaques are displayed with two different colors on the NIRS output. See color figure on page 338

plaque composition; 3) in addition it can be used to explore causes of DES pitfalls and it can be applied in the field of the new polymeric intracoronary devices.

Despite the clear potential of the technology in these areas, its role in daily clinical practice has still to be defined. It is, in fact, unknown if we should

screen for VH-TCFA presence and if we should treat them in order to prevent future adverse events. In case of treatment, efficacious pharmacological or mechanical treatment would be needed. Randomized trials to address these issues would be difficult and costly.

REFERENCES

1. Garcia-Garcia HM, Costa MA, Serruys PW. Imaging of coronary atherosclerosis: Intravascular ultrasound. *Eur Heart J*. 2010;31:2456-2469
2. Mintz GS, Nissen SE, Anderson WD, Bailey SR, Erbel R, Fitzgerald PJ, Pinto FJ, Rosenfield K, Siegel RJ, Tuzcu EM, Yock PG. American college of cardiology clinical expert consensus document on standards for acquisition, measurement and reporting of intravascular ultrasound studies (ivus). A report of the american college of cardiology task force on clinical expert consensus documents. *J Am Coll Cardiol*. 2001;37:1478-1492
3. Garcia-Garcia HM, Costa MA, Serruys PW. Imaging of coronary atherosclerosis: Intravascular ultrasound. *Eur Heart J*. 2010;31:2456-2469
4. Garcia-Garcia HM, Gogas BD, Serruys PW, Bruining N. I.vus-based imaging modalities for tissue characterization: Similarities and differences. *Int J Cardiovasc Imaging*. 2011;27:215-224
5. Nair A, Kuban BD, Tuzcu EM, Schoenhagen P, Nissen SE, Vince DG. Coronary plaque classification with intravascular ultrasound radiofrequency data analysis. *Circulation*. 2002;106:2200-2206
6. Nair A, Margolis MP, Kuban BD, Vince DG. Automated coronary plaque characterisation with intravascular ultrasound backscatter: Ex vivo validation. *EuroIntervention*. 2007;3:113-120
7. Garcia-Garcia HM, Mintz GS, Lerman A, Vince DG, Margolis MP, van Es GA, Morel MA, Nair A, Virmani R, Burke AP, Stone GW, Serruys PW. Tissue characterisation using intravascular radiofrequency data analysis: Recommendations for acquisition, analysis, interpretation and reporting. *EuroIntervention*. 2009;5:177-189
8. Sathyanarayana S, Carlier S, Li W, Thomas L. Characterisation of atherosclerotic plaque by spectral similarity of radiofrequency intravascular ultrasound signals. *EuroIntervention*. 2009;5:133-139
9. Shin ES, Garcia-Garcia HM, Ligthart JM, Witberg K, Schultz C, van der Steen AF, Serruys PW. In vivo findings of tissue characteristics using imap ivus and virtual histology ivus. *EuroIntervention*. 2011;6:1017-1019
10. Virmani R, Burke AP, Farb A, Kolodgie FD. Pathology of the vulnerable plaque. *J Am Coll Cardiol*. 2006;47:C13-18
11. Schaar JA, Muller JE, Falk E, Virmani R, Fuster V, Serruys PW, Colombo A, Stefanadis C, Ward Casscells S, Moreno PR, Maseri A, van der Steen AF. Terminology for high-risk and vulnerable coronary artery plaques. Report of a meeting on the vulnerable plaque, june 17 and 18, 2003, santorini, greece. *Eur Heart J*. 2004;25:1077-1082
12. Cheruvu PK, Finn AV, Gardner C, Caplan J, Goldstein J, Stone GW, Virmani R, Muller JE. Frequency and distribution of thin-cap fibro-atheroma and ruptured plaques in human coronary arteries: A pathologic study. *J Am Coll Cardiol*. 2007;50:940-949
13. Cunningham KS, Gotlieb AI. The role of shear stress in the pathogenesis of atherosclerosis. *Lab Invest*. 2005;85:9-23
14. Virmani R, Kolodgie FD, Burke AP, Farb A, Schwartz SM. Lessons from sudden coronary death: A comprehensive morphological classification scheme for atherosclerotic lesions. *Arterioscler Thromb Vasc Biol*. 2000;20:1262-1275
15. Ross R. Atherosclerosis--an inflammatory disease. *N Engl J Med*. 1999;340:115-126
16. Garcia-Garcia HM, Goedhart D, Schuurbiers JC, Kukreja N, Tanimoto S, Daemen J, Morel MA, Bressers M, van Es GA, Wentzel J, Gijssen F, van der Steen AF, Serruys PW. Virtual histology and remodeling index allow in vivo identification of allegedly high risk coronary plaques in patients with acute coronary syndromes: A three vessel intravascular ultrasound radiofrequency data analysis. *EuroIntervention*. 2006;2:338-344
17. Hong MK, Mintz GS, Lee CW, Lee JW, Park JH, Park DW, Lee SW, Kim YH, Cheong SS, Kim JJ, Park SW, Park SJ. A three-vessel virtual histology intravascular ultrasound analysis of frequency and distribution of thin-cap fibroatheromas in patients with acute coronary syndrome

- or stable angina pectoris. *Am J Cardiol.* 2008;101:568-572
18. Stone GW, Maehara A, Lansky AJ, de Bruyne B, Cristea E, Mintz GS, Mehran R, McPherson J, Farhat N, Marso SP, Parise H, Templin B, White R, Zhang Z, Serruys PW. A prospective natural-history study of coronary atherosclerosis. *N Engl J Med.* 2011;364:226-235
 19. Calvert PA, Obaid DR, O'Sullivan M, Shapiro LM, McNab D, Densem CG, Schofield PM, Braganza D, Clarke SC, Ray KK, West NE, Bennett MR. Association between ivus findings and adverse outcomes in patients with coronary artery disease the viva (vh-ivus in vulnerable atherosclerosis) study. *JACC. Cardiovascular imaging.* 2011;4:894-901
 20. Kubo T, Maehara A, Mintz GS, Doi H, Tsujita K, Choi SY, Katoh O, Nasu K, Koenig A, Pieper M, Rogers JH, Wijns W, Bose D, Margolis MP, Moses JW, Stone GW, Leon MB. The dynamic nature of coronary artery lesion morphology assessed by serial virtual histology intravascular ultrasound tissue characterization. *J Am Coll Cardiol.* 55:1590-1597
 21. Diletti R, Garcia-Garcia HM, Gomez-Lara J, Brugaletta S, Wykrzykowska JJ, van Ditzhuijzen N, van Geuns RJ, Regar E, Ambrosio G, Serruys PW. Assessment of coronary atherosclerosis progression and regression at bifurcations using combined ivus and oct. *JACC. Cardiovascular imaging.* 2011;4:774-780
 22. Nasu K, Tsuchikane E, Katoh O, Tanaka N, Kimura M, Ehara M, Kinoshita Y, Matsubara T, Matsuo H, Asakura K, Asakura Y, Terashima M, Takayama T, Honye J, Hirayama A, Saito S, Suzuki T. Effect of fluvastatin on progression of coronary atherosclerotic plaque evaluated by virtual histology intravascular ultrasound. *JACC Cardiovasc Interv.* 2009;2:689-696
 23. Hong MK, Park DW, Lee CW, Lee SW, Kim YH, Kang DH, Song JK, Kim JJ, Park SW, Park SJ. Effects of statin treatments on coronary plaques assessed by volumetric virtual histology intravascular ultrasound analysis. *JACC Cardiovasc Interv.* 2009;2:679-688
 24. Serruys PW, Garcia-Garcia HM, Buszman P, Erne P, Verheye S, Aschermann M, Duckers H, Bleie O, Dudek D, Botker HE, von Birgelen C, D'Amico D, Hutchinson T, Zambanini A, Mastik F, van Es GA, van der Steen AF, Vince DG, Ganz P, Hamm CW, Wijns W, Zaleski A. Effects of the direct lipoprotein-associated phospholipase a(2) inhibitor darapladib on human coronary atherosclerotic plaque. *Circulation.* 2008;118:1172-1182
 25. Nicholls SJ, Hsu A, Wolski K, Hu B, Bayturan O, Lavoie A, Uno K, Tuzcu EM, Nissen SE. Intravascular ultrasound-derived measures of coronary atherosclerotic plaque burden and clinical outcome. *J Am Coll Cardiol.* 2010;55:2399-2407
 26. Kim SW, Mintz GS, Hong YJ, Pakala R, Park KS, Pichard AD, Satler LF, Kent KM, Suddath WO, Waksman R, Weissman NJ. The virtual histology intravascular ultrasound appearance of newly placed drug-eluting stents. *Am J Cardiol.* 2008;102:1182-1186
 27. Serruys PW, Ormiston JA, Onuma Y, Regar E, Gonzalo N, Garcia-Garcia HM, Nieman K, Bruining N, Dorange C, Miquel-Hebert K, Veldhof S, Webster M, Thuesen L, Dudek D. A bioabsorbable everolimus-eluting coronary stent system (absorb): 2-year outcomes and results from multiple imaging methods. *Lancet.* 2009;373:897-910
 28. Garcia-Garcia HM, Gonzalo N, Pawar R, Kukreja N, Dudek D, Thuesen L, Ormiston JA, Regar E, Serruys PW. Assessment of the absorption process following bioabsorbable everolimus-eluting stent implantation: Temporal changes in strain values and tissue composition using intravascular ultrasound radiofrequency data analysis. A substudy of the absorb clinical trial. *EuroIntervention.* 2009;4:443-448
 29. Sarno G, Onuma Y, Garcia Garcia HM, Garg S, Regar E, Thuesen L, Dudek D, Veldhof S, Dorange C, Ormiston JA, Serruys PW. Ivus radiofrequency analysis in the evaluation of the polymeric struts of the bioabsorbable everolimus-eluting device during the bioabsorption process. *Catheter Cardiovasc Interv.* 2010;75:914-918

30. Ormiston JA, Serruys PW, Regar E, Dudek D, Thuesen L, Webster MW, Onuma Y, Garcia-Garcia HM, McGreevy R, Veldhof S. A bioabsorbable everolimus-eluting coronary stent system for patients with single de-novo coronary artery lesions (absorb): A prospective open-label trial. *Lancet*. 2008;371:899-907
31. Kubo T, Maehara A, Mintz GS, Garcia-Garcia HM, Serruys PW, Suzuki T, Klauss V, Sumitsuji S, Lerman A, Marso SP, Margolis MP, Margolis JR, Foster MC, De Bruyne B, Leon MB, Stone GW. Analysis of the long-term effects of drug-eluting stents on coronary arterial wall morphology as assessed by virtual histology intravascular ultrasound. *Am Heart J*. 159:271-277
32. Aoki J, Abizaid AC, Serruys PW, Ong AT, Boersma E, Sousa JE, Bruining N. Evaluation of four-year coronary artery response after sirolimus-eluting stent implantation using serial quantitative intravascular ultrasound and computer-assisted grayscale value analysis for plaque composition in event-free patients. *J Am Coll Cardiol*. 2005;46:1670-1676
33. Aoki J, Colombo A, Dudek D, Banning AP, Drzewiecki J, Zmudka K, Schiele F, Russell ME, Koglin J, Serruys PW. Persistent remodeling and neointimal suppression 2 years after polymer-based, paclitaxel-eluting stent implantation: Insights from serial intravascular ultrasound analysis in the taxus ii study. *Circulation*. 2005;112:3876-3883
34. Sarno G, Onuma Y, Garcia Garcia HM, Garg S, Regar E, Thuesen L, Dudek D, Veldhof S, Dorange C, Ormiston JA, Serruys PW. Ivus radiofrequency analysis in the evaluation of the polymeric struts of the bioabsorbable everolimus-eluting device during the bioabsorption process. *Catheter Cardiovasc Interv*. 75:914-918
35. Brugaletta S, Garcia-Garcia HM, Garg S, Gomez-Lara J, Diletti R, Onuma Y, van Geuns RJ, McClean D, Dudek D, Thuesen L, Chevalier B, Windecker S, Whitbourn R, Dorange C, Miquel-Hebert K, Sudhir K, Ormiston JA, Serruys PW. Temporal changes of coronary artery plaque located behind the struts of the everolimus eluting bioresorbable vascular scaffold. *Int J Cardiovasc Imaging*. 2010;Epub ahead of print
36. Farb A, Burke AP, Kolodgie FD, Virmani R. Pathological mechanisms of fatal late coronary stent thrombosis in humans. *Circulation*. 2003;108:1701-1706
37. Nair A MP, Kuban BD, Vince DG. Automated coronary plaque characterization with intravascular ultrasound backscatter: Ex vivo validation. *Eurointervention*. 2007;3:113-130
38. Garcia-Garcia HM, Goedhart D, Serruys PW. Relation of plaque size to necrotic core in the three major coronary arteries in patients with acute coronary syndrome as determined by intravascular ultrasonic imaging radiofrequency. *Am J Cardiol*. 2007;99:790-792
39. Ramcharitar S, Gonzalo N, van Geuns RJ, Garcia-Garcia HM, Wykrzykowska JJ, Ligthart JM, Regar E, Serruys PW. First case of stenting of a vulnerable plaque in the secret trial-the dawn of a new era? *Nat Rev Cardiol*. 2009;6:374-378
40. Garcia-Garcia HM, Gonzalo N, Tanimoto S, Meliga E, de Jaegere P, Serruys PW. Characterization of edge effects with paclitaxel-eluting stents using serial intravascular ultrasound radiofrequency data analysis: The betax (beside taxus) study. *Rev Esp Cardiol*. 2008;61:1013-1019
41. Sawada T, Shite J, Garcia-Garcia HM, Shinke T, Watanabe S, Otake H, Matsumoto D, Tanino Y, Ogasawara D, Kawamori H, Kato H, Miyoshi N, Yokoyama M, Serruys PW, Hirata K. Feasibility of combined use of intravascular ultrasound radiofrequency data analysis and optical coherence tomography for detecting thin-cap fibroatheroma. *Eur Heart J*. 2008;29:1136-1146
42. Gonzalo N, Garcia-Garcia HM, Regar E, Barlis P, Wentzel J, Onuma Y, Ligthart J, Serruys PW. In vivo assessment of high-risk coronary plaques at bifurcations with combined intravascular ultrasound and optical coherence tomography. *JACC Cardiovasc Imaging*. 2009;2:473-482
43. Manfrini O, Mont E, Leone O, Arbustini E, Eusebi V, Virmani R, Bugiardini R. Sources of error

- and interpretation of plaque morphology by optical coherence tomography. *Am J Cardiol.* 2006;98:156-159
44. Brugaletta S, Garcia-Garcia HM, Shen ZJ, Gomez-Lara J, Diletti R, Sarno G, Gonzalo N, Wijns W, de Bruyne B, Alfonso F, Serruys PW. Morphology of coronary artery lesions assessed by virtual histology intravascular ultrasound tissue characterization and fractional flow reserve. *Int J Cardiovasc Imaging.* 2011
45. Brugaletta S, Garcia-Garcia HM, Serruys PW, de Boer S, Ligthart J, Gomez-Lara J, Witberg K, Diletti R, Wykrzykowska J, van Geuns RJ, Schultz C, Regar E, Duckers HJ, van Mieghem N, de Jaegere P, Madden SP, Muller JE, van der Steen AF, van der Giessen WJ, Boersma E. NIRS and iMap for characterization of atherosclerosis in patients undergoing coronary angiography. *J Am Coll Cardiol Imaging.* 2011;4:647-655
46. Voros S, Rinehart S, Qian Z, Joshi P, Vazquez G, Fischer C, Belur P, Hulten E, Villines TC. Coronary atherosclerosis imaging by coronary ct angiography: Current status, correlation with intravascular interrogation and meta-analysis. *JACC. Cardiovascular imaging.* 2011;4:537-548
47. Voros S, Rinehart S, Qian Z, Vazquez G, Anderson H, Murrieta L, Wilmer C, Carlson H, Taylor K, Ballard W, Karpaliotis D, Kalynych A, Brown C, 3rd. Prospective validation of standardized, 3-dimensional, quantitative coronary computed tomographic plaque measurements using radiofrequency backscatter intravascular ultrasound as reference standard in intermediate coronary arterial lesions: Results from the atlanta (assessment of tissue characteristics, lesion morphology, and hemodynamics by angiography with fractional flow reserve, intravascular ultrasound and virtual histology, and noninvasive computed tomography in atherosclerotic plaques) i study. *JACC. Cardiovascular interventions.* 2011;4:198-208

1.2

Reproducibility of intravascular ultrasound iMAP for radiofrequency data analysis: implications for design of longitudinal studies

Jung Ho Heo*; Salvatore Brugaletta*; Hector M. Garcia-Garcia; Josep Gomez-Lara; Jurgen M. R. Ligthart; Karen Witberg; Michael Magro; Eun-Seok Shin; Patrick W. Serruys.

* These authors have equally contributed to this manuscript.

Catheterization Cardiovascular Intervention 2012, In press

ABSTRACT

Background: iMAP is a new intravascular ultrasound (IVUS) derived technique for tissue characterization using spectral analysis. Since there is a need for reproducibility data to design longitudinal studies, we sought to assess the in vivo reproducibility of this imaging technique.

Methods: iMAP (40 MHz, Boston Scientific Corporation) was performed in patients referred for elective percutaneous intervention and in whom a non-intervened vessel was judged suitable for a safe IVUS analysis. Overall 20 patients with 20 non angiographically significant lesions were assessed by 2 independent observers. Five out of these 20 patients received an additional iMAP analysis using a new IVUS catheter and using the same catheter after its dis-engagement and re-engagement.

Results: The inter-observer relative difference in plaque area was 2.5%. Limits of agreement for lumen, vessel and plaque area measurements were 1.62, -2.47 mm²; 2.09, -3.71 mm²; 2.80, -3.72 mm²; respectively. Limits of agreement for fibrotic, lipidic, necrotic and calcified measurements were 1.32, -1.44 mm²; 0.24, -0.36 mm²; 1.50, -2.26 mm²; 0.09, -0.11 mm²; respectively. The inter-catheter and intra-catheter relative difference in plaque area were 0.9% and 4.1%, respectively. Although the variability for compositional measurements increased using two different catheters or using the same catheter twice, the variability for compositional measurements keeps always below 10%.

Conclusions: Our analysis demonstrates that the geometrical and compositional iMAP analysis is acceptably reproducible.

INTRODUCTION

In interventional cardiology practice, intravascular ultrasound (IVUS) has been used for quantification of the extent, severity, distribution and morphology of coronary atherosclerosis.¹ In addition it has also been used to evaluate the temporal effect of novel therapies on plaque progression.²⁻⁵

Over the last years, *in vivo* ultrasound tissue characterization interpreting the backscattering signal has been developed in order to provide some important additional information on coronary atherosclerosis.⁶ Necrotic core detected by IVUS-virtual histology (VH) has been extensively studied⁷ and related to clinical characteristics⁸ and cardiovascular risk score⁹ and associated with high risk of events in the PROSPECT trial.¹⁰ IVUS-VH has also been used for testing the efficacy of novel therapies.¹¹ The reproducibility of this technique was shown to be acceptable for use in longitudinal studies.¹²

Recently, a new intravascular ultrasound-based catheter (iMAP, Boston Scientific Corporation) for tissue interpretation has been developed, using a pattern recognition algorithm on the spectra obtained from a fast fourier transformation and histology-derived database.¹³

We sought to study the inter- and intra-observer, intra-catheter and inter-catheter variabilities of iMAP measurements at a single time-point, simulating a longitudinal study. Particularly, we focused on the assessment of the variability of the necrotic core because it is one of the most clinically relevant parameters.

METHODS

Patient population

This was a prospective, investigators-driven study that sought to explore the *in vivo* reproducibility of spectral analysis of iMAP-IVUS (Boston Scientific Corporation). The study population consisted of

consecutive patients, who were referred for elective percutaneous coronary interventions and in whom a non-intervened vessels was judged suitable for IVUS analysis of a vessel segment of at least 30 mm. Two institutions participated in this study, Erasmus Medical Center in Rotterdam, the Netherlands and Ulsan University Hospital, Ulsan, Korea.

Exclusion criteria included the presence of severe calcification and/or vessel tortuosity and patient's hemodynamic instability.

iMap-IVUS catheter and acquisition

iMap IVUS uses a 40 MHz single rotational transducer on a drive shaft and can acquire radiofrequency data continuously, when connected to Boston Scientific's iLab® Ultrasound Imaging System. As it uses a 40Mhz transducer, iMap-IVUS has high axial resolution but displays specific artifacts such as non-uniform rotational distortion because it is a rotational catheter. iMap uses a pattern recognition algorithm on a spectra obtained from a fast fourier transformation and a histology-derived database.¹³ Using a color-code, iMap depicts fibrotic tissue as light green, lipidic tissue as yellow, necrotic tissue as pink and calcified tissue as blue.¹⁴

The IVUS catheters used were commercially available mechanical array catheters (Boston Scientific Corporation). The catheter probe, after intracoronary administration of isosorbide di-nitrate, was advanced at least 10 mm distal to a clearly visible side branch and angiographic cine runs, before and during contrast injection, were performed to define the position of the IVUS catheter before the pullback was started. The catheter was withdrawn at a continuous automated pullback of 0.5 mm/sec. Subsequently, some of the patients included, underwent the same procedure using a new catheter (iMAP 40MHz, Boston Scientific Corporation) or using the same catheter, after its dis-engagement and re-engagement, with the same side branches as landmarks. Data acquired were stored in a DVD for offline analysis.

iMap-IVUS analysis

A region of interest (ROI) was identified between one proximal and one distal side branch. Contour detection of the lumen and the media-adventitia interface was performed by two independent experienced IVUS analysts, using a dedicated software (QIvus, Medis, Leiden, The Netherlands). One of these two IVUS analyst re-analyzed the same cases at time interval of 6 weeks, leading to the possibility of multiple comparisons: inter-observer variability (observer 1 and 2); intra-observer variability (2 times observer 1); inter catheter variability [observer 1 (catheter 1 and catheter 2)] and intra-catheter variability [observer 1 (same catheter with two pullbacks)]. (Figure 1) Intra-catheter, inter-catheter and inter-observer agreement were calculated per ROI.

As the software used for the analysis allows the analyst to mask the shadow of the guidewire, usually detected as necrotic core, and to detect as black the signal underneath calcium, we also evaluated the variability introduced by these software features in the compositional measurements within a pullback, using the same catheter with the same geometrical contours.

The contours of the external elastic membrane (EEM) and the lumen-intima interface enclosed an area that was defined as the coronary plaque plus media area. Geometrical data were obtained

for each cross-sectional area and an average was calculated for each ROI. Compositional data were obtained for each ROI as volume and calculated for each cross-sectional area as percentage.

Statistical analysis

Discrete variables are presented as counts and percentages. Continuous variables are presented as mean \pm standard deviation (SD). Correlation test and using Bland-Altman plots were performed.¹⁶ Limits of agreement were determined by adding two standard deviations to the mean difference for the upper limit and by subtracting two standard deviations from the mean difference for the lower limit. A two-sided p value of less than 0.05 indicated statistical significance. Statistical analysis was performed with SPSS 16.0 software (SPSS Inc., Chicago IL, USA).

RESULTS

Patient population

Twenty consecutive patients with 20 non-significant lesions were included in the study. Baseline characteristics of the patients are shown in table 1. There were no peri-procedural complications. The length of the ROI was 32.9 ± 11.5 mm.

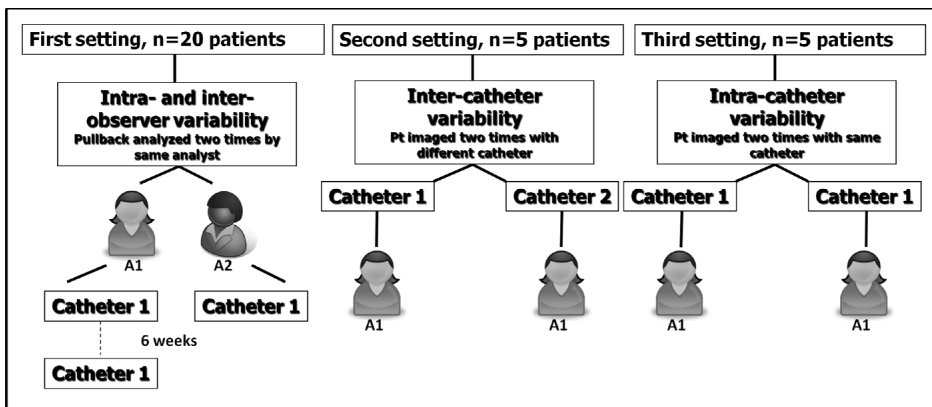


Figure 1. Study design flow-chart

Table 1. Baseline clinical characteristics (n=20)

Clinical characteristics	Patients (n=20), n (%)
Age (years \pm SD)	66.1 \pm 11.1
Male sex	16 (80)
Hypertension	14 (70)
Diabetes Mellitus	5 (25)
Smoking	3 (15)
Family history of coronary disease	8 (40)
Hypercholesterolemia	15 (75)
Lipid lowering agents	14 (70)
Clinical presentation	5 (25)
Stable angina	15 (75)
ACS	5 (25)
Study vessel	
Left anterior descending	15 (75)
Left circumflex artery	2 (10)
Right coronary artery	3 (15)

Inter- and intra-observer agreement (table 2 and 3)

For the assessment of the inter- and intra-observer agreement, a comparison between the same matched ROI analyzed by the two independent analysts or by the same analysis was done. The two datasets were merged resulting in a paired inter- and intra-observer agreement evaluation of 7832 frames.

The relative inter-observer differences regarding geometrical measurements were acceptable. Narrow limits of agreement were found between observers for geometrical (limits of agreement for lumen, vessel and plaque area measurements of 1.62, -2.47 mm²; 2.09, -3.71 mm²; 2.80, -3.72 mm²; respectively). With regards to the compositional measurements, the largest relative difference was found in necrotic tissue measurement, limits of agreement for fibrotic, lipidic, necrotic and calcified measurements of 1.32, -1.44 mm²; 0.24, -0.36 mm²; 1.50, -2.26 mm²; 0.09, -0.11 mm²; respectively. (**Figure 2 and 3**) In particular calcified volumes showed the highest agreement within the compositional measurements.

The relative intra-observer differences regarding geometrical and compositional measurements

were better than the inter-observer differences. In particular, the improvement in geometrical measurement difference resulted in a reduced difference in necrotic core detection. (table 3).

Inter- and intra-catheter agreement (table 4 and 5)

For the assessment of the inter-catheter agreement, a comparison between the same ROI acquired with two different catheters and analyzed by one observer was done. For the assessment of the intra-catheter agreement, a comparison between the same ROI acquired with the same catheter and analyzed by one observer was done. The relative inter-catheter differences regarding geometrical measurements were negligible in both analyses and better than the inter-observer differences, as only one observer analyzed these data. With regards to the compositional measurements, the largest relative difference was found either in necrotic or calcific tissues measurement. (**Figure 4**)

Variability according to various tool of the analysis software (table 6)

Using the guidewire mask and the black pixel classification features of the software, the variability in detecting the various compositional components

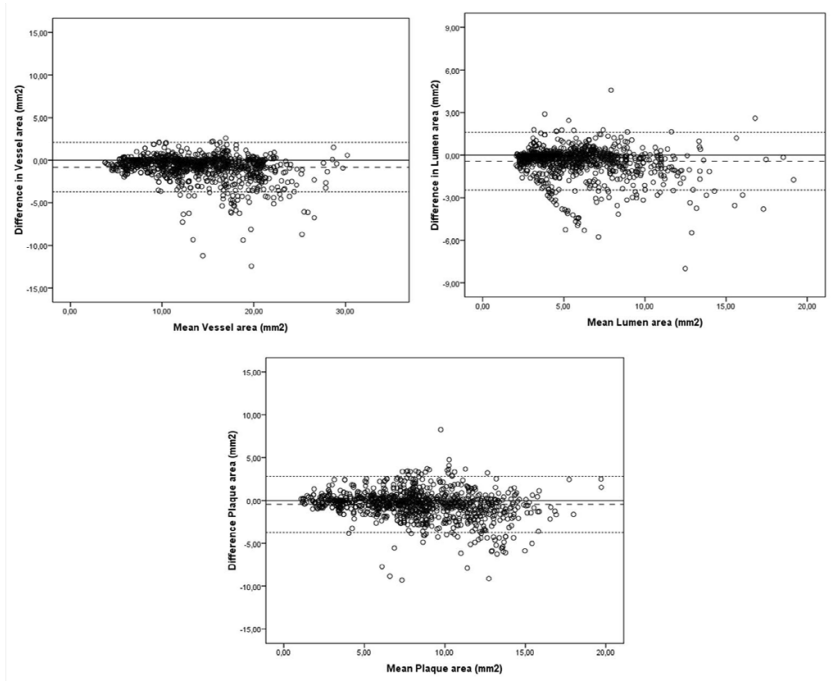


Figure 2. Bland-Altman depicting the inter-observer agreement for geometrical measurement (n=20).

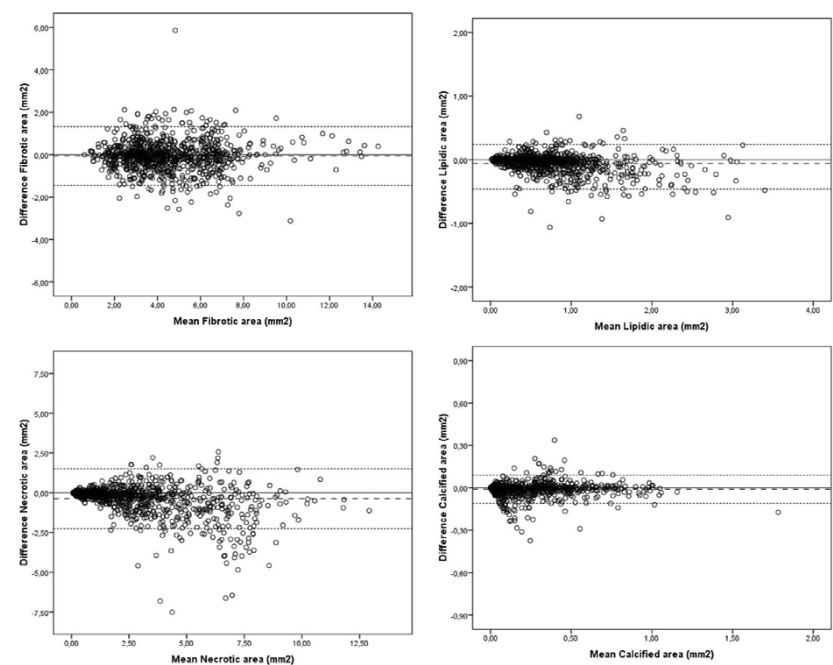


Figure 3. Bland-Altman plots depicting the inter-observer agreement for compositional measurement (n=20).

Table 2. Geometrical and compositional measurement of matched ROI between different observers (n=20)

	Observer 1	Observer 2	Absolute Δ	Relative Δ (%)
Geometrical data				
Lumen CSA (mm ²)	5.94±1.90	6.10±1.93	0.15±0.19	2.5
Lumen volume (mm ³)	191.47±89.41	195.82±93.11	4.34±6.28	1.7
Lumen max diameter (mm)	3.49±0.63	3.58±0.76	0.08±0.20	1.4
Lumen min diameter (mm)	1.92±0.32	2.01±0.27	0.09±0.11	4.6
Lumen mean diameter (mm)	2.65±0.41	2.72±0.43	0.07±0.06	2.4
Vessel CSA (mm ²)	15.18±4.37	15.15±4.35	0.03±0.24	0.2
Vessel volume (mm ³)	486.91±206.69	486.26±200.63	0.65±10.09	0.1
Vessel max diameter (mm)	4.94±0.65	5.11±0.67	0.17±0.24	3.1
Vessel min diameter (mm)	3.48±0.84	3.61±0.85	0.13±0.15	3.5
Vessel mean diameter (mm)	4.20±0.61	4.33±0.65	0.13±0.10	2.9
Plaque CSA (mm ²)	9.23±2.83	9.05±2.83	0.15±0.19	2.5
Plaque volume (mm ³)	295.43±122.77	290.44±115.62	4.99±13.75	1.4
Plaque burden (%)	60.80±5.80	59.63±6.04	1.16±1.14	1.9
Compositional data				
Fibrotic volume (mm ³)	151.91±62.50	151.32±60.61	0.60±6.90	0.2
Fibrotic area (mm ²)	4.59±1.84	4.61±1.89	0.01±0.20	0.1
Fibrotic tissue (%)	53.13±15.79	53.66±15.61	0.53±1.38	1.2
Lipidic volume (mm ³)	26.14±17.58	25.84±16.19	0.30±2.03	2.0
Lipidic area (mm ²)	0.78±0.49	0.79±0.53	0.01±0.06	0.3
Lipidic tissue (%)	8.46±2.10	8.58±2.13	0.11±0.34	0.3
Necrotic volume (mm ³)	112.09±81.60	107.49±74.57	4.60±10.20	10.2
Necrotic area (mm ²)	3.26±2.26	3.40±2.48	0.14±0.31	3.5
Necrotic tissue (%)	35.14±14.02	35.14±13.58	0.70±1.35	1.9
Calcific volume (mm ³)	7.33±4.16	7.40±4.34	0.07±0.48	0.4
Calcific area (mm ²)	0.22±0.13	0.22±0.12	0.01±0.01	0.7
Calcific tissue (%)	2.58±1.30	2.63±1.31	0.04±0.15	0.7

increases within the same pullback. In particular the relative difference in detecting necrotic core was shown to be the highest.

DISCUSSION

The main findings of the present study are: 1) iMAP geometrical measurements have an acceptable reproducibility, while compositional measurements showed lower reproducibility results; 2) in particular, necrotic core tissue had the worst reproducibility in general, while calcified tissue had acceptable reproducibility in the inter-observer setting, but high variability in the inter- and intra-catheter variability. In addition our study has the unique

characteristic to have used two iMAP-IVUS catheters and a same iMAP-IVUS catheter twice for the evaluation of a same ROI, thus simulating a scenario of a longitudinal study.

Compositional measurements, in particular necrotic tissue, have a high variability depending on the geometrical measurements. This was an expected result, which confirms our previous findings in studying the reproducibility of the other ultrasound-based tissue technique so far available (IVUS-VH).¹² Equal to our previous report on IVUS-VH technique, we found that inter-observer and inter-catheter differences are at highest 10%, highly correlated and with a good agreement. Of note is that necrotic tissue showed the largest variability in the various analyses performed. This finding has an

Table 3. Geometrical and compositional measurement of matched ROI between the same observer (n=20)

	Observer 1 (1 st time)	Observer 1 (2 nd time)	Absolute Δ	Relative Δ (%)
Geometrical data				
Lumen CSA (mm ²)	5.94±1.90	5.93±1.89	0.01±0.13	0.03
Lumen volume (mm ³)	191.47±89.41	189.46±88.83	2.02±6.48	1.4
Lumen max diameter (mm)	3.49±0.63	3.47±0.58	0.02±0.05	0.04
Lumen min diameter (mm)	1.92±0.32	1.89±0.25	0.03±0.07	0.1
Lumen mean diameter (mm)	2.65±0.41	2.68±0.43	0.03±0.02	0.1
Vessel CSA (mm ²)	15.18±4.37	15.30±4.40	0.12±0.26	0.7
Vessel volume (mm ³)	486.91±206.69	489.47±208.54	2.57±9.71	0.6
Vessel max diameter (mm)	4.94±0.65	4.90±0.58	0.04±0.27	0.4
Vessel min diameter (mm)	3.48±0.84	3.38±0.71	0.10±0.13	0.6
Vessel mean diameter (mm)	4.20±0.61	4.35±0.65	0.15±0.04	0.6
Plaque CSA (mm ²)	9.23±2.83	9.37±2.82	0.13±0.29	1.6
Plaque volume (mm ³)	295.43±122.77	300.01±124.71	4.58±7.32	1.9
Plaque burden (%)	60.80±5.80	61.21±5.05	0.41±1.14	0.8
Compositional data				
Fibrotic volume (mm ³)	151.91±62.50	153.96±63.36	2.05±4.72	1.5
Fibrotic area (mm ²)	5.11±2.13	5.19±2.17	0.08±0.15	1.6
Fibrotic tissue (%)	53.13±15.79	53.04±15.77	0.09±0.95	0.1
Lipidic volume (mm ³)	26.14±17.58	26.45±17.79	0.31±0.81	1.5
Lipidic area (mm ²)	0.88±0.59	0.89±0.60	0.01±0.02	1.6
Lipidic tissue (%)	8.46±2.10	8.45±2.09	0.01±0.09	0.1
Necrotic volume (mm ³)	112.09±81.60	113.46±81.58	1.37±4.03	2.1
Necrotic area (mm ²)	3.77±2.76	3.83±2.77	0.05±0.13	1.9
Necrotic tissue (%)	35.14±14.02	35.94±13.94	0.11±0.84	0.4
Calcific volume (mm ³)	7.33±4.16	7.44±4.29	0.10±0.52	0.7
Calcific area (mm ²)	0.24±0.14	0.25±0.14	0.01±0.01	0.8
Calcific tissue (%)	2.58±1.30	2.57±1.32	0.01±0.17	1.1

extreme importance in the design of longitudinal studies, as necrotic tissue is the most relevant and studied component of coronary plaques¹⁰ and its variability between two observers and/or two different iMAP pullbacks has to be taken into account to evaluate its temporal change.

It is noteworthy that geometrical contours detection is important in the reproducibility of the compositional iMAP measurements. In particular, some of the observed variability in necrotic volume tissue detection (10.2%) may be due to the inter-observer variability (plaque burden difference between observers was 1.9%), whereas inter-catheter variability contributes with 5.2% in necrotic tissue detection. Interestingly, although

the intra-catheter variability was 1.3% in plaque burden, the necrotic tissue detection was still high compared to the previous variabilities. One of the reasons may be due to the fact the iMAP classifies as necrotic tissue all the attenuated areas within the plaque (deeper plaque) and also the areas behind the calcium. Indeed drawing the vessel contour behind the calcium introduces important variability and the magnitude depends on the extension of the arc of calcification.¹⁷ Calcium measurements showed a higher variability in the inter- and intra-catheter analyses than in the inter-observer analysis, despite a lower variability in geometrical measurements. Use of different catheters with different piezoelectric crystals or “fatigue” of the same

Table 4. Geometrical and compositional measurement of matched ROI between two catheters (n=5)

	Catheter 1	Catheter 2	Absolute Δ	Relative Δ (%)
Geometrical data				
Lumen CSA (mm ²)	8.73±2.68	8.80±2.66	0.08±0.15	1.6
Lumen volume (mm ³)	206.54±82.75	204.26±85.68	2.27±4.83	1.7
Lumen max diameter (mm)	5.06±0.78	5.18±0.86	0.12±0.17	2.2
Lumen min diameter (mm)	3.74±0.56	3.64±0.66	0.10±0.16	3.2
Lumen mean diameter (mm)	4.40±0.57	4.39±0.58	0.00±0.02	0.1
Vessel CSA (mm ²)	15.53±4.09	15.52±4.14	0.00±0.10	0.1
Vessel volume (mm ³)	471.30±178.00	470.93±178.32	0.36±2.74	0.1
Vessel max diameter (mm)	5.06±0.78	5.18±0.86	0.12±0.17	2.2
Vessel min diameter (mm)	3.75±0.48	3.91±0.59	0.16±0.27	3.7
Vessel mean diameter (mm)	4.40±0.57	4.39±0.58	0.00±0.02	0.1
Plaque CSA (mm ²)	8.73±2.68	8.80±2.66	0.08±0.13	0.9
Plaque volume (mm ³)	264.76±103.17	266.67±100.89	1.91±4.16	1.0
Plaque burden (%)	55.80±7.17	56.42±7.29	0.61±1.01	1.0
Compositional data				
Fibrotic volume (mm ³)	164.24±56.90	163.25±56.62	0.99±4.04	0.7
Fibrotic area (mm ²)	5.54±1.92	5.53±1.91	0.01±0.13	0.4
Fibrotic tissue (%)	63.85±12.43	62.79±12.43	1.06±1.29	1.7
Lipidic volume (mm ³)	25.05±12.73	25.25±11.76	0.20±2.30	1.2
Lipidic area (mm ²)	0.84±0.43	0.85±0.39	0.01±0.07	1.6
Lipidic tissue (%)	9.41±2.63	9.57±3.18	0.16±0.96	0.2
Necrotic volume (mm ³)	72.55±53.24	75.36±53.71	2.81±0.61	5.2
Necrotic area (mm ²)	2.45±1.79	2.55±1.82	0.10±0.02	5.5
Necrotic tissue (%)	25.13±11.63	26.10±11.54	0.96±0.64	4.2
Calcific volume (mm ³)	4.11±1.85	3.97±1.83	0.14±0.43	6.4
Calcific area (mm ²)	0.14±0.06	0.13±0.06	0.01±0.01	6.0
Calcific tissue (%)	1.59±0.51	1.52±0.57	0.07±0.20	7.3

catheter used twice could explain these findings. **(Figure 5)** The variability of the other iMAP plaque components also increases from the inter-catheter to the intra-catheter analysis. Our study with this regard may provide some thresholds over which changes are statistically significant.

It is also important to consider that iMAP-IVUS catheter is a sheath based mechanical imaging catheter and compared with electronic non-sheath based IVUS-VH imaging catheter enables to obtain with more probability an uniform pullback, having that a clear importance on size and compositional measurements of atherosclerotic plaques.

Of note is also that iMAP-IVUS catheter recognizes the shadow of the guidewire as necrotic core. Although the software helps to mask this shadow,

some information is lost, depending on where the shadow is located. If the shadow is projected on the coronary plaque, a bigger part of the plaque is excluded from the analysis, as compared if the shadow is projected on a part of the vessel wall without plaque. **(Figure 6)** Although the reproducibility in compositional measurements is not different from that already demonstrated in the VH software, the presence of the guidewire shadow and the possibility to use the black pixel classification tool in the analysis software should be taken into account as they further increase the variability of the measurements, especially of necrotic core detection.

Table 5. Geometrical and compositional measurement of matched ROI within the same catheter (n=5)

	Catheter 1 (1 st pullback)	Catheter 1 (2 nd pullback)	Absolute Δ	Relative Δ (%)
Geometrical data				
Lumen CSA (mm ²)	6.52±2.21	6.53±1.99	0.01±0.29	0.9
Lumen volume (mm ³)	193.78±69.59	195.08±67.87	1.30±8.87	1.1
Lumen max diameter (mm)	3.63±0.84	3.72±0.86	0.08±0.20	2.3
Lumen min diameter (mm)	2.15±0.29	2.13±0.27	0.02±0.09	0.8
Lumen mean diameter (mm)	2.83±0.43	2.83±0.39	0.01±0.06	0.3
Vessel CSA (mm ²)	14.85±4.42	15.21±4.31	0.35±0.55	2.6
Vessel volume (mm ³)	492.92±111.45	434.39±108.86	4.47±9.02	1.2
Vessel max diameter (mm)	4.98±0.80	5.01±0.78	0.03±0.05	0.7
Vessel min diameter (mm)	3.87±0.58	3.93±0.54	0.05±0.07	1.3
Vessel mean diameter (mm)	4.30±0.62	4.36±0.61	0.05±0.07	1.3
Plaque CSA (mm ²)	8.33±3.10	8.68±3.29	0.34±0.41	4.1
Plaque volume (mm ³)	236.13±67.72	239.31±65.17	3.18±5.72	1.7
Plaque burden (%)	55.32±9.13	56.04±9.02	0.72±1.26	1.3
Compositional data				
Fibrotic volume (mm ³)	122.11±26.17	126.97±26.80	4.86±2.02	4.0
Fibrotic area (mm ²)	4.09±0.87	4.25±0.89	0.16±0.06	3.8
Fibrotic tissue (%)	53.29±15.40	53.54±17.43	0.25±2.96	0.1
Lipidic volume (mm ³)	21.50±12.27	21.87±11.66	0.37±1.49	1.9
Lipidic area (mm ²)	0.72±0.41	0.73±0.39	0.01±0.05	1.4
Lipidic tissue (%)	8.64±3.21	8.47±3.14	0.17±0.48	2.3
Necrotic volume (mm ³)	87.87±45.03	87.46±47.75	0.42±7.52	3.9
Necrotic area (mm ²)	2.94±1.51	2.93±1.60	0.01±0.25	5.5
Necrotic tissue (%)	35.08±12.88	34.33±14.62	0.75±2.40	5.2
Calcific volume (mm ³)	7.23±2.71	7.14±2.63	0.09±0.73	1.1
Calcific area (mm ²)	0.24±0.09	0.23±0.08	0.01±0.02	1.8
Calcific tissue (%)	2.99±0.56	2.85±0.75	0.13±0.28	5.1

Limitations

The studied population was relatively small. The selection of a population of patients with non tortuous and non severely calcified vessels could not reproduce the same agreement of the technique in a more challenging population.

Conclusions

Our study showed that compositional measurements of iMAP are acceptably reproducible with regards to the variability in IVUS geometrical measurements. These results can aid investigators to perform power calculation for longitudinal studies using iMAP.

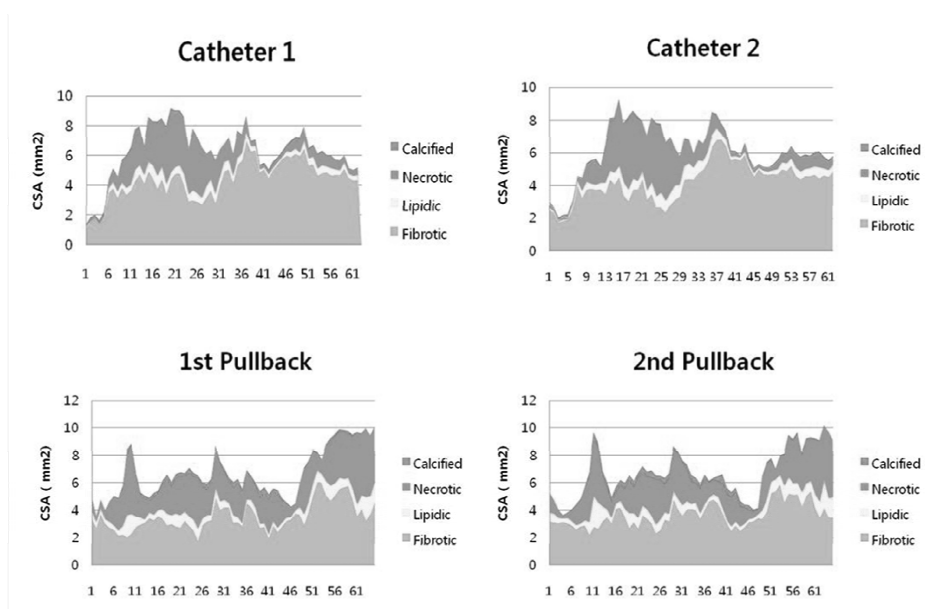


Figure 4. Sequential plotting of a matched ROI interrogated with two different catheters (on the top) or with two different pullbacks (on the bottom). The mean Cross Sectional area(y axis) of each plaque component is color-coded (calcium: blue, necrotic: pink, lipidic: yellow, and fibrotic: green). These figures show examples of the impact of different catheters of pullbacks on compositional measurements. ROI = region of interest. See color figure on page 339

Table 6. Geometrical and compositional measurement of matched ROI within the same catheter using the various tools of the software(n=5)

	Conventional analysis	Mask guidewire	Absolute Δ	Relative Δ (%)	Mask guidewire + black pixel classification	Absolute Δ	Relative Δ (%)
Compositional data							
Fibrotic tissue (%)	53.29 \pm 15.40	53.08 \pm 15.31	0.20 \pm 0.11	0.3	50.49 \pm 17.21	2.80 \pm 2.82	6.1
Lipidic tissue (%)	8.64 \pm 3.21	8.39 \pm 3.12	0.25 \pm 0.15	3.1	8.24 \pm 3.17	0.40 \pm 0.22	5.0
Necrotic tissue (%)	35.08 \pm 12.88	33.28 \pm 13.28	1.80 \pm 1.20	6.8	19.44 \pm 6.21	15.64 \pm 8.06	41.7
Calcific tissue (%)	2.99 \pm 0.56	2.97 \pm 0.54	0.01 \pm 0.02	0.3	2.89 \pm 0.54	0.10 \pm 0.11	3.1

Note: Regarding tissue characterization guidewire (GW) artifact of the image is to be considered as un-analyzable. Similarly, an adequate spectral analysis is not present behind the calcium, due to the drop of the signal. Therefore, this table shows a comparison between the conventional analysis (without excluding parts of the iMAP image) and an analysis excluding these parts by masking the GW artifact of the region behind the calcium.

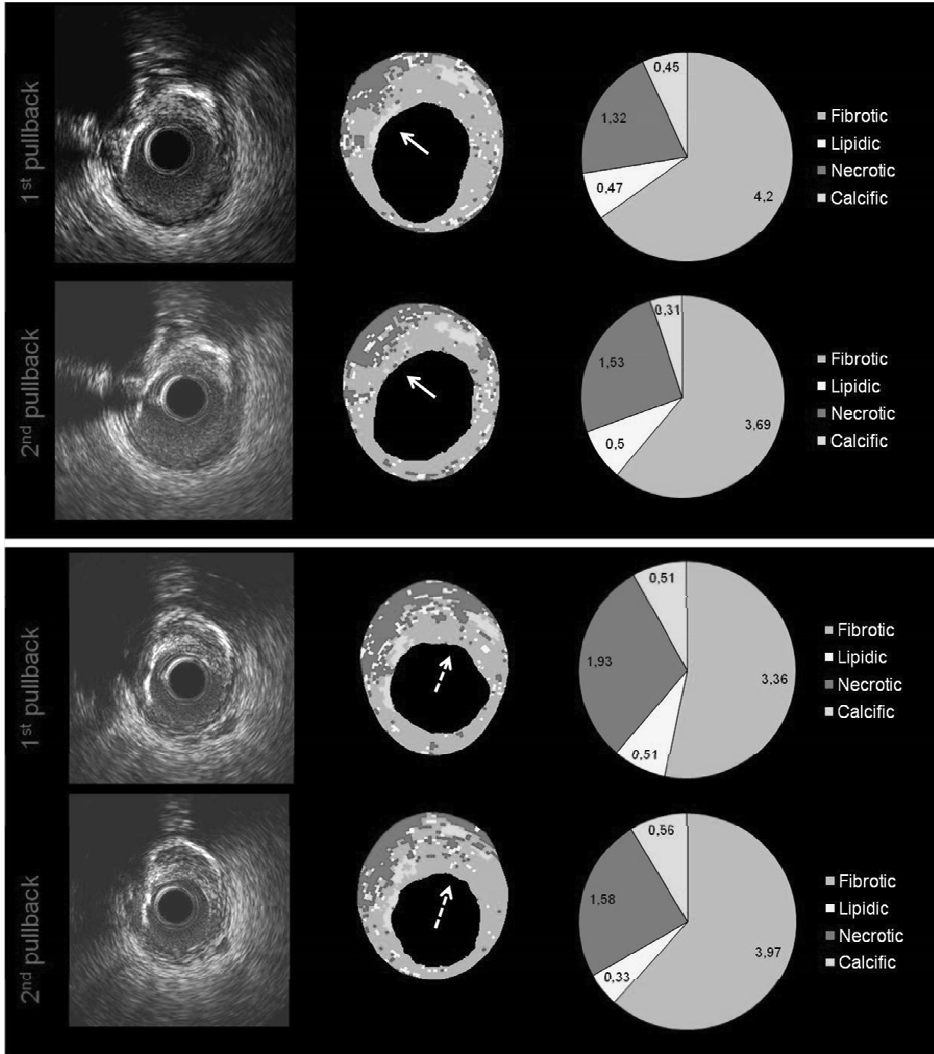


Figure 5. Examples of the impact of two different pullbacks acquired with the same catheter on the calcium (white continuous arrows on the top panel) and necrotic core (white dotted arrows on the bottom panel) detection. Note the difference in terms of brightness between the two pullbacks. See color figure on page 340

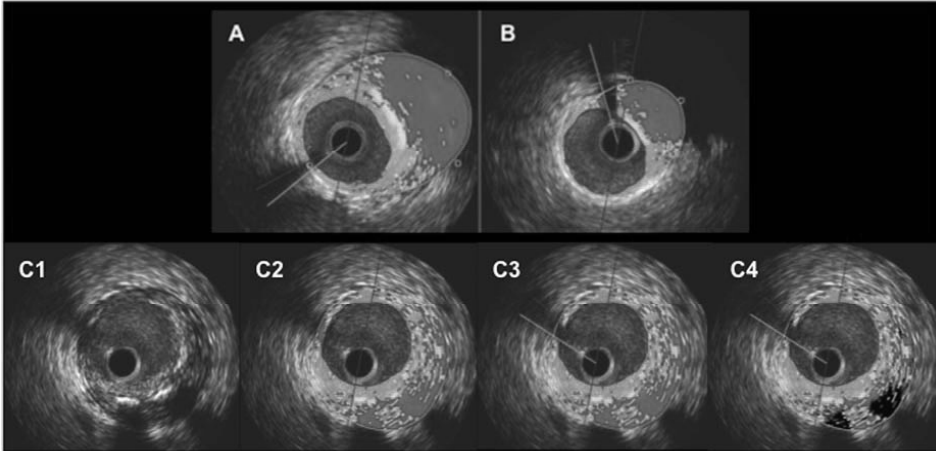


Figure 6. The information lost due to the wire shadow is depending on where the shadow is located. If the shadow is projected on the coronary plaque, a bigger part of the plaque is excluded from the analysis (**B**), as compared if the shadow is projected on a part of the vessel wall without plaque (**A**). The software used for the analysis allows the exclusion of the wire shadow from the tissue characterization (**C1-C3**) and/or the exclusion of the tissue underneath calcification, where an adequate spectral analysis is not possible due to the drop of the signal (**C4**). See color figure on page 341

REFERENCES

1. Brugaletta, S., Costa, J.R., Jr. & Garcia-Garcia, H.M. Assessment of drug-eluting stents and bioresorbable stents by grayscale IVUS and IVUS-based imaging modalities. *Int J Cardiovasc Imaging*.
2. Hirohata, A., et al. Impact of olmesartan on progression of coronary atherosclerosis a serial volumetric intravascular ultrasound analysis from the OLIVUS (impact of OLmesarten on progression of coronary atherosclerosis: evaluation by intravascular ultrasound) trial. *J Am Coll Cardiol* **55**, 976-982.
3. Takayama, T., et al. Effect of rosuvastatin on coronary atheroma in stable coronary artery disease: multicenter coronary atherosclerosis study measuring effects of rosuvastatin using intravascular ultrasound in Japanese subjects (COSMOS). *Circ J* **73**, 2110-2117 (2009).
4. Schoenhagen, P., et al. Determinants of arterial wall remodeling during lipid-lowering therapy: serial intravascular ultrasound observations from the Reversal of Atherosclerosis with Aggressive Lipid Lowering Therapy (REVERSAL) trial. *Circulation* **113**, 2826-2834 (2006).
5. Nissen, S.E., et al. Effect of very high-intensity statin therapy on regression of coronary atherosclerosis: the ASTEROID trial. *JAMA* **295**, 1556-1565 (2006).
6. Nair, A., et al. Coronary plaque classification with intravascular ultrasound radiofrequency data analysis. *Circulation* **106**, 2200-2206 (2002).
7. Burke, A.P., et al. Morphologic findings of coronary atherosclerotic plaques in diabetics: a postmortem study. *Arterioscler Thromb Vasc Biol* **24**, 1266-1271 (2004).
8. Garcia-Garcia, H.M., et al. Synergistic effect of cardiovascular risk factors on necrotic core in coronary arteries: a report from the global intravascular radiofrequency data analysis registry. *JACC Cardiovasc Imaging* **2**, 629-636 (2009).
9. Marso, S.P., et al. Intravascular ultrasound measures of coronary atherosclerosis are associated with the Framingham risk score: an analysis from a global IVUS registry. *EuroIntervention* **5**, 212-218 (2009).
10. Stone, G.W., et al. A prospective natural-history study of coronary atherosclerosis. *N Engl J Med* **364**, 226-235.
11. Serruys, P.W., et al. Effects of the direct lipoprotein-associated phospholipase A(2) inhibitor darapladib on human coronary atherosclerotic plaque. *Circulation* **118**, 1172-1182 (2008).
12. Rodriguez-Granillo, G.A., et al. Reproducibility of intravascular ultrasound radiofrequency data analysis: implications for the design of longitudinal studies. *Int J Cardiovasc Imaging* **22**, 621-631 (2006).
13. Sathyanarayana, S., Carlier, S., Li, W. & Thomas, L. Characterisation of atherosclerotic plaque by spectral similarity of radiofrequency intravascular ultrasound signals. *EuroIntervention* **5**, 133-139 (2009).
14. Shin, E.S., et al. In vivo findings of tissue characteristics using iMap IVUS and Virtual Histology IVUS. *EuroIntervention* **6**, 1017-1019.
15. Shin, E.S., et al. Reproducibility of Shin's method for necrotic core and calcium content in atherosclerotic coronary lesions treated with bioresorbable everolimus-eluting vascular scaffolds using volumetric intravascular ultrasound radiofrequency-based analysis. *Int J Cardiovasc Imaging*.
16. Bland, J.M. & Altman, D.G. Statistical methods for assessing agreement between two methods of clinical measurement. *Lancet* **1**, 307-310 (1986).
17. Bruining, N., et al. Three-dimensional and quantitative analysis of atherosclerotic plaque composition by automated differential echogenicity. *Catheter Cardiovasc Interv* **70**, 968-978 (2007).

Chapter 2

Coronary plaque characterization through near infra-red spectroscopy

2.1

Assessment of Coronary Plaque Composition with Near Infrared Spectroscopy

James A. Goldstein, MD,* Salvatore Brugaletta, MD,‡** Sean P Madden, PhD,† Stephen T Sum, PhD,† Simon R. Dixon, MBChB,* Ryan D. Madder, MD,* Patrick W. Serruys, MD, PhD**; James E Muller, MD.†

*Department of Cardiovascular Medicine, Beaumont Health System, 3601 West 13 Mile Road, Royal Oak, Michigan 48073, USA

‡Thorax Institute, Department of Cardiology, Hospital Clinic, University of Barcelona, Barcelona, Spain

**Thoraxcenter, Erasmus MC, Rotterdam, The Netherlands

†InfraReDx, Inc., 34 Third Ave., Burlington, MA 01803, USA

The PCR-EAPCI Textbook, In press

SECTION TITLE	PAGE
Limitations of coronary angiography and importance of plaque composition: need for improved imaging techniques	x
Rationale for direct coronary imaging techniques	x
Diffuse reflectance near infrared spectroscopy (NIRS)	x
NIRS principles of operation and validation	x
NIRS-IVUS clinical applications	x
Prevention of Peri-Procedural MI	x
Optimization of PCI	x
Identification of vulnerable plaque	x
Additional clinical uses	x
Conclusions	x
Personal perspective	x
References	x

SUMMARY

Intracoronary near infrared spectroscopy (NIRS) is a novel method for the identification and quantification of lipid core within the composition of atherosclerotic plaque. The principles of operation, system development, method validation and early clinical use of intracoronary NIRS are described. The main advantage of NIRS over other plaque characterisation methods is its ability to directly identify chemical composition – the primary use of spectroscopy for other applications. Identification of lipid core plaque (LCP) with NIRS has potential, hypothetically, to improve the safety of stenting, including optimisation of length of vessel to stent, assurance of adequate stent implantation, and identification of lipid-core lesions at higher risk of distal embolisation, possibly leading to effective utilisation of distal embolic protection devices in the native coronaries. NIRS by itself does not display structures, but a combination device with co-registered intravascular ultrasound (IVUS) has been developed to give simultaneous and complementary structural and compositional information. The NIRS-IVUS device also has promise in the identification of vulnerable plaque, which may lead to strategies to prevent future coronary events.

KEYWORDS

- Distal embolisation
- Intravascular ultrasound
- Lipid-core plaque
- Near-infrared spectroscopy
- Plaque characterisation
- Percutaneous coronary intervention

LIMITATIONS OF CORONARY ANGIOGRAPHY AND IMPORTANCE OF PLAQUE COMPOSITION: NEED FOR IMPROVED IMAGING TECHNIQUES

In the past 3 years, the findings of several large-scale clinical studies have had substantial impact on the management of patients with coronary artery disease [1-4]. Observations from these studies emphasise that clinical decision-making in these patients is complex and often surrounded by uncertainty. For example, the clinician is faced daily with challenging decisions regarding revascularisation strategies (whether percutaneous coronary intervention (PCI) should be offered versus bypass surgery) and important procedural issues regarding performance of PCI (e.g., identification of which lesions to treat, length of vessel to treat, optimal stent deployment, prevention of distal embolisation and periprocedural myocardial infarction, etc.).

Unfortunately, coronary angiography alone fails to provide adequate information for such decisions. Although a crucial tool to delineate the gross presence of disease and quantify the degree of stenosis, angiography underestimates the magnitude of atherosclerotic burden, particularly in earlier stage disease during which positive vascular remodelling may allow “normal” lumen calibre despite substantial vascular wall plaque. Importantly, angiography also has significant limitations in the precise delineation of plaque architecture and does not provide data on plaque composition or its biological activity.

Plaque composition has been shown to have some important clinical implications (➤ Table 1): the presence of a lipid pool specifically appears to be a critical determinant of plaque instability [4-8]. Whereas fibrous plaques are thought to be more stable, lipid core plaques (LCP) are implicated in more rapid progression of coronary atherosclerosis, plaque rupture resulting in acute coronary syndromes and sudden cardiac death, as well as distal embolisation complications during PCI [6-11]. The recognition of the ubiquity of substantial but non-flow limiting lesions that may be at high risk for subsequent plaque rupture has resulted in a paradigm shift in thinking about the pathophysiology of coronary artery disease, with the focus no longer solely on the degree of arterial luminal narrowing. This growing need for more information about coronary atherosclerosis in order to identify patients and lesions at risk of complications during PCI, and for future adverse cardiac events, has been the primary impetus for the development of novel intra-coronary imaging methods able to detect plaque composition, in particular the presence of a lipid pool.

TABLE 1
Implications of lipid core plaque

More rapid plaque progression
Plaque vulnerability (ACS and SCD)
Complications during PCI <ul style="list-style-type: none"> • Embolisation-periprocedural infarction • Subacute and late stent thrombosis • Stent edge restenosis

FOCUS BOX 1 Invasive direct coronary imaging

- Coronary angiography gives a semi-quantitative assessment of percent diameter stenosis
- Coronary angiography provides no quantitative or qualitative information on atheroma burden or plaque
- LCP has important implications for plaque progression, stability and may influence the outcome of PCI
- Present and future direct multi-modality direct coronary imaging gives accurate information on atheroma architecture as well as composition and is likely to become a standard tool for invasive evaluation and therapy

RATIONALE FOR DIRECT CORONARY IMAGING TECHNIQUES

The ideal invasive tool for characterisation of coronary plaque should provide, for example, a complete roadmap of atherosclerotic burden throughout the coronary tree and in particular the morphological and compositional data of each plaque. Specific parameters should include: (1) extent of luminal stenosis; (2) lesion length; (3) coronary blood flow reserve through any given stenosis; (4) intramural plaque architecture including atheroma burden, eccentricity, and local vascular remodelling; (5) plaque composition, specifically lipid content; (6) fibrous cap thickness; and (7) presence of inflammation.

Direct intra-coronary imaging methods offer new insight into opportunities to improve PCI treatment of flow-limiting target lesions, and to identify the vulnerable plaques responsible for subsequent events (➤ Table 2). IVUS may provide useful information on plaque architecture, luminal stenosis and vessel remodelling and can be used to quantify the extent of lesion calcification and to assist in optimal stent deployment. By IVUS, complex unstable plaques are typically bulky, eccentric and exhibit features of disruption, such as ulceration, intimal flap and thrombus [6-9,12]. Characterisation of coronary plaques by IVUS greyscale is, however, not completely reliable, as, for example, echolucent and attenuated plaques have been variously related to high lipid content in some histological studies and to non-lipid component in other studies [13-

TABLE 2
Comparison of direct coronary imaging techniques

	IVUS (40 MHz)	VH (20 MHz)	OCT	NEAR-INFRARED SPECTROSCOPY	ANGIOSCOPY
Axial resolution, μm	100	200	10	NA	10 to 50
PCI (stent expansion) and complications	++	+	++	-	+
Necrotic core	+	+	+	++	+
TCFA	-	+	++	+	+
Thrombus	+	-	+	+	++
Stent tissue coverage	+	+	++	-	++
Expansive remodelling	++	++	+	-	-

++ Indicates excellence / + Good / + Possible / - Impossible.

16]. Culprit lesions in patients with ACS demonstrated more expansive/positive remodelling by IVUS than culprit lesions of patients with stable angina, suggesting that expansive remodelling might be associated with plaque vulnerability [4,7,8].

IVUS with Virtual Histology (VH) is being investigated as a tool to characterise plaque structure and composition, based on pattern classification of the backscattering ultrasound signals coming from the coronary plaque, with a sensitivity and specificity to identify necrotic core of approximately 90% [4,17-20]. The PROSPECT Study recently demonstrated that certain plaque features obtained with greyscale IVUS, such as plaque burden >70% and minimal luminal area < 4mm², and the identification of VH-derived thin cap fibroatheroma may predict the occurrence of subsequent events in 700 patients after an ACS at a median follow-up of 3.4 years [4]. Although the PROSPECT Study validated the concept that direct coronary imaging can prospectively characterise “vulnerable” lesions at risk of adverse events, the authors noted that the low specificity of the findings can limit their clinical utility.

OCT is an evolving imaging modality that was introduced into cardiology to provide high-resolution (10 micron) images of the coronary arteries [21,22]. OCT achieves the highest spatial resolution of existing imaging modalities (10 microns, versus 100 microns for IVUS) and is the best method to measure the thickness of the cap overlying lipid-cores. OCT is also an excellent method to identify intra-coronary thrombus, stent expansion, and coverage of stent struts. It requires removal of blood from the field of view, which is accomplished by an intra-coronary injection of saline or contrast material. OCT has been reported to be of use in the detection of LCP [21]. Nevertheless, identification of LCP by OCT is primarily dependent on subjective image interpretation largely relying on the absence of signal, which can be confounded by the presence of calcification and by lack of depth of penetration. In addition, the limited penetration depth prevents detection of the external elastic membrane (EEM) border impeding the calculation of plaque burden.

FOCUS BOX 2

Rationale for direct coronary imaging techniques

Direct coronary imaging with IVUS and OCT provides key data regarding plaque architecture; insights that help delineate the significance of a lesion and guide interventional therapy

DIFFUSE REFLECTANCE NEAR INFRARED SPECTROSCOPY (NIRS)

A near-infrared intravascular spectroscopy (NIRS) catheter system (Lipiscan™, InfraReDx, Burlington, MA, USA) has been recently developed for the invasive detection of LCP. [23-26] This device is comprised of a scanning near-infrared laser and a fibre optic catheter similar in size and use to an IVUS catheter, and an automated pullback and rotation device (🔗 Figure 1).

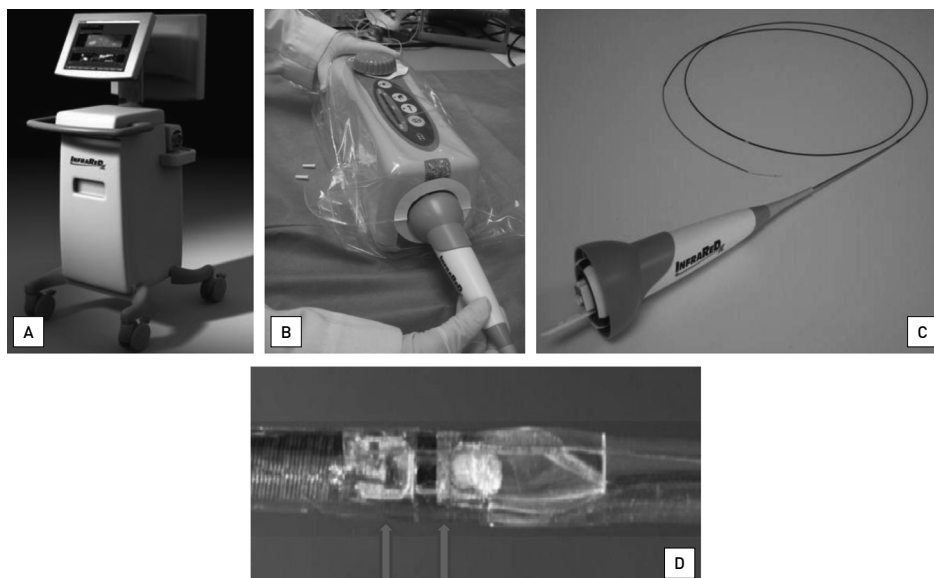
In particular, the NIRS catheter is a monorail system which can be advanced over a 0.014 guidewire up to a reference point distal to the target lesion, like an IVUS catheter. Scanning with automated rotational pullback is performed at a speed of 0.5 mm/second and 240 RPM with the goal of terminating the pullback after the imaging element enters the guiding catheter (🔗 Table 3).

The system performs approximately 8000 chemical measurements per 100 mm of artery scanned. A predictive algorithm calculates the probability that a LCP is present at each interrogated location in the artery.

The data are immediately and automatically displayed on a two dimensional map of the vessel called “chemogram.” The x-axis of the chemogram represents mm of pullback in the artery and the y-axis represents degrees of rotation; a colour scale from red to yellow indicates increasing algorithm probability that a LCP is present (🔗 Figure 2).

FIGURE 1

NIRS catheter system components, including console (A), pullback and rotation (PBR) device (B), catheter (C) and magnified view of catheter tip (D) illustrating NIRS and IVUS components



NIR mirrors IVUS

TABLE 3

NIR spectroscopy

Scans artery through blood
20 msec spectra acquisition
System acquires 1,000 measures /12.5 mm
Each measurement interrogates 1-2 sq mm
Majority of data obtained from a depth of 1 mm
Identifies chemical composition of vessel wall
Spectra processed by algorithm and displayed as chemogram of LCP probability
<ul style="list-style-type: none"> • Sensitivity and specificity > 85% <i>ex vivo</i>

The “block chemogram” provides a summary of the results for each 2 mm section of artery. The numerical value of each block in the block chemogram represents the 90th percentile of all pixel values in the corresponding 2 mm chemogram seg-

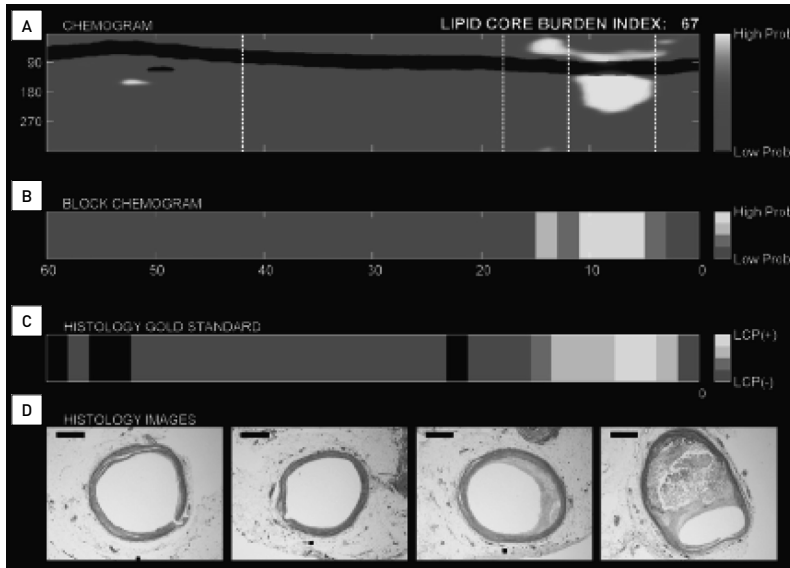
ment. The block chemogram is mapped to the same colour scale as the chemogram and the display uses four discreet colours to aid in the visual interpretation of the algorithm probability that a LCP is present in that 2 mm block (red: $p < 0.57$, orange: $0.57 \leq p \leq 0.84$, tan: $0.84 \leq p \leq 0.98$, yellow: $p > 0.98$).

The lipid core burden index (LCBI) is provided as a quantitative summary metric of the LCP presence in the entire scanned region. LCBI is computed as the fraction of valid pixels within the scanned region that exceed an LCP probability of 0.6, multiplied by 1,000. Since the chemogram colour scale transitions from red to yellow near an LCP algorithm probability of 0.6, the LCBI can be viewed as a quantitative measure of the amount of yellow present on the chemogram.

The radio-opaque marker on the NIRS catheter can be used to identify the location of the catheter and imaging element in relationship to target vessel fiducial landmarks as detected by coronary angiography (e.g., stenoses of interest, branches, guide catheter, etc.) with the possibility to place a mark on the chemogram and annotate anatomical landmarks at the locations of acquisition of the NIRS spectra.

FIGURE 2**A NIRS scan correlates well to histologic findings in coronary artery from a 65-year-old male with a history of MI**

(A) Chemogram image indicating artery wall lipid content (x axis – pullback in millimetres; y axis – rotation in degrees). Each pixel is marked with red for low probability and yellow for high probability of lipid core plaque of interest (LCP). The lipid core burden index (top right) indicates amount of lipid in scanned artery on a 0-1,000 scale. **(B)** Summary (block chemogram) of LCP presence at 2 mm intervals in 4 probability categories. **(C)** Map of histologic classifications (yellow – LCP; light orange – small or thick-capped fibroatheroma; dark orange – intimal xanthoma and pathologic intimal thickening; red – all other types). **(D)** Movat cross-sections from locations along the artery (dotted lines). Black bars denote 1 mm. Image interpretation: The chemogram shows prominent lipid core signal at 2 to 6 mm, occupying 180°. The block chemogram shows that the strongest LCP signals extend 5 to 11 mm. The NIRS signals at 18 and 42 mm correctly indicate absence of LCP.



The NIRS catheter has been approved by the US FDA and has received a CE mark for detection of LCP of interest in the coronary arteries and measurement of the lipid-core burden index (LCBI) a quantitative summary metric of the total LCP detected in the segment of artery scanned.

A combined NIRS-IVUS catheter (InfraReDx, Inc., Burlington, MA, USA) has recently been introduced and approved by the FDA and has a CE mark [25] (Figure 3). This novel catheter allows a complete characterisation of coronary plaques, providing simultaneous and co-registered acquisition of their structural and compositional information. In particular, NIRS can confirm LCP presence when high plaque burden and hypo-echogenic regions are identified by IVUS, possibly indicating lesions at high risk of distal embolisation during balloon dilation and stenting [27,28].

NIRS PRINCIPLES OF OPERATION AND VALIDATION

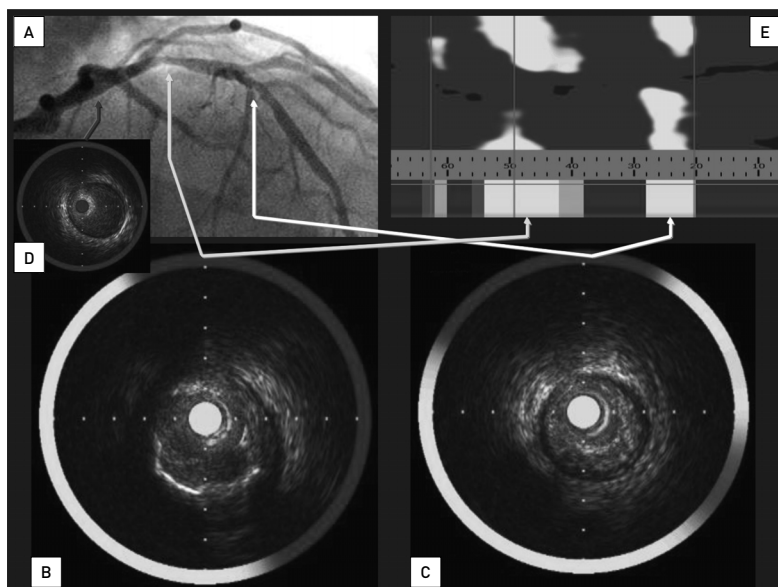
Diffuse reflectance NIRS is widely used in many fields to identify the chemical composition of unknown substances. Spectroscopy can be broadly defined as the measurement of the wavelength dependent interaction of electromagnetic radiation with matter. In diffuse reflectance NIRS, a sample of interest is irradiated with near-infrared light and a detector measures the proportion of diffusely reflected light returned as a function of wavelength. Two quite different processes determine the amount of light that returns to the detector – scattering and absorption.

- *Scattering* occurs when the path of the light is altered by the cellular and extracellular structures (that are larger than the wavelength of light) in the material.

FIGURE 3

Correlation between angiography, IVUS and chemogram obtained with the NIRS-IVUS catheter

Simultaneously obtained co-registered NIRS-IVUS images demonstrating angiographically "mild" disease in the proximal LAD (A, yellow arrow), with a more severe stenosis in the mid-LAD (A, white arrow). In the NIRS-IVUS chemogram, a 2nd block chemogram (E, top) documents that both lesions contain large LCP. Cross-sectional IVUS views (B, C, D), with the chemogram data overlaid in a halo while the block chemogram colour value is portrayed in the central catheter artifact (bottom). IVUS reveals the proximal LAD lesion (B) is a LCP with ulceration and the mid-lesions is a bulky LCP with tight stenosis.



- *Absorption* occurs when light energy is absorbed by chemical bonds of the constituent molecules. Absorbed light is mainly transformed into molecular vibrational energy in the form of oscillations of atoms within their chemical bonds.

To create an advanced algorithm ultimately applicable to interpretation of NIR signals obtained in patients, initial calibration and validation studies were performed in intact and perfused human coronary artery autopsy specimens [23]. NIR spectrographic data were initially compared to the histology gold standard of LCP (fibroatheroma > 60 degrees in circumferential extent >200 microns in thickness on a cross-sectional histologic specimen, with a fibrous cap having a mean thickness of < 450 microns). Spectral similarity was prospectively analysed using common measures of multivariate distance and calibration model residual. In this rigorous, prospective study an area under the receiver operating characteristic curve for detection of LCP of 0.83 (95% confidence interval, 0.70 to 0.93) was observed, satisfying the primary

endpoint of the study. Clinical validation studies with this catheter system were then performed, demonstrating that NIR signals obtained in patients are spectrally similar to those obtained in autopsy specimens [24]. NIRS is well-suited for analysis of LCP in a coronary vessel tissue since it 1) can penetrate blood, 2) can penetrate several millimetres into the tissue, 3) can be done with an ultrafast scanning laser, overcoming the problem of cardiac motion, artefactUltra 4) is capable of acquiring the thousands of spatial measurements required to create an image of the artery, and 5) provides a positive and specific chemical measure of LCP (it does not rely on drop-out of signal as do IVUS and OCT) since cholesterol has prominent features in the NIR region that can distinguish it from other tissue constituents such as collagen.

Overall, results from these studies showed that the NIR system is very accurate and valid for localised detection of LCP, as well as for determination of overall lipid burden of a scanned artery, in patients undergoing coronary angiography.

IVUS and IVUS-VH findings were recently compared with NIRS findings. Larger coronary plaques, identified by grey-scale IVUS, were more likely to be recognised as lipid core plaques (LCP) and as necrotic-core rich plaques by NIRS and VH, respectively; however, the correlation between NIRS and VH was poor. The fundamental differences in the principles of each technique, i.e., VH is based on a pattern classification of the backscattering ultrasound signal, whereas NIRS is based on near-infrared spectral signals, and their respective limitations should be taken into account in the interpretation of the differing results between NIRS and IVUS-VH [26].

FOCUS BOX 3

Principles of operation and validation

- The NIRS catheter is easy to use and has been rigorously validated against histopathology for the detection of LCP
- Ultrafast laser scanning mitigates against cardiac motion artefact
- Positively identifies lipid composition whereas ultrasound relies on acoustic shadowing

NIRS-IVUS CLINICAL APPLICATIONS

Although the safety and efficacy of coronary stenting have steadily improved, patients continue to experience complications during and after PCI procedure. NIRS-IVUS delineation of plaque architecture and composition has the potential to improve safety and long-term outcome of PCI (Table 4) by:

- 1) Identification of large LCP, which are known to be at high risk of distal embolisation and periprocedural MI. In this case pre-PCI identification of such plaques can lead to the use of preventive strategies, employing distal embolic protection devices.
- 2) Delineation of length of vessel to stent with adequate lesion coverage and optimal stent expansion.
- 3) Identification of vulnerable plaques.

TABLE 4

NIRS-IVUS: potential clinical applications

OPTIMAL STENTING PROCEDURES
Determine optimal vessel length to stent <ul style="list-style-type: none"> • Measure precise stent length
Optimise stent deployment <ul style="list-style-type: none"> • Minimise subacute thrombosis and late restenosis
Characterise lesions at embolic risk <ul style="list-style-type: none"> • Assess the need for distal protection devices
CHARACTERISE NON-FLOW LIMITING LESIONS
Identification of vulnerable plaque

PREVENTION OF PERIPROCEDURAL MI

Periprocedural myocardial infarction is associated with short and long-term adverse outcomes. In particular, embolisation of the lipid core of stenotic plaques following PCI has been demonstrated as an important cause of periprocedural no-reflow and MI even in absence of angiographic intra-coronary thrombus. Since periprocedural MI can prolong hospital stay and is an impediment to more frequent performance of stenting in a less costly out-patient setting, pre-PCI identification of such plaques at high risk of embolisation can lead to the use of preventive strategies (e.g., distal embolic protection device), enhancing therefore the safety, efficacy, and cost-effectiveness of stenting [11,29-37].

NIRS appears to be an effective technique for identification of LCP lesions at embolic risk [27,28]. Recent evidence suggested, for example, that large area of LCP identified by NIRS might be associated with distal embolisation and periprocedural MI [27] (Figure 4). The COLOR Registry, an ongoing prospective observational study of patients undergoing NIRS prior to PCI, provided additional evidence of this capability of NIRS [28]. In this study the extent of LCP in the treated region was calculated as the maximal lipid-core burden index (LCBI) for each 4 mm longitudinal segment ($\text{maxLCBI}_{4\text{mm}}$) within the treated region (Figure 5). Results showed that a periprocedural MI developed in 50% of the LCP with a $\text{maxLCBI}_{4\text{mm}}$ of ≥ 500 (22.6% of the lesions) and in only 4.2 % of the LCP with a low $\text{maxLCBI}_{4\text{mm}}$ ($p=0.0002$) (Figure 6). Periprocedural MI can develop in association with post-stent disappearance of yellow LCP, presumably due to rupture and release of LCP contents with distal embolisation (Figure 7).

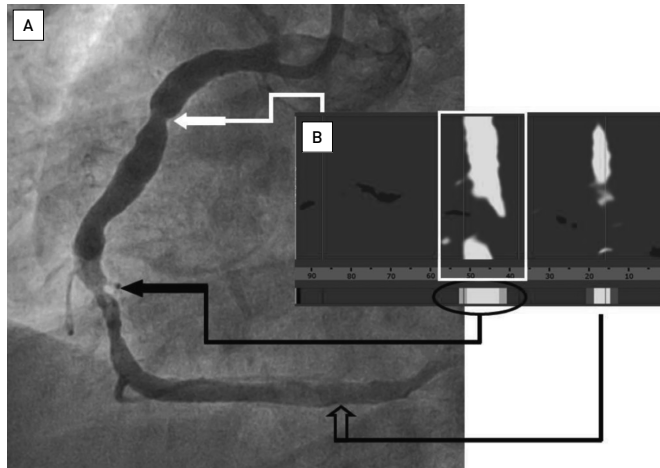
The knowledge that dilatation of a stenosis containing a large LCP, identified by NIRS, carries a 50% risk of causing a periprocedural MI indicates the need for preventive therapy. The use of an embolic protection device (EPD) to prevent distal embolisation of plaque contents, already used in PCI of vein grafts and carotid arteries, is a particularly promising approach. Although prior studies of the use of EPDs during stenting of lesions in the native coronary arteries failed to show clinical benefit, these studies did not characterise, by intra-coronary imaging, the types of plaques most likely to embolise and therefore to benefit from the use of an EPD [38]. The potential ability of NIRS-guided use of an EPD to prevent periprocedural MI will be tested in a prospective randomised trial, named CANARY (Coronary Assessment by Near-infrared of Atherosclerotic Rupture-prone Yellow).

OPTIMISATION OF PCI

The current standard of care consists of selection and placement of a coronary stent on the basis of angiographic infor-

FIGURE 4**Correlation angiogram and chemogram**

Angiogram **(A)** and chemogram **(B)** showing no LCP in a proximal moderate stenosis (solid white arrow), a large, extensive LCP at the stenotic culprit plaque (solid black arrow), and a small LCP in a distal non-stenotic location (open arrow). PCI resulted in abrupt no-reflow associated

**FIGURE 5****Illustration of methodology for determination of the maximum 4 mm sub-segment LCBI ($\text{maxLCBI}_{4\text{mm}}$)**

(A) The chemogram displays the NIRS findings obtained during rotation and pullback of the imaging element within the coronary artery of a patient. The x-axis represents mm of pullback, and the y-axis represents degrees of rotation from zero to 360. Yellow indicates a high probability that LCP is present at the interrogated site. **(B)** $\text{maxLCBI}_{4\text{mm}}$ is determined by defining the intervention region, computing LCBI for all 4 mm sub-segments within the intervention region, and identifying the maximum LCBI sub-segment. [Goldstein et al. *Cir Cardiovasc Intervent* in press]

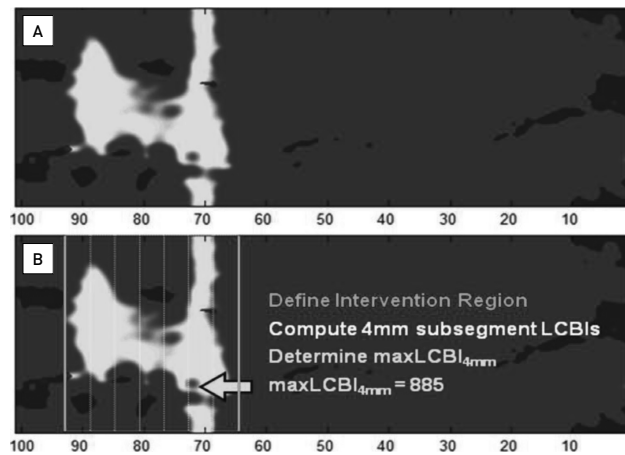
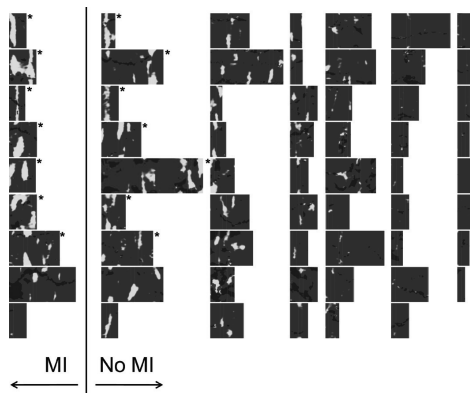
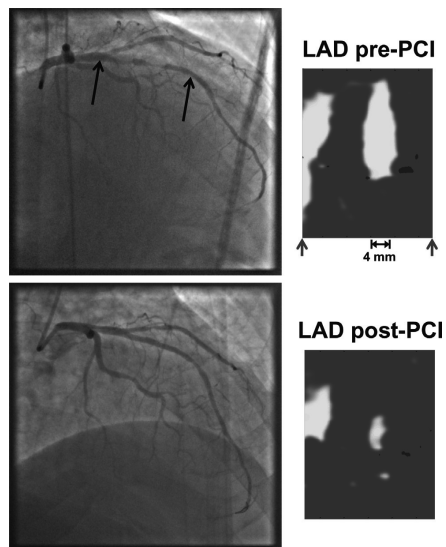


FIGURE 6**A mosaic of the 62 study chemogram intervention zones**

All patients had a coronary stenosis requiring stenting. Chemograms from patients experiencing a periprocedural myocardial infarction (MI) are shown on the left and those without on the right. Chemograms with $\text{maxLCBI}_{4\text{mm}} \geq 500$ are indicated with an asterisk.

**FIGURE 7****Pre and post percutaneous coronary intervention (PCI) angiogram frames and chemograms for a patient experiencing a periprocedural myocardial infarction (MI)**

The black arrows indicate the location on the angiogram of the proximal and distal boundaries of the PCI location and correspond to the boundaries of the chemogram segment. Pre-PCI $\text{maxLCBI}_{4\text{mm}}$ was 591 at the region indicated by the 4 mm mark. The post-PCI chemogram shows substantial reduction in LCP ($\text{maxLCBI}_{4\text{mm}}$ reduced to 189 in the matched region). [Goldstein et al. *Circ Cardiovasc Intervent* in press].



mation alone. Although use of angiography alone generally produces good outcomes, it has been suggested that stent complications (dissection, early or late stent thrombosis, or restenosis) might result from a geographical miss in stent placement (stent ends in an area with high plaque burden) or from incomplete stent expansion or malapposition [39-42]. There is evidence from prior randomised trials that IVUS guidance reduces complications [40,43]. Another application of the NIRS-IVUS device in clinical practice would be therefore to assist in decisions regarding the location and length of artery to be stented. During stenting, sites demonstrating a normal distal and proximal reference diameter are generally chosen for implantation. However, angiography often shows diffuse irregularities and is known to grossly underestimate the extent of disease, even when the vessel segments appear “normal”. Conversely IVUS imaging frequently confirms that sites with normal reference

diameters may have extensive plaque with expansive remodeling. In addition, recent clinical cases (⊙ Figure 8) revealed that placement of the ends of a stent over a LCP could result in high frequency of stent thrombosis [30,42]. NIRS can then help to avoid placement of the ends of a stent in a LCP by accurately and precisely revealing its location. Longer stents can be chosen to extend into vessel free of LCP or conversely the choice of a shorter stent could be supported by the absence of LCP in a given landing zone (⊙ Figure 9). Long-term studies are required to determine whether NIRS-informed stent length decisions result in better clinical outcomes.

IDENTIFICATION OF VULNERABLE PLAQUE

The identification of TCFAs as “suspected” vulnerable plaques provided a useful target that might be identified by novel intracoronary imaging methods [4]. Given the validated capabili-

FIGURE 8

Acute stent thrombosis of a DES edge implanted in a not fully covered LCP. [Jang Circ Img]

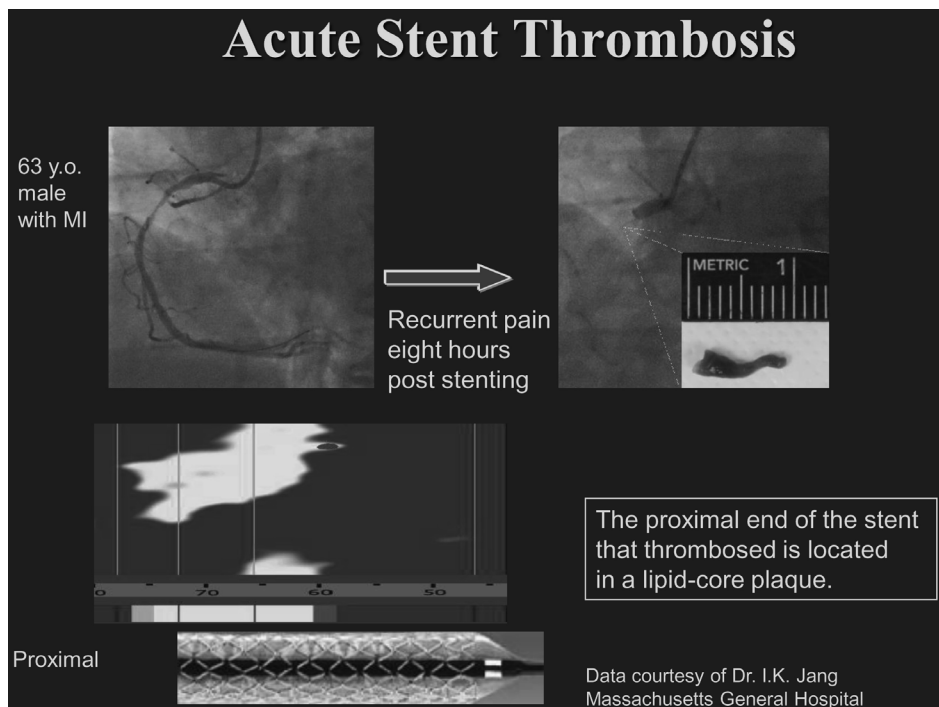
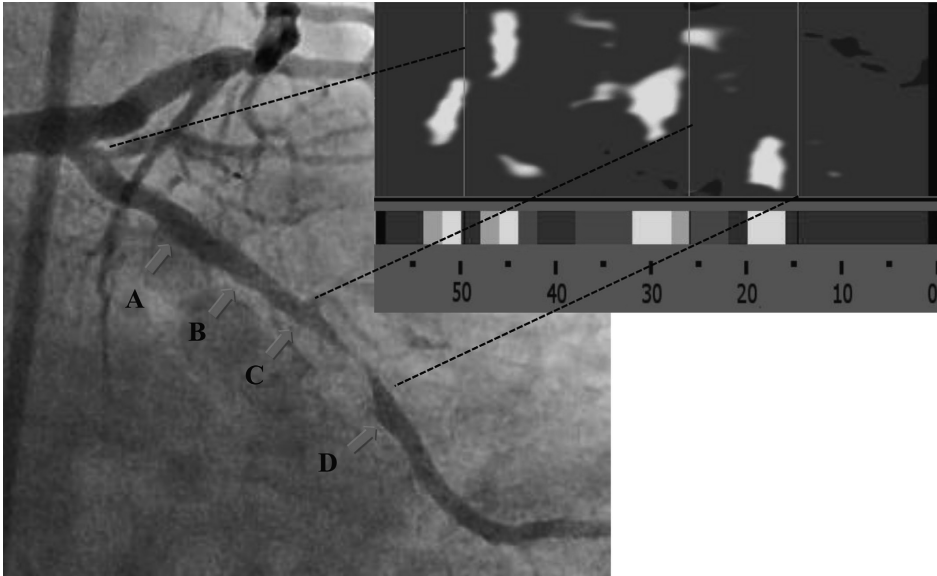


FIGURE 9**Use of NIRS to determine length of vessel to stent**

Severe circumflex stenosis between C and D with corresponding chemogram documenting LCP. Contiguous proximal plaque, though not severely narrowed, also contains LCP (A-B-C).



ties of NIRS for detection of LCP, NIRS-IVUS also has the potential for delineation of vulnerable plaques and in particular for guiding the treatment of lesions causing an intermediate degree of coronary stenosis (⊕ Figure 10). As early evidence mounts for the greater propensity for rupture and more rapid progression when LCPs are present, the presence of LCPs in angiographically intermediate stenosis may support a tailored stenting. A randomised trial of stenting of such LCP lesions of intermediate stenosis needs to be conducted to test this hypothesis. Of note is that InfraReDx, Inc. has initiated an observational study of cholesterol in coronary arteries to determine the relationship between NIRS findings and subsequent events over a 2-year period (COLOR registry, NCT00831116; see <http://clinicaltrials.gov/ct2/show/NCT00831116>). The study aims to enrol 1,000 patients in 14 centres across the USA.

ADDITIONAL CLINICAL USES

NIRS is likely to be helpful in the choice of more intensive lipid modification or anti-thrombotic therapies in some patient subgroups. The presence of extensive LCP might

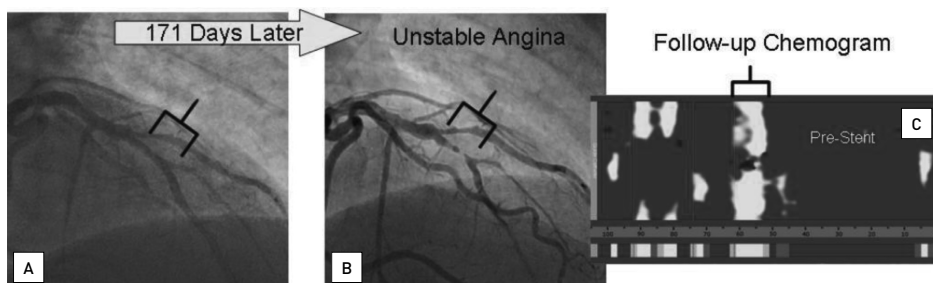
indeed indicate the need for more intensive or different types of LDL-lowering therapies.

NIRS can also be used in the development of anti-atherosclerosis medications by providing a surrogate endpoint in plaque regression/stabilisation studies. In particular, the ability of NIRS to assess the lipid content of plaques may be a more effective means of identifying the beneficial effect of an agent than IVUS. For testing these hypotheses, the IBIS-3 (Integrated Biomarker and Imaging Study) trial has begun enrolling patients at the Thoraxcenter in Rotterdam in order to determine the effect of intensive rosuvastatin therapy on the content of necrotic core (IVUS-VH) and lipid-containing regions (NIRS) at 52 weeks in a non-intervened coronary artery.

Another potential future use could be to more fully inform the decision to perform PCI vs. CABG, based on the presence, patterns and extent of LCP. Most notably changes could be envisioned in the determination of the presence of “three vessel disease” or patients that are “not candidates for PCI.” For example, it is reasonable to hypothesize that LCP-free, fibrotic stenoses in all three coronary vessels may in fact be better treated with

FIGURE 10**Chemogram of a lesion that has progressed in a patient with unstable angina**

(A) Baseline angiogram from a 59 year old male undergoing PCI in the RCA showing little to no angiographic evidence of disease in the LAD. **(B)** 171 day follow-up angiogram after presentation with unstable angina showing progression to near total occlusion. **(C)** Pre-stent chemogram showing high longitudinal and angular extent LCP very likely to also have been present at baseline.



stents. In contrast, diffuse lipid in all three vessels, either stenotic or non-stenotic, may turn out to be better treated by CABG.

FOCUS BOX 4**Potential clinical uses for NIRS**

- NIRS-IVUS delineation of plaque architecture and composition has potential to enhance performance and improve safety of PCI
- The detection of vulnerable plaque
- The identification of patients warranting more intensive lipid lowering therapy
- The accurate identification of lesion length prior to stenting
- The identification of lesions at risk of periprocedural MI

CONCLUSIONS

The structure of coronary artery plaques is an important feature of the coronary artery disease state, but traditional imaging techniques have not been able to provide accurate, easily obtainable information about plaque composition.

The presence or absence of lipid core is one of the most important compositional parameters related to both the safety of stenting and the risk of rupture of a given plaque.

NIRS has a very sound fundamental basis as a reliable method to measure lipid in a biological matrix composed of blood and tissue.

Intracoronary NIRS has been developed and rigorously validated as an accurate method for detection of lipid core plaque in patients undergoing coronary angiography.

A novel device has been constructed combining the compositional measurement provided by NIRS with the complementary structural measurement provided by IVUS in a single catheter.

Early clinical use shows promise for the use of NIRS to assist with common decisions in the catheterisation laboratory such as identification of the risk of embolic infarction following balloon inflation for a stenosis and determination of length of artery to stent.

The ability of NIRS to predict slow- or no-reflow and associated periprocedural MI, suggests the need for preventive strategies, such as NIRS-guided use or an EPD. A randomised trial of this strategy is planned.

Longer term studies are needed to assess the utility of NIRS-guided therapy to improve stenting outcomes and to determine the relationship between NIRS findings and new coronary events.

PERSONAL PERSPECTIVE – JAMES A. GOLDSTEIN

Plaque characterisation with NIRS-IVUS not only provides IVUS data on plaque architecture, but also the most accurate and validated insights on lesion composition, specifically identification of lipid core plaque (LCP). NIRS-IVUS has potential to improve the safety of stenting, including optimisation of length of vessel to stent, assurance of adequate stent deployment, and identification of lipid-core lesions at higher risk of distal embolisation possibly leading to effective utilisation of distal embolic protection devices in the native coronaries. This device also has promise in the identification of vulnerable plaque, which may lead to strategies to prevent future coronary events. Ongoing and future studies will validate whether NIRS-IVUS delineated vulnerable plaques have an increased likelihood of causing cardiac events.

REFERENCES

- Serruys PW, Morice MC, Kappetein AP, Colombo A, Holmes DR, Mack MJ, Stähle E, Feldman TE, van den Brand M, Bass EJ, Van Dyck N, Leadley K, Dawkins KD, Mohr FW; SYNTAX Investigators. Percutaneous coronary intervention versus coronary-artery bypass grafting for severe coronary artery disease. *N Engl J Med.* 2009;360:961-72.
- Boden WE, O'Rourke RA, Teo KK, Hartigan PM, Maron DJ, Kostuk WJ, Knudtson M, Dada M, Casperson P, Harris CL, Chaitman BR, Shaw L, Gosselin G, Nawaz S, Title LM, Gau G, Blaustein AS, Booth DC, Bates ER, Spertus JA, Berman DS, Mancini GB, Weintraub WS; COURAGE Trial Research Group. Optimal medical therapy with or without PCI for stable coronary disease. *N Engl J Med.* 2007;356:1503-16.
- Shaw LJ, Berman DS, Maron DJ, Mancini GB, Hayes SW, Hartigan PM, Weintraub WS, O'Rourke RA, Dada M, Spertus JA, Chaitman BR, Friedman J, Slomka P, Heller GV, Germano G, Gosselin G, Berger P, Kostuk WJ, Schwartz RG, Knudtson M, Veledar E, Bates ER, McCallister B, Teo KK, Boden WE; COURAGE Investigators. Optimal medical therapy with or without percutaneous coronary intervention to reduce ischemic burden: results from the Clinical Outcomes Utilizing Revascularization and Aggressive Drug Evaluation (COURAGE) trial nuclear substudy. *Circulation.* 2008;117:1283-91.
- Stone GW, Machara A, Lansky AJ, de Bruyne B, Cristea E, Mintz GS, Mehran R, McPherson J, Farhat N, Marso SP, Parise H, Templin B, White R, Zhang Z, Serruys PW; PROSPECT Investigators. A prospective natural-history study of coronary atherosclerosis *N Engl J Med.* 2011;20:226-35.
Prospective study in man which identified vulnerable plaques employing IVUS with virtual histology (VH).
- Virmani R, Burke AP, Farb A, Kolodgie FD. Pathology of the vulnerable plaque. *J Am Coll Cardiol.* 2006;47:C13-8.
- Yamagishi M, Terashima M, Awano K, Kijima M, Nakatani S, Daikoku S, Ito K, Yasumura Y, Miyatake K. Morphology of vulnerable coronary plaque: insights from follow-up of patients examined by intravascular ultrasound before an acute coronary syndrome. *J Am Coll Cardiol.* 2000;35:106-11.
- Fujii K, Kobayashi Y, Mintz GS, Takebayashi H, Dangas G, Moussa I, Mehran R, Lansky AJ, Kreps E, Collins M, Colombo A, Stone GW, Leon MB, Moses JW. Intravascular ultrasound assessment of ulcerated ruptured plaques: a comparison of culprit and nonculprit lesions of patients with acute coronary syndromes and lesions in patients without acute coronary syndromes. *Circulation.* 2003;108:2473-8.
- Hong MK, Mintz GS, Lee CW, Lee BK, Yang TH, Kim YH, Song JM, Han KH, Kang DH, Cheong SS, Song JK, Kim JJ, Park SW, Park SJ. The site of plaque rupture in native coronary arteries: a three-vessel intravascular ultrasound analysis. *J Am Coll Cardiol.* 2005;46:261-5.
- Goldstein JA, Demetriou D, Grines CL, Pica M, Shoukfeh M, O'Neill WW. Multiple complex coronary plaques in patients with acute myocardial infarction. *N Engl J Med.* 2000;343:915-22.
- Kolodgie FD, Burke AP, Farb A, *et al.* The thin-cap fibroatheroma: a type of vulnerable plaque: the major precursor lesion to acute coronary syndromes. *Curr Opin Cardiol.* 2001;16:285-92.
- Heusch G, Kleinbongard P, Bose D, Levkau B, Haude M, Schulz R, Erbel R. Coronary microembolization: from bedside to bench and back to bedside. *Circulation.* 2009;120:1822-36.

12. Kolodgie FD, Burke AP, Farb A, Gold HK, Yuan J, Narula J, Finn AV, Virmani R. The thin-cap fibroatheroma: a type of vulnerable plaque: the major precursor lesion to acute coronary syndromes. *Curr Opin Cardiol.* 2001;16:285-92.
Pathological description of TCFA, one of the key lesions felt to be a vulnerable plaque.
13. Prati F, Arbustini E, Labellarte A, Dal Bello B, Sommariva L, Mallus MT, Pagano A, Boccanelli A. Correlation between high frequency intravascular ultrasound and histomorphology in human coronary arteries. *Heart.* 2001;85:567-70.
14. Hiro T, Leung CY, De Guzman S, Caiozzo VJ, Farvid AR, Karimi H, Helfant RH, Tobis JM. Are soft echoes really soft? Intravascular ultrasound assessment of mechanical properties in human atherosclerotic tissue. *Am Heart J.* 1997;133:1-7.
15. Hara H, Tsunoda T, Moroi M, Kubota T, Kunimasa T, Shiba M, Wada M, Tsuji T, Iijima R, Nakajima R, Yoshitama T, Nakamura M. Ultrasound attenuation behind coronary atheroma without calcification: mechanism revealed by autopsy. *Acute cardiac care.* 2006;8:110-2.
16. Yamada R, Okura H, Kume T, Neishi Y, Kawamoto T, Watanabe N, Toyota E, Yoshida K. Histological characteristics of plaque with ultrasonic attenuation: a comparison between intravascular ultrasound and histology. *J Cardiol.* 2007;50:223-8.
17. Nair A, Kuban BD, Tuzcu EM, Schoenhagen P, Nissen SE, Vince DG. Coronary plaque classification with intravascular ultrasound radiofrequency data analysis. *Circulation.* 2002;106:2200-6.
18. Nair A, Margolis MP, Kuban BD, Vince DG. Automated coronary plaque characterisation with intravascular ultrasound backscatter: ex vivo validation. *EuroIntervention.* 2007;3:113-20.
19. Nasu K, Tsuchikane E, Katoh O, Vince DG, Virmani R, Surmely JF, Murata A, Takeda Y, Ito T, Ehara M, Matsubara T, Terashima M, Suzuki T. Accuracy of in vivo coronary plaque morphology assessment: a validation study of in vivo virtual histology compared with in vitro histopathology. *J Am Coll Cardiol.* 2006;47:2405-12.
20. Thim T, Hagnesen MK, Wallace-Bradley D, Granada JF, Kaluza GL, Drouet L, Paaske WP, Botker HE, Falk E. Unreliable assessment of necrotic core by virtual histology intravascular ultrasound in porcine coronary artery disease. *Circ Cardiovasc Imaging.* 2010;3:384-91.
Histopathological study suggesting limitations of IVUS-VH.
21. Jang IK, Tearney GJ, MacNeill B, Takano M, Moselewski F, Iftima N, Shishkov M, Houser S, Aretz HT, Halpern EF, Bouma BE. In vivo characterization of coronary atherosclerotic plaque by use of optical coherence tomography. *Circulation.* 2005;111:1551-5.
22. Kubo T, Imanishi T, Takarada S, Kuroi A, Ueno S, Yamano T, Tanimoto T, Matsuo Y, Masho T, Kitabata H, Tsuda K, Tomobuchi Y, Akasaka T. Assessment of culprit lesion morphology in acute myocardial infarction: ability of optical coherence tomography compared with intravascular ultrasound and coronary angiography. *J Am Coll Cardiol.* 2007;50:933-9.
23. Gardner CM, Tan H, Hull EL, Lissauskas JB, Sum ST, Meese TM, Jiang C, Madden SP, Caplan JD, Burke AP, Virmani R, Goldstein J, Muller JE. Detection of lipid core coronary plaques in autopsy specimens with a novel catheter-based near-infrared spectroscopy system. *JACC Cardiovasc Imaging.* 2008;1:638-48.
Autopsy study validating the accuracy of Lipiscan for the detection of LCP.
24. Waxman S, Dixon SR, L'Allier P, Moses JW, Petersen JL, Cutlip D, Tardif JC, Nesto RW, Muller JE, Hendricks MJ, Sum ST, Gardner CM, Goldstein JA, Stone GW, Krucoff MW. In vivo validation of a catheter-based near-infrared spectroscopy system for detection of lipid core coronary plaques: initial results of the SPECTACL study. *JACC Cardiovasc Imaging.* 2009;2:858-68.
Clinical study of Lipiscan catheter documenting spectral signals in humans similar to those validated by histopathological proof of LCP.
25. Schultz CJ, Serruys PW, van der Ent M, Ligthart J, Mastik F, Garg S, Muller JE, Wilder MA, van de Steen AF, Regar E. First-in-man clinical use of combined near-infrared spectroscopy and intravascular ultrasound: a potential key to predict distal embolization and no-reflow? *J Am Coll Cardiol.* 2010;56:314.
First in man use of the combined multi-modality NIRS-IVUS catheter.
26. Brugaletta S, Garcia-Garcia HM, Serruys PW, de Boer S, Ligthart J, Gomez-Lara J, Witberg K, Diletti R, Wykrzykowska J, van Geuns RJ, Schultz C, Regar E, Duckers HJ, van Mieghem N, de Jaegere P, Madden SP, Muller JE, van der Steen AF, van der Giessen WJ, Boersma E. NIRS and IVUS for Characterization of Atherosclerosis in Patients Undergoing Coronary Angiography. *JACC Cardiovasc Imaging.* 2011;4:647-55.

27. Goldstein JA, Grines C, Fischell T, Virmani R, Rizik D, Muller J, Dixon SR. Coronary embolization following balloon dilation of lipid-core plaques. *JACC Cardiovasc imaging*. 2009;2:1420-4.
28. Goldstein JA, Maini B, Dixon SR, Brilakis ES, Grines CL, Rizik DG, Powers ER, Steinberg DH, Shunk KA, Weisz G, Moreno PR, Kini A, Sharma SK, Hendricks MJ, Sum ST, Madden SP, Muller JE, Stone GW, Kern MJ. Detection of lipid-core plaques by intracoronary near-infrared spectroscopy identifies high Risk of periprocedural myocardial infarction. *Circ Cardiovascular Interv*. 2011;4:429-37.
"Connecting the dots" between LCP and distal embolisation complications.
29. Mauri L, Rogers C, Baim DS. Devices for distal protection during percutaneous coronary revascularization. *Circulation*. 2006;113:2651-6.
30. Saucedo JF, Mehran R, Dangas G, Hong MK, Lansky A, Kent KM, Satler LF, Pichard AD, Stone GW, Leon MB. Long-term clinical events following creatine kinase-myocardial band isoenzyme elevation after successful coronary stenting. *J Am Coll Cardiol*. 2000;35:1134-41.
31. Prasad A, Singh M, Lerman A, Lennon RJ, Holmes DR Jr, Rihal CS. Isolated elevation in troponin T after percutaneous coronary intervention is associated with higher long-term mortality. *J Am Coll Cardiol*. 2006;48:1765-70.
Clinical implications of periprocedural MI.
32. Selvanayagam JB, Porto I, Channon K, Petersen SE, Francis JM, Neubauer S, Banning AP. Troponin elevation after percutaneous coronary intervention directly represents the extent of irreversible myocardial injury: insights from cardiovascular magnetic resonance imaging. *Circulation*. 2005;111:1027-32.
Myocardial Injury due to periprocedural MI.
33. Mehran R, Dangas G, Mintz GS, Lansky AJ, Pichard AD, Satler LF, Kent KM, Stone GW, Leon MB. Atherosclerotic plaque burden and CK-MB enzyme elevation after coronary interventions: intravascular ultrasound study of 2256 patients. *Circulation*. 2000;101:604-10.
34. Hong YJ, Mintz GS, Kim SW, Lee SY, Okabe T, Pichard AD, Satler LF, Waksman R, Kent KM, Suddath WO, Weissman NJ. Impact of plaque composition on cardiac troponin elevation after percutaneous coronary intervention: an ultrasound analysis. *JACC Cardiovasc*. 2009;2:458-68.
35. Kotani J, Nanto S, Mintz GS, Kitakaze M, Ohara T, Morozumi T, Nagata S, Hori M. Plaque gruel of atheromatous coronary lesion may contribute to the no-reflow phenomenon in patients with acute coronary syndrome. *Circulation*. 2002;106:1672-7.
Distal embolisation of lipid contents leading to "no-reflow".
36. Kawamoto T, Okura H, Koyama Y, Toda I, Taguchi H, Tamita K, Yamamuro A, Yoshimura Y, Neishi Y, Toyota E, Yoshida K. The relationship between coronary plaque characteristics and small embolic particles during coronary stent implantation. *J Am Coll Cardiol*. 2007;50:1635-40.
37. Uetani T, Amano T, Ando H, Yokoi K, Arai K, Kato M, Marui N, Nanki M, Matsubara T, Ishii H, Izawa H, Murohara T. The correlation between lipid volume in the target lesion, measured by integrated backscatter intravascular ultrasound, and post-procedural myocardial infarction in patients with elective stent implantation. *Eur Heart J*. 2008;29:1714-20.
38. Lee MS, Park SJ, Kandzari DE, Kirtane AJ, Fearon WF, Brilakis ES, Vermeersch P, Kim YH, Waksman R, Mehilli J, Mauri L, Stone GW. Saphenous vein graft intervention. *JACC Cardiovasc Interv*. 2011;4:831-43.
39. Liu X, Tsujita K, Maehara A, Mintz GS, Weisz G, Dangas GD, Lansky AJ, Kreps EM, Rabbani LE, Collins M, Stone GW, Moses JW, Mehran R, Leon MB. Intravascular ultrasound assessment of the incidence and predictors of edge dissections after drug-eluting stent implantation. *JACC Cardiovasc Interv*. 2009;2:997-1004.
Potential benefits of IVUS to guide optimal stenting.
40. Oemrawsingh PV, Mintz GS, Schaliq MJ, Zwinderman AH, Jukema JW, van der Wall EE. Intravascular ultrasound guidance improves angiographic and clinical outcome of stent implantation for long coronary artery stenoses: final results of a randomized comparison with angiographic guidance (TULIP Study). *Circulation*. 2003;107:62-7.
41. Sakhuja R, Suh WM, Jaffer FA, Jang IK. Residual thrombogenic substrate after rupture of a lipid-rich plaque: possible mechanism of acute stent thrombosis? *Circulation*. 2010;122:2349-50.
Potential risk of subacute stent thrombosis due to uncovered LCP.
42. Waxman S, Freilich MI, Suter MJ, Shishkov M, Bilazarian S, Virmani R, Bouma BE, Tearney GJ. A case of lipid core plaque progression and rupture at the

-
- edge of a coronary stent: elucidating the mechanisms of drug-eluting stent failure. *Circ Cardiovasc Interv.* 2010;3:193-6.
43. Wijns W, Kolh P, Danchin N, Di Mario C, Falk V, Folliguet T, Garg S, Huber K, James S, Knuuti J, Lopez-Sendon J, Marco J, Menicanti L, Ostojic M, Piepoli MF, Pirlet C, Pomar JL, Reifart N, Ribichini FL, Schalij MJ, Sergeant P, Serruys PW, Silber S, Sousa Uva M, Taggart D. Guidelines on myocardial revascularization: The Task Force on Myocardial Revascularization of the European Society of Cardiology (ESC) and the European Association for Cardio-Thoracic Surgery (EACTS). *Eur Heart J.* 2010;31:2501-55.

2.2

In vivo distribution of lipid core containing plaque according to distance from the ostium by near infrared spectroscopy in non-culprit coronary arteries.

Salvatore Brugaletta, Hector M. Garcia-Garcia, Patrick W. Serruys, Josep Gomez-Lara, Sanneke de Boer, Jurgen Ligthart, Karen Witberg, Cihan Simsek, Robert Jan van Geuns, Carl Schultz, Henricus J Duckers, Nicolas van Mieghem, Peter de Jaegere, Sean P. Madden, James E. Muller, Antonius FW van der Steen, Eric Boersma, Wim J van der Giessen, Felix Zijlstra, Evelyn Regar

JACC Cardiovascular Imaging 2012;5:297-9

BRIEF REPORT

Distance of Lipid Core–Rich Plaques From the Ostium by NIRS in Nonculprit Coronary Arteries

Salvatore Brugaletta, MD,*‡ Hector M. Garcia-Garcia, MD, PhD,*†
 Patrick W. Serruys, MD, PhD,* Josep Gomez-Lara, MD,* Sanneke de Boer, MD,*
 Jurgen Ligthart, BSc,* Karen Witberg, RN,* Cihan Simsek, MD,*
 Robert-Jan van Geuns, MD, PhD,* Carl Schultz, MD, PhD,*
 Henricus J. Duckers, MD, PhD,* Nicolas van Mieghem, MD,* Peter de Jaegere, MD, PhD,*
 Sean P. Madden, PhD,§ James E. Muller, MD,§ Antonius F. W. van der Steen, PhD,*
 Eric Boersma, PhD,* Wim J. van der Giessen, MD, PhD,* Felix Zijlstra, MD, PhD,*
 Evelyn Regar, MD, PhD*

Rotterdam, the Netherlands; Barcelona, Spain; and Burlington, Massachusetts

Previous angiographic studies have failed to identify those quiescent plaques prone to progress or rupture, as most of them are non–flow limiting (1). Plaque composition was demonstrated not to be uniformly distributed along each coronary artery, and in patients with ST-segment elevation acute myocardial infarction, culprit lesions tend to cluster within the proximal third of each coronary artery (2,3). Intravascular ultrasound (IVUS) virtual histology (VH), has demonstrated higher necrotic core content of coronary plaque close to the coronary ostium compared with the distal counterpart (4).

Recently, a novel catheter-based intracoronary imaging system, based on near-infrared spectroscopy (NIRS), has been developed for the specific purpose of identification of lipid core plaque (LCP) (5). A weak correlation has been demonstrated between NIRS and VH findings for detecting lipid or necrotic core–rich plaques (6). The aim of the present study is to assess LCP distribution in nonculprit coronary arteries using NIRS.

Sixty-eight consecutive patients, in whom a nonculprit, nontreated vessel was judged suitable for a

safe NIRS pullback of 50 mm or more in length were enrolled (Table 1). The inclusion/exclusion criteria have been previously published (6). The study was conducted under the guidance of the institutional review board, and written informed consent was required.

Each region of interest (ROI), starting from the coronary ostium, was divided into 10-mm segments, corresponding to 5 block chemograms by NIRS (5). For each ROI and 10-mm segment, the mean value of the block chemogram and the number of LCP (absolute and relative) were calculated. A LCP was considered to be present if at least 1 2-mm block chemogram had a strong positive reading as signaled by yellow color, as previously described (5). The presence of at least 3 non–yellow block chemograms in-between 2 LCP was required in order to consider them as 2 independent LCP.

Categorical variables are presented using frequencies and percentages, continuous variables with mean and standard deviations or median and ranges, according to their distribution. A generalized estimating equations approach was used to compensate for any potential cluster effect of multiple lesions in the same patient. Block chemogram values per 10-mm segment are presented as least-square means with 95% confidence intervals (CI). A univariate (including age, sex, dyslipidemia, acute coronary syndrome at presentation, coronary vessel [right coronary artery (RCA) vs. the others], and distance from the ostium [segment 1 vs. the others]) and logistic generalized estimating equations approach (including all variables with a p value ≤ 0.1

From the *Thoraxcenter, Erasmus Medical Center, Rotterdam, the Netherlands; †Cardialysis BV, Rotterdam, the Netherlands; the ‡Department of Cardiology, Thorax Institute, Hospital Clinic, Barcelona, Spain; and §InfraReDx, Inc., Burlington, Massachusetts. Dr. Ligthart has a procor contract (IVUS) with Boston Scientific and teaching contracts with Volcano Inc. and St. Jude Medical. Drs. Madden and Muller are current employees of InfraReDx, Inc. Dr. Madden holds ownership interest in InfraReDx, Inc. All other authors have reported that they have no relationships relevant to the contents of this paper to disclose.

Manuscript received August 16, 2011; revised manuscript received September 21, 2011, accepted September 22, 2011.

Age, yrs	62 ± 10
Sex, male	53 (78)
Clinical history	
Dyslipidemia	41 (60)
Hypertension	40 (58)
Diabetes mellitus	15 (22)
Current smoker	39 (57)
Prior MI	29 (42)
Prior PCI	29 (42)
Prior coronary artery bypass graft	4 (5)
Clinical presentation	
Stable angina	32 (47)
Acute coronary syndromes	36 (53)
Vessel investigated by NIRS	
LAD	22 (32)
LCX	30 (44)
RCA	16 (24)
IVUS analysis	
Lumen volume, mm ³	273.39 ± 157.17
Vessel volume, mm ³	470.64 ± 289.91
Plaque burden, %	38.77 ± 12.75

Values are n (%) or mean ± SD.
 IVUS = intravascular ultrasound; LAD = left anterior descending artery; LCX = left circumflex artery; MI = myocardial infarction; NIRS = near-infrared spectroscopy; PCI = percutaneous coronary interventions; RCA = right coronary artery.

at univariate analysis) were applied to estimate the independent predictors of LCP. A 2-sided p value <0.05 indicated statistical significance. Statistical analyses were performed using SPSS 17.0 software (SPSS Inc., Chicago, Illinois).

Overall, the length of the ROI was 58.0 ± 4.3 mm, with a total of 392 10-mm segments (56 and 67

patients with 6 and 5 10-mm segments available, respectively) and 1,903 block chemograms. Per ROI, the block chemogram value and the IVUS plaque burden were 0.33 ± 0.20% and 38.77 ± 12.75%, respectively. A total of 62 LCP were identified.

Block chemogram values were differently distributed between the 3 coronary arteries (left anterior descending coronary artery [LAD]: 0.24 ± 0.15 vs. left circumflex coronary artery [LCX]: 0.35 ± 0.19 vs. RCA: 0.42 ± 0.23, p = 0.014). Forty-eight percent of the LCP were found in the LCX, 32% in the RCA, and the remaining 20% in the LAD (p = 0.107). At IVUS analysis, plaque burden tended to be higher in the RCA than in the LCx or LAD (45.17 ± 14.60% vs. 38.36 ± 10.19% vs. 35.76 ± 13.71%, p = 0.117).

The block chemogram value stratified per 10-mm segment showed a significantly different distribution in the 60 mm analyzed from the ostium (1st segment: 0.41, 95% CI: [0.34 to 0.48]; 2nd: 0.36, 95% CI: [0.29 to 0.42]; 3rd: 0.37, 95% CI: [0.30 to 0.43]; 4th: 0.32, 95% CI: [0.26 to 0.39]; 5th: 0.26, 95% CI: [0.20 to 0.33]; and 6th: 0.26, 95% CI: [0.19 to 0.33]; p = 0.011). The LCP were also differently distributed between the various segments analyzed, clustering close to the ostium (32.2% in the first 10-mm segment; 17.7% in the 2nd, 3rd, and 4th segments; 6.4% in the 5th segment; and 8.0% in the 6th segment; p < 0.001). The plaque burden did not show a significantly different distribution between the same 10-mm segments (p = 0.784).

Although the block chemogram values were confirmed to be heterogeneously distributed in the LAD and in the LCX, with the highest values closest to the ostium (LAD, p < 0.001. LCX, p = 0.001), in the RCA they were more homogeneously distributed (p = 0.155). The distribution of LCP within the 3 coronary arteries reflects this finding (Figs. 1 and 2). The distribution of plaque burden stratified per 10-mm segment was not statistically different within each coronary artery (data not shown). Distance from the ostium was the only independent predictor of LCP (odds ratio: 0.37 95% CI: [0.20 to 0.69]; p = 0.002).

The present analysis utilizes NIRS to study the longitudinal distribution of LCP in vivo. It has been demonstrated that the ability of this technique in detecting lipid/necrotic core plaques is weakly correlated with VH (6). Nevertheless, our analysis showed that the nonhomogeneity of LCP distribution along the coronary arteries is in agreement with prior anatomopathological, angiographic, and IVUS observations (2–4). In particular, LCP distribution along

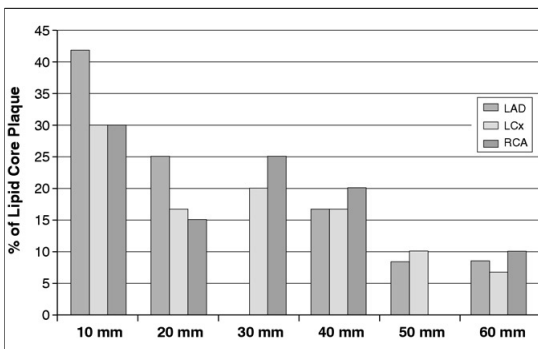


Figure 1. Percentage of LCP in the six 10-mm Segments From the Ostium in the 3 Coronary Arteries

Values of p for the distribution are 0.042 for the left anterior descending coronary artery (LAD), 0.029 for the left circumflex coronary artery (LCX), and 0.041 for the right coronary artery (RCA). LCP = lipid core plaque.

the vessel wall is independently affected by the distance from the coronary ostium, resembling the distribution of the culprit lesions in ST-segment elevation myocardial infarction patients. Presence of tortuosity or frequent branching close to the ostium may explain this finding: significant variation in shear stress has been indeed demonstrated at the level of bifurcations or bending, and low shear stress may be implicated in the migration of lipids and monocytes into the vessel wall, processes that could accelerate the progression of an atherosclerotic lesion toward a vulnerable plaque (7).

Of note is that the distribution of block chemo-gram values and of LCP was different between the 3 coronary arteries: in particular, LCP were mainly located in proximal portions of the LAD and LCX, and were more uniformly distributed in the RCA (Figs. 1 and 2). These findings are also in line with previous anatomopathological studies (2,3).

Our analysis may have important clinical implications, especially for the design and interpretation of future studies. Of note is that LCP distribution is not related to IVUS plaque burden distribution so that NIRS may provide some clues for detecting in vivo vulnerable plaques, which lead to coronary event prediction. Moreover, it is known that percutaneous treatment of LCP can cause embolization of material with periprocedural myocardial infarction (8). For this reason, percutaneous treatment of plaques located close to the LAD or LCX ostia may represent PCI at risk of embolization, whose treatment can benefit from strategies preventing embolization.

Study limitations. The small sample size is a possible limitation of our analysis, although it represents so

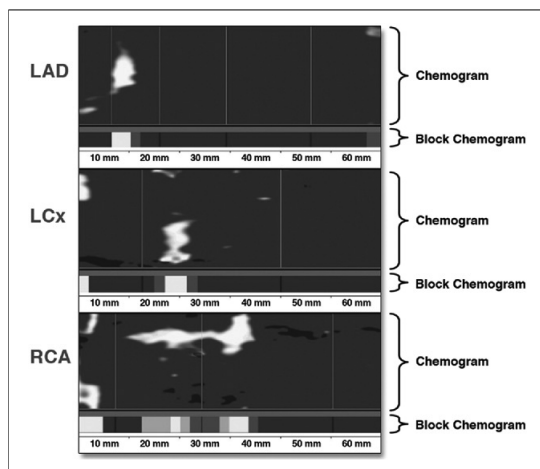


Figure 2. Examples of Distribution of LCP

The presence of LCP is indicated as **yellow**, 2-mm-long block chemo-grams, in the 3 coronary arteries, from the coronary ostium (left) up to 60 mm distally. Abbreviations as in Figure 1.

far the largest cohort of patients who have received a NIRS analysis. Of note is that our study is not a 3-vessel imaging analysis and does not include in the analysis the vessel containing the culprit lesion.

Acknowledgments

This paper is dedicated to Professor Dr. W. J. van der Giessen, who sadly passed away in June 2011.

Reprint requests and correspondence: Dr. P. W. Serruys, Interventional Cardiology Department, Erasmus Medical Center, Thoraxcenter, 's Gravendijkwal 230, 3015 CE, Rotterdam, the Netherlands. *E-mail:* p.w.j.serruys@erasmusmc.nl.

REFERENCES

1. Topol EJ, Nissen SE. Our preoccupation with coronary luminology. The dissociation between clinical and angiographic findings in ischemic heart disease. *Circulation* 1995;92:2333-42.
2. Wang JC, Normand SL, Mauri L, Kuntz RE. Coronary artery spatial distribution of acute myocardial infarction occlusions. *Circulation* 2004; 110:278-84.
3. Cheruvu PK, Finn AV, Gardner C, et al. Frequency and distribution of thin-cap fibroatheroma and ruptured plaques in human coronary arteries: a pathologic study. *J Am Coll Cardiol* 2007; 50:940-9.
4. Valgimigli M, Rodriguez-Granillo GA, Garcia-Garcia HM, et al. Distance from the ostium as an independent determinant of coronary plaque composition in vivo: an intravascular ultrasound study based radiofrequency data analysis in humans. *Eur Heart J* 2006;27:655-63.
5. Waxman S, Dixon SR, L'Allier P, et al. In vivo validation of a catheter-based near-infrared spectroscopy system for detection of lipid core coronary plaques: initial results of the SPECTACL study. *J Am Coll Cardiol Img* 2009;2: 858-68.
6. Brugaletta S, Garcia-Garcia HM, Serruys PW, et al. NIRS and IVUS for characterization of atherosclerosis in patients undergoing coronary angiography. *J Am Coll Cardiol Img* 2011;4: 647-55.
7. Cunningham KS, Gotlieb AI. The role of shear stress in the pathogenesis of atherosclerosis. *Lab Invest* 2005; 85:9-23.
8. Schultz CJ, Serruys PW, van der Ent M, et al. First-in-man clinical use of combined near-infrared spectroscopy and intravascular ultrasound: a potential key to predict distal embolization and no-reflow? *J Am Coll Cardiol* 2010;56:314.

Key Words: atherosclerosis ■ lipid-core plaques ■ near-infrared spectroscopy.

Chapter 3

Combined imaging and functional approaches for coronary atherosclerosis evaluation.

3.1

NIRS and IVUS for characterization of atherosclerosis in patients undergoing coronary angiography.

Salvatore Brugaletta, Hector M Garcia-Garcia, Patrick W. Serruys, Sanneke de Boer, Jurgen Ligthart, Josep Gomez-Lara, Karen Witberg, Roberto Diletti, Joanna Wykrzykowska, Robert Jan van Geuns, Carl Schultz, Evelyn Regar, Henricus J Duckers, Nicolas van Mieghem, Peter de Jaegere, Sean P Madden, James E Muller, Antonius FW van der Steen, Wim J van der Giessen, Eric Boersma

JACC Cardiovascular Imaging 2011;4:647-55

Atherosclerosis in Patients Undergoing Coronary Angiography

Salvatore Brugaletta, MD,*† Hector M. Garcia-Garcia, MD, PhD,*‡
 Patrick W. Serruys, MD, PhD,* Sanneke de Boer, MD,* Jurgen Ligthart, BSc,*
 Josep Gomez-Lara, MD,* Karen Witberg, RN,* Roberto Diletti, MD,*
 Joanna Wykrzykowska, MD,*|| Robert-Jan van Geuns, MD, PhD,*
 Carl Schultz, MD,* Evelyn Regar, MD, PhD,* Henricus J. Duckers, MD, PhD,*
 Nicolas van Mieghem, MD,* Peter de Jaegere, MD, PhD,* Sean P. Madden, PhD,§
 James E. Muller, MD, PhD,§ Antonius F. W. van der Steen, PhD,*
 Wim J. van der Giessen, MD, PhD,* Eric Boersma, PhD*

Rotterdam and Amsterdam, the Netherlands; Barcelona, Spain; and Burlington, Massachusetts

OBJECTIVES The aim of this study was to compare the findings of near-infrared spectroscopy (NIRS), intravascular ultrasound (IVUS) virtual histology (VH), and grayscale IVUS obtained in matched coronary vessel segments of patients undergoing coronary angiography.

BACKGROUND Intravascular ultrasound VH has been developed to add tissue characterization to the grayscale IVUS assessment of coronary plaques. Near-infrared spectroscopy is a new imaging technique able to identify lipid core-containing coronary plaques (LCP).

METHODS We performed NIRS and IVUS-VH pullbacks in a consecutive series of 31 patients with a common region of interest (ROI) between 2 side branches. For each ROI, we analyzed the chemogram blocks by NIRS, plaque area and plaque burden by grayscale IVUS, and tissue types by IVUS-VH. The chemogram block is a summary metric of a 2-mm vertical slice of the chemogram. The value ranges from 0 to 1 according to the presence of lipids and represents the probability of LCP with a color scale from red (low probability) through orange and tan to yellow (high probability).

RESULTS Plaque area (mm²) increases as percentage VH derived-necrotic core (NC) content (4.6 ± 2.7 vs. 7.4 ± 3.5 vs. 8.6 ± 3.4 vs. 7.9 ± 3.3 , grouped in percentage NC quartiles, $p < 0.001$) and chemogram block probability color bin thresholds increase (4.9 ± 3.8 red, 7.3 ± 3.6 orange, 8.1 ± 3.4 tan, and 8.7 ± 3.4 yellow, $p < 0.001$). The correlation between the block chemogram detection of lipid core and percentage NC content by VH was weak ($r = 0.149$). Correction for the presence of calcium does not improve this correlation.

CONCLUSIONS Larger plaque area by grayscale IVUS was more often associated with either elevated percentage VH-NC or LCP by NIRS; however, the correlation between the detection of LCP by NIRS and necrotic core by VH is weak. (J Am Coll Cardiol Img 2011;4:647–55) © 2011 by the American College of Cardiology Foundation

From the *Thoraxcenter, Erasmus Medical Center, Rotterdam, the Netherlands; †Department of Cardiology, Thorax Institute, Hospital Clinic, Barcelona, Spain; ‡Cardialysis BV, Rotterdam, the Netherlands; §InfraReDx, Inc., Burlington, Massachusetts; and the ||Academic Medical Center, Amsterdam, the Netherlands. Drs. Muller and Madden are current employees of InfraReDx, Inc. All other authors have reported that they have no relationships to disclose.

Manuscript received October 18, 2010; revised manuscript received March 7, 2011, accepted March 14, 2011.

lipid core-containing coronary plaques (LCP) are thought to be a cause of most acute coronary syndromes (ACS) (1,2). Near-infrared spectroscopy (NIRS), which is routinely used in science and industry to determine the chemical composition of substances, has the potential to identify such LCP *in vivo*, possibly improving patient risk stratification and guiding therapy (3). A novel intracoronary catheter system, that employs

See page 656

NIRS to detect LCP *in vivo*, has recently been developed. The system was prospectively validated versus histology in a double-blind manner with over 2,500 coronary autopsy sections (4). A clinical trial then documented that similar NIRS spectroscopy data could be acquired *in vivo* (5).

Intravascular ultrasound (IVUS)-based methods have also been developed to detect “necrotic core,” a term considered to be synonymous with “lipid core.” Necrotic core (NC) by IVUS-virtual histology (VH) has been extensively studied (6) and related to clinical characteristics (7) and cardiovascular risk score (8). Intravascular ultrasound VH has also been used for testing the efficacy of novel therapies (9) and has recently been associated with a higher risk of events in a large trial (10). Although NC detection by IVUS-VH is based on pattern classification of backscattering ultrasound signal (11), LCP detection by NIRS is based on near infrared spectral signals from coronary plaques (4).

Therefore, the aim of our study was to explore the relationship between the plaque parameters detected by NIRS (LCP) with those detected by grayscale IVUS (plaque area) and VH (VH components).

METHODS

Population. We prospectively analyzed all the consecutive patients who underwent IVUS-VH and NIRS evaluation in the same artery at our institution (Thoraxcenter, Erasmus Medical Center, Rotterdam, the Netherlands). All patients included were more than 18 years of age, with stable angina pectoris or unstable angina pectoris or with ACS. After percutaneous coronary intervention of the culprit lesion, these patients underwent imaging of a vessel that did not contain the culprit lesion. All

the study coronary vessels included were accessible to the IVUS-VH and Lipiscan (InfraReDx, Burlington, Massachusetts) catheters and had a <50% reduction in lumen diameter by angiographic visual estimation throughout a target segment of at least 40 mm in length. Coronary vessels that received a bypass graft (n = 5) with a minimal lumen diameter <2 mm or with a diameter stenosis >50% by angiographic visual estimation in the segments to be analyzed (n = 11) were excluded.

The study was conducted under the supervision of the institutional review board, and a dedicated written informed consent form was required.

Grayscale and radiofrequency IVUS analysis. Radiofrequency-IVUS with a phased-array, 20-MHz, 3.2-F catheter (Eagle Eye, Volcano Corporation, Rancho Cordova, California) was performed. During motorized catheter pullback, at 0.5 mm/s, grayscale-IVUS and raw radiofrequency data capture gated to the R-wave were recorded (s5i system, Volcano Corporation). Radiofrequency-IVUS uses spectral (frequency) analysis as well as amplitude data from the IVUS signal, which have been validated for tissue characterization against histological samples with high sensitivity and specificity (11,12).

All baseline IVUS images were prospectively analyzed offline by independent core laboratory (Cardialysis BV, Rotterdam, the Netherlands). The IVUS analyses were performed with VIAS software (Volcano Corporation). Contour detection was performed by experienced IVUS analysts who were blinded to the NIRS results (13). Quantitative grayscale IVUS measurements included vessel area, lumen area, plaque area (vessel area – lumen area) and plaque burden ($[\text{plaque area}/\text{vessel area}] \cdot 100$). For the radiofrequency-IVUS analyses, 4 tissue components (NC—red; dense calcium—white; fibrous—dark green; and fibrofatty—light green) were identified with autoregressive classification systems. Each individual tissue component was quantified and color coded in IVUS cross sections, as previously described (11,14).

NIRS analysis. The NIRS system consists of a 3.2-F rapid exchange catheter, a pullback and rotation device, and a console. A motorized catheter pullback, at 0.5 mm/s, was performed in the same artery as IVUS-VH. During the acquisition, as many landmarks as available were identified by the technicians/physicians, under fluoroscopic guidance, identifying fiducial locations such as side branches. These fiducial locations were documented by means

ABBREVIATIONS AND ACRONYMS

ACS = acute coronary syndrome(s)
GUI = graphical user interface
IVUS-VH = intravascular ultrasound-virtual histology
LCP = lipid core-containing coronary plaques
NC = necrotic core
NIRS = near-infrared spectroscopy
ROI = region of interest
VH-NC = virtual histology-necrotic core

Table 1. Demographic, Clinical, and Angiographic Characteristics of the Study Patients (n = 31)

Age, yrs	60.4 ± 9.6
Male	26 (83)
Clinical history	
Hyperlipidemia	21 (67)
Hypertension	20 (64)
Diabetes mellitus	5 (16)
Current smoker	18 (58)
Prior MI	16 (51)
Prior PCI	4 (13)
Prior coronary artery bypass graft	3 (9)
Cerebrovascular accident/transient ischemic attack	2 (6)
Family history of coronary artery disease	17 (54)
Congestive heart failure	2 (6)
Clinical presentation	
Post MI	2 (6)
Unstable angina	16 (51)
Stable angina	13 (43)
Vessel investigated by IVUS-VH and NIRS	
LAD	6 (20)
LCx	16 (51)
RCA	9 (29)

Values are mean ± SD or n (%).
 IVUS-VH = intravascular ultrasound virtual histology; LAD = left anterior descending artery; LCx = left circumflex artery; MI = myocardial infarction; NIRS = near infrared spectroscopy; PCI = percutaneous coronary interventions; RCA = right coronary artery.

of an angiogram, showing the position of the NIRS probe.

The system acquires approximately 1,000 NIRS measurements/12.5 mm of artery scanned. Each measurement interrogates an approximate volume of 1 to 2 mm³ of lumen surface perpendicular to the long axis of the catheter and centered on the optical tip of the catheter. The measurement of the probability of LCP for each scanned arterial segment is displayed as a map, with the x-axis indicating the pullback position in millimeters and the y-axis indicating the circumferential position of the measurement in degrees. The entire display is termed “chemogram,” with the probability of LCP presence coded on a color scale from red to yellow (0 for red, and 1 for yellow). To enhance interpretation of the chemogram and allow block-by-block comparison with histology (4), a summary metric (the chemogram block) is computed to display the probability that an LCP is present in each 2-mm block of the pullback, without regard to rotation. The chemogram block display in the graphical user interface (GUI) uses a binned color scale: red ($p < 0.57$), orange ($0.57 \leq p < 0.84$), tan ($0.84 \leq p < 0.98$) and yellow ($p \geq 0.98$).

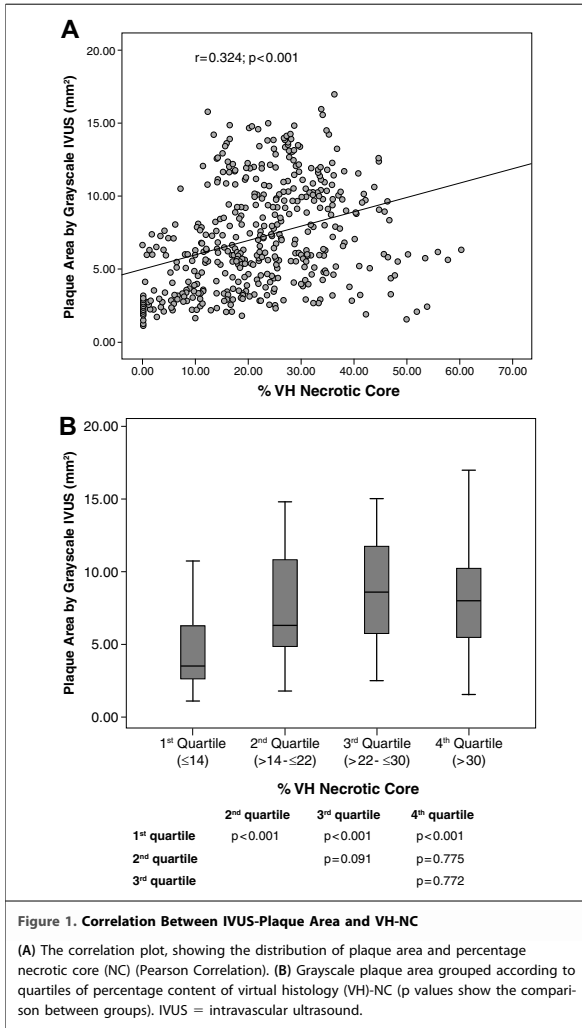
Cross-correlation of the IVUS-VH and NIRS. An independent experienced analyst, blinded to all patient clinical information, used a side-by-side view of both imaging techniques (IVUS-VH and NIRS), color blinded for IVUS-VH data. The cross correlation between the imaging data was obtained by the following 4-step method. First, the landmarks in the NIRS pullback (side branches) were identified in the angiogram. Second, the landmarks in the angiogram and in the NIRS pullback were also identified in the IVUS-VH. Third, the region so identified in NIRS and IVUS-VH pullbacks was defined as our region of interest (ROI). Fourth, the ROI identified in the IVUS-VH was divided into subregions, according to the number of chemogram blocks displayed by NIRS in that ROI (each chemogram block gives information on a region of 2 mm in length), resulting in an average of 4 VH frames/2-mm chemogram block. The percentage content of each VH component for a given collection of frames matched to a chemogram block was done in this manner: [total area of each VH component in those frames/total plaque area in those frames] · 100.

Statistical analysis. Continuous variables are expressed as mean ± SD. The percentage content of NC was divided into quartiles and used as categorical variables. The probability displayed in the chemogram block, that LCP is present, was used as continuous variable (range from 0 to 1) and also transformed into a categorical variable, according to the same values used in the binned

Table 2. Baseline Intracoronary Imaging Data/ROI (n = 31)

Grayscale IVUS and VH data	
Mean vessel area (mm ²)	13.6 ± 6.2
Mean lumen area (mm ²)	7.3 ± 3.1
Plaque burden (%)	39.5 ± 15.6
Mean plaque area (mm ²)	5.9 ± 3.9
Fibrous tissue (%)	55.6 ± 17.9
Fibrofatty tissue (%)	9.1 ± 8.6
NC tissue (%)	22.2 ± 12.1
Dense calcium (%)	12.9 ± 12.2
NIRS data	
Number of blocks/ROI	18 ± 8
Block chemogram value	0.37 ± 0.36
Block chemogram color	
Red	397 (70)
Tan	68 (12)
Orange	42 (7)
Yellow	56 (11)

Values are mean ± SD or n (%).
 NC = necrotic core; ROI = region of interest; other abbreviations as in Table 1.



color scale of the GUI (red, $p < 0.57$; orange, $0.57 \leq p < 0.84$; tan, $0.84 \leq p < 0.98$; and yellow, $p \geq 0.98$). Comparisons between groups and correlations between variables were applied, depending on normal or non-normal distribution of the variables. Statistical analysis for comparison between groups was also performed, with Bonferroni or Dunn corrections for multiple comparisons. The normal distribution was tested with the Kolmogorov-Smirnov test. No adjustments for patient or frame clustering data have been performed. A probabil-

ity value < 0.05 was considered significant, and all tests were 2-tailed. Data were analyzed with SPSS software (version 16.0, SPSS, Inc., Chicago, Illinois).

RESULTS

Population. A total of 31 patients were included in the present analysis. Table 1 shows baseline clinical characteristics. None of the patients experienced an adverse event due to the imaging acquisition.

Intracoronary imaging data. Overall, the average length of ROI was 36.0 mm, and the mean plaque burden/ROI was 39.5% with a mean value of NC of 22.2%. A mean of 18 block chemograms were identified per each ROI, exhibiting a mean value of 0.37. Most of them (70%) were coded as red in the GUI, although 11% were coded as yellow (Table 2). A total of 563 NIRS chemogram blocks were then matched with VH data.

Correlation between grayscale IVUS plaque area and VH-NC/LCP by NIRS. A large plaque area by grayscale IVUS was more often associated with elevated percentage VH-NC content ($r = 0.324$, $p < 0.001$) (Fig. 1A). In particular, grayscale plaque area, grouped according to quartiles of percentage VH-NC content, was significantly different between the quartiles (4.6 ± 2.7 mm² vs. 7.4 ± 3.5 mm² vs. 8.6 ± 3.4 mm² vs. 7.9 ± 3.3 mm², from 1st to 4th quartile, respectively, $p < 0.001$). In further analysis, the p values were statistically significant for the comparison of 1st versus 2nd, 3rd, or 4th quartile, although no differences were found between the other quartiles (Fig. 1B).

A large plaque area by grayscale IVUS was more often associated also with LCP by NIRS ($r = 0.449$, $p < 0.001$) (Fig. 2A). In particular, grayscale plaque area, grouped according to chemogram block probability color bin thresholds, was significantly different between the groups (4.9 ± 3.8 mm² red, 7.3 ± 3.6 mm² orange, 8.1 ± 3.4 mm² tan, and 8.7 ± 3.4 mm² yellow, $p < 0.001$). In the analysis comparing the various groups, p values were statistically significant for the comparison between red versus orange, tan, or yellow (Fig. 2B).

Correlation between VH and NIRS. Overall, 365 NC-rich ($\geq 10\%$ of NC% content) VH-frames were identified. Fifty-two of these (14.2%) were coded as yellow by NIRS, although 225 (61.6%) were coded as red by NIRS. Conversely, 4 of 73 NC-poor ($< 10\%$ of NC content) VH frames by IVUS-VH were coded as yellow by NIRS.

Correlation between percentage VH-NC content of plaque and chemogram block probability was weak ($r = 0.149$, $p = 0.002$) (Fig. 3A). The percentage VH-NC content, grouped according to chemogram block probability color bin thresholds, was significantly different between groups (20.6 ± 11.9 red, 23.5 ± 12.8 orange, 23.0 ± 10.7 tan, and 27.1 ± 11.7 yellow, $p = 0.002$). However, yellow showed a higher percentage VH-NC content compared with red, although no differences were found among the other groups (Fig. 3B).

The correlation between the block chemogram and the total percentage content of VH-NC and fibrofatty tissues was also weak, and the data were widely dispersed ($r = 0.252$, $p < 0.001$). Although in the lesions with a percentage content of dense calcium (DC) $>10\%$, the correlation between percentage VH-NC and block chemograms was significant and weak ($r = 0.203$, $p < 0.001$), in the lesions with a percentage content of DC $<10\%$, this correlation was not significant ($r = 0.130$, $p = 0.054$). In particular, although the block chemogram values were not different between calcified and noncalcified plaques (0.42 ± 0.43 vs. 0.40 ± 0.41 , $p = 0.484$), the percentage VH-NC was significantly higher in calcified plaques, compared with noncalcified plaques ($29.0 \pm 9.3\%$ vs. $15.5 \pm 10.6\%$, $p < 0.001$).

Figures 4 and 5 show some cases of agreement and disagreement between the 2 techniques.

DISCUSSION

The major findings of our study are: 1) NC-rich VH plaques and LCP identified by NIRS have higher grayscale plaque area than corresponding NC/lipid-poor counterparts; and 2) the correlation between the relative VH-NC content of the plaque and the values of the block chemogram of the NIRS is weak.

Near-infrared spectroscopy and IVUS-VH are 2 intracoronary imaging techniques that allow identification of plaque with high lipid/NC content, interpreting the near infrared spectral signals and the intravascular backscattering coming from the atherosclerotic plaque, respectively. There is an important consideration to make with regard to the validation of these techniques. For the validation of NIRS, a lipid core plaque was defined as a fibroatheroma with lipid core $>60^\circ$ in circumferential extent, $>200\text{-}\mu\text{m}$ -thick, with a fibrous cap having a mean thickness $<450\ \mu\text{m}$ and correlated with each chemogram block (4).

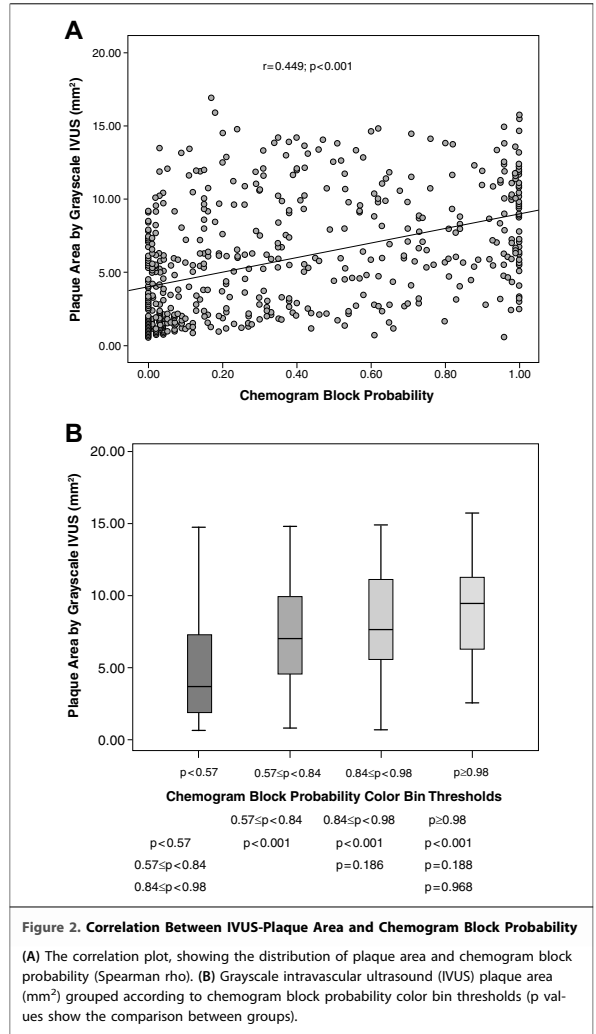


Figure 2. Correlation Between IVUS-Plaque Area and Chemogram Block Probability

(A) The correlation plot, showing the distribution of plaque area and chemogram block probability (Spearman rho). (B) Grayscale intravascular ultrasound (IVUS) plaque area (mm^2) grouped according to chemogram block probability color bin thresholds (p values show the comparison between groups).

For the validation of IVUS-VH, NC was defined as region comprising cholesterol clefts and foam cells. Some lipid components in the presence of collagen are also coded as fibrofatty tissues (11). This is of critical importance, because it might be the source of their different capabilities of detecting NC/lipid.

In this analysis, we found that plaque area increases with the increase of its VH-NC content (Fig. 1). In addition, it also increases according to the block chemogram value, with the plaques

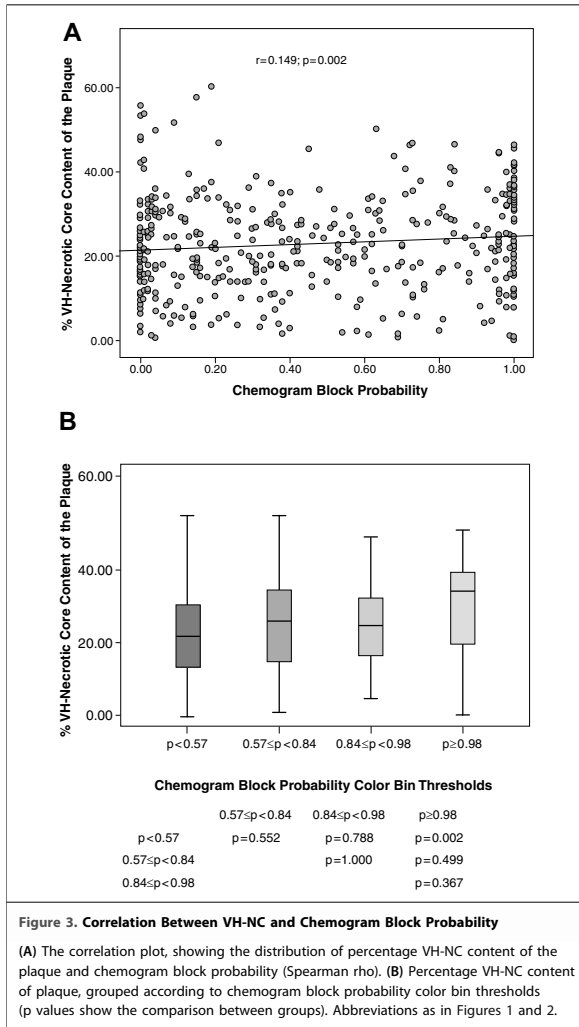


Figure 3. Correlation Between VH-NC and Chemogram Block Probability

(A) The correlation plot, showing the distribution of percentage VH-NC content of the plaque and chemogram block probability (Spearman rho). (B) Percentage VH-NC content of plaque, grouped according to chemogram block probability color bin thresholds (p values show the comparison between groups). Abbreviations as in Figures 1 and 2.

coded as yellow by NIRS having larger area, compared with those coded as red (Fig. 2). Plaque area is, indeed, an estimation of severity of atherosclerosis, and we have previously shown that it correlates with VH-NC size (15,16). Although plaque and lipid/necrotic core size are closely related, the PROSPECT (Providing Regional Observations to Study Predictors of Events in the Coronary Tree) trial has shown that both high plaque burden and thin cap NC-rich VH plaques are independent predictors of long-term events in patients after ACS (10).

Of note is that, although plaques coded as yellow by NIRS tend to have higher VH-NC than those coded as red, the data are widely dispersed, and hence, the correlation between the block chemograms and relative VH-NC is weak with low statistical significance. As previously mentioned, VH-fibrofatty tissue also includes some lipid component. However, considering relative VH-NC and VH-fibrofatty tissue together, its correlation with yellow-block chemogram was still weak.

It is also important to highlight that, unlike ultrasound, NIRS signal is not affected by an inability to cross calcium. Dense calcium was shown to have an impact on a possible artifactual measurement of NC tissue by VH (17). In our analysis we confirm this finding, showing a higher percentage VH-NC in the calcified VH lesions (>10% of DC), compared with the less-calcified counterparts, whereas block chemograms were not influenced by the presence of calcium. Excluding calcified lesions from the analysis, a potential source of incorrect classification of NC, the weak correlation between VH-NC and yellow block chemograms did not improve but rather worsened. The weakness of this correlation cannot be fully explained, because a gold-standard, such as histology, is missing in the present study. The fundamental differences in the principles of each technique—VH is based on pattern classification of backscattering ultrasound signal, whereas NIRS is based on near infrared spectral signals—and their respective limitations should be taken into account in the interpretation of this disagreement between NIRS and IVUS-VH.

In addition to incorrect classification of NC behind calcium, VH has other limitations, related to contours drawing (e.g., in presence of side branches) (18,19) and thrombus classification (18). An important consideration is also that the sensitivity and specificity of NC-VH detection is not 100% but is approximately 90% (11,12,20–22).

Conversely, Gardner et al. (4), comparing the chemogram signals and histological findings, reported that false positive reading of NIRS could be caused by fibroatheromas too small or with caps too thick to meet criteria for LCP of interest or by lesions containing significant lipid but not having NC (intimal xanthoma and pathologic intimal thickening). However, such false positives were not a failure of spectroscopy (i.e., lipid was present and generated a NIRS signal). False negative readings, by contrast, were frequently produced by small lipid cores with extensive calcification and probably dis-

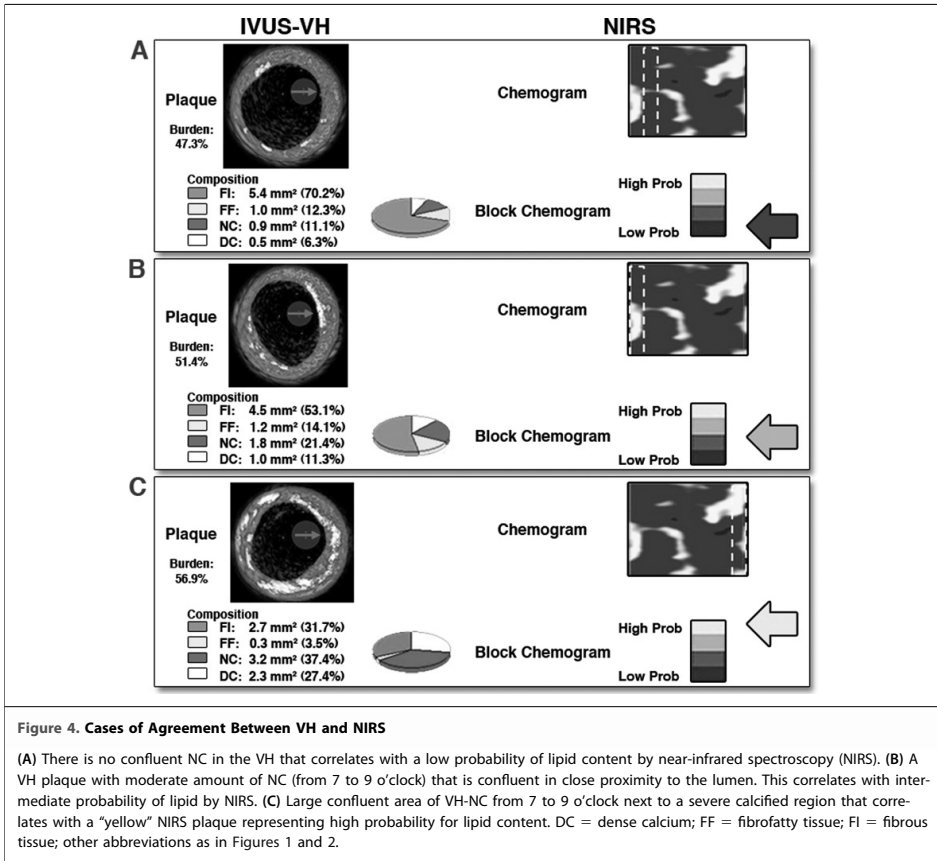


Figure 4. Cases of Agreement Between VH and NIRS

(A) There is no confluent NC in the VH that correlates with a low probability of lipid content by near-infrared spectroscopy (NIRS). (B) A VH plaque with moderate amount of NC (from 7 to 9 o'clock) that is confluent in close proximity to the lumen. This correlates with intermediate probability of lipid by NIRS. (C) Large confluent area of VH-NC from 7 to 9 o'clock next to a severe calcified region that correlates with a "yellow" NIRS plaque representing high probability for lipid content. DC = dense calcium; FF = fibrofatty tissue; FI = fibrous tissue; other abbreviations as in Figures 1 and 2.

placement of lipid by calcium or from signal obtained in a large lumen in which blood obscures the lipid signal. In addition, we can hypothesize that an eccentric position of the NIRS catheter far away from the plaque together with a fibrous cap too thick to allow the transmission of the NIR signal can explain some cases of disagreement between NIRS and VH.

A large and prospective study is necessary to compare the clinical utility of the information coming from these 2 imaging techniques, because so far neither IVUS-VH nor NIRS could be used to make treatment decisions.

Study limitations. We do not know the exact position of the NIRS catheter inside the vessel (close or far away from the plaque), possibly introducing error into the apparent angular extent of NIRS-identified LCP. A new NIRS catheter (Lipiscan IVUS, Infra-Redx) has been developed to simultaneously acquire IVUS and NIRS data, making it possible to

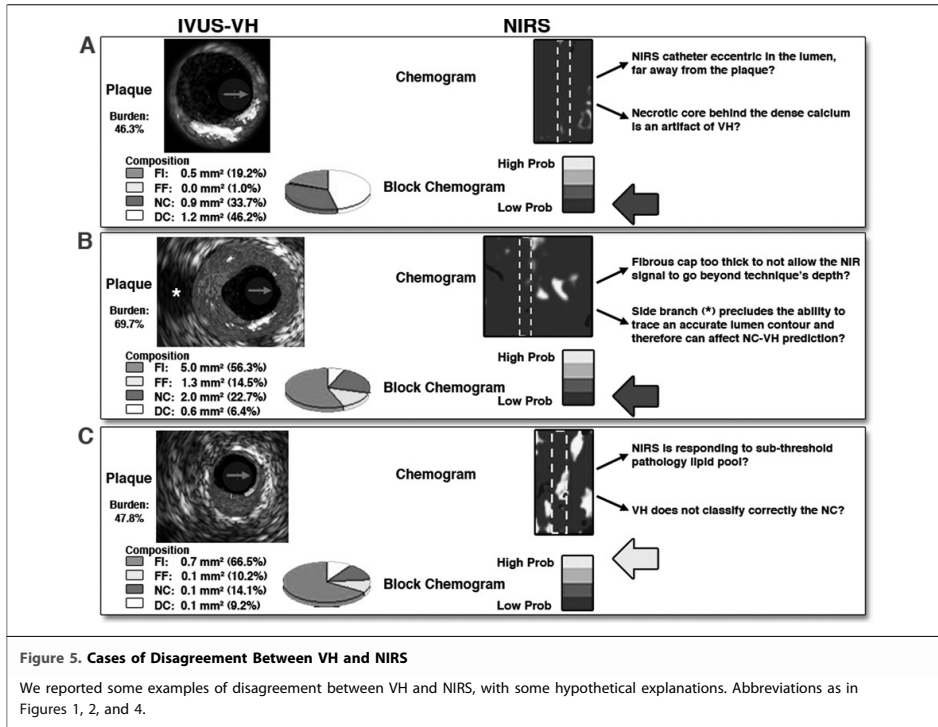
correct for this potential distortion (23,24). Although the greatest care was taken to ensure precise collocation of VH and NIRS sections, it is possible that inherent limitations therein played a role in the accuracy of the matching.

We did not explore the relationships among the cap thickness, NIRS, and VH, because other devices—namely optical coherence tomography—provide a more accurate estimation of cap thickness, compared with IVUS-VH.

Finally, the present study compares the results of 3 imaging techniques without comparison with the gold standard of histology.

CONCLUSIONS

The LCP identified by NIRS and NC-rich VH plaques tend to have bigger plaque area (on IVUS grayscale) than corresponding lipid-poor/necrotic core counterparts. However, the correlation be-



tween the detection of lipid core rich plaque by NIRS and NC by VH is weak. These findings indicate the need for a similar comparative study of the 2 imaging techniques in autopsy specimens in which the imaging results can be compared with the gold standard of histology. A comparative clinical study in which the ability of either

technique to predict clinical outcomes would also be of value.

Reprint requests and correspondence: Dr. Patrick W. Serruys, Thoraxcenter, Ba-583, 's Gravenidijkwal 230, 3015 CE, Rotterdam, the Netherlands. *E-mail:* p.w.j.serruys@erasmusmc.nl.

REFERENCES

- Kolodgie FD, Burke AP, Farb A, et al. The thin-cap fibroatheroma: a type of vulnerable plaque: the major precursor lesion to acute coronary syndromes. *Curr Opin Cardiol* 2001;16:285–92.
- Falk E, Shah PK, Fuster V. Coronary plaque disruption. *Circulation* 1995;92:657–71.
- Jaross W, Neumeister V, Latke P, Schuh D. Determination of cholesterol in atherosclerotic plaques with near infrared diffuse reflection spectroscopy. *Atherosclerosis* 1999;147:327–37.
- Gardner CM, Tan H, Hull EL, et al. Detection of lipid core coronary plaques in autopsy specimens with a novel catheter-based near-infrared spectroscopy system. *J Am Coll Cardiol Img* 2008;1:638–48.
- Waxman S, Dixon SR, L'Allier P, et al. In vivo validation of a catheter-based near-infrared spectroscopy system for detection of lipid core coronary plaques: initial results of the SPECTACL study. *J Am Coll Cardiol Img* 2009;2:858–68.
- Burke AP, Kolodgie FD, Zieske A, et al. Morphologic findings of coronary atherosclerotic plaques in diabetics: a postmortem study. *Arterioscler Thromb Vasc Biol* 2004;24:1266–71.
- Garcia-Garcia HM, Serruys PW, Mintz GS, et al. Synergistic effect of cardiovascular risk factors on necrotic core in coronary arteries: a report from the global intravascular radiofrequency data analysis registry. *J Am Coll Cardiol Img* 2009;2:629–36.
- Marso SP, Frutkin AD, Mehta SK, et al. Intravascular ultrasound measures of coronary atherosclerosis are associated with the Framingham risk score: an analysis from a global IVUS registry. *EuroIntervention* 2009;5:212–8.
- Serruys PW, Garcia-Garcia HM, Buszman P, et al. Effects of the direct lipoprotein-associated phospholipase A(2) inhibitor darapladib on human coronary atherosclerotic plaque. *Circulation* 2008;118:1172–82.
- Stone GW, Machara A, Lansky AJ, et al. A prospective natural-history study of coronary atherosclerosis. *N Engl J Med*;364:226–35.

11. Nair A, Kuban BD, Tuzcu EM, Schoenhagen P, Nissen SE, Vince DG. Coronary plaque classification with intravascular ultrasound radiofrequency data analysis. *Circulation* 2002;106:2200–6.
12. Nair A, Margolis MP, Kuban BD, Vince DG. Automated coronary plaque characterisation with intravascular ultrasound backscatter: ex vivo validation. *EuroIntervention* 2007;3:113–20.
13. Hausmann D, Lundkvist AJ, Friedrich GJ, Mullen WL, Fitzgerald PJ, Yock PG. Intracoronary ultrasound imaging: intraobserver and interobserver variability of morphometric measurements. *Am Heart J* 1994;128:674–80.
14. Serruys PW, Ormiston JA, Onuma Y, et al. A bioabsorbable everolimus-eluting coronary stent system (ABSORB): 2-year outcomes and results from multiple imaging methods. *Lancet* 2009;373:897–910.
15. Garcia-Garcia HM, Goedhart D, Serruys PW. Relation of plaque size to necrotic core in the three major coronary arteries in patients with acute coronary syndrome as determined by intravascular ultrasonic imaging radiofrequency. *Am J Cardiol* 2007;99:790–2.
16. Qian J, Maehara A, Mintz GS, et al. Relation between individual plaque components and overall plaque burden in the prospective, multicenter virtual histology intravascular ultrasound registry. *Am J Cardiol* 2009;104:501–6.
17. Sales FJ, Falcao BA, Falcao JL, et al. Evaluation of plaque composition by intravascular ultrasound “virtual histology”: the impact of dense calcium on the measurement of necrotic tissue. *EuroIntervention* 2010;6:394–9.
18. Garcia-Garcia HM, Mintz GS, Lerman A, et al. Tissue characterisation using intravascular radiofrequency data analysis: recommendations for acquisition, analysis, interpretation and reporting. *EuroIntervention* 2009;5:177–89.
19. Shin ES, Garcia-Garcia HM, Serruys PW. A new method to measure necrotic core and calcium content in coronary plaques using intravascular ultrasound radiofrequency-based analysis. *Int J Cardiovasc Imaging*;26:387–96.
20. Thim T, Hagensen MK, Wallace-Bradley D, et al. Unreliable assessment of necrotic core by virtual histology intravascular ultrasound in porcine coronary artery disease. *Circ Cardiovasc Imaging* 2010;3:384–91.
21. Granada JF, Wallace-Bradley D, Win HK, et al. In vivo plaque characterization using intravascular ultrasound-virtual histology in a porcine model of complex coronary lesions. *Arterioscler Thromb Vasc Biol* 2007;27:387–93.
22. Nasu K, Tsuchikane E, Katoh O, et al. Accuracy of in vivo coronary plaque morphology assessment: a validation study of in vivo virtual histology compared with in vitro histopathology. *J Am Coll Cardiol* 2006;47:2405–12.
23. Schultz CJ, Serruys PW, van der Ent M, et al. First-in-man clinical use of combined near-infrared spectroscopy and intravascular ultrasound: a potential key to predict distal embolization and no-reflow? *J Am Coll Cardiol* 2010;56:314.
24. Garg S, Serruys PW, van der Ent M, et al. First use in patients of a combined near infra-red spectroscopy and intra-vascular ultrasound catheter to identify composition and structure of coronary plaque. *EuroIntervention* 2010;5:755–6.

Key Words: intravascular ultrasound ■ near-infrared spectroscopy ■ virtual histology.

3.2

Assessment of Coronary Atherosclerosis Progression and Regression at Bifurcations Using Combined IVUS and OCT.

Roberto Diletti, Hector M Garcia-Garcia, Josep Gomez-Lara, Salvatore Brugaletta, Joanna J Wykrzykowska, Nienke van Ditzhuijzen, Robert Jan van Geuns, Evelyn Regar, Giuseppe Ambrosio, Patrick W Serruys

JACC Cardiovascular Imaging 2011;4:774-80

Progression and Regression at Bifurcations Using Combined IVUS and OCT

Roberto Diletti, MD,*† Hector M. Garcia-Garcia, MD, PhD,* Josep Gomez-Lara, MD,* Salvatore Brugaletta, MD,* Joanna J. Wykrzykowska, MD,* Nienke van Ditzhuijzen, MSc,* Robert Jan van Geuns, MD, PhD,* Evelyn Regar, MD, PhD,* Giuseppe Ambrosio, MD, PhD,† Patrick W. Serruys, MD, PhD*

Rotterdam, the Netherlands; and Perugia, Italy

OBJECTIVES The aim of this study was to evaluate the progression of atherosclerotic coronary plaques at bifurcations, using combined intravascular ultrasound–virtual histology (IVUS-VH) and optical coherence tomography (OCT).

BACKGROUND Pathological findings reveal that atherosclerotic plaques characterized by the presence of large necrotic cores (NCs) with fibrous cap thicknesses $< 65 \mu\text{m}$ are more prone to rupture. Accuracy in the detection of high-risk plaques could be improved by the combined use of IVUS-VH and OCT.

METHODS IVUS-VH and OCT are 2 imaging modalities with different lateral resolutions and different depths of penetration. To provide a precise matching of the images, bifurcations were used as landmarks. IVUS-VH and OCT were performed in 56 bifurcations from 24 patients at baseline and at 6-month follow-up. All patients were treated with standard medical therapy. Bifurcations were studied at the proximal, in-bifurcation, and distal regions. Plaques were classified according to their composition as assessed by IVUS-VH and fibrous cap thickness as quantified by OCT.

RESULTS At baseline, 27 NC-rich plaques were found. At 6-month follow-up, 22 (81%) did not show any significant change. Four new NC-rich lesions developed. At both time points, percent NC was higher and the fibrous cap was thinner at the proximal bifurcation rim compared with the distal. There were no significant changes in percent NC and fibrous cap thickness in the 3 bifurcation regions between baseline and follow-up examinations. No major cardiovascular events due to bifurcation lesion progression were observed.

CONCLUSIONS The combined use of IVUS-VH and OCT is a reliable tool to serially assess plaque progression and regression, and in the present study it was demonstrated to be safe and feasible. At 6-month follow-up, in this post–percutaneous coronary intervention patient population, most high-risk plaques remained unchanged, retaining their imaging classifications, nevertheless appearing to have remained clinically silent. (*J Am Coll Cardiol Img* 2011;4:774–80) © 2011 by the American College of Cardiology Foundation

From the *Department of Interventional Cardiology, Thoraxcenter, Erasmus Medical Center, Rotterdam, the Netherlands; and the †Division of Cardiology, University of Perugia School of Medicine, Perugia, Italy. All authors have reported that they have no relationships to disclose. Drs. Diletti and Garcia-Garcia contributed equally to this work.

Manuscript received February 14, 2011; accepted April 19, 2011.

Plaque rupture and subsequent activation of the clotting cascade resulting in sudden intraluminal thrombosis are thought to be the most frequent cause of acute coronary syndromes (1,2). In pathology, precursor lesions, known as thin-cap fibroatheromas (TCFA), are characterized by a large pool of necrotic core (NC) covered by a thin fibrous cap <math><65 \mu\text{m}</math> (3). The resolution of current intravascular ultrasound (IVUS) systems (100 to 200 μm) constitutes an important limitation of this technique for the measurement of fibrous cap thickness (4). Optical coherence tomography (OCT), in contrast, has higher resolution (10 to 20 μm) but low signal penetration. This can be a source of inaccurate assessment of NC size, especially in plaques with large plaque burden and positive remodeling, which is a characteristic of TCFA lesions (5). Therefore, combin-

ing the 2 imaging techniques might provide a more accurate method to investigate TCFA (6,7).

There are only a few published reports of the combined use of IVUS and OCT in vivo (6,7) and none describing the longitudinal assessment of plaque progression and regression at bifurcations. The aim of the present study was therefore to evaluate serial changes in plaque type and composition at bifurcations of the main coronary arteries using combined IVUS–virtual histology (VH) and OCT.

ABBREVIATIONS AND ACRONYMS

- IVUS = intravascular ultrasound
- NC = necrotic core
- OCT = optical coherence tomography
- TCFA = thin-cap fibroatheroma
- VH = virtual histology

METHODS

Study population. Fifty-six bifurcations were selected from 24 patients presenting with stable angina, unstable angina, or silent ischemia. All patients were treated at the Thoraxcenter, Erasmus Medical Center (Rotterdam, the Netherlands), and enrolled in 2 different stent studies (ABSORB cohort B and SECRITT). Both studies used IVUS-VH and OCT as part of their protocols.

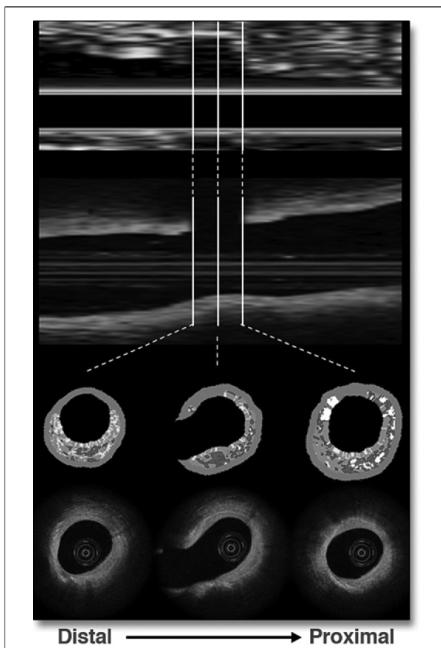


Figure 1. Frame Selection at Bifurcations

A strict selection of the analyzed cross-sections was followed to provide a correct match between the 2 imaging modalities and between baseline and follow-up. Plaques were analyzed only in the main coronary arteries at the proximal rim of the ostium of the side branch (the first frame proximal to the takeoff of the side branch), at the in-bifurcation site (the frame with the larger ostial diameter of the side branch), and at the distal rim of the ostium of the side branch (the first frame distal to the takeoff of the side branch).

Age (yrs)	67 (58–73)
Men	19 (79)
Presentation	
Stable angina	16 (67)
Unstable angina	5 (20)
Silent ischemia	3 (13)
Hypertension	18 (75)
Hypercholesterolemia	17 (71)
Diabetes	4 (17)
Smoking	5 (20)
Family history of CAD	13 (54)
Previous AMI	9 (37)
Previous PCI	10 (42)
Vessel	
LAD	11 (46)
LCX	5 (20)
RCA	8 (33)
Therapy	
Antiplatelet therapy	24 (100)
Beta-blockers	15 (62)
ACE inhibitors/ARBs	13 (54)
Statins	16 (67)
Insulin	1 (4)

Values are median (interquartile range) or n (%).
 ACE = angiotensin-converting enzyme; AMI = acute myocardial infarction;
 ARB = angiotensin II receptor blocker; CAD = coronary artery disease; LAD = left anterior descending coronary artery; LCX = left circumflex coronary artery; PCI = percutaneous coronary intervention; RCA = right coronary artery.

Variable	Baseline	Follow-Up	p Value
Vessel CSA (mm ²)			
Distal	14.01 (10.75–18.06)	13.52 (10.32–16.49)	0.051
In-bifurcation	15.62 (12.47–20.14)	14.75 (12.11–18.77)	0.543
Proximal	15.84 (12.86–20.85)	14.89 (12.23–20.83)	0.262
Luminal CSA (mm ²)			
Distal	7.23 (6.19–9.27)	7.20 (6.19–9.27)	0.012
In-bifurcation	8.46 (7.25–11.05)	7.93 (7.04–10.68)	0.184
Proximal	7.62 (6.80–9.85)	7.27 (6.00–9.75)	0.005
Plaque CSA (mm ²)			
Distal	5.68 (3.74–8.50)	6.26 (4.07–8.30)	0.231
In-bifurcation	5.79 (3.93–8.23)	6.07 (4.36–8.96)	0.144
Proximal	6.84 (5.11–10.72)	7.54 (6.00–10.86)	0.046
Plaque burden (%)			
Distal	42.74 (33.30–57.12)	49.13 (36.61–57.87)	0.004
In-bifurcation	39.38 (30.30–48.86)	42.76 (34.37–48.42)	0.027
Proximal	48.67 (39.32–58.69)	51.50 (46.39–59.54)	0.008
Minimal luminal diameter (mm)			
Distal	2.80 (2.44–3.24)	2.65 (2.29–3.18)	0.007
In-bifurcation	2.87 (2.56–3.21)	2.77 (2.48–3.29)	0.033
Proximal	2.90 (2.60–3.28)	2.78 (2.47–3.16)	0.039
Minimal vessel diameter (mm)			
Distal	3.95 (3.48–4.54)	3.88 (3.41–4.31)	0.075
In-bifurcation	4.06 (3.77–4.59)	4.06 (3.61–4.45)	0.489
Proximal	4.22 (3.81–4.69)	4.13 (3.71–4.72)	0.194
Fibrous CSA (mm ²)			
Distal	1.33 (0.13–3.23)	1.44 (0.45–2.72)	0.423
In-bifurcation	1.53 (0.52–2.83)	1.48 (0.94–2.96)	0.368
Proximal	1.65 (1.20–4.20)	2.57 (1.31–3.49)	0.329
Fibrous tissue (%)			
Distal	60.36 (40.41–70.90)	61.03 (50.83–68.17)	0.922
In-bifurcation	62.63 (50.21–69.14)	59.68 (52.75–66.83)	0.094
Proximal	58.85 (51.09–69.24)	58.18 (50.65–64.23)	0.150
Fibrofatty CSA (mm ²)			
Distal	0.18 (0.02–0.75)	0.30 (0.03–0.87)	0.498
In-bifurcation	0.26 (0.06–0.68)	0.29 (0.07–0.72)	0.739
Proximal	0.50 (0.18–1.09)	0.45 (0.23–1.16)	0.870
Fibrofatty tissue (%)			
Distal	10.54 (1.56–18.02)	10.47 (6.07–18.88)	0.299
In-bifurcation	10.99 (5.24–16.78)	10.55 (3.79–18.84)	0.504
Proximal	13.12 (6.24–23.88)	10.46 (5.53–18.48)	0.339
NC CSA (mm ²)			
Distal	0.19 (0.02–0.62)	0.39 (0.06–0.82)	0.374
In-bifurcation	0.38 (0.05–0.70)	0.50 (0.12–0.88)	0.089
Proximal	0.44 (0.44–0.13)	0.62 (0.28–1.28)	0.265
NC (%)			
Distal	9.90 (1.79–18.13)	13.95 (7.42–21.94)	0.261
In-bifurcation	12.31 (6.52–18.15)	16.10 (8.81–21.65)	0.199
Proximal	12.44 (5.92–23.15)	16.24 (8.65–20.43)	0.280

Continued on next page

Table 2. Continued

Variable	Baseline	Follow-Up	p Value
Dense calcium CSA (mm ²)			
Distal	0.08 (0.00–0.42)	0.20 (0.00–0.40)	0.021
In-bifurcation	0.10 (0.01–0.48)	0.20 (0.01–0.40)	0.005
Proximal	0.17 (0.02–0.53)	0.30 (0.01–0.70)	0.002
Dense calcium (%)			
Distal	3.29 (0.00–9.52)	4.87 (0.43–15.71)	0.031
In-bifurcation	6.70 (0.46–13.85)	7.62 (1.74–13.30)	0.124
Proximal	3.74 (0.92–9.86)	6.60 (1.89–14.55)	0.003

Values are median (interquartile range).
CSA = cross-sectional area; NC = necrotic core.

The bifurcations selected for this study were more than 5 mm away from the stented region and had side branch orifice diameters >1.5 mm as measured by OCT. Only bifurcations imaged with both modalities and for which imaging was of high quality were considered. All bifurcations fitting this inclusion criteria were included. All patients received standard medical therapy, including aspirin, clopidogrel, and statins, for at least 6 months.

IVUS-VH acquisition and analysis. IVUS acquisitions were performed using an Eagle Eye catheter (Volcano Corporation, Rancho Cordova, California) with automatic continuous pullback at a speed of 0.5 mm/s. IVUS grayscale and IVUS-VH analyses were performed offline using dedicated software (8).

OCT acquisition. The OCT M3 (Time Domain-OCT) and C7 (Fourier Domain-OCT) systems were used in this study (LightLab Imaging, Inc., Westford, Massachusetts). For each patient, the same system was used for baseline and follow-up examinations. Measurements were performed offline by 2 independent observers using LightLab imaging software.

OCT analysis. Fibrous cap thickness measurement was performed in each bifurcation frame at the thinnest part of the fibrous cap overlying the pool of NC. The reproducibility of this variable has been previously reported by our group (9).

Bifurcation matching analysis. IVUS-VH and OCT are 2 imaging modalities with different lateral resolutions and different depths of penetration. To provide a precise matching of the images, a strict selection of frames was followed using a method previously described (7). Only the main branches were analyzed, and for each bifurcation the following frames were considered: 1) the proximal rim of the side branch ostium; 2) the in-bifurcation site (the frame with the largest ostial diameter of the side branch); and 3) the distal rim of the side branch ostium (Fig. 1).

Plaque type classification. Plaques were classified according to the following previously described (7) hierarchical classification: 1) those with high percents of fibrotic tissue (adaptive intimal thickening, pathological intimal thickening, fibrotic plaque, and fibrocalcific plaque); and 2) NC-rich plaques (those with more than 10% confluent NC) (fibroatheroma and calcified fibroatheroma); if covered by fibrous caps thinner than 65 μ m, they constitute TCFA and calcified TCFA.

These plaque types are reported per location within the bifurcation (at the distal, in-bifurcation, and proximal frames) and per bifurcation, defined as the worst plaque type within the bifurcation detected among the 3 frames considered.

In addition, we introduce an IVUS-VH and OCT-derived plaque risk index, defined as the ratio between the sum of NC-rich plaques and the sum of non-NC-rich plaques in a given bifurcation region. This index was calculated for each bifurcation region at both baseline and follow-up.

Statistical analysis. Categorical variables are presented as frequencies and percents. Continuous variables are presented as medians and interquartile ranges and were compared using the Wilcoxon signed rank test. A p value <0.05 was considered statistically significant. The bifurcation was the unit of analysis, without correction for correlated observations in the same subjects. Statistical analyses were performed using SPSS version 16.0 for Windows (SPSS, Inc., Chicago, Illinois).

RESULTS

Patients' baseline clinical characteristics are reported in Table 1. The median age was 67 years, and most patients were men (79%). At follow-up, all patients were treated with statins: 6 received rosuvastatin (4 received 10 mg and 2 received 20 mg), 9 patients received simvastatin (7 received 20

Table 3. Plaque Type at Distal Rim, In-Bifurcation, and Proximal Rim at Baseline and Follow-Up and IVUS-VH and OCT-Derived Plaque Risk Index

Segment	Non-NC-Rich Plaques				NC-Rich Plaques				Plaque Risk Index*
	AIT	PIT	FT	FC	FA	CaFA	TCFA	CaTCFA	
Distal rim BL	23 (41)	4 (7.1)	9 (16.1)	3 (5.4)	6 (10.7)	10 (17.9)	0 (0)	1 (1.8)	17/39 = 0.43
Distal rim FU	19 (33.9)	6 (10.7)	10 (17.9)	2 (3.6)	5 (8.9)	12 (21.4)	0 (0)	2 (3.6)	19/37 = 0.51
In-bifurcation BL	17 (30.4)	4 (7.1)	9 (16.1)	7 (12.5)	7 (12.5)	10 (17.9)	0 (0)	2 (3.6)	19/37 = 0.51
In-bifurcation FU	12 (21.4)	6 (10.7)	8 (14.3)	8 (14.3)	9 (16.1)	10 (17.9)	1 (1.8)	2 (3.6)	22/34 = 0.65
Proximal rim BL	14 (25.0)	5 (8.9)	7 (12.5)	6 (10.7)	6 (10.7)	12 (21.4)	2 (3.6)	4 (7.1)	24/32 = 0.75
Proximal rim FU	8 (14.3)	7 (12.5)	9 (16.1)	5 (8.9)	6 (10.7)	14 (25.0)	1 (1.8)	6 (10.7)	27/29 = 0.93

Values are n (%). *Sum of NC-rich/non-NC-rich plaques.
 AIT = adaptive intimal thickening; BL = baseline; CaFA = calcified fibroatheroma; CaTCFA = calcified thin-cap fibroatheroma; FA = fibroatheroma; FC = fibrocalcific plaque; FT = fibrotic plaque; FU = follow-up; IVUS = intravascular ultrasound; NC = necrotic core; OCT = optical coherence tomography; PIT = pathological intimal thickening; TCFA = thin-cap fibroatheroma; VH = virtual histology.

mg and 2 received 40 mg), and 9 patients received atorvastatin (6 received 40 mg, 2 received 20 mg, and 1 received 10 mg).

Results from the geometrical and compositional analysis at the distal rim, in-bifurcation, and proximal rim of the side branch ostium are reported in Table 2.

At follow-up, the median vessel cross-sectional area remained unchanged at the distal, in-bifurcation, and proximal frames, while median luminal cross-sectional area decreased slightly, resulting in an increase in plaque burden (Table 2).

Fibrous and fibrofatty tissue did not change between baseline and follow-up. Median NC cross-

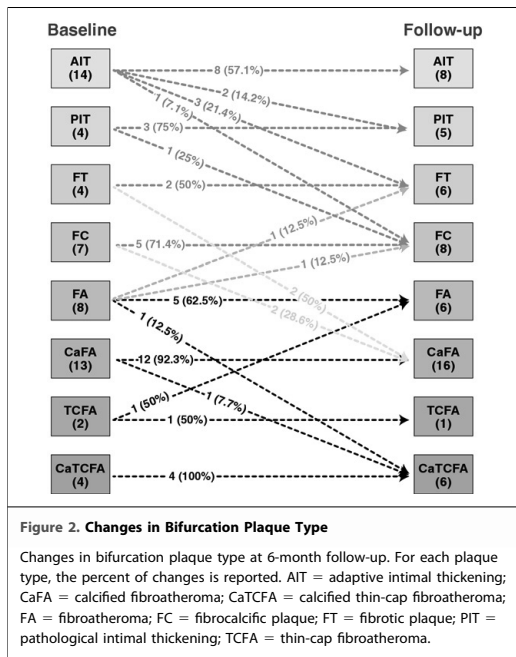
sectional area and percent NC nonsignificantly increased in each region. Dense calcium cross-sectional area significantly increased at the distal, in-bifurcation, and proximal segment (Table 2).

In NC-rich plaques (NC > 10% [fibroatheroma, calcified fibroatheroma, TCFA, and calcified TCFA]), the percent of NC nonsignificantly decreased over time at the distal rim (21.65% vs. 18.54%, $p = 0.193$), in-bifurcation (22.38% vs. 20.25%, $p = 0.573$), and proximal rim (23.15% vs. 18.06%, $p = 0.317$).

Distribution of IVUS-VH and OCT-derived plaque types at the 3 bifurcation regions. The distribution of NC-rich and NC-poor plaques is presented in Table 3. There was a gradient of disease from the proximal to the distal rim. NC-rich plaques were more frequently located at the proximal rim. Non-NC-rich plaques showed an inverse gradient. In addition, the highest value of the IVUS-VH and OCT-derived plaque risk index was found in the proximal rim of the bifurcations at both baseline and follow-up. From baseline to follow-up, the index increased in each region, implying that the number of NC regions relative to non-NC regions also increased (Table 3).

Bifurcation plaque types. At baseline, 27 NC-rich plaques were found, of which 6 were classified as thin-cap lesions (TCFA and calcified TCFA). Two fibroatheroma plaques became fibrotic and fibrocalcific (regressed), and 1 TCFA became a fibroatheroma (regressed). Two fibroatheromas became TCFA (progressed), and 22 (81%) did not change. Four new NC-rich lesions developed from fibrotic and fibrocalcific plaques. Most (83%) thin-cap lesions did not change at 6-month follow-up (Fig. 2).

Fibrous cap thickness, distribution, and changes over time. Fibrous cap thickness significantly decreased from the distal to the proximal region at both baseline and follow-up (Fig. 3). However, no changes in cap thickness were observed from base-



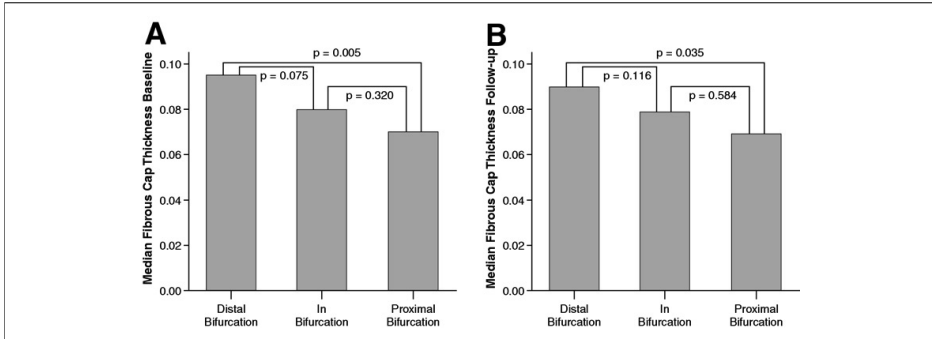


Figure 3. Fibrous Cap Thickness in the Three Regions of the Bifurcation

The fibrous cap was measured in each frame with a plaque more than 600 µm thick assessed by optical coherence tomography and with more than 10% of confluent necrotic core detected by intravascular ultrasound-virtual histology. The fibrous cap showed a progressive reduction in thickness from the distal to the proximal frame at baseline (A) and follow-up (B).

line to follow-up within each of the 3 regions (Table 4, Fig. 4). The same held for frames with thin-cap lesions, for which no changes in cap thickness were observed over time (Table 4).

DISCUSSION

The main findings of our study are as follows: 1) dual-modality acquisition and analysis at 2 different time points for the evaluation of coronary atherosclerosis is feasible, addressing the complementary limitations of the 2 imaging modalities. 2) In a post-percutaneous coronary intervention patient population treated with standard medical therapy, most NC-rich plaques remained unchanged in their composition as measured by IVUS-VH at 6-month follow-up, and most thin-cap lesions remained thin capped (<65 µm) as measured by OCT. 3) Although the study population was small, the serial imaging findings of plaque morphology were in line with the clinical outcomes.

Moreover, we observed that the proximal rim of the side branch ostium is more likely to contain a larger amount of NC and the thinnest fibrous cap within the bifurcation.

The plaque index, defined as the ratio of NC-rich to non-NC-rich frames, increased, implying a progression of the disease at 6 months. This finding is supported by the observation that in this small series, 4 new NC-rich plaques developed and 2 additional plaques became TCFA. This progression was due mostly to an increase of NC in non-NC-rich plaques (development of new NC-rich areas).

To our knowledge, this is the first in vivo study evaluating longitudinal changes in plaque type and

Table 4. Minimal Fibrous Cap Thickness at Distal, In-Bifurcation, and Proximal Segments in All NC-Rich Plaques

NC-Rich Plaques	Segment	Baseline (µm)	Follow-Up (µm)	p Value
Non-thin-cap lesions	Distal	100 (80–130)	90 (70–110)	0.206
	In-bifurcation	80 (70–100)	80 (60–100)	0.670
	Proximal	70 (50–90)	70 (60–100)	0.065
Thin-cap lesions	Distal	50 (40–50)	70 (40–90)	0.317
	In-bifurcation	50 (40–60)	50 (40–50)	0.564
	Proximal	50 (40–60)	50 (50–60)	0.084

Values are median (interquartile range).
NC = necrotic core.

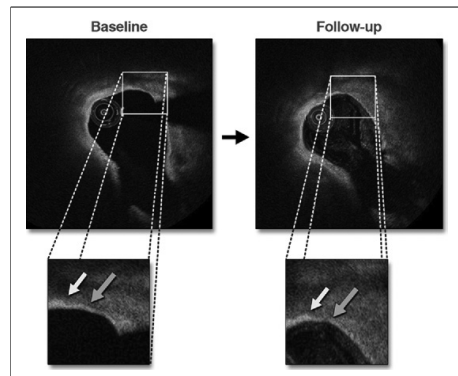


Figure 4. Thin Fibrous Cap at Baseline and Follow-Up

Thin fibrous cap did not show a statistically significant difference in cap thickness at 6-month follow-up (red arrows). The matching of the frames was done using bifurcations and also microstructures (white arrows) as landmarks.

composition using combined plaque assessment with IVUS-VH and OCT.

Sawada et al. (6) recently reported in a small series that 54% of IVUS-VH-derived TCFAs were non-thin-cap lesions by OCT, and 6.3% of OCT-derived TCFAs were not definitively TCFAs. This study strongly supports the combined use of these 2 imaging modalities, which appears to be necessary for the correct detection of high-risk plaques. In addition, Manfrini et al. (5) reported that if used alone, OCT can lead to misinterpretations due to its low signal penetration, which does not allow an accurate detection of signal-poor areas with heterogeneous compositions.

Previously, Kubo et al. (10) reported in a serial population that 75% of TCFAs detected on VH healed at 1-year follow-up. Takarada et al. (11) reported that therapy with statins significantly increased fibrous cap thickness detected with OCT in a population with untreated hypercholesterolemia. However, potentially all single-modality imaging studies could have obtained different results by combining the 2 modalities, virtually increasing accuracy for TCFA detection.

Therefore, further investigations are needed to better understand the evolution of high-risk plaques in patients with optimal medical treatment, and the combined use of IVUS-VH and OCT could be a key tool to characterize the coronary model of future events (12).

Study limitations. This study might have been underpowered to detect differences in plaque composition, and the length of follow-up was short, so the study should be considered exploratory and hypothesis generating, without formal statistical hypotheses.

Local endothelial shear stress was not measured. We cannot exclude that different plaque progression and regression might be also associated in the present series to different shear stress conditions. Because the BVS (Abbott Laboratories, Abbott Park, Illinois) is a drug-eluting device, in bifurcations located distally to the scaffold, the drug might have a considerable impact on the progression or regression of atherosclerosis.

CONCLUSIONS

The combined use of IVUS-VH and OCT is a reliable tool to serially assess plaque progression and regression, and in the present study, it was demonstrated to be safe and feasible. At 6-month follow-up, in this post-percutaneous coronary intervention patient population, most high-risk plaques remained unchanged, retaining their imaging classification, nevertheless appearing to have remained clinically silent.

Reprint requests and correspondence: Dr. Patrick W. Serruys, Erasmus Medical Center, 's-Gravendijkwal 230, 3015 CE Rotterdam, the Netherlands. *E-mail:* p.w.j.c.serruys@erasmusmc.nl.

REFERENCES

- Virmani R, Kolodgie FD, Burke AP, Farb A, Schwartz SM. Lessons from sudden coronary death: a comprehensive morphological classification scheme for atherosclerotic lesions. *Arterioscler Thromb Vasc Biol* 2000;20:1262-75.
- Burke AP, Farb A, Malcom GT, Liang YH, Smialek J, Virmani R. Coronary risk factors and plaque morphology in men with coronary disease who died suddenly. *N Engl J Med* 1997;336:1276-82.
- Virmani R, Burke AP, Farb A, Kolodgie FD. Pathology of the vulnerable plaque. *J Am Coll Cardiol* 2006;47:C13-8.
- Nair A, Vince DG, Calvetti D. "Blind" data calibration of intravascular ultrasound data for automated tissue characterization. *IEEE Ultrason Symp* 2004;2:1126-9.
- Manfrini O, Mont E, Leone O, et al. Sources of error and interpretation of plaque morphology by optical coherence tomography. *Am J Cardiol* 2006;98:156-9.
- Sawada T, Shite J, Garcia-Garcia HM, et al. Feasibility of combined use of intravascular ultrasound radiofrequency data analysis and optical coherence tomography for detecting thin-cap fibroatheroma. *Eur Heart J* 2008;29:1136-46.
- Gonzalo N, Garcia-Garcia HM, Regar E, et al. In vivo assessment of high-risk coronary plaques at bifurcations with combined intravascular ultrasound and optical coherence tomography. *J Am Coll Cardiol Img* 2009;2:473-82.
- García-García HM, Mintz GS, Lerman A, et al. Tissue characterization using intravascular radiofrequency data analysis: recommendations for acquisition, analysis, interpretation and reporting. *EuroIntervention* 2009;5:177-89.
- Barlis P, Serruys PW, Gonzalo N, van der Giessen WJ, de Jaegere PJ, Regar E. Assessment of culprit and remote coronary narrowings using optical coherence tomography with long-term outcomes. *Am J Cardiol* 2008;102:391-5.
- Kubo T, Maehara A, Mintz GS, et al. The dynamic nature of coronary artery lesion morphology assessed by serial virtual histology intravascular ultrasound tissue characterization. *J Am Coll Cardiol*;55:1590-7.
- Takarada S, Imanishi T, Kubo T, et al. Effect of statin therapy on coronary fibrous-cap thickness in patients with acute coronary syndrome: assessment by optical coherence tomography study. *Atherosclerosis* 2009;202:491-7.
- Deliangyris EN. Intravascular ultrasound virtual histology derived thin cap fibroatheroma: now you see it, now you don't. *J Am Coll Cardiol* 2010;55:1598-9.

Key Words: atherosclerosis ■ bifurcations ■ imaging ■ optical coherence tomography ■ virtual histology.

3.3

Assessment of Atherosclerotic Plaques at Coronary Bifurcations with Multidetector Computed Tomography Angiography and Intravascular Ultrasound-Virtual Histology

Stella-Lida Papadopoulou ^{a,b}, MD, Salvatore Brugaletta ^a, MD, Hector M. Garcia-Garcia ^a, MD, PhD, Alexia Rossi ^{a,b}, MD, Chrysaifios Girasis ^a, MD, Anoeshka S. Dharampal ^{a,b}, MD, Lisan A. Neefjes ^{a,b}, MD, Jurgen Ligthart ^a, BSc, Koen Nieman ^{a,b}, MD, PhD, Gabriel P. Krestin ^b, MD, PhD, Patrick W. Serruys ^a, MD, PhD, Pim J. de Feyter ^{a,b}, MD, PhD

a. Department of Cardiology, Thoraxcenter, Erasmus University Medical Center, Rotterdam, The Netherlands

b. Department of Radiology, Erasmus University Medical Center, Rotterdam, The Netherlands

European Heart Journal Cardiovascular Imaging 2012, In Press

ABSTRACT

Aims: We evaluated the distribution and composition of atherosclerotic plaques at bifurcations with intravascular ultrasound–virtual histology (IVUS-VH) and multidetector computed tomography (MDCT) in relation to the bifurcation angle (BA).

Methods and results: In 33 patients (age 63 ± 11 yrs, 79% male) imaged with IVUS-VH and MDCT, 33 bifurcations were matched and studied. The analyzed main vessel was divided into a 5-mm proximal segment, the in-bifurcation segment and a 5-mm distal segment. Plaque contours were manually traced on MDCT and IVUS-VH. Plaques with $>10\%$ confluent necrotic core and $<10\%$ dense calcium on IVUS-VH were considered high-risk, whereas plaque composition by MDCT was graded as non-calcified, calcified or mixed. The maximum bifurcation angle between the main vessel and the side branch was measured on diastolic MDCT datasets.

Overall the mean plaque area decreased from the proximal to the distal segment (8.5 ± 2.8 vs. 6.0 ± 3.0 mm² [$p<0.001$] by IVUS-VH and 9.0 ± 2.6 vs. 6.5 ± 2.5 mm² [$p<0.001$] by MDCT). Similarly, the necrotic core area was higher in the proximal compared to the distal segment (1.12 ± 0.7 vs. 0.71 ± 0.7 mm², $p=0.001$). The proximal segment had the higher percentage of high-risk plaques (13/25, 52%), followed by the in-bifurcation (6/25, 24%) and the distal segment (6/25, 24%); these plaques were characterized by MDCT as non-calcified (72%) or mixed (28%). Presence of high-risk and non-calcified plaques in the proximal segment was associated with higher BA values ($71\pm 19^\circ$ vs. $55\pm 19^\circ$, $p=0.028$ and $74\pm 20^\circ$ vs. $50\pm 14^\circ$, $p=0.001$ respectively).

Conclusion: The proximal segment of bifurcations is more likely to contain high-risk plaques, especially when the branching angle is wide.

INTRODUCTION

In patients with an atherogenic profile, plaque does not develop evenly across the entire coronary tree, but shows a predilection for sites where the laminar blood flow gets disturbed [1]. The low-oscillatory endothelial shear stress has been shown to facilitate atherosclerosis and promote the development of plaques with high-risk features [2-3]; these phenomena may explain the increased incidence of high-risk (i.e. lipid rich) plaques in the vicinity of coronary artery bifurcations [4-5].

Percutaneous treatment of coronary bifurcation lesions remains a challenging task and has been associated with higher restenosis and stent thrombosis rates [6-8]. Better understanding of the underlying pathology, such as the tissue distribution and composition, may allow for safer and more efficient treatment strategies. Intravascular ultrasound–virtual histology (IVUS-VH) is an imaging method that uses the spectral analysis of radiofrequency data to encode four different plaque components, allowing for quantification and characterization of atherosclerotic plaque [9-10].

The complex three-dimensional (3D) geometry of coronary artery bifurcations can affect the local hemodynamic conditions and thereby the plaque distribution and composition. This plausible effect mediated by the bifurcation angle (BA) can only be studied in vivo by means of imaging modalities that provide a 3D reconstruction of the bifurcation, such as multidetector computed tomography (MDCT). MDCT coronary angiography has emerged as a means of non-invasive evaluation of coronary atherosclerotic plaques; its ability to assess plaque burden, remodeling, eccentricity and composition has been based on extensive cross-sectional correlation with IVUS data in both stable and unstable patients [11-13].

The objective of the current study is two-fold: 1) to assess in vivo the distribution, composition and morphology of plaques at bifurcation sites using MDCT and IVUS-VH, and 2) to explore any possible association of the bifurcation angle (BA) with plaque distribution and composition.

METHODS

Study population

All patients admitted to our hospital between March 2008 and March 2010 who underwent both IVUS-VH and MDCT within a 2-month interval, were retrospectively screened for bifurcations adequately visualized by both imaging techniques. The indication for the IVUS-VH was the assessment of angiographically intermediate lesions and/or the result of stent implantation; MDCT was performed for either clinical or research purposes. All patients gave informed consent. Only bifurcations visualized with high quality by both imaging techniques and located at a distance greater than 10 mm from adjacent stents were considered for inclusion.

Bifurcation selection and matching

Bifurcation sites involving a side branch (SB) with an ostial diameter ≥ 1.5 mm on MDCT were only considered for inclusion; left main coronary artery bifurcations were not part of this analysis, because of their entirely different morphology [14]. In order to avoid multiple observations, only a single bifurcation site per patient, the one with the largest SB diameter, was analyzed. To ensure proper matching between IVUS-VH and MDCT, the identical bifurcations were identified using the coronary ostia and other bifurcations as landmarks. We chose to analyze only the main branch; the region of interest (ROI) comprised: 1) the proximal segment, extending 5 mm upstream from the proximal take-off of the SB; 2) the in-bifurcation segment; and 3) the distal

segment, extending 5 mm downstream from the distal take off of the SB. (Fig. 1).

IVUS-VH acquisition and analysis

The IVUS-VH imaging was performed using the Eagle Eye 20 MHz catheter (Volcano Corp., Rancho Cordova, California) with an automatic continuous pullback at a rate of 0.5 mm/s. Grayscale images and radiofrequency data required for VH analysis were acquired during the same pullback. The VH data processing was performed offline by an experienced cardiologist with VIAS software (Volcano Corp., Rancho Cordova, California) that allows semi-automated contour detection and provides the compositional analysis. Quantitative IVUS measurements included vessel area, lumen area, plaque area (vessel area minus lumen area) and plaque burden % ($[\text{plaque area}/\text{vessel area}] * 100$). For the radiofrequency-IVUS

analyses, four color-coded tissue components (necrotic core NC – red; dense calcium DC– white; fibrous FT – dark green; and fibrofatty FF– light green) were identified with autoregressive classification systems. For every frame, each individual tissue component was quantified as cross-sectional area and percentage ($\text{NC} + \text{DC} + \text{FT} + \text{FF} = 100\%$) [9, 15]. Volumetric and compositional parameters obtained per cross-section were averaged for each bifurcation segment.

MDCT acquisition

The patients were scanned with a first generation dual-source CT scanner (Somatom Definition, Siemens Healthcare, Forchheim, Germany) or a second generation dual-source CT scanner (Somatom Definition Flash, Siemens Healthcare, Forchheim, Germany) which was available after May

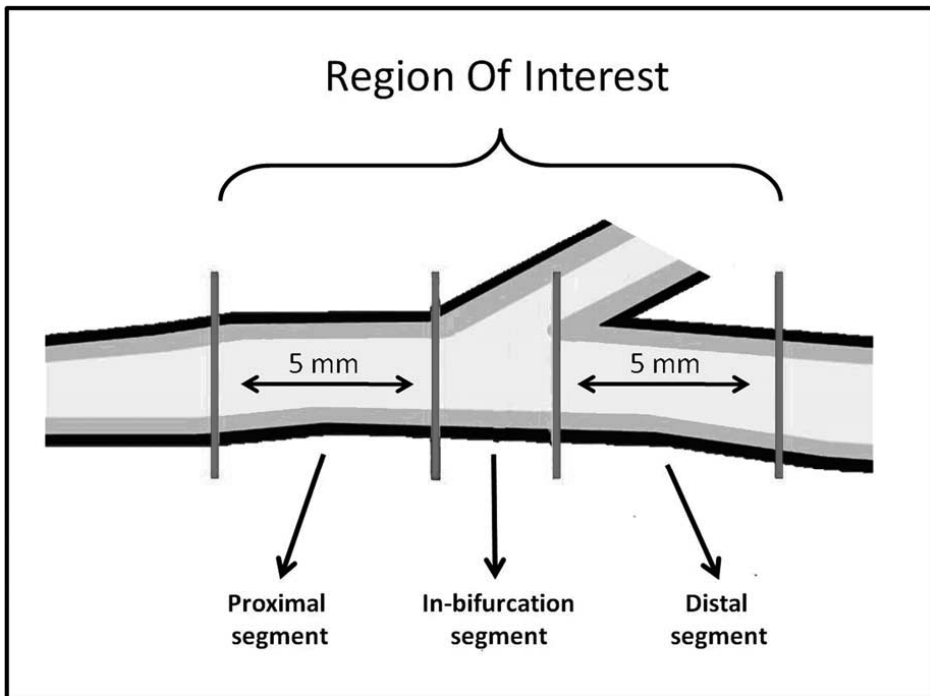


Figure 1. Bifurcation Selection and Region of Interest. Bifurcations that could be identified on both modalities were included. Only the main branch was analyzed. The region of interest consisted of: 1) the proximal 5 mm segment; 2) the in-bifurcation segment; and 3) the distal 5 mm segment.

2009. Sublingual nitroglycerin was administered prior to the scan (0.4 mg/dose), provided there were no contraindications; no prescan beta-blockers were given. An initial non-enhanced ECG gated scan (120-kV tube voltage, 75 mAs tube current and 3-mm slice thickness) was performed to calculate calcium-related scores (Agatston, volume and equivalent mass)[16-18], and was followed by a contrast enhanced CT angiography. The CT angiographic parameters were 1) for first generation dual source scanner: 32 x 2 x 0.6 mm collimation with z-flying focal spot for both detectors, gantry rotation time 330 ms, tube voltage 120 kV, current of 320 to 412 mAs and 2) for the second generation dual source scanner: 64 x 2 x 0.6 mm collimation with z-flying focal spot for both detectors, gantry rotation time 280 ms, tube voltage of 100 to 120 kV, current of 320 to 370 mAs. A bolus of iodinated contrast material (370 mg/mL, Ultravist; Schering, Berlin, Germany), which varied between 60 and 100 mL depending on the expected scan time, was injected intravenously (flow rate, 5.5 mL/sec) followed by a 40 mL saline chaser at the same injection rate. A bolus tracking technique was used to synchronize the arrival of contrast in the coronary arteries and the start of the MDCT acquisition. For acquisitions with the first generation dual source CT scanner, retrospective ECG-gated technique with ECG-pulsing was used; when scanning with the second generation dual source CT either the prospectively ECG-triggered axial scan mode ("step-and-shoot") or the retrospective ECG-gated spiral scan mode with ECG-pulsing was used, depending on the heart rate. The pitch for the retrospective scan was set automatically by the scanner software, prior to scanning. The mean effective radiation dose was 9.0 ± 3.9 mSv, using the dose-length product and a conversion factor k of 0.014 mSv/mGy/cm [19]. All MDCT coronary angiograms were reconstructed with a slice thickness 0.75 mm, an increment 0.4 mm and a medium-to-smooth (B26f) convolution kernel. Optimal datasets with the best

image quality were reconstructed mainly in the mid- to end-diastolic phase.

MDCT image analysis

All datasets from the MDCT angiography scans were transferred to a dedicated workstation (Leonardo; Siemens Medical Systems, Erlangen, Germany) for further analysis by an experienced observer, blinded to the results of the IVUS-VH analysis. After the identification of the bifurcation ROI in the original cross-sectional images, serial multiplanar reformatted images (1.0-mm slice thickness, interval 0.5-mm) orthogonal to the longitudinal axis of the main vessel were rendered to obtain cross-sectional images of the respective vessel segment (Fig. 2A). The settings for window level and width were previously optimized by an independent investigator and fixed at 740 HU and 220 HU respectively [20] (Rengo M. et al. "Optimization of Window-Level Settings in CT Coronary Angiography for the Quantification of Coronary Lumen and Plaque", submitted). Subsequently, lumen and vessel areas were manually traced in each image, and plaque areas were calculated as the difference between the vessel and lumen areas (Fig. 2D). Plaque areas measured on each cross-section were averaged for each segment and reported as mean areas.

Plaque type classification

For each one of the three bifurcation segments, the existing plaque phenotype was examined by both modalities. Based on IVUS-VH, lesions were considered present when the percentage plaque area was $\geq 40\%$ on 3 consecutive frames. Plaques with more than 10% confluent necrotic core and less than 10% dense calcium on 3 consecutive frames were classified as high-risk (i.e. necrotic core rich) and represented thick-capped fibroatheromas (VH-ThCFAs) or thin-cap fibroatheromas (VH-TCFAs), which are considered high-risk plaques according to the American Heart Association and Virmani classifications [21-22].

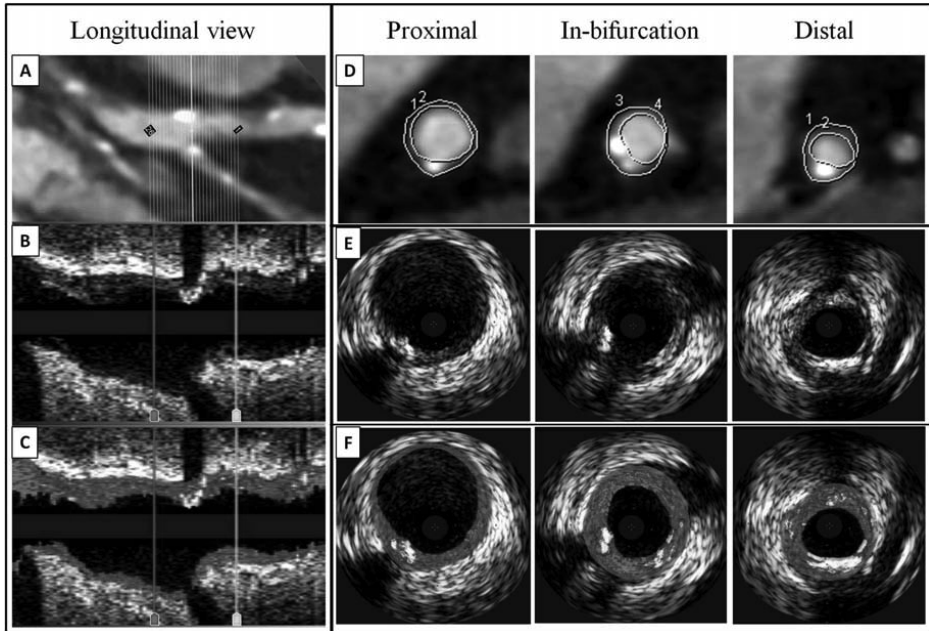


Figure 2. Bifurcation matching and analysis by MDCT and IVUS-VH.

To ensure correct matching of the bifurcations with the 2 techniques, anatomic landmarks and characteristic calcifications were used. Longitudinal vessel view by MDCT (A), grayscale IVUS (B) and virtual histology (C). Examples of corresponding analyzed cross-sections (panels D-F) in the proximal, in-bifurcation and distal segment. IVUS-VH, intravascular ultrasound-virtual histology; MDCT, multidetector computed tomography. See color figure on page 349

Based on MDCT, plaques were classified into three types: calcified plaques ($\geq 50\%$ of the plaque area occupied by calcified tissue), mixed plaques ($< 50\%$ of the plaque area occupied by calcified tissue) and non-calcified plaques which did not contain any calcium at all [11].

Measurement of Bifurcation Angles with MDCT

Multiplanar reconstructions (MPR) were rendered exactly in the plane defined by the main vessel and SB at the bifurcation site, as previously described [23]. The MPR view where the angulation between the main vessel and SB was maximal was used to determine the BA values. The angle was delineated by two centreline vectors drawn along the initial 5-mm course of the distal main vessel and SB

respectively (Fig. 3); only diastolic datasets were used for BA measurements.

Statistical analysis

Continuous variables were presented as means \pm 1 standard deviation, unless otherwise indicated, and categorical variables were reported as counts and/or percentages. The distribution of data was examined with the Shapiro-Wilk test of normality. Continuous variables were compared between different bifurcation segments and between the 2 modalities with the paired samples t-test or the Wilcoxon signed ranks test for 2 dependent samples as appropriate. The BA values were compared between groups using the unpaired t-test. A two-sided p value < 0.05 was considered statistically significant. Statistical analyses were performed using SPSS 17.0 for Windows (SPSS Inc., Chicago, Illinois).

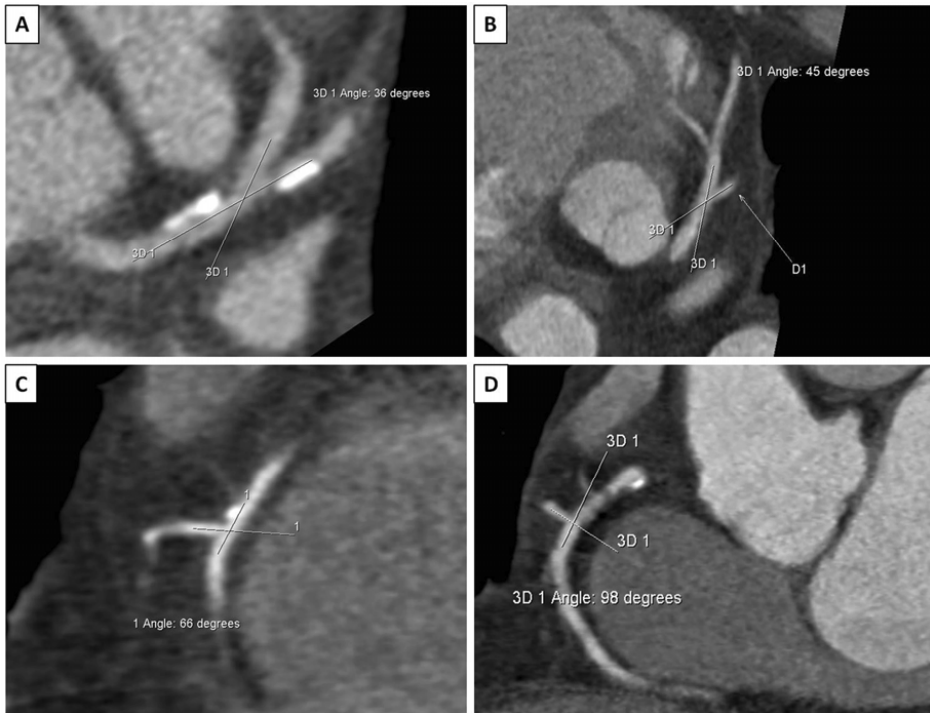


Figure 3. Coronary bifurcation angle measurements with MDCT.

Multiplanar reconstructions were rendered exactly in the plane described by the main vessel and side branch at the bifurcation site. Examples of the bifurcation angles between LAD and D1 (panel A, 36° and panel B, 45°) and between RCA and RVB (panel C, 66° and panel D, 98°). D1, first diagonal branch; LAD, left anterior descending coronary artery; MDCT, multidetector computed tomography; RCA, right coronary artery; RVB, right ventricular branch.

RESULTS

Clinical and procedural characteristics

Out of 64 consecutive patients with IVUS-VH and MDCT imaging that were screened, 38 were eligible for inclusion. Reasons for exclusion were poor MDCT or IVUS-VH image quality ($n=6$), presence of stents within the ROI ($n=9$), lack of true bifurcations (diameter of the SB ostium <1.5 mm), ($n=11$). Moreover, in 5 patients matching of bifurcations between the two imaging modalities was not possible, because more than one bifurcation were located in proximity to each other and could not be reliably identified for analysis. A total of 33 bifurcation sites from 33 patients were analyzed; mean age was 63 ± 11 years, whereas 79% of the patients were male. The

patients' characteristics are summarized in Table 1. Regarding the bifurcation location, 14 LAD/diagonal (42%), 8 LCX/marginal (24%), 8 RCA/right ventricular branch (24%) and 3 RCA/acute marginal branch (9%) were studied.

Plaque volumetric and compositional characteristics

Overall, the mean plaque area was decreased in the proximal compared to the distal segment (IVUS-VH: 8.5 ± 2.8 vs. 6.0 ± 3.0 mm², $p<0.001$ and MDCT: 9.0 ± 2.6 vs. 6.5 ± 2.5 mm², $p<0.001$ respectively). The mean percentage plaque burden was higher in the proximal compared to the distal segment (IVUS-VH: $52\% \pm 13\%$ vs. $44\% \pm 15\%$, $p=0.002$ and MDCT $51\% \pm 11\%$ vs. $46\% \pm 11\%$, $p=0.029$ respectively). The

Table 1. Baseline Patients' Characteristics, n = 33

Age (mean \pm SD), yrs	63 \pm 11
Male gender, n (%)	26 (79)
Risk factors	
Hypertension, n (%)	24 (73)
Hypercholesterolemia, n (%)	27 (82)
Diabetes mellitus, n (%)	6 (18)
Current smoking, n (%)	7 (21)
Family history of CAD, n (%)	15 (45)
Previous ACS, n (%)	10 (30)
Previous PCI, n (%)	8 (24)
Clinical presentation	
Stable angina, n (%)	24 (73)
Unstable angina, n (%)	6 (18)
Acute myocardial infarction, n (%)	3 (9)
Studied vessel	
Left anterior descending, n (%)	14 (42)
Left circumflex, n (%)	8 (24)
Right coronary artery, n (%)	11 (34)
Vessel disease, n (%)	
One vessel disease	16 (50)
Two vessel disease	13 (41)
Three vessel disease	3 (9)
Calcium-related scores*	
Agatston score	313 (147 – 842)
Equivalent mass, mg	59 (29 – 152)
Volume, mm ³	259 (150 – 701)

*Values are median (interquartile range). ACS: acute coronary syndrome; CAD: coronary artery disease; PCI: percutaneous coronary intervention; SD: standard deviation

volumetric data (Table 2) did not differ significantly between the two modalities. Finally, the mean NC area and mean percentage of NC were decreased in the proximal compared to the distal segment (Fig. 4).

Frequency of plaque type

Based on IVUS-VH, 2 bifurcations (6%) had no atherosclerotic plaques at all, whereas in 14 bifurcations (42%) the plaque was contiguous from

Table 2. Volumetric Data in Each Segment of the Bifurcation by MDCT and IVUS-VH

Parameter	Mean Values		
	MDCT (Mean \pm SD)	IVUS-VH (Mean \pm SD)	p-value for t-test
Mean plaque area (mm ²)			
Proximal	9.0 \pm 2.6	8.5 \pm 2.8	0.09
In-bifurcation	7.2 \pm 2.4	7.4 \pm 3.0	0.94
Distal	6.5 \pm 2.5	6.0 \pm 3.0	0.09
Mean plaque burden (%)			
Proximal	51 \pm 11	52 \pm 13	0.69
In-bifurcation	46 \pm 11	45 \pm 13	0.20
Distal	46 \pm 11	44 \pm 15	0.15

IVUS-VH: intravascular ultrasound-virtual histology; MDCT: multidetector computed tomography; SD: standard deviation

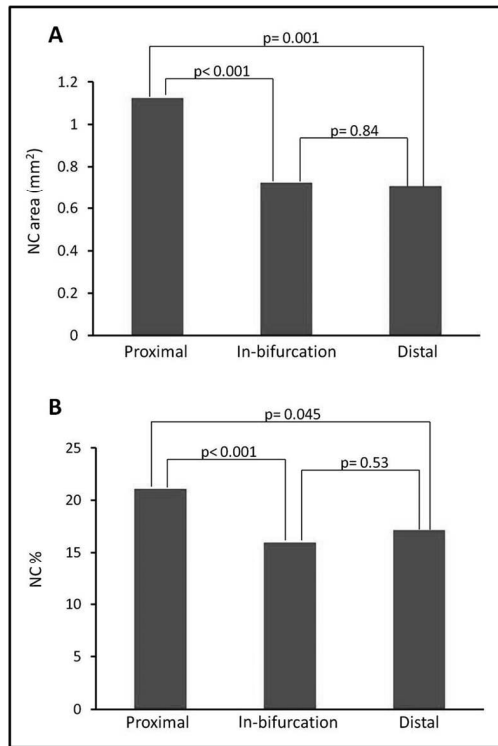


Figure 4. Necrotic core distribution.

Necrotic core (NC) area (A) and necrotic core percentage (B) distribution in the proximal, in-bifurcation and distal segments

the proximal to the distal segment. In total there were 69 bifurcation segments with plaques, 25 of which were high-risk plaques. The proximal segment had the higher percentage of high-risk plaques (13 of 25, 52%), followed by the in-bifurcation segment (6 of 25, 24%) and the distal segment (6 of 25, 24%); the distribution of the different plaque types within each segment is shown in Figure 5A. On MDCT, non-calcified plaques presented more frequently in the proximal segment, whereas the calcified plaques were more frequent in the distal segment (Fig. 5B). The majority of high-risk plaques as determined by IVUS-VH were characterized by MDCT as non-calcified ones (72%); the remaining 28% were classified as mixed. The plaque type distribution per segment is shown in Figure 6.

Plaque distribution and composition in relation to the bifurcation angle

Bifurcations containing plaques in their proximal segments had significantly larger BA values compared to those without ($p=0.002$) (Table 3). Moreover, presence of high-risk and non-calcified plaques in the proximal segment was associated with higher BA values ($71\pm 19^\circ$ vs. $55\pm 19^\circ$, $p=0.028$ and $74\pm 20^\circ$ vs. $50\pm 14^\circ$, $p=0.001$ respectively). Bifurcation angle was not related significantly with either plaque distribution or composition in the other segments.

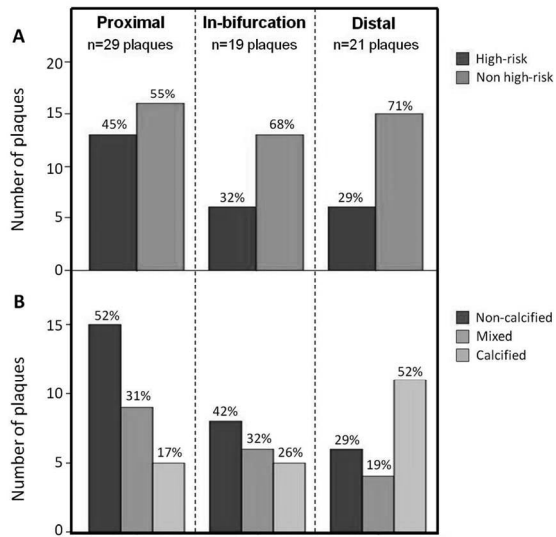


Figure 5. Distribution of the different plaque types in each segment. Panel A: virtual histology, panel B: multidetector computed tomography. The percentages indicate the frequencies of the different plaque types within each segment.

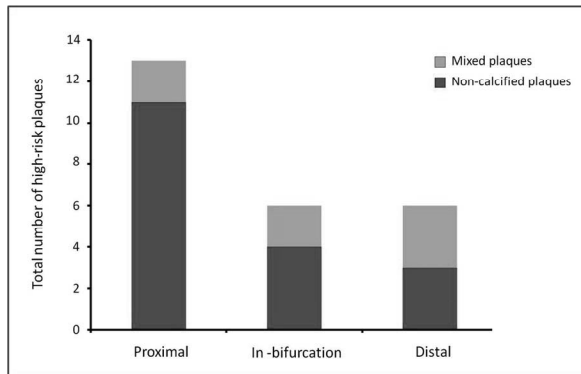


Figure 6. Classification of the high-risk plaques by MDCT.

The IVUS-VH high-risk plaques were characterized by MDCT as non-calcified and mixed. The distribution per segment is presented. IVUS-VH, intravascular ultrasound-virtual histology; MDCT, multidetector computed tomography.

Table 3. Bifurcation Angle in Relation to Plaque Distribution and Composition

Segment	Bifurcation angle		p-value
	Any plaque	No plaque	
Proximal	62 ± 20	46 ± 5	0.002
In-bifurcation	56 ± 18	66 ± 22	0.139
Distal	57 ± 20	66 ± 20	0.186
	High-risk plaques	Non high-risk plaques	
Proximal	71 ± 19	55 ± 19	0.028
In-bifurcation	49 ± 8	58 ± 20	0.155
Distal	60 ± 25	55 ± 17	0.654
	Non-calcified plaques*	Mixed/calcified plaques*	
Proximal	74 ± 20	50 ± 14	0.001
In-bifurcation	61 ± 20	52 ± 16	0.286
Distal	74 ± 22	50 ± 14	0.047

*As characterized by multidetector computed tomography

DISCUSSION

In this exploratory study we evaluated the distribution and composition of atherosclerotic plaques at coronary bifurcations using invasive and non-invasive imaging. To our knowledge, this is the first in vivo study to examine the volumetric and compositional plaque characteristics in combination with the 3D geometry of coronary bifurcations (as expressed by the bifurcation angle).

Our main findings can be summarized as follows: 1) the proximal segment has more extensive plaque burden with more necrotic core; 2) the plaques with high-risk features on IVUS-VH and the non-calcified plaques on MDCT both show a differential distribution along the bifurcation being more frequent in the proximal segment; 3) the distribution and composition of plaques in the proximal segment is associated with the BA values.

The current study corroborates earlier findings on plaque volumetric and compositional characteristics at bifurcation sites. In a previous IVUS study, Badak et al. suggested that significantly more atheroma was located proximal to the bifurcation than distally [24]. Han et al. expanded on these findings [14] using

IVUS-VH to report on tissue characterisation; that study showed that plaque burden and percentage of necrotic core were significantly larger in the proximal segment of the non-left main bifurcations. These data appear to be largely concordant with a prior report by Gonzalo et al. [5] using IVUS-VH and Optical Coherence Tomography (OCT); they suggested that the percentage of necrotic core was higher at the proximal "rim" of the bifurcation. It has been shown that the distribution of inflammatory cells in atherosclerotic plaques is associated with the direction of the arterial flow, with higher content of macrophages in the upstream (proximal) part [25]. The differential distribution of the necrotic core and the high-risk plaques along the coronary tree could be attributed to the influence of local hemodynamic factors altered at bifurcation sites.

Our data demonstrated that predominantly non-calcified plaque type by MDCT corresponded to the IVUS-VH high-risk phenotype. This finding is in agreement with histopathology studies [22] and with previous greyscale IVUS studies showing that plaques with low echogenicity (presumably lipid rich) are mainly soft (non-calcified) by MDCT [11, 26-27]. Conversely, other studies suggested that mixed plaques on MDCT are associated more frequently

with high-risk features on IVUS-VH [28-29]. A recent more systematic evaluation [30] demonstrated that only the non-calcified plaques with small (<1 mm) spotty calcifications on MDCT were associated with plaque characteristics deemed more high-risk on IVUS-VH, however these plaques did not have significantly more VH-TCFAs compared to non-calcified plaques. In our analysis, the ROI included only plaques located within 5-mm long segments proximal and distal to the SB; since atherosclerotic plaque can be diffuse, in case a spotty calcification was located outside this ROI, it would have not been included in our analysis.

The present study extended the assessment of bifurcation lesions beyond volumetric and compositional analysis by integrating the MDCT based BA measurements, which emphasizes the added value of this 3D imaging modality. Our *in vivo* data showed that the presence and phenotype of atherosclerotic plaque in the proximal bifurcation segment is related to the BA size. This finding could be supported by computational fluid dynamics [31-33] and histopathology [34] studies demonstrating that the hemodynamic phenomena important in atherogenesis are more pronounced in widely angulated bifurcations. Moreover, the BA size has been described as a determinant of treatment strategy in bifurcation lesions [35]. In numerous bench and clinical studies [36-40] a wide BA has been associated with a greater risk for suboptimal post-procedural result and long-term adverse clinical events. Additionally, our data demonstrated that a wide BA is associated with greater plaque burden and a high-risk phenotype of bifurcation lesions, which make us speculate that necrotic core rich plaques could be related to the higher restenosis and thrombosis rates [41-43]. Eventually, a comprehensive assessment of bifurcation lesions including plaque characterisation and BA measurements could lead to optimized interventional strategies and improved long-term clinical outcomes

LIMITATIONS

Although this is the first study combining invasive and non-invasive imaging of bifurcations, it was retrospectively performed in a selected patient population undergoing invasive and non-invasive imaging, thus generalization of our results should be done with caution. Given the inclusion of a limited number of patients, the possibility of a type II error should be considered and multivariate analysis for risk factors was not performed. Furthermore, the limited axial resolution of IVUS (approximately 200 μm) does not permit an accurate evaluation of the thin fibrous cap (<65 μm). A proposed method of combined use of IVUS-VH and OCT [5, 44] could facilitate more accurate identification of VH-TCFAs, but was not available for this study. Finally, the radiation exposure during MDCT coronary angiography remains a matter of concern; significant reduction of radiation dose can currently be achieved by implementation of dose-saving techniques [45].

CONCLUSIONS

This study extended the evaluation of bifurcation lesions beyond volumetric and compositional analysis by integrating information on the geometry of coronary bifurcations. Larger plaque burden and increased necrotic core content were found in the proximal bifurcation segments. The high-risk plaques on IVUS-VH and the non-calcified plaques on MDCT tend to accumulate in the proximal bifurcation segments, especially in the presence of a wide BA.

CONFLICT OF INTEREST

The authors declare no conflicts of interest relevant to the content of this paper.

REFERENCES

1. Malek AM, Alper SL, Izumo S. Hemodynamic shear stress and its role in atherosclerosis. *JAMA* 1999;282:2035-2042.
2. Chatzizisis YS, Jonas M, Coskun AU, Beigel R, Stone BV, Maynard C, *et al*. Prediction of the localization of high-risk coronary atherosclerotic plaques on the basis of low endothelial shear stress: an intravascular ultrasound and histopathology natural history study. *Circulation* 2008;117:993-1002.
3. Slager CJ, Wentzel JJ, Gijzen FJ, Schuurbiers JC, van der Wal AC, van der Steen AF, *et al*. The role of shear stress in the generation of rupture-prone vulnerable plaques. *Nat Clin Pract Cardiovasc Med* 2005;2:401-407.
4. Garcia-Garcia HM, Gomez-Lara J, Gonzalo N, Garg S, Shin ES, Goedhart D, *et al*. A comparison of the distribution of necrotic core in bifurcation and non-bifurcation coronary lesions: an in vivo assessment using intravascular ultrasound radiofrequency data analysis. *EuroIntervention* 2010;6:321-327.
5. Gonzalo N, Garcia-Garcia HM, Regar E, Barlis P, Wentzel J, Onuma Y, *et al*. In vivo assessment of high-risk coronary plaques at bifurcations with combined intravascular ultrasound and optical coherence tomography. *JACC Cardiovasc Imaging* 2009;2:473-482.
6. Colombo A, Moses JW, Morice MC, Ludwig J, Holmes DR, Jr., Spanos V, *et al*. Randomized study to evaluate sirolimus-eluting stents implanted at coronary bifurcation lesions. *Circulation* 2004;109:1244-1249.
7. Ge L, Airolidi F, Iakovou I, Cosgrave J, Michev I, Sangiorgi GM, *et al*. Clinical and angiographic outcome after implantation of drug-eluting stents in bifurcation lesions with the crush stent technique: importance of final kissing balloon post-dilation. *J Am Coll Cardiol* 2005;46:613-620.
8. Routledge HC, Lefevre T, Colombo A, Oldroyd KG, Hamm CW, Guagliumi G, *et al*. Three-year clinical outcome of percutaneous treatment of bifurcation lesions in multivessel coronary artery disease with the sirolimus-eluting stent: insights from the Arterial Revascularisation Therapies Study, part II (ARTS II). *EuroIntervention* 2009;5:190-196.
9. Nair A, Kuban BD, Tuzcu EM, Schoenhagen P, Nissen SE, Vince DG. Coronary plaque classification with intravascular ultrasound radiofrequency data analysis. *Circulation* 2002;106:2200-2206.
10. Nasu K, Tsuchikane E, Katoh O, Vince DG, Virmani R, Surmely JF, *et al*. Accuracy of in vivo coronary plaque morphology assessment: a validation study of in vivo virtual histology compared with in vitro histopathology. *J Am Coll Cardiol* 2006;47:2405-2412.
11. Leber AW, Becker A, Knez A, von Ziegler F, Sirol M, Nikolaou K, *et al*. Accuracy of 64-slice computed tomography to classify and quantify plaque volumes in the proximal coronary system: a comparative study using intravascular ultrasound. *J Am Coll Cardiol* 2006;47:672-677.
12. Papadopoulou SL, Neeffes LA, Schaap M, Li HL, Capuano E, van der Giessen AG, *et al*. Detection and quantification of coronary atherosclerotic plaque by 64-slice multidetector CT: A systematic head-to-head comparison with intravascular ultrasound. *Atherosclerosis* 2011.
13. Voros S, Rinehart S, Qian Z, Vazquez G, Anderson H, Murrieta L, *et al*. Prospective validation of standardized, 3-dimensional, quantitative coronary computed tomographic plaque measurements using radiofrequency backscatter intravascular ultrasound as reference standard in intermediate coronary arterial lesions: results from the ATLANTA (assessment of tissue characteristics, lesion morphology, and hemodynamics by angiography with fractional flow reserve, intravascular ultrasound and virtual histology, and noninvasive computed tomography in atherosclerotic plaques) I study. *JACC Cardiovasc Interv* 2011;4:198-208.
14. Han SH, Puma J, Garcia-Garcia HM, Nasu K, Margolis P, Leon MB, *et al*. Tissue characterization of atherosclerotic plaque in coronary artery bifurcations: an intravascular ultrasound

- radiofrequency data analysis in humans. *EuroIntervention* 2010;6:313-320.
15. Garcia-Garcia HM, Mintz GS, Lerman A, Vince DG, Margolis MP, van Es GA, *et al.* Tissue characterisation using intravascular radiofrequency data analysis: recommendations for acquisition, analysis, interpretation and reporting. *EuroIntervention* 2009;5:177-189.
 16. Agatston AS, Janowitz WR, Hildner FJ, Zusmer NR, Viamonte M, Jr., Detrano R. Quantification of coronary artery calcium using ultrafast computed tomography. *J Am Coll Cardiol* 1990;15:827-832.
 17. Callister TQ, Coil B, Raya SP, Lippolis NJ, Russo DJ, Raggi P. Coronary artery disease: improved reproducibility of calcium scoring with an electron-beam CT volumetric method. *Radiology* 1998;208:807-814.
 18. Hoffmann U, Siebert U, Bull-Stewart A, Achenbach S, Ferencik M, Moselewski F, *et al.* Evidence for lower variability of coronary artery calcium mineral mass measurements by multi-detector computed tomography in a community-based cohort--consequences for progression studies. *Eur J Radiol* 2006;57:396-402.
 19. Bongartz G, Golding SJ, Jurik AG, Leonardi M, van Persijn van Meerten E, Rodríguez R, *et al.* 2004 CT Quality Criteria - Appendix C. European Guidelines for Multislice Computed Tomography, European Commission. Available at: http://www.msct.eu/CT_Quality_Criteria.htm.
 20. Mollet NR, Rengo M, Neefjes LA, van der Giesen AG, Weustink AC, Pugliese F, *et al.* Plaque Quantification by CT Coronary Angiography: Optimization of Window Level Settings. Radiological Society of North America, 94th Scientific Assembly and Annual Meeting. Chicago, IL, USA, 2008.
 21. Stary HC, Chandler AB, Dinsmore RE, Fuster V, Glagov S, Insull W, Jr., *et al.* A definition of advanced types of atherosclerotic lesions and a histological classification of atherosclerosis. A report from the Committee on Vascular Lesions of the Council on Arteriosclerosis, American Heart Association. *Arterioscler Thromb Vasc Biol* 1995;15:1512-1531.
 22. Virmani R, Kolodgie FD, Burke AP, Farb A, Schwartz SM. Lessons from sudden coronary death: a comprehensive morphological classification scheme for atherosclerotic lesions. *Arterioscler Thromb Vasc Biol* 2000;20:1262-1275.
 23. Pflederer T, Ludwig J, Ropers D, Daniel WG, Achenbach S. Measurement of coronary artery bifurcation angles by multidetector computed tomography. *Invest Radiol* 2006;41:793-798.
 24. Badak O, Schoenhagen P, Tsunoda T, Magyar WA, Coughlin J, Kapadia S, *et al.* Characteristics of atherosclerotic plaque distribution in coronary artery bifurcations: an intravascular ultrasound analysis. *Coron Artery Dis* 2003;14:309-316.
 25. Dirksen MT, van der Wal AC, van den Berg FM, van der Loos CM, Becker AE. Distribution of inflammatory cells in atherosclerotic plaques relates to the direction of flow. *Circulation* 1998;98:2000-2003.
 26. Leber AW, Knez A, Becker A, Becker C, von Ziegler F, Nikolaou K, *et al.* Accuracy of multidetector spiral computed tomography in identifying and differentiating the composition of coronary atherosclerotic plaques: a comparative study with intracoronary ultrasound. *J Am Coll Cardiol* 2004;43:1241-1247.
 27. Schroeder S, Kopp AF, Baumbach A, Meisner C, Kuettner A, Georg C, *et al.* Noninvasive detection and evaluation of atherosclerotic coronary plaques with multislice computed tomography. *J Am Coll Cardiol* 2001;37:1430-1435.
 28. Pundziute G, Schuijf JD, Jukema JW, Decramer I, Sarno G, Vanhoenacker PK, *et al.* Head-to-head comparison of coronary plaque evaluation between multislice computed tomography and intravascular ultrasound radiofrequency data analysis. *JACC Cardiovasc Interv* 2008;1:176-182.
 29. Sarno G, Vanhoenacker P, Decramer I, Schuijf JD, Pundziute G, Margolis P, *et al.* Characterisation of the "vulnerable" coronary plaque by multi-detector computed tomography: a correlative

- study with intravascular ultrasound-derived radiofrequency analysis of plaque composition. *EuroIntervention* 2008;4:318-323.
30. van Velzen JE, de Graaf FR, de Graaf MA, Schuijff JD, Kroft LJ, de Roos A, *et al.* Comprehensive assessment of spotty calcifications on computed tomography angiography: Comparison to plaque characteristics on intravascular ultrasound with radiofrequency backscatter analysis. *J Nucl Cardiol* 2011.
 31. Perktold K, Resch M, Florian H. Pulsatile non-Newtonian flow characteristics in a three-dimensional human carotid bifurcation model. *J Biomech Eng* 1991;113:464-475.
 32. Markl M, Wegent F, Zech T, Bauer S, Strecker C, Schumacher M, *et al.* In vivo wall shear stress distribution in the carotid artery: effect of bifurcation geometry, internal carotid artery stenosis, and recanalization therapy. *Circ Cardiovasc Imaging* 2010;3:647-655.
 33. Moore JE, Jr., Timmins LH, Ladisa JF, Jr. Coronary artery bifurcation biomechanics and implications for interventional strategies. *Catheter Cardiovasc Interv* 2010;76:836-843.
 34. Friedman MH, Ding Z. Relation between the structural asymmetry of coronary branch vessels and the angle at their origin. *J Biomech* 1998;31:273-278.
 35. Hildick-Smith D, Lassen JF, Albiero R, Lefevre T, Darremont O, Pan M, *et al.* Consensus from the 5th European Bifurcation Club meeting. *EuroIntervention* 2010;6:34-38.
 36. Ormiston JA, Currie E, Webster MW, Kay P, Ruygrok PN, Stewart JT, *et al.* Drug-eluting stents for coronary bifurcations: insights into the crush technique. *Catheter Cardiovasc Interv* 2004;63:332-336.
 37. Murasato Y. Impact of three-dimensional characteristics of the left main coronary artery bifurcation on outcome of crush stenting. *Catheter Cardiovasc Interv* 2007;69:248-256.
 38. Dzavik V, Kharbanda R, Ivanov J, Ing DJ, Bui S, Mackie K, *et al.* Predictors of long-term outcome after crush stenting of coronary bifurcation lesions: importance of the bifurcation angle. *Am Heart J* 2006;152:762-769.
 39. Adriaenssens T, Byrne RA, Dibra A, Iijima R, Mehilli J, Bruskin O, *et al.* Culotte stenting technique in coronary bifurcation disease: angiographic follow-up using dedicated quantitative coronary angiographic analysis and 12-month clinical outcomes. *Eur Heart J* 2008;29:2868-2876.
 40. Collins N, Seidelin PH, Daly P, Ivanov J, Barolet A, Mackie K, *et al.* Long-term outcomes after percutaneous coronary intervention of bifurcation narrowings. *Am J Cardiol* 2008;102:404-410.
 41. Joner M, Finn AV, Farb A, Mont EK, Kolodgie FD, Ladich E, *et al.* Pathology of drug-eluting stents in humans: delayed healing and late thrombotic risk. *J Am Coll Cardiol* 2006;48:193-202.
 42. Kawaguchi R, Oshima S, Jingu M, Tsurugaya H, Toyama T, Hoshizaki H, *et al.* Usefulness of virtual histology intravascular ultrasound to predict distal embolization for ST-segment elevation myocardial infarction. *J Am Coll Cardiol* 2007;50:1641-1646.
 43. Nakazawa G, Yazdani SK, Finn AV, Vorpahl M, Kolodgie FD, Virmani R. Pathological findings at bifurcation lesions: the impact of flow distribution on atherosclerosis and arterial healing after stent implantation. *J Am Coll Cardiol* 2010;55:1679-1687.
 44. Sawada T, Shite J, Garcia-Garcia HM, Shinke T, Watanabe S, Otake H, *et al.* Feasibility of combined use of intravascular ultrasound radiofrequency data analysis and optical coherence tomography for detecting thin-cap fibroatheroma. *Eur Heart J* 2008;29:1136-1146.
 45. Raff GL, Chinnaiyan KM, Share DA, Goraya TY, Kazerooni EA, Moscucci M, *et al.* Radiation dose from cardiac computed tomography before and after implementation of radiation dose-reduction techniques. *JAMA* 2009;301:2340-2348.

3.4

Morphology of coronary artery lesions assessed by virtual histology intravascular ultrasound tissue characterization and fractional flow reserve.

Salvatore Brugaletta, Hector M Garcia-Garcia, Zhu Jun Shen, Josep Gomez-Lara, Roberto Diletti, Giovanna Sarno, Nieves Gonzalo, William Wijns, Bernard de Bruyne, Fernando Alfonso, Patrick W Serruys

Int J Cardiovasc Imaging 2012;28:221-8

Morphology of coronary artery lesions assessed by virtual histology intravascular ultrasound tissue characterization and fractional flow reserve

Salvatore Brugaletta · Hector M. Garcia-Garcia · Zhu Jun Shen ·
 Josep Gomez-Lara · Roberto Diletti · Giovanna Sarno · Nieves Gonzalo ·
 William Wijns · Bernard de Bruyne · Fernando Alfonso · Patrick W. Serruys

Received: 19 October 2010 / Accepted: 20 January 2011
 © Springer Science+Business Media, B.V. 2011

Abstract Fractional flow reserve (FFR) is an index of the physiological significance of a coronary stenosis. Patients who have lesions with a FFR of >0.80 , even optimally treated with medication, have however a MACE rate ranging from 8 to 21%. Coronary plaques at high risk of rupture and clinical events can be also identified by virtual histology intravascular ultrasound (IVUS-VH) as plaques with high amount of necrotic core (NC) abutting the lumen. Aim of this exploratory study was to investigate whether the geometry and composition of lesions with $FFR \leq 0.80$ were different from their counterparts. Fifty-five consecutive patients in whom FFR was clinically indicated on a moderate angiographic

lesion, received also an imaging investigation on the same lesion with IVUS-VH. Data on plaque geometry and composition was analyzed. Patients were subdivided in two groups according to the value of FFR ($>$ or ≤ 0.80). Lesions with a $FFR \leq 0.80$ ($n = 17$) showed a slightly larger plaque burden than those with $FFR > 0.80$ ($n = 38$) ($54.6 \pm 0.7\%$ vs. $51.7 \pm 0.7\%$ $P = 0.1$). In addition, they tend to have less content of necrotic core than their counterparts ($14.2 \pm 8\%$ vs. $19.2 \pm 10.2\%$, $P = 0.08$). No difference was found in the distribution of NC-rich plaques (fibroatheroma and thin-capped fibroatheroma) between groups (82% in $FFR \leq 0.80$ vs. 79% in $FFR > 0.80$, $P = 0.5$). Although $FFR \leq 0.80$ lesions have larger plaque size, they do not differ in composition from the ones with $FFR > 0.80$. Further exploration in a large prospective study is needed to study whether the lesions with $FFR > 0.80$ that are NC rich are the ones associated with the presence of clinical events at follow-up.

S. Brugaletta · H. M. Garcia-Garcia (✉) ·
 Z. J. Shen · J. Gomez-Lara · R. Diletti ·
 G. Sarno · P. W. Serruys
 Z120, Thoraxcentre, Erasmus MC, 's-Gravendijkwal 230,
 3015 CE Rotterdam, The Netherlands
 e-mail: h.garciagarcia@erasmusmc.nl

S. Brugaletta
 Department of Cardiology, Thorax Institute,
 Hospital Clinic, Barcelona, Spain

H. M. Garcia-Garcia
 Cardialysis BV, Rotterdam, The Netherlands

N. Gonzalo · F. Alfonso
 Hospital Clinico, Madrid, Spain

W. Wijns · B. de Bruyne
 Cardiovascular Center, Aalst, Belgium

Keywords Intravascular ultrasound virtual histology · Fractional flow reserve

Introduction

The presence of myocardial ischemia is an important risk factor for an adverse clinical outcome [1]. Revascularization of stenotic coronary lesions that induce ischemia can improve patient's functional

status and outcome [1, 2]. For stenotic lesions that do not induce ischemia, however, the benefit of revascularization is less clear, and medical therapy alone is likely to be equally effective [3, 4].

Fractional flow reserve (FFR) is an index of the physiological significance of a coronary stenosis and is defined as the ratio of maximal blood flow in a stenotic artery to normal maximal flow [5]. A FFR value of 0.80 or less identifies ischemia-causing coronary stenoses with accuracy of more than 90% [5, 6]. Plaques at high risk of rupture and provoking coronary events appear to have high amount of necrotic core [7–10] and this feature can be readily identified by virtual histology intravascular ultrasound (IVUS-VH) [11].

Aim of our study was to explore whether the geometry and composition of lesions with $FFR \leq 0.80$ were different from their counterparts.

Methods

In this exploratory study, all consecutive patients, exhibiting an angiographically moderate lesion on one coronary vessel, admitted from January 2009 to January 2010 in whom FFR was clinically indicated [12, 13], underwent on the same lesion an IVUS-VH analysis to investigate the relationship between functional and morphological/compositional lesion characteristics.

Quantitative coronary angiography analysis

Quantitative coronary angiography (QCA) analyses were performed by one experienced independent observer, blinded to FFR, IVUS-VH and clinical data, using the CAAS II analysis system (Pie Medical BV, Maastricht, Netherlands). The following QCA parameters were computed: computer-defined minimum lumen diameter (MLD), reference vessel diameter (RVD) obtained by the interpolate method, and percentage diameter stenosis [14].

IVUS-VH acquisition and plaque-type classification

The IVUS was performed using the Eagle Eye 20 MHz catheter (Volcano Corp., Rancho Cordova,

California) with an automatic continuous pullback at a rate of 0.5 mm/s (30 frames/sec) at level of the lesion evaluated by FFR. Grayscale images and radiofrequency data required for VH analysis were acquired during the same pullback and raw radiofrequency data capture gated to the R wave (In-Vision Gold, Volcano). The VH processing was performed offline with pcVH 2.1 software (Volcano Corp., Rancho Cordova, California) that permits semi-automated contours detection and provides the compositional structure of the vessel. Quantitative IVUS measurements included vessel area, lumen area, plaque area (vessel area minus lumen area) and plaque burden ($[\text{plaque area}/\text{vessel area}] \times 100$). For the radiofrequency-IVUS analyses, four tissue components (necrotic core—red; dense calcium—white; fibrous—dark green; and fibrofatty—light green) were identified with autoregressive classification systems. Each individual tissue component was quantified and color-coded in IVUS cross sections, as previously described [7, 15].

Lesions were classified by 2 experienced and independent observers, blinded to FFR data, based on plaque composition in 3 consecutive frames within the lesion, as previously described [16]: pathological intimal thickening (PIT), thin-cap fibroatheroma (TCFA), calcified fibroatheroma (CAFA), thick-capped fibroatheroma (ThFA), calcified thick-cap fibroatheroma (CATHFA), fibrotic plaque and fibrocalcific plaque [17, 18]. In case of disagreement, a consensus was reached between the two observers. PIT consisted of mainly a mixture of fibrous and fibrofatty tissue plaque with <10% confluent necrotic core and <10% confluent dense calcium. TCFA was a fibroatheroma without evidence of a fibrous cap: >10% confluent necrotic core with >30° necrotic core in contact with the lumen. Calcified fibroatheroma was a fibroatheroma with >10% confluent dense calcium. ThFA was a fibroatheroma (>10% of confluent necrotic core) with a definable fibrous cap. CATHFA was a ThFA with >10% confluent dense calcium. Fibrotic plaque (FT) consisted of mainly fibrous tissue with <10% confluent necrotic core, <15% fibrofatty tissue and <10% confluent dense calcium. Fibrocalcific plaque (FC) was composed of nearly all fibrous tissue and dense calcium with <10% confluent necrotic core. All the plaques with >10% of necrotic core were also classified as NC-rich plaques.

FFR evaluation

The FFR evaluation was done according to the current guidelines [12, 13]. The FFR was measured with a coronary pressure guidewire (Radi, St.Jude Medical, Uppsala, Sweden) at maximal hyperemia induced by intravenous adenosine, administered at 140 µg/kg/min through a peripheral vein. FFR is calculated as the mean distal coronary pressure (measured with the pressure wire) divided by the mean aortic pressure (measured simultaneously with the guiding catheter) during maximal hyperemia [19]. In the case of diffuse atherosclerosis punctuated by focal areas of more severe stenosis, or in the case of more than one stenosis within the same artery, pressure pullback recordings during hyperemia were performed as described previously [13, 20]. In addition, whenever another significant lesion was detected within the same vessel it was recommended by protocol that the FFR measurements should be performed after this lesion had been treated.

Statistical analysis

Categorical variables were expressed as counts and percentage. Group differences of categorical variables were compared using chi-square or fisher-exact test, as appropriate. Continuous variables were expressed as mean ± standard deviation (SD). The normal distribution of the variables was explored by Kolmogorov-Smirnov test. As the variables were not normally distributed, comparison between groups was done by non parametric tests. A *P* value of <0.05 was considered significant, and all tests were two-tailed. Data were analyzed with SPSS version 16.0 software (SPSS Inc., Chicago, IL).

Results

Baseline clinical and angiographic characteristics

Fifty-five consecutive patients were enrolled in the study. Table 1 shows their clinical and angiographic characteristics. All the patients included had only one-vessel disease, that was investigated by FFR and IVUS-VH analyses. In particular 17 out of these patients (31%) showed a FFR ≤ 0.80 and 13 patients (23%) received stent implantation on the lesion

evaluated by FFR. The remaining 4 patients did not receive any treatment for the following reasons: the minimum lumen area by IVUS was >4 mm² in 3 patients and the FFR was 0.79 in 1 patient. The 38 patients with a FFR ≥ 0.80 did not receive any revascularization treatment and were treated by medical therapy.

QCA analysis confirmed that all the lesions included in the analysis were angiographically moderate lesions (46% mean stenosis), for which the FFR evaluation is indicated according to guidelines. Patients with a FFR ≥ 0.80 exhibited higher RVD and MLD than those patients with a FFR ≤ 0.80 (Table 1).

IVUS geometrical analysis (Table 2)

Plaque burden was slightly larger for those lesions with a FFR ≤ 0.80 (54.6 ± 0.7% vs. 51.7 ± 0.7% *P* = 0.1) accompanied with a reduction in lumen area (7.1 ± 1.8 mm² vs. 7.9 ± 2.4 mm², *P* = 0.1) and without expansion of the vessel area as compared to their counterparts (16.0 ± 5.0 mm² vs. 16.5 ± 4.4 mm², *P* = 0.4). Minimum lumen area was lower for those lesions with a FFR ≤ 0.80 than those with a FFR > 0.80 (*P* = 0.07).

IVUS-VH analysis

Table 2 shows the compositional IVUS-VH data. Plaques with FFR ≤ 0.80 showed higher relative content of fibrofatty tissue (*P* = 0.02) and a trend towards a lower relative content of necrotic core (*P* = 0.08) compared to plaques with FFR > 0.80.

Plaque classification yielded good concordance between the two observers (*κ* = 0.85). Overall, we found 9 PIT, 2 FC, 7 FA, 6 CaFA, 9 TCFA and 22 CaTCFA (Fig. 1). No difference was found in the distribution of VH-plaque type between the two groups (Fig. 2). NC-rich plaque distribution was also not different between groups (82% in FFR ≤ 0.80 vs. 79% in FFR > 0.80, *P* = 0.5).

Discussion

The major finding of this analysis is that, although larger plaques are associated with FFR ≤ 0.80, VH-plaque composition and VH-plaque type are not

Table 1 Clinical and angiographic characteristics

	Patients (<i>n</i> = 55) Lesions (<i>n</i> = 55)	FFR > 0.80 (38 patients)	FFR ≤ 0.80 (17 patients)	<i>P</i> value
Age (years)	61 ± 10	61 ± 9	60 ± 12	0.24
Mean ± SD (<i>n</i>)				
Men (%)	83	81	88	0.70
Smokers (%)	56	55	58	1.00
Diabetes (%)	12	15	5	0.41
Hypertension requiring medication (%)	63	65	58	0.76
Hyperlipidaemia requiring medication (%)	69	68	70	1.00
Stable angina (%)	69	71	65	0.75
Unstable angina (%)	30	29	35	0.63
Target vessel (%)				0.98
Left anterior descending	65	65	64	
Left circumflex	16	15	18	
Right coronary artery	18	20	18	
QCA analysis				
MLD (mm)	1.66 ± 0.37	1.76 ± 0.34	1.43 ± 0.34	0.03
RVD (mm)	3.14 ± 0.52	3.25 ± 0.54	2.90 ± 0.39	0.03
% stenosis	46.1 ± 0.9	45.2 ± 0.8	49.0 ± 0.1	0.16
FFR	0.84 ± 0.08	NA	NA	NA

SD standard deviation, *QCA* quantitative coronary angiography, *MLD* minimum lumen diameter, *RVD* reference vessel diameter, *FFR* fractional flow reserve

different between lesions with FFR more or equal/less than 0.80.

From previous studies it is known that patients, who have lesions with a FFR > 0.80, if optimally treated with medication, have a good prognosis up to 5-years [4]. However, the MACE rate of these patients may range from 8 to 21% [21–25]. We set out this exploratory study to investigate whether plaque composition could be one of the reasons to explain this occurrence of events if these lesions are left untreated, based on FFR findings. Interestingly, QCA already discriminates in our analysis the lesions with a FFR ≤ 0.80 which have smaller MLD and RVD compared with lesions with a FFR ≥ 0.80. However, it appears that although FFR ≤ 0.80 lesions are more stenotic and have larger size, they do not differ in composition from the ones with FFR > 0.80 and left untreated. Rogers et al. [26] demonstrated a heterogeneous VH-plaque type morphology with prevalence of TCFA in FFR-negative lesions. In our study, comparing FFR negative and positive lesions, we found that the relative content of NC seems to be higher in lesions with a FFR > 0.80

(*P* = 0.08). This could be a possible explanation of MACE for those patients with angiographically intermediate lesions, left untreated as no functionally significant by FFR (>0.80) [21]. In addition, lesions with FFR ≤ 0.80 exhibited higher fibrofatty tissue content than those lesions with FFR ≥ 0.80 (*P* = 0.02). This tissue, corresponding to lipids without necrosis, is namely present in PIT, that have been shown able to evolve in VH-fibroatheroma [27].

From pathological studies it is known that specific coronary plaques characteristics, such thin fibrous cap, paucity of smooth muscle cells, heavy inflammatory infiltration of the cap and large necrotic cores correlate with fatal ischemic events [28]. The recent PROSPECT trial has also shown that thin-capped fibroatheroma, identified by IVUS-VH, is a strong independent predictor of events at 3-year follow-up [11]. Angiographic studies before and after myocardial infarction showed that pre-existing lesions at the sites of myocardial infarction are not usually accompanied by hemodynamically significant stenosis [29]. In sudden coronary death, at least 50% of the thrombosis occurred at lesion sites with ≤50%

Table 2 IVUS-VH data

	FFR > 0.80 (n = 38 lesions)	FFR ≤ 0.80 (n = 17 lesions)	P value
IVUS-VH data			
Mean plaque area (mm ²)	8.6 ± 2.6	8.9 ± 3.5	0.8
Plaque burden (%)	51.7 ± 0.7	54.6 ± 0.7	0.1
Mean lumen area (mm ²)	7.9 ± 2.4	7.1 ± 1.8	0.1
Minimum lumen area (mm ²)	5.6 ± 2.3	4.6 ± 1.2	0.07
Mean vessel area (mm ²)	16.5 ± 4.4	16.0 ± 5.0	0.4
Fibrous tissue (mm ²)	2.7 ± 1.4	3.0 ± 1.8	0.6
Fibrous tissue (%)	54.5 ± 10.7	57.3 ± 6.7	0.2
Fibrofatty tissue (mm ²)	0.8 ± 0.8	1.2 ± 1.1	0.07
Fibrofatty tissue (%)	15.1 ± 11.1	21.5 ± 10.8	0.02
Necrotic core tissue (mm ²)	0.9 ± 0.5	0.7 ± 0.4	0.2
Necrotic core tissue (%)	19.2 ± 10.2	14.2 ± 8.0	0.08
Dense calcium (mm ²)	0.5 ± 0.4	0.3 ± 0.3	0.1
Dense calcium (%)	11.0 ± 8.3	6.8 ± 4.8	0.1
VH plaque distribution			
PIT, n (%)	6 (15)	3 (17)	
FC, n (%)	2 (8)	0 (0)	
FA, n (%)	4 (10)	3 (17)	
CaFA, n (%)	5 (13)	1 (8)	
TCFA, n (%)	6 (15)	3 (17)	
CaTCFA, n (%)	15 (39)	7 (41)	

Data are expressed as mean ± standard deviation. FFR fractional flow reserve, PIT pathological intimal thickening, FC fibrocalcific plaque, FA fibroatheroma, CaFA calcified fibroatheroma, TCFA thin-cap fibroatheroma, CaTCFA calcified thin-cap fibroatheroma

angiographic diameter reduction [30]. However, we cannot elucidate from our study whether the lesions with FFR > 0.80 that are NC rich (77% of them) are the ones associated with the presence of clinical events at follow-up. This hypothesis needs further exploration in a larger prospective study.

On the other side, Kubo et al. [27] showed recently that there are various possible pathways in the evolution and stabilization of NC-rich plaques. At 12-month follow-up they found that most of the NC-rich plaques healed or stabilized. The mechanism of healing is not well established. The transformation of hematoma and/or thrombus into fibrous muscular tissue and the formation or increase in thickness of the fibrous cap could lead to plaque stabilization [31]. Some studies have proposed that a silent rupture or a plaque rupture proximal to a lesion might lead to mural thrombus and subsequent formation of a fibrotic cap over the TCFA [32, 33]. This could be the natural evolution of the NC-rich plaques for lesions with a FFR more than 0.80, as the good prognosis of these patients. In addition, it is noteworthy to consider that a large minimum lumen area

could also favor a silent NC-rich plaque rupture, allowing a coronary flow sufficient to avoid a clinical event. In our study, we found, indeed, a lower minimal lumen area in FFR ≤ 0.80 lesions as compared to FFR > 0.80 lesions. This hypothesis also would need further exploration in a larger prospective study.

Finally, it is important to highlight that IVUS-VH and FFR are two different ways to evaluate the significance of a coronary plaque. While FFR is a standardized method evaluating the functional significance of an intermediate coronary stenosis, IVUS-VH analysis provides information on the plaque size and on its tissue characterization through its back-scattering signal. As virtual histology is a sound-based imaging modality using the radiofrequency data to compute 4 different tissue types, it suffers from all limitations as any other ultrasound-derived techniques. While the use of FFR to decide the percutaneous treatment of a coronary lesion has been widely described and correlated with long-term prognosis [13, 34], the use of VH to decide a percutaneous treatment of a coronary plaque is not

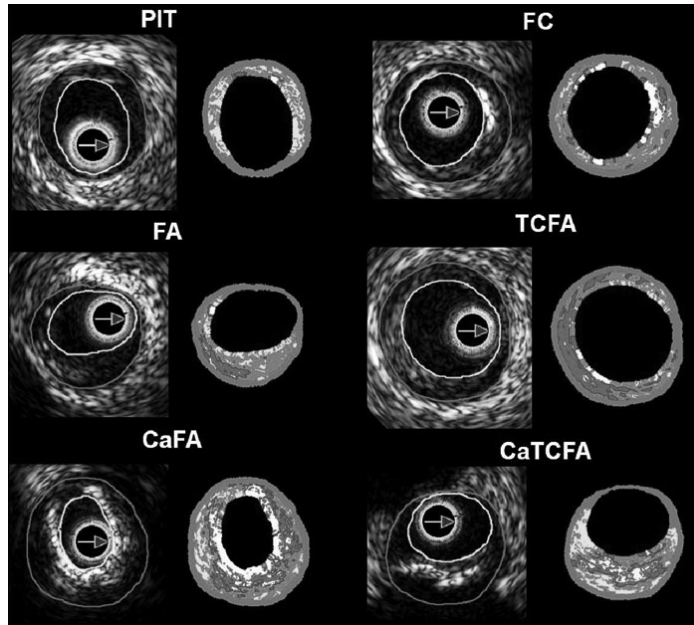


Fig. 1 Examples of various type of VH-plaque found in the analysis with the corresponding IVUS appearance. Lumen contour (yellow line) and vessel contour (red line) are shown. In the VH images, necrotic core is coded as red, dense calcium as white, fibrous tissue as dark green and fibrofatty tissue as

light green. PIT pathological intimal thickening, FC fibrocalcific plaque, FA fibroatheroma, TCFA thin-cap fibroatheroma, CaFA calcified fibroatheroma, CaTCFA calcified thin-cap fibroatheroma

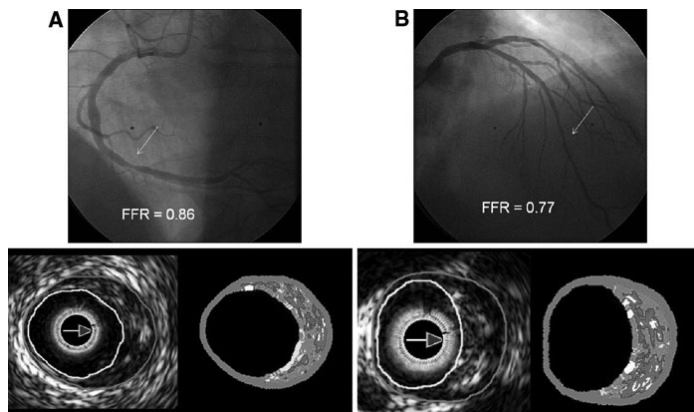


Fig. 2 Examples of two different lesions (white arrows) with a FFR > 0.80 (panel A) and ≤ 0.80 (panel B), both showing a FA VH-plaque type. In the IVUS images red and yellow contours indicate vessel and lumen contours, respectively

well investigated yet. The SECRIT-I trial is ongoing to test the efficacy of preventive treatment of a NC-rich plaque with a self-expanding stent, that allows the formation of a fibrous cap [35].

Limitations

This is a registry study and included a small number of patients. No clinical or angiographic follow-up are available. Our findings only focused on ambiguous/equivocal lesions where the use of FFR was considered of value in the clinical decision process. Whether other lesions causing less significant stenosis have different composition as compared with hemodynamically significant lesions will require additional studies.

Conclusions

Coronary lesions with FFR more or less than 0.80 are not different in terms of plaque composition and virtual histology plaque types from their counterparts. The hypothesis of whether a preventive treatment might be required for those patients who have a NC-rich plaque with FFR > 0.80 needs to be further explored.

Conflict of interest None of the authors have any conflict of interest to declare.

References

- Shaw LJ, Berman DS, Maron DJ, Mancini GB, Hayes SW, Hartigan PM, Weintraub WS, O'Rourke RA, Dada M, Spertus JA, Chaitman BR, Friedman J, Slomka P, Heller GV, Germano G, Gosselin G, Berger P, Kostuk WJ, Schwartz RG, Knudtson M, Veledar E, Bates ER, McCallister B, Teo KK, Boden WE (2008) Optimal medical therapy with or without percutaneous coronary intervention to reduce ischemic burden: results from the clinical outcomes utilizing revascularization and aggressive drug evaluation (courage) trial nuclear substudy. *Circulation* 117(10): 1283–1291. doi:10.1161/CIRCULATIONAHA.107.743963
- Erne P, Schoenenberger AW, Burckhardt D, Zuber M, Kiowski W, Buser PT, Dubach P, Resink TJ, Pfisterer M (2007) Effects of percutaneous coronary interventions in silent ischemia after myocardial infarction: the swiss ii randomized controlled trial. *JAMA* 297(18):1985–1991. doi:10.1001/jama.297.18.1985
- Boden WE, O'Rourke RA, Teo KK, Hartigan PM, Maron DJ, Kostuk WJ, Knudtson M, Dada M, Casperson P, Harris CL, Chaitman BR, Shaw L, Gosselin G, Nawaz S, Title LM, Gau G, Blaustein AS, Booth DC, Bates ER, Spertus JA, Berman DS, Mancini GB, Weintraub WS (2007) Optimal medical therapy with or without pci for stable coronary disease. *N Engl J Med* 356(15):1503–1516. doi: 10.1056/NEJMoa070829
- Pijls NH, van Schaardenburgh P, Manoharan G, Boersma E, Bech JW, van't Veer M, Bar F, Hoorntje J, Koolen J, Wijns W, de Bruyne B (2007) Percutaneous coronary intervention of functionally nonsignificant stenosis: 5-year follow-up of the defer study. *J Am Coll Cardiol* 49(21):2105–2111. doi:10.1016/j.jacc.2007.01.087
- Pijls NH, De Bruyne B, Peels K, Van Der Voort PH, Bonnier HJ, Bartunek JKJ, Koolen JJ (1996) Measurement of fractional flow reserve to assess the functional severity of coronary-artery stenoses. *N Engl J Med* 334(26):1703–1708. doi:10.1056/NEJM199606273342604
- Pijls NH, Van Gelder B, Van der Voort P, Peels K, Bracke FA, Bonnier HJ, el Gamal MI (1995) Fractional flow reserve. A useful index to evaluate the influence of an epicardial coronary stenosis on myocardial blood flow. *Circulation* 92(11):3183–3193
- Nair A, Kuban BD, Tuzcu EM, Schoenhagen P, Nissen SE, Vince DG (2002) Coronary plaque classification with intravascular ultrasound radiofrequency data analysis. *Circulation* 106(17):2200–2206
- Nair A, Margolis MP, Kuban BD, Vince DG (2007) Automated coronary plaque characterisation with intravascular ultrasound backscatter: ex vivo validation. *Euro-Intervention* 3(1):113–120
- Nasu K, Tsuchikane E, Katoh O, Vince DG, Virmani R, Surmely JF, Murata A, Takeda Y, Ito T, Ehara M, Matsu- bara T, Terashima M, Suzuki T (2006) Accuracy of in vivo coronary plaque morphology assessment: a validation study of in vivo virtual histology compared with in vitro histopathology. *J Am Coll Cardiol* 47(12):2405–2412. doi: 10.1016/j.jacc.2006.02.044
- Stary HC, Chandler AB, Dinsmore RE, Fuster V, Glagov S, Insull W Jr, Rosenfeld ME, Schwartz CJ, Wagner WD, Wissler RW (1995) A definition of advanced types of atherosclerotic lesions and a histological classification of atherosclerosis. A report from the committee on vascular lesions of the council on arteriosclerosis, American heart association. *Arterioscler Thromb Vasc Biol* 15(9):1512–1531
- Stone GW, Maehara A, Lansky AJ, de Bruyne B, Cristea E, Mintz GS, Mehran R, McPherson J, Farhat N, Marso SP, Parise H, Templin B, White R, Zhang Z, Serruys PW, PROSPECT Investigators (2011) A prospective natural-history study of coronary atherosclerosis. *N Engl J Med* 364(3):226–235
- De Bruyne B, Pijls NH, Bartunek J, Kulecki K, Bech JW, De Winter H, Van Crombrugge P, Heyndrickx GR, Wijns W (2001) Fractional flow reserve in patients with prior myocardial infarction. *Circulation* 104(2):157–162
- Tonino PA, De Bruyne B, Pijls NH, Siebert U, Ikeno F, van't Veer M, Klauss V, Manoharan G, Engstrom T, Oldroyd KG, Ver Lee PN, MacCarthy PA, Fearon WF (2009) Fractional flow reserve versus angiography for guiding percutaneous coronary intervention. *N Engl J Med* 360(3):213–224. doi:10.1056/NEJMoa0807611
- Reiber JH, Serruys PW (1991) Quantitative coronary angiography: methodologies. *Quantitative Coronary*

- Angiography Dordrecht, vol 98. Kluwer Academic Publishers, The Netherlands, p 102
15. Serruys PW, Ormiston JA, Onuma Y, Regar E, Gonzalo N, Garcia-Garcia HM, Nieman K, Bruining N, Dorange C, Miquel-Hebert K, Veldhof S, Webster M, Thuesen L, Dudek D (2009) A bioabsorbable everolimus-eluting coronary stent system (absorb): 2-year outcomes and results from multiple imaging methods. *Lancet* 373(9667):897–910. doi:10.1016/S0140-6736(09)60325-1
 16. Garcia-Garcia HM, Mintz GS, Lerman A, Vince DG, Margolis MP, van Es GA, Morel MA, Nair A, Virmani R, Burke AP, Stone GW, Serruys PW (2009) Tissue characterisation using intravascular radiofrequency data analysis: recommendations for acquisition, analysis, interpretation and reporting. *EuroIntervention* 5(2):177–189
 17. Rodriguez-Granillo GA, Garcia-Garcia HM, Mc Fadden EP, Valgimigli M, Aoki J, de Feyter P, Serruys PW (2005) In vivo intravascular ultrasound-derived thin-cap fibroatheroma detection using ultrasound radiofrequency data analysis. *J Am Coll Cardiol* 46(11):2038–2042. doi:10.1016/j.jacc.2005.07.064
 18. Konig A, Margolis MP, Virmani R, Holmes D, Klauss V (2008) Technology insight: in vivo coronary plaque classification by intravascular ultrasonography radiofrequency analysis. *Nat Clin Pract Cardiovasc Med* 5(4):219–229. doi:10.1038/npcardio1123
 19. Pijls NH, van Son JA, Kirkeeide RL, De Bruyne B, Gould KL (1993) Experimental basis of determining maximum coronary, myocardial, and collateral blood flow by pressure measurements for assessing functional stenosis severity before and after percutaneous transluminal coronary angioplasty. *Circulation* 87(4):1354–1367
 20. Pijls NH (2004) Optimum guidance of complex pci by coronary pressure measurement. *Heart* 90(9):1085–1093. doi:10.1136/hrt.2003.032151
 21. Bech GJ, De Bruyne B, Pijls NH, de Muinck ED, Hoortje JC, Escaned J, Stella PR, Boersma E, Bartunek J, Koolen JJ, Wijns W (2001) Fractional flow reserve to determine the appropriateness of angioplasty in moderate coronary stenosis: a randomized trial. *Circulation* 103(24):2928–2934
 22. Leesar MA, Abdul-Baki T, Yalamanchili V, Hakim J, Kern M (2003) Conflicting functional assessment of stenoses in patients with previous myocardial infarction. *Catheter Cardiovasc Interv* 59(4):489–495. doi:10.1002/ccd.10550
 23. Hernandez Garcia MJ, Alonso-Briales JH, Jimenez-Navarro M, Gomez-Doblas JJ, Rodriguez Bailon I, de Teresa Galvan E (2001) Clinical management of patients with coronary syndromes and negative fractional flow reserve findings. *J Interv Cardiol* 14(5):505–509
 24. Bech GJ, Pijls NH, De Bruyne B, Peels KH, Michels HR, Bonnier HJ, Koolen JJ (1999) Usefulness of fractional flow reserve to predict clinical outcome after balloon angioplasty. *Circulation* 99(7):883–888
 25. Kern MJ, Lerman A, Bech JW, De Bruyne B, Eeckhout E, Fearon WF, Higano ST, Lim MJ, Meuwissen M, Piek JJ, Pijls NH, Siebes M, Spaan JA (2006) Physiological assessment of coronary artery disease in the cardiac catheterization laboratory: a scientific statement from the American heart association committee on diagnostic and interventional cardiac catheterization, council on clinical cardiology. *Circulation* 114(12):1321–1341. doi:10.1161/CIRCULATIONAHA.106.177276
 26. Rogers JH, Wegelin J, Harder K, Valente R, Low R (2006) Assessment of ffr-negative intermediate coronary artery stenoses by spectral analysis of the radiofrequency intravascular ultrasound signal. *J Invasive Cardiol* 18(10):448–453
 27. Kubo T, Maehara A, Mintz GS, Doi H, Tsujita K, Choi SY, Katoh O, Nasu K, Koenig A, Pieper M, Rogers JH, Wijns W, Bose D, Margolis MP, Moses JW, Stone GW, Leon MB (2010) The dynamic nature of coronary artery lesion morphology assessed by serial virtual histology intravascular ultrasound tissue characterization. *J Am Coll Cardiol* 55 (15):1590–1597. doi:10.1016/j.jacc.2009.07.078
 28. Virmani R, Kolodgie FD, Burke AP, Farb A, Schwartz SM (2000) Lessons from sudden coronary death: a comprehensive morphological classification scheme for atherosclerotic lesions. *Arterioscler Thromb Vasc Biol* 20(5):1262–1275
 29. de Feyter PJ, Ozaki Y, Baptista J, Escaned J, Di Mario C, de Jaegere PP, Serruys PW, Roelandt JR (1995) Ischemia-related lesion characteristics in patients with stable or unstable angina. A study with intracoronary angioscopy and ultrasound. *Circulation* 92(6):1408–1413
 30. Farb A, Tang AL, Burke AP, Sessums L, Liang Y, Virmani R (1995) Sudden coronary death. Frequency of active coronary lesions, inactive coronary lesions, and myocardial infarction. *Circulation* 92(7):1701–1709
 31. Stary HC (2000) Natural history and histological classification of atherosclerotic lesions: an update. *Arterioscler Thromb Vasc Biol* 20(5):1177–1178
 32. Virmani R, Burke AP, Farb A, Kolodgie FD (2006) Pathology of the vulnerable plaque. *J Am Coll Cardiol* 47(8 Suppl):C13–C18. doi:10.1016/j.jacc.2005.10.065
 33. Burke AP, Kolodgie FD, Farb A, Weber DK, Malcom GT, Smialek J, Virmani R (2001) Healed plaque ruptures and sudden coronary death: evidence that subclinical rupture has a role in plaque progression. *Circulation* 103(7):934–940
 34. Pijls NH, Fearon WF, Tonino PA, Siebert U, Ikeno F, Bornschein B, van't Veer M, Klauss V, Manoharan G, Engstrom T, Oldroyd KG, Ver Lee PN, MacCarthy PA, De Bruyne B (2010) Fractional flow reserve versus angiography for guiding percutaneous coronary intervention in patients with multivessel coronary artery disease: 2-year follow-up of the fame (fractional flow reserve versus angiography for multivessel evaluation) study. *J Am Coll Cardiol* 56 (3):177–184. doi:10.1016/j.jacc.2010.04.012
 35. Ramcharitar S, Gonzalo N, van Geuns RJ, Garcia-Garcia HM, Wykrzykowska JJ, Ligthart JM, Regar E, Serruys PW (2009) First case of stenting of a vulnerable plaque in the seccrit i trial-the dawn of a new era? *Nat Rev Cardiol* 6(5):374–378. doi:10.1038/nrcardio.2009.34

3.5

Relationship between palpography and virtual histology in patients with acute coronary syndromes: a sub-analysis from the PROSPECT trial.

Salvatore Brugaletta, Hector M Garcia-Garcia, Patrick W Serruys, Akiko Maehara, Vasim Farooq, Gary S Mintz, Bernard de Bruyne, Steven P Marso, Stefan Verhey, Dariusz Dudek, Christian W Hamm, Nahim Farhat, Francois Schiele, John McPherson, Amir Lerman, Pedro R Moreno, Bertil Wennerblom, Martin Fahy, Barry Templin, Marie-Angele Morel, Gerrit Anne van Es, Gregg W Stone

JACC Cardiovascular Imaging 2012;5:S19-27

Relationship Between Palpography and Virtual Histology in Patients With Acute Coronary Syndromes

Salvatore Brugaletta, MD,*† Hector M. Garcia-Garcia, MD, PhD,*‡ Patrick W. Serruys, MD, PhD,* Akiko Machara, MD,§ Vasim Farooq, MBChB,* Gary S. Mintz, MD,§ Bernard de Bruyne, MD,|| Steven P. Marso, MD,¶ Stefan Verheyde, MD, PhD,# Dariusz Dudek, MD,** Christian W. Hamm, MD,†† Nahim Farhat, MD,‡‡ Francois Schiele, MD,§§ John McPherson, MD,|||| Amir Lerman, MD,¶¶ Pedro R. Moreno, MD,## Bertil Wennerblom, MD,*** Martin Fahy, MSc,§ Barry Templin, MBA,††† Marie-Angel Morel, BSc,‡ Gerrit Anne van Es, PhD,§ Gregg W. Stone, MD§
Rotterdam, the Netherlands; New York, New York; Aalst and Antwerp, Belgium; Kansas City, Missouri; Krakow, Poland; Bad Nauheim, Germany; Elyria, Ohio; Besançon, France; Nashville, Tennessee; Rochester, Minnesota; Göteborg, Sweden; and Santa Clara, California

OBJECTIVES The purpose of this study was to correlate adverse events at long-term follow-up in patients after an acute coronary syndrome with coronary plaque characteristics derived from simultaneous evaluation of their mechanical and compositional properties using virtual histology (intravascular ultrasound virtual histology) and palpography.

BACKGROUND Fibroatheroma is the plaque morphology with the highest risk of causing adverse cardiac events. Palpography can potentially assess the local mechanical plaque properties with the possibility of identifying fibroatheroma with the highest risk of rupture.

METHODS A total of 114 patients with acute coronary syndrome from the PROSPECT (Providing Regional Observations to Study Predictors of Events in the Coronary Tree) trial underwent a single ultrasound imaging investigation of their 3 coronary vessels with the co-registration of intravascular ultrasound virtual histology and palpography. Major adverse cardiac events (MACE) (cardiac death, cardiac arrest, myocardial infarction, or unstable or progressive angina) were collected up to a median follow-up of 3.4 years and adjudicated to originally treated culprit versus untreated nonculprit lesions.

RESULTS In total, 488 necrotic core-rich plaques were identified and subclassified as thin-cap fibroatheroma (n = 111), calcified thick-cap fibroatheroma (n = 213), and noncalcified thick-cap fibroatheroma (n = 164) and matched to their co-registered palpography data. A total of 16 MACE, adjudicated to untreated nonculprit lesions, were recorded at follow-up. In patients in whom MACE developed, fibroatheroma were larger (plaque area 10.0 mm² [range: 8.4 to 11.6 mm²] vs. 8.2 mm² [range: 7.7 to 8.8 mm²] (p = 0.03) compared with patients who were MACE free. By palpography, the maximum and the density strain values did not differ between the varying subtypes of fibroatheroma of patients with or without MACE during follow-up.

CONCLUSIONS In acute coronary syndromes, patients treated with stents and contemporary pharmacotherapy, palpography did not provide additional diagnostic information for the identification of fibroatheroma with a high risk of rupture and MACE during long-term follow-up. (Providing Regional Observations to Study Predictors of Events in the Coronary Tree [PROSPECT]: An Imaging Study in Patients With Unstable Atherosclerotic Lesions; NCT00180466 (J Am Coll Cardiol Img 2012;5:519–27) © 2012 by the American College of Cardiology Foundation

From the *Erasmus University, Thoraxcentrum, Rotterdam, the Netherlands; †Thorax Institute, Department of Cardiology, Hospital Clinic, University of Barcelona, Spain; ‡Cardialysis, Rotterdam, the Netherlands; §Columbia University Medical

ABBREVIATIONS
AND ACRONYMS

ACS = acute coronary syndromes
 CSA = cross-sectional area
 TCFA = calcified thick-cap fibroatheroma
 EEM = external elastic membrane
 hsCRP = high-sensitivity C-reactive protein
 IVUS-VH = intravascular ultrasound virtual histology
 IVUS = intravascular ultrasound
 MACE = major adverse cardiac event(s)
 NC = necrotic core
 NCTFA = noncalcified thick-cap fibroatheroma
 NSTEMI = non-ST-segment elevation myocardial infarction
 ROC = Rotterdam classification
 STEMI = ST-segment elevation myocardial infarction
 TCFA = thin-cap fibroatheroma
 VH = virtual histology

In the modern era of cardiology, the prevention of coronary events through identification of coronary plaques at high risk of events has become a topic of intense research. Several anatomopathologic studies previously showed that most atherosclerotic plaques responsible for acute

atheromas and their prognostic value in predicting future cardiovascular events.

See page S38

coronary syndromes (ACS) are angiographically mild (1,2). The thrombosis associated with rupture of a thin-cap fibroatheroma (TCFA) is the most common cause of myocardial infarction and cardiac death (3–6). Moreover, the degree of mechanical strain exhibited by the plaque is related to the thickness of the cap (7,8).

In patients with ACS recruited in the PROSPECT (Providing Regional Observations to Study Predictors of Events in the Coronary Tree) study (9–16), intravascular ultrasound virtual histology (IVUS-VH) demonstrated that the plaques responsible for major adverse cardiac events (MACE), at a median term follow-up of 3.4 years, had a larger plaque burden and smaller lumen area and/or were mostly virtual histology (VH) TCFA.

IVUS palpography is a technique that can allow the assessment of local mechanical tissue properties, with previous *in vitro* studies suggesting a high sensitivity and specificity for detecting vulnerable plaques (17–19). In a subgroup of patients from the PROSPECT trial, in whom combined IVUS-VH and palpography recordings were performed, we explored the potential relationship between the mechanical and compositional properties of fibro-

METHODS

Population. The study design of the PROSPECT trial has been published (9,10). Briefly, this multicenter, prospective, international study was designed to identify imaging and serologic predictors of vulnerable plaque events in patients who underwent percutaneous coronary intervention for ACS. After treatment of their culprit lesions, patients underwent 3-vessel gray-scale IVUS and IVUS-VH imaging of culprit and nonculprit arteries. The main inclusion criteria were: 1) acute cardiac pain or angina equivalent consistent with unstable angina or myocardial infarction lasting >10 min within the past 72 h; and 2) the presence of any of the following: increased biochemical markers of myocardial necrosis (creatin kinase-myocardial band isoenzyme or troponin I or T) greater than the upper limits of normal; ST-segment depression >1 mm in ≥ 2 contiguous leads or transient ST-segment elevation >1 mm in ≥ 2 contiguous leads lasting <30 min; or ST-segment elevation myocardial infarction with onset >24 h previously, diagnosed with the typical triad of nitrate-unresponsive chest pain lasting >30 min, ST-segment elevation >1 mm in ≥ 2 contiguous leads, or new left bundle branch block. This study was approved by the institutional review boards of the centers where the procedures were performed. Written informed consent was obtained from all patients before cardiac catheterization. Clinical follow-up was undertaken at 30 days, 6 months, and then yearly for at least 2 years. The study was terminated after all patients reached a 3-year follow-up.

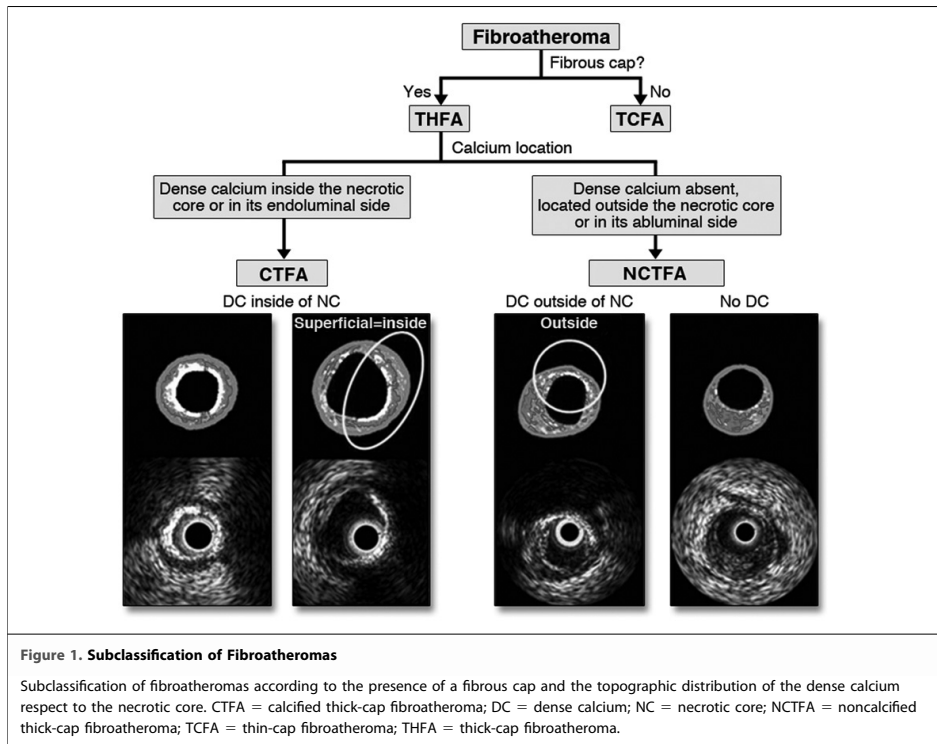
Center/New York-Presbyterian Hospital and the Barcelona, Spain; Cardiovascular Research Foundation, New York, New York; ¶Cardiovascular Center, OLV Hospital, Aalst, Belgium; ¶Saint Luke's Mid America Heart Institute, University of Missouri-Kansas City, Kansas City, Missouri; #Antwerp Cardiovascular Institute Middelheim, Ziektehuis Netwerk Antwerpen, Antwerp, Belgium; **Department of Cardiology, Jagiellonian University, Krakow, Poland; ††Kerckhoff Klinik, Bad Nauheim, Germany; ‡‡EMH Regional Medical Center, Elyria, Ohio; §§University Hospital Jean Minjot, Besançon, France; |||Vanderbilt University Medical Center, Nashville, Tennessee; ¶¶Division of Cardiovascular Diseases, Department of Internal Medicine, Mayo Clinic and College of Medicine, Rochester, Minnesota; ##The Mount Sinai School of Medicine, New York, New York; ***Cardiology Department, Sahlgrenska University Hospital, Göteborg, Sweden; and †††Abbott Vascular, Santa Clara, California. The study was sponsored and funded by Abbott Vascular and Volcano Corporation. Dr. Machara has received a research grant from Boston Scientific and lecture fees from Volcano. Dr. Mintz has received grant support, consulting fees, and honoraria from Volcano and Boston Scientific. Dr. Dudek has received research grants from or served as consultant/advisory board member for Abbott, Adamed, Biotronik, Balton, Bayer, BBraun, BioMatrix, Boston Scientific, Boehringer Ingelheim, Bristol-Myers Squibb, Cordis, Cook, Eli Lilly, EuroCor, Glaxo, InVatec, Medtronic, The Medicines Company, MSD, Nycomed, Orbus-Neich, Pfizer, Possis, Promed, Sanofi-Aventis, Siemens, Solvay, Terumo, and Tyco. Dr. McPherson is a consultant for Abbott Vascular. Dr. Stone has received research grants from Volcano and InfaRed; and is on the scientific advisory board and receives honoraria from Boston Scientific and Abbott Vascular. All other authors have reported that they have no relationships relevant to the contents of this paper to disclose.

Manuscript received September 21, 2010; revised manuscript received December 16, 2010, accepted February 14, 2011.

Radiofrequency IVUS analysis. Radiofrequency IVUS of the left main and proximal 6 to 8 cm of each major epicardial coronary artery using a phased-array, 20-MHz, 3.2-F catheter (Eagle Eye, Volcano Corporation, Rancho Cordova, California) were performed. During motorized catheter pullback, at 0.5 mm/s, gray-scale IVUS was recorded, and raw radiofrequency data capture was gated to the R wave (In-Vision Gold, Volcano Corporation). Radiofrequency IVUS uses spectral (frequency) analysis as well as amplitude data from the IVUS signal, which has been correlated with histologic samples with high sensitivity and specificity (20,21).

All baseline IVUS images were prospectively offline analyzed at independent core laboratory without knowledge of subsequent events (Cardiovascular Research Foundation, New York, New York). Radiofrequency IVUS analyses were performed using: 1) QCU-CMS software (Medis, Leiden, the Netherlands) for contouring; 2) pcVH 2.1 software (Volcano Corporation) for contouring and data output; and 3) proprietary qVH software (Cardiovascular Research Foundation) for segmental qualitative assessment and quantitative data

output. External elastic membrane (EEM) and lumen borders were contoured for all recorded frames (each ~0.4 mm in length). Quantitative IVUS measurements included EEM cross-sectional area (CSA), lumen CSA, plaque and media (EEM minus lumen) CSA, plaque burden (plaque and media divided by EEM CSA), and minimal lumen area. Radiofrequency IVUS plaque components were color coded as dense calcium (white), necrotic core (NC) (red), fibrofatty (light green), and fibrotic tissue (dark green) and reported as percentages of total plaque area. A lesion was defined as a segment with ≥ 3 consecutive frames with $\geq 40\%$ plaque burden. Only the NC-rich plaques, FA, and TCFAs were considered in this study. Because calcium causes attenuation of the backscattering signal and may affect VH-IVUS plaque classification, the NC behind calcium is more likely to be artifactual. Consequently, the core laboratory separately categorized plaques with calcium according to its topographic distribution within the plaque. The NC-rich plaques were therefore classified as: 1) TCFA when the fibrous cap was absent; 2) calcified thick cap fibroatheroma (CTFA) when dense calcium



was located within the NC or at its endoluminal side; 3) noncalcified TCFA (NCTFA) when dense calcium was absent or located outside the NC or on its abluminal side (22,23) (Fig. 1).

IVUS Palpography acquisition and analysis. IVUS palpography is a technique that allows the assessment of local mechanical tissue properties. At a defined pressure difference, soft-tissue (e.g., lipid-rich) components deform more than hard-tissue components (e.g., fibrous-calcified) (10–12). In coronary arteries, the tissue of interest is the vessel wall, whereas the blood pressure, with its physiologic changes during the heart cycle, is used as the excitation force. Radiofrequency data obtained at different pressure levels are compared to determine the local tissue deformation.

Each palpogram represents the strain information for a certain cross section over the full cardiac cycle. The longitudinal resolution of the acquisitions depends on heart rate and pullback speed. With a heart rate of 60 beats/min and a pullback speed of 1.0 mm/s, the longitudinal resolution is 1.0 mm. Palpograms were acquired simultaneously with radiofrequency IVUS using the same 20-MHz phased-array IVUS catheter. Digital radiofrequency data were acquired using a custom-designed workstation.

Data were acquired from the left main and proximal 6 to 8 cm of each major epicardial coronary artery at a pullback speed of 1.0 mm/s using an automated pullback device (Trak Back II, Volcano Corporation) with simultaneous recordings of the electrocardiogram, aortic pressure, and IVUS-VH

data. The data were subsequently stored on a DVD and sent to the imaging core laboratory for offline analyses (Cardialysis BV, Rotterdam, the Netherlands). The local strain was calculated from the gated radiofrequency traces using cross-correlation analyses, displayed and color coded from blue (for 0% strain) through yellow (for 2% strain) via red, as previously described (19). This color-coded information was superimposed on the lumen vessel boundary of the cross-sectional IVUS image. Using previously described methodology, plaque strain values were assigned a Rotterdam classification (ROC) ranging from I to IV (ROC I, 0% to 0.5%; ROC II, 0.6% to <0.9%; ROC III, 0.9% to 1.2%; ROC IV, >1.2%) (8). A region was defined as a high-strain spot when it had high strain (ROC III to IV) that spanned an arc of at least 12° at the surface of a plaque (identified on the IVUS recording) adjacent to low-strain regions (<0.5%). The highest value of strain in the cross section was taken as the strain level of the spot.

Cross-correlation of the techniques. An independent experienced palpography analyst, blinded to the clinical information of all patients, used a color-blinded side-by-side view of both (palpography and IVUS-VH). Because the 2 recordings (electrocardiography-gated IVUS-VH, and nonelectrocardiography-gated palpography) were taken simultaneously from the same coronary region, the time stamps (i.e., time of acquisition) of both techniques were used to superimpose the palpography strain values over the coronary plaques identified by IVUS-VH (Fig. 2). Three different palpography endpoints for each plaque were then calculated.

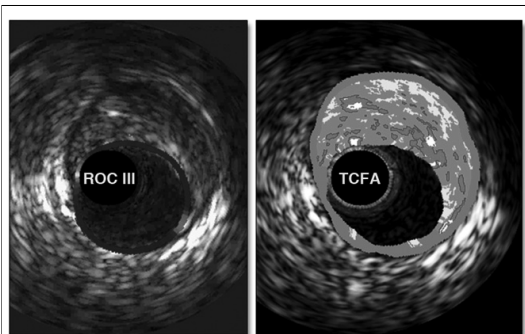


Figure 2. Palpography and IVUS-VH

Side-by-side view of palpography (left) and IVUS-VH (right) for a TCFA. High-strain spots on palpography are present at the edges of the plaque. Note that the time of acquisition of the images for both techniques is the same. IVUS-VH = intravascular ultrasound virtual histology; TCFA = thin-cap fibroatheroma.

1. Endpoint 1 (maximum strain value per plaque): maximum value of strain spots in the region of interest
2. Endpoint 2 (density of ROC III to IV per plaque): cumulative strain of the maximum strain in all ROC III/ROC IV high-strain spots, normalized by the number of cross sections
3. Endpoint 3 (density of ROC I/IV per plaque): cumulative strain of the maximum strain in all ROC I/ROC II/ROC III/ROC IV high-strain spots, normalized by the number of cross sections

Clinical endpoint definitions. The primary endpoint was MACE, defined as a composite of cardiac death, cardiac arrest, myocardial infarction, or unstable or progressive angina requiring rehospitalization or revascularization. On the basis of follow-up

angiography, MACE were adjudicated as occurring at the initially treated lesion site responsible for the original ACS (the index culprit lesion), or at previously untreated coronary segments (nonculprit lesions). If follow-up angiography was not performed, the location of the MACE was classified indeterminate (9,10).

Statistical analysis. Categorical variables are presented using frequencies and percentages, continuous variables with mean \pm SD or median (interquartile range), according to their normal or non-normal distribution. Comparison and correlation among variables were done with different statistical tests according to their distribution. Analysis of normality of the continuous variables was performed with the Kolmogorov-Smirnov test. In particular, comparison among groups for variables normally distributed was performed by analysis of variance and for variables non-normally distributed by the Mann-Whitney or Kruskal-Wallis test. Correlation among variables was done by the Pearson or Spearman test, accordingly to their normal or non-normal distribution, respectively. Palpography endpoints were compared at the plaque level and at the patient level. To relate high-sensitivity C-reactive protein (hsCRP) values to plaque type, because hsCRP is patient specific, each patient was entered in the analysis, according to his or her worst plaque (TCFA, CTFA, or NCTFA). For plaque (i.e., fibroatheroma) or lesion level data, a model with a generalized estimating equations approach was used to compensate for any potential cluster effect of multiple plaques in the same lesion or multiple lesions in the same patient and presented as least-square means with 95% confidential intervals. A 2-sided p value <0.05 indicated statistical significance. Statistical analyses were performed using SPSS software version 13.0 (SPSS Inc., Chicago, Illinois).

RESULTS

Baseline clinical characteristics. Between October 29, 2004, and June 8, 2006, the PROSPECT trial enrolled 697 patients. In a subgroup of 114 patients, IVUS palpography and radiofrequency recordings were simultaneously obtained during a single IVUS pullback. Clinical baseline characteristics are shown in Table 1. At a median follow-up of 3.4 years, a total of 16 MACE were recorded in this population, adjudicated to untreated nonculprit lesions. Because no death or acute myocardial infarction in this subgroup occurred during follow-up, MACE

Table 1. Patient Characteristics, Baseline Laboratory Results, and Index Procedure

Age, yrs	55.7 \pm 10.9
Female	25/114 (22)
Diabetes mellitus	13/114 (11.4)
Requiring insulin	3/114 (2.6)
Metabolic syndrome	31/114 (27.1)
Current cigarette use	65/114 (57.7)
Hypertension	56/114 (49.1)
Hyperlipidemia	62/114 (54.3)
Previous myocardial infarction	12/114 (10.5)
Family history of coronary artery disease	61/114 (53.5)
Framingham risk score	6.3 \pm 3.1
Previous percutaneous coronary intervention	11/114 (9.6)
Clinical presentation	
ST-segment elevation myocardial infarction	44/114 (38.5)
Non-ST-segment elevation myocardial infarction	56/114 (49.3)
Unstable angina with electrocardiographic changes	14/114 (12.2)
Body mass index, kg/m ²	28.3 \pm 5.1
Cholesterol, mg/dl	
Total	172.7 \pm 42.5
LDL	81.4 \pm 48.4
HDL	43.3 \pm 21.1
Triglycerides, mg/dl	128.8 \pm 84.3
Hemoglobin A _{1c} , %	5.8 (5.3–6.1)
Estimated creatinine clearance, ml/min	104.0 (79.0–132.4)
High-sensitivity C-reactive protein, mg/l	7.0 (2.4–16.6)

Values are mean \pm SD, n (%), or median (interquartile range).
HDL = high-density lipoprotein; LDL = low-density lipoprotein.

therefore consisted mainly of new occurrences of unstable or progressive angina requiring rehospitalization or revascularization.

Imaging analysis. A total of 488 NC-rich plaques were identified by radiofrequency IVUS and palpog-

Table 2. Lesion Characterization of Necrotic Core-Rich Plaques (N = 488)

Lumen cross-sectional area, mm ²	7.6 \pm 3.2
External elastic membrane area, mm ²	16.2 \pm 5.5
Plaque cross-sectional area, mm ²	8.6 \pm 3.2
Plaque burden, %	53.5 \pm 9.6
$\geq 70\%$	37 (7.5)
Fibroatheroma length, mm	1.7 (0.9–3.0)
Tissue composition, %	
Fibrotic	29.5 \pm 8.1
Fibrofatty	6.7 \pm 4.4
Dense calcium	7.0 \pm 4.7
Necrotic core	14.1 \pm 4.8
Plaque classification	
Thin-cap fibroatheroma	111 (22.8)
Calcified thick-cap fibroatheroma	213 (43.6)
Noncalcified thick-cap fibroatheroma	164 (33.6)

Values are mean \pm SD, n (%), or median (interquartile range).

	TCFA (n = 111)	CTFA (n = 213)	NCTFA (n = 164)	p Value
Maximum strain value (endpoint #1), %	0.56 ± 0.36 0.45 (0.30–0.70)	0.53 ± 0.44 0.40 (0.30–0.80)	0.58 ± 0.44 0.50 (0.30–0.70)	0.50
Density of ROC III–IV (endpoint #2), ROC/mm	0.08 ± 0.18 0.00 (0.00–0.00)	0.09 ± 0.27 0.00 (0.00–0.00)	0.08 ± 0.20 0.00 (0.00–0.00)	0.80
Density of ROC I–IV (endpoint #3), ROC/mm	0.31 ± 0.20 0.28 (0.15–0.40)	0.33 ± 0.29 0.25 (0.15–0.42)	0.33 ± 0.27 0.25 (0.15–0.44)	0.70

Values are mean ± SD and median (interquartile range).
CTFA = calcified thick-cap fibrotheroma; NCTFA = noncalcified thick-cap fibrotheroma; ROC = Rotterdam classification; TCFA = thin-cap fibrotheroma.

raphy (4.2 per patient). Table 2 shows all imaging data. In particular, 22.8% were classified as TCFA, 43.6% CTFA, and 33.6% NCTFA. No differences were found in palpography endpoints among these 3 types of plaque (Table 3).

The hsCRP values did not differ among the different types of plaque considered at the patient level (TCFA, 8.5 mg/l [interquartile range: 3.0 to 12.4 mg/l]; CTFA, 6.9 mg/l [interquartile range: 2.8 to 19.4 mg/l]; NCTFA, 8.5 mg/l [interquartile range: 4.0 to 19.7 mg/l]; $p = 0.2$). No correlation was found between palpography endpoints and hsCRP at the patient level ($r = -0.004$, $p = 0.975$ for endpoint #1; $r = 0.073$, $p = 0.511$ for endpoint #2; $r = -0.46$, $p = 0.678$ for endpoint #3). Palpography endpoint #1 was higher in patients with a clinical presentation of ST-segment elevation myocardial infarction (STEMI) or non-ST-segment elevation myocardial infarction (NSTEMI) compared with patients with unstable angina (0.31% [inter-

quartile range: 0.25% to 0.50%]); NSTEMI (0.60% [interquartile range: 0.37% to 0.70%]); or STEMI (0.50% [interquartile range: 0.32% to 0.76%]) (Fig. 3). hsCRP values did not differ according to the clinical presentation (unstable angina, 4.5 mg/l [interquartile range: 2.6 to 10.5 mg/l] vs. NSTEMI, 6.6 mg/l [interquartile range: 2.6 to 12.4 mg/l] vs. STEMI, 9.1 mg/l [interquartile range: 2.2 to 20.7 mg/l]; $p = 0.418$). Comparison of the tertiles of endpoint 1 in terms of hsCRP values showed no differences among them (7.9 mg/l [interquartile range: 3.6 to 13.0 mg/l] vs. 6.6 mg/l [interquartile range: 1.6 to 11.1 mg/l] vs. 8.5 mg/ml [interquartile range: 2.4 to 18.0 mg/l], respectively; $p = 0.794$). The other palpography endpoints did not differ among patients according to their clinical presentation.

Plaques with ROC III to IV showed no differences compared with plaques with ROC I to II (Table 4). A weak correlation was found between

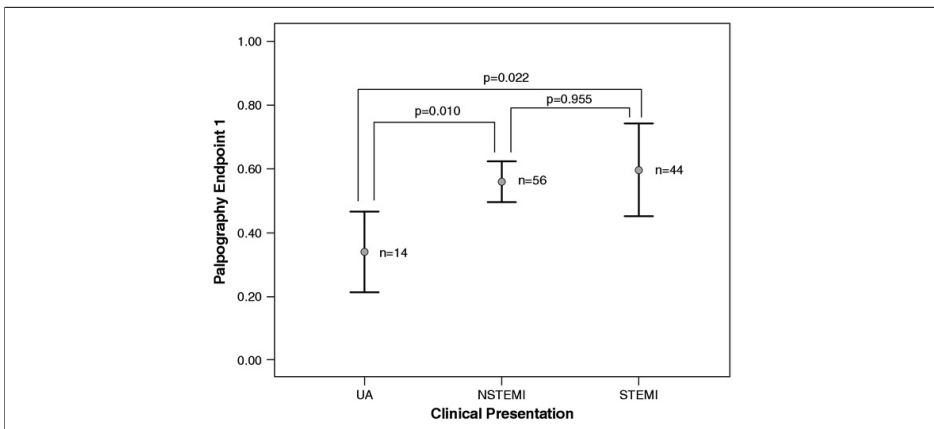


Figure 3. Maximum Strain Value Distribution According to Clinical Presentation

The mean of the maximum strain value (endpoint #1) in the necrotic core-rich plaques by clinical presentation. NSTEMI = non-ST-segment elevation myocardial infarction; STEMI = ST-segment elevation myocardial infarction; UA = unstable angina.

Table 4. Comparison of Radiofrequency IVUS Parameters and ROC Palpography Classification

IVUS-VH	ROC I-II Plaques (n = 404)	ROC III-IV Plaques (n = 84)	p Value
Plaque area, mm ²	8.5 (8.0–9.0)	8.2 (7.3–9.1)	0.40
Dense calcium, %	6.3 (5.6–7.0)	6.2 (5.1–7.2)	0.86
Necrotic core, %	12.9 (12.1–13.6)	12.5 (11.5–13.5)	0.44
Fibrous tissue, %	30.2 (28.9–31.4)	29.3 (27.1–31.5)	0.59
Fibrofatty tissue, %	7.2 (6.5–8.0)	7.53 (6.3–8.6)	0.59

All values are presented as generalized estimating equation-adjusted least mean square (95% confidence interval).
IVUS = intravascular ultrasound; IVUS-VH = intravascular ultrasound virtual histology; ROC = Rotterdam classification.

the palpography endpoint 3 and relative content of fibrous tissue for the TCFA plaques ($r = -0.2$, $p = 0.02$). No correlation was found between the other palpography endpoints and VH component for other VH plaque type (CTFA and NCTFA).

The fibroatheromas identified in the patients in whom MACE developed during follow-up were 49 of 488 (10.0%): TCFA, 11 of 49 (22.4%); CTFA, 22 of 49 (45%), and NCTFA, 16 of 49 (32.6%). These plaques demonstrated higher areas ($p = 0.03$) and a higher fibrofatty component ($p < 0.01$) compared with plaques of patients who were MACE free during follow-up (Table 5). However, in this substudy, no differences were found among the groups according to the distribution of VH plaque classification. No differences were found in palpography endpoints between the plaques of patients with or without MACE during follow-up (Table 5).

DISCUSSION

The principal findings of this substudy are the following: 1) larger fibroatheromas are confirmed to be more frequent in patients in whom cardiac events develop during long-term follow-up; and 2) palpography does not provide any additional diagnostic information with respect to the VH and does not specifically identify plaques at higher risk of events.

The PROSPECT study was the first trial to study atherosclerosis using a multimodality intracoronary imaging approach in patients after successfully treated ACS. This demonstrated that non-culprit lesions with a higher plaque burden and a radiofrequency IVUS morphology of TCFA were independent predictors of cardiovascular events over a 3-year follow-up period (9,11–16).

In our substudy, we focused on NC-rich plaques and analyzed the palpography data of these plaques. As shown in the main study, we

found that larger fibroatheromas were more frequent in patients in whom events developed during follow-up. It is noteworthy to consider that, because previous studies demonstrated a correlation between plaque size and its NC content (24,25), use of gray-scale IVUS could be sufficiently powerful to identify larger and NC-rich plaques. In this substudy, no difference, indeed, was demonstrated in VH plaque distribution between plaques of patients in whom MACE developed during follow-up and those who were MACE free.

Palpography was previously shown to potentially detect differences in deformability (strain) exhibited by different types of plaques, with lipid-rich plaques deforming more and thus showing a higher strain value compared with calcified or fibrous plaques (17,19). Rodriguez-Granillo et al. (8) showed that IVUS-VH had an acceptable sensitivity to detect high strain as assessed by palpography, but a low specificity. However, all of these studies were performed retrospectively and could not identify the predictive value of these techniques in the detection of high-risk plaques. In our subanalysis of the PROSPECT trial, palpography analyses of all 3 coronary vessels were performed and all data were matched to each NC-rich plaque. Our approach was therefore plaque based, whereas Rodriguez-Granillo et al. (8) used a frame-based approach.

Using this plaque-based approach, we found that ROC III to IV plaques did not exhibit any difference in VH composition compared with ROC I to II plaques, confirming the results of our previous frame-based approach (8). In addition, palpography was already validated in an *ex vivo* model to identify thin-capped fibroatheromas. However, in this substudy, the strain values were found to be no different between plaques with a thin or a thick fibrous cap, as evaluated by IVUS (19,26,27).

The number of high-strain spots in the culprit epicardial vessel was previously found to be correlated with clinical presentation and significantly decrease with standard medical therapy (18). In our analysis, we confirmed that the high-strain spot can be correlated with the clinical presentation, finding a higher maximum strain value in patients with a clinical presentation of NSTEMI or STEMI compared with those with unstable angina (18) (Fig. 3). However, we did not achieve any correlation between the high-strain spot and

Table 5. Comparison of Coronary Plaques in Patients With and Without MACE During Follow-Up			
	Plaques in Patients With MACE (n = 49)	Plaques in Patients Without MACE (n = 439)	p Value
Radiofrequency IVUS*			
Plaque area, mm ²	10.0 (8.4–11.6)	8.2 (7.7–8.8)	0.03
Dense calcium, %	6.3 (5.7–7.0)	5.4 (2.8–8.0)	0.51
Necrotic core, %	12.4 (10.2–14.5)	12.9 (12.1–13.7)	0.64
Fibrous tissue, %	32.6 (28.4–36.8)	29.7 (28.4–31.0)	0.19
Fibrofatty tissue, %	10.3 (7.9–12.6)	6.8 (6.1–7.6)	<0.01
VH plaque classification			
TCFA	11 (22)	100 (22)	0.73
CTFA	22 (45)	191 (43)	0.49
NCTFA	16 (33)	148 (35)	0.76
Palpography			
Maximum strain value (endpoint #1), %	0.51 ± 0.38	0.57 ± 0.43	0.409
	0.40 (0.20–0.80)	0.50 (0.30–0.70)	
Density of ROC III–IV (endpoint #2), ROC/mm	0.06 ± 0.20	0.09 ± 0.22	0.399
	0.00 (0.00–0.00)	0.00 (0.00–0.00)	
Density of ROC I–IV (endpoint #3), ROC/mm	0.30 ± 0.23	0.33 ± 0.26	0.420
	0.29 (0.13–0.51)	0.25 (0.15–0.41)	
<small>Values are n (%), mean ± SD, or median (interquartile range). *These values are presented as generalized estimating equation-adjusted least mean square (95% confidence interval). MACE = major adverse cardiac event; VH = virtual histology; other abbreviations as in Tables 3 and 4.</small>			

the C-reactive protein values, as found in a previous study (18).

It is important to highlight that the strain values of palpography were lower in our population compared with previous studies (8,27); these low strain values may be the reason for the low rates of cardiac events recorded in our population. Palpography can, indeed, potentially identify some of the mechanical properties of coronary plaques that are more prone to rupture and lead to a clinical event such as cardiac death or acute myocardial infarction (18,19). However, during the follow-up, no patients experienced either cardiac death or myocardial infarction, only progressive stable or unstable angina. For these reasons, our study, therefore, may have been underpowered to detect possible differences in the mechanical properties of coronary plaques more prone to cause serious cardiac events (cardiac death, cardiac arrest, or myocardial infarction). The low rate of events confirms the results of the main trial in which the 3-year rate of serious adverse events was 4.9%, attesting to the favorable outcomes that may be achieved in this population with high compliance with medical therapy and close clinical follow-up (9).

Study limitations. The main limitations are the small sample size and the low event rate at follow-up. IVUS has an axial resolution of ~100 to 200 μm ,

whereas the pathologic definition of TCFA typically requires a cap thickness <65 μm (3). As such, a proportion of the lesions classified as TCFA by radiofrequency IVUS were more likely to have had thick fibrous caps. At present, no data are available to show that that IVUS-VH could be used to make treatment decisions.

CONCLUSIONS

Our data confirm that larger fibroatheromas occur more frequently in patients in whom cardiac events develop during long-term follow-up, although no statistical differences in VH plaque classification were found between patients with or without MACE. However, a combined approach by IVUS-VH and palpography did not lead to any additional information with regard to aiding diagnostic identification of the fibroatheroma with the higher risk of rupture. In light of these results, the future application of palpography as an intracoronary imaging device to detect high-risk lesions needs to be revisited.

Reprint requests and correspondence: Dr. Patrick W. Serruys, Thoraxcenter, Ba-583, 's Gravendijkwal 230, 3015 CE Rotterdam, the Netherlands. *E-mail:* p.w.j.serruys@erasmusmc.nl.

REFERENCES

1. Ambrose JA, Tannenbaum MA, Alexopoulos D, et al. Angiographic progression of coronary artery disease and the development of myocardial infarction. *J Am Coll Cardiol* 1988; 12:56–62.
2. Glaser R, Selzer F, Faxon DP, et al. Clinical progression of incidental, asymptomatic lesions discovered during culprit vessel coronary intervention. *Circulation* 2005;111:143–9.
3. Virmani R, Burke AP, Farb A, Kolodgie FD. Pathology of the vulnerable plaque. *J Am Coll Cardiol* 2006;47:C13–8.
4. Naghavi M, Libby P, Falk E, et al. From vulnerable plaque to vulnerable patient: a call for new definitions and risk assessment strategies: part II. *Circulation* 2003;108:1772–8.
5. Naghavi M, Libby P, Falk E, et al. From vulnerable plaque to vulnerable patient: a call for new definitions and risk assessment strategies: part I. *Circulation* 2003;108:1664–72.
6. Schaar JA, Muller JE, Falk E, et al. Terminology for high-risk and vulnerable coronary artery plaques. Report of a meeting on the vulnerable plaque, June 17 and 18, 2003, Santorini, Greece. *Eur Heart J* 2004;25: 1077–82.
7. Loree HM, Kamm RD, Stringfellow RG, Lee RT. Effects of fibrous cap thickness on peak circumferential stress in model atherosclerotic vessels. *Circ Res* 1992;71:850–8.
8. Rodriguez-Granillo GA, Garcia-Garcia HM, Valgimigli M, et al. In vivo relationship between compositional and mechanical imaging of coronary arteries. Insights from intravascular ultrasound radiofrequency data analysis. *Am Heart J* 2006;151: 1025.e1–6.
9. Stone G, Maehara A, Lansky AJ, et al. A prospective natural-history study of coronary atherosclerosis. *N Engl J Med* 2011;364:226–35.
10. Maehara A, Cristea E, Mintz GS, et al. Definitions and methodology for the grayscale and radiofrequency intravascular ultrasound and coronary angiographic analyses. *J Am Coll Cardiol* 2012;5 Suppl S:S1–8.
11. Marso SP, Mercado N, Maehara A, et al. Atherosclerotic plaque composition and clinical outcomes in patients with acute coronary syndromes and metabolic syndrome or diabetes. *J Am Coll Cardiol* 2012;5:Suppl S:42–52.
12. Mehran et al. Differences in coronary plaque composition, morphology and outcomes in patients with and without chronic kidney disease presenting with acute coronary syndromes. *J Am Coll Cardiol* 2012;5:Suppl S:xxx–xxx.
13. Lansky AJ, Ng VG, Maehara A, et al. Impact of gender on the extent of coronary atherosclerosis, plaque composition and clinical outcomes in acute coronary syndromes. *J Am Coll Cardiol* 2012;5 Suppl S:S62–72.
14. McPherson JA, Maehara A, Weisz G, et al. Residual plaque burden in patients with acute coronary syndromes after successful percutaneous coronary intervention: extent, characterization, and clinical implications. *J Am Coll Cardiol* 2012;5 Suppl S:S76–85.
15. Brener SJ, Mintz GS, Cristea E, et al. Characteristics and clinical significance of angiographically mild lesions in acute coronary syndromes. *J Am Coll Cardiol* 2012;5 Suppl S:S86–94.
16. Sanidas EA, Mintz GS, Maehara A, et al. Adverse cardiovascular events arising from atherosclerotic lesions with and without angiographic disease progression. *J Am Coll Cardiol* 2012;5 Suppl S:S95–105.
17. Schaar JA, De Korte CL, Mastik F, et al. Characterizing vulnerable plaque features with intravascular elastography. *Circulation* 2003;108:2636–41.
18. Schaar JA, Regar E, Mastik F, et al. Incidence of high-strain patterns in human coronary arteries: assessment with three-dimensional intravascular palpography and correlation with clinical presentation. *Circulation* 2004; 109:2716–9.
19. Schaar JA, van der Steen AF, Mastik F, Baldeusings RA, Serruys PW. Intravascular palpography for vulnerable plaque assessment. *J Am Coll Cardiol* 2006;47:C86–91.
20. Nair A, Kuban BD, Tuzcu EM, Schoenhagen P, Nissen SE, Vince DG. Coronary plaque classification with intravascular ultrasound radiofrequency data analysis. *Circulation* 2002;106:2200–6.
21. Nair A, Margolis MP, Kuban BD, Vince DG. Automated coronary plaque characterisation with intravascular ultrasound backscatter: ex vivo validation. *EuroIntervention* 2007;3: 113–20.
22. Garcia-Garcia HM, Mintz GS, Lerman A, et al. Tissue characterisation using intravascular radiofrequency data analysis: recommendations for acquisition, analysis, interpretation and reporting. *EuroIntervention* 2009;5:177–89.
23. Rodriguez-Granillo GA, Garcia-Garcia HM, McFadden EP, et al. In vivo intravascular ultrasound-derived thin-cap fibroatheroma detection using ultrasound radiofrequency data analysis. *J Am Coll Cardiol* 2005;46: 2038–42.
24. Garcia-Garcia HM, Goedhart D, Serruys PW. Relation of plaque size to necrotic core in the three major coronary arteries in patients with acute coronary syndrome as determined by intravascular ultrasonic imaging radiofrequency. *Am J Cardiol* 2007;99: 790–2.
25. Qian J, Maehara A, Mintz GS, et al. Relation between individual plaque components and overall plaque burden in the prospective, multicenter virtual histology intravascular ultrasound registry. *Am J Cardiol* 2009;104:501–6.
26. de Korte CL, Siervogel MJ, Mastik F, et al. Identification of atherosclerotic plaque components with intravascular ultrasound elastography in vivo: a Yucatan pig study. *Circulation* 2002;105:1627–30.
27. Serruys PW, Garcia-Garcia HM, Buszman P, et al. Effects of the direct lipoprotein-associated phospholipase A(2) inhibitor darapladib on human coronary atherosclerotic plaque. *Circulation* 2008;118:1172–82.

Key Words: intravascular ultrasound ■ palpography.

Chapter 4

Assessment of findings after coronary metallic stent
implantation

4.1

Evaluation of in-stent restenosis in the APPROACH trial (assessment on the prevention of progression by Rosiglitazone on atherosclerosis in diabetes patients with cardiovascular history).

Hector M Garcia-Garcia, Scot Garg, Salvatore Brugaletta, Giorgio Morocutti, Robert E Ratner, Nikheel S Kolatkar, Barbara G Kravitz, Diane M Miller, Chun Huang, Richard W Nestor, Patrick W Serruys

Int J Cardiovasc Imaging 2011, Epub ahead of print

Evaluation of in-stent restenosis in the APPROACH trial (assessment on the prevention of progression by Rosiglitazone on atherosclerosis in diabetes patients with cardiovascular history)

Héctor M. García-García · Scot Garg · Salvatore Brugaletta · Giorgio Morocutti · Robert E. Ratner · Nikheel S. Kolatkar · Barbara G. Kravitz · Diane M. Miller · Chun Huang · Richard W. Nesto · Patrick W. Serruys · The APPROACH study group

Received: 5 October 2010 / Accepted: 16 February 2011

© The Author(s) 2011. This article is published with open access at Springerlink.com

Abstract To determine (1) the medium-term effect of rosiglitazone and glipizide on intra-stent neointima hyperplasia, (2) restenosis pattern as assessed by intravascular ultrasound (IVUS) and quantitative coronary angiography (QCA) in patients with T2DM and coronary artery disease. A total of 462 patients with T2DM were randomized to rosiglitazone or glipizide for up to 18 months in the APPROACH trial, and had evaluable baseline and follow-up IVUS examinations. There was no significant difference in the size of plaque behind stent between the rosiglitazone and glipizide groups at 18 months among those treated with a bare metal stent (-5.6 mm^3 vs. 1.9 mm^3 ; $P = 0.61$) or with a drug-eluting stent (12.1 mm^3 vs. 5.5 mm^3 ; $P = 0.09$). Similarly, there was no significant difference in

percentage intimal hyperplasia volume between the rosiglitazone and glipizide groups at 18 months among those treated with a bare metal stent (24.1% vs. 19.8%; $P = 0.38$) or with a drug-eluting stent (9.8% vs. 8.3%; $P = 0.57$). QCA data (intra-stent late loss, intra-stent diameter stenosis or binary restenosis) were not different between the rosiglitazone and glipizide groups. This study suggests that both rosiglitazone and glipizide have a similar effect on neointimal growth at medium term follow-up, a finding that warrants investigation in dedicated randomized trials.

Keywords Restenosis · Type 2 diabetes · IVUS · Atherosclerosis

Trial Registration: Clinicaltrials.gov NCT00116831.
<http://clinicaltrials.gov/ct2/show/NCT00116831>.

The members of the APPROACH study group are given in "Appendix".

H. M. García-García (✉) · S. Garg · S. Brugaletta · P. W. Serruys
 Erasmus Medical Center., Z120 Thoraxcentre,
 Gravendijkwal 230, 3015 CE Rotterdam, The Netherlands
 e-mail: h.garciagarcia@erasmusmc.nl

H. M. García-García
 Cardialysis, Rotterdam, The Netherlands

G. Morocutti
 Cardiologia, Azienda Ospedaliera, Universitaria S. Maria
 della Misericordia, Udine, Italy

Introduction

The APPROACH (Assessment on the Prevention of Progression by Rosiglitazone On Atherosclerosis in diabetes patients with Cardiovascular History) study

R. E. Ratner
 MedStar Research Institute, Washington, DC, USA

N. S. Kolatkar · B. G. Kravitz · D. M. Miller · C. Huang
 GlaxoSmithKline Research and Development,
 King of Prussia, PA, USA

R. W. Nesto
 Lahey Clinic, Burlington, MA, USA

was a double-blind randomized clinical trial comparing the effects of rosiglitazone with glipizide on the progression of coronary atherosclerosis [1, 2]. Patients with Type 2 diabetes mellitus (T2DM) are at increased risk for restenosis after intracoronary stent placement [3–6]. Moreover, prior studies have suggested that thiazolidinediones, which improve insulin sensitivity and have effects on vascular smooth muscle cell proliferation and neointimal hyperplasia, may reduce rates of in-stent restenosis in patients irrespective of their diabetic status [7–15].

The objectives of this pre-specified APPROACH sub-study were: (1) to determine the effect of rosiglitazone and glipizide on intra-stent neointima hyperplasia in patients with T2DM and coronary artery disease (CAD); (2) to determine the restenosis parameters measured by intravascular ultrasound (plaque behind stent, intra-stent intima hyperplasia volume); and (3) to report the quantitative coronary angiography (QCA) intra-stent late loss, intra-stent diameter stenosis [DS], and binary angiographic restenosis.

Materials and methods

Study design and eligibility criteria

A detailed description of the APPROACH trial has been previously published [1]. In brief, the APPROACH study was a prospective multicenter,

double-blind, randomized, active-controlled trial (Fig. 1) of 672 patients from 92 centers in 19 countries, who were aged 30–80 years with established T2DM and who had clinically indicated coronary angiography or percutaneous coronary intervention (PCI) between February 2005 and January 2007. Patients were included if they had at least one atherosclerotic plaque with >50% luminal narrowing in a coronary artery, and if their diabetes was treated with either lifestyle approaches alone (with an HbA1C > 7 and ≤10%), or with oral agents comprising 1 oral agent at any dose, or 2 oral agents where each was prescribed at ≤50% of its maximal dose (with an HbA1C > 6.5 and ≤8.5%). Exclusion criteria were: ST-segment elevation myocardial infarction in the prior 30 days; coronary artery bypass graft surgery; severe valvular heart disease; left ventricular ejection fraction <40%; any heart failure (New York Heart Association class I–IV); uncontrolled hypertension (systolic blood pressure >170 mmHg or diastolic blood pressure >100 mmHg); renal insufficiency (serum creatinine ≥1.5 mg/dl for men or ≥1.4 mg/dl for women); and active liver disease. Participant safety was monitored by an Independent Data Monitoring. Data analysis was performed according to a pre-specified plan that was developed with the approval of the steering committee.

In this pre-specified analysis, all patients who underwent stent placement during APPROACH and

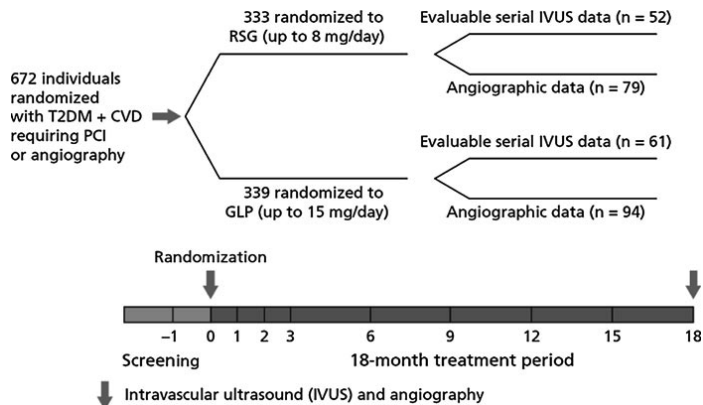


Fig. 1 Patient disposition. CVD cardiovascular disease, GLP glipizide, IVUS intravascular ultrasound, PCI percutaneous coronary intervention, RSG rosiglitazone, T2DM type 2 diabetes mellitus

had available serial IVUS or QCA measurements were included.

Quantitative angiography analysis

The angiograms were stored in DICOM format and analyzed offline by Core laboratory personnel (Cardialysis, Rotterdam, The Netherlands), using the CASS II analysis system (Pie Medical BV, Maastricht, The Netherlands). The following quantitative coronary angiography (QCA) analysis parameters were measured: computed-defined minimal luminal diameter (MLD) and reference vessel diameter (RVD) obtained by an interpolate method.

Quantitative coronary angiography endpoints

Late loss was defined as the difference in minimum lumen diameter between baseline and follow-up.

Percent diameter stenosis was defined as the minimum lumen diameter divided by the reference vessel diameter at the site of the MLD $\times 100$.

Binary angiographic restenosis was defined as follow-up stenosis $>50\%$. This is reported as frequency and percentage.

Management of glycemia and follow-up

Patients were randomized in a 1:1 ratio to receive masked rosiglitazone (4 mg/day) or glipizide (5 mg/day) in one pill. After 2 and 3 months, the dose of masked study drug was increased if tolerated and if the mean daily glucose level calculated from the patient's logbook of capillary tests in the 3 days prior to the visit was ≥ 126 mg/dl (7.0 mmol/l). If more than 1 titration was required, 2 pills per day were given. Open-label metformin (maximal total daily dose 2,550 mg) and then once-daily basal insulin, or both was added after the first 3 months if needed to maintain a $\text{HbA1c} \leq 7\%$ using a glyceemic titration algorithm designed to provide comparable glyceemic control between treatment groups. Non-study drugs were reduced before study drugs in the event of hypoglycemia requiring dose reductions. Unless informed consent was formally withdrawn, all patients were followed until 18 months from randomization and clinical status ascertained regardless of whether they continued to take study medication.

Intravascular ultrasound examination and image analysis

Following stent implantation IVUS was performed. After intracoronary administration of nitroglycerin, an ultrasound catheter (2.5F Atlantis SR Pro Imaging 40 MHz) connected to a Galaxy G2 digital imaging console (Boston Scientific, Natick, MA) was advanced into the target vessel. The imaging transducer was positioned just distal to an identifiable side branch, and then motorized pullback of the transducer was performed at 0.5 mm/s. If a participant required cardiac catheterization for a clinical indication between 9 and 18 months, follow-up IVUS examination could be performed at that time instead of at study completion.

Intravascular ultrasound outcomes

Core laboratory personnel (Cardialysis, Rotterdam, The Netherlands) who were blinded to treatment assignment analyzed all IVUS images using validated software (Curad, version 3.1, Wijk bij Duurstede, The Netherlands), that facilitates detection of luminal and external elastic membrane (EEM—also called vessel contour) boundaries in reconstructed longitudinal planes. In order to obtain a smooth appearance of the vessel wall structures in the longitudinal views, the Intelligate™ image-based gating method was applied [16, 17].

Intravascular ultrasound endpoints

Plaque behind stent was derived by subtracting the mean stent area from the vessel mean area.

Percentage volume of intimal hyperplasia (%vol IH) was defined as IH volume divided by stent volume.

Statistical methods

For baseline characteristics, continuous variables are expressed as mean and standard deviation, or median and interquartile range if non-normally distributed, with categorical variables reported as percentage. For continuous variables *P* values were based on Wilcoxon test, while for categorical variables *P* values were based on Fisher's exact test. The *P* values for treatment difference of continuous IVUS and QCA

variables were based on analysis of covariance model (ANCOVA) with terms for treatment, baseline measurement, region, gender, cardiac procedure, and prior OAD medication. Two sample test was used for group comparisons at baseline and follow-up. For binary angiographic restenosis, Fisher's exact test was used.

Results

Participants

In total 672 (68% men) of mean (SD) age 61 (9) years, median diabetes duration of 4.8 years and mean haemoglobin HbA1C of 7.2 (0.9) % were randomized to either glipizide ($N = 339$) or rosiglitazone ($N = 333$) from 92 sites in 19 countries (Fig. 1). At the end of the study, 462 randomized patients had evaluable baseline and follow-up IVUS examinations. 173 had evaluable angiographic data and 113 had serial IVUS data from a vessel with PCI at baseline.

Patients were followed for a median of 18.6 months (IQR 18.2–18.9) and a mean (SD) of 16 (6) months; patients allocated to glipizide were adherent at 90.7% of visits and those allocated to rosiglitazone were adherent at 92.7% of visits.

In this analysis, 231 patients who underwent stent placement during the study and had available serial IVUS or QCA measurements were included. Patients who underwent stent placement do not represent randomized groups, however the distribution of these patients was similar between the randomized groups (glipizide $N = 118$, rosiglitazone $N = 113$).

Baseline characteristics were generally similar between the groups. (Table 1). Patients in the rosiglitazone group had slightly higher serum creatinine, compared with glipizide ($P = 0.01$).

All the DES implanted were from 1st DES generation. No difference in stent size were found between groups (Table 2).

Effect on intravascular ultrasound endpoints

There was no significant difference in the size of plaque behind stent between the rosiglitazone and glipizide groups at 18 months among those treated with a bare metal stent (-5.6 mm^3 vs. 1.9 mm^3 ; $P = 0.61$) or with

a drug-eluting stent (12.1 mm^3 vs. 5.5 mm^3 ; $P = 0.09$) (Table 3). Similarly, there was no significant difference in percentage intimal hyperplasia volume between the rosiglitazone and glipizide groups at 18 months among those treated with a bare metal stent (24.1% vs. 19.8%; $P = 0.38$) or with a drug-eluting stent (9.8% vs. 8.3%; $P = 0.57$) (Table 3).

Effect on QCA endpoints

Intra-stent late loss did not differ between the rosiglitazone and glipizide groups among those with a bare metal stent (0.76 mm vs. 0.71 mm; $P = 0.51$) or a drug-eluting stent (0.37 vs. 0.25; $P = 0.41$) (Table 3). There was no difference in intra-stent diameter stenosis between the rosiglitazone and glipizide groups among those with a bare metal stent (32.3% vs. 30.4%; $P = 0.50$) or a drug-eluting stent (22.1% vs. 17.9%; $P = 0.28$) (Table 3). The percentage of patients with binary angiographic restenosis did not differ between the rosiglitazone and glipizide groups among those with a bare metal stent (22.9% vs. 10.8%; $P = 0.21$) or a drug-eluting stent (4.6% vs. 1.8%; $P = 0.58$) (Table 3).

Safety

As noted previously, the patients who underwent stent placement do not represent randomized groups, however, there were no significant differences in cardiovascular events between the rosiglitazone and glipizide groups, which occurred infrequently during the trial (Table 4).

In the rosiglitazone group, 5 cardiovascular events occurred within 5 days of the baseline cardiac catheterization and were classified as procedure-related. These events included one revascularization, two nonfatal myocardial infarctions, one nonfatal stroke and one cardiovascular death.

Discussion

This study demonstrates no additional advantage of using rosiglitazone over glipizide in Type 2 diabetic patients for the reduction of in-stent restenosis; however it did demonstrate that both drugs have comparable effect on neointimal growth up to 18-months after coronary stent implantation.

Table 1 Baseline characteristics of intervened patients

	Glipizide (<i>N</i> = 118)	Rosiglitazone (<i>N</i> = 113)	P value
<i>Demographic characteristics</i>			
Age, mean (SD), years	60.4 (9.1)	62.4 (8.1)	0.14
Male, <i>n</i> (%)	84 (71.2%)	92 (81.4%)	0.09
Weight, mean (SD), kg	81.9 (17.5)	80.2 (17.3)	0.56
BMI, mean (SD), kg/m ²	29.2 (4.9)	28.7 (5.3)	0.30
Duration of diabetes, median [IQR], years	4.5 [1.5–9.5]	4.5 [1.9–8.7]	0.77
Hypertension, <i>n</i> (%)	91 (77.1%)	88 (77.9%)	1.00
Dyslipidemia, <i>n</i> (%)	72 (61.0%)	74 (65.5%)	0.50
Prior myocardial infarction, <i>n</i> (%)	38 (32.2%)	28 (24.8%)	0.24
Presenting condition, <i>n</i> (%)			
Acute coronary syndrome	60 (50.9%)	55 (48.7%)	0.79
Elective procedure	58 (49.2%)	58 (51.3%)	
Baseline procedure, <i>n</i> (%)			
Coronary angiography	6 (5.1%)	6 (5.3%)	1.00
Percutaneous coronary intervention	112 (94.9%)	107 (94.7%)	
Current smoker, <i>n</i> (%)	20 (17.0%)	24 (21.2%)	0.50
ACC/AHA lesion type, <i>n</i> (%)			
A	14 (11.7)	14 (12.1)	0.53
B1	49 (41.5)	48 (42.6)	
B2	35 (29.7)	32 (28.3)	
C	20 (17.1)	19 (17.0)	
<i>Prior medication use</i>			
Aspirin	106 (89.8%)	102 (90.3%)	1.00
Other anti-platelet	109 (92.4%)	108 (95.6%)	0.41
Beta-blocker	88 (74.6%)	86 (76.1%)	0.88
ACE inhibitor or ARB	80 (67.8%)	71 (62.8%)	0.49
Nitrates	57 (48.3%)	56 (49.6%)	0.90
Statin	97 (82.2%)	94 (83.2%)	0.86
Fibrate or other lipid-lowering agent	7 (5.93%)	10 (8.9%)	0.46
<i>Vital signs and laboratory values</i>			
Blood pressure, mean (SD), mmHg			
Systolic	129.9 (15.5)	126.6 (15.5)	0.17
Diastolic	74.5 (9.5)	73.2 (10.3)	0.41
HbA1c, mean (SD), %	7.1 (0.8)	7.0 (0.7)	0.14
Serum creatinine, mean (SD), μmol/L	85.2 (19.5)	93.7 (26.0)	0.01
BNP, median [IQR], pg/mL	30 [14–68]	25 [12–58]	0.50
Fasting insulin, median [IQR], μU/mL	12.1 [8.6–19.0]	13.0 [8.6–18.1]	0.96
LDL cholesterol, mean (SD), mg/dL	87.6 (38.0)	85.5 (36.6)	0.66
HDL cholesterol, mean (SD), mg/dL	41.2 (10.5)	40.9 (9.9)	0.79
Triglycerides, median [IQR], mg/dL	154.0 [113.7–200.9]	161.1 [123.9–192.0]	0.61
hsCRP, median [IQR], mg/L	5.1 [2.4–11.7]	6.1 [3.7–13.3]	0.19
MMP-9, median [IQR], μg/L	102.1 [48.1–202.4]	73.2 [38.4–159.9]	0.38

Table 2 Stent size distribution in the groups

	Bare metal stent			Drug-eluting stent		
	Glipizide <i>N</i> = 21	Rosiglitazone <i>N</i> = 21	<i>P</i> value	Glipizide <i>N</i> = 40	Rosiglitazone <i>N</i> = 31	<i>P</i> value
Diameter	2.79 ± 0.60	3.05 ± 0.83	0.126	2.58 ± 0.71	2.68 ± 0.54	0.592
Length	18.00 ± 7.20	17.25 ± 5.10	0.833	21.45 ± 7.81	19.58 ± 7.02	0.257

In this post-hoc analysis, neither rosiglitazone nor glipizide are randomized groups

On face value these results appear to contrast with the majority of the previously conducted studies, which have all reported significant reductions in the rates of in-stent restenosis in patients treated with thiazolidinediones compared to controls [7–15]. However it must be appreciated that these previous studies have inherent limitations which include: small sample sizes; a single-center location; the lack of independent core lab analysis; short follow-up; and PCI performed using only BMS. The recent POPPS study by Takagi et al. [7] is an exception in view of its multi-center recruitment, and use of an independent core lab; however patients were still only treated with BMS, and follow-up was reported at only 6-months. On the contrary, the current study has distinct advantages in addition to being the largest single assessment to date of in-stent restenosis in patients treated with thiazolidinediones. These additional advantages include medium term follow-up, the use of both bare and drug eluting stents, and IVUS/QCA analysis performed by an independent core lab.

In the recent POPPS study, the neointimal growth index (neointimal volume/stent volume × 100) at 6-months amongst patients who were received a BMS, and treatment with pioglitazone and controls was 31 and 40% respectively [7]; similarly in the current study the respective values of this index at 18-months for rosiglitazone and glipizide were 24 and 19%, respectively. Whilst the results for rosiglitazone are perhaps expected, the change noted with glipizide although welcome is unexpected, and obviously warrants further investigation.

The significance of the different follow-up periods, which were between 6–9 months in the earlier studies and 18-months in the current study, cannot be overstated. Previous IVUS studies have clearly demonstrated that neointimal growth continues to progress up to 18-months after implantation of a BMS, before regressing [18]. This key observation not only highlights the importance of documenting

the point in time when IVUS measurements are made, and keeping this in mind when interpreting the IVUS findings; but also indicates the arduous nature of trying to compare results from the current study to previous studies. Nevertheless, in the present study the comparatively lower rates of neointimal growth seen at 18-months, reiterates a comparable effect of both rosiglitazone and glipizide.

In-stent restenosis remains one of the undesired consequences of PCI, and although the introduction of drug eluting stents in 2002 improved rates of restenosis, they have been unable to eliminate it [19]. There is a widely held misconception that restenosis is a benign phenomenon; however it is associated with both morbidity and mortality. In simplistic terms, restenosis increases the requirement for a repeat PCI procedure, which in itself is not risk free. For example a mortality rate of 2.5% was observed in the Ontario registry in those patients having target vessel revascularisation within a month of their initial PCI procedure [20]. In addition rates of MI related to restenosis have been reported to be between 2 and 19% [21, 22].

In view of this it is no surprise that there is a great desire to identify adjunctive agents which may help reduce in-stent restenosis. This problem is particularly pertinent in diabetic patients owing to the identification of diabetes as an independent predictor of in-stent restenosis [3, 4]. The mechanisms underlying this increased risk are poorly understood, however it is considered amongst others to be the result of a combination of the greater degree of the vascular inflammation, and endothelial dysfunction seen in diabetics [23, 24]. The risk of in-stent restenosis is further compounded in T2DM patients because insulin resistance can aggravate restenosis, through the direct growth-factor like effect of insulin on vascular smooth muscle and neointimal cells [25].

Poor glycaemic control is also implicated in promoting restenosis [26], however previous studies

Table 3 Results of quantitative coronary angiographic analysis

IVUS measurement	Bare metal stent		<i>P</i> value	Drug-eluting stent		<i>P</i> value
	Glipizide <i>N</i> = 21	Rosiglitazone <i>N</i> = 21		Glipizide <i>N</i> = 40	Rosiglitazone <i>N</i> = 31	
<i>Vessel volume</i>						
Baseline	302.3 (161.4)	245.1 (104.3)	0.18	278.6 (132.6)	302.4 (110.1)	0.42
Follow-up	302.3 (160.5)	241.0 (110.0)	0.16	288.6 (141.9)	317.3 (102.6)	0.35
Change from baseline	0.0 (29.3)	-4.1 (39.8)		10.0 (23.0)	14.9 (34.1)	
Model-adjusted change (SE)	8.7 (16.6), <i>P</i> = 0.60	9.8 (16.3), <i>P</i> = 0.55		6.7 (13.9) <i>P</i> = 0.62	14.0 (14.3), <i>P</i> = 0.33	
Treatment difference (95% CI)	1.1 (-24.9, 27.1)		0.93	7.3 (-7.4, 22.0)		0.32
<i>Stent volume</i>						
Baseline	147.4 (81.1)	125.8 (53.1)	0.31	140.5 (64.4)	152.9 (61.0)	0.42
Follow-up	145.5 (78.7)	127.3 (60.0)	0.41	145.0 (65.8)	155.7 (53.4)	0.47
Change from baseline	-1.9 (15.4)	1.5 (16.4)		4.5 (10.8)	2.8 (17.3)	
Model-adjusted change (SE)	-1.2 (7.9), <i>P</i> = 0.88	3.5 (7.6), <i>P</i> = 0.65		0.3 (6.7), <i>P</i> = 0.96	-0.4 (6.9), <i>P</i> = 0.95	
Treatment difference (95% CI)	4.7 (-7.3, 16.6)		0.43	-0.7 (-7.8, 6.4)		0.84
<i>Plaque behind stent</i>						
Baseline	154.9 (83.3)	119.3 (57.5)	0.11	138.1 (77.9)	149.6 (59.7)	0.50
Follow-up	156.8 (85.2)	113.7 (54.4)	0.06	143.6 (83.6)	161.7 (58.7)	0.29
Change from baseline	1.9 (19.1)	-5.6 (26.0)		5.5 (16.9)	12.1 (22.4)	
Model-adjusted change (SE)	10.3 (10.5), <i>P</i> = 0.33	6.0 (10.6), <i>P</i> = 0.58		5.7 (9.4), <i>P</i> = 0.54	14.3 (9.7), <i>P</i> = 0.15	
Treatment difference (95% CI)	-4.3 (-21.2, 12.6)		0.61	8.6 (-1.4, 18.5)		0.09
<i>%volume of IH*</i>						
Baseline	-0.1 (0.2)	-0.01 (0.1)	0.25	-0.3 (1.0)	-0.3 (0.80)	0.75
Follow-up	19.7 (11.1)	24.1 (17.1)	0.33	8.0 (8.7)	9.6 (11.3)	0.51
Change from baseline	19.8 (11.1)	24.1 (17.1)		8.3 (8.7)	9.8 (11.3)	
Model-adjusted change (SE)	19.1 (7.2), <i>P</i> = 0.01	23.9 (7.17), <i>P</i> = 0.002		19.7 (4.3), <i>P</i> < 0.0001	21.0 (4.4), <i>P</i> < 0.0001	
Treatment difference (95% CI)	4.9 (-6.2, 15.9)		0.38	1.3 (-3.2, 5.8)		0.57
<i>QCA measurement</i>						
	Bare metal stent		<i>P</i> value	Drug-eluting stent		<i>P</i> value
	Glipizide <i>N</i> = 37	Rosiglitazone <i>N</i> = 35		Glipizide <i>N</i> = 57	Rosiglitazone <i>N</i> = 44	
<i>In-stent late loss (mm)</i>						
Mean	0.71	0.76		0.25	0.37	
SD	0.380	0.572		0.304	0.586	
Model-adjusted Mean at month 18 (SE)	0.85 (0.151)	0.93 (0.162)	0.51	0.75 (0.177)	0.82 (0.183)	0.41
<i>In-stent DS (%)</i>						
Mean	30.4	32.3		17.9	22.1	
SD	15	18		12	20	
Model-adjusted Mean at month 18 (SE)	32.98 (5.32)	35.92 (5.678)	0.50	32.57 (6.346)	35.82 (6.53)	0.28

Table 3 continued

QCA measurement	Bare metal stent		<i>P</i> value	Drug-eluting stent		<i>P</i> value
	Glipizide <i>N</i> = 37	Rosiglitazone <i>N</i> = 35		Glipizide <i>N</i> = 57	Rosiglitazone <i>N</i> = 44	
<i>RVD (mm)</i>						
Mean	2.62	2.58		2.62	2.78	
SD	0.51	0.47		0.42	0.44	
Model-adjusted Mean at month 18 (SE)	2.51 (0.100)	2.53 (0.108)	0.76	2.61 (0.121)	2.67 (0.125)	0.32
<i>MLD (mm)</i>						
Mean	1.84	1.75		2.15	2.27	
SD	0.59	0.56		0.46	0.45	
Model-adjusted Mean at month 18 (SE)	1.68 (0.151)	1.60 (0.162)	0.50	1.78 (0.141)	1.79 (0.146)	0.86
<i>Binary angiographic restenosis, n(%)</i>	4 (10.81)	8 (22.86)	0.21	1 (1.75)	2 (4.55)	0.58

In this post-hoc analysis, neither rosiglitazone nor glipizide are randomized groups; *%vol *IH* percentage volume of intimal hyperplasia

Table 4 Adverse cardiovascular events occurring either on-therapy or post-therapy

Patients with an event, <i>n</i> (%)	Glipizide (<i>N</i> = 118) (%)	Rosiglitazone (<i>N</i> = 113) (%)
All-cause death	3 (2.5)	5 (4.4)
Cardiovascular death	1 (0.8)	2 (1.8)
Stroke	0 (0.0)	2 (1.8)
Myocardial infarction	2 (1.7)	5 (4.4)
Nonfatal MI	1 (0.8)	4 (3.5)
Fatal MI	1 (0.8)	1 (0.9)
Cardiovascular death, nonfatal stroke, or nonfatal MI	2 (1.7)	7 (6.2)
Coronary revascularisation	14 (11.9)	15 (13.3)

In this post-hoc analysis, neither rosiglitazone nor glipizide are randomized groups

which have reported the benefit of thiazolidinediones in reducing restenosis have indicated that this benefit occurs independently of the drug's effect on glycaemic control [7]. There are many potential mechanisms by which thiazolidinediones may reduce in-stent restenosis including: (a) the inhibition of smooth muscle cell migration and proliferation [27, 28]; (b) the increased apoptosis in vascular smooth muscle cells [29]; (c) a beneficial effect on local inflammation [30, 31]; (d) an anti-thrombotic effect [32]; and (e) a beneficial effect on fasting insulin levels, thereby preventing insulin driven atherosclerosis [25, 33].

In the end, it is important to highlight recent concerns associated with rosiglitazone use. Following drug launch, a metanalysis published in 2007 showed, indeed, an increased risk of myocardial infarction and cardiovascular death associated with rosiglitazone [34]. The recent RECORD trial also demonstrated an increased risk of heart failure events in people treated with rosiglitazone [35]. Eventually, the FDA mandated a study comparing rosiglitazone and pioglitazone with placebo, known as TIDE and then stopped the inclusion of the patients. Rosiglitazone has subsequently been removed from the EU market however it remains available on the US market albeit with severe restrictions.

Limitations

IVUS analyses were available in half of the patients included in the present study and could not be representative of overall population. Stent design was not pre-specified for the different groups.

Conclusions

This study indicates that both rosiglitazone and glipizide have a similar effect on neointimal growth at medium term follow-up, a finding that warrants investigation in dedicated randomized trials.

Acknowledgments This study was funded by GlaxoSmith-Kline Pharmaceuticals. The authors of this manuscript have certified that they comply with the Principles of Ethical Publishing in the International Journal of Cardiology [36].

Conflict of interest Dr Garcia-Garcia received honoraria from GlaxoSmith-Kline; Dr Garg, Dr Brugaletta and Dr Morocutti have no conflict of interest to declare. Dr Ratner has received grants from AstraZeneca, Bayhill Therapeutics, GlaxoSmithKline, Novo Nordisk, Takeda; served as an advisor to Amylin, AstraZeneca, Novo Nordisk, Roche, Sanofi-Aventis, and Tethys; and holds stock (\geq \$10,000 value) in Abbott, Johnson and Johnson, and Merck. Dr. Serruys received honoraria from GlaxoSmith-Kline. Dr Nesto has served on speakers' bureaus for GlaxoSmithKline and Takeda and served as an advisor to GlaxoSmithKline. Drs Kolatkar, Miller, and Huang and B.G. Kravitz are employed by and own stock in GlaxoSmithKline.

Open Access This article is distributed under the terms of the Creative Commons Attribution Noncommercial License which permits any noncommercial use, distribution, and reproduction in any medium, provided the original author(s) and source are credited.

Appendix

Steering Committee: R. Ratner, P. Fitzgerald (co-chairs), C. Cannon, H. Gerstein, R. Nesto, P. Serruys, G-A Van Es, A. Zalewski.

Statistical Data and Analysis Center: Axio Research, Seattle, WA. L. Shemanski, A. Slee.

Endpoint Adjudication Committee: M. Savage (chair), H. Weitz, I. Ahmed.

APPROACH Study Management Team: R.P. Aftiring, N. Kolatkar, B. Kravitz, A. Wolstenholme, K. Saarinen, R. Fowler, Janet Hoffman, D. Steele-Norwood, R. Russell, S. Young and former team members Hubert Chou, Steve McMorn, Courtney Kirsch, Bonnie Louridas, Teresa Oliviera, and Debra Mattioli.

APPROACH Statistics and Data Management Team: D. Miller, C. Huang, C. Nguyen, L. Jahnke.

Independent Data Monitoring Committee- G. Mintz, J. Lachin (co-chairs), M. Abrahamson, P. Carson, P. Jones.

References

1. Ratner RE, Cannon CP, Gerstein HC, Nesto RW, Serruys PW, Van Es GA, Kolatkar NS, Kravitz BG, Zalewski A, Fitzgerald PJ (2008) Assessment on the prevention of progression by rosiglitazone on atherosclerosis in diabetes patients with cardiovascular history (approach): Study design and baseline characteristics. *Am Heart J* 156(6): 1074–1079. doi:10.1016/j.ahj.2008.07.025
2. Gerstein HC, Ratner RE, Cannon CP, Serruys PW, Garcia-Garcia HM, van Es GA, Kolatkar NS, Kravitz BG, Miller DM, Huang C, Fitzgerald PJ, Nesto RW Effect of rosiglitazone on progression of coronary atherosclerosis in patients with type 2 diabetes mellitus and coronary artery disease. The assessment on the prevention of progression by rosiglitazone on atherosclerosis in diabetes patients with cardiovascular history trial. *Circulation*. doi:10.1161/CIRCULATIONAHA.109.881003
3. Abizaid A, Kornowski R, Mintz GS, Hong MK, Abizaid AS, Mehran R, Pichard AD, Kent KM, Satler LF, Wu H, Popma JJ, Leon MB (1998) The influence of diabetes mellitus on acute and late clinical outcomes following coronary stent implantation. *J Am Coll Cardiol* 32(3): 584–589. doi:S0735-1097(98)00286-1
4. Lemos PA, Hoye A, Goedhart D, Arampatzis CA, Saia F, van der Giessen WJ, McFadden E, Sianos G, Smits PC, Hofma SH, de Feyter PJ, van Domburg RT, Serruys PW (2004) Clinical, angiographic, and procedural predictors of angiographic restenosis after sirolimus-eluting stent implantation in complex patients: An evaluation from the rapamycin-eluting stent evaluated at rotterdam cardiology hospital (research) study. *Circulation* 109(11):1366–1370. doi:10.1161/01.CIR.0000121358.26097.06
5. Scheen AJ, Warzee F, Legrand VM (2004) Drug-eluting stents: meta-analysis in diabetic patients. *Eur Heart J* 25(23): 2167–2168; author reply 2168–2169. doi:10.1016/j.ehj.2004.07.041
6. Moussa I, Leon MB, Baim DS, O'Neill WW, Popma JJ, Buchbinder M, Midwall J, Simonton CA, Keim E, Wang P, Kuntz RE, Moses JW (2004) Impact of sirolimus-eluting stents on outcome in diabetic patients: A sirolimus-coated bx velocity balloon-expandable stent in the treatment of patients with de novo coronary artery lesions) substudy. *Circulation* 109(19):2273–2278. doi:10.1161/01.CIR.0000129767.45513.71
7. Takagi T, Okura H, Kobayashi Y, Kataoka T, Taguchi H, Toda I, Tamita K, Yamamoto A, Sakanoue Y, Ito A, Yanagi S, Shimeno K, Waseda K, Yamasaki M, Fitzgerald PJ, Ikeno F, Honda Y, Yoshiyama M, Yoshikawa J (2009) A prospective, multicenter, randomized trial to assess efficacy of pioglitazone on in-stent neointimal suppression in type 2 diabetes: Popps (prevention of in-stent neointimal proliferation by pioglitazone study). *JACC Cardiovasc Interv* 2(6):524–531. doi:10.1016/j.jcin.2009.04.007
8. Takagi T, Yamamoto A, Tamita K, Yamabe K, Katayama M, Mizoguchi S, Ibuki M, Tani T, Tanabe K, Nagai K, Shiratori K, Morioka S, Yoshikawa J (2003) Pioglitazone reduces neointimal tissue proliferation after coronary stent implantation in patients with type 2 diabetes mellitus: An intravascular ultrasound scanning study. *Am Heart J* 146(2):E5. doi:10.1016/S0002-8703(03)00146-7
9. Law RE, Goetze S, Xi XP, Jackson S, Kawano Y, Demer L, Fishbein MC, Meehan WP, Hsueh WA (2000) Expression and function of ppargamma in rat and human vascular smooth muscle cells. *Circulation* 101(11):1311–1318
10. Choi D, Kim SK, Choi SH, Ko YG, Ahn CW, Jang Y, Lim SK, Lee HC, Cha BS (2004) Preventative effects of

- rosiglitazone on restenosis after coronary stent implantation in patients with type 2 diabetes. *Diabetes Care* 27(11):2654–2660. doi:27/11/2654
11. Geng DF, Jin DM, Wu W, Wang Z, Wang JF (2009) Effect of thiazolidinediones on in-stent restenosis in patients after coronary stenting: A meta-analysis of randomized controlled trials. *Atherosclerosis* 202(2):521–528. doi:10.1016/j.atherosclerosis.2008.05.029
 12. Katayama T, Ueba H, Tsuboi K, Kubo N, Yasu T, Kuroki M, Saito M, Momomura S, Kawakami M (2007) Reduction of neointimal hyperplasia after coronary stenting by pioglitazone in nondiabetic patients with metabolic syndrome. *Am Heart J* 153(5):762 e761–762 e767. doi:10.1016/j.ahj.2007.02.022
 13. Marx N, Wohrle J, Nusser T, Walcher D, Rinker A, Hombach V, Koenig W, Hoher M (2005) Pioglitazone reduces neointima volume after coronary stent implantation: A randomized, placebo-controlled, double-blind trial in nondiabetic patients. *Circulation* 112(18):2792–2798. doi:10.1161/CIRCULATIONAHA.105.535484
 14. Osman A, Otero J, Brizolara A, Waxman S, Stouffer G, Fitzgerald P, Uretsky BF (2004) Effect of rosiglitazone on restenosis after coronary stenting in patients with type 2 diabetes. *Am Heart J* 147(5):e23. doi:10.1016/j.ahj.2003.12.006
 15. Nishio K, Sakurai M, Kusuyama T, Shigemitsu M, Fukui T, Kawamura K, Itoh S, Konno N, Katagiri T (2006) A randomized comparison of pioglitazone to inhibit restenosis after coronary stenting in patients with type 2 diabetes. *Diabetes Care* 29(1):101–106. doi:29/1/101
 16. Rodriguez-Granillo GA, Vos J, Bruining N, Garcia-Garcia HM, de Winter S, Ligthart JM, Deckers JW, Bertrand M, Simoons ML, Ferrari R, Fox KM, Remme W, De Feyter PJ (2007) Long-term effect of perindopril on coronary atherosclerosis progression (from the perindopril's prospective effect on coronary atherosclerosis by angiography and intravascular ultrasound evaluation [perspective] study). *Am J Cardiol* 100(2):159–163. doi:10.1016/j.amjcard.2007.02.073
 17. De Winter SA, Hamers R, Degertekin M, Tanabe K, Lemos PA, Serruys PW, Roelandt JR, Bruining N (2004) Retrospective image-based gating of intracoronary ultrasound images for improved quantitative analysis: The intelligate method. *Catheter Cardiovasc Interv* 61(1):84–94. doi:10.1002/ccd.10693
 18. Aoki J, Colombo A, Dudek D, Banning AP, Drzewiecki J, Zmudka K, Schiele F, Russell ME, Koglin J, Serruys PW (2005) Persistent remodeling and neointimal suppression 2 years after polymer-based, paclitaxel-eluting stent implantation: Insights from serial intravascular ultrasound analysis in the taxus ii study. *Circulation* 112(25):3876–3883. doi:10.1161/CIRCULATIONAHA.105.558601
 19. Stettler C, Wandel S, Allemann S, Kastrati A, Morice MC, Schomig A, Pfisterer ME, Stone GW, Leon MB, de Lezo JS, Goy JJ, Park SJ, Sabate M, Sirtop MJ, Kelback H, Spaulding C, Menicelli M, Vermeersch P, Dirksen MT, Cervinka P, Petronio AS, Nordmann AJ, Diem P, Meier B, Zwahlen M, Reichenbach S, Trelle S, Windecker S, Juni P (2007) Outcomes associated with drug-eluting and bare-metal stents: A collaborative network meta-analysis. *Lancet* 370(9591):937–948. doi:10.1016/S0140-6736(07)61444-5
 20. Tu JV, Bowen J, Chiu M, Ko DT, Austin PC, He Y, Hopkins R, Tarride JE, Blackhouse G, Lazzam C, Cohen EA, Goeree R (2007) Effectiveness and safety of drug-eluting stents in ontario. *N Engl J Med* 357(14):1393–1402. doi:10.1056/NEJMoa071076
 21. Windecker S, Juni P (2008) Safety of drug-eluting stents. *Nat Clin Pract Cardiovasc Med* 5(6):316–328. doi:10.1038/npcardio1189
 22. Daemen J, Wenaweser P, Tsuchida K, Abrecht L, Vaina S, Morger C, Kukreja N, Juni P, Sianos G, Hellige G, van Domburg RT, Hess OM, Boersma E, Meier B, Windecker S, Serruys PW (2007) Early and late coronary stent thrombosis of sirolimus-eluting and paclitaxel-eluting stents in routine clinical practice: Data from a large two-institutional cohort study. *Lancet* 369(9562):667–678. doi:10.1016/S0140-6736(07)60314-6
 23. Kereiakes DJ, Young JJ (2005) Percutaneous coronary revascularization of diabetic patients in the era of drug-eluting stents. *Rev Cardiovasc Med* 6(Suppl 1):S48–S58
 24. Aronson D, Bloomgarden Z, Rayfield EJ (1996) Potential mechanisms promoting restenosis in diabetic patients. *J Am Coll Cardiol* 27(3):528–535. doi:0735-1097(95)00496-3
 25. Beckman JA, Creager MA, Libby P (2002) Diabetes and atherosclerosis: Epidemiology, pathophysiology, and management. *JAMA* 287(19):2570–2581. doi:jrv10119
 26. Corpus RA, George PB, House JA, Dixon SR, Ajluni SC, Devlin WH, Timmis GC, Balasubramanian M, O'Neill WW (2004) Optimal glycemic control is associated with a lower rate of target vessel revascularization in treated type ii diabetic patients undergoing elective percutaneous coronary intervention. *J Am Coll Cardiol* 43(1):8–14. doi:S073510970301324X
 27. Goetze S, Xi XP, Graf K, Fleck E, Hsueh WA, Law RE (1999) Troglitazone inhibits angiotensin ii-induced extracellular signal-regulated kinase 1/2 nuclear translocation and activation in vascular smooth muscle cells. *FEBS Lett* 452(3):277–282. doi:S0014-5793(99)00624-9
 28. Yasunari K, Kohno M, Kano H, Yokokawa K, Minami M, Yoshikawa J (1997) Mechanisms of action of troglitazone in the prevention of high glucose-induced migration and proliferation of cultured coronary smooth muscle cells. *Circ Res* 81(6):953–962
 29. Aizawa Y, Kawabe J, Hasebe N, Takehara N, Kikuchi K (2001) Pioglitazone enhances cytokine-induced apoptosis in vascular smooth muscle cells and reduces intimal hyperplasia. *Circulation* 104(4):455–460
 30. Ishibashi M, Egashira K, Hiasa K, Inoue S, Ni W, Zhao Q, Usui M, Kitamoto S, Ichiki T, Takeshita A (2002) Anti-inflammatory and antiarteriosclerotic effects of pioglitazone. *Hypertension* 40(5):687–693
 31. Kasai T, Miyauchi K, Yokoyama T, Kajimoto K, Sumiyoshi K, Kubota N, Ikeda E, Daida H (2008) Pioglitazone attenuates neointimal thickening via suppression of the early inflammatory response in a porcine coronary after stenting. *Atherosclerosis* 197(2):612–619. doi:10.1016/j.atherosclerosis.2007.08.030

32. Li D, Chen K, Sinha N, Zhang X, Wang Y, Sinha AK, Romeo F, Mehta JL (2005) The effects of ppar-gamma ligand pioglitazone on platelet aggregation and arterial thrombus formation. *Cardiovasc Res* 65(4):907–912. doi: 10.1016/j.cardiores.2004.11.027
33. Takagi T, Yoshida K, Akasaka T, Kaji S, Kawamoto T, Honda Y, Yamamuro A, Hozumi T, Morioka S (2000) Hyperinsulinemia during oral glucose tolerance test is associated with increased neointimal tissue proliferation after coronary stent implantation in nondiabetic patients: A serial intravascular ultrasound study. *J Am Coll Cardiol* 36(3):731–738. doi:S0735-1097(00)00799-3
34. Nissen SE, Wolski K (2007) Effect of rosiglitazone on the risk of myocardial infarction and death from cardiovascular causes. *N Engl J Med* 356(24):2457–2471. doi:10.1056/NEJMoa072761
35. Komajda M, McMurray JJ, Beck-Nielsen H, Gomis R, Hanefeld M, Pocock SJ, Curtis PS, Jones NP, Home PD (2010) Heart failure events with rosiglitazone in type 2 diabetes: Data from the record clinical trial. *Eur Heart J* 31(7):824–831. doi:10.1093/eurheartj/ehp604
36. Coats AJ (2009) Ethical authorship and publishing. *Int J Cardiol* 131(2):149–150. doi:10.1016/j.ijcard.2008.11.048

4.2

Poor Agreement Of Qualitative Assessment of Stent Struts Coverage By Optical Coherence Tomography.

Salvatore Brugaletta, Hector M Garcia-Garcia, Josep Gomez-Lara, Maria D Radu, Ravindra Pawar, Jamal Khachabi, Nico Bruining, Manel Sabaté, Patrick W Serruys

Int J Cardiovasc Imaging 2012, Epub ahead of print

Reproducibility of qualitative assessment of stent struts coverage by optical coherence tomography

Salvatore Brugaletta · Hector M. Garcia-Garcia · Josep Gomez-Lara · Maria D. Radu · Ravindra Pawar · Jamal Khachabi · Nico Bruining · Manel Sabaté · Patrick W. Serruys

Received: 19 August 2011 / Accepted: 10 February 2012
© The Author(s) 2012. This article is published with open access at Springerlink.com

Abstract Assessment of stent strut coverage by optical coherence tomography (OCT) is not standardized. The methodology most commonly used is based on a visual binary qualitative assessment (strut covered or not). However, the influence of magnification (zoom setting) to the inter- and intra-observer agreements has not yet been evaluated. Aim of our study was therefore to evaluate the agreements of this approach, taking into account various zoom settings. 126 struts from 10 selected frames were independently evaluated by four observers using a stepwise approach increasing the zoom setting as following: (1) full view of the lumen (FV), (2) half view of the lumen (HV) and (3) a quarter view of the lumen (QV). Intra- and inter-observer agreements (κ) were assessed. The rate of uncoverage was determined for each strut as the number of times it was defined as uncovered divided by the total number of observations (maximum

12 = 3 zoom settings \times 4 analysts) and expressed as percentage. The inter-observer κ values (mean [range]) were 0.32 [0.07–0.63], 0.40 [0.18–0.69] and 0.33 [0.09–0.6], within FV, HV and QV respectively. The intra-observer κ values were 0.60 [0.50–0.70], 0.75 [0.75–0.76] and 0.60 [0.50–0.70], within FV, HV and QV respectively. By increasing zoom setting the κ value of intra-observer agreement was 0.74 [0.58–0.83] (from FV to HV), 0.70 [0.56–0.83] (from HV to QV) and 0.70 [0.37–0.86] (from FV to QV). Overall, the rate of uncoverage was 15.5% [8.3–100%]. The OCT qualitative evaluation of strut coverage has wide inter and intra-observer agreements and is dependent of the zoom setting used during the analysis. A more reproducible approach would be needed to eventually increase the probability to link uncovered struts with clinical events.

Keywords OCT · Coverage · Strut · Stent

S. Brugaletta · H. M. Garcia-Garcia (✉) · J. Gomez-Lara · M. D. Radu · N. Bruining · P. W. Serruys
Z120, Thoraxcentre, Erasmus MC, 's-Gravendijkwal 230, 3015 CE Rotterdam, The Netherlands
e-mail: h.garciagarcia@erasmusmc.nl

S. Brugaletta · M. Sabaté
Department of Cardiology, Thorax Institute, Hospital Clinic, Barcelona, Spain

H. M. Garcia-Garcia · R. Pawar · J. Khachabi
Cardialysis BV, Rotterdam, The Netherlands

Introduction

Optical coherence tomography (OCT) is a light-based imaging modality that can provide in vivo high-resolution images of coronary stents, with detailed information about struts apposition and tissue coverage [1]. Pathological studies have suggested that the absence of stent strut coverage due to delayed vascular

healing and the persistence of fibrin may be the most important determinants of late stent thrombosis, together with lesion and procedure-related settings [2, 3]. For this reason, coverage at strut-level analysis by OCT is the most common surrogate endpoint in OCT studies, providing a measurable variable for the comparison between different stents and being also an important parameter for the approval of new drug eluting stents by regulatory agencies [4].

The inter- and intra-observer reproducibility for strut count, strut apposition and quantitative strut tissue coverage measurement (e.g. neointima thickness) has been shown to be good [5, 6]. However, strut coverage evaluation is not standardized. The most commonly used approach is the visual qualitative assessment, evaluating strut coverage as a binary variable (covered or not covered). Moreover, independently from the methodology used, the zoom setting used for magnifying the OCT images may influence the assessment and thereby the reproducibility of strut coverage assessment.

The objective of the present study was to revise this qualitative approach for the assessment of strut coverage by measuring the inter- and intra-observer agreement and evaluating the influence of various zoom settings.

Methods

Study population

From our OCT database all patients, who received an OCT pullback at 6 months after stent implantation, were selected. After an initial quality check, an independent analyst (not involved in the assessment of coverage) randomly selected 10 frames from the OCT pullbacks identifying 126 struts, according to the following definitions:

- Highly reflective surface with cast dorsal and radial shadows;
- Highly reflective surface without dorsal shadowing.

The stent implanted was Resolute Endeavor in all the frames analyzed. Struts were termed “covered” by OCT if tissue could be identified above the struts, as previously defined [7].

OCT acquisition

The OCT acquisition was performed using a commercially available system for intracoronary imaging (C7XR Fourier-Domain System; LightLab Imaging, Westford, Massachusetts). Pullback was performed during continuous injection of contrast medium (3 mL/s, Iodixanol 370, Visipaque, GE Health Care, Cork, Ireland) through the guide catheter with an injection pump. The automated pullback rate was 20 mm/s and the frame rate was 100 images/s.

Qualitative evaluation of strut coverage

Four independent and expert observers separately analyzed the selected frames in order to qualify the coverage of the struts, previously defined, as a qualitative binary variable (yes/no). In particular, two analysts (Obs 1 and Obs 2) were interventional cardiologists with wide expertise in OCT evaluation; the remaining two (Obs 3 and Obs 4) were senior OCT CoreLab analysts, without experience in cardiology practice. All of them repeated the analysis with three different zoom settings 1 week later at each step in order to estimate the intra-observer agreement, related to the zoom setting (Fig. 1). Two of the analysts repeated all the analyses 4 weeks later with the same stepwise protocol in order to estimate also the intra-observer agreement within the same zoom setting. The predefined zoom settings used were: full view of the lumen, half view of the lumen and quarter view of the lumen (Fig. 2). Each strut was then evaluated 12 times (four different observers with three different zoom settings).

For the purpose of the study, the rate of uncoverage of each strut was determined according to the following formula:

$$100 \times \frac{\text{Number of times a strut is defined as uncovered}}{\text{Total number of observation}}$$

Statistical analysis

The agreement in the number of struts evaluated as covered was estimated by the kappa test for agreement. The kappa values are presented as mean and range within the various zoom setting. According to previous publications: ≤ 0 indicates poor agreement, 0–0.20 indicates slight agreement, 0.21–0.40 indicates fair agreement, 0.41–0.60 indicates moderate agreement,

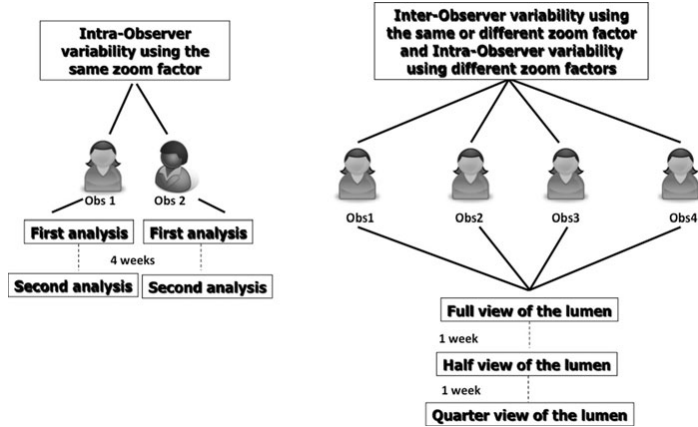


Fig. 1 Flow-chart of the study analysis

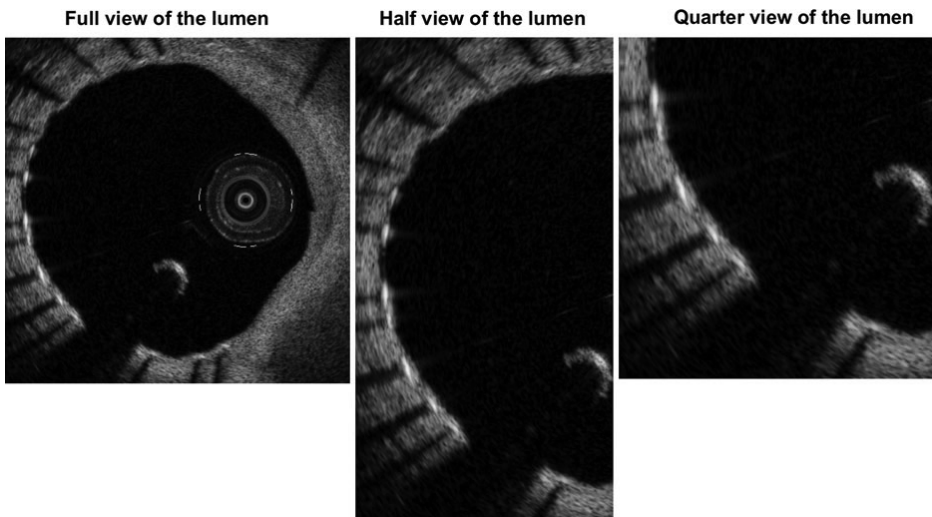


Fig. 2 Examples of the various zoom settings used in the analysis

0.61–0.80 indicates good agreement, and 0.81–1.0 indicates excellent agreement [8, 9]. Wilcoxon paired test was used to compare the number of struts assessed as covered between the various zoom factors. Comparison between groups was performed by Mann–Whitney test. Data were analyzed with SPSS version 16.0 software (SPSS Inc., Chicago, IL).

Results

Inter-observer agreement within the same zoom setting

Table 1 reports the inter-observer agreements according to the various zoom settings used. The κ values

Table 1 Inter-observer agreement within a same zoom setting

	Observer 1	Observer 2	Observer 3	Observer 4
Full view of the lumen				
Observer 1		0.40	0.07	0.20
Observer 2	0.40		0.25	0.63
Observer 3	0.07	0.25		0.41
Observer 4	0.20	0.63	0.41	
Half view of the lumen				
Observer 1		0.69	0.18	0.45
Observer 2	0.69		0.18	0.45
Observer 3	0.18	0.18		0.47
Observer 4	0.45	0.45	0.47	
Quarter view of the lumen				
Observer 1		0.65	0.09	0.25
Observer 2	0.65		0.18	0.37
Observer 3	0.09	0.18		0.47
Observer 4	0.25	0.37	0.47	

K value are reported

were 0.32 [0.07–0.63], 0.40 [0.18–0.69] and 0.33 [0.09–0.65], from the full view of the lumen, through half view up to quarter view of the lumen, respectively. Out of 126 struts, the average number of the struts evaluated as uncovered by the analysts was 21.5 [range: 3–50] using the full view of the lumen, 20.2 [7–46] with half view of the lumen and 17.2 [3–42] with quarter view of the lumen.

Overall, there was on average a progressive decrease in the struts detected uncovered going from full to half view of the lumen (–5.8%; $p = 0.275$), from full to quarter view of the lumen (–14%; $p = 0.001$), and from half to quarter view of the lumen (–17%; $p = 0.018$).

Intra-observer agreement changing the zoom setting

Increasing the zoom setting from full to half view of the lumen, the intra-observer agreement (k-value) was 0.74 [0.58–0.83], while from half to quarter view of the lumen it was 0.70 [0.56–0.83] and from full to quarter view of the lumen 0.70 [0.37–0.86] (Table 2). In particular, the intra-observer agreement was higher within Obs 3 and 4 (senior OCT CoreLab analysts) than within Obs 1 and 2 (interventional cardiologists with wide expertise in OCT evaluation) (0.82 [0.76–0.86] vs. 0.61 [0.37–0.76]; $p = 0.002$).

Table 2 Intra-observer agreement, according to the zoom setting

From lumen to half view of the lumen	
1st Observer	0.58
2nd Observer	0.76
3rd Observer	0.83
4th Observer	0.80
From lumen to quarter view of the lumen	
1st Observer	0.65
2nd Observer	0.56
3rd Observer	0.83
4th Observer	0.76
From half to quarter view of the lumen	
1st Observer	0.37
2nd Observer	0.75
3rd Observer	0.86
4th Observer	0.85

K value are reported

Intra-observer agreement within the same zoom setting

Two analysts have assessed the intra-observer agreement within the same zoom setting. Using full view of the lumen the average k-value of agreement for each observer was 0.60 (0.70 and 0.50 for the two observers, respectively), using half view of the lumen it was 0.75 (0.76 and 0.75 for the two observers, respectively) and using quarter view of the lumen 0.60 (0.50 and 0.70 for the two observers, respectively).

Rate of uncoverage of the struts

Overall, the rate of uncoverage for each strut was 15.5% [8.3–100%]. Within full view of the lumen it was 16.9% [25–100%], half view 16.0% [25–100%], quarter view 13.6% [25–100%] (Fig. 3).

Discussion

Our analysis demonstrates a wide inter- and intra-observer agreement for uncovered struts evaluated visually by OCT, which is highly dependent of the zoom setting used in the analysis.

Vascular healing of metallic stent has been extensively studied by anatomic-pathologists, as the delaying of this process has been related to the occurrence of

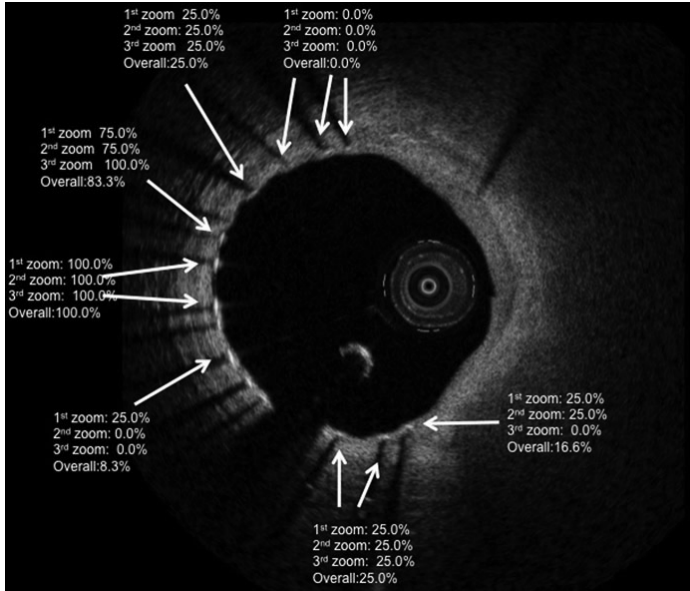


Fig. 3 Example of the wide variability of the rate of uncoverage, according to the various zoom settings used in the analysis. Some struts are adjudicated by all the analysts as

uncovered, independently from the zoom setting (rate of uncoverage 100%). Some struts have a probability to be defined as uncovered from 8.3 to 83.3%

very late stent thrombosis [2]. In vivo, OCT is highly suited for the evaluation of strut coverage due to its high resolution and image quality [10]. Assessment of stent strut coverage, however, is not standardized and a quantitative or qualitative approach can be used. In the first methodology, struts coverage is evaluated through quantification of tissue coverage area: the operator manually traced the stent and lumen area, deriving the tissue coverage area. Using this kind of approach, a good intra- and inter-observer agreement has been reported for the neointima thickness measurement [5, 11, 12]. In a further step, in order to report these data at strut level, a predefined threshold of neointima thickness is used in a semi-quantitative fashion to define a strut as covered [13, 14]. However, some important concerns must be highlighted in the interpretation of these results. The use of a threshold is quite arbitrary and has some therein limitations, as it is not standardized for different stent and even for the same stent. In addition, Murata et al. comparing the

morphometric differences at the strut level between OCT and histology have shown that the correlation between these techniques is much dependent on the amount of the neointima present. OCT seems to correlate appropriately with histology only in either the absence ($<20 \mu\text{m}$) or the presence ($>100 \mu\text{m}$) of robust neointima. It should be also considered that the strut blooming is about $37 \mu\text{m}$ in thickness and extends bi-directionally toward and away from the catheter light source, complicating the measurement of low neointimal coverage ($<20 \mu\text{m}$) [15]. Of note is that $10\text{--}20 \mu\text{m}$ represents the OCT resolution and that the majority of the drug eluting stents report a neointima thickness between 20 and $100 \mu\text{m}$. For these reasons, the choice of an arbitrary threshold should be carefully considered. In addition, the zoom setting used in the analysis, seldom reported in the majority of the OCT-stent papers, is not standardized and can further increase the variability of the assessment.

The second and most used approach to evaluate the strut coverage is a visual qualitative classification of strut coverage as a binary variable (covered or not covered) [16]. This qualitative assessment is sometimes performed at a distance interval different from that used in the quantitative OCT measurement (e.g. each frame vs. 0.33 mm interval) and no reproducibility is reported [17]. The zoom setting, of utmost importance in this qualitative evaluation as compared to the quantitative approach, is neither standardized nor specified. In our analysis, we tested the agreement of this approach in a Core Lab, using different zoom settings. We demonstrated that the zoom setting is an important bias and the range of intra-observer agreement according to the zoom used is very wide: a same strut can range from 0 to 25% probability to be considered as uncovered, using different zoom. In particular, moving from the first (lumen) to the second zoom (half lumen), there was a slight decrease in the number of the strut detected as uncovered. Increasing further the zoom (quarter lumen), there was a significant decrease in the struts detected as uncovered. Using the same zoom setting, the intra-observer agreement was on average good, but with wide variability. Although overall the inter and intra-agreement was not high (e.g. close to 1), looking at the various k-value per zoom factor the half view of the lumen appeared as the zoom factor with a higher reproducibility between and within the observers as compared to the others and could be used as a reference in future studies.

Of note is that in a careful evaluation of our results two different kind of analysts can be identified: the Core Lab analysts (Obs 3 and Obs 4) showed a good intra-observer agreement changing the zoom setting, compared to the interventional cardiologists with wide experience in OCT evaluation (Obs 1 and Obs 2), who exhibited a low agreement in their measurements changing the zoom setting. This observation supports the presence of a CoreLab for performing such analysis, which should be blinded to the clinical meaning of the measurements and only based on a phenomenological description of strut coverage.

The poor agreement in qualitative assessment of strut coverage raises some concerns about the clinical interpretation of these findings. OCT was, indeed, advocated as the gold standard to evaluate the reliability of the degree of incomplete coverage, identifying those patients at increased risk of late

stent thrombosis. Nevertheless, it is unable to distinguish between fibrin, giant cells, granulomatous reaction and degree of endothelialization and our results could be considered as supportive of this limitation, as each analysts thinks differently about the “status” of coverage of each strut.

Limitations

A small number of frames have been analyzed in the current study to allow multiple evaluations by the 4 different observers. The fact that the k-value could improve by increasing the number of observation should be acknowledged. Nevertheless, it is of note that four different observers, who assessed the frames up to 4 times, have been used in our analysis.

Conclusions

Qualitative evaluation of strut coverage by OCT has wide inter and intra-observer agreements, extremely dependent from the zoom setting used during the analysis.

Conflict of interest None.

Open Access This article is distributed under the terms of the Creative Commons Attribution License which permits any use, distribution, and reproduction in any medium, provided the original author(s) and the source are credited.

References

1. Gonzalo N, Serruys PW, Regar E (2008) Optical coherence tomography: clinical applications and the evaluation of DES. *Minerva Cardioangiol* 56(5):511–525
2. Joner M, Finn AV, Farb A, Mont EK, Kolodgie FD, Ladich E, Kutys R, Skorija K, Gold HK, Virmani R (2006) Pathology of drug-eluting stents in humans: delayed healing and late thrombotic risk. *J Am Coll Cardiol* 48(1):193–202. doi:10.1016/j.jacc.2006.03.042
3. Finn AV, Joner M, Nakazawa G, Kolodgie F, Newell J, John MC, Gold HK, Virmani R (2007) Pathological correlates of late drug-eluting stent thrombosis: strut coverage as a marker of endothelialization. *Circulation* 115(18):2435–2441
4. Tahara S, Chamie D, Baibars M, Alraies C, Costa M (2011) Optical coherence tomography endpoints in stent clinical investigations: strut coverage. *Int J Cardiovasc Imaging* 27(2):271–287. doi:10.1007/s10554-011-9796-3

5. Gonzalo N, Garcia-Garcia HM, Serruys PW, Commissaris KH, Bezerra H, Gobbens P, Costa M, Regar E (2009) Reproducibility of quantitative optical coherence tomography for stent analysis. *EuroIntervention* 5(2):224–232. doi:10.4244/EIJV5I2A35
6. Okamura T, Gonzalo N, Gutierrez-Chico JL, Serruys PW, Bruining N, de Winter S, Dijkstra J, Comossaris KH, van Geuns RJ, van Soest G, Ligthart J, Regar E (2010) Reproducibility of coronary Fourier domain optical coherence tomography: quantitative analysis of in vivo stented coronary arteries using three different software packages. *EuroIntervention* 6 (3):371–379. doi:10.4244/EIJV6I1A62
7. Standards for acquisition, measurement, and reporting of intravascular OCT (IVOCT) studies. A consensus report from the International Working Group for Intravascular OCT standardization and validation (2012). *J Am Coll Cardiol* (in press)
8. Cohen J (1960) A coefficient of agreement for nominal scales. *Educ Psychol Meas* 20:37–46
9. Fleiss J (1981) *Statistical methods for rates and proportions*, 2nd edn. Wiley, New York
10. Bouma BE, Tearney GJ, Yabushita H, Shishkov M, Kauffman CR, DeJoseph Gauthier D, MacNeill BD, Houser SL, Aretz HT, Halpern EF, Jang IK (2003) Evaluation of intracoronary stenting by intravascular optical coherence tomography. *Heart* 89(3):317–320
11. Prati F, Zimarino M, Stabile E, Pizzicannella G, Fouad T, Rabozzi R, Filippini A, Pizzicannella J, Cera M, De Caterina R (2008) Does optical coherence tomography identify arterial healing after stenting? An in vivo comparison with histology, in a rabbit carotid model. *Heart* 94(2):217–221. doi:10.1136/hrt.2006.112482
12. Xie Y, Takano M, Murakami D, Yamamoto M, Okamatsu K, Inami S, Seimiya K, Ohba T, Seino Y, Mizuno K (2008) Comparison of neointimal coverage by optical coherence tomography of a sirolimus-eluting stent versus a bare-metal stent three months after implantation. *Am J Cardiol* 102(1):27–31. doi:10.1016/j.amjcard.2008.02.091
13. Kim JS, Jang IK, Fan C, Kim TH, Park SM, Choi EY, Lee SH, Ko YG, Choi D, Hong MK, Jang Y (2009) Evaluation in 3 months duration of neointimal coverage after zotarolimus-eluting stent implantation by optical coherence tomography: the ENDEAVOR OCT trial. *JACC Cardiovasc Interv* 2(12):1240–1247. doi:10.1016/j.jcin.2009.10.006
14. Kim JS, Kim TH, Fan C, Lee JM, Kim W, Ko YG, Choi D, Hong MK, Jang Y (2010) Comparison of neointimal coverage of sirolimus-eluting stents and paclitaxel-eluting stents using optical coherence tomography at 9 months after implantation. *Circ J* 74 (2):320–326
15. Murata A, Wallace-Bradley D, Tellez A, Alviar C, Aboodi M, Sheehy A, Coleman L, Perkins L, Nakazawa G, Mintz G, Kaluza GL, Virmani R, Granada JF (2010) Accuracy of optical coherence tomography in the evaluation of neointimal coverage after stent implantation. *JACC Cardiovasc Imaging* 3(1):76–84. doi:10.1016/j.jcmg.2009.09.018
16. Guagliumi G, Musumeci G, Sirbu V, Bezerra HG, Suzuki N, Fiocca L, Matiashvili A, Lortkipanidze N, Trivisonno A, Valsecchi O, Biondi-Zoccai G, Costa MA (2010) Optical coherence tomography assessment of in vivo vascular response after implantation of overlapping bare-metal and drug-eluting stents. *JACC Cardiovasc Interv* 3 (5):531–539. doi:10.1016/j.jcin.2010.02.008
17. Guagliumi G, Costa MA, Sirbu V, Musumeci G, Bezerra HG, Suzuki N, Matiashvili A, Lortkipanidze N, Mihalesik L, Trivisonno A, Valsecchi O, Mintz GS, Dressler O, Parise H, Maehara A, Cristea E, Lansky AJ, Mehran R, Stone GW (2011) Strut coverage and late malapposition with paclitaxel-eluting stents compared with bare metal stents in acute myocardial infarction: optical coherence tomography sub-study of the Harmonizing Outcomes with Revascularization and Stents in Acute Myocardial Infarction (HORIZONS-AMI) Trial. *Circulation* 123(3):274–281. doi:10.1161/CIRCULATIONAHA.110.963181

Chapter 5

Use of imaging techniques for the assessment of bioresorbable vascular scaffolds.

5.1

Comparison between the first and second generation bioresorbable vascular scaffolds: a six month virtual histology study.

Salvatore Brugaletta, Hector M Garcia-Garcia, Roberto Diletti, Josep Gomez-Lara, Scot Garg, Yoshinobu Onuma, Eun-Seok Shin, Robert Jan van Geuns, Bernard de Bruyne, Dariusz Dudek, Leif Thuesen, Bernard Chevalier, Dougal McClean, Stephan Windecker, Robert Whitbourn, Cecile Dorange, Susan Veldhof, Richard Rapoza, Krishnankutty Sudhir, Nico Bruining, John A Ormiston, Patrick W Serruys

Eurointervention 2011;6:1110-1116

Comparison between the first and second generation bioresorbable vascular scaffolds: a six month virtual histology study

Salvatore Brugaletta¹, MD; Hector M. Garcia-Garcia¹, MD, PhD; Roberto Diletti¹, MD; Josep Gomez-Lara¹, MD; Scot Garg¹, MBChB, MRCP; Yoshinobu Onuma¹, MD; Eun-Seok Shin¹, MD, PhD; Robert Jan van Geuns¹, MD, PhD; Bernard de Bruyne², MD; Dariusz Dudek³, MD; Leif Thuesen⁴, MD; Bernard Chevalier⁵, MD; Dougal McClean⁶, MD; Stephan Windecker⁷, MD, PhD; Robert Whitbourn⁸, MD; Cecile Dorange⁹, MSc; Susan Veldhof⁹, RN; Richard Rapoza¹⁰, PhD; Krishnankutty Sudhir¹⁰, MD, PhD; Nico Bruining¹, PhD; John A. Ormiston¹, MBChB, PhD; Patrick W. Serruys^{1*}, MD, PhD, FACC, FESC

1. Thoraxcenter, Erasmus MC, Rotterdam, The Netherlands; 2. Cardiovascular Center Aalst, Belgium; 3. Department of Cardiology, Jagiellonian University, Krakow, Poland; 4. Department of Cardiology, Skejby Sygehus, Aarhus University Hospital, Skejby, Denmark; 5. Department of Cardiology, Institute Hosp. Jacques Cartier, Massy, France; 6. Department of Cardiology, Christchurch Hospital, Christchurch, New Zealand; 7. Department of Cardiology, Bern University Hospital, Switzerland; 8. Department of Cardiology, St Vincents Hospital, Melbourne, Fitzroy, Australia; 9. Abbott Vascular, Diegem, Belgium; 10. Abbott Vascular, Santa Clara, CA, USA; 11. Department of Cardiology, Auckland City Hospital, Auckland, New Zealand

Cecile Dorange, Susan Veldhof, Richard Rapoza and Krishnankutty Sudhir are employed by Abbott Vascular, the other authors have no conflict of interest to declare.

KEYWORDS

Bioresorbable vascular scaffold, intravascular ultrasound virtual histology

Abstract

Aims: To compare the intravascular ultrasound virtual histology (IVUS-VH) appearance of the polymeric struts of the first (Revision 1.0) and the second (Revision 1.1) generation bioresorbable vascular scaffold (BVS).

Methods and results: IVUS-VH misrepresents polymeric struts as dense calcium (DC) and necrotic core (NC) so that their presence and disappearance could be used as potential artifactual surrogate of bioresorption. DC and NC were assessed in both revisions of the BVS by analysing IVUS-VH from all patients in the ABSORB cohort A (Revision 1.0) and cohort B (Revision 1.1) study who had an IVUS-VH post-treatment and at 6-month follow-up. Post-treatment and 6-month follow-up IVUS-VH results, available in 60 patients (BVS 1.0 n=28; BVS 1.1 n=32), indicated an insignificant rise in DC+NC area compared to baseline with Revision 1.1 ($0.10 \pm 0.46 \text{ mm}^2$, $p=0.2$), whilst a significant reduction was seen with Revision 1.0 ($-0.57 \pm 1.3 \text{ mm}^2$, $p=0.02$). A significant correlation has been found between the change in the DC+NC area and the change in external elastic membrane area ($y=0.68x-0.1$; $r=0.58$, $p=0.03$).

Conclusions: Based on 6-months IVUS-VH analysis, the BVS 1.1 appears to have a different backscattering signal compared to the BVS 1.0, which may reflect differences in the speed of chemical and structural alteration.

Introduction

The bioresorption process of new bioresorbable vascular scaffolds (BVS) is crucial in the determination of their performance at medium and long-term. A BVS should have enough radial strength to counteract acute vessel recoil following angioplasty and should also be able to maintain its mechanical integrity until late recoil forces subside. The fully resorbable BVS (Abbott Vascular, Santa Clara, CA, USA) has been tested in 30-patient in the first-in-man ABSORB cohort A study and demonstrated excellent long-term clinical results up to two years with a major adverse cardiac event rate of 3.6%.¹ However, due to faster degradation, the first generation BVS showed higher late recoil than conventional metallic platform stents.^{1,3}

To prolong the mechanical strength of the scaffold and reduce late recoil, a second generation BVS –Revision 1.1– has recently been introduced, and this is currently undergoing clinical evaluation in the ABSORB cohort B study.⁴ Compared to the Revision 1.0 which was used in the ABSORB cohort A study, the Revision 1.1 has a smaller maximum circular unsupported surface area,⁵ a more uniform strut distribution and improved stent retention. Importantly, these changes have not resulted in an increased amount of polymeric material or an increase in strut thickness. Proprietary process changes have been implemented to increase radial strength. In addition, these changes have reduced polymer degradation rates at early time points and thus prolonged mechanical integrity of the scaffold throughout the first few months following implantation.

Intravascular ultrasound virtual histology (IVUS-VH), a tool developed to assess tissue composition of intact native coronary arteries, mis-classifies polymeric stent struts as “dense calcium” and “necrotic core” (white and red in the VH colour code).⁶ This could potentially be used as surrogate marker of alteration of the polymeric struts and to assess in vivo the degradation process of a BVS.^{7,8} Shin’s method, for IVUS-VH analysis, allows a more accurate detection of dense calcium and necrotic core so that the bioresorption process can be better explored.⁹

The aim of this study was; 1) to evaluate temporal changes in the IVUS-VH signal of the BVS 1.1 and BVS 1.0; 2) to assess the correlation between the changes in IVUS-VH signal for BVS 1.1 and 1.0, and the change in external elastic membrane (EEM) area.

Methods

Study design

All patients from cohort A and cohort B of the ABSORB trial with paired post-BVS implantation and 6-month follow-up IVUS-VH data were included. The ABSORB cohort A study is described elsewhere.¹ In brief, for cohort A and cohort B, patients were suitable for inclusion if they were older than 18 years, with a diagnosis of stable, unstable or silent ischaemia. All treated lesions were *de novo* lesions in a native coronary artery with a reference vessel diameter of 3.0 mm, with a percent diameter stenosis $\geq 50\%$ and $< 100\%$ and a thrombolysis in myocardial infarction (TIMI) flow grade of ≥ 1 . The BVS 1.0 was used in patients in cohort A, whilst Revision 1.1 was used in cohort B.⁴ Major exclusion criteria were:

patients presenting with an acute myocardial infarction, unstable arrhythmias or patients who had left ventricular ejection fraction $\leq 30\%$, restenotic lesions, lesions located in the left main coronary artery, lesions involving a side branch > 2 mm in diameter, and the presence of thrombus or another clinically significant stenosis in the target vessel. Both ABSORB trials were approved by ethics committee at each participating institution and each patient gave written informed consent before inclusion.

Study device

The BVS has an amorphous poly-DL-lactide (PDLLA) coating that contains and controls the release of the anti-proliferative drug everolimus. The scaffold body is made of semi-crystalline poly-L-lactide (PLLA). PLLA is completely degraded via hydrolysis and bioresorbed via the lactate shuttle. There are no differences in polymeric material, drug dose, drug release or strut thickness between BVS Revisions 1.0 and 1.1. Of note, the BVS Revision 1.1 has a smaller maximum circular unsupported surface area compared to Revision 1.0.⁵ Processing changes in Revision 1.1 have resulted in higher and prolonged mechanical strength and stability post implantation. (Figure 1)

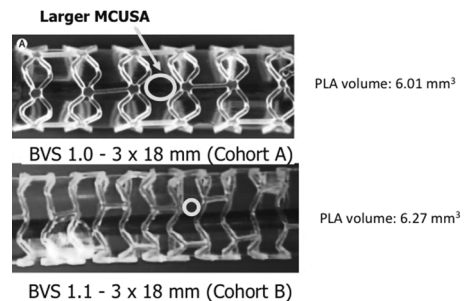


Figure 1. Although the scaffold design is different between revision 1.0 and revision 1.1, the content of polymer is nearly the same. MCUSA: maximum circular unsupported surface area; BVS: bioresorbable vascular scaffold; PLA: polylactide

BVS implantation procedure

In both cohorts, lesions were treated with routine interventional techniques that included mandatory pre-dilatation using a balloon shorter than the study device and 0.5 mm less in diameter. All patients were pre-treated with aspirin and a loading dose of at least 300 mg of clopidogrel was administered according to local hospital practise. After the procedure, all patients received aspirin ≥ 75 mg for the study duration (five years) and clopidogrel 75 mg daily for a minimum of six months. Anticoagulation and glycoprotein IIb/IIIa use was according to local hospital practise.

Imaging procedure and acquisition

IVUS-VH post-BVS implantation and at 6-month follow-up were obtained from patients from both cohorts. Imaging techniques were

acquired simultaneously with a phased array 20MHz intravascular ultrasound catheter (EagleEye™; Volcano Corporation, Rancho Cordova, CA, USA) using an automated pullback of 0.5 mm per second. Four tissue components (necrotic core – red; dense calcium – white; fibrous – green; and fibrofatty – light green) were identified with autoregressive classification systems.^{10,11} Each individual tissue component was quantified and colour coded in all IVUS cross sections as previously described.¹⁰ All IVUS-VH analyses were performed offline using pcVH 2.1 (Volcano Corporation, Rancho Cordova, CA, USA). We carefully matched the region received BVS implantation using anatomical markers to compare the post implantation and 6-month follow-up IVUS-VH images. Regions received non-BVS stent implantation were not analysed. For each cross section, polymeric struts were detected as areas of apparent “dense calcium” and “necrotic core”. The quantitative changes in dense calcium (DC) and necrotic core (NC) content were used as a surrogate marker of alteration of the polymeric struts, as previously described.^{1,7,12,13} Only changes in DC and NC, which can be seen as the fingerprint of the BVS, were required, therefore the lumen contour was drawn around the IVUS catheter without following the leading edge of the interface lumen intima, as previously described by Shin et al.⁹ Using this approach, the BVS struts closest to the lumen were better detected and recognised as DC and NC by the VH software and the ones overlying small plaques (thinner side of an eccentric plaque) were not obscured by the imposed grey medial stripe seen with IVUS-VH. (Figure 2) We also recorded in all patients the interface between plaque+media and the adventitia (EEM area). Lumen area and plaque area cannot be recorded using this method.

Statistical analysis

Discrete variables are presented as counts and percentages. Continuous variables are presented as mean \pm standard deviation (SD). The DC and NC values have been statistically tested separately post-procedure and 6-month follow-up. The VH

fingerprint of the BVS in the artery was defined as the sum of the changes in DC and NC, as IVUS-VH detects stent struts as dense calcium surrounded by necrotic core halo.⁶ The calculation of the changes between post-treatment and six months was as follows: mean six month area minus mean post-procedure area for both NC and DC. Paired comparisons between post-procedure and 6-month follow-up were performed using the Wilcoxon signed rank test. Comparisons between groups were assessed using non parametric tests, whilst correlations between parameters were performed by using a Spearman test. A two-side p -value of less than 0.05 indicated statistical significance. Statistical analyses were performed with use of SPSS 13.0 software (SPSS Inc., Chicago IL, USA).

Results

The comparison between post-procedure and 6-month follow-up IVUS-VH included 28 patients from cohort A and 32 patients from cohort B. (Figure 3)

Table 1 shows clinical and angiographic data in both cohorts. Compositional changes from post-treatment to six month follow-up by IVUS-VH (Table 2).

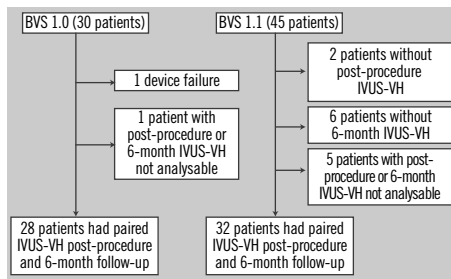


Figure 3. Flow chart of paired IVUS-VH data available for both cohorts.

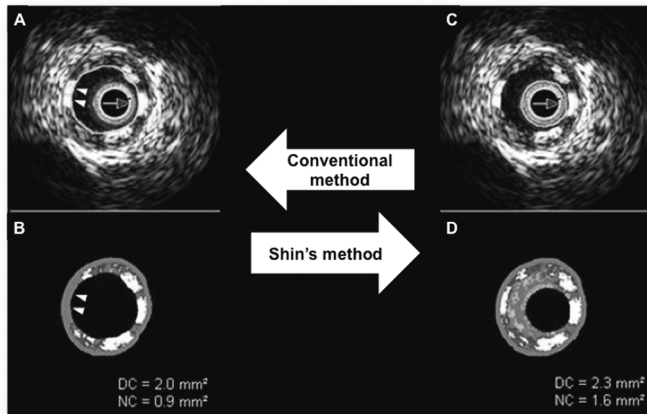


Figure 2. The conventional method (A and B) does not show some necrotic core and dense calcium (two white arrow heads), hidden by the grey medial stripe (two white arrow heads), that are showed by the Shin's method (C and D). DC: dense calcium, NC: necrotic core

Table 1. Baseline demographics, risk factors and lesion characteristics.

	Cohort A (N=28) (Lesions=28)	Cohort B (N=32) (Lesions=32)	P-Value
Age (years)			
Mean±SD	62.03±9.00	62.83±10.01	0.67 ¹
Men, % (n)	57.1% (16)	65.6% (21)	0.43 ²
Smokers, % (n)	21.4% (6)	12.5% (4)	0.49 ²
Diabetes, % (n)	3.6% (1)	15.6% (5)	0.19 ²
Hypertension requiring medication, % (n)	57.1% (16)	59.3% (19)	0.79 ²
Hypertlipidaemia requiring medication, % (n)	63.0% (17)	87.5% (28)	0.02 ²
Previous target vessel intervention, % (n)	3.6% (1)	6.2% (2)	1.00 ²
Previous myocardial infarction, % (n)	3.5% (1)	37.5% (12)	<0.01 ²
Stable angina, % (n)	67.9% (19)	68.7% (22)	1.00 ²
Unstable angina, % (n)	28.6% (8)	15.6% (5)	0.34 ²
Silent ischaemia, % (n)	3.6% (1)	0.0% (0)	0.47 ²
Target vessel, % (n)			
Left anterior descending	50.0% (14)	37.5% (12)	0.30 ²
Left circumflex	28.6% (8)	25.0% (8)	1.00 ²
Right coronary artery	21.4% (6)	37.5% (12)	0.17 ²
AHA/ACC lesion classification, % (n)			
A	0.0% (0)	3.1% (1)	1.00 ²
B1	64.3% (18)	43.8% (14)	0.19 ²
B2	35.7% (10)	50.0% (16)	0.43 ²
C	0.0% (0)	3.1% (1)	1.00 ²
Mean reference vessel diameter (mm), Mean±SD (n)	2.70±0.47 (28)	2.60±0.45 (32)	0.39 ¹
Minimum luminal diameter (mm), Mean±SD (n)	1.08±0.25 (28)	1.08±0.31 (32)	0.77 ¹
Diameter stenosis (%), Mean±SD (n)	59.13±11.28 (28)	57.81±12.60 (32)	0.87 ¹
Lesion length (mm), Mean±SD (n)	8.79±3.67 (28)	10.08±3.50 (32)	0.09 ¹

1. from Wilcoxon's rank sum test; 2. from Fisher's exact test; AHA/ACC: American Heart Association/American College of Cardiology; SD: standard deviation

Table 2. IVUS-VH data between post-procedure and 6-month follow-up.

	Cohort A (BVS 1.0), n=28			Cohort B (BVS 1.1), n=32			P value	
	Post-procedure	6-month follow-up	p value	Post-procedure	6-month follow-up	p value	Cohort A vs. Cohort B Post	Cohort A vs. Cohort B 6-month follow-up
DC area (mm ²)	1.07±0.55	0.85±0.54	0.08	1.08±0.69	1.18±0.66	0.2	0.9	0.01
DC (%)	7.73±3.70	6.21±3.69	0.1	8.87±4.58	10.39±5.64	0.09	0.2	<0.001
NC area (mm ²)	1.71±1.03	1.36±0.91	0.02	1.84±1.14	1.91±0.93	0.1	0.5	0.001
NC (%)	11.35±4.78	9.44±4.84	0.001	15.3±6.81	16.04±6.69	0.2	0.01	<0.001
NC+DC area (mm ²)	2.78±1.42	2.21±1.29	0.02	2.91±1.76	3.08±1.47	0.2	0.7	0.003
NC+DC (%)	19.08±6.89	15.65±7.34	0.03	23.90±10.71	26.43±11.28	0.2	0.05	<0.001
EEM area (mm ²)	14.13±3.53	13.96±3.38	0.4	14.1±3.7	14.25±3.72	0.1	0.5	0.3
Absolute DC change (mm ²)		-0.22±0.62			0.10±0.46			0.06
Absolute NC change (mm ²)		-0.35±0.79			0.07±0.79			0.007
Absolute DC+NC change (mm ²)		-0.57±1.3			0.16±1.16			0.013

Data are expressed as mean±SD; DC: dense calcium; NC: necrotic core; BVS: bioresorbable vascular scaffold

In cohort A, there was a relative 20% decrease in both DC and NC (p=0.08 and p=0.02) between post-procedure and 6-month follow-up. Conversely, over the same time period in cohort B, a small relative increase in DC and NC of 9% (p=0.2) and of 4% (p=0.1) respectively, was observed. (Figure 4) At 6-month follow-up, while in cohort A there was regression in the calcified pattern in 16 out of 27 patients (59%) and in the necrotic

pattern in 20 out of 27 patients (74%), in cohort B there was regression in the calcified pattern in 11 out of 26 patients (42%) and in necrotic pattern in seven out of 26 patients (27%). Overall, the absolute DC+NC decrease was significantly larger in cohort A than cohort B, suggesting an earlier IVUS-VH alteration of the polymeric struts with the BVS 1.0 as compared to the BVS 1.1.

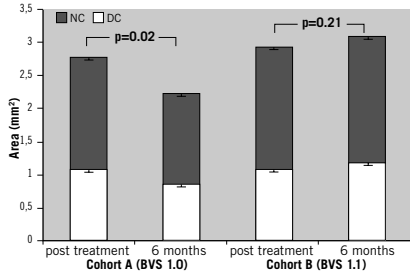


Figure 4. DC and NC area at six months compared to post-treatment in BVS 1.0 and BVS 1.1. Error bars portray standard error of the mean. DC: dense calcium; NC: necrotic core

Grey-scale intravascular ultrasound data and correlation with IVUS-VH alteration of BVS 1.0 and 1.1

On average, at six month follow-up, the EEM area did not significantly differ from post-treatment status in both cohorts (Table 2).

Classifying patients according to reduction in the EEM area at 6-month follow-up, we analysed changes in absolute area of DC and NC core in both cohorts. In patients from cohort A, those with reduction of the EEM area at 6-month ($n=15$) showed a significantly lower absolute area change of NC compared to other patients ($n=13$) ($-0.69 \pm 0.73 \text{ mm}^2$ vs. $0.05 \pm 0.68 \text{ mm}^2$, $p=0.017$) (Figure 5). Reduction of DC was no different ($-0.40 \pm 0.63 \text{ mm}^2$ vs. $-0.02 \pm 0.56 \text{ mm}^2$, $p=0.1$). Overall no correlation was found between changes in EEM area and the sum of absolute change in DC+NC area (Figure 6A).

On the other hand, in patients from cohort B with a reduction in the EEM area ($n=16$), there was a significantly lower change in absolute area of DC and NC at follow-up compared to other patients ($n=16$)

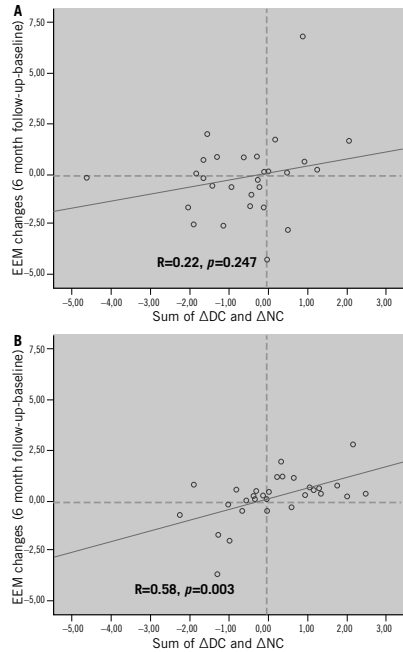


Figure 6. Bioresorption of the scaffold, measured by sum of absolute change in dense calcium and necrotic core area is significantly correlated with change of EEM area in cohort B (Panel B), but not in cohort A (Panel A). In the lower left quadrant of both panels, patients with bioresorption of BVS and reduction of EEM area are shown. EEM: external elastic membrane; DC: dense calcium, NC: necrotic core; BVS: bioresorbable vascular scaffold

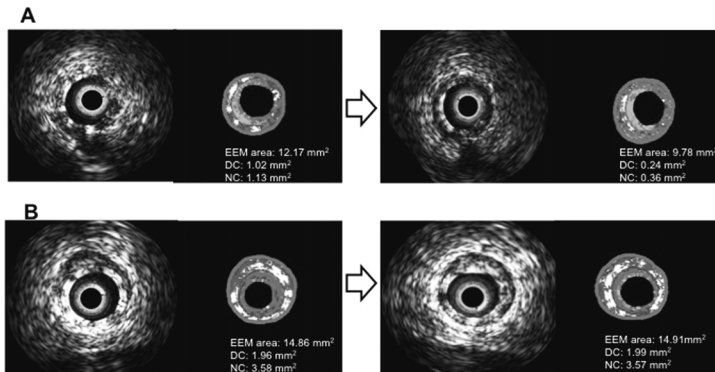


Figure 5. In the A panels, an extreme example of bioresorption at 6-months correlated with EEM area reduction. In the B panels, the persistence of the stent at six months is not associated with EEM area reduction. With the Shin method, blood surrounding ultrasound catheter is detected as fibrous and fibrous-fatty tissues. The boundaries of the lumen area are not depicted or superimposed on the figures. EEM: external elastic membrane; DC: dense calcium; NC: necrotic core

(respectively for DC -0.12 ± 0.41 mm² vs. 0.30 ± 0.42 mm², $p=0.007$; for NC -0.38 ± 0.84 mm² vs. 0.50 ± 0.45 mm², $p<0.001$). In the overall population, the change in DC+NC area correlated significantly with the change in EEM area. ($R=0.58$, $p=0.003$). (Figure 6B).

Discussion

The major findings of our study are: 1) the changes in design, degradation rate and mechanical durability of the BVS 1.1 compared to BVS 1.0 significantly influenced its IVUS-VH changes over a period of six months (i.e., less reduction in DC and NC at six months); 2) a relationship exists between change overtime in EEM area and in DC+NC area.

Kim et al have previously shown that metallic stents eluting sirolimus and paclitaxel introduce artifacts in IVUS-VH images, that interfere with the classification of plaque behind the struts.⁶ Normally struts of drug-eluting stents appear as DC, surrounded by a red halo. Although the BVS is made of non-metallic materials, it was also recognised by IVUS-VH software as DC and NC. For this scaffold, the presence of "pseudo" DC and NC could be used as surrogate marker of alteration of the polymeric struts.^{1,7,8,12-14} Garcia-Garcia et al have already shown in a sub-study of ABSORB cohort A trial that polymeric struts are identified with radiofrequency backscattering as calcific structures. Using IVUS-VH, it has been shown that there was an important increase in DC and NC immediately after BVS implantation.⁷ This sudden change in DC and NC has been attributed to the introduction of polymeric struts and might represent their VH fingerprint. Our data confirm that polymeric struts appear as DC and NC and that IVUS-VH is a potential approach to semi-quantify or state the presence of the polymer. The ability of IVUS-VH to recognise polymeric struts is important also to potentially follow the mechanical support or bioresorption process. Our study demonstrated that while for the BVS Revision 1.0 there is a reduction in DC and NC after six months,⁷ for the BVS Revision 1.1 the IVUS-VH signature appears to be unchanged over the same period. This stable backscattering signal with the BVS 1.1 suggests unchanging polymeric structure and/or stable mechanical properties due to slower degradation *in vivo*, as intended. The first revision of the BVS showed slightly higher acute recoil than conventional metallic platform stents² and at six months an 11.7% reduction in scaffold area of the BVS 1.0 area was documented.³ Of note, the longer-lasting mechanical integrity of the BVS Revision 1.1, –as suggested by unaltered IVUS-VH signature over a period of six months, may prevent this loss in structural integrity and reduction in scaffold area.^{1,15} This observation of constancy in radiofrequency backscattering of BVS 1.1 is largely confirmed by the absence of qualitative alterations of the appearance of the polymeric struts of BVS 1.1 with optical coherence tomography (OCT).⁴ They uniformly keep their "preserved box" appearance, whereas with the BVS 1.0 only 3% of preserved box were present at six months follow-up.¹²

Our data also showed that the change in DC+NC area detected by IVUS-VH may be associated with shrinkage of the EEM area. For Revision 1.1, we found a significant correlation between the reduction of the EEM area at follow-up and changes in the sum of DC and NC. In particular, it seems to be a trend between the EEM shrinkage and the positive/negative value of sum of changes in DC

and NC. In the case of Revision 1.0, the absence of any relationship between the change in IVUS-VH and the change in EEM area may be the result of a different phenomenon, or it may relate to a broader biological and/or sample variability; in particular looking at Figure 6, the two lines for both the cohorts seem similar and one is significant but not the other probably because of less variability. It is interesting to note that for both scaffolds the IVUS-VH changes (and potentially the bioresorption process) are not uniform in all patients. It depends not only on the hydrolysis of the scaffold, but probably also on the nature of the underlying plaque (composition and inflammatory state), and the further recruitment of macrophages to the site of the scaffold implantation. OCT of the presence of macrophages surrounding the scaffold, and the analysis of plaque composition behind the scaffold will enhance the understanding of the bioresorption process of the BVS.

In conclusion, IVUS-VH is a clinical method that can detect differences in behaviour between BVS Revision 1.0 and 1.1. Their IVUS-VH fingerprints may be influenced by changes in mechanical design or in product processing. Stability in the IVUS-VH signal of the BVS 1.1 through to 6-months follow-up might suggest a more durable mechanical integrity than the BVS 1.0.

Limitations

We acknowledge that the classification tree of IVUS radiofrequency analysis has not been validated for polymeric struts. We did not collect data about change in fibrous tissue, because it is known that polymeric struts only appear as dense calcium and necrotic core on IVUS-VH. At the same time, using Shin's method, we did not collect data on changes to the lumen area and plaque burden. Changes in DC and NC at follow-up are probably not only related to the BVS, but also to the natural history of the atherosclerotic disease.

References

- Serruys PW, Ormiston JA, Onuma Y, Regar E, Gonzalo N, Garcia-Garcia HM, Nieman K, Bruining N, Dorange C, Miquel-Hebert K, Veldhof S, Webster M, Thuesen L, Dudek D. A bioabsorbable everolimus-eluting coronary stent system (ABSORB): 2-year outcomes and results from multiple imaging methods. *Lancet* 2009; 373:897-910.
- Tanimoto S, Serruys PW, Thuesen L, Dudek D, de Bruyne B, Chevalier B, Ormiston JA. Comparison of *in vivo* acute stent recoil between the bioabsorbable everolimus-eluting coronary stent and the everolimus-eluting cobalt chromium coronary stent: insights from the ABSORB and SPIRIT trials. *Catheter Cardiovasc Interv* 2007;70:515-523.
- Tanimoto S, Bruining N, van Domburg RT, Rotger D, Radeva P, Ligthart JM, Serruys PW. Late stent recoil of the bioabsorbable everolimus-eluting coronary stent and its relationship with plaque morphology. *J Am Coll Cardiol* 2008; 52:1616-1620.
- Serruys PW, Onuma Y, Ormiston JA, De Bruyne B, Regar E, Dudek D, Thuesen L, Smith P, Chevalier B, McClean D, Koolen J, Windecker S, Whitbourn R, Meredith I, Dorange C, Veldhof S, Miquel-Hebert K, Rapoza R, Garcia Garcia HM. Evaluation of the second generation of a bioresorbable everolimus drug-eluting vascular scaffold for treatment of de novo coronary artery stenosis: 6-month clinical and imaging outcomes. *Circulation*, 2010;122:2301-12.
- Okamura T, Garg S, Gutierrez-Chico JL, Shin ES, Onuma Y, Garcia HM, Rapoza R, Sudhir K, Regar E, Serruys PW. In-vivo evaluation of stent strut

distribution patterns in the bioabsorbable everolimus-eluting device: An OCT ad hoc analysis of the Revision 1.0 and Revision 1.1 stent design in the ABSORB clinical trial. *EuroIntervention* 2010;9:932-938.

6. Kim SW, Mintz GS, Hong YJ, Pakala R, Park KS, Pichard AD, Satler LF, Kent KM, Suddath WO, Waksman R, Weissman NJ. The virtual histology intravascular ultrasound appearance of newly placed drug-eluting stents. *Am J Cardiol* 2008; 102:1182-1186.
7. Garcia-Garcia HM, Gonzalo N, Pawar R, Kukreja N, Dudek D, Thuesen L, Ormiston JA, Regar E, Serruys PW. Assessment of the absorption process following bioabsorbable everolimus-eluting stent implantation: temporal changes in strain values and tissue composition using intravascular ultrasound radiofrequency data analysis. A substudy of the ABSORB clinical trial. *EuroIntervention* 2009;4:443-448.
8. Sarno G, Onuma Y, Garcia Garcia HM, Garg S, Regar E, Thuesen L, Dudek D, Veldhof S, Dorange C, Ormiston JA, Serruys PW. IVUS radiofrequency analysis in the evaluation of the polymeric struts of the bioabsorbable everolimus-eluting device during the bioabsorption process. *Catheter Cardiovasc Interv*. 2010;75:914-918.
9. Shin ES, Garcia-Garcia HM, Serruys PW. A new method to measure necrotic core and calcium content in coronary plaques using intravascular ultrasound radiofrequency-based analysis. *Int J Cardiovasc Imaging* 2010;26:387-396.
10. Nair A, Kuban BD, Tuzcu EM, Schoenhagen P, Nissen SE, Vince DG. Coronary plaque classification with intravascular ultrasound radiofrequency data analysis. *Circulation* 2002;106:2200-2206.
11. Nasu K, Tsuchikane E, Katoh O, Vince DG, Virmani R, Surmely JF, Murata A, Takeda Y, Ito T, Ehara M, Matsubara T, Terashima M, Suzuki T. Accuracy of in vivo coronary plaque morphology assessment: a validation study of in vivo virtual histology compared with in vitro histopathology. *J Am Coll Cardiol* 2006;47:2405-2412.
12. Ormiston JA, Serruys PW, Regar E, Dudek D, Thuesen L, Webster MW, Onuma Y, Garcia-Garcia HM, McGreevy R, Veldhof S. A bioabsorbable everolimus-eluting coronary stent system for patients with single de-novo coronary artery lesions (ABSORB): a prospective open-label trial. *Lancet* 2008; 371:899-907.
13. Ormiston JA, Webster MW, Armstrong G. First-in-human implantation of a fully bioabsorbable drug-eluting stent: the BVS poly-L-lactic acid everolimus-eluting coronary stent. *Catheter Cardiovasc Interv* 2007;69:128-131.
14. Bruining N, de Winter S, Roelandt JR, Regar E, Heller I, van Domburg RT, Hamers R, Onuma Y, Dudek D, Webster MW, Thuesen L, Ormiston JA, Cheong WF, Miquel-Hebert K, Veldhof S, Serruys PW. Monitoring in vivo absorption of a drug-eluting bioabsorbable stent with intravascular ultrasound-derived parameters a feasibility study. *JACC Cardiovasc Interv*. 2010;3:449-456.
15. Mintz GS, Popma JJ, Pichard AD, Kent KM, Satler LF, Wong C, Hong MK, Kovach JA, Leon MB. Arterial remodeling after coronary angioplasty: a serial intravascular ultrasound study. *Circulation* 1996;94:35-43.

5.2

A comparative assessment by optical coherence tomography of the performance of the first and second generation of the everolimus-eluting bioresorbable vascular scaffolds.

Josep Gomez-Lara, Salvatore Brugaletta, Roberto Diletti, Scot Garg, Yoshinobu Onuma, Bill D Gogas, Robert Jan van Geuns, Cecile Dorange, Susan Veldhof, Richard Rapoza, Robert Whitbourn, Stephan Windecker, Hector M Garcia-Garcia, Patrick W Serruys

Eur Heart J 2011;32:294-304

A comparative assessment by optical coherence tomography of the performance of the first and second generation of the everolimus-eluting bioresorbable vascular scaffolds

Josep Gomez-Lara^{1†}, Salvatore Brugaletta¹, Roberto Diletti¹, Scot Garg¹, Yoshinobu Onuma¹, Bill D. Gogas¹, Robert Jan van Geuns¹, Cécile Dorange², Susan Veldhof², Richard Rapoza², Robert Whitbourn³, Stephan Windecker⁴, Hector M. Garcia-Garcia¹, Evelyn Regar¹, and Patrick W. Serruys^{1*†}

¹Department of Interventional Cardiology, Ba583a, Thoraxcenter, Erasmus MC, s-Gravendijkwal 230, 3015 CE Rotterdam, The Netherlands; ²Abbott Vascular, Diegem, Belgium; ³St Vincent's Hospital, Melbourne, Australia; and ⁴Swiss Cardiovascular Centre, Bern, Switzerland

Received 8 September 2010; revised 28 October 2010; accepted 18 November 2010

Aims	The first generation of the everolimus-eluting bioresorbable vascular scaffold (BVS 1.0) showed an angiographic late loss higher than the metallic everolimus-eluting stent Xience V due to scaffold shrinkage. The new generation (BVS 1.1) presents a different design and manufacturing process than the BVS 1.0. This study sought to evaluate the differences in late shrinkage, neointimal response, and bioresorption process between these two scaffold generations using optical coherence tomography (OCT).
Methods and results	A total of 12 lesions treated with the BVS 1.0 and 12 selected lesions treated with the revised BVS 1.1 were imaged at baseline and 6-month follow-up with OCT. Late shrinkage and neointimal area (NIA) were derived from OCT area measurements. Neointimal thickness was measured in each strut. Strut appearance has been classified as previously described. Baseline clinical, angiographic, and OCT characteristics were mainly similar in the two groups. At 6 months, absolute and relative shrinkages were significantly larger for the BVS 1.0 than for the BVS 1.1 (0.98 vs. 0.07 mm ² and 13.0 vs. 1.0%, respectively; $P = 0.01$). Neointimal area was significantly higher in the BVS 1.0 than in the BVS 1.1 (in-scaffold area obstruction of 23.6 vs. 12.3%; $P < 0.01$). Neointimal thickness was also larger in the BVS 1.0 than in the BVS 1.1 (166.0 vs. 76.4 μm ; $P < 0.01$). Consequently, OCT, intravascular ultrasound, and angiographic luminal losses were higher with the BVS 1.0 than with the BVS 1.1. At 6 months, strut appearance was preserved in only 2.9% of the BVS 1.0 struts, but remained unchanged with the BVS 1.1 indicating different state of strut microstructure and/or their reflectivity.
Conclusion	The BVS 1.1 has less late shrinkage and less neointimal growth at 6-month follow-up compared with the BVS 1.0. A difference in polymer degradation leading to changes in microstructure and reflectivity is the most plausible explanation for this finding.
Keywords	Bioresorbable vascular scaffold • Shrinkage • Optical coherence tomography • Bioresorption

Background

The first generation of the everolimus-eluting bioresorbable vascular scaffold (BVS 1.0) was tested in 30 patients enrolled in the ABSORB Cohort A study. At 6-month follow-up, this device showed a late shrinkage of the scaffold area of 11.8% as assessed by intravascular ultrasound (IVUS) and rapid changes in strut appearance, documented by multiple imaging modalities.¹

At variance with metallic stents, which do not exhibit late shrinkage,² the reduction of the BVS 1.0 scaffold area was the main component of late luminal loss at 6 months.

The BVS 1.1 represents a new generation of bioresorbable devices. It utilizes a novel platform design and polymer processing different than the previous BVS 1.0. This new generation is designed to improve the radial force and to slow-down the loss in mechanical integrity, without substantially affecting the bioresorption process.³ It has been investigated in 101 patients enrolled in the ABSORB cohort B trial. Forty-five of these patients were scheduled for a 6-month control with conventional angiography and multiple intravascular imaging techniques.

Optical coherence tomography (OCT) is a high resolution imaging technique capable of an accurate assessment of the polymeric struts, changes in luminal and scaffold dimensions, and the quantification of neointimal hyperplasia.^{4–6}

Our aim is to compare the late shrinkage and neointimal response of the two polymeric devices using OCT imaging and to assess the qualitative changes in strut appearance as a marker of bioresorption at 6-month follow-up.

Materials and methods

Study design and population

The ABSORB trial is a non-randomized, multicentre, single-arm, efficacy–safety study. The first Cohort (A) included 30 patients treated with the BVS 1.0; the trial design and results up to 3-year follow-up have been already published.^{1,4,7} The second Cohort (B) included 101 patients with 102 lesions treated with a single size 3 × 18 mm of the BVS 1.1 design; the study design is available at clinicaltrials.gov (NCT00856856).

The inclusion criteria were similar in both studies: patients aged 18 years or older diagnosed with stable, unstable, or silent ischaemia, with a *de novo* lesion in a native coronary artery between 50 and 99% of the luminal diameter and a Thrombolysis In Myocardial Infarction (TIMI) flow grade of 1 or more. Exclusions included patients with an evolving myocardial infarction, stenosis of an unprotected left main or ostial right coronary artery (RCA), presence of intracoronary thrombus or heavy calcification. Excessive tortuosity and lesions involving a side branch more than 2 mm in diameter were also exclusion criteria. The ethics committee at each participating institution approved the protocol and each patient gave written informed consent before inclusion.

Four centres (Auckland, Aarhus, Krakow, and Rotterdam) participated in the Absorb Cohort A in 2006 using the BVS 1.0.¹ In this first-in-man study, angiography and IVUS were mandatory investigations at 6 and 24 months of follow-up. Optical coherence tomography was an optional investigation that was only executed and performed in Rotterdam with the available system at that time (M2 Light Lab). Subsequently, the Rotterdam group performed OCT follow-up of their patients at 6 and 24 months. As a result, 13 patients in Cohort A had sequential OCT investigation at baseline and 6 months.⁴ The Cohort B study was started during 2009 using the BVS 1.1. In this study, 7 of the 12 participating centres performed OCT at baseline and follow-up and three of them (Rotterdam = 9, Melbourne = 2, and Bern = 1) used the most advanced system (C7 Light Lab). As a result, 12 patients in Cohort B have been imaged with the OCT C7 system. This limited but almost equal number of patients represents a unique opportunity to analyse, with the high

resolution of OCT, the mechanical behaviour of the first and second generation of everolimus-eluting BVS at baseline and at 6-month follow-up.

Devices

The BVS 1.0 (Abbott Vascular, Santa Clara, CA, USA) is a balloon expandable device built on a backbone of semi-crystalline poly-L-lactide (PLLA) polymer. The polymer consists of crystalline and amorphous domains. The balance between the crystalline and amorphous fractions and the molecular orientation state of these phases depends on their thermal and deformation history. The platform is coated with the poly-D,L-lactide (PDLLA) copolymer that contains and controls the release of the antiproliferative everolimus (Novartis, Switzerland). Both PLLA and PDLLA are fully bioresorbable. The strut thickness is 150 µm and the struts are distributed as circumferential out-of-phase zigzag hoops linked together by three longitudinal bridges between each hoop. The BVS 1.0 design is shown in Figure 1.

The manufacturing process the BVS 1.1 (Abbott Vascular, Santa Clara, CA, USA) has been modified to enhance the mechanical strength and mechanical durability of the struts. Moreover, the new design has in-phase zigzag hoops linked by bridges that allow for a more uniform strut distribution, reduce maximum circular unsupported surface area, and provide more uniform vessel wall support and drug transfer.³ The polymer mass, coating content, amount of drug, and the strut thickness remain the same. The BVS 1.1 design is also shown in Figure 1.

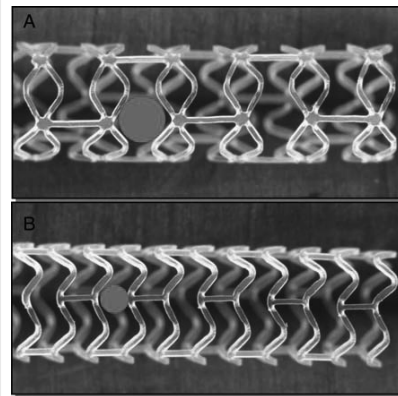


Figure 1 Design of the different bioresorbable vascular scaffold (BVS). (A) BVS 1.0 design. The struts are distributed as circumferential out-of-phase zigzag hoops linked together by three longitudinal bridges between each hoop. The maximal circular unsupported surface area is drawn as a red circle. (B) BVS 1.1 design. The struts are arranged as in-phase zigzag hoops linked together by three longitudinal bridges. The strut distribution is more uniform and allows the maximal circular unsupported surface area (red circle) to be smaller than in the BVS 1.0.

Treatment procedure

All procedures were performed electively. Lesions were treated with routine interventional techniques that included mandatory pre-dilatation. The study protocol forbade the use of pre-dilatation balloons longer than the pre-specified length of the device (18 mm), and recommended using balloons 0.5 mm smaller in diameter than the reference vessel diameter (RVD). The BVS had to be implanted at a pressure not exceeding the rated burst pressure (16 atmospheres). Post-dilation was allowed at the operator's discretion with shorter balloons than the BVS length and inflated at diameters that fit within the boundaries of the scaffold. Bail-out stenting was also allowed at operator's discretion.

Quantitative angiography analysis

The 2D angiograms were stored in DICOM format and analysed offline by the core lab (Cardiagnosis, Rotterdam, The Netherlands) using the CASS II analysis system (Pie Medical BV, Maastricht, The Netherlands). In each patient, the treated region and the peri-treated regions (defined by a length of 5 mm proximal and distal to the device edge) were analysed. The following quantitative coronary angiography (QCA) analysis parameters were measured: computer-defined minimal luminal diameter (MLD), RVD obtained by an interpolated method, and percentage of diameter stenosis (DS). Late loss was defined as the difference between MLD post-procedure and MLD at follow-up.⁸

Optical coherence tomography acquisition

In the ABSORB Cohort A, baseline and follow-up OCT acquisition was executed with an M2 Time-Domain System (LightLab Imaging, Westford, MA, USA) using the balloon occlusion method. The occlusion balloon Helios (Goodman, Japan) was advanced distal to the treated region over a conventional angioplasty guidewire of 0.014". Then, the conventional guidewire was replaced by the OCT ImageWire (LightLab Imaging, Westford, MA, USA) and the occlusion balloon catheter was positioned proximal to the segment of interest. Pullback of the ImageWire was performed with automated pullback at 1 mm/s and 15.6 frames/s during the occlusion of the artery by the balloon at low pressure (0.5–0.7 atm), and during simultaneous flushing of the vessel distal to the occlusion with lactated Ringer's solution at 37°C (flow rate 0.8 mL/s).

In ABSORB Cohort B, the baseline and follow-up OCT acquisitions were performed with the C7 XR Fourier-Domain System (LightLab Imaging, Westford, MA, USA) without occluding the coronary artery. In these cases, a conventional wire was placed distal to the segment of interest. Then the OCT imaging catheter (RX ImageWire II; LightLab Imaging, Westford, MA, USA) was advanced distally to the treated region. Removal of the conventional wire was left to the operator's discretion. The pullback was performed during a continuous injection of 3 mL/s of contrast medium (Iodixanol 370, Visipaque, GE Health Care, Cork, Ireland) injected at a maximum pressure of 300 psi through the guiding catheter using an injection pump. In this case, the automated pullback rate was 20 mm/s and the frame rate was 100 images/s.

The resolution of both OCT systems is exactly the same (15–20 µm of lateral resolution and 15–20 µm of axial resolution).⁹

Optical coherence tomography analysis

The OCT measurements were performed with proprietary software for offline analysis (LightLab Imaging, Westford, MA, USA). Adjusting for the pullback speed, the analysis of contiguous cross-sections was performed at each 1 mm longitudinal intervals within the treated segment.

The monochromatic peak wavelength of the OCT is differently reflected, refracted, and absorbed by the polymeric or metallic struts. A great deal of the OCT light energy is transmitted through the polymeric struts, such that only part of it is reflected at the endoluminal and abluminal sides of the struts generating a visible optical frame border; the core of the polymeric struts is imaged as a black square at baseline. As a consequence, the vessel wall is easily imaged through the struts without any major signs of shadowing (Figure 2). Thus, OCT analysis of the BVS has several advantages over that of metallic stents. First, at baseline, the vessel wall/lumen and its luminal area can be readily measured behind the polymeric struts. At follow-up, most of the struts are fully covered and embedded in the vessel wall and the luminal area can be drawn with an automated detection algorithm available in the Light Lab proprietary software; manual corrections are performed if necessary. Second, since polymeric struts are accurately imaged at baseline, the device area can be obtained manually by joining the middle point of each consecutive strut around the circumference. In frames with only a few struts, the BVS area was adjusted to follow the lumen area in the regions where its contour was outside the lumen area. At follow-up, the BVS area was also measured by joining the middle point of the struts (Figure 3).

Device shrinkage is defined as the decrease over time of the device area with respect to the area measured immediately after the deployment.^{10,11} Absolute late shrinkage has been measured as the difference between the mean BVS area at baseline minus the mean BVS area at follow-up. Relative late shrinkage has been measured as: [(absolute late shrinkage)/baseline mean BVS area] × 100 (Figure 3).

In case of incomplete scaffold/strut apposition (ISA), the area between the backside of the struts and the vessel wall has been measured as ISA area. The neointimal area (NIA) has been measured at follow-up as: BVS area – (Lumen Area – ISA area). The neointimal thickness (NIT) has been measured at follow-up with the 'thickness ruler' tool from the endoluminal border of the black strut core to the lumen.

Moreover, a qualitative assessment of the appearance of polymeric struts has been obtained at follow-up. Basically, the struts were classified as preserved box, open box, dissolved bright box, and dissolved black box in order of decreasing reflectivity (Figure 4).¹ The kappa index to detect the four types of strut appearance was 0.58.¹² Strut tissue coverage was assessed qualitatively when clear neointimal tissue covered the polymeric strut.

Intra-vascular ultrasound acquisition and analysis

The scaffolded segments were examined with phased array IVUS catheters (EagleEye; Volcano Corporation, Rancho Cordova, CA, USA) with an automated pullback at 0.5 mm/s. Lumen area was measured with a validated computer-based contour detection programme (CURAD BV, Wijk bij Duurstede, The Netherlands) that allows for semi-automatic detection of lumen.¹³

Statistical analysis

Normality distribution of continuous variables was explored with the Kolmogorov–Smirnov test. All continuous variables had normal distribution and have been expressed as means and 1 standard deviation (SD). Categorical variables are presented as counts (%). Paired comparisons of continuous variables within groups between the different time points were done by the Wilcoxon's signed rank test. Comparison of continuous variables between Cohorts A and B has been made using the U-Mann–Whitney test. Comparisons of absolute differences

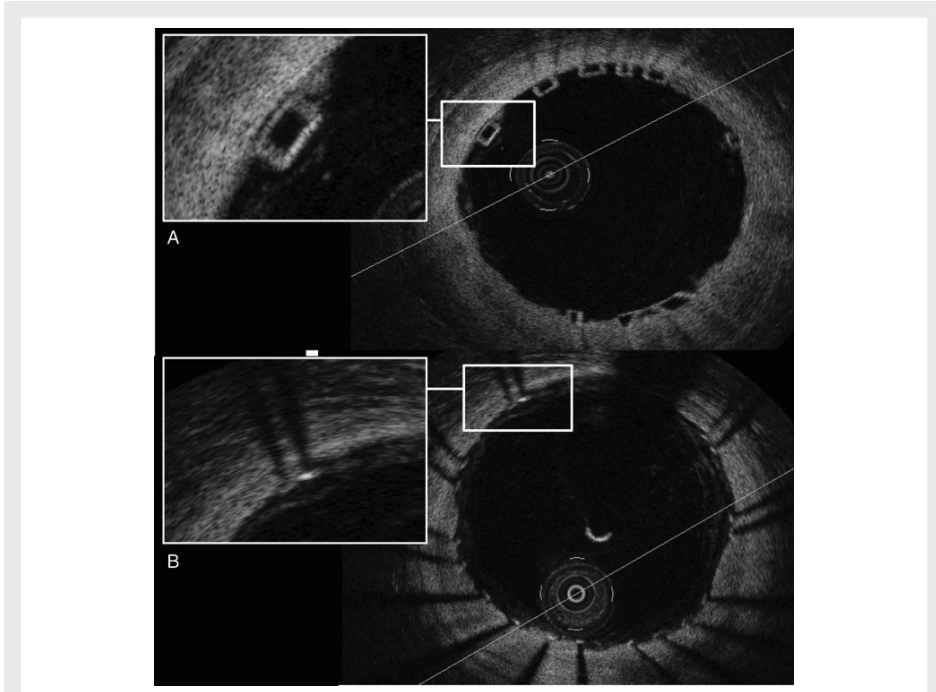


Figure 2 Optical coherence tomography (OCT) imaging of the bioresorbable scaffolds and metallic platform stents. (A) Bioresorbable vascular scaffold imaged with OCT. The strut appearance is translucent and allows a perfect imaging of the vessel wall. (B) Metallic platform stent imaged with OCT. The metallic struts are opaque to the OCT light and produce the typical shadow into the vessel wall.

between baseline and follow-up have also been made with the U-Mann-Whitney test. Comparisons of categorical variables between groups have been made using the Chi-square test or the Fisher test when one of the cells had less than five events. A two-sided P -value ≤ 0.05 was considered statistically significant. All the statistics have been performed with the SPSS 15.0 version for Windows (IL, US).

Results

Study population

A total of 13 lesions in 13 patients had baseline and follow-up OCT imaging in the ABSORB Cohort A study.¹ One of these patients underwent a non-ischæmia driven target lesion revascularization treated with a metallic platform stent at Day 42. The OCT imaging at that time showed strut discontinuation with attached thrombi probably due to overstretching of the BVS during implantation.⁷ This patient has not been included in the present study. In the ABSORB Cohort B study, 28 patients with scheduled imaging control at 6-month follow-up were studied with OCT at baseline.

Two of them were excluded due to the sub-optimal quality of the imaging, and of the remaining 26 patients, 13 were imaged with the M3 OCT system and 13 were imaged with the OCT C7. None of the 13 patients imaged with the M3 system needed an unscheduled angiography and all of them were studied with OCT at 6 months. One patient imaged with the C7 system presented with a symptomatic peri-procedural myocardial infarction at the index procedure secondary to an occlusion of a small diagonal after the implantation of the BVS in the left anterior descending. This patient refused invasive imaging at 6-month follow-up. Finally, 24 patients were included in the present study: 12 were treated with the BVS 1.0 and 12 were treated with the BVS 1.1. None of those patients had BVS fractures at baseline or 6-month follow-up.

The baseline clinical characteristics are shown in Table 1. Both groups were similar in gender and age. There was a trend toward lower percentage of hypercholesterolaemia (72.7 vs. 100.0%; $P = 0.06$) and prior acute myocardial infarction (8.3 vs. 41.7%; $P = 0.06$) in the BVS 1.0 than in the BVS 1.1 group, respectively. There was a significant difference in the smoking status favouring the BVS 1.1 group (33 vs. 0%, respectively; $P = 0.03$).

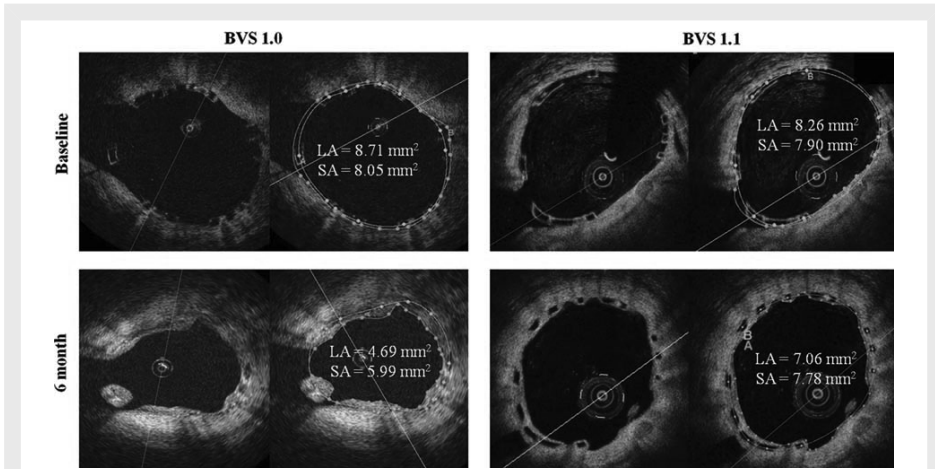


Figure 3 Late shrinkage assessment. Optical coherence tomography (OCT) imaging of the BVS 1.0 and 1.1. At baseline, the scaffold area (SA; blue line) is usually drawn into the luminal area (LA; green line). At follow-up, the neointima covers the polymeric struts and then, the scaffold area usually is drawn outside of the luminal area. The absolute late shrinkage for the BVS 1.0 is 2.06 mm² (relative shrinkage of 25.6%) and for the BVS 1.1 is 0.12 mm² (relative shrinkage of 1.5%).

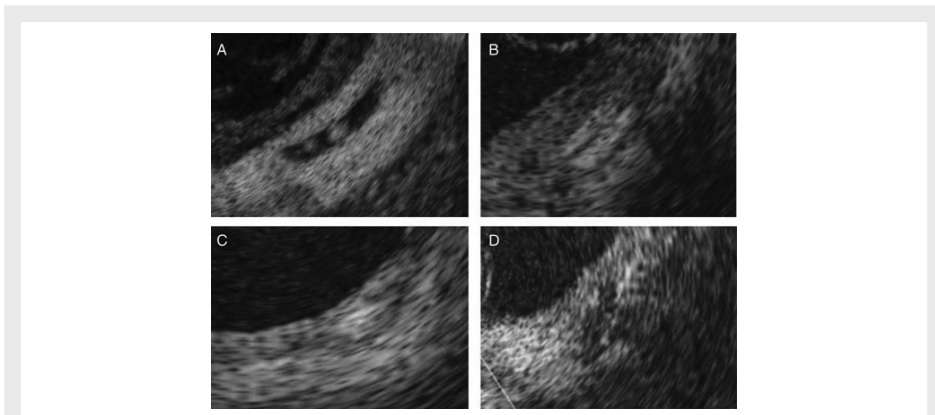


Figure 4 Strut appearance of the bioresorbable vascular scaffold at follow-up. (A) Preserved box appearance: sharp defined, bright reflection borders with preserved box-shaped appearance; strut body shows low reflection; (B) open box: luminal and abluminal long-axis borders thickened bright reflection; short-axis borders not visible; (C) dissolved bright box: partially visible bright spot, contours poorly defined; no box-shaped appearance; (D) dissolved black box: black spot, contours poorly defined, often confluent; no box-shaped appearance.

A total of 11 patients in ABSORB Cohort A were treated with a BVS 1.0 of 3 × 12 mm and 1 was treated with a BVS 1.0 of 3 × 18 mm. All patients of the ABSORB Cohort B were treated with a BVS 1.1 of 3 × 18 mm.

Quantitative coronary angiography results

Baseline and follow-up angiographic parameters are shown in Table 2. Both groups had similar angiographic characteristics at

Table 1 Baseline clinical and angiographic characteristics

	BVS 1.0 (n = 12)	BVS 1.1 (n = 12)	P-value
Male	8 (66.7)	9 (75.0)	0.65
Age (years ± SD)	59.5 ± 8.3	61.2 ± 9.6	0.76
Hypertension	6 (50.0)	7 (58.3)	0.68
Hypercholesterolaemia	8 (72.7)	12 (100.0)	0.06
Diabetes mellitus	1 (8.3)	1 (8.3)	1.00
Smoke	4 (33.3)	0	0.03
Prior MI	1 (8.3)	5 (41.7)	0.06
Prior PCI	2 (16.7)	3 (25.0)	0.62
Clinical indication			0.27
Stable or silent angina	11 (91.7)	9 (75.0)	
Unstable angina	1 (8.3)	3 (25.0)	
Number of vessel disease			0.14
One	12 (100.0)	10 (83.3)	
Two	0	2 (16.7)	
Culprit vessel			0.22
LAD	4 (33.3)	6 (50.0)	
LCX	6 (50.0)	2 (16.7)	
RCA	2 (16.7)	4 (33.3)	
BVS size			<0.01
3 × 12 mm	11 (91.7)	0	
3 × 18 mm	1 (8.3)	12 (100.0)	

Values are expressed as count (%), except for age.

MI, myocardial infarction; PCI, percutaneous coronary intervention; LAD, left anterior descending; LCX, left circumflex; RCA, right coronary artery; BVS, bioresorbable vascular scaffold.

pre-implantation. Patients treated with the BVS 1.0 tended to have a larger RVD than patients treated with the BVS 1.1 (2.95 vs. 2.69 mm; $P = 0.14$).

At 6-month follow-up, patients treated with the BVS 1.0 had a significant decrease in MLD (angiographic late loss) of 0.43 mm ($P = 0.01$), whereas a non-significant 0.08 mm decrease was seen in those treated with the BVS 1.1. The difference in late loss between the BVS 1.0 and 1.1, although numerically appreciable, failed to reach statistical significance at 6 months ($P = 0.07$). The serial individual changes in MLD between baseline and follow-up are shown in *Figure 5*.

Optical coherence tomography results

Baseline and follow-up quantitative OCT and IVUS findings are shown in *Table 3*. Both groups had similar OCT findings at baseline after the deployment of the BVS. At 6 months, the BVS 1.0 had a significantly higher late shrinkage than the BVS 1.1 (absolute shrinkage of 0.98 vs. 0.07 mm² and relative shrinkage of 13.0 vs. 1.0%, respectively; $P = 0.01$). Neointimal area was significantly higher with the BVS 1.0 when compared with the BVS 1.1 (1.44 vs. 0.87 mm², respectively; $P < 0.01$). NIH was also larger in the

BVS 1.0 than in the BVS 1.1 (166.0 vs. 76.4 μm; $P < 0.01$). These findings at 6 months caused a significantly higher reduction in mean lumen area (relative difference of 35.1 vs. 16.1%; $P < 0.01$) and in minimal luminal area (47.0 vs. 20.7%; $P < 0.01$) with the BVS 1.0 than with the BVS 1.1 as assessed by OCT. Serial individual changes of the BVS area and of the minimal lumen area as assessed by OCT are shown in *Figure 5*. The ISA area of the BVS 1.0 at 6 months increased significantly with respect to the baseline (0.10 mm²; CI 95%: from -0.02 to 0.21 mm²; $P = 0.04$), while the ISA area of the BVS 1.1 remained unchanged (0.02 mm²; -0.18 to 0.22 mm²; $P = 0.26$).

A total of 662 struts of the BVS 1.0 and 1575 of the BVS 1.1 were detected at baseline. After deployment, all struts appear as preserved box in both BVS devices. At follow-up, 620 struts and 1639 struts were analysed. The strut appearance of the BVS 1.0 showed substantial changes in appearance: at 6 months struts had changed from 100% preserved black box to 29.7% open box, 51.4% dissolved bright box, 16.0% dissolved black box, and only 2.9% were preserved black box. For the BVS 1.1, all struts maintained a preserved black box appearance at 6 months ($P < 0.01$). Uncovered struts were less frequent in the BVS 1.0 (1.1%) than in the BVS 1.1 (5.3%) ($P = 0.01$).

Intravascular-ultrasound results

IVUS results are shown in *Table 3*. The reduction in mean lumen area was larger with the BVS 1.0 than with the BVS 1.1 (12.71 vs. 6.93%), but this difference was not statistically significant ($P = 0.17$). The reduction in minimal lumen area was significantly larger with the BVS 1.0 than with the BVS 1.1 (22.83 vs. 4.81%; $P < 0.01$).

Reproducibility of optical coherence tomography measurements

The scaffold area reproducibility using our method has been assessed specifically for our study. Two independent analysts measured the scaffold area in 100 images at follow-up. After 1 week, one of the analysts re-analysed the same frames. The inter-observer R^2 for repeated measures was 0.88 and the intraobserver R^2 was 0.98.

Discussion

The main findings of our study are: (i) the BVS 1.1 does not show late shrinkage at 6 months with respect to the baseline scaffold area; (ii) the BVS 1.0 has higher neointimal response and higher in-scaffold area obstruction than the BVS 1.1; (iii) these changes resulted in a higher OCT and IVUS luminal losses and angiographic late loss in the BVS 1.0 than in the BVS 1.1; (iv) the overall strut appearance at 6-month follow-up is dramatically different between the two generations of BVS, which may reflect differences in the polymer's interaction with light, arising from differences in microstructure and its degradation.

A pre-clinical animal study involving histological samples at differing time points divided the evolution process of the BVS into two parts:¹² first, the BVS resorption process, which consists of the disappearance of the polymeric PLA and the subsequent

Table 2 Quantitative coronary angiography findings at baseline and 6-month follow-up

BVS	Pre-deployment	Post-deployment	6-month FU	Difference post-pre (CI 95%)	P-value*	Difference post – 6 m FU (CI 95%)	P-value**	P-value†
QCA								
Lesion length (mm) ^a								
BVS 1.0	9.86 (3.46)	10.34 (1.70)	10.17 (2.20)	-0.48 (-2.90 to 1.94)	0.18	0.18 (-0.26 to 0.61)	0.64	0.93
BVS 1.1	8.99 (2.89)	17.08 (1.12)	16.08 (1.48)	-8.09 (-9.82 to -6.35)	<0.01	1.00 (-0.16 to 2.16)	0.13	
RVD (mm)								
BVS 1.0	2.95 (0.38)	3.03 (0.39)	2.87 (0.41)	0.08 (-0.10 to 0.26)	0.31	0.16 (0.01 to 0.31)	0.04	0.24
BVS 1.1	2.69 (0.35)	2.64 (0.23)	2.53 (0.22)	-0.05 (-0.21 to 0.11)	0.70	0.11 (0.02 to 0.20)	0.03	
MLD (mm)								
BVS 1.0	1.13 (0.30)	2.46 (0.38)	2.03 (0.30)	1.32 (1.03 to 1.62)	<0.01	0.43 (0.13 to 0.73)	0.01	0.07
BVS 1.1	1.23 (0.44)	2.26 (0.28)	2.18 (0.25)	1.03 (0.69 to 1.37)	<0.01	0.08 (-0.14 to 0.30)	0.24	
DS (%)								
BVS 1.0	60.8 (13.4)	18.6 (9.4)	27.8 (16.0)	-42.3 (-50.8 to -33.7)	<0.01	-9.3 (-18.7 to 0.2)	0.07	0.24
BVS 1.1	57.6 (13.1)	14.7 (7.5)	15.7 (9.3)	-42.9 (-50.9 to -35.0)	<0.01	-1.0 (-5.5 to 3.5)	0.66	

Data are expressed as mean (SD).

QCA, quantitative coronary angiography; BVS, bioresorbable vascular scaffold; FU, follow-up; RVD, reference vessel diameter; MLD, minimal lumen diameter; DS, diameter stenosis.

^aLesion length at post-procedure and at follow-up has been measured between the platinum markers of the BVS.

*Paired comparison between pre- and post-deployment within each group.

**Paired comparison between post-deployment and follow-up within each group.

†Comparison of the difference post-deployment—follow-up between the two groups. Comparison between groups at pre-deployment and post-deployment were non-significant ($P > 0.10$).

filling of the strut voids with proteoglycan material; second, the BVS integration process, which consists of the formation of organized tissue with connective cells and connective extracellular matrices replacing the polymeric and the proteoglycan material. In the same study, the strut appearance as assessed by OCT was compared with matched histological sections.¹² At 24 months, all the struts were discernible by OCT and 80.4% of them were classified as having the preserved box appearance (similar to the BVS 1.1 at 6 months). At that point of time, matched histological samples showed that almost all the strut footprints were occupied by proteoglycans and the analysis with gel permeation chromatography did not find traces of the polymeric material. This demonstrated that the polymer was already resorbed at that time, and therefore OCT imaging was not able to assess the resorption process. At 3- and 4-year follow-up, almost all the struts were not discernible and the few observed struts were classified as a dissolved bright or dissolved black box (similar to the BVS 1.0 at 6 months). There was poor correlation of these types of OCT strut appearance with the particular patterns observed on histology. But, the indiscernible struts and the dissolved black box appearance as assessed by OCT were observed as circumscribed regions of dense connective tissue with low cellularity on histology.

Therefore, as assessed by OCT, the most advanced resorption/integration states were characterized as: (i) observation of other types of strut appearance rather than the preserved box; and (ii) the reduction of discernible struts over time jointly with the observation of a dissolved black box strut appearance.¹²

In our study, the number of discernible struts of the BVS 1.1 was slightly lower at baseline than at follow-up (1575 vs. 1639, respectively; $P = 0.06$). At 6 months, the strut appearance was 'preserved' in all the patients. In contrast, the number of discernible struts of the BVS 1.0 was higher at baseline than at follow-up (662 vs. 620, respectively; $P = 0.05$) and at 6 months, only 2.9% of the discernible struts had a preserved box appearance. The correlation of our findings with the animal study shows that the BVS 1.0 had a more advanced resorption/integration state than the BVS 1.1 at 6 months. Our hypothesis is that this faster resorption/integration state is the main cause of the higher late shrinkage and greater neointimal response of the BVS 1.0 compared with the BVS 1.1.

Late shrinkage is a phenomenon resulting from the loss of structural integrity of the polymeric scaffold in conjunction with fatigue and constrictive remodelling of the vessel in the first months following the vessel injury. Loss of structural integrity is an inevitable part of the resorption process of these polymeric devices. The poly-L-lactic acid (PLLA) polymer has a lifecycle which can be divided in five

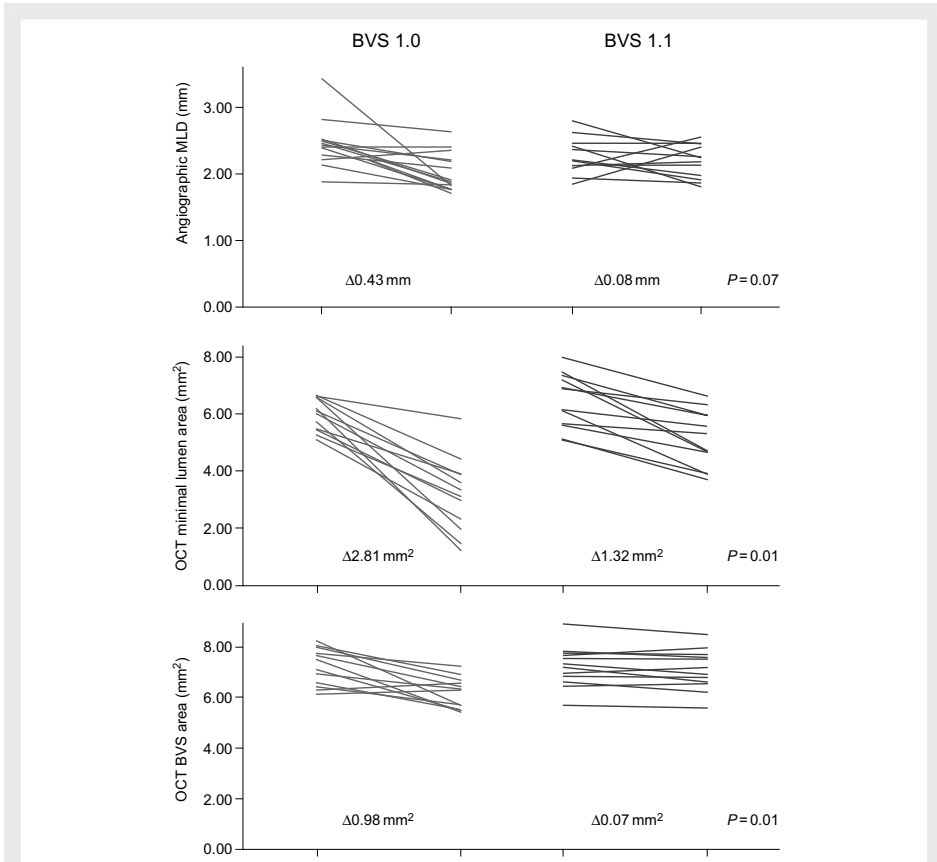


Figure 5 Serial changes in angiographic late lumen loss, BVS area (late shrinkage) and minimal lumen area as assessed by optical coherence tomography.

phases.¹⁴ First, immediately after the deployment, the polymer absorbs water from blood and surrounding tissues. Second, the long chains of PLLA degrade by hydrolysis into smaller chains without affecting the device's structure. Third, the hydrolysis process continues and causes a loss in integrity, with fragmentation of the struts and loss of radial strength. Fourth, soluble monomeric anions dissolve into the intercellular fluid and microparticles of less than 2 μm may be phagocytosed by the macrophages; manifesting in mass loss and bioresorption. Finally, the soluble L-lactate is converted into pyruvate, which enters the Krebs cycle, being eventually converted into carbon dioxide and water. The initial degradation process of the PLLA semi-crystalline polymer depends on the length of the polymers chain (molecular weight), the hydrophilicity, and the degree of crystallinity. In BVS 1.1, initial degradation rate (i.e.

losses in molecular weight leading to structural degradation) has been reduced through changes in the manufacturing process. This slower degradation allows for maintenance of the radial strength over months following the implantation.

The second cause of late shrinkage is the constrictive remodeling of the treated vessel in the first few months after implantation. In the era of balloon angioplasty, more than 70% of the restenotic process was attributed to negative remodeling of the vessel in the treated segment, and less than 30% was done to neointimal growth.¹⁵ In the metallic stent era, late lumen loss within the stent correlated strongly with tissue growth ($r = 0.975$), eliminating negative remodeling as the common cause of restenosis.^{16,17} Thus, the key question for intracoronary bioresorbable scaffolds is for how long radial strength (i.e. scaffolding) must be maintained

Table 3 Quantitative optical coherence tomography and intravascular ultrasound findings at baseline and 6-month follow-up

BVS (n = 12 vs. 12)	Baseline (post-deployment)	6-month FU	Absolute difference between BL and FU (CI 95%)	Relative difference between BL and FU (%)	P-value*	P-value**
OCT						
Mean luminal area (mm ²)						
1.0 BVS	7.63 (0.79)	4.94 (1.10)	2.69 (1.99–3.39)	35.07 (13.31)	<0.01	<0.01
1.1 BVS	7.67 (0.94)	6.44 (0.93)	1.23 (0.89–1.57)	16.09 (6.48)	0.01	
Minimal luminal area (mm ²)						
1.0 BVS	5.99 (0.57)	3.19 (1.28)	2.81 (2.03–3.59)	46.97 (19.67)	<0.01	<0.01
1.1 BVS	6.32 (0.96)	5.01 (0.97)	1.32 (0.83–1.80)	20.65 (10.94)	<0.01	
Mean BVS area (mm ²)						
1.0 BVS	7.18 (0.73)	6.20 (0.64)	0.98 (0.42–1.54)	12.95 (11.70)	0.01	0.01
1.1 BVS	7.21 (0.82)	7.14 (0.84)	0.07 (–0.10 to 0.24)	0.97 (3.73)	0.37	
Minimal BVS area (mm ²)						
1.0 BVS	5.82 (0.60)	4.75 (0.83)	1.07 (0.49–1.66)	17.90 (14.26)	<0.01	0.01
1.1 BVS	6.21 (0.98)	6.00 (0.85)	0.21 (–0.14 to 0.56)	2.81 (8.11)	0.29	
ISA area (mm ²)						
1.0 BVS	0.14 (0.25)	0.22 (0.31)	–0.10 (–0.21 to 0.02)	–36.36 (10.33)	0.04	0.88
1.1 BVS	0.15 (0.30)	0.17 (0.18)	–0.02 (–0.22 to 0.18)	–11.76 (15.35)	0.26	
NIA (mm ²)						
1.0 BVS	NA	1.44 (0.32)	NA	NA	NA	<0.01 ^a
1.1 BVS	NA	0.87 (0.22)	NA	NA	NA	
NIT (mm)						
1.0 BVS	NA	0.17 (0.04)	NA	NA	NA	<0.01 ^a
1.1 BVS	NA	0.08 (0.02)	NA	NA	NA	
In-device area obstruction (%)						
1.0 BVS	NA	23.62 (6.55)	NA	NA	NA	<0.01 ^a
1.1 BVS	NA	12.28 (3.38)	NA	NA	NA	
IVUS						
Mean luminal area (mm ²)						
1.0 BVS	6.84 (0.74)	5.94 (0.67)	0.90 (0.43–1.37)	12.71 (9.89)	<0.01	0.17
1.1 BVS	6.69 (0.81)	6.20 (0.76)	0.47 (0.24–0.69)	6.93 (4.68)	<0.01	
Minimal luminal area (mm ²)						
1.0 BVS	5.75 (0.52)	4.41 (0.70)	1.34 (0.83–1.84)	22.83 (12.73)	<0.01	<0.01
1.1 BVS	5.51 (0.78)	5.15 (0.73)	0.28 (–0.01 to 0.57)	4.81 (7.20)	0.09	

Data are expressed in mean (SD).

OCT, optical coherence tomography; IVUS, intravascular ultrasound; ISA, incomplete scaffold/strut apposition; NIA, neointimal area; NIT, neointimal thickness; NA, not applicable.

Comparison of the OCT and IVUS findings at baseline between groups showed no significant differences.

^aComparison of the neointimal hyperplasia (NIA and NIT) and in-device area obstruction at follow-up between groups.

*P-value between baseline and follow-up within groups.

**P-value comparing the absolute differences between groups.

to avoid constrictive remodelling. In a cohort of patients consecutively re-catheterized at 1, 2, 3, and 4 months, Serruys et al.¹⁸ demonstrated that the restenotic process after balloon angioplasty ceases to progress after 4 months. It is possible that after this time, scaffolding is no longer needed, and the structural degradation and bioresorption processes can commence.

It is uncertain whether the constrictive remodelling is more focused in the regions of the vessel with more plaque burden or is equally distributed. This can affect the results of our study due

to the differences in the BVS lengths according to the lesion length. The lesion length prior to the implantation was similar in both groups (around 9–10 mm), but the device length as assessed by QCA at post-deployment was significantly higher in the BVS 1.1 than in the BVS 1.0 (17.08 vs. 10.34 mm; $P < 0.01$). This difference resulted from the fact that all patients treated in the ABSORB Cohort B study received a single size device (3 × 18 mm), while in the ABSORB Cohort A there were two different sizes (3 × 12 and 3 × 18 mm). A sub-analysis of the 12 central millimetre

of the scaffold imaged by OCT (that part of the scaffold is more likely to be located at the nadir of the narrowing) in the patients treated with a 3 × 18 mm showed that the mean scaffold area at baseline and at 6-month follow-up was 7.18 and 6.19 mm² with the BVS 1.0 (relative shrinkage of 13.09%) and 7.14 and 7.10 mm² with the BVS 1.1 (relative shrinkage of 0.50%); $P = 0.01$.

Until now, four different fully bioresorbable scaffolds have been tested in humans. The polymeric PLLA non-drug-eluting Igaki-Tamai device was the first fully bioresorbable scaffold used in humans. The IVUS analysis did not show bioresorption of the polymeric struts at 6 months and this absence of ultrasonic changes in struts was parallel to the absence of scaffold shrinkage. This device presented a target vessel revascularization of 6.7% at 6 months and a low rate of major cardiac events at 10 years.^{19,20} Conversely, the PROGRESS-AMS magnesium platform non-drug-eluting bioresorbable scaffold had a rapid resorption which was complete at 4-month follow-up. This swift resorption produced an important reduction of the lumen (60% of the late lumen loss) and a high incidence of restenosis (47.5% assessed by QCA).²¹ The REVA device is a poly (iodinated desaminotyrosyl-tyrosine ethyl ester) carbonate non-drug-eluting scaffold. The closed design and the lifecycle of the carbonate provide enough radial strength during the first 3 months following the implantation without appreciable shrinkage. However, focal mechanical failures driven by polymer embrittlement led to a high rate of TLR (66.7%) between 4- and 6-month follow-up.²² Finally, the IDEAL™ Poly (Anhydride Ester) Salicylic acid sirolimus-eluting device has been tested in only 11 patients.²³

The shrinkage phenomenon observed in the BVS 1.0 was linked to a significant increase of the ISA area with respect to baseline and with higher neointimal response with respect to the BVS 1.1. The increasing of the ISA area with the BVS 1.0 can be explained by the scaffold shrinkage itself. At baseline, 95% of the struts were apposed or aligned, while in the follow-up only 93% of the struts were apposed to the vessel wall. Moreover, less than 10% of the malapposed struts at baseline were resolved at follow-up.¹ The NIA measured in this population was significantly different between the two generations of BVS (1.44 mm² for the BVS 1.0 vs. 0.87 mm² for the BVS 1.1). In-scaffold area obstruction was also different between BVS 1.0 and 1.1 (23.6 vs. 12.3%, respectively). The significantly lower neointimal response of the BVS 1.1 with respect to the BVS 1.0 has no clear explanation. Both generations of BVS are built with the same polymer mass, strut thickness, drug, and coating elution and the same amount of drug. One hypothesis is that the loss in scaffold area leads to a decreased efficiency in drug transfer to the vessel wall and thus, a reduction in antiproliferative efficacy. Another hypothesis is that the more accelerated resorption/integration process of the BVS 1.0 compared with the BVS 1.1 could generate a larger neointimal response. Unfortunately, this cannot be assessed by OCT due to the lack of correlation between the different types of strut appearance and the histological findings based on animal studies.¹² An exploratory analysis of the patients treated with the BVS 1.0 in our study relating the NIT measured above the preserved box appearance ($0.15 \pm 0.04 \mu\text{m}$) with the NIT measured above the other types of strut appearance (0.18 ± 0.06) failed to be significant ($P = 0.27$). The same patients treated with the BVS 1.0

studied with OCT at 2 years showed few discernible struts with no measurable neointima. Nevertheless, the mean lumen area increased up to 19% from 6-month to 2-year follow-up.⁴ This fact may be a sign of vessel remodeling at the neointimal level but the low number of patients are a clear limitation to this conclusion. This hypothesis will be examined further when the strut appearance of patients treated with the BVS 1.1 changes in future scheduled imaging controls.

The OCT performance of the BVS 1.1 can be compared with some drug-eluting stents (DES). The NIT observed in the BVS 1.1 (0.08 mm) is similar to that seen with the sirolimus-DES (from 0.05 to 0.12 mm) at 6-month follow-up.^{24,25} Paclitaxel-DES and zotarolimus-DES showed a NIT of 0.20 and 0.33 mm, respectively.²⁴ The late shrinkage of metallic DES has not been yet explored with OCT. Using IVUS, the everolimus-DES showed a relative difference in mean stent area of 0.3% at 6-month follow-up.²⁶ This value is similar to the 1.0% found in our study with the BVS 1.1. Based on this information, the BVS 1.1 presents a similar profile as the metallic DES as assessed by OCT.

In summary, our study represents the first comparison of two generations of bioresorbable devices in terms of late shrinkage, neointimal response, and bioresorption state using the most sophisticated intravascular imaging technique (OCT) and the same methodology for both devices. The OCT findings at 6 months show the improvement of the new generation of BVS with respect to the previous generation. The slower bioresorption process of the BVS 1.1, compared with the BVS 1.0, is the most plausible explanation for the near elimination of the late shrinkage and for the higher inhibition of the neointimal response. Further investigations will be required to assess the preservation of these results after 6-month follow-up for the BVS 1.1. A more advanced bioresorption state can contribute to a very late shrinkage of the device or later neointimal responses.

Limitations

The result of the present analysis must be interpreted with caution as a major limitation of our study is the small number of patients who have been enrolled in a non-randomized comparison. Figure 5 shows that there is a homogeneous trend of higher late shrinkage and higher loss in minimal lumen area in the BVS 1.0 than in the BVS 1.1. The histogram distribution of the NIA in the two populations also shows this trend of higher neointimal growth in the BVS 1.0 than in the BVS 1.1 (data not shown). This trend, however, is not observed with the angiographic late lumen loss in which one outlier can be influencing the higher late lumen loss in the BVS 1.0. Moreover, two eligible patients imaged at baseline and scheduled for an invasive follow-up at 6 months did not undergo repeat invasive imaging. It is uncertain how this lack of serial imaging in those patients affects the global results of our study. Although the small number of patients, we have used the maximal number of 'historical' cases performed with the BVS 1.0 and imaged with the best available OCT system M2 at that time and compared with the same number of patients of the BVS 1.1 imaged with the best available system nowadays (OCT C7 system).

These differences in OCT systems are inherent to the fact that the ABSORB Cohort A trial was conducted in 2006, when a

balloon occlusive technique was needed due to the lower frame/rate and acquisition speed of the available systems at that time. One *in vitro* study showed less accuracy in the lumen area measurement with lower frame rate and acquisition speed than with higher frame/rate and speed.²⁷ An *in vivo* study, comparing the non-occlusive and the occlusive technique in the same non-scaffolded native coronary artery, showed systematically smaller mean and minimal lumen areas with the occlusive technique than with the non-occlusive technique (relative differences of 13.2 and 28.2%, respectively).²⁸ These differences were probably produced by the lack of physiological pressurization of the vessel during the occlusive technique imaging and/or the over-pressurization of the vessel during the contrast infusion of the non-occlusive technique.²⁸ These differences represent an important limitation of our study because the two different devices were imaged with different OCT techniques (occlusive for the BVS 1.0 and non-occlusive for the BVS 1.1). However, in our study, the baseline and follow-up acquisition were performed using the same imaging technique in each cohort of patients and also, the analysed region is scaffolded by the BVS. The scaffolded region is probably less susceptible to changes in volumetric parameters according to the intravascular pressure. Unfortunately, there is no current information comparing the changes in lumen areas within the scaffolded regions with the two different OCT techniques.

The method of analysis used in our study is slightly different from the current method of OCT measurement of polymeric scaffold. The strut appearance of the BVS 1.0 at 6 months (and probably the appearance of the BVS 1.1 in later controls) does not permit the delineation of the strut contour at the front or backside of the strut. Using the central part of the strut as landmark for measurement is the most reliable method to assess the scaffold area. However, it must be recognized that the neointima area as such determined is an arbitrary entity resulting from the difference between the luminal area and the scaffold area, and does not depict accurately the neointimal tissue that has grown between, on the top and behind the struts either biologically altered in the case of the BVS 1.0 or almost intact in the case of the BVS 1.1.

Finally, the differences in device lengths in the two groups may be favourable to the BVS 1.1 due to a better anchoring in the healthy part of the vessel that can be subjected to a less constrictive modelling of the vessel.

Conclusion

The two generations of the everolimus-eluting bioresorbable vascular scaffold have different OCT findings at 6-month follow-up. The BVS 1.1 has less late shrinkage and less neointimal growth at 6-month follow-up compared with the BVS 1.0. Consequently, less angiographic late loss and less OCT and IVUS luminal losses were observed with the BVS 1.1. A difference in polymer degradation leading to changes in microstructure and reflectivity is the most plausible explanation for this finding.

Conflict of interest: S.W. is a consultant for Abbott, Biosensors, Boston Scientific, Cordis and Medtronic.

Funding

This work was supported by Abbott.

References

- Ormiston JA, Serruys PW, Regar E, Dudek D, Thuesen L, Webster MW, Onuma Y, Garcia-Garcia HM, McGreevy R, Veldhof S. A bioabsorbable everolimus-eluting coronary stent system for patients with single de-novo coronary artery lesions (ABSORB): a prospective open-label trial. *Lancet* 2008;**371**: 899–907.
- Painter JA, Mintz GS, Wong SC, Popma JJ, Pichard AD, Kent KM, Satler LF, Leon MB. Serial intravascular ultrasound studies fail to show evidence of chronic Palmaz-Schatz stent recoil. *Am J Cardiol* 1995;**75**:398–400.
- Okamura T, Garg S, Gutierrez-Chico JL, Shin ES, Onuma Y, Garcia-Garcia HM, Rapoza R, Sudhir K, Regar E, Serruys PW. In vivo evaluation of stent strut distribution patterns in the bioabsorbable everolimus-eluting device: an OCT ad hoc analysis of the revision 1.0 and revision 1.1 stent design in the ABSORB clinical trial. *EuroIntervention* 2010;**5**:932–938.
- Serruys PW, Ormiston JA, Onuma Y, Regar E, Gonzalo N, Garcia-Garcia HM, Nieman K, Bruining N, Dorange C, Miquel-Hebert K, Veldhof S, Webster M, Thuesen L, Dudek D. A bioabsorbable everolimus-eluting coronary stent system (ABSORB): 2-year outcomes and results from multiple imaging methods. *Lancet* 2009;**373**:897–910.
- Kawase Y, Hoshino K, Yoneyama R, McGregor J, Hajjar RJ, Jang IK, Hayase M. In vivo volumetric analysis of coronary stent using optical coherence tomography with a novel balloon occlusion-flushing catheter: a comparison with intravascular ultrasound. *Ultrasound Med Biol* 2005;**31**:1343–1349.
- Suzuki Y, Ikano F, Koizumi T, Tio F, Yeung AC, Yock PG, Fitzgerald PJ, Fearon WF. In vivo comparison between optical coherence tomography and intravascular ultrasound for detecting small degrees of in-stent neointima after stent implantation. *JACC Cardiovasc Interv* 2008;**1**:168–173.
- Onuma Y, Serruys PW, Ormiston JA, Regar E, Webster M, Thuesen L, Dudek D, Veldhof S, Rapoza R. Three-year results of clinical follow-up after a bioresorbable everolimus-eluting scaffold in patients with de novo coronary artery disease: the ABSORB trial. *EuroInterv* 2010;**6**:447–453.
- Reiber JH, Serruys PW, Kooijman CJ, Wjns W, Slager CJ, Gerbrands JJ, Schuurbers JC, den Boer A, Hugenholz PG. Assessment of short-, medium-, and long-term variations in arterial dimensions from computer-assisted quantitation of coronary cineangiograms. *Circulation* 1985;**71**:280–288.
- Takarada S, Imanishi T, Liu Y, Ikejima H, Tsujioka H, Kuroi A, Ishibashi K, Komukai K, Tanimoto T, Ino Y, Kitabata H, Kubo T, Nakamura N, Hirata K, Tanaka A, Mizukoshi M, Akasaka T. Advantage of next-generation frequency-domain optical coherence tomography compared with conventional time-domain system in the assessment of coronary lesion. *Catheter Cardiovasc Interv* 2009;**75**: 202–206.
- Tanimoto S, Serruys PW, Thuesen L, Dudek D, de Bruyne B, Chevalier B, Ormiston JA. Comparison of in vivo acute stent recoil between the bioabsorbable everolimus-eluting coronary stent and the everolimus-eluting cobalt chromium coronary stent: insights from the ABSORB and SPIRIT trials. *Catheter Cardiovasc Interv* 2007;**70**:515–523.
- Tanimoto S, Bruining N, van Domburg RT, Rotger D, Radeva P, Ligthart JM, Serruys PW. Late stent recoil of the bioabsorbable everolimus-eluting coronary stent and its relationship with plaque morphology. *J Am Coll Cardiol* 2008;**52**: 1616–1620.
- Onuma Y, Serruys P, Perkins L, Okamura T, Gonzalo N, Garcia-Garcia HM, Regar E, Kamberi M, Powers JC, Rapoza R, van Beusekom H, van der Giessen W, Virmani R. Intracoronary optical coherence tomography (OCT) and histology at 1 month, at 2, 3 and 4 years after implantation of everolimus-eluting bioresorbable vascular scaffolds in a porcine coronary artery model: An attempt to decipher the human OCT images in the ABSORB trial. *Circulation* 2010; Published online ahead of print 25 October 2010.
- von Birgelen C, de Vrey EA, Mintz GS, Nicosia A, Bruining N, Li W, Slager CJ, Roelandt JR, Serruys PW, de Feyter PJ. ECG-gated three-dimensional intravascular ultrasound: feasibility and reproducibility of the automated analysis of coronary lumen and atherosclerotic plaque dimensions in humans. *Circulation* 1997;**96**: 2944–2952.
- Aalst M, Eenink M, Kruff M, van Tuil R. ABC's of bioabsorption: application of lactide based polymers in fully resorbable cardiovascular stents. *EuroIntervention* 2009;**5**(Suppl. F):F23–F27.
- Mintz GS, Popma JJ, Pichard AD, Kent KM, Satler LF, Wong C, Hong MK, Kovach JA, Leon MB. Arterial remodeling after coronary angioplasty: a serial intravascular ultrasound study. *Circulation* 1996;**94**:35–43.
- Hoffmann R, Mintz GS, Dussallant GR, Popma JJ, Pichard AD, Satler LF, Kent KM, Griffin J, Leon MB. Patterns and mechanisms of in-stent restenosis. A serial intravascular ultrasound study. *Circulation* 1996;**94**:1247–1254.

17. Nakamura M, Yock PG, Bonneau HN, Kitamura K, Aizawa T, Tamai H, Fitzgerald PJ, Honda Y. Impact of peri-stent remodeling on restenosis: a volumetric intravascular ultrasound study. *Circulation* 2001;**103**:2130–2132.
18. Serruys PW, Luijten HE, Beatt KJ, Geuskens R, de Feyter PJ, van den Brand M, Reiber JH, ten Katen HJ, van Es GA, Hugenholz PG. Incidence of restenosis after successful coronary angioplasty: a time-related phenomenon. A quantitative angiographic study in 342 consecutive patients at 1, 2, 3, and 4 months. *Circulation* 1988;**77**:361–371.
19. Tamai H, Igaki K, Kyo E, Kosuga K, Kawashima A, Matsui S, Komori H, Tsuji T, Motohara S, Uehata H. Initial and 6-month results of biodegradable poly-L-lactic acid coronary stents in humans. *Circulation* 2000;**102**:399–404.
20. Nishio S, Kosuga K, Okada M, Harita T, Ishii M, Kawata Y, Takeda S, Takeuchi Y, Hata T, Ikeguchi S. Long term (> 10 years) clinical outcomes of the first-in-man biodegradable poly-L-lactic acid coronary stents. Oral presentation. Paris: EuroPCR; 2010.
21. Erbel R, Di Mario C, Bartunek J, Bonnier J, de Bruyne B, Eberli FR, Erne P, Haude M, Heublein B, Herrigan M, Ilesley C, Bose D, Koolen J, Luscher TF, Weissman N, Waksman R. Temporary scaffolding of coronary arteries with bioabsorbable magnesium stents: a prospective, non-randomised multicentre trial. *Lancet* 2007;**369**:1869–1875.
22. Pollman M. Engineering a bioresorbable stent: the REVA programme update. *Euro-Intervention* 2009;**5**(Suppl. F):F54–F57.
23. Jabara R. *Polyanhydride Basic on Salicylic Acid and Adipic Acid Anhydride*. Barcelona: EuroPCR; 2009.
24. Guagliumi G, Musumeci G, Sirbu V, Bezerra HG, Suzuki N, Fiocca L, Matiashvili A, Lortkipanidze N, Trivisonno A, Valsecchi O, Biondi-Zoccai G, Costa MA. Optical coherence tomography assessment of in vivo vascular response after implantation of overlapping bare-metal and drug-eluting stents. *JACC Cardiovasc Interv* 2010;**3**: 531–539.
25. Matsumoto D, Shite J, Shinke T, Otake H, Tanino Y, Ogasawara D, Sawada T, Paredes OL, Hirata K, Yokoyama M. Neointimal coverage of sirolimus-eluting stents at 6-month follow-up: evaluated by optical coherence tomography. *Eur Heart J* 2007;**28**:961–967.
26. Serruys PW, Ong AT, Piek JJ, Neumann FJ, van der Giessen WJ, Wiemer M, Zeiher A, Grube E, Haase J, Thuesen L, Hamm C, Otto-Terlouw PC. A randomized comparison of a durable polymer Everolimus-eluting stent with a bare metal coronary stent: The SPIRIT first trial. *EuroIntervention* 2005;**1**:58–65.
27. Sawada T, Shite J, Negi N, Shinke T, Tanino Y, Ogasawara D, Kawamori H, Kato H, Miyoshi N, Yoshino N, Kozuki A, Koto M, Hirata K. Factors that influence measurements and accurate evaluation of stent apposition by optical coherence tomography. Assessment using a phantom model. *Circ J* 2009;**73**: 1841–1847.
28. Gonzalo N, Serruys PW, Garcia-Garcia HM, van Soest G, Okamura T, Ligthart J, Knaapen M, Verheyde S, Bruijning N, Regar E. Quantitative ex vivo and in vivo comparison of lumen dimensions measured by optical coherence tomography and intravascular ultrasound in human coronary arteries. *Rev Esp Cardiol* 2009;**62**: 615–624.

5.3

Agreement and reproducibility of intravascular ultrasound and optical coherence tomography for the analysis of the bioresorbable vascular scaffold.

Josep Gómez-Lara, MD¹; Salvatore Brugaletta, MD¹; Roberto Diletti, MD¹; Bill D. Gogas, MD¹; Vasim Farooq, MBChB MRCP¹; Maria Radu, MD¹; Yoshinobu Onuma, MD¹; Pierre Gobbens, BSc²; Gerrit Anne Van Es, PhD²; Karine Miquel-Hebert, BSc³; Susan Veldhof, RN³; Hector M. García-García, MD PhD^{1,2}; Patrick W. Serruys, MD, PhD¹.

¹ ThoraxCenter, Erasmus Medical Center, Rotterdam, the Netherlands.

² Cardialysis, Rotterdam, the Netherlands

³ Abbott Vascular, Diegem, Belgium

Catheter Cardiovasc Intervention 2012, Epub ahead of print.

ABSTRACT

Objective: To report the agreement between IVUS and OCT in assessing the BVS structures and their respective reproducibility.

Background: Bioresorbable Vascular Scaffolds (BVS) are composed of an erodible polymer. Ultrasound and light signals backscattered from polymeric material differs from metallic stents using intravascular ultrasound (IVUS) and optical coherence tomography (OCT).

Methods: Forty-five patients included in the ABSORB study were treated with a 3.0x18 mm BVS and imaged with IVUS 20 MHz and OCT post-implantation. Qualitative (ISA, side-branch struts, protrusion and dissections) and quantitative (number of struts, lumen and scaffold area) measurements were assessed by two investigators. The agreement and the inter- and intra-observer reproducibility were investigated using the kappa (κ) and the inter-class correlation coefficient (ICC).

Results: IVUS and OCT agreement was predominantly poor at a lesion, frame and strut level analysis (κ and ICC <0.4) for qualitative measurements. IVUS demonstrated a reduced ability to detect cross-sections with ISA (4.5% vs. 20.6%), side-branch (SB) struts (6.3% vs. 7.8%), protrusions (3.2% vs. 9.6%) and dissections (0.2% vs. 9.0%) compared to OCT. IVUS reproducibility was poor-moderate (κ and ICC <0.6) except for ISA and SB-struts (κ and ICC between 0.2 and 0.75). OCT showed an excellent reproducibility (κ and ICC >0.75) except for the assessment of tissue protrusion (κ and ICC between 0.47 and 0.94). IVUS reproducibility was poor-moderate (ICC \leq 0.5) in assessing the number of struts but excellent with OCT (ICC >0.85). The reproducibility to assess lumen and scaffold areas were excellent using both techniques (ICC >0.85).

Conclusions: IVUS has a poor capacity to detect qualitative findings post-BVS implantation and its reproducibility is low compared to OCT. IVUS should be limited to assess lumen and scaffold areas.

INTRODUCTION

Bioresorbable Vascular Scaffolds (BVS) are a new generation of intravascular devices constructed of polymeric material. The ultrasonic and light wave beams from the intravascular ultrasound (IVUS) and optical coherence tomography (OCT) catheters are backscattered in different ways from the polymeric structures as compared to metallic structures. Consequently, IVUS and OCT render the BVS structures differently compared to metallic stents (1,2). IVUS imaging, with a 20 MHz catheter, renders the polymeric struts as hyper-refractive boxes with an important echogenic blooming effect that confers a

double strut appearance. The polymeric struts have an echogenic intensity similar to calcium tissue, but without acoustic shadowing behind the struts (**Figure 1**). OCT shows the polymeric struts as a black central core surrounded by a light-scattering frame. The four sides of the polymeric struts are clearly visible without the typical shadowing observed behind metallic structures (**Figure 1**).

The IVUS and OCT agreement and their respective inter- and intra-observer reproducibility to assess qualitative and quantitative findings immediately after BVS implantation remain unknown. The aim of our study is to report the agreement of IVUS and OCT in assessing qualitative and quantitative

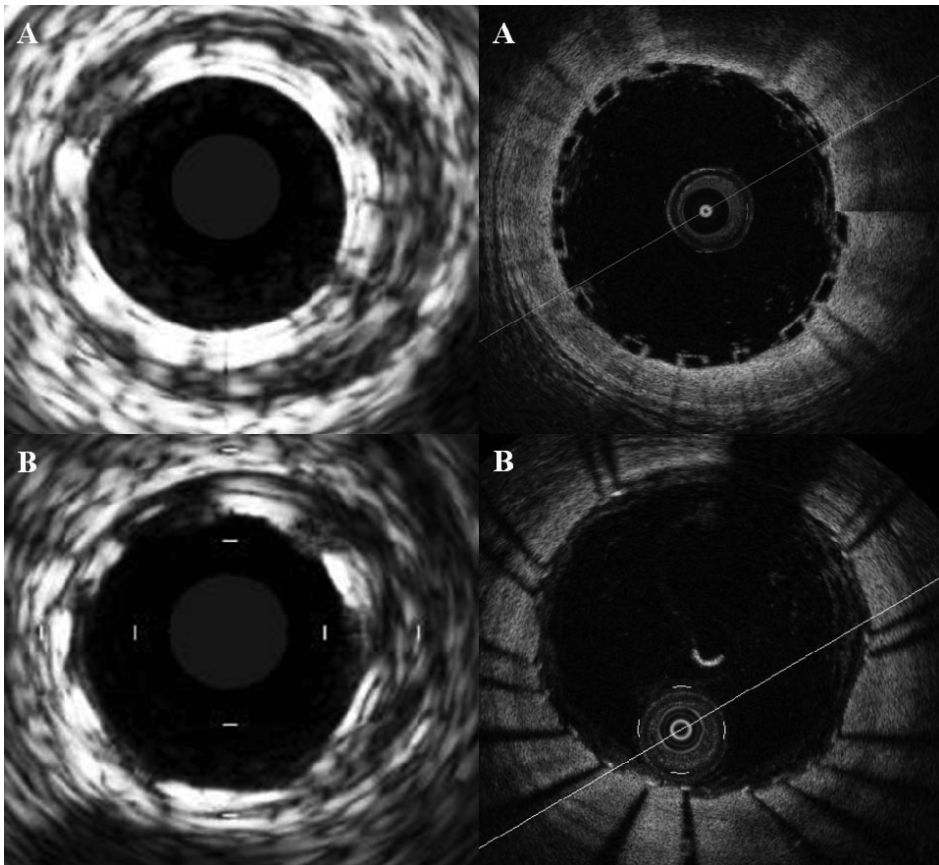


Figure 1. IVUS and OCT imaging of the bioresorbable scaffolds and metallic stents
IVUS and OCT imaging of a bioresorbable vascular scaffold (A) and a metallic stent (B)

BVS findings post-implantation and to assess their inter- and intra-observer reproducibility.

MATERIAL AND METHODS

Population

The ABSORB Cohort B trial is a non-randomized, multicenter, single arm, efficacy-safety study. The study design has been previously reported (3). In brief, patients were eligible when aged 18 years or older and were diagnosed with stable, unstable or silent ischemia. Patients with a stenosis of the left main or ostial right coronary artery (RCA), presence of angiographic intracoronary thrombus, heavy calcification, excessive tortuosity and with lesions involving a side branch >2 mm were excluded. All patients were treated with a single size 3.0x18 mm BVS.

At baseline, IVUS 20 MHz imaging was performed in all patients. OCT imaging was performed in selected centers as an optional additional investigation. Both imaging techniques were performed after the last dilatation of the BVS. The present study included only those patients imaged simultaneously with IVUS and OCT immediately after BVS deployment.

Study Device

The BVS balloon expandable device (Abbott Vascular, Santa Clara, CA, US) consists of a polymer backbone of Poly-L lactide (PLLA) coated with a thin layer of a 1:1 mixture of Poly-D, L-lactide (PDLLA) polymer, and the anti-proliferative drug everolimus to form an amorphous drug eluting coating matrix containing 100 micrograms of everolimus/cm² of scaffold. The strut thickness is 150 microns. The implant is radiolucent, but has two platinum markers at each end that allow easy visualization on angiography and other imaging modalities.

IVUS 20 MHz acquisition

IVUS acquisition was performed with the Eagle Eye 20 MHz catheter (Volcano Corporation, Rancho Cordova, CA, USA). The acquisition was performed according to standard procedures (4). After intracoronary nitroglycerin injection, the catheter probe was advanced distally to the lesion. Using an automated pullback device, the transducer was withdrawn at a continuous speed of 0.5 mm/s. The image data was stored on DVD for off-line analysis.

OCT ACQUISITION

OCT imaging was performed using two different OCT systems (M3 Time-Domain System and C7XR Fourier-Domain System; LightLab Imaging, Westford, MA, USA). The M3 OCT system uses a standard intracoronary guide wire to cross the target lesion. This conventional wire was subsequently exchanged for the Light Lab Image wire using a single or double lumen intracoronary catheter. Pullback was performed during continuous injection of contrast medium (1-3 mL/s, Iodixanol 370, Visipaque, GE Health Care, Cork, Ireland) through the guide catheter with an injection pump. The automated pullback was performed at 3 mm/second with a frame rate of 20 images/second.

The C7XR system uses a conventional wire to cross the segment of interest. The OCT imaging catheter (RX ImageWire II; LightLab Imaging, Westford, MA, USA) was then advanced distally to the treated region. The pullback was performed during a continuous injection of 3 ml/second of contrast medium (Iodixanol 370, Visipaque, GE Health Care, Cork, Ireland) injected at a maximum pressure of 300 psi through the guiding catheter with an injection pump. In these cases, the automated pullback rate was 20 mm/second and the frame rate was 100 images/second.

IVUS and OCT definitions and analysis

IVUS and OCT analyses were performed by two experienced analysts. Taking into account the acquisition frame rate and the pullback speed, both IVUS and OCT were analyzed at intervals of 1 mm within the scaffold and 5 mm proximal and distal to the scaffold edges whenever possible. The first cross-section of the corresponding pullbacks with struts observed in the 4 quadrants of the lumen perimeter was used as a landmark to establish the scaffold length. Two analysts investigated the same cross-sections and one investigator repeated the same measurements one month later. IVUS analysis was performed using the Q-IVUS 2.0 software analysis (Medis, Leiden, The Netherlands). OCT analysis was performed with the proprietary software for offline analysis (LightLab Imaging, Westford, MA, USA). The selected cross-sections were investigated to assess:

Number of struts: Using IVUS, the polymeric struts were defined as independent, hyper-echogenic and double-box shapes without echogenic shadow behind. Using OCT, the polymeric struts were assessed as box-shape light-scattering frames delimiting a black central core (**Figure 1**) (1).

Number of malapposed struts: ISA was defined when the abluminal side of the polymeric strut was clearly separated from the vessel wall in the absence of a side branch (4) (**Figure 2**).

Number of side-branch struts: Side-branches were assessed longitudinally and in the immediately proximal and distal 2D cross-sections. Whenever the polymeric struts were not in contact with the vessel wall at the site of the take-off of the side-branch, they were classified as side-branch struts (**Figure 2**).

Tissue protrusion: Tissue protrusion was defined as when convex shaped tissue protruded between the endoluminal sides of adjacent struts and extended within the lumen as a circular arc connecting the adjacent struts (5,6) (**Figure 2**).

In-BVS, proximal and distal dissections: Dissections were defined when a disruption of the luminal vessel surface with an overhanging flap within the lumen was observed within the BVS segment or at 5 mm proximal or distal to the scaffold edges (6) (**Figure 2**).

Lumen and scaffold area. Using IVUS, the lumen area was drawn following the endoluminal vessel wall contour. IVUS-derived scaffold area was drawn following the endoluminal side of the polymeric struts. Using OCT, in contrast, the lumen area was

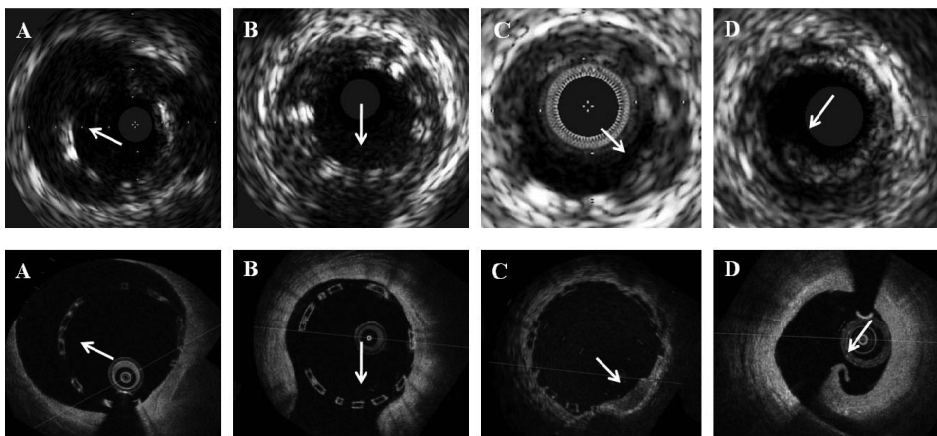


Figure 2. IVUS and OCT assessment of qualitative findings

Matched images between IVUS and OCT of incomplete strut/scaffold apposition (A), side-branch struts (B), tissue protrusion (C) and edge dissection (D)

defined behind the polymeric struts following the endoluminal vessel contour and the scaffold area was drawn following the abluminal side of the polymeric struts.

STATISTICAL ANALYSIS

Discrete variables are presented as counts and percentages. Continuous variables are presented as means \pm (SD) standard deviation. Due to the clustered nature of the IVUS and OCT data at different levels of dependence (strut, cross-sections, lesions and patients) and the lack of correlation between IVUS and OCT cross-sections, all qualitative measurements have been adjusted at a lesion level dividing the number of observations by the total amount of frames/struts in each lesion. Quantitative measurements to assess the inter- and intra-observer reproducibility are presented at cross-section level analysis.

The IVUS and OCT agreement at lesion level analysis were estimated by the Cohen's κ (kappa) test for concordance (7). According to previous publications: <0 indicates poor agreement, 0 to 0.20 indicates slight agreement, 0.21 to 0.40 indicates fair agreement, 0.41 to 0.60 indicates moderate agreement, 0.61 to 0.80 indicates good agreement, and 0.81 to 1.0 indicates excellent agreement (8). Due to the higher reproducibility and the higher resolution of OCT when compared to IVUS, we have estimated the sensitivity, specificity and global efficiency of IVUS 20 MHz with respect to the OCT (as reference). The IVUS and OCT agreement of qualitative measurements at frame and strut level were estimated with the inter-class correlation coefficient (ICC) for concordance (ICCc) and absolute agreement (ICCa). An ICC <0.4 indicates bad agreement, an ICC between 0.4 and 0.75 indicates moderate agreement and ICC values >0.75 indicates excellent agreement (9).

The inter- and intra-observer reproducibility of qualitative measurements was assessed using the kappa value and the inter-class correlation coefficient as previously explained. The absolute differences between the percentages of qualitative findings (at lesion level) between observers/ observations were estimated for each variable. Bland–Altman plots were drawn for the percentage of malapposed struts and SB-struts at lesion level analysis (10). Inter- and intra-observer reproducibility of IVUS and OCT to assess quantitative measurements (number of struts, lumen and scaffold area) were performed in 150 randomly selected cross-sections in 15 patients. Bland–Altman plots were drawn for these quantitative parameters at frame level analysis. Due to the lack of matching images between IVUS and OCT, the agreement of both techniques to assess the number of struts and lumen and scaffold areas were not performed.

RESULTS

Population characteristics

The ABSORB Cohort B trial included 102 lesions in 101 patients. A total of 46 lesions in 45 patients were imaged with both IVUS 20 MHz and OCT immediately after the BVS implantation. A total of 892 and 888 cross-sections and 6313 and 6452 struts were analyzed with IVUS 20 MHz and OCT respectively.

The baseline clinical and angiographic characteristics are shown in **Table 1**. In general, patients were predominantly males (71%), had hypercholesterolemia (87%) and were treated due to stable angina (87%).

OCT and IVUS agreement of qualitative measurements

Agreement of qualitative measurements between IVUS and OCT at lesion level analysis are shown in **Table 2**. The agreement between IVUS and OCT

Table 1. Baseline clinical and angiographic characteristics (n=45 patients)

Males	32 (71.1)
Age (years)	61.5 ± 10.3
Hypertension	28 (62.2)
Hypercholesterolemia	39 (86.7)
Diabetes mellitus	4 (8.9)
Smokers	11 (24.4)
Previous myocardial infarction	13 (28.9)
Previous coronary revascularization	9 (20.0)
Clinical indication:	
Stable angina	39 (86.7)
Acute coronary syndrome	6 (13.3)
Culprit vessel:	
Left anterior descending	24 (53.3)
Left circumflex	9 (20.0)
Right coronary artery	12 (26.7)
Number of vessels disease:	
One	39 (86.7)
Two	6 (13.3)
Three	0

Table 2. Qualitative agreement between OCT and IVUS 20 MHz (lesion level analysis)

n=46 lesions		OCT			Kappa	Accuracy of IVUS with respect to OCT (%)	
		No	Yes	Total			
IVUS 20 MHz	Proximal dissection	No	30	9	39	NA	Se = 0
		Yes	0	0	0		Sp = 100
		Total	30	9	39		Eff = 77
	Distal dissection	No	28	8	36	0.16	Se = 11
		Yes	0	1	1		Sp = 100
		Total	28	9	37		Eff = 78
	Dissection within BVS	No	20	25	45	0.03	Se = 4
		Yes	0	1	1		Sp = 100
		Total	20	26	46		Eff = 46
	ISA	No	6	21	27	0.15	Se = 46
		Yes	1	18	19		Sp = 86
		Total	7	39	46		Eff = 52
	SB struts	No	10	13	23	0.26	Se = 59
		Yes	4	19	23		Sp = 71
		Total	14	32	46		Eff = 63
Tissue protrusion	No	17	22	39	0.00	Se = 15	
	Yes	3	4	7		Sp = 85	
	Total	20	26	46		Eff = 46	

ISA= incomplete scaffold/strut apposition; SB= side-branch; NA= not applicable; Se= sensitivity; Sp= specificity; Eff= efficiency

to assess scaffolds with at least one cross-section with ISA, tissue protrusion and dissections were slight. Assessment of at least one cross-section with SB struts showed fair agreement between both techniques. Sensitivity and global efficiency of IVUS analysis were extremely low in all parameters compared to OCT (as reference), but IVUS specificity was moderate to high.

Qualitative agreement of both IVUS and OCT at frame and strut level analysis are shown in **Table 3**. By OCT, a higher number of cross-sections with ISA, SB-struts, tissue protrusions and dissections were detected compared to IVUS. Moreover, the agreement of both techniques to assess these parameters at a frame level analysis was poor. At a strut level analysis, the agreement of IVUS and OCT was also poor in detecting ISA and SB-struts.

IVUS reproducibility of qualitative measurements

The inter- and intra-observer reproducibility of IVUS 20 MHz to assess qualitative findings at a lesion

level analysis is shown in **Table 4**. Inter-observer reproducibility to assess tissue protrusion and dissections within the scaffold length was poor to slight. Distal dissections demonstrated a fair reproducibility and ISA and SB-struts had moderate agreement. Intra-observer reproducibility was fair for tissue protrusion and dissections within the scaffold length. Detection of scaffolds with ISA or SB-struts had moderate and good agreement. Intra-observer reproducibility of distal edge dissections was excellent.

Inter- and intra-observer reproducibility of IVUS 20 MHz at frame and strut level analysis are shown in **Tables 5 and 6**. Inter- and intra-observer reproducibility of IVUS 20 MHz to assess cross-sections with tissue protrusion and dissection within the BVS were bad. Inter- and intra-observer reproducibility to assess cross-sections with ISA or SB-struts was poor to moderate. At strut level analysis, the inter- and intra-observer reproducibility of IVUS 20 MHz was moderate to excellent. The Bland – Altman plots of IVUS inter- and intra- observer reproducibility to

Table 3. Inter-observer agreement between OCT and IVUS 20 MHz (frame and strut level analysis)

	IVUS	OCT	Absolute difference, % (CI 95%)	ICCc (CI 95%)	ICCa (CI 95%)	
Frame level	Frames with ISA, n	37	181			
	% Frames with ISA per lesion, mean (SD)	4.5 (7.7)	20.6 (20.9)	-16.05 (-21.72 to -10.39)	0.27 (-0.02 to 0.52)	0.18 (-0.07 to 0.42)
	Frames with SB struts, n	57	69			
	% Frames with SB struts per lesion, mean (SD)	6.3 (8.3)	7.8 (6.4)	-1.48 (-4.15 to 1.19)	0.26 (-0.03 to 0.51)	0.26 (-0.02 to 0.51)
	Frames with tissue protrusion, n	10	69			
% Frames with tissue protrusion per lesion, mean (SD)	1.2 (3.2)	7.7 (9.6)	-6.47 (-9.29 to -3.66)	0.12 (-0.17 to 0.39)	0.09 (-0.12 to 0.31)	
Strut level	Frames with Dissection (within BVS), n	1	79			
	% Frames with dissection per lesion, mean (SD)	0.2 (1.1)	9.0 (12.4)	-8.87 (-12.44 to -5.29)	0.06 (-0.23 to 0.34)	0.04 (-0.14 to 0.25)
	Struts with ISA, n	74	348			
	% ISA struts per lesion, mean (SD)	1.3 (4.0)	5.5 (8.1)	-4.23 (-6.35 to -2.10)	0.37 (0.09 to 0.59)	0.31 (0.02 to 0.54)
	Struts at SB, n	84	77			
% SB struts per lesion, mean (SD)	1.3 (1.9)	1.2 (1.2)	0.12 (-0.49 to 0.73)	0.18 (-0.11 to 0.45)	0.19 (-0.11 to 0.45)	

ISA= incomplete scaffold/strut apposition; SB= side-branch; ICC= inter-class correlation coefficient; CI= confidence interval.

Table 4. Inter and intra-observer reproducibility of IVUS 20 MHz and OCT (lesion level)

n=46 lesions			Observer A			Observer B (2nd)						
			No	Yes	Total	Inter-observer agreement (Kappa)	No	Yes	Total	Intra-observer agreement (Kappa)		
IVUS 20 MHz	Observer B (1st)	Proximal dissection	No	41	2	43	NA	42	1	43	NA	
			Yes	0	0	0		0	0	0		
			Total	41	2	43		42	1	43		
		Distal dissection	No	35	3	38	0.37	38	0	38	1.00	
			Yes	0	1	1		0	1	1		
			Total	35	4	39		38	1	39		
		Dissection within BVS	No	38	7	45	-0.04	42	3	45	0.38	
			Yes	1	0	1		0	1	1		
			Total	39	7	46		42	4	46		
	ISA	No	26	1	27	0.47	20	7	27	0.47		
		Yes	10	9	19		5	14	19			
		Total	36	10	46		25	21	46			
	SB struts	No	20	3	23	0.48	20	3	23	0.61		
		Yes	9	14	23		6	17	23			
		Total	29	17	46		26	20	46			
	Tissue protrusion	No	29	5	34	0.02	26	2	28	0.23		
		Yes	10	2	12		13	5	18			
		Total	39	7	46		38	7	46			
	OCT	Observer 1 (observation 1)	Proximal dissection	No	32	0	32	1.00	32	0	32	1.00
				Yes	0	9	9		0	9	9	
				Total	32	9	41		32	9	41	
Distal dissection			No	30	1	31	0.94	31	0	31	1.00	
			Yes	0	10	10		0	10	10		
			Total	30	11	41		31	10	41		
Dissection within BVS			No	16	4	20	0.76	19	1	20	0.96	
			Yes	1	25	26		0	26	26		
			Total	17	29	46		19	27	46		
ISA		No	7	0	7	0.85	7	0	7	1.00		
		Yes	2	37	39		0	39	39			
		Total	7	37	46		7	39	46			
SB struts		No	12	2	14	0.89	14	0	14	1.00		
		Yes	0	32	32		0	32	32			
		Total	12	34	46		14	32	46			
Tissue protrusion		No	16	4	20	0.73	18	2	20	0.91		
		Yes	2	24	26		0	26	26			
		Total	18	28	46		18	28	46			

ISA= incomplete scaffold/strut apposition; SB= side-branch; NA= not applicable

Table 5. Inter-observer reproducibility of IVUS 20 MHz and OCT (frame and strut level analysis)

		Observer A	Observer B	Margin of error of the 95% CI of the absolute difference (%)	ICC (CI 95%)	ICCa (CI 95%)	
IVUS 20 MHz	Frame level (892 cross-sections)	Frames with ISA, n	37	45			
		% Frames with ISA, mean (SD)	4.5 (7.7)	5.2 (1.5)	7.32	0.21 (-0.08 to 0.47)	0.22 (-0.08 to 0.48)
		Frames with SB struts, n	57	43			
		% Frames with SB struts, mean (SD)	6.3 (8.3)	4.9 (7.8)	4.68	0.53 (0.28 to 0.71)	0.52 (0.28 to 0.70)
	Frames with protrusion, n	10	54				
	% Frames with tissue protrusion, mean (SD)	1.2 (3.2)	6.2 (10.9)	6.28	-0.05 (-0.33 to 0.25)	-0.05 (-0.33 to 0.24)	
	Frames with dissection (within BVS), n	1	7				
	% Frames with dissection, mean (SD)	0.2 (1.1)	0.7 (1.7)	1.24	0.15 (-0.14 to 0.43)	0.13 (-0.12 to 0.38)	
	Strut level (6313 struts)	Struts with ISA, n	74	65			
		% ISA struts, mean (SD)	1.3 (4.0)	1.0 (2.6)	1.50	0.72 (0.54 to 0.83)	0.84 (0.71 to 0.91)
	Struts at SB, n	84	85				
	% SB struts, mean (SD)	1.3 (1.9)	1.2 (2.2)	1.28	0.44 (0.18 to 0.65)	0.45 (0.18 to 0.65)	
OCT	Frame level (888 cross-sections)	Frames with ISA, n	181	175			
		% Frames with ISA, mean (SD)	20.6 (20.9)	19.8 (20.4)	4.57	0.93 (0.88 to 0.96)	0.93 (0.88 to 0.96)
		Frames with SB struts, n	69	67			
		% Frames with SB struts, mean (SD)	7.8 (6.4)	7.6 (6.0)	1.96	0.86 (0.76 to 0.92)	0.86 (0.76 to 0.92)
	Frames with tissue, n	69	87				
	% Frames with tissue protrusion, mean (SD)	7.7 (9.6)	9.8 (10.8)	6.21	0.48 (0.22 to 0.67)	0.47 (0.22 to 0.67)	
	Frames with dissection (within BVS), n	79	109				
	% Frames with dissection, mean (SD)	9.0 (12.4)	12.4 (13.9)	4.16	0.86 (0.76 to 0.92)	0.83 (0.67 to 0.91)	
	Strut level (6452 struts)	Struts with ISA, n	348	315			
		% ISA struts, mean (SD)	5.5 (8.1)	5.0 (7.3)	1.15	0.99 (0.97 to 0.99)	0.98 (0.97 to 0.99)
	Struts at SB, n	77	82				
	% SB struts, mean (SD)	1.2 (1.2)	1.3 (1.1)	0.15	0.78 (0.63 to 0.87)	0.78 (0.63 to 0.87)	

ISA= incomplete scaffold/strut apposition; SB= side-branch; ICC= inter-class correlation coefficient; CI= confidence interval.

Table 6. Intra-observer reproducibility of IVUS 20 MHz and OCT (frame and strut level analysis)

		Observation 1	Observation 2	Margin of error of the 95% CI of the absolute difference (%)	ICc (CI 95%)	ICCa (CI 95%)	
IVUS 20 MHz	Frame level (892 cross-sections)	Frames with ISA, n	37	61			
		<i>% Frames with ISA, mean (SD)</i>	4.5 (7.7)	7.1 (11.1)	5.13	0.59 (0.37 to 0.75)	0.58 (0.35 to 0.74)
		Frames with SB struts, n	57	36			
		<i>% Frames with SB struts, mean (SD)</i>	6.3 (8.3)	4.0 (5.4)	3.17	0.71 (0.53 to 0.83)	0.68 (0.46 to 0.82)
	Strut level (6313 struts)	Frames with protrusion, n	10	19			
		<i>% Frames with tissue protrusion, mean (SD)</i>	1.2 (3.2)	2.2 (4.2)	3.19	0.15 (-0.14 to 0.43)	0.13 (-0.12 to 0.38)
		Frames with dissection (within BVS), n	1	6			
		<i>% Frames with dissection, mean (SD)</i>	0.2 (1.1)	0.66 (2.3)	3.17	-0.05 (-0.33 to 0.24)	-0.05 (-0.33 to 0.24)
Strut level (6313 struts)	Struts with ISA, n	74	128				
	<i>% ISA struts, mean (SD)</i>	1.3 (4.0)	2.2 (4.8)	1.71	0.79 (0.65 to 0.88)	0.77 (0.62 to 0.87)	
Strut level (6313 struts)	Struts at SB, n	84	47				
	<i>% SB struts, mean (SD)</i>	1.3 (1.9)	0.70 (1.1)	0.72	0.69 (0.50 to .82)	0.65 (0.39 to 0.80)	
OCT	Frame level (888 cross-sections)	Frames with ISA, n	181	181			
		<i>% Frames with ISA, mean (SD)</i>	20.6 (20.9)	20.6 (20.9)	0	1.00 (1.00 to 1.00)	1.00 (1.00 to 1.00)
		Frames with SB struts, n	69	69			
		<i>% Frames with SB struts, mean (SD)</i>	7.80 (6.4)	7.80 (6.4)	0	1.00 (1.00 to 1.00)	1.00 (1.00 to 1.00)
	Strut level (6452 struts)	Frames with protrusion, n	69	73			
		<i>% Frames with tissue protrusion, mean (SD)</i>	7.7 (9.6)	8.2 (9.1)	0.95	0.94 (0.90 to 0.97)	0.94 (0.90 to 0.97)
		Frames with dissection (within BVS), n	79	66			
		<i>% Frames with dissection, mean (SD)</i>	9.0 (12.4)	7.5 (9.7)	3.17	0.88 (0.80 to 0.93)	0.88 (0.79 to 0.93)
Strut level (6452 struts)	Struts with ISA, n	348	340				
	<i>% ISA struts, mean (SD)</i>	5.5 (8.1)	5.4 (7.8)	0.36	1.00 (0.99 to 1.00)	1.00 (0.99 to 1.00)	
Strut level (6452 struts)	Struts at SB, n	77	79				
	<i>% SB struts, mean (SD)</i>	1.2 (1.2)	1.2 (1.2)	0.21	0.96 (0.93 to 0.98)	0.96 (0.93 to 0.98)	

ISA= incomplete scaffold/strut apposition; SB= side-branch; ICc= inter-class correlation coefficient; CI= confidence interval.

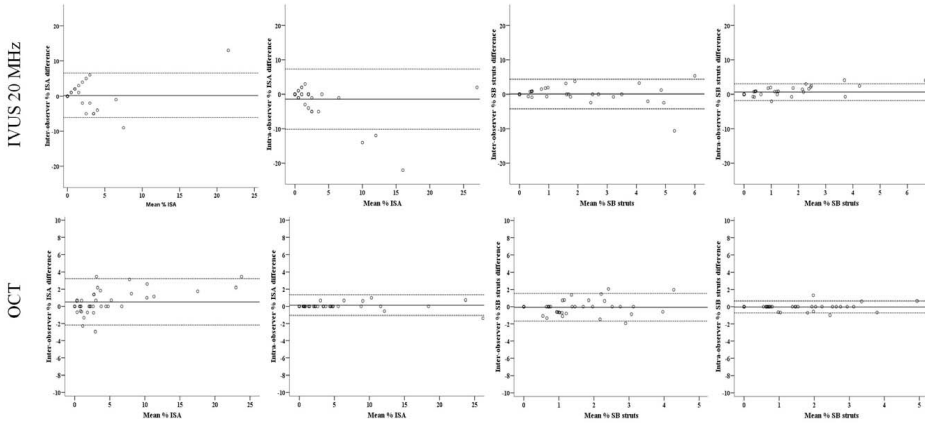


Figure 3. Bland-Altman graph of the inter- and intra-observer reproducibility of IVUS 20 MHz and OCT to assess malapposed and side-branch struts (strut level)

Table 7. Inter- and Intra-observer variability of quantitative measurements of IVUS and OCT

n = 150 cross-sections	Observer A	Observer B (1st)	Observer B (2nd)	Inter-observer variability			Intra-observer variability			
				absolute difference (95% CI)	ICCc	ICCa	Absolute difference (95% CI)	ICCc	ICCa	
IVUS	N of struts, n	906	1097	1070						
	struts x frame, mean (SD)	6.71 (2.05)	8.13 (2.28)	7.93 (2.50)	-1.41 (-1.92 to -0.91)	0.06 (-0.11 to 0.23)	0.05 (-0.09 to 0.20)	0.20 (-0.21 to 0.61)	0.50 (0.36 to 0.62)	0.50 (0.36 to 0.62)
	Lumen area (mm²)	6.15 (1.59)	6.24 (1.48)	6.42 (1.53)	-0.09 (-0.17 to 0.00)	0.94 (0.92 to 0.96)	0.94 (0.92 to 0.96)	-0.19 (-0.24 to -0.13)	0.97 (0.96 to 0.98)	0.97 (0.93 to 0.98)
	Scaffold area (mm²)	6.82 (1.77)	6.24 (1.47)	6.33 (1.51)	0.58 (0.49 to 0.67)	0.94 (0.92 to 0.96)	0.88 (0.42 to 0.96)	-0.09 (-0.14 to -0.04)	0.98 (0.97 to 0.98)	0.98 (0.96 to 0.98)
OCT	N of struts, n	1032	1020	1017						
	struts x frame, mean (SD)	7.64 (2.44)	7.53 (2.40)	7.56 (2.33)	0.11 (-0.10 to 0.32)	0.87 (0.82 to 0.90)	0.87 (0.82 to 0.90)	-0.02 (-0.19 to 0.14)	0.92 (0.88 to 0.94)	0.92 (0.88 to 0.94)
	Lumen area (mm²)	6.86 (1.76)	7.15 (1.81)	6.98 (1.77)	-0.29 (-0.33 to -0.26)	0.99 (0.99 to 0.99)	0.98 (0.63 to 0.99)	0.17 (0.14 to 0.21)	0.99 (0.99 to 0.99)	0.99 (0.95 to 1.00)
	Scaffold area (mm²)	7.47 (1.71)	7.62 (1.77)	7.50 (1.77)	0.14 (0.10 to 0.19)	0.99 (0.98 to 0.99)	0.98 (0.97 to 0.99)	-0.03 (-0.07 to 0.02)	0.99 (0.98 to 0.99)	0.99 (0.98 to 0.99)

Data are expressed in mean (SD).

ICC= inter-class correlation coefficient; CI= confidence interval.

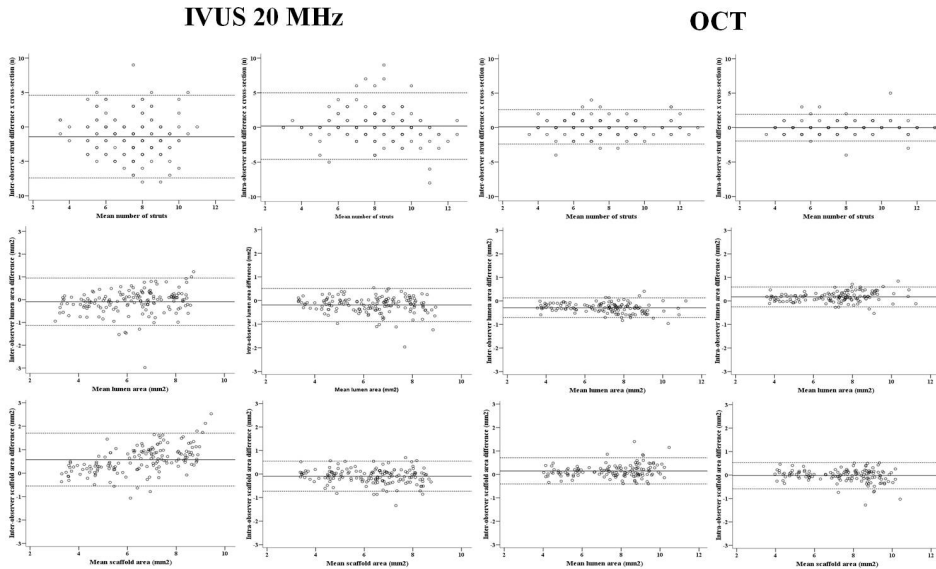


Figure 4. Bland-Altman graphs of the inter- and intra-observer reproducibility to assess number of struts, lumen area and scaffold area between IVUS 20 MHz and OCT

assess percentage of ISA and SB struts are shown in **Figure 3**.

OCT reproducibility of qualitative measurements

The inter- and intra-observer reproducibility of OCT to assess qualitative findings at lesion level analysis is shown in **Table 4**. Inter- and intra-observer reproducibility to assess scaffolds with at least one cross-section with dissection, ISA, SB-struts, tissue protrusion and thrombus was excellent except for the inter-observer reproducibility of tissue protrusion (moderate).

Inter- and intra-observer reproducibility at a frame and a strut level analysis are shown in **Tables 5 and 6**. Inter- and intra-observer reproducibility of OCT was excellent for all parameters except the inter-observer reproducibility of frames with tissue protrusion (moderate). The Bland – Altman plots of OCT inter- and intra-observer reproducibility to assess the percentage of ISA and SB struts are shown in **Figure 3**.

IVUS and OCT reproducibility of quantitative measurements

IVUS and OCT inter- and intra-observer reproducibility of quantitative measures are shown in **Table 7**. Assessment of number of struts per cross-section had poor to moderate inter- and intra-observer reproducibility with IVUS-20 MHz and excellent with OCT. Lumen and scaffold areas showed excellent reproducibility with both IVUS and OCT. Bland – Altman plots of the inter- and intra-observer reproducibility to assess number of struts, lumen area and scaffold area are shown in **Figure 4**.

DISCUSSION

The main results of our study are: 1) The agreement of IVUS and OCT to assess qualitative scaffold parameters immediately after the BVS implantation was predominantly poor at lesion, frame and strut level analysis; 2) OCT demonstrated a higher ability to detect ISA, SB-struts, tissue protrusion and dissections compared to IVUS; 3) Inter- and intra-observer

reproducibility to assess qualitative findings and number of struts per cross-section was poor to moderate with IVUS and excellent with OCT; 4) Lumen and scaffold areas had an excellent inter- and intra- observer reproducibility with both IVUS and OCT; but IVUS showed a margin of error (2 standard deviation of the difference between observers/ observations) larger than OCT in all measurements.

Intravascular imaging techniques are usually compared according to their spatial resolution. The spatial resolution can be defined as the ability to discriminate small objects in the axial and lateral plans (4). The axial and lateral resolution of the IVUS 20 MHz systems is 80 and 200-250 microns, respectively (4). OCT has an axial and lateral resolution of 15-20 and 20-40 microns respectively (11). The larger wavelength of the IVUS beam (35-80 microns), compared to the near-infrared light beam of the OCT (1 micron), allows higher tissue penetration and scan diameters but has less spatial resolution (11). This fact explains the higher accuracy of OCT to detect ISA, tissue protrusion and dissections compared to IVUS in metallic stents (5).

Using polymeric scaffolds, the larger echogenic blooming effect of the polymeric struts compared to the metallic stents challenges even more the assessment of the BVS structures with IVUS 20 MHz; especially when the vessel wall is rich in calcium tissue or the plaque is hyper-echogenic. It is uncertain if the visualization of the BVS structures with a high frequency IVUS system (≥ 30 MHz) would improve the assessment and reproducibility of these parameters. High frequency IVUS systems have previously been shown to demonstrate a better image quality when compared to low frequency IVUS (e.g. 20 MHz) (12). In the ABSORB trial, it was decided to use the IVUS 20 MHz system to assess the temporal changes of the vessel wall composition. The spectral analysis of the raw backscattered ultrasound data allows the correlation of the vessel wall composition with 4 different types of IVUS-derived tissue (fibrous tissue, fibro-fatty tissue, necrotic core and dense

calcium) (13). As of present, the IVUS 20 MHz Eagle Eye catheter (Volcano Corporation, Rancho Cordova, CA, USA) has been the only system validated for tissue characterization (virtual histology) (14), and has been used to assess the bioresorbtion process of the BVS (15).

Although the sensitivity and efficiency of IVUS to assess qualitative findings at a frame or a strut level analysis was low compared to OCT, the specificity of IVUS to assess qualitative findings at a lesion level analysis was high (**Table 2**). The good specificity of IVUS was probably due to the capability to detect the more severe cases of dissections, tissue protrusion and ISA without false positive observations. On the other hand, the low sensitivity of IVUS was probably due to the omission of the "less severe" cases when the lower resolution of the IVUS did not allow the visualization of these findings (e.g. malapposed struts separated from the vessel wall by less than 200 microns). The assessment of tissue coverage with IVUS presented similar results to our study; IVUS was less able to assess a few degrees of neointimal coverage compared to OCT (16,17). On the other hand, the assessment of SB struts is a special case in which the take-off of the side branch is usually easily observed by IVUS. In our study, the assessment of SB struts showed better alignment between IVUS and OCT at a lesion and a frame level analysis than the other qualitative findings.

However, the poor to moderate inter- and intra-observer reproducibility of IVUS 20 MHz qualitative measurements represent a clear limitation of the use of this imaging technique. Only the ISA and SB-strut assessment at a strut level analysis showed good reproducibility. However, the comparison of the IVUS 20 MHz inter- and intra-observer reproducibility to assess ISA and SB struts using the Bland-Altman graphs at a strut level analysis, showed a margin of error 2-3 times larger than with OCT (**Figures 3 and 4**). On the other hand, OCT showed excellent reproducibility for qualitative findings and number of struts per cross-section. These results are similar

to those reported by Gonzalo *et al.* using metallic stents (18). The inter- and intra-observer reproducibility for lumen and scaffold areas was excellent for both IVUS and OCT. These results are congruent with other studies using IVUS and OCT (18,19). However, our study shows that the inter- and intra-observer margin of error of those measurements was larger with IVUS than with OCT (**Figure 4**).

LIMITATIONS

The main limitation of this study is the lack of matching between IVUS and OCT image cross-sections. Although we tried to assess the same number of cross-sections per lesion measured at each 1 mm with respect to the pullback landmark, the disparity of the scaffold lengths between both techniques did not allow us to ensure the same sequence of cross-sections. Therefore, the percentages of

qualitative findings adjusted per lesion may differ and adds variability to the agreement between the two techniques. The second limitation of the study is the use of two different OCT systems. The visualization of the guide-wire and its shadowing in the OCT images obtained with the C7 system did not allow the complete analysis of the lumen/scaffold perimeter. On the other hand, the M3 system and the IVUS 20 MHz catheter allowed the complete visualization of the lumen/scaffold perimeter.

CONCLUSION

Qualitative assessment of BVS structures using IVUS 20 MHz should be avoided due to its poor agreement and reproducibility when compared to OCT. Both IVUS and OCT have good reproducibility to assess lumen and scaffold areas but the margin of error with IVUS is larger than with OCT.

REFERENCES

1. Ormiston JA, Serruys PW, Regar E, Dudek D, Thuesen L, Webster MW, Onuma Y, Garcia-Garcia HM, McGreevy R, Veldhof S. A bioabsorbable everolimus-eluting coronary stent system for patients with single de-novo coronary artery lesions (ABSORB): a prospective open-label trial. *Lancet* 2008;371(9616):899-907.
2. Serruys PW, Ormiston JA, Onuma Y, Regar E, Gonzalo N, Garcia-Garcia HM, Nieman K, Bruining N, Dorange C, Miquel-Hebert K and others. A bioabsorbable everolimus-eluting coronary stent system (ABSORB): 2-year outcomes and results from multiple imaging methods. *Lancet* 2009;373(9667):897-910.
3. Serruys PW, Onuma Y, Ormiston JA, de Bruyne B, Regar E, Dudek D, Thuesen L, Smits PC, Chevalier B, McClean D and others. Evaluation of the Second Generation of a Bioresorbable Everolimus Drug-Eluting Vascular Scaffold for Treatment of De Novo Coronary Artery Stenosis: Six-Month Clinical and Imaging Outcomes. *Circulation*.
4. Mintz GS, Nissen SE, Anderson WD, Bailey SR, Erbel R, Fitzgerald PJ, Pinto FJ, Rosenfield K, Siegel RJ, Tuzcu EM and others. American College of Cardiology Clinical Expert Consensus Document on Standards for Acquisition, Measurement and Reporting of Intravascular Ultrasound Studies (IVUS). A report of the American College of Cardiology Task Force on Clinical Expert Consensus Documents. *J Am Coll Cardiol* 2001;37(5):1478-92.
5. Bouma BE, Tearney GJ, Yabushita H, Shishkov M, Kauffman CR, DeJoseph Gauthier D, MacNeill BD, Houser SL, Aretz HT, Halpern EF and others. Evaluation of intracoronary stenting by intravascular optical coherence tomography. *Heart* 2003;89(3):317-20.
6. Gonzalo N, Serruys PW, Okamura T, Shen ZJ, Onuma Y, Garcia-Garcia HM, Sarno G, Schultz C, van Geuns RJ, Ligthart J and others. Optical coherence tomography assessment of the acute effects of stent implantation on the vessel wall: a systematic quantitative approach. *Heart* 2009;95(23):1913-9.
7. Cohen J. A coefficient of agreement for nominal scales. *Educ Psychol Meas* 1960;20:37-46.
8. Fleiss J. 1981. *Statistical methods for rates and proportions*. New York: John Wiley & Son.
9. Fleiss J. 1986. *The design and analysis of clinical experiments*. New York.: John Wiley & Sons.
10. Bland JM, Altman DG. *Statistical methods for assessing agreement between two methods of clinical measurement*. *Lancet* 1986;1(8476):307-10.
11. Prati F, Regar E, Mintz GS, Arbustini E, Di Mario C, Jang IK, Akasaka T, Costa M, Guagliumi G, Grube E and others. Expert review document on methodology, terminology, and clinical applications of optical coherence tomography: physical principles, methodology of image acquisition, and clinical application for assessment of coronary arteries and atherosclerosis. *Eur Heart J* 2010;31(4):401-15.
12. Fort S, Freeman NA, Johnston P, Cohen EA, Foster FS. In vitro and in vivo comparison of three different intravascular ultrasound catheter designs. *Catheter Cardiovasc Interv* 2001;52(3):382-92.
13. Garcia-Garcia HM, Mintz GS, Lerman A, Vince G, Margolis MP, Van Es GA, Morel MA, Nair A, Virmani R, Burke J and others. Tissue characterization using intravascular radiofrequency data analysis: recommendations for acquisition, analysis, interpretation and reporting. *EuroIntervention* 2009;5:177-189.
14. Nair A, Kuban BD, Tuzcu EM, Schoenhagen P, Nissen SE, Vince DG. Coronary plaque classification with intravascular ultrasound radiofrequency data analysis. *Circulation* 2002;106(17):2200-6.
15. Garcia-Garcia HM, Gonzalo N, Pawar R, Kukreja N, Dudek D, Thuesen L, Ormiston JA, Regar E, Serruys PW. Assessment of the absorption process following bioabsorbable everolimus-eluting stent implantation: temporal changes in strain values and tissue composition using intravascular ultrasound radiofrequency data

- analysis. A substudy of the ABSORB clinical trial. *EuroIntervention* 2009;4(4):443-8.
16. Suzuki Y, Ikeno F, Koizumi T, Tio F, Yeung AC, Yock PG, Fitzgerald PJ, Fearon WF. In vivo comparison between optical coherence tomography and intravascular ultrasound for detecting small degrees of in-stent neointima after stent implantation. *JACC Cardiovasc Interv* 2008;1(2):168-73.
 17. Capodanno D, Prati F, Pawlowsky T, Cera M, La Manna A, Albertucci M, Tamburino C. Comparison of optical coherence tomography and intravascular ultrasound for the assessment of in-stent tissue coverage after stent implantation. *EuroIntervention* 2009;5(5):538-43.
 18. Gonzalo N, Garcia-Garcia HM, Serruys PW, Commissaris KH, Bezerra H, Gobbens P, Costa M, Regar E. Reproducibility of quantitative optical coherence tomography for stent analysis. *EuroIntervention* 2009;5(2):224-32.
 19. Mintz GS, Griffin J, Chuang YC, Pichard AD, Kent KM, Satler LF, Popma JJ, Leon MB. Reproducibility of the intravascular ultrasound assessment of stent implantation in saphenous vein grafts. *Am J Cardiol* 1995;75(17):1267-70.

Chapter 6

Evaluation of mechanical properties of bioresorbable vascular scaffolds.

6.1

Angiographic geometric changes of the lumen arterial wall after bioresorbable vascular scaffolds and metallic platform stents at 1-year follow-up.

Josep Gomez-Lara, Salvatore Brugaletta, Vasim Farooq, Robert Jan van Geuns, Bernard de Bruyne, Stephan Windecker, Dougal McClean, Leif Thuesen, Dariusz Dudek, Jacques Koolen, Robert Whitbourn, Pieter C Smits, Bernard Chevalier, Marie-Angele Morel, Cecile Dorange, Susan Veldhof, Richard Rapoza, Hector M Garcia-Garcia, John A Ormiston, Patrick W Serruys

JACC Cardiovascular Interventions 2011;4:789-99

Angiographic Geometric Changes of the Lumen Arterial Wall After Bioresorbable Vascular Scaffolds and Metallic Platform Stents at 1-Year Follow-Up

Josep Gomez-Lara, MD,* Salvatore Brugaletta, MD,* Vasim Farooq, MBChB,* Robert Jan van Geuns, MD, PhD,* Bernard De Bruyne, MD, PhD,† Stephan Windecker, MD,‡ Douglas McClean, MD,§ Leif Thuesen, MD,|| Dariusz Dudek, MD,¶ Jacques Koolen, MD, PhD,# Robert Whitbourn, MD,** Pieter C. Smits, MD, PhD,†† Bernard Chevalier, MD,‡‡ Marie-Angèle Morel, BSc,§§ Cécile Dorange, MSc,||| Susan Veldhof, RN,|||| Richard Rapoza, PhD,¶¶ Hector M. Garcia-Garcia, MD, PhD,*§§ John A. Ormiston, MBChB, PhD,## Patrick W. Serruys, MD, PhD*

Rotterdam and Eindhoven, the Netherlands; Aalst and Diegem, Belgium; Bern, Switzerland; Christchurch and Auckland, New Zealand; Skejby, Denmark; Krakow, Poland; Melbourne, Australia; Massy, France; and Santa Clara, California

Objectives The aim of this study was to compare the angiographic changes in coronary geometry of the bioresorbable vascular scaffolds (BVS) and metallic platform stent (MPS) between baseline and follow-up.

Background Coronary geometry changes after stenting might result in wall shear stress changes and adverse events. The BVS have better conformability, compared with MPS, but still modify artery geometry. It is uncertain whether the BVS resorption can restore the coronary anatomical configuration at midterm follow-up.

Methods All patients of the ABSORB (A Clinical Evaluation of the Bioabsorbable Everolimus Eluting Coronary Stent System [BVS EECSS] in the Treatment of Patients With de Novo Native Coronary Artery Lesions) and SPIRIT (A Clinical Evaluation of the XIENCE V Everolimus Eluting Coronary Stent System in the Treatment of Patients With de Novo Native Coronary Artery Lesions) trials treated with a single 3.0 × 18 mm device and imaged at baseline and 6- to 12-month follow-up were eligible. Coronary geometry changes were assessed with quantitative angiography as changes in curvature and angulation. Curvature and angulation changes between systole and diastole were investigated to assess hinging movements of the coronary artery.

Results One hundred sixty-one patients (86 BVS, and 75 MPS) were included. Baseline angiographic characteristics were similar. From post-implantation to follow-up, curvature increased 8.4% ($p < 0.01$) with BVS and decreased 1.9% ($p = 0.54$) with MPS; $p = 0.01$. Angulation increased 11.3% with BVS ($p < 0.01$) and 3.8% with MPS ($p = 0.01$); $p < 0.01$. From pre-implantation to follow-up, BVS decreased 3.4% the artery curvature ($p = 0.05$) and 3.9% the artery angulation ($p = 0.16$), whereas MPS presented with 26.1% decrease in curvature ($p < 0.01$) and 26.9% decrease in angulation ($p < 0.01$), being larger with MPS ($p < 0.01$, both). Hinging movements in curvature from pre-implantation to follow-up decreased 19.7% with BVS and 39.0% with MPS ($p = 0.27$) and decreased 3.9% with BVS and 26.9% with MPS in angulation ($p < 0.01$).

Conclusions At midterm follow-up, the BVS tended to restore the coronary configuration and the systo-diastolic movements to those seen before implantation. The coronary geometry remained similar to that seen at after implantation with MPS. (A Clinical Evaluation of the Bioabsorbable Everolimus Eluting Coronary Stent System [BVS EECSS] in the Treatment of Patients With de Novo Native Coronary Artery Lesions; NCT00856856) (J Am Coll Cardiol Intv 2011;4:789–99) © 2011 by the American College of Cardiology Foundation

From the *Department of Interventional Cardiology, Thoraxcenter, Erasmus Medical Center, Rotterdam, the Netherlands; †Cardiovascular Center, Aalst, Belgium; ‡Swiss Cardiovascular Center, Bern, Switzerland; §Christchurch Hospital, Christchurch, New Zealand; ||Skejby Sygehus, Aarhus University Hospital, Skejby, Denmark; ¶Jagiellonian University, Krakow, Poland;

Coronary geometry is the major determinant of the shear stress inflicted on the endothelial cells lining the artery wall. Physiological wall shear stress (WSS) induces the alignment of the endothelial cells in the flow direction and the secretion of numerous antiatherogenic substances such as endothelin and nitric oxide. In contrast, oscillatory or low WSS induces the secretion of pro-atherogenic substances, which carries a higher risk of plaque progression (1). As a result, atherosclerotic plaques are more frequently located at regions with low WSS, such as at the inner walls of curved arteries (2–4).

See page 800

Coronary stenting also modifies shear stress. The local WSS decreases along the entire length of the stent after implantation

Abbreviations and Acronyms

- BMS = bare-metal stent(s)
- BVS = bioresorbable vascular scaffolds
- DS = diameter stenosis
- ICCa = interclass correlation coefficient for absolute agreement
- MLD = minimal lumen diameter
- MPS = metallic platform stent
- PES = paclitaxel-eluting stent(s)
- QCA = quantitative coronary angiography
- SES = sirolimus-eluting stent(s)
- TLR = target lesion revascularization
- WSS = wall shear stress

(5). Moreover, stented regions exposed to lower WSS have been shown to exhibit higher grades of neointimal response compared with regions with physiological WSS; this has been shown to be applicable for both bare-metal stents (BMS) and paclitaxel-eluting stents (PES) at 6-month follow-up (6,7). Consequently, straightening of curved coronary arteries after implantation has been related to a higher neointimal response with BMS and PES at midterm follow-up (7–9). Conversely, sirolimus-eluting stents (SES) have been demonstrated to avoid the relationship between low WSS and a higher neointimal response at 6 months (7). As a result, some clinical studies using first-generation SES showed no relationship between angulated lesions and angiographic restenosis

at 9 months (10,11). It is still unknown whether the progressive loss of angiographic minimal lumen diameter (MLD) experienced by the SES at long-term follow-up can modify the relationships among artery bend, curvature, and angulation

with stent restenosis (12). At 2 years, SES and PES presented with similar angiographic lumen loss (12).

The most important device property that determines acute changes in coronary geometry is the conformability of the stent. Stent conformability is dependent on both material and design (13). The everolimus-eluting bioresorbable vascular scaffold (BVS) have shown better conformability in its ability to adapt to the coronary geometry immediately after implantation, compared with the Multi-link Vision and Xience V metallic platform stents (MPS) (Abbott Vascular, Santa Clara, California) (14). However, both the MPS and BVS devices have previously been demonstrated to decrease the artery curvature and angulation from pre- to post-implantation (14). Therefore, it is uncertain how these changes in artery geometry are maintained in both devices at midterm follow-up. This fact is especially important with the BVS, because bioresorption of the polymeric scaffolds might potentially allow for the restoration of the coronary artery to its original anatomical configuration seen before implantation. By design, the mechanical integrity of the BVS and the scaffold support to the artery wall eventually disappear a few months after the implantation (15), with complete resorption of the polymer approximately 2 years after implantation (16).

The aim of the present study is to compare the changes in coronary geometry from post-implantation to 6 to 12 months of follow-up between BVS and MPS. The clinical outcomes of both BVS and MPS are also explored.

Methods

Population and study design. The ABSORB Cohort B (A Clinical Evaluation of the Bioabsorbable Everolimus Eluting Coronary Stent System [BVS EECSS] in the Treatment of Patients With de Novo Native Coronary Artery Lesions) trial is a single-arm trial that included 101 patients treated with a single 3.0 × 18 mm BVS. The global population was divided into 2 groups with different invasive angiographic controls at 6-month (n = 45) and 12-month (n = 56) follow-up. The study design and the clinical outcomes of the first cohort of patients (with 6-month follow-up invasive control) have been reported (17). The SPIRIT (A Clinical Evaluation of the XIENCE V Everoli-

#Catharina Ziekenhuis, Eindhoven, the Netherlands; **Cardiovascular Research Center, St. Vincent's Hospital, Melbourne, Australia; ††Maasstad Ziekenhuis, Rotterdam, the Netherlands; ‡‡Institut cardio-vasculaire Paris-Sud, Massy, France; §§CardiAlysis, Rotterdam, the Netherlands; |||Abbott Vascular, Diegem, Belgium; ¶¶Abbott Vascular, Santa Clara, California; and the ##Auckland City Hospital, Auckland, New Zealand. The ABSORB Cohort B and the SPIRIT I and II trials have been supported by Abbott Vascular. Dr. Windecker has received research grants from Abbott, Cordis, Medtronic, Biosensors, and Boston Scientific. Dr. Dudek has received research grants or served as a consultant/advisory board member for Abbott, Adamed, AstraZeneca, Biotronik, Balton, Bayer, BBraun, BioMatrix, Boston Scientific, Boehringer Ingelheim, Bristol-Myers Squibb,

Cordis, Cook, Eli Lilly, EuroCor, GlaxoSmithKline, Invatec, Medtronic, The Medicines Company, Merck Sharp & Dohme, Nycomed, Orbus-Neich, Pfizer, Possis, Promed, Sanofi-Aventis, Siemens, Solvay, Terumo, and Tyco. Dr. Smits has received speaker and travel fees from Abbott Vascular. Dr. Chevalier is a consultant for Abbott Vascular. Cécile Dorange, Susan Veldhof, and Dr. Rapoza are employees of Abbott Vascular. Dr. Ormiston is on the advisory boards for Abbott and Boston Scientific; and has received minor honoraria from Abbott and Boston Scientific. All other authors have reported that they have no relationships to disclose. Eric Bates, MD, served as Guest Editor for this paper.

Manuscript received January 25, 2011; revised manuscript received March 29, 2011, accepted April 11, 2011.

mus Eluting Coronary Stent System in the Treatment of Patients With de Novo Native Coronary Artery Lesions) I trial is a randomized trial that included 60 patients treated with a single Xience V ($n = 28$) or a Multi-link Vision ($n = 32$) 3.0×18 mm stent. The SPIRIT II trial randomized 300 patients to PES or to Xience V stent. A total of 223 patients were treated with different sizes of Xience V stent. All patients included in the SPIRIT I and II trials were scheduled for an angiographic control at 6-month follow-up.

The study design and clinical outcomes of the SPIRIT I and II trials have been reported (18,19). In brief, the inclusion criteria of the ABSORB and SPIRIT trials were similar: patients with stable or non-ST-segment elevation acute coronary syndrome and with a de novo lesion in a native coronary artery with a diameter stenosis (DS) between 50% and 99% were eligible. Patients with ostial lesions, heavily calcified arteries, or extreme angulated lesions ($>90^\circ$) were excluded.

Acute changes in coronary geometry assessed before and after implantation of both BVS and MPS (Multi-link Vision or Xience V) have previously been investigated and reported by our group (14). In brief, 89 patients included in the ABSORB Cohort B trial treated with the BVS and 102 patients of the SPIRIT I and II trials treated with the Multi-link Vision or Xience V stents were included (14). This report presents a continuation of the previous study with the same population that underwent angiographic control at 6- or 12-month follow-up.

Treatment procedure and devices. All lesions were treated with routine interventional techniques that included mandatory pre-dilation with a balloon shorter and 0.5 mm smaller in diameter than the study device. Post-dilation with a balloon shorter than the implanted device was allowed at the discretion of the operator, as was bailout treatment.

The ABSORB Bioabsorbable Vascular Scaffold (Abbott Vascular) is a device consisting of a backbone of a fully resorbable polymer (poly-L-lactide), coated with a copolymer (poly-D,L-lactide) that contains and releases the antiproliferative drug (everolimus). Two platinum markers at each end outline the boundaries of the scaffold and remain embedded in the coronary wall after the scaffold resorbs. The Multi-link Vision and the Xience V stents (Abbott Vascular) share the same metallic platform composed of a cobalt-chromium alloy. The Xience V stent is coated with a biocompatible fluorinated copolymer that contains and releases the same amount of antiproliferative drug ($100 \mu\text{g}/\text{cm}^2$ of everolimus) within a similar period.

Quantitative coronary angiography analysis. The operators were requested to select an angiographic view with minimal foreshortening of the lesion and limited overlap with other arteries. This angiographic view was used at baseline (before and after implantation) and at follow-up. The 2-dimensional angiograms were analyzed by an independent core laboratory (Cardialysis, Rotterdam, the Netherlands) with the

CAAS II analysis system (Pie Medical BV, Maastricht, the Netherlands). In each patient, the treated region and the peritreated regions (defined by 5 mm proximal and distal to the device edge) were analyzed. The following quantitative coronary angiography (QCA) parameters were measured: the interpolated-reference artery diameter, the MLD, and the percentage DS. Late luminal loss was derived from the difference between the MLD after implantation and at follow-up with matched angiographic views.

Curvature and angulation were measured before and after implantation and at follow-up with the same angiographic views (with a maximal difference of 10°). Both parameters were assessed within the treated region with clear landmarks to assess the treated region before implantation and with the radio-opaque markers after implantation and at follow-up. Both curvature and angulation were estimated with QCA (CAAS II version 1.2 Beta or CAAS 5.9 research version; Pie Medical Imaging) as previously reported (14). Briefly, "curvature" is defined as the infinitesimal rate of change in the tangent vector at each point of the center-line. This measurement has a reciprocal relationship to the radius of the perfect circle defined by the curve at each point. The curvature value is calculated as $1/\text{radius}$ of the circle in cm^{-1} (14). "Angulation" is defined as the angle in degrees that the tip of an intracoronary guidewire would need to reach the distal part of a coronary bend (14). Cyclical changes in coronary curvature and angulation were estimated as: curvature/angle at the end-diastole - curvature/angle at the end-systole. End-diastole curvature/angulation was assessed in the still angiographic view corresponding to the peak of the QRS complex of the electrocardiogram; and end-systole curvature/angulation was assessed in the still angiographic view corresponding with the peak of the T wave of the electrocardiogram. Relative differences, before and after implantation, were estimated at the end-diastole as: (absolute difference in curvature or angulation between pre- and post-implantation/curvature or angulation at pre-implantation) $\times 100$.

Statistical analysis. The Kolmogorov-Smirnov test was used to evaluate the normality assumptions of all continuous variables. Because curvature, angulation, and cyclical changes of curvature and angulation did not have a normal distribution, all QCA geometry variables were expressed as median (interquartile range). The rest of the continuous variables were expressed as mean ± 1 SD. Categorical variables were presented as counts (%). Paired comparisons of continuous variables within groups between different time-points were estimated with the Wilcoxon test. Non-paired comparisons between BVS and MPS were estimated with the Mann-Whitney U test when variables were non-normally distributed and with the Student t test when normally distributed. Comparisons of categorical variables were estimated with the chi-square test.

To assess the interobserver reproducibility of curvature and angle measurements, 2 observers analyzed 40 randomly selected cases. The interobserver reproducibility was assessed with the r^2 Pearson correlation coefficient and the interclass correlation coefficient for absolute agreement (ICCa). An ICCa <0.4 indicated bad agreement, an ICCa between 0.4 and 0.75 indicated moderate agreement, and ICCa values >0.75 indicated excellent agreement (20).

All statistical tests were carried out with a 2-sided 5% level of significance. All measures were obtained with the SPSS software (version 15.0, SPSS, Inc., Chicago Illinois).

Results

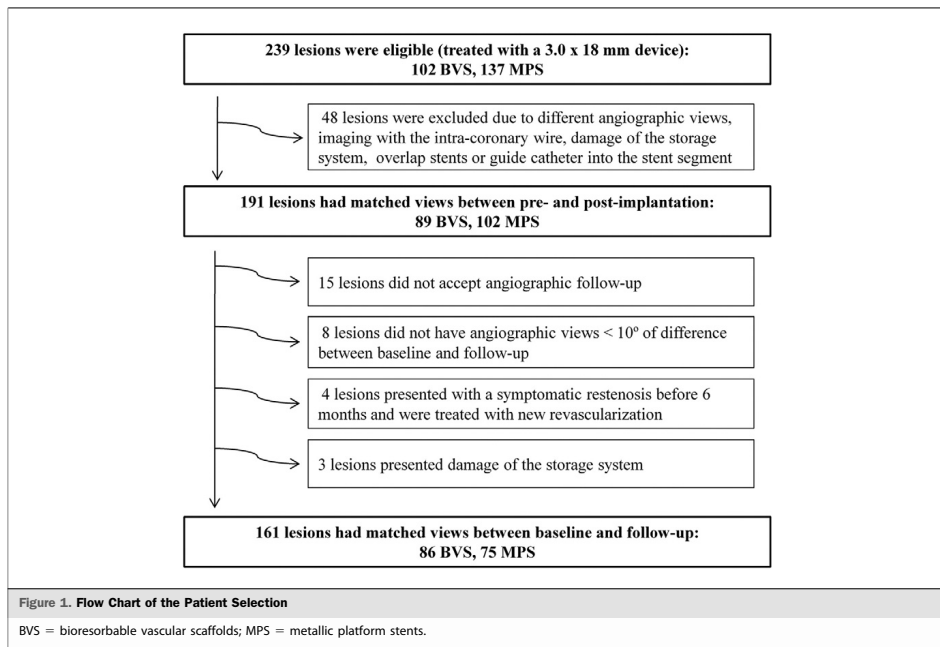
Population and baseline clinical characteristics. A total of 86 patients treated with BVS and 75 patients treated with MPS (58 Xiience V, and 17 Multi-link Vision) were included in the present study. A flow chart of the patient selection is shown in Figure 1. Briefly, 30 patients were excluded because of: declined invasive angiographic follow-up, different angiographic views between baseline and follow-up, target lesion revascularization (TLR) before the scheduled invasive control, and damage to the data storage media. Angiographic follow-up of the BVS group was performed at 6 months in 37 patients and at 12 months in

49 patients. All patients treated with MPS were planned for invasive angiographic follow-up at 6 months.

The baseline clinical characteristics are shown in Table 1. Both groups were similar in age, sex, and cardiovascular risk factors except for smoking history (BVS 16.3% vs. MPS 37.3%; $p < 0.01$). Although there were no differences in the treated artery, the BVS group had a trend toward more patients with the culprit lesion located in the right coronary artery (33.7% vs. 20.9%, respectively). The left anterior descending was the most commonly treated artery with both BVS and MPS (45.4% vs. 50.7%, respectively).

Angiographic changes unrelated to coronary geometry. Angiographic findings unrelated to coronary geometry are shown in Table 2. Both BVS and MPS showed similar angiographic parameters before implantation. After implantation the BVS demonstrated a smaller MLD (2.05 mm vs. 2.14 mm, respectively; $p < 0.01$) and higher DS (15.4% vs. 12.7%, respectively; $p < 0.01$) compared with MPS. At follow-up, the DS, MLD, and late luminal loss were nonstatistically different between BVS and MPS.

Angiographic changes related to coronary geometry. Angiographic findings related to coronary geometry are shown in Table 3. Before implantation both groups presented with similar median values of curvature (BVS 0.297 cm^{-1} and



	BVS (n = 86)	MPS (n = 75)	p Value
Age (yrs)	61.6 ± 8.4	62.6 ± 10.2	0.50
Men	62 (72.1)	52 (69.3)	0.70
Hypertension	55 (64.0)	44 (58.7)	0.47
Hypercholesterolemia	71 (82.6)	55 (73.3)	0.16
Diabetes mellitus	15 (17.4)	12 (16.0)	0.81
Smoking history	14 (16.3)	28 (37.3)	<0.01
Previous MI	20 (23.3)	25 (33.3)	0.23
Previous PCI	15 (17.4)	14 (18.7)	0.84
Previous CABG	2 (2.3)	1 (1.3)	0.64
Clinical presentation			0.41
Stable angina	72 (83.7)	59 (78.7)	
Acute coronary syndrome	14 (16.3)	16 (21.3)	
Culprit artery			0.13
LAD	39 (45.4)	38 (50.7)	
LCX	18 (20.9)	22 (29.3)	
RCA	29 (33.7)	15 (20.0)	

Values are mean ± SD or count (%).

BVS = bioresorbable vascular scaffolds; CABG = coronary artery bypass graft; LAD = left anterior descending artery; LCX = left circumflex artery; MI = myocardial infarction; MPS = metallic platform stents; PCI = percutaneous coronary intervention; RCA = right coronary artery.

MPS 0.365 cm^{-1} ; $p = 0.99$) and angulation (33.1° vs. 36.5° , respectively; $p = 0.84$). Cyclical changes in curvature (0.109 cm^{-1} vs. 0.091 cm^{-1} , respectively; $p = 0.80$) and angulation (5.6° vs. 8.4° , respectively; $p = 0.11$) were also similar between groups.

From pre- to post-implantation, curvature and angulation significantly decreased in both groups. However, the BVS group experienced a smaller reduction in curvature

(15.3% vs. 21.9%, respectively; $p = 0.11$) and angulation (17.4° vs. 31.8° , respectively; $p = 0.02$) compared with MPS. The BVS also presented with a smaller decrease in systo-diastolic (cyclical) changes in curvature (23.1% vs. 39.9%, respectively; $p = 0.09$) and angulation (29.6% vs. 51.0%, respectively; $p = 0.06$) compared with MPS.

From post-implantation to follow-up, the BVS showed an 8.4% increase in curvature ($p < 0.01$) and 11.3% increase in angulation ($p < 0.01$). Conversely, the MPS remained with a similar curvature (1.9% reduction, $p = 0.54$) but presented with a mild increase in angulation (3.8%, $p = 0.01$). The comparison of the absolute changes in curvature and angulation from post-implantation to follow-up between BVS and MPS was statistically significant for both parameters. The cyclical changes in coronary curvature and angulation observed at follow-up were similar to that observed after implantation in both groups, without any significant differences between devices.

From pre-implantation to follow-up, the BVS demonstrated a trend toward a reduction in artery curvature (3.4%; $p = 0.05$) and angulation (3.9%; $p = 0.16$). However, the MPS demonstrated a significant reduction in curvature of 26.1% ($p < 0.01$) and a reduction in angulation of 26.9% ($p < 0.01$); this was shown to be significantly larger than the BVS ($p < 0.01$ for curvature and angulation). Similarly, the BVS experienced fewer changes of systo-diastolic changes in curvature (19.7% reduction; $p = 0.11$) and angulation (0.3% increase; $p = 0.51$). However, the MPS showed an important decrease in cyclical changes of curvature (39.0%; $p < 0.01$) and angulation (49.9%; $p < 0.01$). The comparison between devices resulted in a lower reduction with the

		Pre-Implantation	Post-Implantation	Follow-Up	p Value*	p Value†	p Value‡
Lesion/scaffold length (mm)	BVS	10.08 (3.77)	16.33 (1.50)	16.33 (1.73)	0.11	0.23	0.10
	MPS	11.03 (3.69)	16.69 (1.13)	16.87 (1.19)			
RVD (mm)	BVS	2.60 (0.37)	2.67 (0.31)	2.53 (0.34)	0.37	0.32	<0.01
	MPS	2.65 (0.31)	2.72 (0.32)	2.68 (0.32)			
MLD (mm)	BVS	1.06 (0.27)	2.28 (0.25)	2.05 (0.30)	0.62	<0.01	0.14
	MPS	1.03 (0.34)	2.41 (0.25)	2.14 (0.49)			
	BMS	1.05 (0.31)	2.40 (0.33)	1.51 (0.44)			
	DES	1.03 (0.35)	2.41 (0.23)	2.33 (0.31)			
LLL	BVS	—	—	0.23 (0.27)	—	—	0.47
	MPS	—	—	0.27 (0.43)			
	BMS			0.89 (0.40)			
	DES			0.08 (0.21)			
DS (%)	BVS	59.12 (9.90)	15.44 (6.00)	20.12 (8.95)	0.76	<0.01	
	MPS	61.19 (11.48)	12.66 (4.39)	20.67 (13.94)			
	BMS	60.73 (9.34)	13.70 (5.10)	39.53 (15.19)			
	DES	61.32 (12.11)	12.35 (4.16)	14.95 (6.64)			

Bare-metal stents (BMS) = 17; drug-eluting stents (DES) = 58. *p = comparison between BVS (n = 86) and MPS (n = 75) before implantation; †p = comparison between BVS and MPS after implantation; ‡p = comparison between BVS and MPS at follow-up.

DS = diameter stenosis; LLL = late luminal loss; MLD = minimal lumen diameter; RVD = reference vessel diameter; other abbreviations as in Table 1.

Table 3. Coronary Geometric Changes at Baseline and Follow-Up

		Pre-implantation	Post-implantation	Follow-Up	Relative Change Post-Pre (%)		Relative Change FU-Post (%)		Relative Change FU-Pre (%)		p Value*	p Value†	p Value‡
					Median	p1	Median	p2	Median	p3			
Curvature (cm ⁻¹)	BVS	0.297 (0.179–0.573)	0.269 (0.133–0.473)	0.299 (0.154–0.550)	-15.3	<0.01	8.4	<0.01	-3.4	0.05	0.11	0.01	<0.01
	MPS	0.365 (0.186–0.556)	0.265 (0.130–0.400)	0.261 (0.133–0.397)	-21.9	<0.01	-1.9	0.54	-26.1	<0.01			
Cyclic changes in curvature (cm ⁻¹)	BVS	0.109 (0.043–0.167)	0.070 (0.032–0.149)	0.078 (0.026–0.149)	-23.1	0.01	10.7	0.30	-19.7	0.11	0.09	0.93	0.27
	MPS	0.091 (0.045–0.173)	0.046 (0.022–0.100)	0.060 (0.026–0.112)	-39.9	<0.01	11.5	0.27	-39.0	<0.01			
Angle (°)	BVS	33.13 (15.62–55.40)	26.26 (13.33–43.82)	32.44 (18.86–49.53)	-17.4	<0.01	11.3	<0.01	-3.9	0.16	0.02	<0.01	<0.01
	MPS	36.49 (23.08–58.19)	24.94 (13.46–36.60)	24.55 (14.86–36.14)	-31.8	<0.01	3.8	0.01	-26.9	<0.01			
Cyclic changes in angle (°)	BVS	5.64 (2.37–12.14)	4.63 (1.85–8.22)	4.51 (2.59–10.02)	-29.6	0.01	4.6	0.26	0.3	0.51	0.06	0.51	<0.01
	MPS	8.35 (3.40–13.20)	3.70 (1.55–6.46)	4.54 (2.03–6.80)	-51.0	<0.01	3.7	0.72	-49.9	<0.01			

Values are median (interquartile range). *p = comparison between BVS (n = 86) and MPS (n = 75) of the absolute difference post-implantation – pre-implantation; †p = comparison between BVS and MPS of the absolute difference follow-up (FU) – post-implantation; ‡p = comparison between BVS and MPS of the absolute difference FU – pre-implantation.
 p1 = paired comparison between pre- and post-implantation; p2 = paired comparison between post-implantation and follow-up; p3 = paired comparison between pre-implantation and follow-up; other abbreviations as in Table 1.

BVS compared with the MPS for cyclical changes in angulation (p < 0.01) but not for the cyclical changes in curvature (p = 0.27).

Geometric changes in coronary geometry in the subset of patients with larger pre-implantation curvature and angle.

Because geometric changes are expected to be greater in curved arteries compared with straight arteries; the one-half of the overall population with larger median values of curvature (≥0.324 cm⁻¹) and angulation (≥34.3°) before implantation were selected and are shown in Figure 2.

From pre- to post-implantation, the BVS demonstrated a smaller reduction in curvature (from 0.579 to 0.480 cm⁻¹; 15.9%) compared with MPS (from 0.553 to 0.400 cm⁻¹; 25.5%); this difference almost reached statistical significance when both scaffolds were compared (p = 0.09). The BVS also showed a trend toward a lower reduction in angulation (from 57.7° to 43.9°; 20.6%) compared with MPS (from 56.7° to 36.4°; 36.1%); without statistical significance (p = 0.14).

From post-implantation to follow-up, the BVS showed a 6.2% increase in artery curvature (from 0.480 to 0.547 cm⁻¹) and a 7.8% increase in angulation (from 43.9° to 52.8°; 7.8%). The MPS demonstrated a 3.7% reduction in curvature (from 0.400 to 0.356 cm⁻¹) and 3.2% increase in angulation (from 36.4° to 35.7°). As a result, the BVS had a statistically significant larger increase in curvature and angulation than MPS (p < 0.01 for both measurements).

From pre-implantation to follow-up, the BVS demonstrated a 0.019 cm⁻¹ (3.4%) reduction in curvature and a 6.1° (10.4%) reduction in angulation. The MPS demonstrated a 0.211 cm⁻¹ (39.1%) reduction in curvature and a 20.1° (32.6%) reduction in angulation. The absolute reduction in curvature and angulation were significantly lower with the BVS compared with the MPS (p < 0.01 for both curvature and angulation).

Geometric changes of the BVS group at 6- and 12-month follow-up.

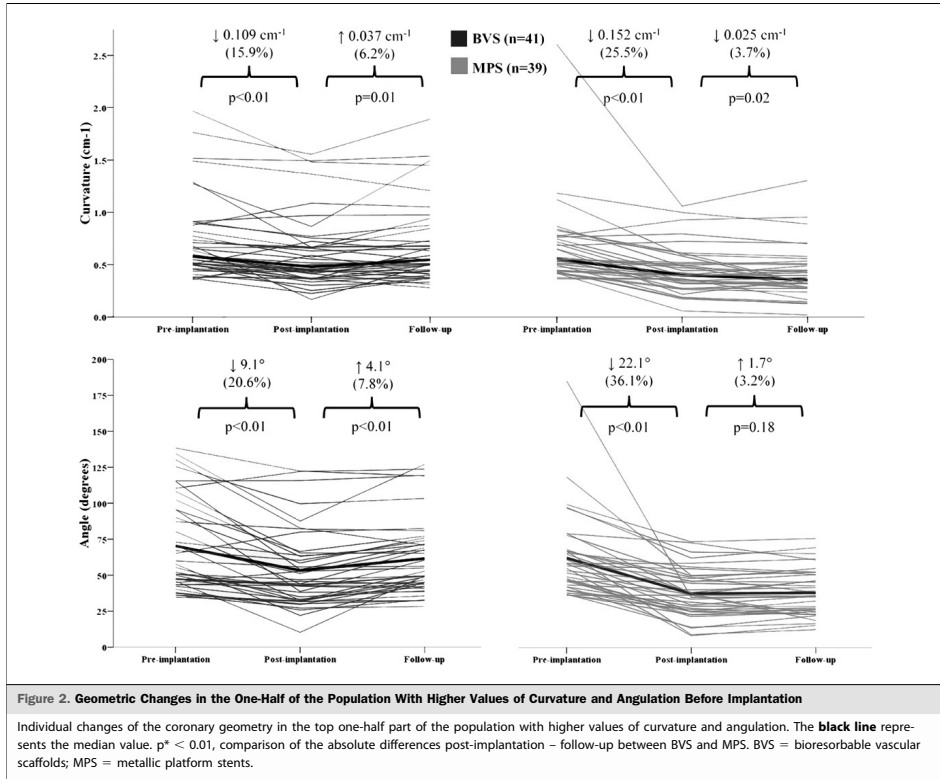
Figure 3 shows the individual data of the BVS patients divided according to the invasive follow-up (6 vs. 12 months). From post-implantation to follow-up, the cohort of patients who underwent 12-month follow-up tended to have larger changes in curvature (14.8% vs. 2.9%, respectively; p = 0.24) and angulation (11.4% vs. 6.2%, respectively; p = 0.36) compared with the cohort of patients who had 6-month follow-up.

Clinical outcomes related to coronary curvature/angulation.

A total of 191 patients (89 BVS and 102 MPS: 77 Xience V and 25 Multi-link Vision) were investigated before implantation for geometric parameters. There were no deaths during the first year of follow-up. A total of 14 patients (7.3%) presented with TLR during the first 12 months after implantation: 4 patients (4.5%) treated with the BVS, 3 patients (3.9%) treated with the Xience V stent, and 7 patients (28.0%) treated with the Multi-link Vision stent. None of the patients with TLR were diabetic. All TLR events were ischemia-driven, except for 2 patients (1 BVS and 1 Multi-link Vision).

Figure 4 shows the box-plot values of curvature and angulation before implantation according to the treatment device. In the overall population, patients with TLR at 1 year showed larger median values of curvature (0.454 cm⁻¹ vs. 0.307 cm⁻¹, respectively; p = 0.72) and angulation (41.9° vs. 31.4°, respectively; p = 0.23) compared with patients without TLR, although these differences did not reach statistical significance.

Reproducibility of curvature and angle measurements. Interobserver reproducibility for curvature assessment had an r² Pearson correlation coefficient of 0.84 and ICCa of 0.92 (excellent agreement). The mean ± SD difference between observers was 0.022 ± 0.175 cm⁻¹. Interobserver reproducibility for angulation assessment was 0.86 for the r² Pearson correlation



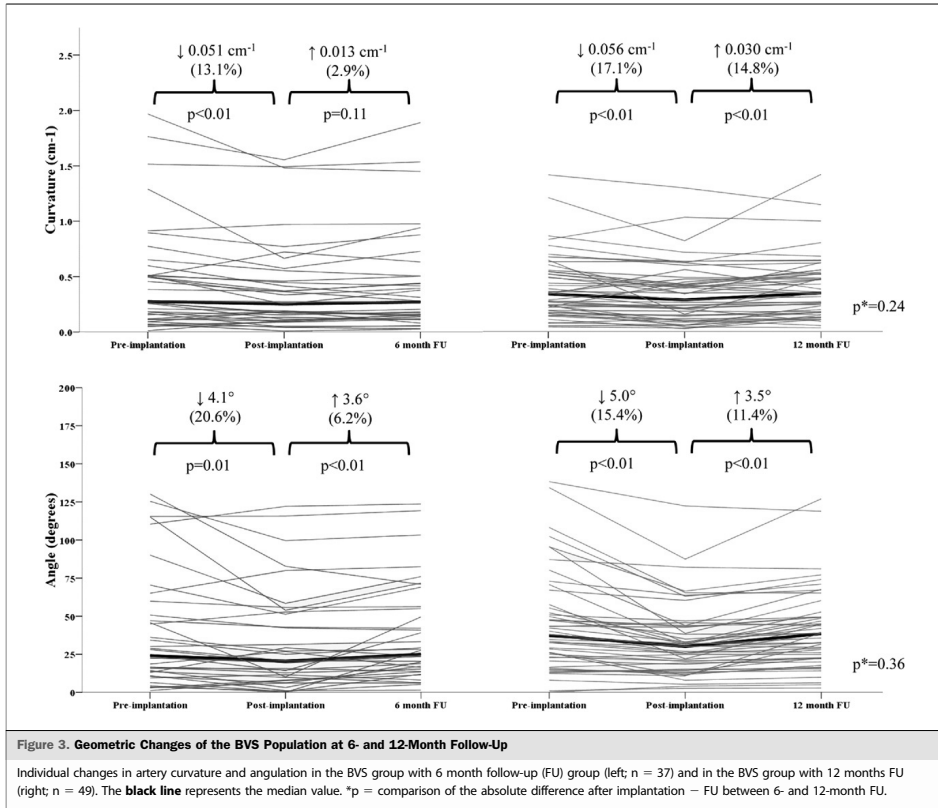
coefficient and 0.91 for the ICCa (excellent agreement). The mean \pm SD difference between observers was $5.3^\circ \pm 11.2^\circ$.

Discussion

The major findings of the present study are: 1) both BVS and MPS decreased the coronary curvature, angulation, and systo-diastolic changes from pre- to post-implantation; 2) from post-implantation to follow-up, the BVS significantly increased the artery curvature and angulation except for the systo-diastolic changes in curvature and angulation, and the MPS showed a slight increase in angulation but retained the artery curvature and the systo-diastolic changes in curvature and angulation as measured after implantation; 3) at follow-up, the BVS presented with a minor reduction in coronary curvature with respect to that seen before implantation, although the coronary angulation and the cyclical changes in curvature and angulation were similar to that seen before implantation; and 4) from pre-implantation to

follow-up, the MPS presented with an important reduction in all geometric parameters. These results were larger and more evident when the one-half of the population with higher values of curvature and angulation was investigated.

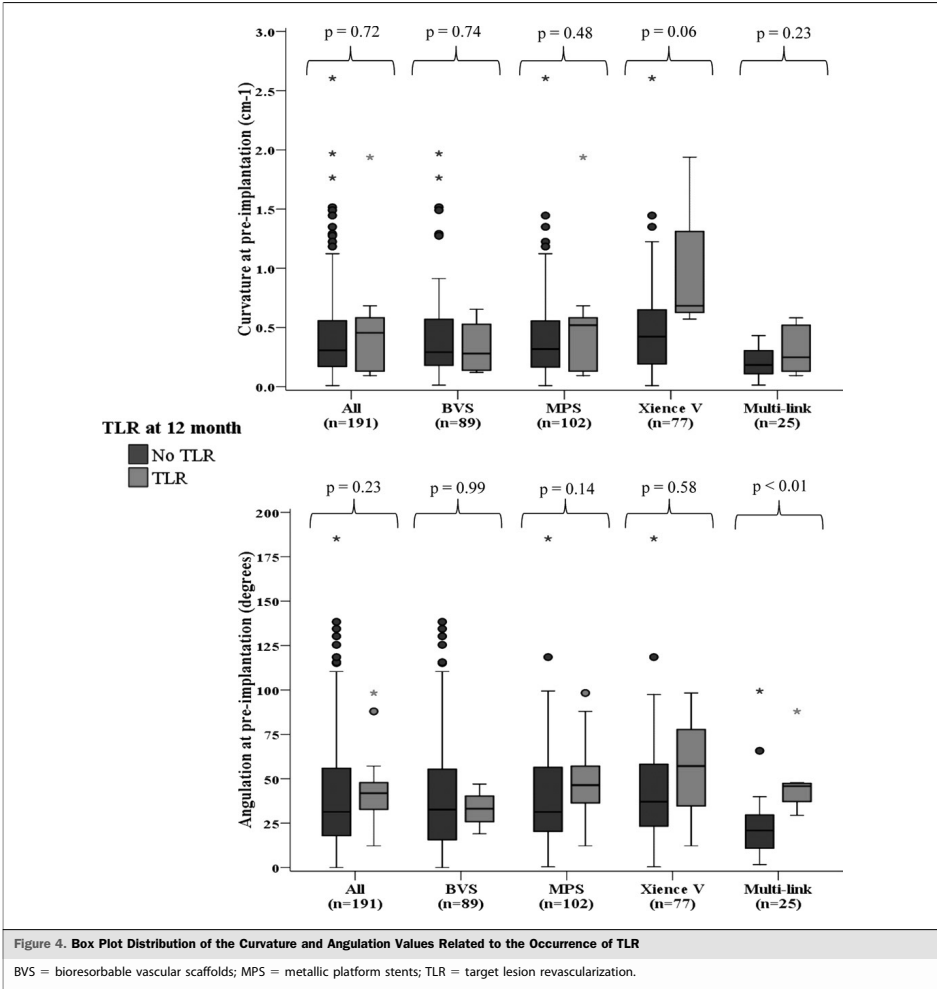
To the best of our knowledge, the present study is the first to report an increase in geometric parameters from post-implantation to follow-up in scaffolded segments. At 6- or 12-month follow-up, the anatomical configuration of the arteries treated with the ABSORB BVS allowed restoration of coronary geometry to values close to those measured before implantation. However, these differences were slightly different according to the follow-up. Patients with angiographic control at 12 months tended to show larger changes in geometric parameters compared with patients with angiographic control at 6 months. Figure 5 shows the changes in coronary geometry in 2 patients treated with the BVS and imaged at different follow-up periods (6 and 12 months). The most plausible explanation for the coronary



geometric changes observed in the present study is the gradual reduction in artery support and disappearance of the mechanical integrity of the scaffold in most of the patients at 6- to 12-month follow-up but especially in those patients who underwent angiographic control at 12 months. The first-generation BVS (1.0) showed an accelerated loss of the artery support during the first 6 months that resulted in an important shrinkage of the scaffold (21). The new generation of BVS (ABSORB) was redesigned to slow down the loss of artery support, compared with its previous generation, through modification of the manufacturing processes of the polymer and platform design (17). According to the manufacturer, the artery wall support provided by the ABSORB BVS is designed to gradually decrease during this period of restoration (3 to 12 months). By the end of the first year, the vast majority of amorphous polymer that links the crystalline lamella is hydrolyzed (15). Therefore, the

scaffold has gradually lost continuity of structure, allowing restoration of the original anatomical configuration.

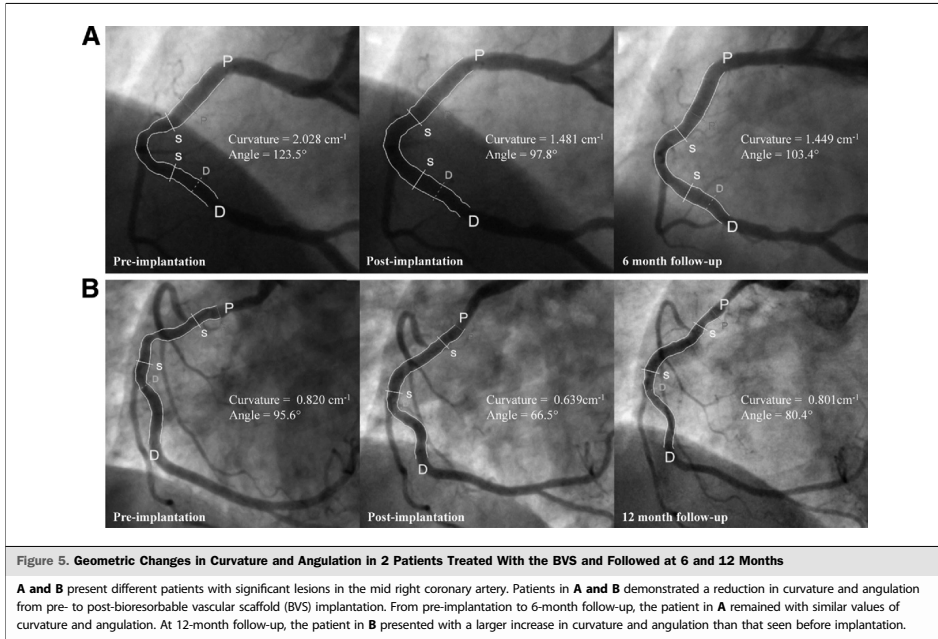
The potential clinical implications related to the restoration of the coronary geometry at follow-up are uncertain. It is noteworthy that, before the scaffold implantation, the physiological geometry of the treated segment developed an atherosclerotic lesion. The first bioresorbable scaffolds implanted in human coronary arteries (Igaki-Tamai, Igaki Medical Planning Company, Kyoto, Japan) have fulfilled 10-year clinical and intravascular ultrasound follow-up. The intravascular ultrasound imaging in patients that required TLR at long-term follow-up showed the presence of neoatherosclerotic plaques within the scaffolded segment (22). Therefore, it seems plausible that the restoration of the coronary anatomical configuration similar to that seen before implantation might also potentially restore the WSS conditions that triggered the formation of atherosclerotic plaques, if drastic preventive measures are not taken.



Conversely, Figure 4 shows a trend toward higher values of curvature and angulation before implantation in patients with TLR at 12 months, compared with those without revascularization. These differences mildly differed, depending on the implanted stent/scaffold. With BVS, differences in curvature and angulation before implantation in patients without TLR (median values: 0.292 cm^{-1} and 32.6° , respectively) and with TLR at 12 months (0.280 cm^{-1} and 33.1° , respectively) were minimal ($p = 0.74$ and $p = 0.99$, respectively). With MPS,

curvature and angulation tended to be slightly smaller in patients without TLR (0.318 cm^{-1} and 31.4° , respectively), compared with patients with TLR at 12 months (0.519 cm^{-1} and 46.4° , respectively); $p = 0.48$ and $p = 0.14$, respectively. However, the present study was not sufficiently powered to relate coronary geometric parameters with clinical outcomes, and these results should be interpreted carefully.

Previous reports using BMS found higher risk of restenosis in angulated and curved arteries. A pre-treatment



angulation $\geq 33.5^{\circ}$ was found as an independent predictor of restenosis at 10 months of follow-up (8). However, with the use of SES, to date no study has been able to relate the artery curvature/angulation before implantation with a greater neointimal response or higher risk of restenosis (7,10,23). However, most of these studies are limited to clinical outcomes at midterm follow-up. It is uncertain whether the progressive late lumen loss experienced by SES at long-term follow-up can modify the relationship between artery bend, curvature, and angulation and stent restenosis at longer-term follow-up. The first-generation SES has shown a progressive reduction of MLD from 6 to 18 months of 0.28 mm, whereas the delayed late lumen loss was smaller with the first-generation PES in the same period (0.10 mm; $p < 0.01$) (12). The Xience everolimus-eluting stent has also been associated with a progressive reduction in the MLD from 6 to 24 months (delayed late lumen loss of 0.16 mm) and therefore can also be influenced by the effect of WSS at long-term follow-up (24).

Study limitations. The first limitation of the present study is the use of 2-dimensional images to assess the geometric parameters of coronary arteries. Coronary arteries have a 3-dimensional geometric shape that is in continuous movement (4-dimensional), despite the use of the least foreshort-

ened view. For these reasons, the 2-dimensional analysis of coronary geometry is clearly biased by foreshortening of the angiographic views. However, a reliable 3-dimensional reconstruction of coronary arteries, based on angiographic images, requires a biplane system or rotational angiography (25,26). Almost all images of patients included in the ABSORB and SPIRIT trials were acquired with monoplane angiograms in such way that the 3-dimensional reconstruction would not have been reliable. Second, the non-normal distribution of curvature and angulation values, with a relatively high number of extreme values, caused a moderate variability for repeated measures between different observers when extreme values of curvature and angulation were assessed. The exclusion of extreme curved and angulated lesions (curvature $>0.900 \text{ cm}^{-1}$ and angulation $>90^{\circ}$) substantially improved the variability between observers to $0.016 \pm 0.086 \text{ cm}^{-1}$ for curvature and $4.3 \pm 7.2^{\circ}$ for angulation. The results of the present study were also reproducible (data not shown), taking into account the interobserver variability for repeated measurements ($2 \times \text{SD}$), with and without extreme values. The third limitation is the small number of patients included in our study. The possible relationship between coronary geometry and clinical outcomes reported in the present study is clearly underpowered and needs to be interpreted with caution. Finally, the fourth limitation of

the study is the difference in the time of follow-up of the ABSORB trial patients. It was decided, as per protocol, to split the population into 2 groups to assess the bioresorption process with multiple intravascular imaging techniques in different time-points. Although a possible restoration of the coronary artery to its pre-implantation anatomical configuration in patients treated with metallic stents at 12-month follow-up seems improbable, we do not have angiographic control at 12 months for MPS SPIRIT patients.

Conclusions

At midterm follow-up, the BVS tended to allow restoration of the coronary geometry and systo-diastolic movements of the coronary arteries similar to that seen before implantation. Coronary geometry and systo-diastolic movements of coronary arteries treated with MPS remained similar to that seen after implantation. Potential clinical benefits of restoring the pre-implantation coronary anatomy will require longer-term clinical follow-up in a larger patient group.

Acknowledgments

The authors thank Pie Medical for reviewing the manuscript. The authors also thank the Biomedical Research Institution of Bellvitge (IDIBELL) for the grant awarded to Dr. Gomez-Lara.

Reprint requests and correspondence: Dr. Patrick W. Serruys, Department of Interventional Cardiology, Thoraxcenter, Erasmus MC, 's-Gravendijkwal 230, 3015 CE, Rotterdam, the Netherlands. E-mail: p.w.j.c.serruys@erasmusmc.nl.

REFERENCES

- Malek AM, Alper SL, Izumo S. Hemodynamic shear stress and its role in atherosclerosis. *JAMA* 1999;282:2035–42.
- Asakura T, Karino T. Flow patterns and spatial distribution of atherosclerotic lesions in human coronary arteries. *Circ Res* 1990;66:1045–66.
- Wentzel JJ, Janssen E, Vos J, et al. Extension of increased atherosclerotic wall thickness into high shear stress regions is associated with loss of compensatory remodeling. *Circulation* 2003;108:17–23.
- Koskinas KC, Feldman CL, Chatzizisis YS, et al. Natural history of experimental coronary atherosclerosis and vascular remodeling in relation to endothelial shear stress: a serial, in vivo intravascular ultrasound study. *Circulation* 2010;121:2092–101.
- LaDisa JF Jr., Guler I, Olson LE, et al. Three-dimensional computational fluid dynamics modeling of alterations in coronary wall shear stress produced by stent implantation. *Ann Biomed Eng* 2003;31:972–80.
- Wentzel JJ, Krams R, Schuurbers JC, et al. Relationship between neointimal thickness and shear stress after Wallstent implantation in human coronary arteries. *Circulation* 2001;103:1740–5.
- Papafaklis MI, Bourantas CV, Theodorakis PE, et al. The effect of shear stress on neointimal response following sirolimus- and paclitaxel-eluting stent implantation compared with bare-metal stents in humans. *J Am Coll Cardiol Intv* 2010;3:1181–9.
- Gyongyosi M, Yang P, Khorsand A, Glogar D, Austrian Wiktor Stent Study Group and European Paragon Stent Investigators. Longitudinal straightening effect of stents is an additional predictor for major adverse cardiac events. *J Am Coll Cardiol* 2000;35:1580–9.
- Phillips PS, Alfonso F, Segovia J, et al. Effects of Palmaz-Schatz stents on angled coronary arteries. *Am J Cardiol* 1997;79:191–3.
- Fukuda Y, Shirai K, Miura S, et al. The impact of angulated lesions on angiographic late loss in patients with drug-eluting stent implantation. *J Cardiol* 2009;53:396–401.
- Rathore S, Terashima M, Kato H, et al. Predictors of angiographic restenosis after drug eluting stents in the coronary arteries: contemporary practice in real world patients. *EuroIntervention* 2009;5:349–54.
- Park KW, Kim CH, Lee HY, et al. Does "late catch-up" exist in drug-eluting stents: insights from a serial quantitative coronary angiography analysis of sirolimus versus paclitaxel-eluting stents. *Am Heart J* 2010;159:446–53.e3.
- Schmidt W, Lanzer P, Behrens P, Topoleski LD, Schmitz KP. A comparison of the mechanical performance characteristics of seven drug-eluting stent systems. *Catheter Cardiovasc Interv* 2009;73:350–60.
- Gomez-Lara J, Garcia-Garcia HM, Onuma Y, et al. A comparison of the conformability of everolimus-eluting bioresorbable vascular scaffolds to metal platform coronary stents. *J Am Coll Cardiol Intv* 2010;3:1190–8.
- Oberhauser J, Hossainy S, Rapoza R. Design principles and performance of bioresorbable polymeric vascular scaffolds. *EuroIntervention* 2009;5 Suppl F:F15–22.
- Onuma Y, Serruys PW, Perkins LE, et al. Intracoronary optical coherence tomography and histology at 1 month and 2, 3, and 4 years after implantation of everolimus-eluting bioresorbable vascular scaffolds in a porcine coronary artery model: an attempt to decipher the human optical coherence tomography images in the ABSORB trial. *Circulation* 2010;122:2288–300.
- Serruys PW, Onuma Y, Ormiston JA, et al. Evaluation of the second generation of a bioresorbable everolimus drug-eluting vascular scaffold for treatment of de novo coronary artery stenosis: six-month clinical and imaging outcomes. *Circulation* 2010;122:2301–12.
- Serruys PW, Ong AT, Piek JJ, et al. A randomized comparison of a durable polymer everolimus-eluting stent with a bare metal coronary stent: the SPIRIT first trial. *EuroIntervention* 2005;1:58–65.
- Serruys PW, Ruygrok P, Neuzner J, et al. A randomised comparison of an everolimus-eluting coronary stent with a paclitaxel-eluting coronary stent: the SPIRIT II trial. *EuroIntervention* 2006;2:286–94.
- Fleiss J. *The Design and Analysis of Clinical Experiments*. New York, NY: John Wiley & Sons, 1986.
- Ormiston JA, Serruys PW, Regar E, et al. A bioabsorbable everolimus-eluting coronary stent system for patients with single de-novo coronary artery lesions (ABSORB): a prospective open-label trial. *Lancet* 2008;371:899–907.
- Nishio S, Kosuga K, Okada M, et al. Long Term (>10 Years) Clinical Outcomes of the First-In-Man Biodegradable Poly-L-Lactic Acid Coronary Stents. Presented at: EuroPCR 2010; Paris, France.
- Gijsen FJ, Oortman RM, Wentzel JJ, et al. Usefulness of shear stress pattern in predicting neointima distribution in sirolimus-eluting stents in coronary arteries. *Am J Cardiol* 2003;92:1325–8.
- Claessen BE, Beijk MA, Legrand V, et al. Two-year clinical, angiographic, and intravascular ultrasound follow-up of the XIENCE V everolimus-eluting stent in the treatment of patients with de novo native coronary artery lesions: the SPIRIT II trial. *Circ Cardiovasc Interv* 2009;2:339–47.
- Tu S, Koning G, Jukema W, Reiber H. Assessment of obstruction length and optimal viewing angle from biplane X-ray angiograms. *Int J Cardiovasc Imaging* 2010;26:5–17.
- Bruining N, Tanimoto S, Otsuka M, et al. Quantitative multi-modality imaging analysis of a bioabsorbable poly-L-lactic acid stent design in the acute phase: a comparison between 2- and 3D-QCA, QCU and QMSCT-CA. *EuroIntervention* 2008;4:285–91.

Key Words: bioresorbable vascular scaffolds (BVS) ■ coronary geometry ■ metallic platform stent (MPS).

6.2

Comparison of in vivo eccentricity and symmetry indices between metallic stents and bioresorbable vascular scaffolds: Insights from the ABSORB and SPIRIT trials.

Salvatore Brugaletta, Josep Gomez-Lara, Roberto Diletti, Vasim Farooq, Robert Jan van Geuns, Bernard de Bruyne, Dariusz Dudek, Hector M Garcia-Garcia, John A Ormiston, Patrick W Serruys

Catheter Cardiovasc Interv 2012;79:219-28

Comparison of In Vivo Eccentricity and Symmetry Indices Between Metallic Stents and Bioresorbable Vascular Scaffolds: Insights From the ABSORB and SPIRIT Trials

Salvatore Brugaletta,^{1,2} MD, Josep Gomez-Lara,¹ MD, Roberto Diletti,¹ MD, Vasim Farooq,¹ MBChB, MRCP, Robert Jan van Geuns,¹ MD, Bernard de Bruyne,³ MD, Dariusz Dudek,⁴ MD, Hector M. Garcia-Garcia,^{1,5} MD, PhD, John A. Ormiston,⁶ MBChB, PhD, and Patrick W. Serruys,^{1*} MD, PhD

Objective: To compare the geometrical parameters of a bioresorbable vascular scaffold (BVS) with a standard metallic stent. **Background:** The introduction of polymeric bioresorbable materials in the design of novel coronary scaffolds may affect some geometrical parameters, such as eccentricity and symmetry indices, previously introduced as IVUS criteria for optimal metallic stent deployment. **Methods:** From ABSORB Cohort A, ABSORB Cohort B, SPIRIT I, and SPIRIT II, all patients implanted with BVS 1.0, BVS 1.1, or XIENCE V, respectively and intravascular ultrasound analyses post-implantation were selected. The eccentricity index was calculated frame by frame and expressed as an average per device (minimum diameter/maximum diameter). The symmetry index of the device was reported as [(maximum diameter – minimum diameter)/maximum diameter]. Six months major adverse cardiac events (MACE) were analyzed. **Results:** A total of 242 patients were selected (BVS 1.0: $n = 28$, BVS 1.1: $n = 94$, XIENCE V: $n = 120$). The BVS exhibited a significantly lower eccentricity index (BVS 1.0: 0.83 ± 0.09 ; BVS 1.1: 0.85 ± 0.08 ; XIENCE V: 0.90 ± 0.06 ; $P < 0.01$) and a significantly higher symmetry index (BVS 1.0: 0.30 ± 0.07 ; BVS 1.1: 0.31 ± 0.06 , XIENCE V 0.26 ± 0.07 ; $P < 0.01$) as compared to the XIENCE V. An inverse correlation was found between the symmetry and eccentricity indices for both (BVS $r = -0.69$, $P < 0.01$; XIENCE V $r = -0.61$, $P < 0.01$). No differences in MACE were detected between the groups according to their geometrical parameters. **Conclusions:** The introduction of a new polymeric material in the design of BVS resulted in a lower eccentricity index and a higher symmetry index as compared to metallic stents, without detectable impact in MACE, at 6 months. © 2011 Wiley-Liss, Inc.

Key words: BVS; eccentricity; symmetry; IVUS; XIENCE V

INTRODUCTION

The introduction of intravascular ultrasound (IVUS) and high pressure implantation of coronary stents in

interventional cardiology practice have had a significant impact on stent deployment [1,2]. The MUSIC trial showed how the use of IVUS criteria (such as

¹Thoraxcenter, Erasmus MC, Rotterdam, The Netherlands

²Thorax Institute, Hospital Clinic, University of Barcelona, Barcelona, Spain

³Cardiovascular Center Aalst, Belgium

⁴Jagiellonian University, Krakow, Poland

⁵Cardialysis B.V., Rotterdam, The Netherlands

⁶Auckland City Hospital, Auckland, New Zealand

Conflict of interest: Nothing to report.

*Correspondence to: Prof. Patrick W. Serruys, MD, PhD, Thoraxcenter, Ba-583's Gravendijkwal 230,3015 CE Rotterdam, The Netherlands. E-mail: p.w.j.c.serruys@erasmusmc.nl

Received 10 January 2011; Revision accepted 16 January 2011

DOI 10.1002/ccd.22996

Published online in Wiley Online Library (wileyonlinelibrary.com)

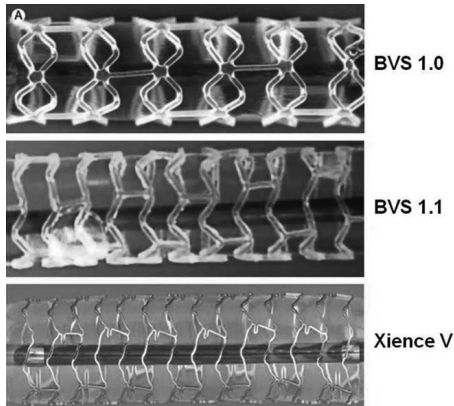


Fig. 1. Pictures of BVS 1.0, BVS 1.1, and XIENCE V.

complete apposition of the stent against the vessel wall; in-stent minimal lumen area $\geq 90\%$ of the average reference lumen area; eccentricity index ≥ 0.7), may positively contribute to the immediate and 6-month clinical and angiographic outcomes [3]. A meta-analysis from the BENESTENT and MUSIC trials further confirmed how the IVUS guidance is responsible for reduction in restenosis rate [4,5].

Some geometrical stent parameters, such as eccentricity and symmetry, easily detectable by IVUS, have previously been demonstrated to be related to either favorable or adverse clinical outcomes [3,6]. With the transition from a metallic stent to a polymeric bioresorbable platform, the need for the re-evaluation of these geometrical parameters is required at short and long term.

In the present analysis, we evaluated the eccentricity and symmetry indices of the bioresorbable vascular scaffold (BVS) in the ABSORB trials and compared these to the XIENCE V stent from the SPIRIT trials.

METHODS

Study Population

For the present analysis, we screened all patients from ABSORB (Cohort A and B) and SPIRIT I [7] and II [8] trials, and selected all the patients with available IVUS data post-device implantation. These patients were then subdivided into three groups according to the device implanted (BVS 1.0, BVS 1.1 and XIENCE V, all Abbott Vascular, Santa Clara, CA). The design of the ABSORB studies has been previously described [9–11].

Briefly, in the ABSORB Cohort A trial (NCT00300131), patients with a diagnosis of stable or unstable angina or silent ischemia, were enrolled. All treated lesions were single and de novo in a native coronary artery of 3.0 mm diameter, shorter than 8 mm for the 12-mm stent and shorter than 14 mm for the 18-mm stent, with a diameter stenosis greater than 50% and less than 100%, and with a thrombolysis in myocardial infarction (TIMI) flow grade more than 1. All lesions were treated by implantation of BVS 1.0 (3.0 \times 12 mm and 3.0 \times 18 mm). The ABSORB Cohort B trial (NCT00856856) enrolled patients with the same clinical profile and lesion type. All lesions were treated by implantation of a BVS 1.1 (3.0 \times 18 mm) [11].

The SPIRIT trials were planned to assess the safety and efficacy of the everolimus eluting stent (XIENCE V) in patients with coronary artery disease. SPIRIT I and II were prospective, multicenter, single-blinded, randomized-controlled clinical investigations which compared XIENCE V with either the bare Multi-Link VISION metal (Abbott Vascular, Santa Clara, CA, SPIRIT I trial, NCT00180453) or paclitaxel-eluting (Boston Scientific, Natick, MA, SPIRIT II trial, NCT00180310) stents [7,8]. The exclusion criteria of the two SPIRIT trials were similar to those of the ABSORB trials. All the trials had previously been approved by the ethics committee at each participating institution with written informed consent obtained for each patient before inclusion.

Quantitative Coronary Angiography Analysis of Vessels Pretreatment

Quantitative coronary angiography (QCA) pre-treatment was performed by an independent core laboratory (Cardialysis BV, Rotterdam, The Netherlands), using the CAAS II analysis system (Pie Medical BV, Maastricht, Netherlands). For each pre-treatment angiogram, the treated and the peri-treated regions (defined by a length of 5-mm proximal and distal to the device edge) were analyzed. The following QCA parameters were computed: computer-defined minimum lumen diameter (MLD), reference vessel diameter (RVD), obtained by the interpolate method, and percentage diameter stenosis [12].

Study Devices

The BVS has an amorphous poly-DL-lactide (PDLLA) coating that contains and controls the release of the anti-proliferative drug everolimus (Fig. 1). The scaffold body is made of semi-crystalline poly-L-lactide (PLLA). PLLA is completely degraded via hydrolysis and bioresorbed via the Krebs cycle [9,10]. Physically, the scaffold has struts with an approximate thickness of 150 μm .

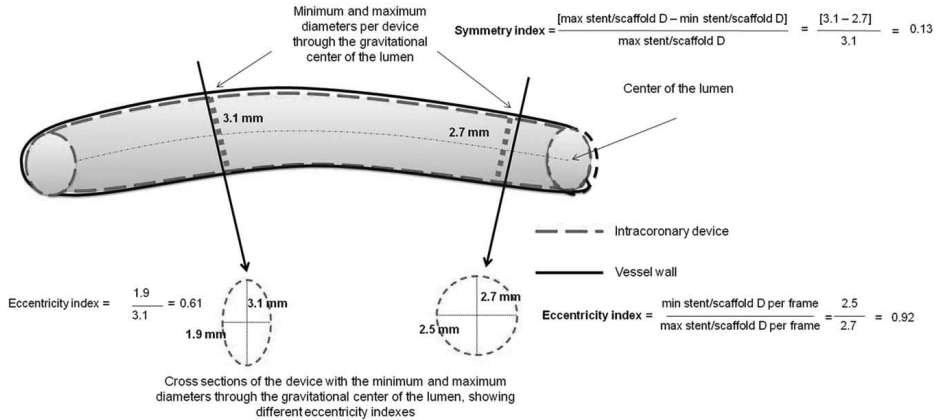


Fig. 2. Relationship between the symmetry and eccentricity indices of an intracoronary device. Minimum and maximum diameters over the length of the device are shown. Two cross-sections with different eccentricity indexes are also shown.

There are no differences in polymeric material, drug dose, drug release, or strut thickness between BVS revisions 1.0 and 1.1. Of note, the BVS revision 1.1 has a smaller maximum circular unsupported surface area compared to revision 1.0, with the struts arranged as in-phase zigzag hoops linked together by three longitudinal links, similar to the XIENCE V design [13].

The XIENCE V stent is an everolimus-eluting, cobalt chromium alloy device with a platform consisting of serpentine rings connected by links fabricated from a single piece. The strut thickness is 81 μm with the polymer and drug coating adding a further thickness of 7 μm to the overall thickness.

Lesions were treated with standard interventional techniques, with mandatory pre-dilatation, using a balloon shorter and 0.5 mm smaller in diameter than the study device. The study device was implanted at a pressure not exceeding the rated burst pressure. Post-dilatation with a balloon shorter than the implanted device was allowed at the operator's discretion, as was bailout treatment.

Intravascular Ultrasound Analysis

Post-procedure treated vessel segments were examined with mechanical (Atlantis, Boston Scientific, Natick, MA) or phased array (Eagle-eye Volcano, Rancho Cordova, CA) intravascular ultrasound (IVUS), using automated pullbacks at 0.5 mm per second after administration of 0.2 mg intracoronary nitroglycerin. IVUS analyses were performed by an independent core

laboratory (Cardialysis BV, Rotterdam, The Netherlands). Only the lesions implanted with a BVS 1.0, BVS 1.1, or a XIENCE V were included in the analysis. A computer-based contour detection program was used for automated 2D reconstruction of the treated segment. The lumen, stent/scaffold boundaries and external elastic membrane (vessel boundaries) were detected using a minimum cost algorithm [14].

For each treated vessel segment, we analyzed frame by frame the lumen, device implanted (stent/scaffold), plaque, and vessel area and upfront selected the site (single frame) of minimum stent/scaffold area (MSA). The MSA is classically described as the flow-limiting area and has been previously related to angiographic and clinical outcomes [15,16]. In each frame, we obtained the "projected" diameters of the stent/scaffold, as previously described and validated [17].

For each device implanted we therefore calculated:

- Eccentricity index at the MSA frame, as a ratio between the minimum and maximum diameters in that frame; [3,18]
- Eccentricity index, as the average of all eccentricity indices of each frame; [3,18]
- Symmetry index as [maximum stent/scaffold diameter in a single frame minus minimum stent/scaffold diameter in a single frame] divided by the maximum stent/scaffold diameter [19]. Note that the maximum and the minimum stent/scaffold diameters in this calculation were possibly located in two different frames over the length of the device implanted (Fig. 2).

Intravascular Ultrasound Assessment of Lesion Calcification

The MSA frames selected upfront for each lesion were also assessed by two experienced cardiologists to quantify calcium, as previously described [19–22]. Calcium produced bright echoes (using the adventitia as reference) with acoustic shadowing (attenuation) of deeper arterial structures. The extent and distribution of lesion calcification were assessed as follows:

- The location of the calcium was defined as superficial (calcium at the intimal/lumen interface or closer to the lumen than to the adventitia), deep (calcium at the media/adventitia border or closer to the adventitia than to the lumen), or both.
- The largest arc of calcium was measured in degrees with a protractor centered on the lumen. If there was more than one deposit of calcium in the frame, the total arc of calcium for that frame was obtained by adding up the arcs of each individual deposit. Calcification was then classified as none, one-quadrant ($\leq 90^\circ$), two-quadrant (91° to 180°), three-quadrant (181° to 270°), or four-quadrant (271° to 360°) calcification.

Statistical Analysis

Categorical variables are presented as counts and percentages and compared by means of the Chi-square test. Continuous variables are presented as means \pm standard deviation (SD). The distribution of the variables was tested as normal or non normal by Kolmogorov-Smirnov test. Depending on the distribution of the data, comparison between groups was made with the ANOVA test with Bonferroni correction or with the Kruskal-Wallis test with Dunn correction for multiple comparisons. Correlation between parameters was performed by Pearson or Spearman test, depending on their distribution. Cardiac death, any acute myocardial infarction and ischemia-driven target lesion revascularization at 6-month follow-up were considered as major cardiac events (MACE), according to the original protocol of ABSORB A and B trials, and SPIRIT I and II trials [7,8,10]. The threshold between the considered normal and non normal value for the eccentricity index was ≥ 0.7 , as previously described [3,11]. A multivariate linear regression analysis was tested for the independent predictors of eccentricity index: symmetry index, type of lesion according to AHA/ACC classification, target vessel, size of the device as a categorical variable (size of 3.0×18 mm or not) and device implanted (BVS vs. XIENCE V) were introduced in the model. A two side P -value < 0.05 was considered as significant. Statistical analyses were performed with use of SPSS 13.0 software (SPSS, Chicago, IL).

RESULTS

Baseline Clinical and Angiographic Characteristics

We studied 242 patients (249 lesions) with available post-stent/scaffold implantation IVUS analyses and subdivided these into three groups according to the device implanted. Group 1 (28 patients): ABSORB Cohort A trial, BVS 1.0; group 2 (94 patients): ABSORB Cohort B trial, BVS 1.1, and group 3 (120 patients/127 lesions): SPIRIT I and II trials, XIENCE V stent. Table I shows the baseline clinical characteristics.

No significant differences were found between the groups in the pre-treatment QCA analysis. The diameter and the length of the stents/scaffold implanted were significantly different between the groups (both $P < 0.0001$). In particular, only two (7.1%) patients from group 1 received a BVS 1.0 3.0×18 mm, while all the patients (100%) from group 2 received a BVS 1.1 3.0×18 mm, and 37 patients (31%) from group 3 received a XIENCE V 3.0×18 mm.

Six-month follow-up data were available in 225 patients (92.9%). A total of 7 MACE were recorded: 1 (3.5%) MACE was recorded for BVS 1.0 [9], 4 (4.2%) MACE for BVS 1.1 [11], and 2 (1.9%) MACE for XIENCE V [7,8].

Intravascular Ultrasound Analysis After Implantation

Both the mean lumen area and the MSA were significantly lower for the BVS 1.0 and 1.1 compared to XIENCE V ($P < 0.001$; Table II). However, in a further sub-analysis, including only the stents with the same size (3.0×18 mm²), no significant differences were found between the groups in terms of mean lumen area ($P = 0.368$) and post-procedural MSA ($P = 0.268$).

Eccentricity and Symmetry Index After Implantation

The eccentricity index, either average-of-all-frames or at the MSA, was significantly lower for BVS 1.0 and 1.1 as compared to XIENCE V (both $P < 0.001$). Conversely, the symmetry index was significantly lower for XIENCE V compared to BVS 1.0 and BVS 1.1 ($P < 0.001$) (Fig. 3). Analyzing the 3.0×18 mm stents alone, the BVS maintained a lower eccentricity index and a higher symmetry index compared to XIENCE V (both $P < 0.001$). No significant differences were found, in terms of eccentricity and symmetry index, when comparing the 3.0×18 mm devices against other sizes (Table III).

Whilst no patients demonstrated an average eccentricity index per stent below the threshold of 0.7, 10

TABLE I. Clinical and Angiographic Baseline Characteristics

	BVS 1.0 (patients/lesions = 28)	BVS 1.1 (patients/lesions = 94)	XIENCE V (patients = 120; lesions = 127)	P-value
Age, mean \pm SD	62.0 \pm 9.0	60.7 \pm 8.9	61.6 \pm 10.5	0.90
Male, % (n)	57.1 (16)	61.7 (58)	76.6 (92)	0.23
Hypertension requiring medication, % (n)	57.1 (16)	56.3 (53)	68.3 (82)	0.49
Hyperlipidaemia requiring medication, % (n)	60.7 (17)	65.9 (62)	77.5 (93)	0.57
Smokers, % (n)	21.4 (6)	15.9 (15)	36.6 (44)	0.05
Diabetes, % (n)	3.5 (1)	15.9 (15)	20 (24)	0.20
Previous PCI, % (n)	3.5 (1)	4.2 (4)	6.6 (8)	0.82
Previous AMI, % (n)	7.1 (2)	17.0 (16)	40 (48)	0.04
Renal Impairment, % (n)	3.5 (1)	2.1 (2)	1.6 (2)	0.71
Stable angina, % (n)	71.4 (20)	63.8 (60)	64.1 (77)	0.41
Unstable angina, % (n)	25.1 (7)	31.9 (30)	33.3 (40)	0.01
Silent ischaemia, % (n)	3.5 (1)	4.3 (4)	2.6 (3)	0.48
Target vessel, % (n)				
Left anterior descending	53.5 (15)	44.6 (42)	48.8 (62)	0.83
Left Circumflex	25.0 (7)	22.3 (21)	22.8 (29)	0.69
Right coronary artery	21.5 (6)	33.1 (31)	28.4 (36)	0.78
AHA/ACC lesion classification, % (n)				
A	0 (0)	1 (1.1)	2 (1.5)	0.46
B1	18 (64.3)	52 (55.3)	34 (26.7)	0.01
B2	10 (35.7)	38 (40.4)	76 (59.8)	0.01
C	0 (0)	3 (3.2)	15 (12)	0.01
Diameter of stent implanted (mean \pm SD, mm)	3.0 \pm 0.0	3.0 \pm 0.0	3.17 \pm 0.3	0.01
Length of stent implanted (mean \pm SD, mm)	12.2 \pm 1.1	18.0 \pm 0.0	22.8 \pm 8.5	0.01
QCA analysis pre-treatment				
RVD (mean \pm SD, mm)	2.69 \pm 0.47	2.61 \pm 0.37	2.66 \pm 0.44	0.71
MLD (mean \pm SD, mm)	1.05 \pm 0.26	1.06 \pm 0.28	1.10 \pm 0.30	0.67
Diameter stenosis (mean \pm SD, %)	60 \pm 11	58 \pm 9	58 \pm 8	0.83

PCI = percutaneous coronary interventions; AMI = acute myocardial infarction; AHA/ACC = American heart association/American college of Cardiology; QCA = quantitative coronary angiography; RVD=reference vessel diameter; MLD: minimum lumen diameter.

TABLE II. Intravascular Ultrasound Postprocedure Data

	BVS 1.0 (28 lesions)	BVS 1.1 (94 lesions)	XIENCE V (127 lesions)	P-value between the groups	P-value XIENCE V vs. BVS 1.0 and BVS 1.1
Mean vessel area (mm ²)	13.22 \pm 3.65	14.13 \pm 3.38	14.84 \pm 3.91	0.113	0.151 vs. BVS 1.0 0.632 vs. BVS 1.1
Mean lumen area (mm ²)	6.01 \pm 1.09	6.42 \pm 1.03	7.22 \pm 1.65	<0.001	<0.001 for both
Mean plaque area (mm ²)	7.21 \pm 2.78	7.68 \pm 2.64	7.65 \pm 2.72	0.726	1.000 for both
Minimum stent/scaffold area (mm ²)	5.04 \pm 1.00	5.28 \pm 0.99	5.96 \pm 1.52	<0.001	<0.001 for both
Eccentricity index	0.86 \pm 0.05	0.88 \pm 0.03	0.92 \pm 0.03	<0.001	<0.001 for both
Eccentricity index at MSA frame	0.83 \pm 0.09	0.85 \pm 0.08	0.90 \pm 0.06	<0.001	<0.001 for both
Stent/scaffold symmetry index	0.30 \pm 0.07	0.31 \pm 0.06	0.26 \pm 0.07	<0.001	<0.001 for both

Data are expressed as mean \pm SD. BVS: bioresorbable vascular scaffold; MSA: Minimum stent/scaffold area.

patients (4.1%) exhibited an eccentricity index at the MSA below 0.7: two (7.1%) of these had a BVS 1.0, seven (7.4%) a BVS 1.1, and one (0.8%) a XIENCE V ($P = 0.023$). Only one MACE (10%) occurred in the patients with a value <0.7 ($n = 10$), whilst the remaining six MACE (2.5%) occurred in those patients with a value ≥ 0.7 ($n = 239$) (log rank test $P = 0.283$).

There was an inverse correlation between the symmetry and eccentricity indices for the XIENCE V ($r = -0.61$, $P < 0.01$) and BVS ($r = -0.69$, $P < 0.001$) (Fig. 4). Multivariate analysis demonstrated that independent

predictors of eccentricity index were the symmetry index ($P < 0.001$) and the implanted device ($P < 0.001$).

Eccentricity Index at MSA According to Lesion Calcification

By IVUS, calcium was identified at MSA in 129 frames (52%). When present, it was only superficial in 44 (34%), only deep in 57 (44%) and both superficial and deep in 28 (22%). The maximum arc of calcium measured was $42^\circ \pm 57^\circ$. The distribution of the

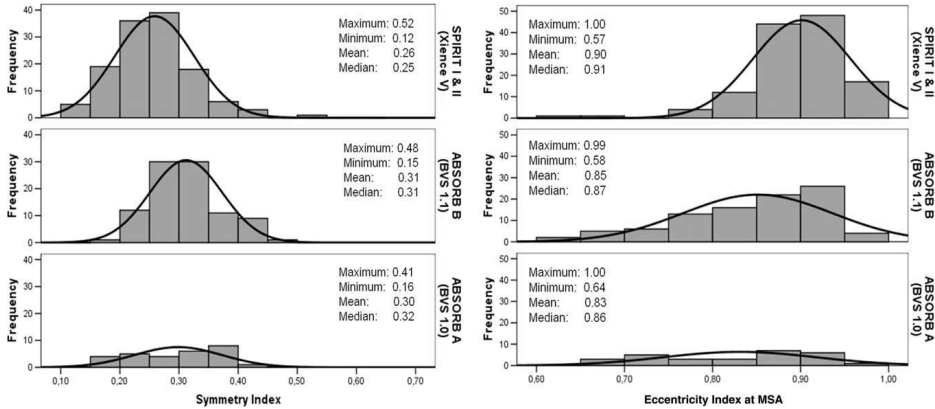


Fig. 3. Distribution of symmetry (left panel) and eccentricity index at MSA (right panel) between the groups. XIENCE V shows the lowest symmetry index and highest eccentricity index, significantly different compared to that of BVS 1.0 and BVS 1.1 ($P < 0.001$ in the comparison between all the groups, and $P < 0.001$ in post-hoc statistical analysis between XIENCE V vs. BVS 1.0 and BVS 1.1). MSA = minimum stent/scaffold area.

TABLE III. Eccentricity and Symmetry Index According to the Size of the Device

	3.0 × 18 mm	Other sizes	P-value
Eccentricity index XIENCE V	0.91 ± 0.03	0.92 ± 0.03	0.256
Symmetry index XIENCE V	0.27 ± 0.07	0.25 ± 0.07	0.101
Eccentricity index BVS	0.88 ± 0.03	0.86 ± 0.05	0.126
Symmetry index BVS	0.31 ± 0.06	0.30 ± 0.07	0.759

Data are expressed as mean ± SD. BVS: bioresorbable vascular scaffold.

maximum arc of calcium was one-quadrant in 76 (59%), two-quadrant in 41 (32%), three-quadrant in 12 (9%). Table IV shows the frequency and distribution of calcium between the groups.

Both BVS (0.82 ± 0.09 vs. 0.87 ± 0.08 , $P < 0.01$) and XIENCE V (0.89 ± 0.04 vs. 0.92 ± 0.04 , $P < 0.01$) exhibited a significantly lower eccentricity index at the MSA in presence of calcium compared to its absence. The eccentricity index at the MSA of BVS was significantly lower compared to XIENCE V, either with or without the presence of calcium, (both $P < 0.01$) (Fig. 5). No difference in eccentricity index was found between the groups according to the localization of calcium (deep, superficial or both). We observed that when there was a maximum arc of calcium in two or three quadrants, the eccentricity indices for both BVS (one-quadrant 0.85 ± 0.08 , two-quadrant 0.81 ± 0.08 , three-quadrant 0.72 , $P = 0.101$) and Xience V (one quadrant 0.91 ± 0.05 , two-quadrant 0.87 ± 0.06 , three-quadrant 0.87 ± 0.05 , $P = 0.005$) were lower as compared to the maximum arc of calcium being present in only one quadrant.

DISCUSSION

The major findings of our analysis are: (1) BVS exhibits a lower eccentricity index when compared to a metallic stent; (2) BVS tends to have a higher symmetry index compared to a metallic stent; nevertheless (3) these differences in geometrical parameters did not seem to generate clinical events in the small cohort of patients studied at 6 months.

Some properties influenced by stent material and design, such as conformability and flexibility, have previously been studied in various metallic stent platforms [23–25]. However, these geometrical parameters seen in the metallic stent era have to be re-evaluated with the recent introduction of the polymeric bioresorbable scaffolds [26,27].

The BVS 1.0 and 1.1 have different geometrical designs, but are manufactured from the same material. The BVS 1.1 and the XIENCE V have similar designs, but are made from differing materials. Our study shows that different values of eccentricity and symmetry are observed when comparing BVS with conventional metallic stents. We found that while an everolimus-eluting metallic stent tends to exhibit a symmetrical shape and a high eccentricity index after deployment, the everolimus-eluting BVS tends to have a less symmetrical shape and a low eccentricity index (Fig. 5). The relationship between these two parameters is inversely correlated for both devices, but the slope of this correlation is different (Fig. 3). Thus, device symmetry and

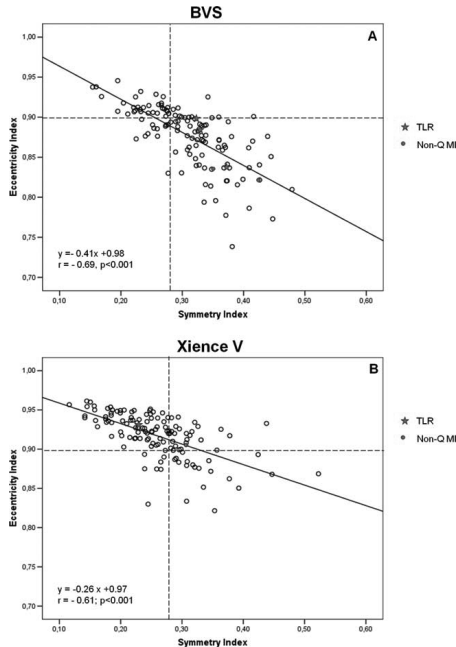


Fig. 4. Correlation between the symmetry and the eccentricity indices for BVS (Panel A) and XIENCE V (Panel B). Dotted lines represent the median value of symmetry and eccentricity indices in the overall population. Full dots and stars represent the patients who developed a MACE during the 6-month follow-up. Note that the majority of the BVS are distributed in the quadrant lower/right, while the XIENCE V in the quadrant upper/left. TLR = ischemia-driven target lesion revascularization; non-Q MI = non-Q myocardial infarction.

eccentricity seem to be related to the material rather than to the device design itself. The size of the device, and in particular its length, do not seem to have any significant influence on the eccentricity and symmetry of the devices, but—as expected—differences in device sizes appear to have an impact on the mean lumen area and the MSA after implantation. The characteristics of the lesion treated, evaluated by the ACC/AHA classification, do not seem to influence the eccentricity index, although they were differently distributed between the groups. Multivariate analysis, indeed, demonstrated symmetry index and type of the device implanted (BVS vs. XIENCE V) to be the only independent predictors of the eccentricity index.

We explored also the influence of lesion's calcification, estimated by IVUS, on the eccentricity index in

the MSA frame. As not all the patients included in the analysis received an intravascular ultrasound virtual histology (VH) imaging, we used a validated grey-scale IVUS methodology for calcium quantification [22]. In addition use of greyscale IVUS data overcomes the problem of VH dense calcium overestimation in the presence of a BVS or metallic stent, as the stent/scaffold struts are recognized as dense calcium by the VH [28,29]. We found that in presence of calcium the eccentricity at MSA frame for both devices is lower, confirming that BVS exhibits a lower eccentricity index compared to XIENCE V (Fig. 5).

It is noteworthy to consider that despite these differences in geometrical properties, BVS has previously been shown to have an acute recoil only slightly higher, but insignificantly different, from that of the XIENCE V, implying for both devices a sufficient radial strength to counteract the recoil of the vessel [26].

The different grade of eccentricity and symmetry of the BVS does not seem to generate clinical events, although our study was obviously underpowered to demonstrate this. An eccentricity value of 0.7 has previously been shown to be an acceptable cut-off in the evaluation of good stent expansion in the MUSIC trial, with favorable angiographic results seen at 6-month follow-up [3]. Otake et al. found that a low eccentricity index may be associated with thrombus formation after sirolimus-eluting stent implantation [6]. Alfonso et al., analyzing the IVUS data of 12 consecutive patients with stent thrombosis, found that MUSIC criteria were not fulfilled in any patient [30]. Nevertheless, closer analysis of the single MUSIC criteria in each patient showed that the eccentricity index was above 0.7 in every case. Stent under-expansion or malapposition, inflow/outflow disease or edge dissections were suggested to be more important. These findings have also been confirmed in larger IVUS studies [31–33].

Limitations

The low risk nature of these patients may have contributed to their favorable outcomes and lower rate of MACE during follow-up. Therefore, the results may be difficult to generalize or to apply to a less selected patient population treated in different settings. A more complex type of lesions and patients are currently recruited in the ABSORB EXTEND registry that will enroll 1,000 patients.

CONCLUSION

The bioresorbable vascular scaffold appears to have reduced eccentricity index and increased symmetry index, when compared to conventional metallic stents,

TABLE IV. Frequency and Distribution of Calcium Between the Groups

	BVS 1.0 (28 lesions)	BVS 1.1 (94 lesions)	XIENCE V (127 lesions)	<i>P</i> value between the groups
Presence and location of calcium, <i>n</i> (%)				
No calcium	16 (57)	48 (51)	56 (44)	0.151
Only superficial	1 (3)	16 (17)	27 (21)	0.032
Only deep	9 (32)	20 (21)	28 (22)	0.346
Both superficial and deep	2 (8)	10 (11)	16 (13)	0.335
Distribution of the maximum arc, <i>n</i> (%)				
One quadrant ($\leq 90^\circ$)	10 (83)	34 (74)	32 (45)	0.041
Two-quadrant (91° – 180°)	2 (17)	11 (24)	28 (39)	0.038
Three-quadrant (181° – 270°)	0 (0)	1 (2)	11 (16)	0.061
Four-quadrant (271° – 360°)	0 (0)	0 (0)	0 (0)	na

BVS: bioresorbable vascular scaffold.

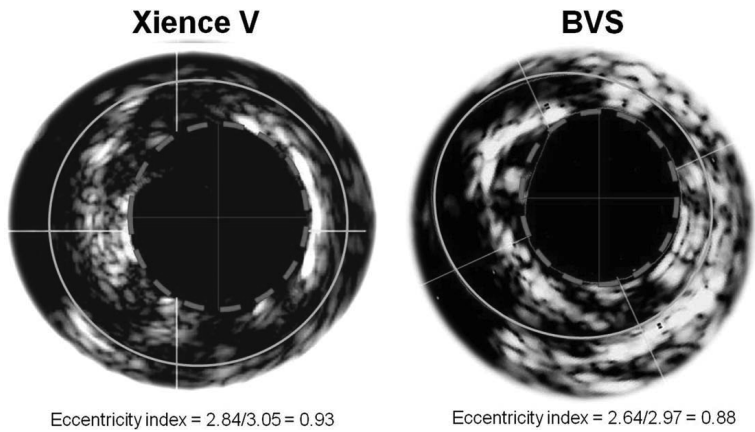


Fig. 5. Two examples of eccentricity index of XIENCE V and BVS in MSA frames in presence of calcium (from 7 to 11 o'clock). Red circles with dotted lines represent the stent/scaffold contours; the minimum and maximum diameters are drawn inside as continuous red line. Green lines represent the external elastic membrane. Note that the polymeric struts of the BVS are brighter and thicker than struts of XIENCE.

without detectable impact on 6-month MACE. Long term IVUS follow-up is required to assess the geometrical outcome of these devices and to ascertain the impact of these peri-procedural IVUS parameters on the long-term outcome.

ACKNOWLEDGEMENTS

The authors thank Leif Thuesen, Bernard Chevalier, Pieter Smits, Jacques Koolen, Dougal McClean, Stephan Windecker, Robert Whitbourn, and Ian Meredith for their help in recruiting the patients used in the present analysis. They thank Maria Radu, Cecile Dorange,

Dong Li, Susan Veldhof, Yoshinobu Onuma, and Nico Bruining for the critical review of the present manuscript.

REFERENCES

1. Goldberg SL, Colombo A, Nakamura S, Almagor Y, Maiello L, Tobis JM. Benefit of intracoronary ultrasound in the deployment of Palmaz-Schatz stents. *J Am Coll Cardiol* 1994;24:996–1003.
2. Serruys PW, Emanuelsson H, van der Giessen W, Lunn AC, Kiemeneij F, Macaya C, Rutsch W, Heyndrickx G, Suryapranata H, Legrand V, et al. Heparin-coated Palmaz-Schatz stents in human coronary arteries. Early outcome of the Benestent-II Pilot Study. *Circulation* 1996;93:412–422.

3. de Jaegere P, Mudra H, Figulla H, Almagor Y, Doucet S, Penn I, Colombo A, Hamm C, Bartorelli A, Rothman M, et al. Intravascular ultrasound-guided optimized stent deployment. Immediate and 6 months clinical and angiographic results from the multicenter ultrasound stenting in coronaries study (MUSIC Study). *Eur Heart J* 1998;19:1214-1223.
4. Serruys PW, Kay IP, Disco C, Deshpande NV, de Feyter PJ. Periprocedural quantitative coronary angiography after Palmaz-Schatz stent implantation predicts the restenosis rate at six months: Results of a meta-analysis of the Belgian Netherlands Stent study (BENESTENT) I. BENESTENT II Pilot, BENESTENT II, and MUSIC trials. Multicenter ultrasound stent in coronaries. *J Am Coll Cardiol* 1999;34:1067-1074.
5. de Feyter PJ, Kay P, Disco C, Serruys PW. Reference chart derived from post-stent-implantation intravascular ultrasound predictors of 6-month expected restenosis on quantitative coronary angiography. *Circulation* 1999;100:1777-1783.
6. Otake H, Shite J, Ako J, Shinke T, Tanino Y, Ogasawara D, Sawada T, Miyoshi N, Kato H, Koo BK, et al. Local determinants of thrombus formation following sirolimus-eluting stent implantation assessed by optical coherence tomography. *JACC Cardiovasc Interv* 2009;2:459-466.
7. Serruys PW, Ong AT, Piek JJ, Neumann FJ, van der Giessen WJ, Wiemer M, Zeiher A, Grube E, Haase J, Thuesen L, et al. A randomized comparison of a durable polymer Everolimus-eluting stent with a bare metal coronary stent: The SPIRIT I trial. *EuroIntervention* 2005;1:58-65.
8. Serruys PW, Ruysgrok P, Neuzner J, Piek JJ, Seth A, Schofer JJ, Richardt G, Wiemer M, Carrie D, Thuesen L, et al. A randomised comparison of an everolimus-eluting coronary stent with a paclitaxel-eluting coronary stent: The SPIRIT II trial. *EuroIntervention* 2006;2:286-294.
9. Ormiston JA, Serruys PW, Regar E, Dudek D, Thuesen L, Webster MW, Onuma Y, Garcia-Garcia HM, McGreevy R, Veldhof S. A bioabsorbable everolimus-eluting coronary stent system for patients with single de-novo coronary artery lesions (ABSORB): A prospective open-label trial. *Lancet* 2008;371:899-907.
10. Serruys PW, Ormiston JA, Onuma Y, Regar E, Gonzalo N, Garcia-Garcia HM, Nieman K, Bruining N, Dorange C, Miquel-Hebert K, et al. A bioabsorbable everolimus-eluting coronary stent system (ABSORB): 2-year outcomes and results from multiple imaging methods. *Lancet* 2009;373:897-910.
11. Serruys PW, Onuma Y, Ormiston JA, de Bruyne B, Regar E, Dudek D, Thuesen L, Smits PC, Chevalier B, McClean D, et al. Evaluation of the second generation of a bioresorbable everolimus drug-eluting vascular scaffold for treatment of de novo coronary artery stenosis: Six-month clinical and imaging outcomes. *Circulation* 2010;122:2301-2312.
12. Reiber JH, Serruys PW. *Quantitative Coronary Angiography: Methodologies*. Quantitative Coronary Angiography. Dordrecht, The Netherlands: Kluwer Academic Publishers; 1991, Vol. 98, p 102.
13. Okamura T, Garg S, Gutierrez-Chico JL, Shin ES, Onuma Y, Garcia HM, Rapoza R, Sudhir K, Regar E, Serruys PW. In-vivo evaluation of stent strut distribution patterns in the bioabsorbable everolimus-eluting device: An OCT ad hoc analysis of the Revision 1.0 and Revision 1.1 stent design in the ABSORB clinical trial. *EuroIntervention* 2010;932-938.
14. Hamers R, Bruining N, Knook M, Sabate M. A novel approach to quantitative analysis of intravascular ultrasound images. *Computers Cardiol* 2008;28:589-592.
15. Doi H, Maehara A, Mintz GS, Yu A, Wang H, Mandinov L, Popma JJ, Ellis SG, Grube E, Dawkins KD, et al. Impact of post-intervention minimal stent area on 9-month follow-up patency of paclitaxel-eluting stents: An integrated intravascular ultrasound analysis from the TAXUS IV, V, and VI and TAXUS ATLAS workhorse, long lesion, and direct stent trials. *JACC Cardiovasc Interv* 2009;2:1269-1275.
16. Sonoda S, Morino Y, Ako J, Terashima M, Hassan AH, Bonneau HN, Leon MB, Moses JW, Yock PG, Honda Y, et al. Impact of final stent dimensions on long-term results following sirolimus-eluting stent implantation: Serial intravascular ultrasound analysis from the sirius trial. *J Am Coll Cardiol* 2004;43:1959-1963.
17. Tsuchida K, Garcia-Garcia HM, Ong AT, Valgimigli M, Aoki J, Rademaker TA, Morel MA, van Es GA, Bruining N, Serruys PW. Revisiting late loss and neointimal volumetric measurements in a drug-eluting stent trial: Analysis from the SPIRIT I trial. *Catheter Cardiovasc Interv* 2006;67:188-197.
18. Costa MA, Sabate M, Kay IP, de Feyter PJ, Kozuma K, Serrano P, de Valk V, Albertal M, Ligthart JM, Disco C, et al. Three-dimensional intravascular ultrasonic volumetric quantification of stent recoil and neointimal formation of two new generation tubular stents. *Am J Cardiol* 2000;85:135-139.
19. Mintz GS, Nissen SE, Anderson WD, Bailey SR, Erbel R, Fitzgerald PJ, Pinto FJ, Rosenfield K, Siegel RJ, Tuzcu EM, et al. American college of cardiology clinical expert consensus document on standards for acquisition, measurement and reporting of intravascular ultrasound studies (IVUS). A report of the American college of cardiology task force on clinical expert consensus documents. *J Am Coll Cardiol* 2001;37:1478-1492.
20. Mintz GS, Pichard AD, Popma JJ, Kent KM, Satler LF, Bucher TA, Leon MB. Determinants and correlates of target lesion calcium in coronary artery disease: A clinical, angiographic and intravascular ultrasound study. *J Am Coll Cardiol* 1997;29:268-274.
21. Kostamaa H, Donovan J, Kasaoka S, Tobis J, Fitzpatrick L. Calcified plaque cross-sectional area in human arteries: Correlation between intravascular ultrasound and undecalcified histology. *Am Heart J* 1999;137:482-488.
22. Mintz GS, Popma JJ, Pichard AD, Kent KM, Satler LF, Chuang YC, Ditrano CJ, Leon MB. Patterns of calcification in coronary artery disease. A statistical analysis of intravascular ultrasound and coronary angiography in 1155 lesions. *Circulation* 1995;91:1959-1965.
23. Schmidt W, Lanzer P, Behrens P, Topoleski LD, Schmitz KP. A comparison of the mechanical performance characteristics of seven drug-eluting stent systems. *Catheter Cardiovasc Interv* 2009;73:350-360.
24. Sangiorgi G, Melzi G, Agostoni P, Cola C, Clementi F, Romitelli P, Virmani R, Colombo A. Engineering aspects of stents design and their translation into clinical practice. *Ann Ist Super Sanita* 2007;43:89-100.
25. Rieu R, Barragan P, Garitey V, Roquebert PO, Fuseri J, Commeau P, Sainsous J. Assessment of the trackability, flexibility, and conformability of coronary stents: A comparative analysis. *Catheter Cardiovasc Interv* 2003;59:496-503.
26. Tanimoto S, Serruys PW, Thuesen L, Dudek D, de Bruyne B, Chevalier B, Ormiston JA. Comparison of in vivo acute stent recoil between the bioabsorbable everolimus-eluting coronary stent and the everolimus-eluting cobalt chromium coronary stent: Insights from the ABSORB and SPIRIT trials. *Catheter Cardiovasc Interv* 2007;70:515-523.
27. Gomez-Lara J, Garcia-Garcia HM, Onuma Y, Garg S, Regar E, De Bruyne B, Windecker S, McClean D, Thuesen L, Dudek D, et al. A comparison of the conformability of everolimus-eluting bioresorbable vascular scaffolds to metal platform coronary stents. *JACC Cardiovasc Interv* 2010;3:1190-1198.
28. Kim SW, Mintz GS, Hong YJ, Pakala R, Park KS, Pichard AD, Satler LF, Kent KM, Suddath WO, Waksman R, et al. The virtual histology intravascular ultrasound appearance of newly placed drug-eluting stents. *Am J Cardiol* 2008;102:1182-1186.

29. Brugaletta S, Garcia-Garcia HM, Garg SJ, G-L, Diletti R, Onuma Y, Van Geuns RJ, McClean D, Dudek D, Thuesen L, Chevalier B, Windecker S, Whitbourn R, Dorange C, Miquel-Hebert K, Sudhir K, Ormiston JA, Serruys PW. Temporal changes of coronary artery plaque located behind the struts of the everolimus eluting bioresorbable vascular scaffold. *Int J Cardiovasc Imaging* 2010, Oct 13 [epub ahead of print] (in press).
30. Alfonso F, Suarez A, Perez-Vizcayno MJ, Moreno R, Escaned J, Banuelos C, Jimenez P, Bernardo E, Angiolillo DJ, Hernandez R, et al. Intravascular ultrasound findings during episodes of drug-eluting stent thrombosis. *J Am Coll Cardiol* 2007;50:2095–2097.
31. Uren NG, Schwarzacher SP, Metz JA, Lee DP, Honda Y, Yeung AC, Fitzgerald PJ, Yock PG. Predictors and outcomes of stent thrombosis: An intravascular ultrasound registry. *Eur Heart J* 2002;23:124–132.
32. Cheneau E, Leborgne L, Mintz GS, Kotani J, Pichard AD, Satler LF, Canos D, Castagna M, Weissman NJ, Waksman R. Predictors of subacute stent thrombosis: Results of a systematic intravascular ultrasound study. *Circulation* 2003;108:43–47.
33. Alfonso F, Suarez A, Angiolillo DJ, Sabate M, Escaned J, Moreno R, Hernandez R, Banuelos C, Macaya C. Findings of intravascular ultrasound during acute stent thrombosis. *Heart* 2004;90:1455–1459.

6.3

Vascular compliance changes of the coronary vessel wall after bioresorbable vascular scaffold implantation in the treated and adjacent segments.

Salvatore Brugaletta, Bill D Gogas, Hector M Garcia-Garcia, Vasim Farooq, Chrysafios Girasis, Jun Ho Heo, Robert Jan van Geuns, Bernard de Bruyne, Dariusz Dudek, Jacques Koolen, Pieter Smits, Susan Veldhof, Richard Rapoza, Yoshinobu Onuma, John Ormiston, Patrick W Serruys

Circulation Journal 2012, In press

Vascular Compliance Changes of the Coronary Vessel Wall After Bioresorbable Vascular Scaffold Implantation in the Treated and Adjacent Segments

Salvatore Brugaletta, MD, PhD; Bill D. Gogas, MD; Hector M. Garcia-Garcia, MD, PhD; Vasim Farooq, MD; Chrysaifios Girasis, MD; Jung Ho Heo, MD; Robert Jan van Geuns, MD, PhD; Bernard de Bruyne, MD, PhD; Dariuz Dudek, MD; Jacques Koolen, MD, PhD; Pieter Smits, MD, PhD; Susan Veldhof, BSc; Richard Rapoza, PhD; Yoshinobu Onuma, MD; John Ormiston, MD; Patrick W. Serruys, MD, PhD

Background: Implantation of a metallic prosthesis creates local stiffness with a subsequent mismatch in the compliance of the vessel wall, disturbances in flow and heterogeneous distribution of wall shear stress. Polymeric bioresorbable ABSORB scaffolds have less stiffness than metallic platform stents. We sought to analyze the mismatch in vascular compliance after ABSORB implantation and its long-term resolution with bioresorption.

Methods and Results: A total of 83 patients from the ABSORB trials underwent palpography investigations (30 and 53 patients from ABSORB Cohorts A and B, respectively) to measure the compliance of the scaffolded and adjacent segments at various time points (from pre-implantation up to 24 months). The mean of the maximum strain values was calculated per segment by utilizing the Rotterdam Classification (ROC) score and expressed as ROC/mm. Scaffold implantation led to a significant decrease in vascular compliance (median [IQR]) at the scaffolded segment (from 0.37 [0.24–0.45] to 0.14 [0.09–0.23], $P < 0.001$) with mismatch in compliance in a paired analysis between the scaffolded and adjacent segments (proximal: 0.23 [0.12–0.34], scaffold: 0.12 [0.07–0.19], distal: 0.15 [0.05–0.26], $P = 0.042$). This reported compliance mismatch disappears at short- and mid-term follow-up.

Conclusions: The ABSORB scaffold decreases vascular compliance at the site of scaffold implantation. A compliance mismatch is evident immediately post-implantation and in contrast to metallic stents disappears in the mid-term, likely leading to a normalization of the rheological behavior of the scaffolded segment. (*Circ J* 2011; ■■: ■■■■–■■■■)

Key Words: ABSORB; Poly-lactide; Vascular compliance

Over the past 20 years percutaneous implantation of metallic prostheses has increasingly been used to alleviate flow-limiting lesions by overstretching the plaque and underlying vessel wall.¹ From a mechanical perspective this treatment may locally stiffen the artery, reducing its compliance and creating a mismatch in compliance with respect to the segments contiguous to the implanted device.² This mismatch may eventually provoke flow disturbances and wall shear stress alterations with subsequent blood stasis³ (Figure 1). The wall shear stress distribution in a stented artery has been

reported as a determinant factor for cellular growth and the occurrence of thrombus formation.⁴

The ABSORB everolimus-eluting bioresorbable vascular scaffold system (ABSORB BVS) theoretically has many advantages over rigid metallic stents. In particular, because the scaffold is completely made of poly-lactide, it does not have the same stiffness as metal, thereby having the potential to overcome in part the problems related to local stiffening of the artery and compliance mismatch associated with metallic platform stents. In addition, the mismatch in compliance after

Received December 5, 2011; revised manuscript received February 25, 2012; accepted March 12, 2012; released online Xxxx XX, 20XX
Time for primary review: 31 days

Thoraxcenter, Erasmus MC, Rotterdam (S.B., B.D.G., H.M.G.-G., V.F., C.G., J.H.H., R.J.v.G., Y.O., P.W.S.); Maasstad Hospital, Rotterdam (P.S.); Cardialysis B.V., Rotterdam (H.M.G.-G.); Catharina Hospital, Eindhoven (J.K.), The Netherlands; Department of Cardiology, Thorax Institute, University Hospital Clinic, Barcelona (S.B.), Spain; Cardiovascular Center, Aalst (B.d.B.), Belgium; Jagiellonian University, Krakow (D.D.), Poland; Abbott Vascular, Diegem (S.V.), Belgium; Abbott Vascular, Santa Clara, CA (R.R.), USA; Auckland City Hospital, Auckland (J.O.), New Zealand

Mailing address: Patrick W. Serruys, Professor, MD, PhD, Head of the Interventional Cardiology Department, Erasmus MC, Thoraxcenter, 's Gravedijkwal 230,3015 CE, Rotterdam, The Netherlands. E-mail: p.w.j.c.serruys@erasmusmc.nl

ISSN-1346-9843 doi:10.1253/circj.CJ-11-1416

All rights are reserved to the Japanese Circulation Society. For permissions, please e-mail: cj@j-circ.or.jp

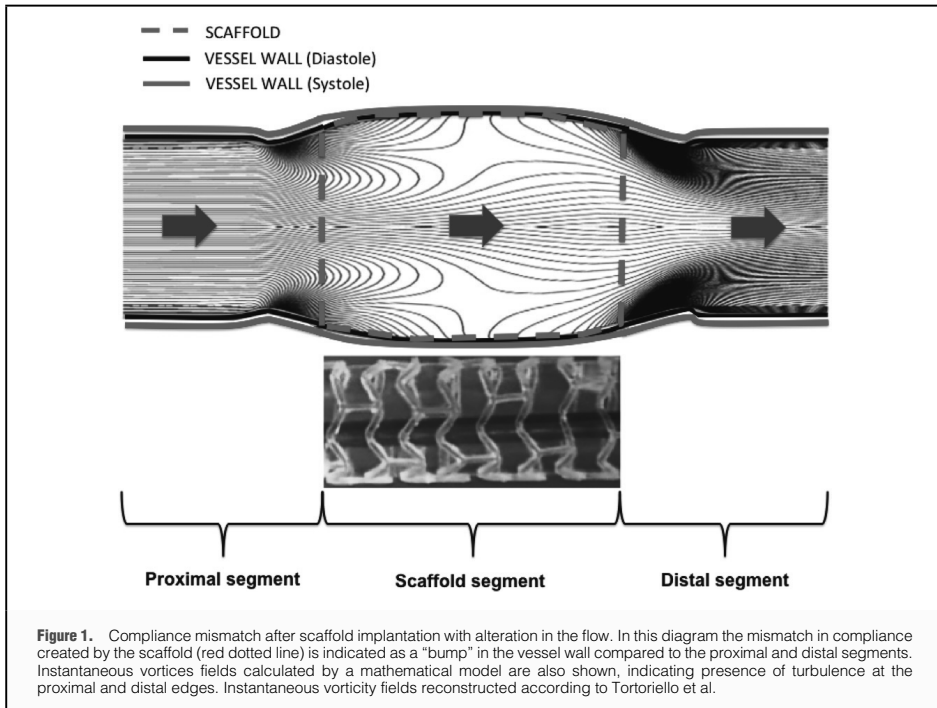


Figure 1. Compliance mismatch after scaffold implantation with alteration in the flow. In this diagram the mismatch in compliance created by the scaffold (red dotted line) is indicated as a "bump" in the vessel wall compared to the proximal and distal segments. Instantaneous vorticity fields calculated by a mathematical model are also shown, indicating presence of turbulence at the proximal and distal edges. Instantaneous vorticity fields reconstructed according to Tortoriello et al.

scaffold implantation may potentially disappear in the long-term once the scaffold is completely bioresorbed.

The aim of the present analysis was to investigate the vascular compliance of the coronary segments treated with the bioresorbable scaffold and the adjacent proximal and distal edges, by measuring: (1) the changes in compliance immediately after ABSORB BVS implantation and at 6-, 12- and 24-month follow-up; and (2) the compliance mismatch between these 3 segments at the various time points.

Methods

Study Population

The ABSORB trial includes the ABSORB Cohorts A and B trials. In brief, the ABSORB Cohort A trial (NCT00300131) enrolled 30 patients with a diagnosis of stable or unstable angina or silent ischemia. All treated lesions were single and de novo in a native coronary artery of 3.0mm diameter, shorter than 8 mm for the 12-mm scaffold and shorter than 14 mm for the 18-mm scaffold, with a diameter stenosis $\geq 50\%$ and $< 100\%$, and with a Thrombolysis in Myocardial Infarction flow grade ≥ 1 . Major exclusion criteria were acute myocardial infarction, unstable arrhythmias or left ventricular ejection fraction $< 30\%$, restenotic lesions, lesions located in the left main coronary artery, lesions involving an epicardial side branch ≥ 2 mm in diameter by visual assessment, and the presence of thrombus or other clinically significant stenosis in the target vessel. All

lesions were treated by implantation of ABSORB BVS first-generation scaffold (Generation 1.0) and invasively imaged at 6- and 24-month follow-up. The ABSORB Cohort B trial (NCT00856856) enrolled 101 patients with the same clinical profile and lesion type, divided into 2 groups according to the timeline of invasive follow-up: ABSORB Cohort B1 with invasive imaging at 6 and 24 months; ABSORB Cohort B2 with the same invasive imaging at 12 and 36 months. The 12-month follow-up has been reported.⁵ All lesions were treated by implantation of an ABSORB BVS second generation scaffold (Generation 1.1) (3.0 \times 18mm).⁶ The ethics committee at each participating institution approved the protocol and each patient gave written informed consent before inclusion.

Study Device

The ABSORB BVS scaffold (Abbott Vascular, Santa Clara, CA, USA) consists of a polymer backbone of poly-L lactide (PLLA) coated with a thin layer of a 1:1 mixture of poly-D, L-lactide (PDLLA) polymer, and the antiproliferative drug, everolimus, to form an amorphous drug-eluting coating matrix containing 100 μ g of everolimus/cm² of scaffold. The details of the device have been previously described.⁷⁻¹¹ The ABSORB Cohort A and Cohort B trials evaluated the ABSORB BVS scaffold generations 1.0 and 1.1, respectively.^{12,13} The ABSORB BVS scaffold 1.1 has a smaller maximum circular unsupported surface area compared to 1.0, with the struts arranged as in-phase zigzag hoops linked together by 3 longitudi-

Table 1. Clinical Baseline Characteristics				
	All patients (n=83)	Cohort A (n=30)	Cohort B (n=53)	P value
Patient demographic and clinical data				
Age, years	61.71±8.59	62.46±8.98	61.28±8.41	0.605
Male, n (%)	56 (67.5)	18 (60.0)	38 (71.7)	0.332
Hypertension, n (%)	51 (62.2)	18 (60.0)	33 (63.5)	0.815
Hypercholesterolemia, n (%)	61 (74.4)	19 (65.5)	42 (79.2)	0.194
Diabetes, n (%)	10 (12.0)	1 (3.3)	9 (17.0)	0.085
Current smoking, n (%)	14 (17.0)	6 (20.0)	8 (15.1)	0.559
Prior PCI, n (%)	18 (21.7)	6 (20.0)	12 (22.6)	1.000
Prior MI, n (%)	13 (15.7)	3 (10.0)	10 (18.9)	0.359
Stable angina, n (%)	18 (21.7)	6 (20.0)	12 (22.6)	1.000
Unstable angina, n (%)	13 (15.7)	8 (26.7)	5 (9.4)	0.058
Silent ischemia, n (%)	2 (2.4)	1 (3.3)	1 (1.9)	1.000
Lesion and angiographic characteristics				
Treated vessel, n (%)				
Left anterior descending artery	39 (47.0)	14 (46.7)	25 (47.2)	1.000
Left circumflex artery	22 (26.5)	9 (30.0)	13 (24.5)	0.612
Right coronary artery	22 (26.5)	7 (23.3)	15 (28.3)	0.796
ACC/AHA lesion type, n (%)				
Type A	0 (0)	0 (0)	0 (0)	NA
Type B1	50 (61.0)	18 (60.0)	32 (61.5)	1.000
Type B2	31 (37.8)	12 (40.0)	19 (36.0)	0.815
Type C	1 (1.2)	0 (0)	1 (1.9)	1.000
QCA analysis pre-treatment				
RVD (mean±SD, mm)	2.64±0.39	2.69±0.47	2.61±0.34	0.628
MLD (mean±SD, mm)	1.04±0.26	1.05±0.26	1.04±0.27	0.837
Diameter stenosis, (mean±SD, %)	59.85±10.41	59.92±11.30	59.80±9.96	0.980
Medical treatment, n (%)				
β-blocker	62 (75)	21 (73)	41 (77)	0.646
ACEI	37 (45)	13 (44)	24 (45)	0.837
Statin	81 (98)	29 (98)	52 (98)	1.000

Continuous variables are expressed as mean±SD.

MI, myocardial infarction; NA, not applicable; RVD, reference vessel diameter; MLD, minimum lumen diameter; ACEI, angiotensin-converting enzyme inhibitor; SD, standard deviation.

dinal links, similar to the XIENCE V design.^{8,14} No differences in polymeric material, drug dose, drug release kinetics or strut thickness exist between the 2 generations. Of note is that changes implemented in the manufacture of ABSORB BVS 1.1 resulted in more prolonged luminal support post-implantation.^{6,15,16}

Study Procedure and Intravascular Ultrasound (IVUS) Acquisition/Analysis

Target lesions were treated using standard interventional techniques with mandatory pre-dilation. Post-dilation with a balloon that was shorter than the implanted scaffold was allowed at the operator's discretion up to the prescribed maximal post-dilation diameter.

IVUS palpography analyses were performed using the Eagle Eye 20MHz catheter (Volcano Corp, Rancho Cordova, CA, USA) with an automated continuous pullback (0.5 mm/s, 30 frames/s) at the level of the scaffolded and adjacent segments, with simultaneous recordings of the electrocardiogram and aortic pressure, at various follow-up time points.

IVUS Palpography Acquisition and Analysis

IVUS palpography is a technique that allows for the assess-

ment of local mechanical tissue properties. The underlying principle is that at defined pressure differences soft tissue (eg, lipid-rich) components deform more than hard tissue components (eg, fibrous-calcified).¹⁷⁻¹⁹ In coronary arteries the tissue of interest is the vessel wall, whereas blood pressure, with its physiological changes during the heart cycle, is used as the excitation force. Radiofrequency data obtained at different pressure levels are compared to determine the local tissue deformation. The strain value is normalized to a pressure difference of 2.5 mmHg per frame: this allows the construction of a "strain" image in which hard (low strain/compliance) and soft (high strain/compliance) values range between 0% and 2%.¹⁷ In postmortem coronary arteries the sensitivity and specificity of palpography to detect high strain values have previously been reported as 88% and 89%, respectively.¹⁸

Digital radiofrequency data were acquired using a custom-designed workstation and subsequently stored on a DVD for sending to the imaging core laboratory for offline analyses (Cardialysis, Rotterdam, The Netherlands). Both the scaffolded and the 5-mm proximal and distal segments were analyzed.²⁰ Local strain was calculated from the gated radiofrequency traces using cross-correlation analyses, displayed and color-coded from blue (for 0% strain) to yellow (for 2% strain)

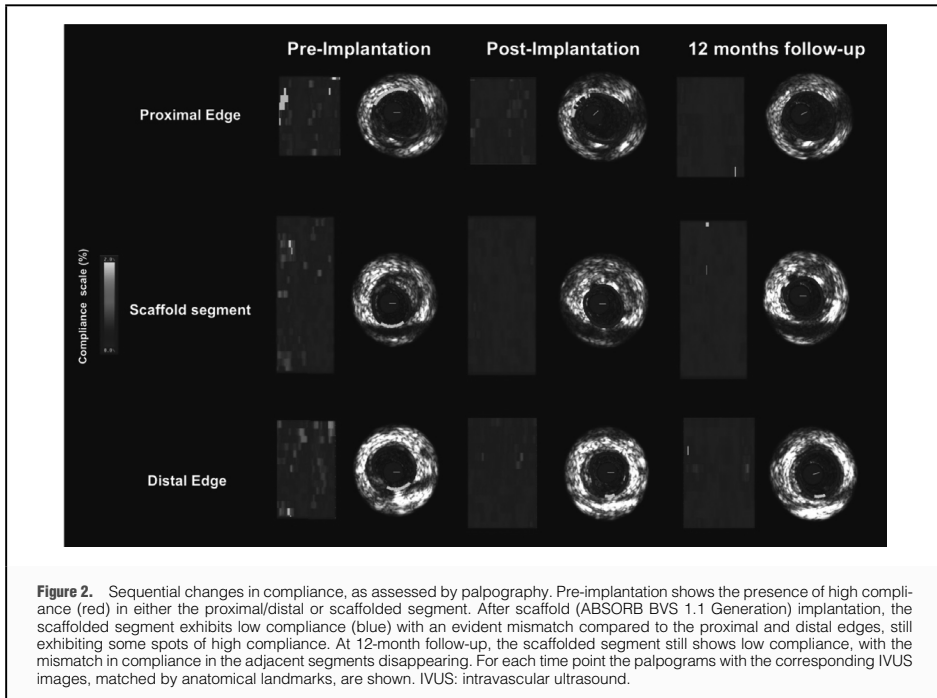


Figure 2. Sequential changes in compliance, as assessed by palpography. Pre-implantation shows the presence of high compliance (red) in either the proximal/distal or scaffolded segment. After scaffold (ABSORB BVS 1.1 Generation) implantation, the scaffolded segment exhibits low compliance (blue) with an evident mismatch compared to the proximal and distal edges, still exhibiting some spots of high compliance. At 12-month follow-up, the scaffolded segment still shows low compliance, with the mismatch in compliance in the adjacent segments disappearing. For each time point the palpograms with the corresponding IVUS images, matched by anatomical landmarks, are shown. IVUS: intravascular ultrasound.

via red as previously described.¹⁹

Strain values were assigned a Rotterdam classification (ROC) score ranging from I to IV (ROC I, 0–0.5%; ROC II, 0.6–<0.9%; ROC III, 0.9–1.2%; ROC IV, >1.2%).²¹ A region was defined as high strain when it had ROC III–IV that spanned an arc of at least 12° at the surface of a plaque (identified on the IVUS recording), as previously reported. The highest value of strain in the cross-section was taken as the strain level of the site.²¹ The compliance of each segment was calculated per segment (proximal edge, scaffold segment and distal edge) and defined as the mean of the maximum strain values per cross-section in ROC I/II/III/IV sites, expressed as ROC/mm.^{22,23}

Ideally, the absence of a mismatch is the absence of difference in compliance along the vessel wall. For the purpose of the present analysis, mismatch was defined as statistically significant differences in compliance between the 3 segments analyzed on a paired basis, using a statistical test for trend (Figure 1).

Statistical Analysis

Categorical variables are presented using frequencies and percentages. Continuous variables are presented with mean and standard deviations or median and interquartile ranges, according to their distribution. Analyses of normality of the continuous variables were performed with the Kolmogorov-Smirnov test. Changes in compliance between various time points were evaluated by means of paired Wilcoxon signed rank test. Differences in compliance between the 3 segments analyzed

(scaffold, proximal and distal edges) at each time point were evaluated by the paired Friedman test. Comparison between 2 groups was performed with the Mann-Whitney test. A 2-sided P-value <0.05 indicated statistical significance. Statistical analyses were performed with SPSS 18.0 software (SPSS, Chicago, IL, USA).

Results

Baseline Clinical Characteristics (Table 1)

A total of 83 patients from the ABSORB Cohort A and B trials underwent palpography investigations (30 and 53 patients from ABSORB Cohort A and Cohort B, respectively). Specifically, palpography analyses were performed in 27 patients pre-scaffold implantation (13 and 14 from ABSORB Cohort A and Cohort B), 71 patients post-scaffold implantation (27 and 44 from ABSORB Cohort A and Cohort B), 42 patients at 6 months (27 and 15 from ABSORB Cohort A and Cohort B), 26 patients at 12 months and in 21 patients at 24 months.

Palpography analyses were completed for all 3 segments (scaffold, proximal and distal segments) in 14 patients at pre-scaffold implantation (5 and 9 from ABSORB Cohort A and Cohort B), 35 patients post-implantation (14 and 11 from ABSORB Cohort A and Cohort B), 27 patients at 6 months (16 and 11 from ABSORB Cohort A and ABSORB Cohort B), 11 patients at 12 months and 14 patients at 24 months.

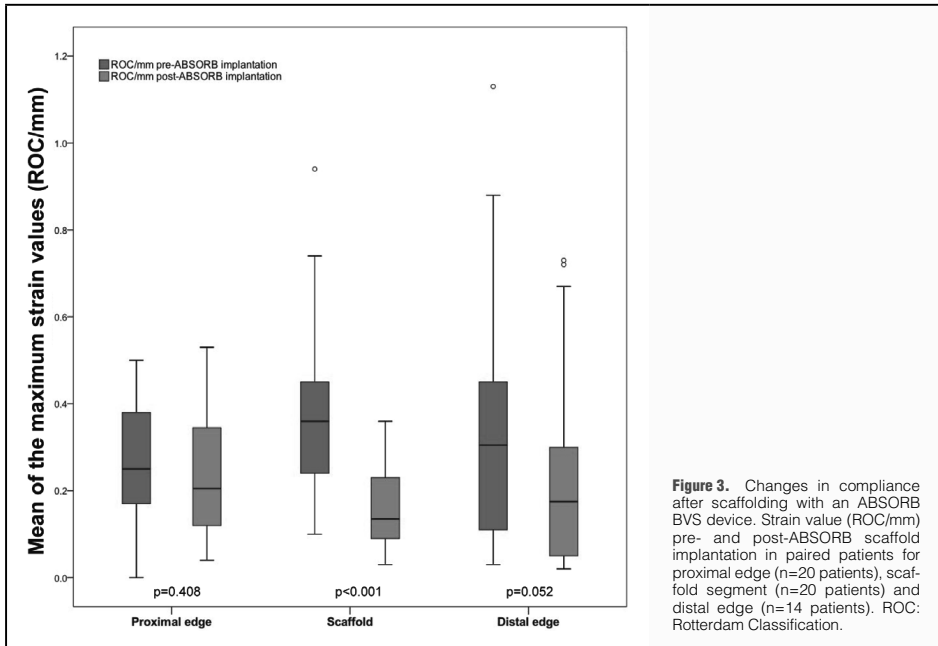


Figure 3. Changes in compliance after scaffolding with an ABSORB BVS device. Strain value (ROC/mm) pre- and post-ABSORB scaffold implantation in paired patients for proximal edge (n=20 patients), scaffold segment (n=20 patients) and distal edge (n=14 patients). ROC: Rotterdam Classification.

Modification in Vascular Compliance From Pre- to Post-Scaffold Implantation (Figure 2)

After scaffold implantation a significant decrease in compliance in the scaffolded segment was evident with no modification in the proximal/distal edges compliance. Of note, a trend towards a reduction in compliance was evident in the distal edge (Figure 3). The modifications in compliance after scaffold implantation did not significantly differ between ABSORB Cohort A and Cohort B in the 3 segments (scaffolded segment P=0.820; proximal edge P=0.310; distal edge P=0.606).

A mismatch in compliance tended to be present immediately after scaffold implantation (Figure 4).

Modification in Vascular Compliance During Follow-up (Tables 2,3)

In ABSORB Cohort A there was a significant increase in the compliance of the scaffolded segment at 6 and 24 months compared to post-implantation. Conversely, in ABSORB Cohort B no changes in compliance of the scaffolded segment were evident at either 6 (P<0.001 as compared to ABSORB Cohort A) or 12 months, compared to post-implantation. No other significant changes were found at the proximal/distal edges in either ABSORB Cohort A or B at the various time points.

At the various follow-up time points, no mismatch in compliance was found either in Cohort A (6 months=proximal edge 0.29 [0.18–0.35] vs. scaffold segment 0.10 [0.06–0.22] vs. distal edge 0.16 [0.05–0.24]; P=0.146; 24 months proximal edge 0.20 [0.09–0.30] vs. scaffold segment 0.24 [0.17–0.29] vs. distal edge 0.11 [0.05–0.24]; P=0.052) or Cohort B

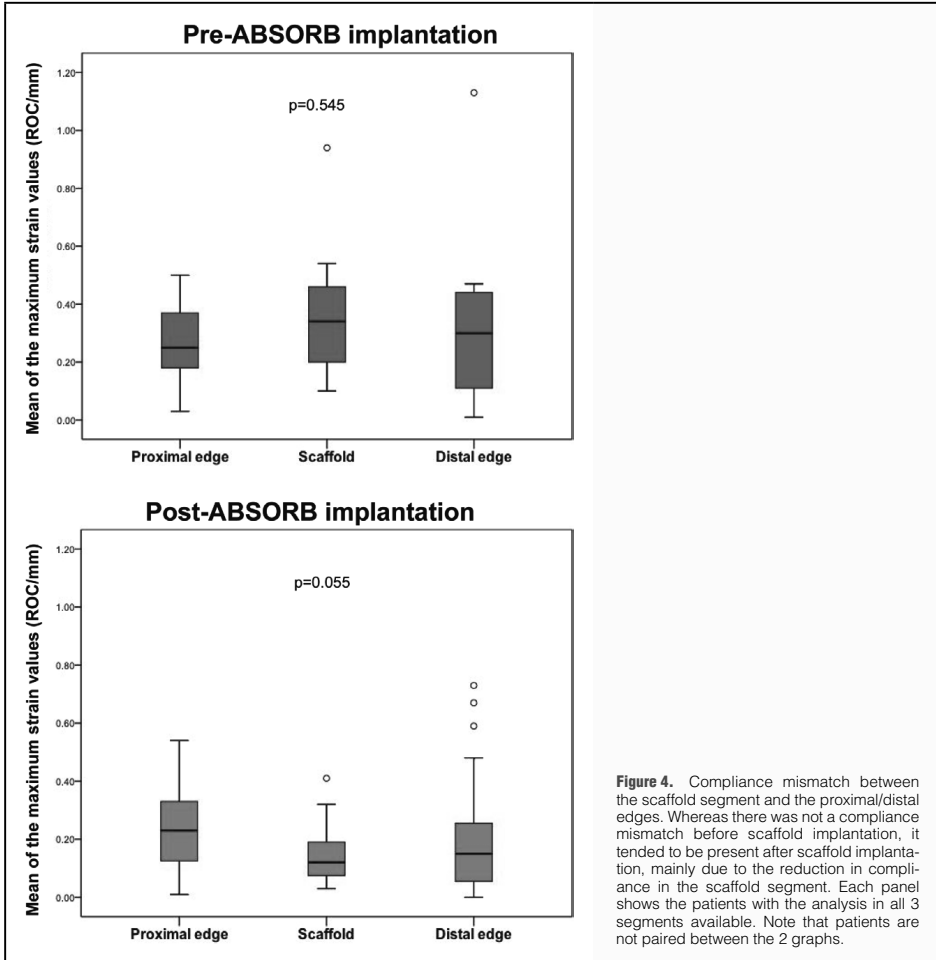
(6 months=proximal edge 0.28 [0.16–0.46] vs. scaffold segment 0.23 [0.14–0.29] vs. distal edge 0.11 [0.05–0.17]; P=0.449; 12 months=proximal edge 0.18 [0.10–0.36] vs. scaffold segment 0.16 [0.08–0.26] vs. distal edge 0.11 [0.02–0.20]; P=0.618).

Discussion

The major findings of the present analysis are: (1) scaffolding of a diseased vessel wall by an ABSORB BVS significantly reduces its compliance, with the compliance of the segment immediately distal to the device tending also to be reduced; (2) the mismatch in compliance that is present immediately after scaffold implantation disappears in the short- to mid-term; (3) the prolonged duration of mechanical support of the ABSORB BVS generation 1.1, compared to BVS 1.0, is responsible for the differing changes in vascular compliance in the scaffold segment between the 2 devices at 6 months.

Compliance and Pulsatility of the Scaffolded Segment

Palpography is a technique of assessing the elastic properties of the coronary vessel wall; in particular, it analyzes the ability of the artery to be distended, providing a measurement of its compliance.^{17,19,24} Deployment of a stiff metallic stent over coronary plaque may mechanically reduce the local compliance of the coronary vessel wall.²⁵ This reduction may be further explained by the fact that the foreign scaffold material may partially interfere with the palpography measurements due to the artificial acoustic properties of the stent struts themselves.²⁵



Implantation of an ABSORB BVS, made of polymeric material, reduces the local compliance of the scaffolded segment and possibly the acute vulnerability of the treated coronary plaque.^{19,25} Nevertheless, with the first ABSORB Revision 1.0 at long term, an increase in compliance was observed in parallel with bioresorption of the scaffold.^{9,25} It is noteworthy that with the progressive disappearance of the polymeric scaffold, the vessel wall can recover a normal response to physiologic pulsatile cyclic strain and to shear stress; this positive interplay between cyclical strain and shear stress can be translated into chemical signals by cells with upregulation of the e-NOS gene, prostacyclin and metalloproteinases production, expression of anti-inflammatory genes, low permeability and low oxidative stress in the endothelial cells and in the smooth muscle cells.^{26–29} The presence of endothelial-dependent vaso-

motion in the vascular segment scaffolded by an ABSORB BVS device suggests that all these biological processes work appropriately.^{5,13} Conversely, cell signaling is altered in metallic scaffolded segments, where the vessel's distensibility is eliminated by metallic caging and it is exposed to static and non-pulsatile strain.^{30–32}

It should be also noted that the vessel wall compliance over time may be modulated differently according to the type of polymeric device implanted. The 2 generations of ABSORB BVS were compared at post-implantation and at 6-month follow-up. No differences in their ability to reduce vascular compliance immediately after implantation were found, confirming the absence of differences in acute mechanical properties, such as acute recoil, between the 2 BVS generations.³³ Nevertheless, at 6 months the compliance of the scaffolded segment

Table 2. Modification in Strain Values After ABSORB Cohort A Scaffold Implantation (Generation 1.0)

	Post-scaffolding	6-month follow-up	24-month follow-up	P value*	P value**	P value***
Proximal edge	0.33 [0.18–0.40] (17)	0.25 [0.15–0.38] (18)	0.20 [0.09–0.36] (16)	0.679 (15)	0.275 (13)	0.391 (14)
Scaffolded segment	0.12 [0.07–0.25] (27)	0.25 [0.17–0.37] (27)	0.26 [0.17–0.32] (21)	<0.001 (25)	0.003 (19)	0.746 (20)
Distal edge	0.17 [0.05–0.30] (18)	0.16 [0.09–0.41] (18)	0.12 [0.07–0.28] (16)	0.715 (15)	0.127 (14)	0.391 (14)

All P-values are calculated by Wilcoxon paired test.

*Post vs. 6-month follow-up; **Post vs. 24-month follow-up; ***6- vs. 24-month follow-up.

Values are reported as median [IQR] (n). IQR, interquartile range.

Table 3. Modification in Strain Values After ABSORB Cohort B Scaffold Implantation (Generation 1.1)

	Post-scaffolding	6-months follow-up	P value
Cohort B1			
Proximal edge	0.25 [0.11–0.41] (12)	0.17 [0.11–0.34] (11)	0.313 (7)
Scaffolded segment	0.22 [0.13–0.28] (16)	0.20 [0.12–0.28] (15)	0.053(11)
Distal edge	0.22 [0.11–0.31] (10)	0.19 [0.10–0.37] (14)	0.313 (7)
Cohort B2			
Proximal edge	0.23 [0.10–0.35] (17)	0.17 [0.13–0.34] (17)	0.531 (14)
Scaffolded segment	0.17 [0.09–0.32] (28)	0.16 [0.11–0.21] (26)	0.226 (21)
Distal edge	0.15 [0.03–0.20] (18)	0.08 [0.04–0.23] (16)	0.747 (11)

All P-values are calculated by Wilcoxon paired test.

Values are reported as median [IQR] (n). IQR, interquartile range.

increased after ABSORB 1.0 implantation, whereas it tended to further decrease after ABSORB 1.1 implantation. These findings are in line with expectations: smaller maximum circular unsupported surface area and a slower rate of degradation of the generation 1.1 compared to 1.0 aim to improve and prolong the duration of lumen scaffolding and to avoid the “late recoil” phenomenon (scaffold area reduction over time), likely explaining the differing changes over time in compliance of the scaffolded segment between the 2 generations.^{5,6,14–16}

Compliance Mismatch Between the Scaffolded and Contiguous Segments

Local stiffness due to metallic stent implantation, in contrast to the compliance of the contiguous vascular segments, generates a compliance mismatch (Figures 1,2). Vernhet et al previously showed that metallic stent implantation within the normal rabbit abdominal aorta causes a persistent increase in upstream compliance, while simultaneously abolishing compliance in the stented segment, creating a compliance mismatch.³⁴ Similar findings have been demonstrated in human carotid arteries after stenting.³⁵ It has also been shown that ring vortices with in-flow stagnation points and rapid variations of wall shear stress can form at the edges of the prosthesis.^{3,26,36} All of these findings, in particular the increase in upstream compliance, have been related to the observation that late plaque rupture after stenting in human coronary arteries is more likely to occur at the stent inflow compared to elsewhere.²⁰

At variance with these metallic stent observations, ABSORB BVS implantation did not increase the compliance in the in-flow segment, but conversely tended to decrease it in the outflow segment (Figure 3). Normally, there is propagation of pressure waves along the vessel wall (the so-called Windkessel effect) and at sites where this process is interrupted (eg, side branches, stent/scaffold) there is a reflection of pressure waves with prevention of their propagation.³⁷ This may eventually reduce wall motion and compliance distally, explaining the changes observed in the present analysis in the segment

distal to the scaffold.^{38,39}

Although a compliance mismatch between the scaffolded and adjacent segments was demonstrated immediately after polymeric scaffold implantation, it disappeared at 6 months in contrast to metallic stents (Figure 2). The abolition of a step-up compliance at the scaffold edges can theoretically lead to laminar flow, exposing the endothelial cells to a homogeneous shear stress, which can eventually result in atheroprotective and anti-restenosis effects.^{20,26,39,40} Long-term data from the ABSORB B trial up to 3 years are awaited to confirm these findings.

Study Limitations

The major limitation of the present analysis is the small group of patients with paired palpography analysis at the various time points. This cohort of patients does, however, currently represent the sole set of available data on polymeric scaffold and vascular compliance. The lack of a control group testing a metallic stent is another limitation to fully interpreting the present findings; other investigators have, however, previously studied the phenomenon of mismatch compliance in vessel scaffolded with metal.^{34,35}

Conclusions

Scaffold implantation with an ABSORB BVS device transiently reduces the vascular distensibility of a treated coronary segment. In contrast to metallic stents, the created mismatch in compliance with the proximal and distal segments disappeared at mid-term due to the bioresorption and disappearance of the scaffold. Potential clinical benefits of these findings, related to restoration of vessel wall pulsatility and absence of mismatch, will require longer term clinical follow-up in a larger population.

Acknowledgments

The ABSORB Trial is sponsored and funded by Abbott Vascular, Santa

Clara, California, USA. Susan Veldhof and Richard Rapozo are employees of Abbott Vascular.

References

- Garg S, Serruys PW. Coronary stents: Current status. *J Am Coll Cardiol* 2010; **56**(10 Suppl): S1–S42.
- Surovtsova I. Effects of compliance mismatch on blood flow in an artery with endovascular prosthesis. *J Biomech* 2005; **38**: 2078–2086.
- Tortoriello A, Pedrizzetti G. Flow-tissue interaction with compliance mismatch in a model stented artery. *J Biomech* 2004; **37**: 1–11.
- Wentzel JJ, Whelan DM, van der Giessen WJ, van Beusekom HM, Andhyswara I, Serruys PW, et al. Coronary stent implantation changes 3-D vessel geometry and 3-D shear stress distribution. *J Biomech* 2000; **33**: 1287–1295.
- Serruys PW, Onuma Y, Dudek D, Smits PC, Koolen J, Chevalier B, et al. Evaluation of the second generation of a bioresorbable everolimus-eluting vascular scaffold for the treatment of de novo coronary artery stenosis 12-month clinical and imaging outcomes. *J Am Coll Cardiol* 2011; **58**: 1578–1588.
- Serruys PW, Onuma Y, Ormiston JA, de Bruyne B, Regar E, Dudek D, et al. Evaluation of the second generation of a bioresorbable everolimus drug-eluting vascular scaffold for treatment of de novo coronary artery stenosis: Six-month clinical and imaging outcomes. *Circulation* 2010; **122**: 2301–2312.
- Ormiston JA, Webster MW, Armstrong G. First-in-human implantation of a fully bioabsorbable drug-eluting stent: The BVS poly-L-lactic acid everolimus-eluting coronary stent. *Catheter Cardiovasc Interv* 2007; **69**: 128–131.
- Okamura T, Garg S, Gutierrez-Chico JL, Shin ES, Onuma Y, Garcia HM, et al. In-vivo evaluation of stent strut distribution patterns in the bioabsorbable everolimus-eluting device: An OCT ad hoc analysis of the Revision 1.0 and Revision 1.1 stent design in the ABSORB clinical trial. *EuroIntervention* 2010; **5**: 932–938.
- Onuma Y, Serruys PW, Perkins LE, Okamura T, Gonzalo N, Garcia-Garcia HM, et al. Intracoronary optical coherence tomography and histology at 1 month and 2, 3, and 4 years after implantation of everolimus-eluting bioresorbable vascular scaffolds in a porcine coronary artery model: An attempt to decipher the human optical coherence tomography images in the ABSORB Trial. *Circulation* 2010; **122**: 2288–2300.
- Onuma Y, Ormiston J, Serruys PW. Bioresorbable scaffold technologies. *Circ J* 2011; **75**: 509–520.
- Gutierrez-Chico JL, Radu MD, Diletti R, Sheehy A, Kossuth MB, Oberhauser JP, et al. Spatial distribution and temporal evolution of scattering centers by optical coherence tomography in the poly(l-lactide) backbone of a bioresorbable vascular scaffold. *Circ J* 2012; **76**: 342–350.
- Ormiston JA, Serruys PW, Regar E, Dudek D, Thuesen L, Webster MW, et al. A bioabsorbable everolimus-eluting coronary stent system for patients with single de-novo coronary artery lesions (ABSORB): A prospective open-label trial. *Lancet* 2008; **371**: 899–907.
- Serruys PW, Ormiston JA, Onuma Y, Regar E, Gonzalo N, Garcia-Garcia HM, et al. A bioabsorbable everolimus-eluting coronary stent system (ABSORB): 2-year outcomes and results from multiple imaging methods. *Lancet* 2009; **373**: 897–910.
- Brugaletta S, Garcia-Garcia HM, Diletti R, Gomez-Lara J, Garg S, Onuma Y, et al. Comparison between the first and second generation bioresorbable vascular scaffolds: A six month virtual histology study. *EuroIntervention* 2011; **6**: 1110–1116.
- Brugaletta S, Gomez-Lara J, Serruys PW, Farooq V, van Geuns RJ, Thuesen L, et al. Serial in vivo intravascular ultrasound-based echogenicity changes of everolimus-eluting bioresorbable vascular scaffold during the first 12 months after implantation insights from the ABSORB B Trial. *J Am Coll Cardiol Interv* 2011; **4**: 1281–1289.
- Gomez-Lara J, Brugaletta S, Diletti R, Garg S, Onuma Y, Gogas BD, et al. A comparative assessment by optical coherence tomography of the performance of the first and second generation of the everolimus-eluting bioresorbable vascular scaffolds. *Eur Heart J* 2011; **32**: 294–304.
- Schaar JA, De Korte CL, Mastik F, Srijder C, Pasterkamp G, Boersma E, et al. Characterizing vulnerable plaque features with intravascular elastography. *Circulation* 2003; **108**: 2636–2641.
- Schaar JA, Regar E, Mastik F, McFadden EP, Saia F, Disco C, et al. Incidence of high-strain patterns in human coronary arteries: Assessment with three-dimensional intravascular palpography and correlation with clinical presentation. *Circulation* 2004; **109**: 2716–2719.
- Schaar JA, van der Steen AF, Mastik F, Baldeawsing RA, Serruys PW. Intravascular palpography for vulnerable plaque assessment. *J Am Coll Cardiol* 2006; **47**(Suppl): C86–C91.
- Ward MR, Hibi K, Shaw JA, Furukawa E, Resnic FS, Kimura K. Effect of stent implantation on upstream coronary artery compliance—a cause of late plaque rupture? *Am J Cardiol* 2005; **96**: 673–675.
- Rodríguez-Granillo GA, Garcia-Garcia HM, Valgimigli M, Schaar JA, Pawar R, van der Giessen WJ, et al. In vivo relationship between compositional and mechanical imaging of coronary arteries: Insights from intravascular ultrasound radiofrequency data analysis. *Am Heart J* 2006; **151**: 1025 e1–e6.
- Serruys PW, Garcia-Garcia HM, Buszman P, Erne P, Verheyhe S, Aschermann M, et al. Effects of the direct lipoprotein-associated phospholipase A(2) inhibitor darapladib on human coronary atherosclerotic plaque. *Circulation* 2008; **118**: 1172–1182.
- Van Mieghem CA, McFadden EP, de Feyter PJ, Bruining N, Schaar JA, Mollet NR, et al. Noninvasive detection of subclinical coronary atherosclerosis coupled with assessment of changes in plaque characteristics using novel invasive imaging modalities: The Integrated Biomarker and Imaging Study (IBIS). *J Am Coll Cardiol* 2006; **47**: 1134–1142.
- Wada T, Fujishiro K, Fukumoto T, Yamazaki S. Relationship between ultrasound assessment of arterial wall properties and blood pressure. *Angiology* 1997; **48**: 893–900.
- Garcia-Garcia HM, Gonzalo N, Pawar R, Kukreja N, Dudek D, Thuesen L, et al. Assessment of the absorption process following bioabsorbable everolimus-eluting stent implantation: Temporal changes in strain values and tissue composition using intravascular ultrasound radiofrequency data analysis: A substudy of the ABSORB clinical trial. *EuroIntervention* 2009; **4**: 443–448.
- Hahn C, Schwartz MA. Mechanotransduction in vascular physiology and atherogenesis. *Nat Rev Mol Cell Biol* 2009; **10**: 53–62.
- Gupta V, Grande-Allen KJ. Effects of static and cyclic loading in regulating extracellular matrix synthesis by cardiovascular cells. *Cardiovasc Res* 2006; **72**: 375–383.
- Slager CJ, Wentzel JJ, Gijzen FJ, Schuurbiens JC, van der Wal AC, van der Steen AF, et al. The role of shear stress in the generation of rupture-prone vulnerable plaques. *Nat Clin Pract Cardiovasc Med* 2005; **2**: 401–407.
- Khattab A, Windecker S. Vascular restoration therapy: What should the clinical and angiographic measures for success be? *EuroIntervention* 2009; **5**(Suppl): F49–F57.
- Awolesi MA, Sessa WC, Sumpio BE. Cyclic strain upregulates nitric oxide synthase in cultured bovine aortic endothelial cells. *J Clin Invest* 1995; **96**: 1449–1454.
- Peng X, Haldar S, Deshpande S, Irani K, Kass DA. Wall stiffness suppresses Akt/eNOS and cytoprotection in pulse-perfused endothelium. *Hypertension* 2003; **41**: 378–381.
- Balligand JL, Feron O, Dessy C. eNOS activation by physical forces: From short-term regulation of contraction to chronic remodeling of cardiovascular tissues. *Physiol Rev* 2009; **89**: 481–534.
- Onuma Y, Serruys PW, Gomez J, de Bruyne B, Dudek D, Thuesen L, et al. Comparison of in vivo acute stent recoil between the bioresorbable everolimus-eluting coronary scaffolds (revision 1.0 and 1.1) and the metallic everolimus-eluting stent. *Catheter Cardiovasc Interv* 2011; **78**: 3–12.
- Vernhet H, Juan JM, Demaria R, Oliva-Lauraire MC, Senac JP, Dauzat M. Acute changes in aortic wall mechanical properties after stent placement in rabbits. *J Vasc Interv Radiol* 2000; **11**: 634–638.
- Vernhet H, Jean B, Lust S, Laroche JP, Bonafe A, Senac JP, et al. Wall mechanics of the stented extracranial carotid artery. *Stroke* 2003; **34**: e222–e224.
- Yazdani SK, Moore JE Jr, Berry JL, Vlachos PP. DPIV measurements of flow disturbances in stented artery models: Adverse effects of compliance mismatch. *J Biomech Eng* 2004; **126**: 559–566.
- Van Den Bos GC, Westerhof N, Elzinga G, Sipkema P. Reflection in the systemic arterial system: Effects of aortic and carotid occlusion. *Cardiovasc Res* 1976; **10**: 565–573.
- Lyon RT, Runyon-Hass A, Davis HR, Glagov S, Zarins CK. Protection from atherosclerotic lesion formation by reduction of artery wall motion. *J Vasc Surg* 1987; **5**: 59–67.
- Schwarzacher SP, Tsao PS, Ward M, Hayase M, Niebauer J, Cooke JP, et al. Effects of stenting on adjacent vascular distensibility and neointima formation: Role of nitric oxide. *Vasc Med* 2001; **6**: 139–144.
- Benard N, Coisne D, Donal E, Perrault R. Experimental study of laminar blood flow through an artery treated by a stent implantation: Characterisation of intra-stent wall shear stress. *J Biomech* 2003; **36**: 991–998.

Chapter 7

Assessment of changes in the structure of bioresorbable vascular scaffolds overtime.

7.1

Serial in vivo IVUS-based echogenicity changes of everolimus-eluting bioresorbable vascular scaffold during the first 12 months after implantation. Insights from ABSORB B trial.

Salvatore Brugaletta, Josep Gomez-Lara, Patrick W Serruys, Vasim Farooq, Robert Jan van Geuns, Leif Thuesen, Dariusz Dudek, Jacques Koolen, Bernard Chevalier, Dougal McClearn, Stephan Windecker, Pieter C Smits, Bernard de Bruyne, Robert Whitbourn, Ian Meredith, Ron T van Domburg, Kenij Sihan, Sebastiaan de Winter, Susan Veldhof, Karine Miquel-Hebert, Richard Rapoza, Hector M Garcia-Garcia, John A Ormiston, Nico Bruining

JACC Cardiovascular Intervention 2011;4:1281-9

Serial In Vivo Intravascular Ultrasound-Based Echogenicity Changes of Everolimus-Eluting Bioresorbable Vascular Scaffold During the First 12 Months After Implantation

Insights From the ABSORB B Trial

Salvatore Brugaletta, MD,*|| Josep Gomez-Lara, MD,* Patrick W. Serruys, MD, PhD,* Vasim Farooq, MBChB,* Robert Jan van Geuns, MD,* Leif Thuesen, MD,¶ Dariusz Dudek, MD,# Jacques Koolen, MD, PhD,§ Bernard Chevalier, MD,** Dougal McClean, MD,‡‡ Stephan Windecker, MD, PhD,§§ Pieter C. Smits, MD, PhD,† Bernard de Bruyne, MD,||| Robert Whitbourn, MD,## Ian Meredith, MD, PhD,*** Ron T. van Domburg, PhD,* Kenij Sihan, MSc,* Sebastiaan de Winter, BSc,* Susan Veldhof, RN,¶¶ Karine Miquel-Hebert, PhD,¶¶ Richard Rapoza, PhD,††† Hector M. Garcia-Garcia, MD, PhD,*‡ John A. Ormiston, MBChB, PhD,†† Nico Bruining, PhD*

Rotterdam and Eindhoven, the Netherlands; Barcelona, Spain; Aarhus, Denmark; Krakow, Poland; Masy, France; Auckland and Christchurch, New Zealand; Bern, Switzerland; Aalst and Diegem, Belgium; Fitzroy and Melbourne, Australia; and Santa Clara, California

Objectives This study sought to investigate quantitative and homogeneity differential echogenicity changes of the ABSORB scaffold (1.1) during the first year after implantation.

Background The imaging of the ABSORB bioresorbable vascular scaffold degradation by intravascular ultrasound (IVUS) has previously demonstrated diminishing gray-level intensity of the struts over time that can be evaluated by IVUS-based differential echogenicity. The first generation of ABSORB (1.0) showed a 50% reduction in hyperechogenicity at 6 months and restoration of the pre-ABSORB implantation values at 2 years. The second generation of ABSORB (1.1), investigated in the ABSORB B trial, was modified to prolong the duration of luminal scaffolding.

Methods A total of 63 patients were examined by IVUS immediately post-implantation and at 6-month (Cohort B1, n = 28) or 12-month (Cohort B2, n = 35) follow-up. IVUS-based tissue composition analysis software was used to quantify changes in hyperechogenicity over time in the scaffolded regions. Relative changes in hyperechogenicity were calculated as: $100 \times (\% \text{ hyperechogenicity at follow-up} - \% \text{ hyperechogenicity at baseline}) / \% \text{ hyperechogenicity at baseline}$.

Results At 6- and 12-month follow-up, there was a 15% (from $22.58 \pm 9.77\%$ to $17.42 \pm 6.69\%$, $p = 0.001$) and 20% (from $23.51 \pm 8.57\%$ to $18.25 \pm 7.19\%$, $p < 0.001$) reduction in hyperechogenicity, respectively, compared with post-implantation values. No difference in hyperechogenicity changes were observed between the proximal, medial, or distal part of the scaffolded segment.

Conclusions Quantitative differential echogenicity changes of the ABSORB scaffold (1.1) during the first 12 months after implantation are lower compared with those previously observed with its first generation (1.0), confirming the value of the manufacturing changes and suggesting a slower degradation rate of the scaffold. (*J Am Coll Cardiol Intv* 2011;4:1281–9) © 2011 by the American College of Cardiology Foundation

Bioresorbable everolimus-eluting vascular scaffolds (ABSORB, Abbott Vascular, Santa Clara, California) are a novel approach for treating coronary disease in that they provide transient vessel support with drug delivery capability, but without the long-term limitations of metallic stents (1–5). Monitoring the *in vivo* bioresorption represents a challenge because the information can only be derived indirectly. However, evaluation of degradation and bioresorption of the ABSORB scaffold at different time points is important in order to relate it to other relevant clinical parameters, such as late changes in scaffold geometry and restoration of vasomotor function (6).

Intravascular ultrasound (IVUS)-derived quantitative echogenicity has previously been shown to be valuable to monitor the degradation and bioresorption processes of the scaffold. Previous benchwork showed that degradation of polymers results in different acoustical properties of the material, and with respect to the *in vivo* ABSORB scaffold degradation process, this is detected by IVUS as diminishing gray-level intensities of the struts over time (7,8).

The first-generation ABSORB scaffold (1.0), tested in the ABSORB Cohort A trial, showed a reduction in IVUS-derived hyperechogenicity from 20.9% at post-implantation to 10% at 6 months and to 6.0% at 2 years, the latter of which was close to the pre-ABSORB implantation value of the scaffolded segment (9). This reduction in hyperechogenicity was accompanied by a significant reduction in scaffold area during the first 6 months and restoration of vasomotor function at 2 years (6,8,10,11).

The second generation of the ABSORB scaffold (1.1) was modified to prolong the mechanical integrity of the device, with the aim of reducing the change in scaffold area over time, especially in the early phase: this is currently being evaluated in the ABSORB Cohort B trial (12,13). Of note is that these enhancements resulted in the absence of the scaffold area changes at 6-month follow-up that were previously observed with the first generation of ABSORB (9,14).

The objective of this study is to investigate the amount and homogeneity of the changes in IVUS-derived hyperechogenicity of the ABSORB scaffold (1.1) from post-implantation to 6- and 12-month follow-up.

Methods

Study population. The ABSORB Cohort B trial enrolled patients older than 18 years of age with a diagnosis of stable, unstable, or silent ischemia. The trial was subdivided into 2 subgroups of patients: the first group (Cohort B1) with invasive imaging with quantitative coronary angiography, IVUS, IVUS-virtual histology, and optical coherence tomography at 6- and 24-month follow-up; the second group (Cohort B2) with the same invasive imaging but at different follow-up intervals, namely 12 and 36 months (9). All lesions were *de novo*, in a native coronary artery with a reference vessel diameter of 3.0 mm, with a percentage diameter stenosis $\geq 50\%$ and $< 100\%$, and a Thrombolysis In Myocardial Infarction flow grade of ≥ 1 , and were treated with implantation of an ABSORB scaffold 1.1 (3.0 \times 18 mm). Major exclusion criteria were patients with an acute myocardial infarction, with unstable arrhythmias, or with a left ventricular ejection fraction $< 30\%$, restenotic lesions, lesions located in the left main coronary artery, lesions involving a side branch ≥ 2 mm in diameter, and the presence of thrombus or other clinically significant stenoses in the target vessel. The ethics committee at each participating institution approved the trial, and each patient gave written informed consent before inclusion.

In the present study, all patients from Cohort B1 and B2 of the ABSORB trial who underwent paired IVUS studies post-implantation and at 6- or 12-month follow-up were analyzed.

Scaffold design. The ABSORB is a fully absorbable intracoronary device comprised of semicrystalline poly(L-lactide) (PLLA) coated with amorphous poly(D,L-lactide) (PDLLA) copolymer that contains and controls the release of the antiproliferative drug everolimus. Both polylactide materials are completely degraded via hydrolysis. PLLA is bioresorbed via the Krebs's energy cycle, and PDLLA is physio-

Abbreviations and Acronyms

IVUS = intravascular ultrasound

PDLLA = amorphous poly(D,L-lactide)

PLLA = semicrystalline poly(L-lactide)

From the *Thoraxcenter, Erasmus Medical Center, Rotterdam, the Netherlands; †Maasstad Hospital, Rotterdam, the Netherlands; ‡Cardialysis BV, Rotterdam, the Netherlands; §Catharina Hospital, Eindhoven, the Netherlands; |Department of Cardiology, Thorax Institute, Hospital Clinic, University of Barcelona, Barcelona, Spain; ¶Skejby Sygehus, Aarhus University Hospital, Aarhus, Denmark; #Jagiellonian University, Krakow, Poland; **Institut Cardiovasculaire Paris Sud, Massy, France; ††Auckland City Hospital, Auckland, New Zealand; †††Christchurch Hospital, Christchurch, New Zealand; §§Bern University Hospital, Bern, Switzerland; |||Cardiovascular Center, Aalst, Belgium; ¶¶Abbott Laboratories Ltd. Vascular, Diegem, Belgium; ##St. Vincent's Hospital, Fitzroy, Australia; ***Monash Cardiovascular Research Centre, Melbourne, Australia; and ††††Abbott Laboratories Ltd. Vascular, Santa Clara, California. The ABSORB trial is sponsored and funded by Abbott Vascular, Santa Clara, California. Prof. Dudek has received research grants or served as consultant/advisory board member for Abbott, Adamed, AstraZeneca,

Biotronik, Balton, Bayer, BBraun, BioMatrix, Boston Scientific, Boehringer Ingelheim, Bristol-Myers Squibb, Cordis, Cook, Eli Lilly, EuroCor, GlaxoSmithKline, Invatec, Medtronic, The Medicines Company, Merck & Co. and Schering-Plough, Nycomed, Orbus-Neich, Pfizer, Possis, Promed, Sanofi-Aventis, Siemens, Solvay, Terumo, and Tyco. Dr. Chevalier is a consultant for Abbott Vascular. Dr. Windecker received research grants to the institution from Abbott, Biotronik, Biosensors, Boston Scientific, Cordis, and Medtronic. Dr. Smits received travel and speaking fees from Abbott Vascular and is a consultant for Blue Medical. Dr. Meredith is a consultant for Medtronic, Boston Scientific, and Abbott Vascular. Ms. Veldhof, Dr. Hebert, and Dr. Rapoza are full-time employees of Abbott Vascular. Dr. Ormiston is on the advisory board for and received minor honoraria from Abbott Vascular and Boston Scientific. Michael Kutcher, MD, served as Guest Editor for this paper. Manuscript received March 22, 2011; revised manuscript received July 27, 2011, accepted August 11, 2011.

logically processed via both Krieb's cycle and methylglyoxal metabolism (8,10,15). As previously shown, when this process is imaged by IVUS, individual cross-sectional images show a diminishing gray-level intensity of the struts over time (7).

Study procedure and imaging acquisition. All lesions were treated with routine interventional techniques that included mandatory pre-dilation using a balloon shorter and 0.5 mm smaller in diameter than the study device. IVUS examinations were performed at the different specified time points (post-implantation, 6-month, or 12-month follow-up) with either a phased-array 20-MHz IVUS catheter (EagleEye; Volcano Corporation, Rancho Cordova, California) or a mechanical rotating single-element catheter operating at 40 MHz (Atlantis, Boston Scientific, Natick, Massachusetts) applying an automated pullback speed of 0.5 mm/s (16). Rotational, mechanical IVUS probes, operating at a frequency of 40 MHz, rotate a single piezoelectric transducer at 1,800 rpm, whereas electronic phased-array systems operate at a center frequency of approximately 20 MHz. Higher ultrasound frequencies are associated with higher image resolution, but have decreased tissue penetration capabilities (17). Electronic systems have up to 64 transducer elements in an annular array that are active sequentially to generate the cross-sectional image (18). In general, electronic catheter designs are slightly easier to set up and use, whereas mechanical probes offer superior image quality.

Quantitative IVUS analysis. To analyze and compare the IVUS data consistently, only IVUS examinations acquired with the same type of catheter and/or ultrasound consoles (20 or 40 MHz) at baseline and follow-up were included in this study (19). Before quantitative IVUS was performed, the IVUS data were retrospectively electrocardiogram-gated by the previously validated Intelligate method (19,20). This method selects fully automatic, near end-diastolic-acquired IVUS frames from a nongated IVUS study. Consequently, this process allows for a smoother appearance of the coronary vessel wall, which results in enhanced matching between baseline and follow-up studies, longitudinal contouring, and echogenicity analysis (21,22). Of note is that a low frame rate (e.g., 10 frames/s instead of the optimal setting of 30 frames/s) does not allow accurate detection of near end-diastolic frames and cannot be processed by the Intelligate algorithm.

The post-procedural and follow-up IVUS images were therefore analyzed side by side, comparing the matched segments, as previously described (11). Only the treated segments, identified by the first and the last cross sections containing visible scaffold struts, were analyzed. The lumen, scaffold, and external elastic membrane contours were detected using previously validated IVUS analysis software (CURAD Vessel Analysis, Curad BV, Wijk bij Duurstede, the Netherlands) in longitudinal reconstructed views of the coronary vessels (23). The contours of the analysis were

subsequently used to perform the echogenicity analysis of the scaffolded segment.

Echogenicity analysis. Fully automated quantitative echogenicity analysis software, previously developed in-house and validated, was used to quantify the hyperechogenicity changes in the scaffolded segment (7,24). In brief, the mean gray value of the adventitia was used to classify tissue components as either hypo- or hyperechogenic. The adventitia surrounding the coronary artery was defined as a layer extending from 0.2 to 0.5 mm outside the external elastic membrane. To avoid artifacts, tissue within acoustic shadowed areas is excluded, and very high gray-level pixels are identified as upper tissue (24). After the tissue identification process, the relative fraction of hypo- versus hyperechogenic tissue volumes was calculated for the entire scaffolded segment. At 6- and 12-month follow-up, the echogenicity was calculated between the scaffold and the external elastic membrane contours, as previously described (7). The software calculated the echogenicity as a volume and percentage for each scaffolded segment (setting hypoechogenicity and hyperechogenicity to 100%).

The Δ hyperechogenicity was calculated for each scaffolded coronary segment, as follows:

$$\frac{\% \text{ hyperechogenicity 6 months} - \% \text{ hyperechogenicity post ABSORB scaffold implantation}}{\% \text{ hyperechogenicity post ABSORB scaffold implantation}} \times 100\%$$

The same formula was also applied to calculate the relative change in hyperechogenicity at 12-month follow-up.

In a further analysis, the scaffold was subdivided into 3 segments of equal length (proximal, medial, and distal), and the homogeneity of the hyperechogenicity changes at the various pre-specified time points was investigated.

Statistical analysis. Categorical variables are expressed as counts and percentages. Continuous variables are presented as mean \pm SD. The normal distribution of the variables was analyzed by the Kolmogorov-Smirnov test. IVUS-derived parameters across all time points were compared with parametric (paired sample *t* test) and nonparametric tests (Wilcoxon test) for paired data, as appropriate, according to their distribution. Correlation between plaque volume and Δ hyperechogenicity was done by Spearman rank test, as these variables were not normally distributed.

A 2-tailed value of $p < 0.05$ was considered statistically significant. Statistical analyses were performed with SPSS 16.0 software (SPSS Inc., Chicago, Illinois).

Results

Study patients. Overall, 37 and 54 patients underwent paired IVUS imaging post-procedural and at 6- or 12-month follow-up in ABSORB Cohorts B1 and B2,

respectively. For the purpose of the study, 9 and 19 patients were excluded from the Cohorts B1 and B2, respectively, because different IVUS catheters (20 or 40 MHz) were used at baseline and/or follow-up (n = 7) or the quality of the pullbacks did not allow further post-processing (n = 21). Eventually, 63 patients (28 with 6-month and 35 with 12-month follow-up) were included in the analysis (Table 1). No differences were found between the patients included and those excluded from the analysis in terms of baseline or angiographic characteristics.

Table 2 shows the IVUS data for both cohorts. At 6 months, there was a small, significant reduction in mean scaffold and lumen areas, whereas the mean vessel area remained unchanged. At 12 months, no changes were found in mean scaffold, lumen, and vessel areas.

Quantitative echogenicity analysis from post-implantation to 6 months. There was a nonsignificant increase of plaque volume (Table 3). The % hyperechogenicity decreased significantly between post-ABSORB implantation and the 6-month follow-up (p = 0.001) (Fig. 1A). Overall, there was on average a Δ hyperechogenicity of -15.51% (95% confidence interval: -27.51 to -7.52).

There were no differences in Δ hyperechogenicity between proximal (-4.22 ± 35.57%), medial (-10.7 ± 31.78%), and distal segments (-10.80 ± 45.41%; p = 0.487) (Fig. 2A). No correlation was found between baseline plaque volume and Δ hyperechogenicity (Spearman rho = 0.194, p = 0.322).

Quantitative echogenicity analysis from post-implantation to 12 months. At 12 months, there was a nonsignificant increase of plaque volume (Table 4). The % hyperechoge-

Table 1. Clinical and Lesion Characteristics		
	Cohort B1 (n = 28)	Cohort B2 (n = 35)
Patient demographic and clinical data		
Age, yrs	62.1 ± 10.1	60.4 ± 8.1
Male	19 (68)	23 (66)
Hypertension	17 (61)	25 (74)
Hypercholesterolemia	26 (93)	23 (66)
Diabetes	5 (18)	7 (20)
Current smoking	4 (14)	7 (20)
Prior PCI	5 (18)	5 (14)
Prior myocardial infarction	10 (36)	5 (15)
Stable angina	21 (75)	22 (63)
Unstable angina	3 (11)	6 (17)
Silent ischemia	0 (0)	3 (9)
Lesion and angiographic characteristics		
Treated vessel		
Left anterior descending artery	7 (25)	19 (53)
Left circumflex artery	8 (29)	6 (17)
Right coronary artery	13 (46)	11 (31)
ACC/AHA lesion type		
Type A	1 (4)	0
Type B1	13 (46)	25 (71)
Type B2	13 (46)	8 (23)
Type C	1 (4)	2 (6)
QCA analysis pretreatment		
Mean RVD, mm	2.68 ± 0.47	2.61 ± 0.30
MLD, mm	1.06 ± 0.33	1.04 ± 0.26
Diameter stenosis, %	60.10 ± 10.93	59.92 ± 9.66
Medical treatment		
Beta-blockers	22 (80)	28 (82)
ACE inhibitors	13 (47)	15 (44)
Statins	26 (96)	32 (94)
<small>Values are mean ± SD or n (%). ACC/AHA American College of Cardiology/American Heart Association; ACE = angiotensin-converting enzyme; MLD = minimum lumen diameter; PCI = percutaneous coronary intervention; QCA = quantitative coronary angiography; RVD = reference vessel diameter.</small>		

Table 2. IVUS Data From the Same Patients Used for the Echogenicity Analysis			
Paired Patients (n = 28)	Post-Implantation	6-Month Follow-Up	p Value
Mean lumen area	6.62 ± 1.22	6.35 ± 1.11	0.007
Mean vessel area	14.42 ± 3.82	14.70 ± 3.74	0.161
Mean scaffold area	6.60 ± 1.16	6.42 ± 1.09	0.004
Mean plaque area	7.80 ± 2.87	8.35 ± 2.83	0.002
Paired Patients (n = 35)	12-Month Follow-Up		
Mean lumen area	6.27 ± 1.02	6.13 ± 1.02	0.118
Mean vessel area	14.24 ± 3.48	14.58 ± 3.47	0.196
Mean scaffold area	6.24 ± 0.97	6.15 ± 0.94	0.162
Mean plaque area	7.97 ± 2.81	8.45 ± 2.68	0.023
Values are mean ± SD.			
IVUS = intravascular ultrasound.			

nicity decreased significantly ($p < 0.001$) (Fig. 1B). On average, there was a Δ hyperechogenicity of -20.00% (95% confidence interval: -27.32 to -12.00).

There were no differences in Δ hyperechogenicity between proximal ($-15.38 \pm 26.77\%$), medial ($-12.15 \pm 30.32\%$), and distal segments ($-11.20 \pm 40.81\%$; $p = 0.920$) (Fig. 2B). No correlation was found between baseline plaque volume and Δ hyperechogenicity (Spearman's $\rho = 0.101$, $p = 0.564$).

Discussion

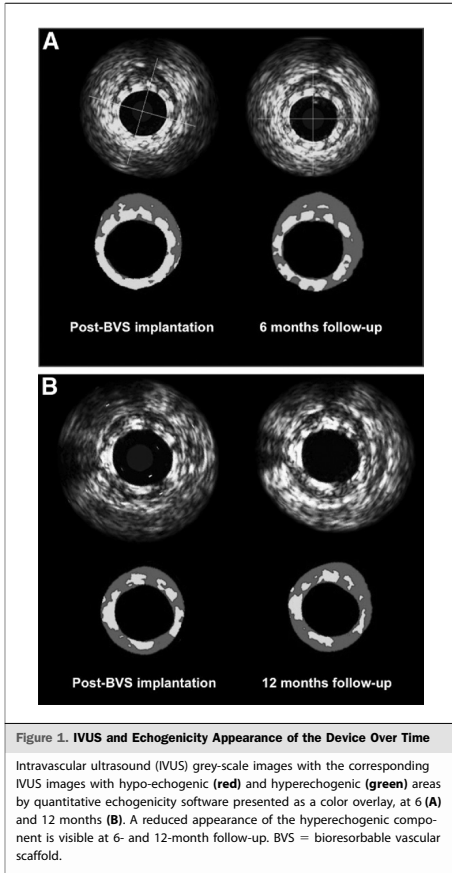
The major findings of this study are: 1) the ABSORB (1.1) demonstrates a smaller reduction in hyperechogenicity during the first 6-month follow-up, as compared with the first generation (1.0). This observation may be representative of a slower degradation rate of the scaffold; 2) at 12 months, the relative reduction of hyperechogenicity was slightly higher than that observed at 6 months; and 3) the hyperechogenicity reduction was homogeneous over the length of the scaffold and did not correlate with the underlying plaque volume.

Changes in material properties of polylactide have previously been demonstrated to be measurable by changes in the acoustic properties of the material over time. Specifically, acoustic properties are influenced by

molecular weight, viscoelasticity, copolymer ratio, and crystallinity changes in polylactide (25). Additionally, Wu et al. (26), confirming that property changes of biodegradable polymers can be detected by ultrasonic waves, have further shown that the degradation behavior of biodegradable polymers can potentially be monitored through the application of ultrasonic techniques. In the ABSORB Cohort A study, we demonstrated that quantitative differential echogenicity, as a method of determining the acoustic property changes of the ABSORB, could be applied to monitor *in vivo* changes of the scaffold (7,8). At the expected time of total degradation and bioresorption (approximately 2 years), the acoustic signals showed only little evidence of polymer residues (7). Furthermore, histological studies in animal models at 2 to 4 years have demonstrated that the previous locations of the struts were replaced by proteoglycans with occasional microcalcification and ultimately by connective tissue (8,27). Gel permeation chromatography confirmed that the molecular weight of the PLLA was unquantifiable at 2 years after implantation and that the polymer mass loss increases by 20%, 60%, and 90% at 1, 1.5, and 2 years, respectively, becoming undetectable at 3 years (27).

In the present study, focusing on the first-year follow-up after ABSORB bioresorbable vascular scaffold

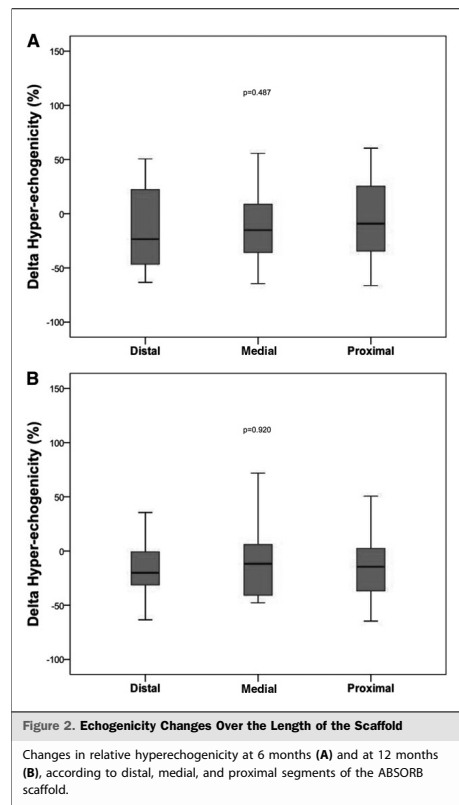
Table 3. Echogenicity Analysis Post-ABSORB Implantation and at 6 Months (n = 28)				
	Post-Implantation	6-Month Follow-Up	Relative Difference Based on Individual Data, %	p Value
Plaque volume, mm ³	186.51 ± 71.74	199.60 ± 69.50	12.67 ± 32.98	0.127
Calcification volume, mm ³	0.11 ± 0.21	0.10 ± 0.22	-15.75 ± 51.24	0.520
Upper volume, mm ³	2.38 ± 4.79	0.72 ± 2.07	-57.50 ± 79.61	0.001
Hyperechogenicity, mm ³	38.91 ± 20.19	33.31 ± 16.26	-6.65 ± 26.29	0.094
Hyperechogenicity, %	22.58 ± 9.77	17.42 ± 6.69	-15.01 ± 28.68	0.001
Values are mean ± SD.				



(1.1) implantation, we demonstrated a smaller change in Δ hyperechogenicity at 6 months as compared with its first generation (1.0) ($p = 0.001$) (Fig. 3). No difference in baseline hyperechogenicity was present between Cohorts B1 and B2 ($22.58 \pm 9.77\%$ vs. $23.51 \pm 8.57\%$, $p = 0.742$). The accuracy of this method has been previously reported (7,24). At 12 months, the Δ hyperechogenicity of the ABSORB (1.1) was slightly higher when compared with 6 months. Although these data came from 2 different groups of patients (Cohorts B1 and B2), a small hyperechogenicity reduction of ABSORB 1.1 could nevertheless be extrapolated for the period between 6 and 12 months, further supporting a low in vivo degradation rate of the second-generation ABSORB scaffold. It is note-

worthy that although in an animal model there was a significant molecular weight degradation of ABSORB over the first 12 months (27), in humans, the small change in hyperechogenicity at 12 months may suggest that the microstructural features, which drive the hyperechogenicity signal of the scaffold, are retained for longer times post-implantation. Because the preservation of semicrystalline microstructure is necessary for enduring luminal support, this hypothesis is also consistent with the observation of reduced scaffold area loss at 6 months with ABSORB (1.1) compared with its first-generation device (9,14). Further studies are, however, required to correlate the ABSORB degradation process with the changes in its mechanical properties (28).

In a further subanalysis, we also showed that the Δ hyperechogenicity is homogeneous over the entire length of the scaffold and does not differ in relation to the



	Post-Implantation	12-Month Follow-Up	Relative Difference Based on Individual Data, %	p Value
Plaque volume, mm ³	176.31 ± 88.19	197.13 ± 67.90	33.07 ± 70.58	0.219
Calcification volume, mm ³	0.12 ± 0.21	0.16 ± 0.31	22.55 ± 69.67	0.611
Upper volume, mm ³	2.00 ± 3.00	1.39 ± 2.17	-56.92 ± 51.17	0.590
Hyperechogenicity, mm ³	39.06 ± 20.24	34.06 ± 15.02	-3.17 ± 54.43	0.050
Hyperechogenicity, %	23.51 ± 8.57	18.25 ± 7.19	-19.66 ± 22.32	<0.001

Values are mean ± SD.

volume of the baseline underlying plaque. We hypothesized that Δ hyperechogenicity, used as a surrogate of the ABSORB property changes, could not only be due to intrinsic material property changes caused by degradation, but might also depend upon specific characteristics of the scaffolded plaque, such as size and histochemical characteristics (e.g., presence of macrophages) (29). However, we found no correlation between plaque size and change in hyperechogenicity at the various time points. IVUS-virtual histology could be used to evaluate the characteristics of the scaffolded plaque: the overestimation of virtual histology—dense calcium and necrotic core after ABSORB implantation precludes this kind of analysis (30,31).

It is of interest to note that although at 6 months there was a significant reduction in mean scaffold area and in mean lumen area, this was not observed at 12 months. This phenomenon is supported by the fact that a constrictive remodeling after balloon angioplasty, possibly inducing a

restenotic process, ceased to be active after 4 months (32). Hypothetically then, at 12-month follow-up, it seems that there are no elastic vessel forces active anymore on the scaffold, whose radial force has conversely partially subsided as indicated by the vasoconstriction and vasodilatation induced by vasoactive drugs (33). Further follow-up at future time points (e.g., at 2 and 3 years) is required to extend the significance of the current findings.

Finally, our standardized software analysis method to assess the echogenicity of the scaffolded segment over time represents a clinically relevant tool for the bioresorbable scaffold era. This analysis approach may provide indirect information on scaffold degradation, performance of these devices in various types of lesions (calcified, fibrotic, eccentric, degenerated vein graft) and a method to compare other types of present and future bioresorbable scaffold platforms. **Study limitations.** The main limitation of this observational study is the relatively small study population. To maintain the highest quality for analysis, we had to

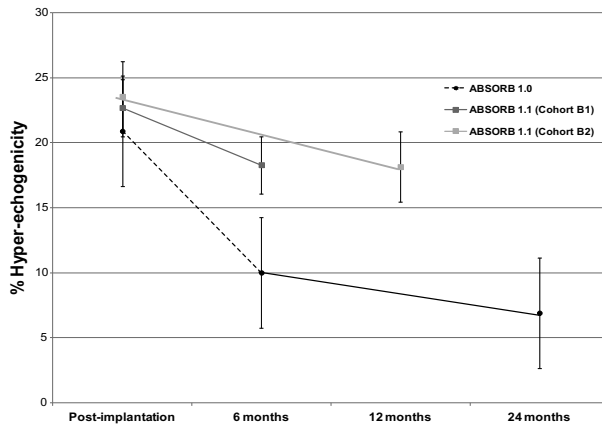


Figure 3. Comparison in Terms of Echogenicity Changes Between ABSORB 1.0 and 1.1

Comparison between ABSORB 1.0 and 1.1 in terms of serial changes in hyperechogenicity. Mean values and standard errors are reported.

exclude some patients for whom the data were acquired with different ultrasound catheters or with a low frame rate, making baseline and follow-up paired matching unreliable (34). The use of 20-MHz IVUS catheters may affect the accurate detection of the scaffold as a result of its relatively low IVUS resolution (as compared with the commercially available 40-MHz catheters); conversely, a relatively low resolution comes with a relatively high acoustic energy, which improves the sensitivity to pick up the scaffold struts.

Conclusions

The second-generation ABSORB scaffold (1.1) demonstrated a reduced amount of change in ultrasound-derived parameters (e.g., changes in hyperechogenicity) at 6 and 12 months (-15% and -20%, respectively), compared with its first generation (1.0). This observation may be representative of a slower degradation rate of the scaffold. Longer follow-up is required to confirm these findings and their clinical significance.

Reprint requests and correspondence: Dr. Nico Bruining, Thoraxcenter, Erasmus Medical Center, P.O. Box 1738, 3000 DR, Rotterdam, the Netherlands. E-mail: n.bruining@erasmusmc.nl

REFERENCES

1. Ormiston JA, Serruys PWS. Bioabsorbable coronary stents. *Circ Cardiovasc Interv* 2009;2:255-60.
2. Waksman R. Biodegradable stents: they do their job and disappear. *J Invasive Cardiol* 2006;18:70-4.
3. Finn AV, Joner M, Nakazawa G, et al. Pathological correlates of late drug-eluting stent thrombosis: strut coverage as a marker of endothelialization. *Circulation* 2007;115:2455-41.
4. Joner M, Finn AV, Farb A, et al. Pathology of drug-eluting stents in humans: delayed healing and late thrombotic risk. *J Am Coll Cardiol* 2006;48:193-202.
5. Togni M, Windecker S, Cocchia R, et al. Sirolimus-eluting stents associated with paradoxical coronary vasoconstriction. *J Am Coll Cardiol* 2005;46:231-6.
6. Sarno G, Bruining N, Onuma Y, et al. Morphological and functional evaluation of the bioresorption of the bioresorbable everolimus-eluting vascular scaffold using IVUS, echogenicity and vasomotion testing at two year follow-up: a patient level insight into the ABSORB A clinical trial. *Int J Cardiovasc Imaging* 2011 Jan 7 [E-pub ahead of print].
7. Bruining N, de Winter S, Roelandt JR, et al. Monitoring in vivo absorption of a drug-eluting bioabsorbable stent with intravascular ultrasound-derived parameters a feasibility study. *J Am Coll Cardiol Interv* 2010;3:449-56.
8. Serruys PW, Ormiston JA, Onuma Y, et al. A bioabsorbable everolimus-eluting coronary stent system (ABSORB): 2-year outcomes and results from multiple imaging methods. *Lancet* 2009;373:897-910.
9. Serruys PW, Onuma Y, Ormiston JA, et al. Evaluation of the second generation of a bioresorbable everolimus drug-eluting vascular scaffold for treatment of de novo coronary artery stenosis: six-month clinical and imaging outcomes. *Circulation* 2010;122:2301-12.
10. Ormiston JA, Serruys PW, Regar E, et al. A bioabsorbable everolimus-eluting coronary stent system for patients with single de-novo coronary artery lesions (ABSORB): a prospective open-label trial. *Lancet* 2008;371:899-907.

11. Tanimoto S, Bruining N, van Domburg RT, et al. Late stent recoil of the bioabsorbable everolimus-eluting coronary stent and its relationship with plaque morphology. *J Am Coll Cardiol* 2008;52:1616-20.
12. Waksman R, Eribel R, Di Mario C, et al. Early- and long-term intravascular ultrasound and angiographic findings after bioabsorbable magnesium stent implantation in human coronary arteries. *J Am Coll Cardiol Interv* 2009;2:312-20.
13. Okamura T, Garg S, Gutiérrez-Chico JL, et al. In vivo evaluation of stent strut distribution patterns in the bioabsorbable everolimus-eluting device: an OCT ad hoc analysis of the revision 1.0 and revision 1.1 stent design in the ABSORB clinical trial. *EuroIntervention* 2010;5:932-8.
14. Gomez-Lara J, Brugaletta S, Diletti R, et al. A comparative assessment by optical coherence tomography of the performance of the first and second generation of the everolimus-eluting bioresorbable vascular scaffolds. *Eur Heart J* 2011;32:294-304.
15. Ewaschuk JB, Naylor JM, Zello GA. D-lactate in human and ruminant metabolism. *J Nutr* 2005;135:1619-25.
16. Mintz GS, Nissen SE, Anderson WD, et al. American College of Cardiology clinical expert consensus document on standards for acquisition, measurement and reporting of intravascular ultrasound studies (IVUS). A report of the American College of Cardiology Task Force on Clinical Expert Consensus Documents. *J Am Coll Cardiol* 2001;37:1478-92.
17. Lockwood GR, Ryan LK, Hunt JW, Foster FS. Measurement of the ultrasonic properties of vascular tissues and blood from 35-65 MHz. *Ultrasound Med Biol* 1991;17:653-66.
18. Bridal SL, Fornès P, Bruneval P, Berger G. Parametric (integrated backscatter and attenuation) images constructed using backscattered radio frequency signals (25-56 MHz) from human aortae in vitro. *Ultrasound Med Biol* 1997;23:215-29.
19. Rodriguez-Granillo GA, McFadden EP, Aoki J, et al. In vivo variability in quantitative coronary ultrasound and tissue characterization measurements with mechanical and phased-array catheters. *Int J Cardiovasc Imaging* 2006;22:47-53.
20. De Winter SA, Hamers R, Degertekin M, et al. Retrospective image-based gating of intracoronary ultrasound images for improved quantitative analysis: the Intelligate method. *Catheter Cardiovasc Interv* 2004;61:84-94.
21. Bruining N, von Birgelen C, de Feyter PJ, et al. ECG-gated versus nongated three-dimensional intracoronary ultrasound analysis: implications for volumetric measurements. *Catheter Cardiovasc Diagn* 1998;43:254-60.
22. von Birgelen C, Mintz GS, Nicosia A, et al. Electrocardiogram-gated intravascular ultrasound image acquisition after coronary stent deployment facilitates on-line three-dimensional reconstruction and automated lumen quantification. *J Am Coll Cardiol* 1997;30:436-43.
23. Hamers R, Bruining N, Knook M, Sabate M. A novel approach to quantitative analysis of intravascular ultrasound images. *Comput Cardiol* 2008;28:589-92.
24. Bruining N, Verheye S, Knaapen M, et al. Three-dimensional and quantitative analysis of atherosclerotic plaque composition by automated differential echogenicity. *Catheter Cardiovasc Interv* 2007;70:968-78.
25. Parker NG, Mather ML, Morgan SP, Povey MJ. Longitudinal acoustic properties of poly(lactic acid) and poly(lactic-co-glycolic acid). *Biomed Mater* 2010;5:055004.
26. Wu HC, Shen FW, Hong X, Chang WV, Winet H. Monitoring the degradation process of biopolymers by ultrasonic longitudinal wave pulse-echo technique. *Biomaterials* 2003;24:3871-6.
27. Onuma Y, Serruys PW, Perkins LE, et al. Intracoronary optical coherence tomography and histology at 1 month and 2, 3, and 4 years after implantation of everolimus-eluting bioresorbable vascular scaffolds in a porcine coronary artery model: an attempt to decipher the human optical coherence tomography images in the ABSORB trial. *Circulation* 2010;122:2288-300.
28. Nuutinen JP, Clerc C, Reinikainen R, Törmälä P. Mechanical properties and in vitro degradation of bioabsorbable self-expanding braided stents. *J Biomater Sci Polym Ed* 2003;14:255-66.
29. Jiang WW, Su SH, Eberhart RC, Tang L. Phagocyte responses to degradable polymers. *J Biomed Mater Res A* 2007;82:492-7.

30. Kim SW, Mintz GS, Hong YJ, et al. The virtual histology intravascular ultrasound appearance of newly placed drug-eluting stents. *Am J Cardiol* 2008;102:1182–6.
31. Sales FJ, Falcao BA, Falcao JL, et al. Evaluation of plaque composition by intravascular ultrasound “virtual histology”: the impact of dense calcium on the measurement of necrotic tissue. *EuroIntervention* 2010;6:394–9.
32. Serruys PW, Luijten HE, Beatt KJ, et al. Incidence of restenosis after successful coronary angioplasty: a time-related phenomenon. A quantitative angiographic study in 342 consecutive patients at 1, 2, 3 and 4 months. *Circulation* 1988;77:361–71.
33. Serruys PW, Onuma Y, Dudek D, et al. Evaluation of the second generation of a bioresorbable everolimus-eluting vascular scaffold for the treatment of de novo coronary artery stenosis: 12-month clinical and imaging outcomes. *J Am Coll Cardiol* 2011;58:1578–88.
34. Rodriguez-Granillo GA, Vaina S, García-García HM, et al. Reproducibility of intravascular ultrasound radiofrequency data analysis: implications for the design of longitudinal studies. *Int J Cardiovasc Imaging* 2006;22:621–31.

Key Words: ABSORB bioresorbable vascular scaffold ■ echogenicity ■ IVUS.

7.2

Serial analysis of the malapposed and uncovered struts of the new generation of everolimus-eluting bioresorbable scaffold using optical coherence tomography.

Josep Gomez-Lara, Maria Radu, Salvatore Brugaletta, Vasim Farooq, Roberto Diletti, Yoshinobu Onuma, Stephan Windecker, Leif Thuesen, Dougal McClean, Jacques Koolen, Robert Whitbourn, Dariusz Dudek, Pieter C Smits, Evelyn Regar, Susan Veldhof, Richard Rapoza, John A Ormiston, Hector M Garcia-Garcia, Patrick W Serruys

JACC Cardiovascular Intervention 2011;4:992-1001

Serial Analysis of the Malapposed and Uncovered Struts of the New Generation of Everolimus-Eluting Bioresorbable Scaffold With Optical Coherence Tomography

Josep Gomez-Lara, MD,* Maria Radu, MD,* Salvatore Brugaletta, MD,*
 Vasim Farooq, MChB,* Roberto Diletti, MD,* Yoshinobu Onuma, MD,*
 Stephan Windecker, MD,† Leif Thuesen, MD,‡ Dougal McClean, MD,§
 Jacques Koolen, MD, PhD,|| Robert Whitbourn, MD,¶ Dariusz Dudek, MD,#
 Pieter C. Smits, MD, PhD,** Evelyn Regar, MD, PhD,* Susan Veldhof, RN,††
 Richard Rapoza, PhD,‡‡ John A. Ormiston, MChB, PhD,§§
 Hector M. Garcia-Garcia, MD, PhD,* Patrick W. Serruys, MD, PhD*

Rotterdam and Eindeboven, the Netherlands; Bern, Switzerland; Aarhus, Denmark; Christchurch and Auckland, New Zealand; Fitzroy, Australia; Krakow, Poland; Diegem, Belgium; and Santa Clara, California

Objectives The aim of this study is to assess the serial changes in strut apposition and coverage of the bioresorbable vascular scaffolds (BVS) and to relate this with the presence of intraluminal masses at 6 months with optical coherence tomography (OCT).

Background Incomplete strut/scaffold apposition (ISA) and uncovered struts are related to a higher risk of scaffold thrombosis. Bioresorbable vascular scaffolds can potentially avoid the risk of scaffold thrombosis because of its complete resorption. However, during the resorption period, the risk of scaffold thrombosis is unknown.

Methods OCT was performed in 25 patients at baseline and 6 months. Struts were classified according to apposition, coverage, and presence of intraluminal masses. Persistent ISA was defined as malapposed struts present at baseline and follow-up, and late acquired ISA as ISA developing at follow-up, and scaffold pattern irregularities when the strut distribution suggested scaffold fracture.

Results At baseline, 3,686 struts were analyzed: 128 (4%) were ISA, and 53 (1%) were located over side-branches (SB). At 6 months, 3,905 struts were analyzed: 32 (1%) ISA, and 35 (1%) at the SB. Persistent ISA was observed more frequently than late acquired-ISA (81% vs. 16%, respectively; 3% were unmatchable). Late acquired ISA was associated with scaffold pattern irregularities, which were related to overstretching of the scaffold. Uncovered struts (63 struts, 2%) were more frequently observed in ISA and SB struts, compared with apposed struts (29% vs. 1%; $p < 0.01$). Intraluminal masses (14 cross-sections, 3%; in 6 patients, 24%) were more frequently located at the site of ISA and/or uncovered struts (39% vs. 2% and 13% vs. 2%, respectively; $p < 0.01$).

Conclusions The lack of strut apposition at baseline is related to the presence of uncovered struts and intraluminal masses at 6 month. An appropriate balloon/artery ratio respecting the actual vessel size and avoiding the overstretching of the scaffold can potentially decrease the risk of scaffold thrombosis. (ABSORB Clinical Investigation, Cohort B [ABSORB B]; NCT00856856) (J Am Coll Cardiol Intv 2011;4:992-1001) © 2011 by the American College of Cardiology Foundation

From the *Thoraxcenter, Erasmus Medical Center, Rotterdam, the Netherlands; †Swiss Cardiovascular Center, Bern, Switzerland; ‡Skejby Sygehus, Aarhus University Hospital, Aarhus, Denmark; §Christchurch Hospital, Christchurch, New Zealand; ||Catharina Ziekenhuis, Eindhoven, the Netherlands; ¶St. Vincent's Hospital, Fitzroy, Australia; #Jagiellonian University, Krakow, Poland; **Maasstad Ziekenhuis, Rotterdam, the Netherlands; ††Abbott Laboratories, Ltd., Vascular, Diegem, Belgium; ‡‡Abbott Laboratories, Ltd., Vascular, Santa Clara, California; and the §§Auckland City Hospital, Auckland, New Zealand. The Absorb

Serial intravascular ultrasound (IVUS) imaging of metallic drug-eluting stents (DES) has shown that incomplete stent/strut apposition (ISA) at follow-up can be caused by the persistence of ISA observed at baseline or by the new appearance of late acquired incomplete scaffold/strut apposition (LAISA) (1,2). Recent reports suggest that strut apposition is important for the development of strut coverage, because malapposed struts are more frequently uncovered at follow-up, as compared with apposed struts (3,4). Furthermore, the absence of neointimal coverage as well as the presence of malapposed struts have been related to late stent thrombosis, even in patients treated with dual antiplatelet therapy (5,6).

The novel everolimus-eluting bioresorbable vascular scaffolds (BVS) are promising intravascular devices that can potentially circumvent the risk of malapposed and uncovered struts at follow-up. Notably, at 2 years after implantation, the polymeric material has been shown to be resorbed with the disappearance of struts that were initially malapposed or at side branches (SBs) (7). The first-generation BVS (version 1.0) demonstrated a high rate of malapposed struts before complete resorption, with a rate of malapposed struts at 6 months higher than at baseline (6% vs. 5%, respectively; $p < 0.01$). This uncommon phenomenon was caused by a low rate of resolved malapposed struts and by the occurrence of LAISA at 6-month follow-up (8). The late scaffold area reduction (shrinkage) observed at 6 months was the most plausible explanation for the higher rate of ISA observed at follow-up compared with baseline. Despite this, only 1% of struts remained uncovered at 6-month follow-up (8).

The new-generation BVS (version 1.1) uses a new platform design and a different processing of the polymer, as compared with the previous generation of BVS (version 1.0), resulting in an increased radial force and longer retention of mechanical integrity (9). Consequently, there is now no detectable loss in scaffold area at 6 months (10,11). Nevertheless, ISA and uncovered struts can still be detected with the new generation of BVS, but the fate of these struts is unknown.

The aim of our study is to describe the serial changes of ISA and uncovered struts at baseline and at 6-month follow-up of the new generation of BVS (version 1.1), as assessed by optical coherence tomography (OCT).

Methods

Population. The ABSORB Cohort B (A Clinical Evaluation of the Bioabsorbable Everolimus Eluting Coronary Stent System [BVS EECS] in the Treatment of Patients With de Novo Native Coronary Artery Lesions) trial is a nonrandomized, multicenter, single-arm, efficacy-safety study (12). The study included 101 patients that were allocated to 6-month angiographic and intravascular imaging control (cohort B1) or 12-month angiographic and intravascular imaging control (cohort B2). All lesions were treated with a single-size device (3×18 mm) of the new generation of BVS (version 1.1). The OCT imaging was an optional investigation performed in selected participating centers. In brief, the common inclusion criteria were patients 18 years of age or older, with a diagnosis of stable, unstable, or silent ischemia that presented with a de novo lesion in a native coronary artery between 50% and 99% of the luminal diameter and a Thrombolysis In Myocardial Infarction flow grade of 1 or more. Exclusion criteria included patients with an evolving myocardial infarction, stenosis of the left main or ostial right coronary artery, presence of intracoronary thrombus, or heavy calcification.

The present study is a post hoc analysis of those patients included in the ABSORB cohort B1 that were serially imaged with OCT at baseline and at 6-month follow-up.

BVS. The BVS version 1.1 revision is a balloon-expandable device, consisting of a polymer backbone of poly-L-lactide coated with a thin layer of a 1:1 mixture of an amorphous matrix of poly-D,L-lactide polymer containing $100 \mu\text{g}/\text{cm}^2$ of the antiproliferative drug everolimus. The implant is radiolucent but has 2 platinum markers at each edge, which allows visualization on angiography and other imaging modalities. Physically, the scaffold has struts with an approximate thickness of $150 \mu\text{m}$ arranged as in-phase zigzag hoops linked together by 3 longitudinal bridges.

Abbreviations and Acronyms

BVS = bioresorbable vascular scaffolds
DES = drug-eluting stents
ISA = incomplete scaffold/strut apposition
IVUS = intravascular ultrasound
LAISA = late acquired incomplete scaffold/strut apposition
OCT = optical coherence tomography
SB = side branch

Cohort B study has been funded by Abbott Vascular (Santa Clara, California). Dr. Windecker has received research grants from Abbott, Cordis, Medtronic, Biosensors, and Boston Scientific. Dr. Dudek has received research grants or served as consultant/advisory board member for Abbott, Adamed, AstraZeneca, Biotronik, Balton, Bayer, B Braun, BioMatrix, Boston Scientific, Boehringer Ingelheim, Bristol-Myers Squibb, Cordis, Cook, Eli Lilly, EuroCor, Glaxo, InVatec, Medtronic, The Medicines Co., MSD, Nycomed, Orbus-Neich, Pfizer, Possis, Promed, Sanofi-Aventis, Siemens, Solvay, Terumo, and Tyco. Dr. Smits has

received travel fees from Abbott Vascular. Ms. Susan Veldhof and Dr. Rapoza are employees of Abbott Vascular. Dr. Ormiston is on the advisory board of and has received minor honoraria from Abbott Vascular and Boston Scientific. All other authors have reported that they have no relationships relevant to the contents of this paper to disclose.

Manuscript received November 30, 2010; revised manuscript received March 18, 2011, accepted March 28, 2011.

Treatment procedure. Lesions were treated with routine interventional techniques. As per protocol, pre-dilation with conventional balloons was mandatory. Pre-dilation balloons should be shorter than the length of the scaffold and 0.5-mm smaller in diameter than the reference vessel. The BVS implantation should not exceed the burst pressure as indicated by the product chart (16 atm). Post-dilation with a balloon shorter than the implanted device was allowed at the discretion of the operator but, when performed, should only be done with balloons sized to fit within the boundaries of the scaffold. Intravascular imaging techniques were performed when optimal BVS placement was obtained according to the judgment of the physician on the basis of angiographic results. In case of suboptimal deployment as assessed by intravascular imaging techniques, post-dilations were allowed at discretion of the operator until optimal stent placement was achieved (on the basis of angiography). After the last post-dilation, a new intravascular imaging acquisition was performed and was used for the study analysis.

OCT acquisition. The OCT imaging was performed with 2 different OCT systems (M3 Time-Domain System and C7XR Fourier-Domain System; LightLab Imaging, Westford, Massachusetts). The M3 OCT system used a standard intracoronary guidewire to cross the target lesion, and then a single-lumen (e.g., Transit, Cordis, Johnson and Johnson, Miami, Florida, or ProGreat, Terumo, Tokyo, Japan) or double-lumen catheter (0.023-inch TwinPass, Vascular Solutions, Inc., Minneapolis, Minnesota) was required to exchange the conventional wire with the LightLab Imaging ImageWire. Pullback was performed during continuous injection of contrast medium (1 to 3 ml/s, iodixanol 370; Visipaque, GE Healthcare, Cork, Ireland) through the guide catheter with an injection pump. The automated pullback was performed at 3 mm/s with a frame rate of 20 images/s.

The C7XR system used a conventional wire to cross the segment of interest. The OCT imaging catheter (Dragonfly, LightLab Imaging) was then advanced distally to the treated region. Pullback was performed during continuous injection of contrast medium (3 ml/s, iodixanol 370; Visipaque) through the guide catheter with an injection pump. The automated pullback rate was 20 mm/s, and the frame rate was 100 images/s.

OCT analysis. Offline OCT qualitative data analysis was carried out by 2 expert analysts with the proprietary software for offline analysis (LightLab Imaging). Both investigators were blinded to the patient, procedural, and clinical characteristics as well as to the clinical outcomes. Adjusting for the pullback speed, the analysis of contiguous cross-sections was performed at 1-mm longitudinal intervals within the treated segment (7 cross-sections/mm in case of M3 OCT system and 5 cross-sections/mm in case of C7 OCT system).

At baseline, embedded struts were defined as present when more than one-half thickness of the strut was im-

acted into the vessel wall; protruding struts were defined as struts being in contact with the vessel wall but with less than one-half strut thickness impacted into the vessel wall. Both embedded and protruding struts presented with different degrees of apposed struts at follow-up, but we made no distinction. At baseline and follow-up, malapposed struts were defined as struts where the abluminal surfaces were separated from the vessel wall by flush; and SB struts were defined as struts overlying the ostium of an SB (Fig. 1). It is noteworthy that, in contrast with metallic stents, the BVS allows the assessment of the structures located behind the struts without the usual shadowing of metallic struts. Therefore, strut malapposition can be easily assessed when the polymeric strut is separated from the vessel wall. At follow-up, the absence of strut coverage was defined when 1 of the strut corners preserved the right angle shape without signs of neointimal tissue (Fig. 1). Although strut apposition and coverage was measured as a consensus between 2 analysts, a total of 100 random images of 10 different patients were analyzed separately by 2 analysts to ensure the agreement of the qualitative assessments. Scaffold pattern irregularities were defined when struts were found in locations incongruent with the scaffold pattern. They were classified into 2 categories: 1) 2 struts overhanging each other in the same angular sector of the lumen perimeter, with or without malapposition; and/or 2) isolated struts located more or less at the center of the vessel without obvious connection to the expected adjacent strut pattern. At follow-up, protruding masses attached to the vessel wall or floating masses without contact with the vessel wall have been suggested to be thrombi (3). However, the distinction between thrombi and neointimal protrusions into the lumen is not always possible. Therefore, any irregular mass attached to the polymeric struts or floating into the lumen has been classified as intraluminal mass without distinction between thrombus and neointima.

With clear landmarks in the longitudinal OCT images, all cross-sections with at least 1 ISA or SB strut at baseline were matched with the corresponding image of all the possible cross-sections of the entire recording at follow-up (every 7 cross-sections/mm in case of M3 OCT system and every 5 cross-sections/mm in case of C7 OCT system). Every single ISA or SB strut at baseline was investigated at follow-up, to assess its apposition and the state of neointimal coverage. Similarly, those images with at least 1 ISA and/or uncovered struts at follow-up were matched to the corresponding image at baseline of all possible cross-sections of the entire recording at baseline and investigated to assess the original state of strut apposition.

Statistical analysis. Statistical analysis was performed with the SPSS software (version 15.0, SPSS, Inc., Chicago, Illinois). Discrete variables are presented as counts and percentages and continuous variables as mean \pm SD. Comparisons of continuous variables between baseline and

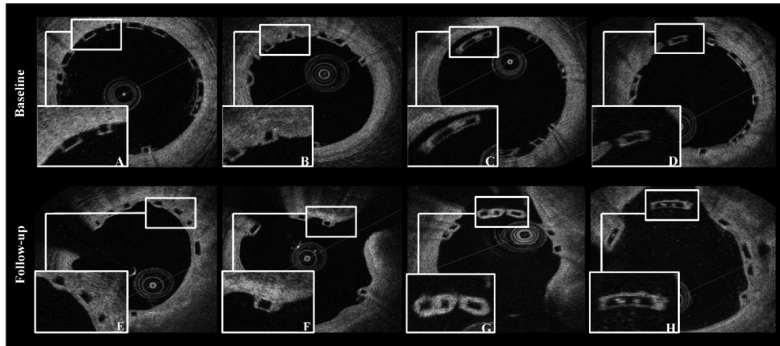


Figure 1. Strut Apposition and Coverage Assessment

Apposition assessment at baseline: (A) protruding struts: less than one-half thickness of the strut is impacted into the vessel wall; (B) embedded strut: more than one-half thickness of the strut is impacted into the vessel wall; (C) incomplete strut/scaffold apposition (ISA): the back-side of the strut is separated from the vessel wall; (D) side-branches (SB) strut: the strut is located in the take-off of an SB without any contact with the vessel wall. Strut coverage assessment at follow-up: (E) apposed and covered strut: the 4 corners of the polymeric strut have lost the right angle shape with signs of tissue coverage; (F) apposed and uncovered strut: 1 of the 2 endoluminal strut corners preserves the right angle shape without signs of tissue coverage; (G) ISA/SB and covered strut: the 4 strut corners have lost the right angle shape with signs of tissue coverage; (H) ISA/SB and uncovered: 1 of the 4 strut corners preserves the right angle shape without signs of tissue coverage.

follow-up have been estimated with the nonparametric Wilcoxon signed-rank test. Comparison of percentages of uncovered struts between apposed and nonapposed struts has been performed with the Mann-Whitney *U* test at strut level analysis. Adjustments for clustering data at the patient and frame level analysis have not been performed. A 2-sided *p* value ≤ 0.05 was considered statistically significant.

The interobserver agreement for qualitative measurements was quantified by the Cohen's kappa test for concordance (13). In accordance with previous publications, a value < 0 indicates poor agreement, 0 to 0.20 indicates slight agreement, 0.21 to 0.40 indicates fair agreement, 0.41 to 0.60 indicates moderate agreement, 0.61 to 0.80 indicates good agreement, and 0.81 to 1.0 indicates excellent agreement (14).

Results

Population. The ABSORB Cohort B1 study included 45 patients, 28 of whom were imaged with OCT at baseline. Two patients were excluded due to suboptimal quality of the OCT recording (lack of imaging of the full length and/or perimeter of the implant); and 1 asymptomatic patient withdrew consent to invasive control at 6-month follow-up. The remaining 25 patients, all of whom were serially imaged with OCT at baseline and 6-month follow-up, were included in the present study. A total of 11 and 9 patients were imaged with the M3 OCT system at baseline and

follow-up, respectively; whereas 14 and 16 patients were imaged with the C7 OCT system at baseline and follow-up, respectively. Only 2 patients were imaged with different OCT systems at baseline and follow-up.

Male	20 (80.0)
Age (yrs)	62.4 \pm 10.0
Hypertension	14 (56.0)
Hypercholesterolemia	24 (96.0)
Diabetes	2 (8.0)
Smokers	5 (20.0)
Prior MI	11 (44.0)
Prior PCI	6 (24.0)
Clinical indication	
Stable angina	21 (84.0)
Unstable angina	4 (16.0)
Number of vessel disease	
1	21 (84.0)
2	3 (12.0)
3	1 (4.0)
Target vessel	
Left anterior descending	11 (44.0)
Left circumflex	6 (24.0)
Right coronary artery	8 (32.0)
Values are count (%) or mean \pm SD.	
MI = myocardial infarction; PCI = percutaneous coronary intervention.	

Number of struts	3,686
Protruding	2,554 (69.3%)
Embedded	951 (25.8%)
ISA	128 (3.5%)
SB	53 (1.4%)
Matched ISA at baseline that at 6 months became	128
Apposed + covered	97 (75.8%)
Apposed + uncovered	6 (4.7%)
Persistent ISA + covered	15 (11.7%)
Persistent ISA + uncovered	4 (3.1%)
Unmatchable	6 (4.7%)
Matched SB struts at baseline that at 6 months became	53
Apposed + covered	12 (22.7%)
Apposed + uncovered	1 (1.9%)
SB + covered	27 (50.9%)
SB + uncovered	5 (9.4%)
Unmatchable	8 (15.1%)

ISA = incomplete scaffold/strut apposition; OCT = optical coherence tomography; SB = side branch.

Baseline clinical and angiographic characteristics are shown in Table 1. Mean age was 62.4 years; 80% were men, and 8% were diabetic. The clinical indication of the index procedure was stable angina in 84% of patients. A total of 85% of patients had single-vessel disease.

Qualitative OCT findings at baseline. Qualitative OCT findings at baseline are shown in Table 2. At baseline, 3,686 struts in 424 frames were analyzed: 2,554 were classified as

protruding (69.3%), 951 as embedded (25.8%), 128 as ISA (3.5%), and 53 struts were overlying an SB (1.4%). Figure 2 shows the distribution of malapposed and SB struts throughout the length of the BVS.

Matched cross-sections. A total of 80 of 90 baseline images with ISA and/or SB struts were properly matched with the corresponding frame at 6-month follow-up. Therefore, 95.3% of malapposed and 84.9% of SB struts were properly matched between time points. At follow-up, the fate of the malapposed struts observed at baseline was: 80.5% resolved into apposed struts, and 14.8% persisted as ISA (4.7% were unmatchable).

Qualitative OCT findings at 6-month follow-up. At 6 months, all polymeric struts were visible, remaining with the preserved box appearance. Qualitative OCT findings are shown in Table 3. At follow-up, 3,905 struts in 433 frames were analyzed: 3,838 were apposed (98.3%), 32 were malapposed (0.8%), and 35 were located over an SB (0.9%). Lack of tissue coverage was detected in 63 struts (1.6%). Distribution of ISA, SB, and uncovered struts throughout the length of the BVS is shown in Figure 2.

Strut coverage. A total of 43 of 3,838 apposed struts (1.1%) were uncovered, whereas 10 of 32 ISA struts (31.3%) and 10 of 35 SB struts (28.6%) were uncovered. The comparison of the rate of uncovered plus apposed struts (1.1%) with the rate of uncovered plus ISA or SB struts (29.0%) was statistically significant ($p < 0.01$) (Fig. 3).

Intraluminal masses. At 6 months, intraluminal masses were observed in 14 cross-sections (2.9%) in 6 patients (24.0%).

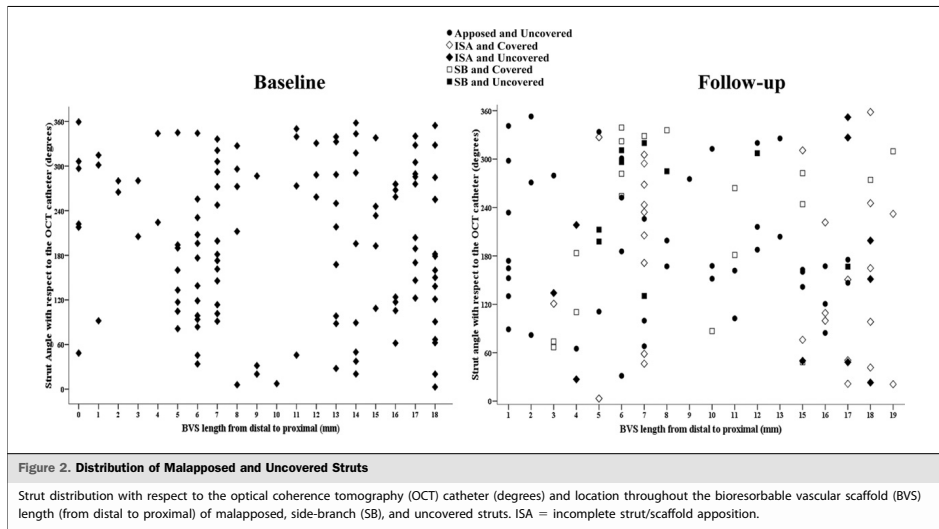


Table 3. Qualitative OCT Findings at 6-Month Follow-Up	
Number of struts at 6 months	3,905
Apposed + covered	3,795 (97.2%)
Apposed + uncovered	43 (1.1%)
ISA + covered	22 (0.5%)
ISA + uncovered	10 (0.3%)
SB + covered	25 (0.6%)
SB + uncovered	10 (0.3%)
Number of struts with attached intraluminal masses at 6 months*	21 (0.5%)
Apposed + covered	9 (0.2%)
Apposed + uncovered	4 (9.3%)
ISA + covered	4 (18.2%)
ISA + uncovered	4 (40%)
SB + covered	0
SB + uncovered	0
Matched ISA struts at follow-up that at baseline were:	32 (0.8%)
ISA	26 (81.3%)
Protruding	5 (15.6%)
Embedded	0
Unmatchable	1 (3.1%)
Matched uncovered struts at follow-up that at baseline were:	63 (1.6%)
Protruding	36 (57.1%)
Embedded	4 (6.3%)
ISA	10 (15.9%)
SB	10 (15.9%)
Unmatchable	3 (4.8%)
Matched ISA + uncovered struts at follow-up that at baseline were:	10 (0.3%)
Protruding	5 (50.0%)
ISA	5 (50.0%)
N = 25. *Percentages are estimated according to the total amount of each strut type. Abbreviations as in Table 2.	

Notably, intraluminal masses were more often associated with malapposed and/or uncovered struts rather than apposed and covered struts. Of struts with attached intraluminal masses, 40.0% of struts were malapposed and uncovered, 18.2% were malapposed and covered, 9.3% were apposed and uncovered, and 0.9% were apposed and covered ($p < 0.01$).

Matched cross-sections. A total of 51 of 53 cross-sections with ISA or uncovered struts were properly matched with the corresponding image at baseline. Likewise, 97.1% of malapposed and 95.2% of uncovered struts were properly matched. The ISA was more frequently caused by persistent ISA (81.3%) rather than LAISA (15.6%); 3.1% of the struts were unmatchable. Late acquired ISA was only found in 2 patients (8.0%). Serial analysis of uncovered struts showed that, at baseline, 36 matched struts were classified as protruding (57.1%), 4 as embedded (6.3%), and 10 as ISA (15.9%), and 10 struts were overlying an SB (15.9%); 4.8% were unmatchable.

Clinical outcomes. At 6-month follow-up, no death, spontaneous acute myocardial infarction, scaffold thrombosis, or target lesion revascularization of the 25 patients included in the present study were documented. One patient experi-

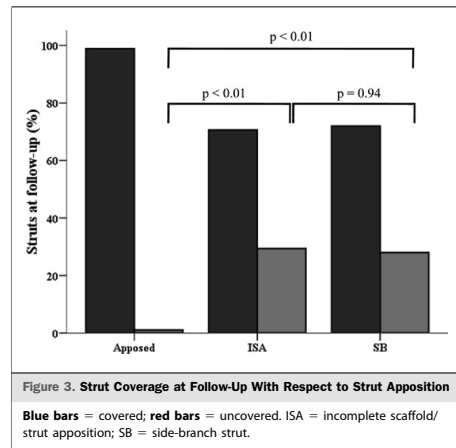
enced a periprocedural acute myocardial infarction at the time of the index procedure without any further complications. Another patient with suboptimal OCT imaging at baseline (and excluded from our study) presented with nonclinically driven target lesion revascularization at day 33. At that time, OCT imaging showed scaffold pattern irregularities demonstrating substantial structural distortion, with intraluminal masses attached to the malapposed struts. At the time of the index procedure, this patient was also treated with a post-dilation balloon that achieved a larger predicted diameter than the maximum limit recommended for the BVS.

Qualitative coverage agreement between the 2 analysts. Two analysts investigated, in separate analyses, 100 selected cross-sections of 10 different patients with 767 struts. Both analysts agreed in 710 and 35 covered and uncovered struts, respectively. The Kappa index was 0.75 (good agreement).

Discussion

The main findings of our study are: 1) with the BVS version 1.1, the number of malapposed struts decreased from baseline to 6-month follow-up; 2) 80% of the malapposed struts observed at baseline resolved into apposed struts at follow-up, with a relatively low rate of LAISA at 6 months; 3) as at baseline and follow-up, ISA and SB struts were associated with a lack of strut coverage at 6 months; and 4) intraluminal masses were rarely observed but were more frequently associated with ISA and uncovered struts.

Acute ISA. With metallic-DES, acute ISA ranged from 3.7% to 11.6% of the total amount of struts in patients without ST-segment elevation myocardial infarction



(15,16). Patients with at least 1 malapposed strut ranged from 32% to 88% in the same clinical setting (17,18). Our study observed a rate of acute ISA of 3.5%; and 17 patients (68%) presented with at least 1 malapposed strut. These findings suggest that the BVS might have a similar rate of acute ISA, as compared with metallic-DES.

Figure 2 shows the distribution of the malapposed struts throughout the BVS length. According to this figure, malapposed struts were distributed with a particular pattern and were more frequently located at the 2 edges (especially at the proximal edge), with few malapposed struts being located in the central segments of the BVS. This is probably caused by the placement of the central segment of the BVS at the site of the minimal lumen area and by the use of post-dilation balloons (in 56% of patients), shorter than the length of the scaffold, applied at the central segment of the BVS. At baseline, 2 of 25 patients presented with scaffold pattern irregularities resulting in acute strut malapposition. Both patients were treated with post-dilation balloons immediately after the BVS implantation. In both cases, post-dilation balloons were inflated at pressures that resulted in predicted device diameters (according to the manufacturer's chart) larger than the recommended limits for the BVS implantation (3.3 mm for a 3.0-mm nominal diameter BVS). Scaffold pattern irregularities were located at the proximal edges and extended over 2 to 4 mm of the scaffold length. In these images, the number of ISAs were 2 and 5 struts, respectively. Additionally, no intraluminal mass was observed in these frames.

ISA at 6 months. Malapposed struts of different metallic-DES ranged from 0% to 15% of the total amount of struts at 6 months in non-ST-segment elevation myocardial infarction patients (19–21). In a single study comparing different metallic-DES, zotarolimus DES presented with lower rates of malapposed struts (0.0%), as compared with paclitaxel (0.7%) or sirolimus DES (1.9%) (19). All serial OCT imaging studies performed with metallic-DES have found a progressively decreasing amount of malapposed struts over time (21,22). Unfortunately, at the time of the present study, no OCT data were available for the everolimus DES at 6-month follow-up.

The healing process of the different metallic-DES is extremely heterogeneous, with little data being available with regard to the healing process of malapposed struts. Serial OCT imaging of sirolimus DES at baseline and 10-month follow-up showed a high rate of persistent malapposed struts, with 65% of ISA struts observed at baseline remaining malapposed at follow-up. Late acquired ISA was observed in 7.3% of malapposed struts at follow-up (3). Although there are many IVUS studies with serial strut analysis at baseline and at follow-up, the low sensitivity of IVUS to assess ISA—when compared with OCT—challenges the comparability of the results (23). Nevertheless, IVUS was able to identify some of the mechanisms

involved in the appearance of LAISA with metallic-DES. Some patients experienced positive remodeling due to vessel and lumen enlargement without increasing the plaque area. In these cases, the vessel wall separated from the apposed strut causing LAISA. This mechanism was more frequently related to sirolimus DES (24,25) rather than paclitaxel DES (1,25), everolimus DES (26), or zotarolimus DES (27).

The first generation of the everolimus-eluting BVS (version 1.0) presented with more malapposed struts at 6 months than at baseline. A total of 78% of malapposed struts observed at baseline persisted at 6 months. Late acquired ISA was observed in 1.0% of the total amount of struts and represented 16% of the total amount of ISA at follow-up (8). The most plausible explanation for this phenomenon was the loss in scaffold area observed during the first 6 months, when the BVS version 1.0 had a premature loss of its radial force and structural continuity (10). This phenomenon caused the displacement of the scaffold into the lumen and probably delayed the healing of previously (baseline) malapposed struts. Likewise, this probably caused the appearance of new malapposed struts at follow-up that were apposed at baseline (LAISA). As assessed by IVUS (8), positive remodeling was not observed with the BVS (version 1.0), unlike what was previously reported in DES.

In our study, with the new generation of BVS (version 1.1), the percentage of malapposed struts at 6-month follow-up was inferior to that at baseline (0.8% vs. 3.5%, respectively; $p < 0.01$). Only 15% of the malapposed struts at baseline persisted at follow-up. Late acquired ISA was observed in 5 struts (1.0%) in 2 patients and represented 16% of malapposed struts at follow-up. The mechanism owing to LAISA in these 2 patients was the emergence of scaffold pattern irregularities not observed at baseline. Scaffold pattern irregularities were extended over 4 mm throughout the length of the BVS and were mainly located at the proximal edge. The IVUS analysis showed the absence of positive remodeling at the site of the external elastic membrane in those patients (data not shown). Figures 4 and 5 show matched OCT images from baseline to 6-month follow-up of the 2 patients with LAISA caused by the emergence of scaffold pattern irregularities. Although scaffold pattern irregularities were not observed in any of those patients at baseline, it is remarkable that the respective patients had been treated with post-dilation with balloons that over-stretched the BVS to larger diameters than the recommended maximum device diameter of 3.3 mm.

The matched images of the 7 struts with acute ISA due to acute scaffold pattern irregularities (at baseline) evolved to ISA + covered (3 struts) and to ISA + uncovered (4 struts) at 6 months. None of the cases were related to LAISA.

Strut coverage at 6-month follow-up. Strut coverage of different metallic-DES is extremely heterogeneous. At 6

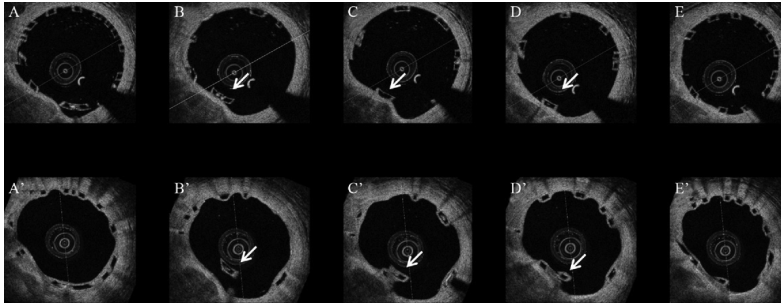


Figure 4. Late Acquired ISA

Consecutive, matched OCT images at baseline (**A to E**) and 6 months (**A' to E'**) of 1 patient treated with excessive post-dilation (3.4 mm). At baseline, the scaffold pattern is regular. **B, C, and D** show 1 apposed strut at baseline (**arrows**) that at follow-up evolved to acquired malapposed strut (**arrows**) due to scaffold pattern irregularities. Abbreviations as in Figure 2.

months, sirolimus DES presented with a rate of uncovered struts from 8.7% to 15.0% (19–22). Uncovered struts with paclitaxel DES ranged from 2.7% to 5.0% (19,20), and zotarolimus DES presented with 0% of uncovered struts in a single report (19).

In our study, with the new generation of BVS (version 1.1), a total of 1.6% of struts were uncovered at 6-month follow-up. The distribution of uncovered struts throughout the BVS length did not show any particular pattern (Fig. 2). However, uncovered struts at follow-up were relatively more frequently found in struts that at baseline were ISA and SB struts rather than apposed struts. Similar results have been obtained with serial OCT imaging of sirolimus DES. Ozaki

et al. (3) found a higher percentage of uncovered struts, at 10-month follow-up, in struts that were malapposed at baseline (65.4%) as compared with struts that were apposed (8.6%). The first generation of everolimus-eluting BVS (version 1.0) presented with 1.0% of uncovered struts at 6-month follow-up (8). Although the rate of ISA at 6 months was relatively high, uncovered struts were not commonly found. Moreover, the mean neointimal hyperplasia area was statistically higher with the BVS version 1.0 than with the BVS version 1.1 (10). There is no clear explanation for these findings. One hypothesis is that the advanced resorption state and the strut appearance changes observed with the BVS version 1.0 at 6 months as compared

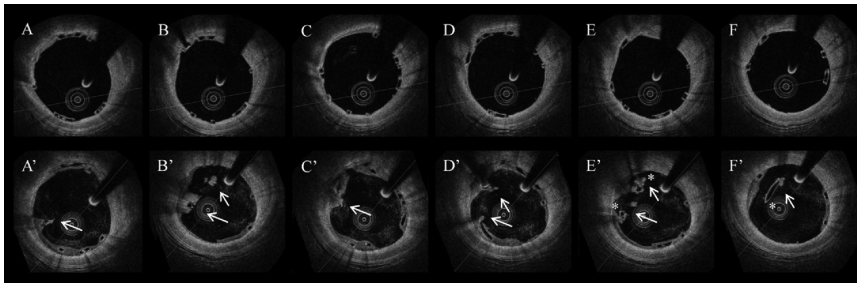


Figure 5. Late Acquired ISA With Attached Intraluminal Masses

Consecutive, matched OCT images at baseline (**A to F**) and 6-month follow-up (**A' to F'**). At baseline, the scaffold was post-dilated up to 3.4 mm of predicted device diameter. The OCT images show all struts are apposed to the vessel wall without scaffold pattern irregularities. At 6 months, the scaffold presents with pattern irregularities resulting in strut malapposition and lack of tissue coverage (*). Irregular intraluminal masses (**arrows**) with mild shadowing behind are attached to the malapposed and uncovered struts. Abbreviations as in Figure 2.

with the BVS 1.1 could trigger a higher neointimal response and strut coverage.

Intraluminal masses at 6-month follow-up. Lack of neointimal coverage of different DES was proposed as the best predictor of late stent thrombosis in pathological studies (6). However, although sirolimus DES presented with a higher percentage of uncovered struts compared with paclitaxel DES, thrombi were more frequently found with paclitaxel DES (20). This observation supports the concept of a multicausal pathogenesis of late stent thrombosis, including malapposition, expansive vessel remodeling, and other factors that can initiate thrombus formation (28,29). Due to its high resolution, OCT is able to visualize, with great detail, many of the proposed predictors of late stent thrombosis in vivo (3,30). With sirolimus DES, Ozaki et al. (3) found 4.1% of frames with thrombi at 10-month follow-up; thrombi were more frequently observed in frames with ISA than in those without this feature (21% vs. 2%, respectively, $p < 0.01$). Our study found 14 cross-sections (2.9%) in 6 patients (24%) containing intraluminal masses at 6-month follow-up. Intraluminal masses were more frequently observed in cross-sections with ISA than without (39% vs. 2%; $p < 0.01$) and in cross-sections with uncovered struts than without (13% vs. 2%; $p < 0.01$), supporting that malapposition and absence of coverage can initiate thrombosis. However, whether this is of clinical importance needs to be further investigated. Figure 5 shows intraluminal masses attached to malapposed and uncovered struts in 1 patient with acquired scaffold pattern irregularities and LAISA at 6 months.

Clinical implications. In our study, the new generation of BVS presented with a lower rate of ISA, uncovered struts, and intraluminal masses as compared with sirolimus DES at 6-month follow-up. The polymeric nature of this new technology, however, could render it susceptible to iatrogenically induced scaffold pattern irregularities. These can lead to ISA and lack of strut coverage at 6-month follow-up. The 5 cases reported in our study were treated with aggressive post-dilations, probably resulting in overstretching of the scaffold at the time of the implantation. A third generation of the device is intended to raise the limit of deployment of the 3.0-mm nominal diameter device to 3.8 mm. Nevertheless, the previous generation of the BVS (version 1.0) showed a complete resorption of its components at 2-year follow-up without any malapposed or uncovered struts (7). Therefore, in this case, the treatment with dual antiplatelet therapy can become unnecessary. It is, however, currently uncertain whether the new generation of the BVS (version 1.1) will exhibit similar resorption characteristics at 2 years.

Study limitations. The first limitation of the present study is the limited number of patients. However, our report is 1 of the largest OCT studies with serial imaging of the same intracoronary device at baseline and at follow-up. The

second limitation is the lack of statistical adjustment for clinical and anatomic covariables. The clustering essence of the OCT data (patient level, stent level, frame level, and strut level) needs a multilevel regression analysis not applied in our study. Moreover, the different OCT pullback speed, frame/rate, and quality of the image of the 2 OCT systems used in the present study hamper the matching of cross-sections between baseline and follow-up. A total of 12 cross-sections were unmatchable from baseline to follow-up or vice versa: 8 cross-sections were imaged with the M3 OCT system and 4 cross-sections were imaged with the C7 OCT system in both baseline and follow-up. Finally, the last limitation is the lack of results at very-long-term follow-up. The extrapolation of the 2-year follow-up results observed with the first generation of BVS (version 1.0) with the new generation of BVS (version 1.1) is purely speculative. However, all patients included in the ABSORB cohort B study will be reinvestigated at 2-year follow-up with invasive imaging techniques.

Conclusions

The new generation of BVS exhibited a low rate of acute, persistent, and late acquired incomplete strut/scaffold malapposition as well as uncovered struts. At baseline and follow-up, malapposed and SB struts were related to a lack of tissue coverage at 6 months. Scaffold pattern irregularities were the only cause observed in our study of late acquired malapposed struts and were also related to a lack of tissue coverage. Attached intraluminal masses occurred more frequently in malapposed and uncovered struts at 6 months. A more careful device implantation, with appropriate sizing of the vessel and respecting the deployment limits of inflation, will reduce the rates of acute ISA and scaffold pattern irregularities and, therefore, could circumvent most of the ISA, uncovered struts, and intraluminal masses observed at midterm follow-up.

Reprint requests and correspondence: Dr. Patrick W. Serruys, Thoraxcenter, Erasmus University Medical Center, 's-Gravendijkwal 230, Ba-583, 3015 CE Rotterdam, the Netherlands. E-mail: p.w.j.c.serruys@erasmusmc.nl

REFERENCES

1. Tanabe K, Serruys PW, Degertekin M, et al. Incomplete stent apposition after implantation of paclitaxel-eluting stents or bare metal stents: insights from the randomized TAXUS II trial. *Circulation* 2005;111:900–5.
2. Degertekin M, Serruys PW, Tanabe K, et al. Long-term follow-up of incomplete stent apposition in patients who received sirolimus-eluting stent for de novo coronary lesions: an intravascular ultrasound analysis. *Circulation* 2003;108:2747–50.
3. Ozaki Y, Okumura M, Ismail TF, et al. The fate of incomplete stent apposition with drug-eluting stents: an optical coherence tomography-based natural history study. *Eur Heart J* 2010;31:1470–6.

4. Matsumoto D, Shite J, Shinke T, et al. Neointimal coverage of sirolimus-eluting stents at 6-month follow-up: evaluated by optical coherence tomography. *Eur Heart J* 2007;28:961-7.
5. Cook S, Wenaweser P, Togni M, et al. Incomplete stent apposition and very late stent thrombosis after drug-eluting stent implantation. *Circulation* 2007;115:2426-34.
6. Finn AV, Joner M, Nakazawa G, et al. Pathological correlates of late drug-eluting stent thrombosis: strut coverage as a marker of endothelialization. *Circulation* 2007;115:2435-41.
7. Serruys PW, Ormiston JA, Onuma Y, et al. A bioabsorbable everolimus-eluting coronary stent system (ABSORB): 2-year outcomes and results from multiple imaging methods. *Lancet* 2009;373:897-910.
8. Ormiston JA, Serruys PW, Regar E, et al. A bioabsorbable everolimus-eluting coronary stent system for patients with single de-novo coronary artery lesions (ABSORB): a prospective open-label trial. *Lancet* 2008;371:899-907.
9. Okamura T, Garg S, Gutierrez-Chico JL, et al. In vivo evaluation of stent strut distribution patterns in the bioabsorbable everolimus-eluting device: an OCT ad hoc analysis of the revision 1.0 and revision 1.1 stent design in the ABSORB clinical trial. *EuroIntervention* 2010;5:932-8.
10. Gomez-Lara J, Brugaletta S, Diletti R, et al. A comparative assessment by optical coherence tomography of the performance of the first and second generation of the everolimus-eluting bioresorbable vascular scaffolds. *Eur Heart J* 2011;32:294-304.
11. Brugaletta S, Garcia-Garcia HM, Diletti R, et al. Comparison between the first and second generation bioresorbable vascular scaffolds: a six month virtual histology study. *EuroIntervention* 2010;6:1110-6.
12. Serruys PW, Onuma Y, Ormiston JA, et al. Evaluation of the second generation of a bioresorbable everolimus drug-eluting vascular scaffold for treatment of de novo coronary artery stenosis: six-month clinical and imaging outcomes. *Circulation* 2010;122:2301-12.
13. Cohen J. A coefficient of agreement for nominal scales. *Educ Psychol Meas* 1960;20:37-46.
14. Fleiss J. *Statistical Methods for Rates and Proportions*. 2nd edition. New York, NY: John Wiley, 1981.
15. Tanigawa J, Barlis P, Dimopoulos K, Dalby M, Moore P, Di Mario C. The influence of strut thickness and cell design on immediate apposition of drug-eluting stents assessed by optical coherence tomography. *Int J Cardiol* 2009;134:180-8.
16. Kim JS, Jang IK, Fan C, et al. Evaluation in 3 months duration of neointimal coverage after zotarolimus-eluting stent implantation by optical coherence tomography: the ENDEAVOR OCT trial. *J Am Coll Cardiol Intv* 2009;2:1240-7.
17. Kubo T, Imanishi T, Kitabata H, et al. Comparison of vascular response after sirolimus-eluting stent implantation between patients with unstable and stable angina pectoris: a serial optical coherence tomography study. *J Am Coll Cardiol Img* 2008;1:475-84.
18. Tanigawa J, Barlis P, Dimopoulos K, Di Mario C. Optical coherence tomography to assess malapposition in overlapping drug-eluting stents. *EuroIntervention* 2008;3:580-3.
19. Guagliumi G, Musumeci G, Sirbu V, et al. Optical coherence tomography assessment of in vivo vascular response after implantation of overlapping bare-metal and drug-eluting stents. *J Am Coll Cardiol Intv* 2010;3:531-9.
20. Murakami D, Takano M, Yamamoto M, et al. Advanced neointimal growth is not associated with a low risk of in-stent thrombus. Optical coherence tomographic findings after first-generation drug-eluting stent implantation. *Circ J* 2009;73:1627-34.
21. Katoh H, Shite J, Shinke T, et al. Delayed neointimalization on sirolimus-eluting stents: 6-month and 12-month follow up by optical coherence tomography. *Circ J* 2009;73:1033-7.
22. Ishigami K, Uemura S, Morikawa Y, et al. Long-term follow-up of neointimal coverage of sirolimus-eluting stents: evaluation with optical coherence tomography. *Circ J* 2009;73:2300-7.
23. Bouma BE, Tearney GJ, Yabushita H, et al. Evaluation of intracoronary stenting by intravascular optical coherence tomography. *Heart* 2003;89:317-20.
24. Ako J, Morino Y, Honda Y, et al. Late incomplete stent apposition after sirolimus-eluting stent implantation: a serial intravascular ultrasound analysis. *J Am Coll Cardiol* 2005;46:1002-5.
25. Hong MK, Mintz GS, Lee CW, et al. Late stent malapposition after drug-eluting stent implantation: an intravascular ultrasound analysis with long-term follow-up. *Circulation* 2006;113:414-9.
26. Tsuchiya Y, Lansky AJ, Costa RA, et al. Effect of everolimus-eluting stents in different vessel sizes (from the pooled FUTURE I and II trials). *Am J Cardiol* 2006;98:464-9.
27. Miyazawa A, Ako J, Hongo Y, et al. Comparison of vascular response to zotarolimus-eluting stent versus sirolimus-eluting stent: intravascular ultrasound results from ENDEAVOR. *Am Heart J* 2008;III:155:108-13.
28. Oikawa Y, Yajima J, Costa M, et al. Intravascular ultrasound, angioscopic and histopathological characterization of heterogeneous patterns of restenosis after sirolimus-eluting stent implantation: insights into potential "thromborestenosis" phenomenon. *EuroIntervention* 2010;6:380-7.
29. Joner M, Finn AV, Farb A, et al. Pathology of drug-eluting stents in humans: delayed healing and late thrombotic risk. *J Am Coll Cardiol* 2006;48:193-202.
30. Otake H, Shite J, Ako J, et al. Local determinants of thrombus formation following sirolimus-eluting stent implantation assessed by optical coherence tomography. *J Am Coll Cardiol Intv* 2009;2:459-66.

Key Words: bioresorbable scaffolds ■ incomplete stent ■ late acquired incomplete stent ■ optical coherence tomography ■ strut apposition ■ uncovered struts.

7.3

Head to head comparison of optical coherence tomography, intravascular ultrasound echogenicity and virtual histology for the detection of changes in polymeric struts over time. Insights from the ABSORB trial.

Salvatore Brugaletta, Josep Gomez-Lara, Nico Bruining, Maria D Radu, Robert Jan van Geuns, Leif Thuesen, Dougal McClean, Jacques Koolen, Stephan Windecker, Robert Whitbourn, James Oberhauser, Richard Rapoza, John A Ormiston, Hector M Garcia-Garcia, Patrick W Serruys

Eurointervention 2011, Epub ahead of print

Head to head comparison of optical coherence tomography, intravascular ultrasound echogenicity and virtual histology for the detection of changes in polymeric struts over time. Insights from the ABSORB trial

Salvatore Brugaletta^{1,2}, MD; Josep Gomez-Lara¹, MD; Nico Bruining¹, PhD; Maria D. Radu¹, MD; Robert-Jan van Geuns¹, MD, PhD; Leif Thuesen³, MD; Dougal McClean⁴, MD; Jacques Koolen⁵, MD, PhD; Stephan Windecker⁶, MD, PhD; Robert Whitbourn⁷, MD; James Oberhauser⁸, PhD; Richard Rapoza⁸, PhD; John A. Ormiston⁹, MBChB, PhD; Hector M. Garcia-Garcia^{1,10}, MD, PhD; Patrick W. Serruys^{1*}, MD, PhD

1. Thoraxcenter; Erasmus MC, Rotterdam, The Netherlands; 2. Thorax Institute, Department of Cardiology, Hospital Clinic, Barcelona, Spain; 3. Skejby Sygehus, Aarhus University Hospital, Aarhus, Denmark; 4. Christchurch Hospital, Christchurch, New Zealand; 5. Catharina Hospital, Eindhoven, The Netherlands; 6. Bern University Hospital, Bern, Switzerland; 7. St Vincent's Hospital, Fitzroy, Australia; 8. Abbott Vascular, Santa Clara, CA, USA; 9. Auckland City Hospital, Auckland, New Zealand; 10. Cardialysis BV, Rotterdam, The Netherlands

KEYWORDS

- virtual histology
- OCT
- imaging

Abstract

Aims: To analyse and to compare the changes in the various optical coherence tomography (OCT), echogenicity and intra-vascular ultrasound virtual histology (VH) of the everolimus-eluting bioresorbable scaffold (ABSORB) degradation parameters during the first 12 months after ABSORB implantation. In the ABSORB study, changes in the appearance of the ABSORB scaffold were monitored over time using various intracoronary imaging modalities. The scaffold struts exhibited a progressive change in their black core area by OCT, in their ultrasound derived grey level intensity quantified by echogenicity, and in their backscattering ultrasound signal, identified as “pseudo dense-calcium” (DC) by VH.

Methods and results: From the ABSORB Cohort B trial 35 patients had paired OCT, echogenicity and VH assessment at baseline and at six- (n=18) or 12-months follow-up (n=17). Changes in OCT strut core area, hyper-echogenicity and VH-derived DC were analysed and compared at the various time points. At six months, the change (median[IQR]) in OCT strut core area was -7.2% (-14.0-+0.9) (p=0.053), in hyper-echogenicity -12.7% (-33.7-+1.4) (p=0.048) and VH-DC 22.1% (-10.8-+48.8) (p=0.102). At 12 months, all the imaging modalities showed a decrease in the various parameters considered (OCT: -12.2% [-17.5- -1.9], p=0.093; hyper-echogenicity -24.64% [-36.6- -16.5], p=0.001; VH-DC: -24.66% [-32.0- -7.0], p=0.071). However, the correlation between the relative changes in these parameters was statistically poor (Spearman's rho <0.4).

Conclusions: OCT, echogenicity and VH were able to detect changes in the ABSORB scaffold struts, although the correlation between those changes was poor. This is likely due to the fact that each imaging modality interrogates different material properties on different length scales. Further studies are needed to explore these hypotheses.

*Corresponding author: Erasmus MC, Thoraxcenter, 's Gravendijkwal 230,3015 CE, Rotterdam, The Netherlands.
E-mail: p.w.j.serruys@erasmusmc.nl

Abbreviations

IVUS	intra vascular ultrasound
LLI	LightLab Imaging
OCT	optical coherence tomography
PDLLA	poly(D,L-lactide)
PLA	polylactide
PLLA	poly(L-lactide)
VH	virtual histology

Introduction

The everolimus-eluting bioresorbable ABSORB scaffold (Abbott Vascular, Santa Clara, CA, USA) represents a novel approach for the treatment of coronary lesions, providing transient luminal support and vessel wall drug delivery without the long-term limitations of conventional metallic drug-eluting stents^{1,3}.

In the ABSORB trials, multi-modality imaging techniques were applied, including optical coherence tomography (OCT), intravascular ultrasound (IVUS) greyscale and virtual histology (VH). These modalities have been extensively used, primarily to investigate geometric changes to the vessel wall and lumen and secondarily to assess changes in the appearance of the struts, as surrogate for changes in polymer microstructure caused by hydrolytic degradation of the polymer over time. OCT, for example, monitored the progressive integration of the scaffold into the vessel wall, with modification in the reflectivity of the strut core area and in the size of the black strut core area^{3,4}; IVUS showed a progressive reduction in the grey level intensity of the polymeric struts over time, detected by change in hyper-echogenicity⁵, and VH reported changes in dense calcium areas (DC) as the struts are detected by the software as “pseudo dense-calcium”^{2,3,6,7}.

However, no systematic and serial comparison between these three intra-coronary imaging modalities and their derived parameters, detecting the polymer microstructural changes, has been made. With this “pilot-study”, we tried to quantitatively compare the material property changes of the scaffold as detected by OCT, echogenicity and VH *in vivo* at six and 12 months after ABSORB implantation.

Methods

STUDY POPULATION

The ABSORB Cohort B study enrolled 101 patients older than 18 years of age with a diagnosis of stable/unstable angina or silent ischaemia (Trial number: NCT00856856). Those patients were divided into two groups: the first group (Cohort B1) underwent invasive imaging including greyscale IVUS, IVUS-VH and OCT at six-month follow-up; the second group (Cohort B2) had the same invasive imaging at 12 months³. All lesions were *de novo*, in a native coronary artery with a reference vessel diameter of 3.0 mm, a percentage diameter stenosis $\geq 50\%$ and $< 100\%$, a thrombolysis in myocardial infarction flow grade of ≥ 1 , and were treated with implantation of an ABSORB scaffold (3.0 \times 18 mm). Major exclusion criteria were: patients with an acute myocardial infarction, unstable arrhythmias or who had a left ventricular ejection fraction

$< 30\%$, restenotic lesions, lesions located in the left main coronary artery, lesions involving a side branch ≥ 2 mm in diameter, and the presence of thrombus or other clinically significant stenoses in the target vessel. The local ethics committee at each participating institution approved the trial and each patient gave written informed consent before inclusion.

Only patients with paired IVUS-VH, echogenicity and OCT data were included in the present analysis.

ABSORB SCAFFOLD

The ABSORB scaffold is a fully bioresorbable intra-coronary device made from semi-crystalline poly(L-lactide) (PLLA) coated with an amorphous poly(D,L-lactide) (PDLLA) copolymer that contains and controls the release of the anti-proliferative drug everolimus. The primary mechanism for molecular weight degradation of both polylactide (PLA) materials is hydrolysis, a process in which the ester bonds present in the monomeric subunit of PLA molecules are progressively cleaved. Ultimately, PLLA and PDLLA degrade to lactic acid, which is readily converted to lactate and processed via both the Krebs' cycle (for L-lactate) and methylglyoxal metabolism (for D-lactate^{2,8}). Based on preclinical studies, the time for complete resorption is assumed to be approximately two years⁹.

The ABSORB Cohort A and Cohort B trials evaluated the ABSORB scaffold generation 1.0 and 1.1, respectively^{1,2}. There are no differences in polymeric material, drug dose, drug release rate or strut thickness between the two generations. Of note, the ABSORB 1.1 has a smaller maximum circular unsupported surface area than the ABSORB 1.0⁹. Controls implemented in the manufacturing of ABSORB 1.1 have resulted in more prolonged luminal support post-implantation³.

IVUS ACQUISITION

Treated vessels were examined post-procedure and at follow-up with 20 MHz phased array intravascular ultrasound (IVUS) Eagle-eye[®] catheters (Volcano Corporation, Rancho Cordova, CA, USA), using automated pullback at 0.5 mm per second after administration of 0.2 mg intracoronary nitroglycerin. IVUS analyses were performed by an independent core laboratory (Cardialysis BV, Rotterdam, The Netherlands).

IVUS-VH ANALYSIS

Backscattering of radiofrequency signals provides information on vessel wall tissue composition¹¹. All IVUS-VH analyses were performed offline using the pcVH 2.1 software (Volcano Corporation, Rancho Cordova, CA, USA). Four tissue components (necrotic core: red; dense calcium: white; fibrous: green; and fibrofatty: light green) were identified with autoregressive classification systems^{11,12}. Each individual tissue component was quantified, colour coded in all IVUS cross sections and reported as absolute and relative areas¹¹. As previously shown, the polymeric struts are normally classified as areas of “pseudo dense calcium” (DC)^{2,3,6,7,13}. For this reason, we assessed the change in DC areas between post-implantation and follow-up as previously reported^{1,2,6}.

IVUS ECHOGENICITY ANALYSIS

Fully-automated quantitative echogenicity analysis software, previously developed in-house and validated, was used to quantify the hyper-echogenicity in the treated segment^{5,14}. Briefly, the mean grey value of the adventitia is used to classify tissue components as either hypo- or hyper-echogenic. The adventitia circumscribing the coronary artery is defined as a layer extending from 0.2 to 0.5 mm outside the external elastic membrane. To minimise artefacts, tissue within acoustic shadowed areas is excluded and very high grey level pixels are identified as upper tissue¹⁴. After the tissue identification process, the relative fraction of hypo- versus hyper-echogenic tissue volumes are calculated for the entire scaffold segment⁵. As the polymeric struts, due to a high grey value intensity, are identified as hyper-echogenic tissue and show a continuous decrease of their grey level intensity during the degradation process, we therefore used changes in hyper-echogenicity as a surrogate for scaffold degradation, as previously described^{5,15,16}.

OCT ACQUISITION AND ANALYSIS

OCT imaging was performed as an optional investigation in selected centres, using either time domain (M3 system; LightLab Imaging [LLI], Westford, MA, USA) or frequency domain OCT systems (C7XR system, LLI) at baseline and follow-up^{10,17-21}. The OCT measurements were performed with proprietary software for offline analysis (LightLab Imaging). Adjusting for the pullback speed, the analysis of continuous cross-sections was performed at 1 mm longitudinal intervals within the treated segment.

The ABSORB scaffold shows important differences with respect to metallic stents when imaged by OCT. The optically translucent polymer allows imaging of both luminal and abluminal boundaries of the strut, which appears as a box with a black central core (strut core area) framed by highly reflective borders⁵. The second generation ABSORB 1.1 shows, up to 12 months, a progressive decrease in strut core area, and none of the changes in morphological strut appearance that were seen with the first generation ABSORB 1.0¹². In this analysis, we therefore focus on the changes in the strut core area between post-implantation and follow-up, as a surrogate for scaffold degradation^{3,4}.

STATISTICAL ANALYSIS

Categorical variables are expressed as counts and percentages. Continuous variables are presented as mean±standard deviation or median and interquartile range, according to their normal or not normal distribution. Normality of the data was evaluated using the Kolmogorov-Smirnov test. The correlation between various parameters across all time points was performed with the Spearman's test, as the data were not normally distributed.

The percentage changes for VH-derived dense calcium, hyper-echogenicity and strut core area by OCT were calculated for each scaffolded coronary segment as follows:

$$\frac{(\text{Follow-up} - \text{post ABSORB scaffold implantation})}{\text{post ABSORB scaffold implantation}} \times 100\%$$

A two-tailed value of $p < 0.05$ was considered statistically significant. Statistical analyses were performed with SPSS 16.0 software (SPSS Inc., Chicago, IL, USA).

Results

BASELINE CLINICAL AND ANGIOGRAPHIC CHARACTERISTICS

Overall, 35 patients had paired multi-modality imaging analyses post-implantation and at follow-up. Of these, 17 patients were followed-up at six months, and the remaining 18 were followed up at 12 months. Clinical and angiographic characteristics are shown in **Table 1**.

Table 1. Clinical and angiographic baseline characteristics.

	Cohort B1 (n=17)	Cohort B2 (n=18)
Age (years) mean±SD (n)	61.0±9.0	60.0±9.1
Men, n (%)	13 (76)	13 (72)
Smokers, n (%)	4 (23)	5 (27)
Diabetes, n (%)	2 (12)	2 (11)
Hypertension requiring medication, n (%)	8 (47)	11 (61)
Hyperlipidaemia requiring medication, n (%)	15 (88)	11 (61)
Previous target vessel intervention, n (%)	4 (23)	3 (16)
Previous myocardial infarction, n (%)	8 (47)	2 (11)
Clinical presentation, n (%)		
Stable angina	14 (82)	13 (72)
Unstable angina	2 (12)	3 (16)
Silent ischaemia	0 (0)	2 (12)
Target vessel, n (%)		
Left anterior descending	6 (35)	11 (61)
Left circumflex	5 (30)	4 (22)
Right coronary artery	6 (35)	3 (17)
SD: standard deviation		

MULTI-IMAGING ANALYSES FROM OCT, IVUS-VH AND ECHOGENICITY AT SIX AND 12 MONTHS

Table 2 shows the mean strut core area, mean absolute and relative VH-DC area, mean absolute and relative hyper-echogenicity values immediately after ABSORB implantation and at six and 12 month follow-up.

At six months, the change in strut core area by OCT was -7.25% (-14.07 – $+0.98$) ($p=0.053$), in VH-DC 22.13% (-10.82 – $+48.85$) ($p=0.102$) and in hyper-echogenicity -12.71% (-33.70 – $+1.41$) ($p=0.048$). At 12 months, the change in strut core area was -12.20% (-17.55 – -1.98) ($p=0.093$), in VH-DC -24.66% (-32.07 – -7.01) ($p=0.071$) and in hyper-echogenicity -24.64% (-36.63 – -16.51) ($p=0.001$) (**Figure 1**).

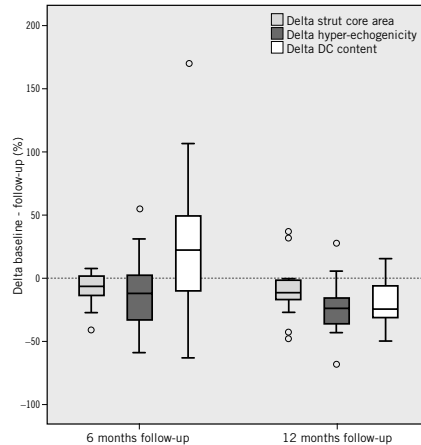
CORRELATION BETWEEN OCT, IVUS-VH AND ECHOGENICITY

There was a poor correlation between the changes in the evaluated parameters both at six and at 12 months (six months: OCT vs. hyper-echogenicity Spearman's $\rho = -0.361$, $p=0.141$; OCT vs. VH-DC Spearman's $\rho = 0.362$, $p=0.139$; hyper-echogenicity vs. VH-DC Spearman's $\rho = -0.218$, $p=0.385$; 12 months: OCT vs.

Table 2. Multi-imaging data from both cohorts.

	Cohort B1 (n=17)			Cohort B2 (n=18)		
	Baseline	6-month	p-value	Baseline	12-month	p-value
Mean strut core area (mm ²)	0.21±0.03	0.20±0.05	0.053	0.19±0.03	0.17±0.06	0.093
Mean DC area (mm ²)	1.15±0.90	1.39±0.82	0.050	1.47±0.72	1.23±0.49	0.029
Mean DC (%)	14.10±7.08	16.27±6.67	0.102	17.38±5.62	13.75±3.92	0.071
Mean hyper-echogenicity volume (mm ³)	36.6±13.7	34.5±19.0	0.446	38.2±14.3	33.2±41.0	0.093
Mean hyper-echogenicity (%)	23.1±9.4	19.2±8.9	0.048	24.4±10.5	18.2±8.9	0.001

DC: dense calcium

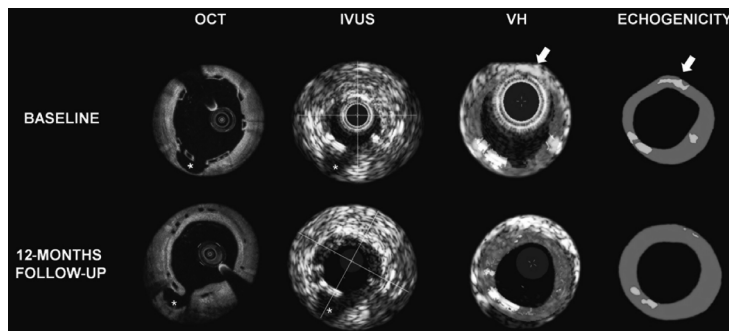
**Figure 1.** Relative reduction in strut core area, hyper-echogenicity and DC content between baseline and 6/12 months follow-up. DC: dense calcium

hyper-echogenicity Spearman's $\rho=0.262$, $p=0.309$; OCT vs. VH-DC Spearman's $\rho=0.233$, $p=0.368$; hyper-echogenicity vs. VH-DC Spearman's $\rho=0.368$, $p=0.233$). The correlation did not improve when considering the data from six and 12 months together (OCT vs. hyper-echogenicity Spearman's $\rho=-0.038$, $p=0.830$; OCT vs. VH-DC Spearman's $\rho=0.281$, $p=0.102$; hyper-echogenicity vs. VH-DC Spearman's $\rho=0.071$, $p=0.683$) (Figure 2).

Discussion

The main findings of the analysis are: 1) there appears to be a reduction in strut core area by OCT and in hyper-echogenicity values both at six and 12 month follow-up; 2) VH detects contrasting changes in dense-calcium between six and 12 months; 3) at the patient level, the correlation between the various parameters detected by the three imaging modalities is poor.

One of the most interesting concepts of the ABSORB scaffold is the temporary lumen scaffolding: in contrast with metallic stents, the polymeric scaffold does not involve a permanent caging of the vessel, as it is bioresorbed over time^{22,23}. In keeping with this concept, much interest has been focused on the use of intra-coronary imaging techniques and their capabilities in detecting *in vivo* changes in scaffold material properties.

**Figure 2.** Examples of OCT, IVUS, VH and echogenicity findings of corresponding cross-sectional images with a side branch (*) selected as an anatomical landmark. The white arrows indicate a hyper-echogenic tissue in echogenicity analysis, hidden by the grey media stripe in the VH analysis; OCT: optical coherence tomography; IVUS: intravascular ultrasound; VH: virtual histology

With regard to OCT, it is sensitive to refractive index changes on a length scale greater than the wavelength of the light emitted from the catheter. For this reason, it detects the polymeric struts as being highly reflective compared to the lumen and the vessel wall. Conversely, the black strut core area, despite the heterogeneity of the semi-crystalline polymer structure, has a light-poor signal after ABSORB implantation, indicating that changes in refractive index occur on a length scale less than that of the wavelength of the OCT light. However, as hydrolytic degradation progresses, it is reasonable to expect that this polymer microstructural heterogeneity coarsens, leading eventually to an increase in OCT reflectivity. For example, in the ABSORB Cohort A trial, testing the first generation ABSORB device, OCT showed that at six months, only 3% of the strut boxes kept the so-called “preserved box” appearance seen at post-implantation, whereas the remaining 97% changed their reflectivity, becoming “open box, dissolved bright box or dissolved black box”²⁷. Each of these OCT appearances was related to different histological characteristics in an animal study, where it was shown that reduction in strut core area and transition from preserved to open/dissolved box may represent indirect signs of scaffold degradation (e.g.; polymer microstructural heterogeneity) and integration into the vessel wall⁹. Conversely, in the ABSORB Cohort B trial, using the second generation ABSORB device, the scaffold struts maintained the OCT-defined “preserved box” appearance both at six and at 12-month follow-up exhibiting a progressive reduction in black strut core area by OCT^{3,24}. Concomitantly, IVUS greyscale showed a progressive reduction in the grey level intensity of the struts; this phenomenon was quantified by echogenicity analysis, demonstrating a reduction in the hyper-echogenicity values of the polymeric struts over time⁵. In the ABSORB Cohort A study, quantitative differential echogenicity was already applied to monitor *in vivo* changes of the scaffold by means of the acoustic property changes, showing an increase of hyper-echogenicity tissue immediately after the ABSORB implantation, which was back to pre-implantation values at the time of expected degradation and bioresorption (approximately two years^{2,5}). At six months, the differences in hyper-echogenicity reduction between the ABSORB Cohort A and Cohort B (50% vs. 17%) were in line with the differences in the struts’ OCT appearance and in the late loss (0.43 mm vs. 0.19 mm), further supporting differences in hydrolytic degradation rate characteristics between the two ABSORB devices³.

At variance with these findings, a slight increase in the backscattering signal of the struts interpreted as dense calcium by VH was detected at six months with a subsequent decrease at 12 months. It should be kept in mind that not only the polymeric scaffold – with its presence and degradation – but also the tissue surrounding the struts contributes to the VH-derived dense calcium quantification, which may explain this contrasting finding^{6,25}. In particular, our global evaluation of the area comprised between the lumen and the medial stripe integrates into our quantification of dense calcium also the backscattering signal not related to the sole struts, but, for instance, to the plaque behind the scaffold. Changes in composition

of this plaque are therefore also detected by VH. In a porcine model some inflammatory cells, such as granuloma and giant cells, were found surrounding the polymeric struts in the early stages after implantation, before decreasing over time⁹. At six months, focusing on the VH appearance of the plaque behind the scaffold, we confirmed this observation in humans, finding a progression in the NC content²⁵. Of note is that dense calcium is a frequent finding within the necrotic core region; in this case it is frequently “speckled” and can be due to calcification of a “nidus” of macrophages²⁶. Changes over time in strut core area and in hyper-echogenicity are instead probably less related to the plaque changes.

It is important to highlight that despite an overall agreement between hyper-echogenicity and strut core area in terms of reduction of both parameters during the first 12 months, analysis at the patient level revealed that the correlation between these imaging parameters is poor. This is not surprising, since the optical and ultrasonic parameters reflect different aspects of scaffold degradation. From our animal experience, we learnt that the polymer is first hydrolysed into small oligomers digested by macrophages and that the strut voids initially occupied by the polymeric struts are then filled with proteoglycan and eventually integrated into the vessel wall. Hence, the changes in black strut core area by OCT do not reflect the molecular dissolution of the polylactide, as the polymer and the proteoglycan material have the same optical properties, but rather the filling of the strut voids by connective tissue ultimately making the struts undetectable by OCT and in histology⁹. Conversely, changes in the material properties of polylactide (e.g., crystallinity, molecular weight, stiffness, etc.) have previously been demonstrated to predominantly affect the acoustic properties of the material over time, and these can be detected by ultrasonic waves^{15,16}.

Although both echogenicity and VH data are based on the application of ultrasound, the correlation between them was also poor. This lack of correlation may be explained by the differences of methodologies used in these two techniques. Whilst the echogenicity software analyses the complete image and the echo intensity (envelope amplitude), which is normally used in the formation of the greyscale-IVUS image, the VH software analyses the frequency of the signal underlying the amplitude (radiofrequency backscattering). As the classification tree of VH was not validated for recognition of metallic/polymeric struts, the backscattering signal, derived from a stent/scaffold, was usually interpreted by the software as dense calcium, such as found in heavily calcified coronary segments^{6,27}. Conversely, echogenicity analysis excluded from its tissue quantification the acoustically shadowed areas, resulting in a likely better discrimination between polymeric struts and calcified coronary segments. Another important point to consider in the VH detection of the polymeric struts is that some scaffold strut information may be missed because of the presence of the medial grey stripe and it is extremely dependent on the contours drawing^{28,29} (Figure 2). In addition no data are available to date correlating the backscattering signal changes with the physical and mechanical properties of polylactide.

Finally, it is important to highlight the difference in variability of the various changes explored by these techniques, with OCT exhibiting the least variability (Figure 1). The fundamental differences in the principles and spatial resolution of each technique should be taken into account in the interpretation of this variability and also of their poor correlation^{30,31}.

Limitations

A major limitation of our analysis is the small number of patients compared to the total number of patients enrolled in the trial. For this reason the p-values of the modification over time in the various parameters investigated have to be considered as exploratory. Nevertheless, limiting the analysis to only patients receiving all three imaging modalities allows a more accurate comparison between the various parameters investigated. Lack of data about the polylactide degradation has also to be taken into account as a possible limitation of our comparison. An *in vitro* or *ex vivo* study would be required to correlate these parameters with the scaffold/polymer degradation.

Conclusions

Our analysis showed that during the first 12 months after ABSORB scaffold implantation there is a reduction in black strut core area, as measured by OCT, and in hyper-echogenicity of the scaffold, representing independent signs of scaffold/polymer degradation. In contrast, VH only showed a reduction in "pseudo dense-calcium" at 12 months indicating some limitations in monitoring scaffold property changes.

Acknowledgments

The ABSORB Trial is sponsored and funded by Abbott Vascular, Santa Clara, CA, USA.

Conflict of interest statement

James Oberhauser and Richard Rapoza are employees of Abbott Vascular. None of the other authors have conflicts of interest relevant to the subject material in this paper.

References

1. Ormiston JA, Serruys PW, Regar E, Dudek D, Thuesen L, Webster MW, Onuma Y, Garcia-Garcia HM, McGreevy R, Veldhof S. A bioabsorbable everolimus-eluting coronary stent system for patients with single de-novo coronary artery lesions (absorb): A prospective open-label trial. *Lancet*. 2008;371:899-907.
2. Serruys PW, Ormiston JA, Onuma Y, Regar E, Gonzalo N, Garcia-Garcia HM, Nieman K, Bruining N, Dorange C, Miquel-Hebert K, Veldhof S, Webster M, Thuesen L, Dudek D. A bioabsorbable everolimus-eluting coronary stent system (absorb): 2-year outcomes and results from multiple imaging methods. *Lancet*. 2009;373:897-910.
3. Serruys PW, Onuma Y, Ormiston JA, de Bruyne B, Regar E, Dudek D, Thuesen L, Smits PC, Chevalier B, McClean D, Koolen J, Windecker S, Whitbourn R, Meredith I, Dorange C, Veldhof S,

Miquel-Hebert K, Rapoza R, Garcia-Garcia HM. Evaluation of the second generation of a bioresorbable everolimus drug-eluting vascular scaffold for treatment of de novo coronary artery stenosis: Six-month clinical and imaging outcomes. *Circulation*. 2010;122:2301-2312.

4. Gomez-Lara J, Brugaletta S, Diletti R, Garg S, Onuma Y, Gogas BD, van Geuns RJ, Dorange C, Veldhof S, Rapoza R, Whitbourn R, Windecker S, Garcia-Garcia HM, Regar E, Serruys PW. A comparative assessment by optical coherence tomography of the performance of the first and second generation of the everolimus-eluting bioresorbable vascular scaffolds. *Eur Heart J*. 2011;32:294-304.

5. Bruining N, de Winter S, Roelandt JR, Regar E, Heller I, van Domburg RT, Hamers R, Onuma Y, Dudek D, Webster MW, Thuesen L, Ormiston JA, Cheong WF, Miquel-Hebert K, Veldhof S, Serruys PW. Monitoring in vivo absorption of a drug-eluting bioabsorbable stent with intravascular ultrasound-derived parameters a feasibility study. *JACC Cardiovasc Interv*. 2010;3:449-456.

6. Garcia-Garcia HM, Gonzalo N, Pawar R, Kukreja N, Dudek D, Thuesen L, Ormiston JA, Regar E, Serruys PW. Assessment of the absorption process following bioabsorbable everolimus-eluting stent implantation: Temporal changes in strain values and tissue composition using intravascular ultrasound radiofrequency data analysis. A substudy of the absorb clinical trial. *EuroIntervention*. 2009;4:443-448.

7. Brugaletta S, Garcia-Garcia HM, Diletti R, Gomez-Lara J, Garg S, Onuma Y, Shin ES, Van Geuns RJ, De Bruyne B, Dudek D, Thuesen L, Chevalier B, McClean D, Windecker S, Whitbourn R, Dorange C, Veldhof S, Rapoza R, Sudhir K, Bruining N, Ormiston J, Serruys P. Comparison between the first and second generation bioresorbable vascular scaffolds: A six month virtual histology study. *EuroIntervention*. 2011;6:1110-6.

8. Ewaschuk JB, Naylor JM, Zello GA. D-lactate in human and ruminant metabolism. *J Nutr*. 2005;135:1619-1625.

9. Onuma Y, Serruys PW, Perkins LE, Okamura T, Gonzalo N, Garcia-Garcia HM, Regar E, Kammer M, Powers JC, Rapoza R, van Beusekom H, van der Giessen W, Virmani R. Intracoronary optical coherence tomography and histology at 1 month and 2, 3, and 4 years after implantation of everolimus-eluting bioresorbable vascular scaffolds in a porcine coronary artery model: An attempt to decipher the human optical coherence tomography images in the absorb trial. *Circulation*. 2010;122:2288-2300.

10. Okamura T, Garg S, Gutierrez-Chico JL, Shin ES, Onuma Y, Garcia HM, Rapoza R, Sudhir K, Regar E, Serruys PW. In-vivo evaluation of stent strut distribution patterns in the bioabsorbable everolimus-eluting device: An OCT ad hoc analysis of the revision 1.0 and revision 1.1 stent design in the absorb clinical trial. *EuroIntervention*. 2010;6:932-938.

11. Nair A, Kuban BD, Tuzcu EM, Schoenhagen P, Nissen SE, Vince DG. Coronary plaque classification with intravascular ultrasound radiofrequency data analysis. *Circulation*. 2002;106: 2200-2206.

12. Nasu K, Tsuchikane E, Katoh O, Vince DG, Virmani R, Surmely JF, Murata A, Takeda Y, Ito T, Ehara M, Matsubara T, Terashima M, Suzuki T. Accuracy of in vivo coronary plaque mor-

- phology assessment: A validation study of in vivo virtual histology compared with in vitro histopathology. *J Am Coll Cardiol.* 2006;47:2405-2412.
13. Serruys PW, Onuma Y, Dudek D, Smits PC, Koolen J, Chevalier B, De Bruyne B, Thuesen L, McClean D, van Geuns RJ, Windecker S, Whitbourn R, Meredith C, Dorange C, Veldhof S, Miquel-Hebert K, Sudhir K, Garcia-Garcia HM, Ormiston JA. Evaluation of the second generation of a bioresorbable everolimus-eluting vascular scaffold for the treatment of de novo coronary artery stenosis: 12-month clinical and imaging outcomes. *J Am Coll Cardiol.* 2011;58:1578-88.
 14. Bruining N, Verheye S, Knaapen M, Somers P, Roelandt JR, Regar E, Heller I, de Winter S, Ligthart J, Van Langenhove G, de Feijter PJ, Serruys PW, Hamers R. Three-dimensional and quantitative analysis of atherosclerotic plaque composition by automated differential echogenicity. *Catheter Cardiovasc Interv.* 2007;70: 968-978.
 15. Wu HC, Shen FW, Hong X, Chang WV, Winet H. Monitoring the degradation process of biopolymers by ultrasonic longitudinal wave pulse-echo technique. *Biomaterials.* 2003;24:3871-3876.
 16. Parker NG, Mather ML, Morgan SP, Povey MJ. Longitudinal acoustic properties of poly(lactic acid) and poly(lactic-co-glycolic acid). *Biomed Mater.* 2010;5:055004.
 17. Sihan K, Botha C, Post F, de Winter S, Gonzalo N, Regar E, Serruys PJ, Hamers R, Bruining N. Fully automatic three-dimensional quantitative analysis of intracoronary optical coherence tomography: Method and validation. *Catheter Cardiovasc Interv.* 2009;74:1058-1065.
 18. Prati F, Regar E, Mintz GS, Arbustini E, Di Mario C, Jang IK, Akasaka T, Costa M, Guagliumi G, Grube E, Ozaki Y, Pinto F, Serruys PW. Expert review document on methodology, terminology, and clinical applications of optical coherence tomography: Physical principles, methodology of image acquisition, and clinical application for assessment of coronary arteries and atherosclerosis. *Eur Heart J.* 2010;31:401-415.
 19. Gonzalo N, Serruys PW, Okamura T, Shen ZJ, Onuma Y, Garcia-Garcia HM, Sarno G, Schultz C, van Geuns RJ, Ligthart J, Regar E. Optical coherence tomography assessment of the acute effects of stent implantation on the vessel wall: A systematic quantitative approach. *Heart.* 2009;95:1913-1919.
 20. Regar E, Leeuwen AMGJv, Serruys PW. Optical coherence tomography in cardiovascular research. *Informa Healthcare;* 2007.
 21. Gonzalo N, Serruys PW, Garcia-Garcia HM, van Soest G, Okamura T, Ligthart J, Knaapen M, Verheye S, Bruining N, Regar E. Quantitative ex vivo and in vivo comparison of lumen dimensions measured by optical coherence tomography and intravascular ultrasound in human coronary arteries. *Rev Esp Cardiol.* 2009;62: 615-624.
 22. Onuma Y, Serruys PW. Bioresorbable scaffold: The advent of a new era in percutaneous coronary and peripheral revascularization? *Circulation.* 2011;123:779-797.
 23. Oberhauser JP, Hossainy S, Rapoza R. Design principles and performance of bioresorbable polymeric vascular scaffolds. *EuroIntervention.* 2009;5:F15-F22.
 24. Brugaletta S, Garcia-Garcia HM, Garg S, Gomez-Lara J, Diletti R, Onuma Y, van Geuns RJ, McClean D, Dudek D, Thuesen L, Chevalier B, Windecker S, Whitbourn R, Dorange C, Miquel-Hebert K, Sudhir K, Ormiston JA, Serruys PW. Temporal changes of coronary artery plaque located behind the struts of the everolimus eluting bioresorbable vascular scaffold. *Int J Cardiovasc Imaging.* 2011;27:859-866.
 25. Garcia-Garcia HM, Mintz GS, Lerman A, Vince DG, Margolis MP, van Es GA, Morel MA, Nair A, Virmani R, Burke AP, Stone GW, Serruys PW. Tissue characterisation using intravascular radiofrequency data analysis: Recommendations for acquisition, analysis, interpretation and reporting. *EuroIntervention.* 2009;5: 177-189.
 26. Kubo T, Maehara A, Mintz GS, Garcia-Garcia HM, Serruys PW, Suzuki T, Klaus V, Sumitsuji S, Lerman A, Marso SP, Margolis MP, Margolis JR, Foster MC, De Bruyne B, Leon MB, Stone GW. Analysis of the long-term effects of drug-eluting stents on coronary arterial wall morphology as assessed by virtual histology intravascular ultrasound. *Am Heart J.* 2010;159:271-277.
 27. Shin ES, Garcia-Garcia HM, Garg S, Ligthart J, Thuesen L, Dudek D, Ormiston JA, Serruys PW. Assessment of the serial changes of vessel wall contents in atherosclerotic coronary lesion with bioresorbable everolimus-eluting vascular scaffolds using shin's method: An IVUS study. *Int J Cardiovasc Imaging.* 2011;27: 931-7.
 28. Mintz GS, Nissen SE, Anderson WD, Bailey SR, Erbel R, Fitzgerald PJ, Pinto FJ, Rosenfield K, Siegel RJ, Tuzcu EM, Yock PG. American college of cardiology clinical expert consensus document on standards for acquisition, measurement and reporting of intravascular ultrasound studies (ivus). A report of the american college of cardiology task force on clinical expert consensus documents. *J Am Coll Cardiol.* 2001;37:1478-1492.
 29. Bezerra HG, Costa MA, Guagliumi G, Rollins AM, Simon DI. Intracoronary optical coherence tomography: A comprehensive review clinical and research applications. *JACC Cardiovasc Interv.* 2009;2:1035-1046.

Chapter 8

Assessment of morphological and functional modifications in the coronary artery after bioresorbable vascular scaffolds implantation.

8.1

Temporal changes of coronary artery plaque located behind the struts of the everolimus eluting bioresorbable vascular scaffold.

Salvatore Brugaletta, Hector M Garcia-Garcia, Scot Garg, Josep Gomez-Lara, Roberto Diletti, Yoshinobu Onuma, Robert Jan van Geuns, Dougal McClean, Dariusz Dudek, Leif Theisen, Bernard Chevalier, Stephan Windecker, Robert Whitbourn, Cecile Dorange, Karine Miquel-Hebert, Krishnankutty Sudhir, John A Ormiston, Patrick W Serruys

Int J Cardiovasc Imaging 2011;27:859-66

Temporal changes of coronary artery plaque located behind the struts of the everolimus eluting bioresorbable vascular scaffold

Salvatore Brugaletta · Hector M. Garcia-Garcia · Scot Garg · Josep Gomez-Lara · Roberto Diletti · Yoshinobu Onuma · Robert Jan van Geuns · Dougal McClean · Dariusz Dudek · Leif Thuesen · Bernard Chevalier · Stephan Windecker · Robert Whitbourn · Cecile Dorange · Karine Miquel-Hebert · Krishnankutty Sudhir · John A. Ormiston · Patrick W. Serruys

Received: 10 June 2010 / Accepted: 29 September 2010
© Springer Science+Business Media, B.V. 2010

Abstract Implantation of a coronary stent results in a mechanical enlargement of the coronary lumen with stretching of the surrounding atherosclerotic plaque. Using intravascular ultrasound virtual-histology (IVUS-VH) we examined the temporal changes in composition of the plaque behind the struts (PBS) following the implantation of the everolimus eluting bioresorbable vascular scaffold (BVS). Using IVUS-VH and dedicated software, the composition of plaque was analyzed in all patients from the ABSORB B trial who were imaged with a commercially available IVUS-VH console (s5i system, Volcano Corporation, Rancho Cordova, CA, USA) post-treatment and at

6-month follow-up. This dedicated software enabled analysis of the PBS after subtraction of the VH signal generated by the struts. The presence of necrotic core (NC) in contact with the lumen was also evaluated at baseline and follow-up. IVUS-VH data, recorded with s5i system, were available at baseline and 6-month follow-up in 15 patients and demonstrated an increase in both the area of PBS ($2.45 \pm 1.93 \text{ mm}^2$ vs. $3.19 \pm 2.48 \text{ mm}^2$, $P = 0.005$) and the external elastic membrane area ($13.76 \pm 4.07 \text{ mm}^2$ vs. $14.76 \pm 4.56 \text{ mm}^2$, $P = 0.006$). Compared to baseline there was a significant progression in the NC ($0.85 \pm 0.70 \text{ mm}^2$ vs. $1.21 \pm 0.92 \text{ mm}^2$, $P = 0.010$) and fibrous tissue area

S. Brugaletta · H. M. Garcia-Garcia · S. Garg · J. Gomez-Lara · R. Diletti · Y. Onuma · R. J. van Geuns · P. W. Serruys (✉)
Thoraxcenter, Erasmus MC, Ba-583, 's Gravendijkwal 230, 3015 CE Rotterdam, The Netherlands
e-mail: p.w.j.c.serruys@erasmusmc.nl

H. M. Garcia-Garcia
Cardialysis B.V., Rotterdam, The Netherlands

D. McClean
Chrischurch Hospital, Chrischurch, New Zealand

D. Dudek
Jagiellonian University, Krakow, Poland

L. Thuesen
Skejby Sygehus, Aarhus, Denmark

B. Chevalier
Institut Cardiovasculaire Paris Sud, Massy, France

S. Windecker
Bern University Hospital, Bern, Switzerland

R. Whitbourn
St Vincents Hospital, Fitzroy, Australia

C. Dorange · K. Miquel-Hebert · K. Sudhir
Abbott Vascular, Diegem, Belgium

J. A. Ormiston
Department of Cardiology, Auckland City Hospital, Auckland, New Zealand

($0.88 \pm 0.79 \text{ mm}^2$ vs. $1.15 \pm 1.05 \text{ mm}^2$, $P = 0.027$) of the PBS. The NC in contact with the lumen in the treated segment did not increase with follow-up (7.33 vs. 6.36%, $P = 0.2$). Serial IVUS-VH analysis of BVS-treated lesions at 6-month demonstrated a progression in the NC and fibrous tissue content of PBS.

Keywords Bioresorbable vascular scaffold · Coronary plaque · IVUS-VH · Everolimus

Introduction

Percutaneous treatment of atherosclerotic lesions has been improved by the introduction of bare- and drug-eluting metallic stents [1]. Implantation of a metallic stent does not remove atherosclerotic plaque; instead the plaque is stretched during baro-trauma. The metallic stent platform and the eluted drug may affect not only the intra-stent neo-intima growth, but also the plaque behind the struts. With regards to the vascular response to a foreign body (i.e. a metallic stent), [2, 3] animal models have demonstrated that metallic stents eluting sirolimus and paclitaxel induce inflammatory changes adjacent to almost all struts [4].

Evaluation of plaque behind the metallic struts can be performed using intravascular ultrasound virtual histology (IVUS-VH), which facilitates qualitative and quantitative analyses of the plaque. Since metallic stent's struts are mistakenly recognized by IVUS-VH as dense calcium and necrotic core, careful evaluation of the sole plaque behind the stent struts should be done to avoid any misclassification of the actual tissue [5, 6]. Previous reports using serial IVUS-VH analysis of lesions treated with drug-eluting stents have demonstrated a greater frequency of "unstable lesion morphometry" at follow-up, compared with bare metal stents [7]. Temporary scaffolding with an everolimus eluting bioresorbable vascular scaffold (BVS; Abbott Vascular, Santa Clara, USA) may have differential effects on peristrut plaque, due to the polymeric nature of the fast resorbable coating made of a mixture of L and D racemic forms of poly-lactide [8].

Therefore, we assessed the vascular response to implantation of the BVS at 6-months follow-up using IVUS-VH, and customized software to selectively analyze the plaque behind the struts.

Methods

Study population

For the present analysis, we initially screened patients from Cohort B1 of the ABSORB trial with paired post-implantation and 6-month follow-up IVUS-VH. Briefly, ABSORB Cohort B trial enrolled patients older than 18 years, with a diagnosis of stable, unstable or silent ischemia. This trial was subdivided in two subgroups of patients: the first group (cohort B1) has to undergo invasive imaging such as QCA, IVUS, IVUS-VH and OCT at 6 and 24 months whereas the second group (cohort B2) will undergo this invasive imaging at 12 and 24 months. All lesions were de novo, in a native coronary artery with a reference vessel diameter of 3.0 mm, with a % diameter stenosis ≥ 50 and $< 100\%$ and a thrombolysis in myocardial infarction (TIMI) flow grade of ≥ 1 . All lesions were treated by implantation of the BVS revision 1.1 (3.0 \times 18 mm). Major exclusion criteria were: patients presenting with an acute myocardial infarction, unstable arrhythmias or patients who had left ventricular ejection fraction $\leq 30\%$, restenotic lesions, lesions located in the left main coronary artery, lesions involving a side branch > 2 mm in diameter, and the presence of thrombus or another clinically significant stenosis in the target vessel. This trial was approved by ethics committee at each participating institution and each patient gave written informed consent before inclusion.

The BVS has an amorphous poly-DL-lactide (PDLLA) coating that contains and controls the release of the anti-proliferative drug everolimus. The scaffold body is made of semi-crystalline poly-L-lactide (PLLA). PLA is completely degraded via hydrolysis and bioresorbed via the Krebs cycle [8, 9].

Lesions were treated with routine interventional techniques that included mandatory pre-dilatation using a balloon shorter than the study device and 0.5 mm less in diameter. All patients were pre-treated with aspirin and a loading dose of at least 300 mg of clopidogrel was administered according to local hospital practise. After the procedure, all patients received aspirin ≥ 75 mg for the study duration (5 years) and clopidogrel 75 mg daily for a minimum of 6 months. Anticoagulation and glycoprotein IIb/IIIa use was according to local hospital practice.

Imaging procedure and acquisition

IVUS-VH post-implantation and 6 months follow-up were acquired with a phased array 20 MHz intravascular ultrasound catheter (EagleEye™; Volcano Corporation, Rancho Cordova, CA, USA) using an automated pullback of 0.5 mm per second. These files were stored on DVD and sent to the Corelab for independent analyses (Cardialysis, BV, Rotterdam, The Netherlands).

Image analysis

Customized offline IVUS-VH software was the QIVUs (Medis, Leiden, The Netherlands). Unlike other IVUS-VH software (pcVH and VIAS), this package allows the user to draw, in a semi-automatic fashion, a third contour (i.e. the scaffold contour). One limitation, however, is the ability of the software to read only IVUS-VH data acquired using a specific commercially available IVUS-VH console (s5i system, Volcano Corporation, Rancho Cordova, CA, USA). Contour detection was performed by experienced IVUS analysts who were blinded to the time of acquisition of the data (e.g. baseline or 6-month follow-up) [10]. Four tissue components (necrotic core—red; dense calcium—white; fibrous—green; and fibrofatty—light green) were identified with autoregressive classification systems. Each individual tissue component was quantified and colour coded in all IVUS cross sections as previously described [8, 11].

It has already been reported that the polymeric struts of the BVS (150 μm strut's thickness) are misinterpreted by IVUS-VH as areas of apparent “dense calcium” and “necrotic core”, [8] therefore drawing

this third contour, behind the polymeric struts of the BVS, delineates a new region of interest excluding the polymeric struts and their ultrasonic signature (Fig. 1).

In addition, we evaluated the presence of necrotic core in contact with the lumen, defined as a confluent necrotic core >10% of plaque area without evidence of overlying non-necrotic core tissue in the treated segment and in the edges (5 mm length adjacent to each BVS edge). Importantly, as polymeric struts are recognized as dense calcium surrounded by necrotic core, this surrounding necrotic core identified with the help of the corresponding grey-scale image, was not interpreted as necrotic core in contact with the lumen [5, 7, 12].

Ultimately, we drew the interface between plaque + media and the adventitia (external elastic membrane area, EEM), as well as the contours of the BVS area. We calculated the plaque area behind the struts (PBS) as the sum of all IVUS-VH components of the plaque behind the struts, excluding the grey medial stripe seen with IVUS-VH.

Statistical analysis

Discrete variables are presented as counts and percentages. Continuous variables are presented as means \pm standard deviation (SD). The calculation of the changes of each IVUS-VH plaque component between post-treatment and 6 months was as follows: mean 6 months area minus mean post-procedure area. The ratio between the number of frames with necrotic core in contact with the lumen and the total number of frames analyzed has been defined as incidence of necrotic core in contact with the lumen for the treated segment and the edges. Paired comparisons between

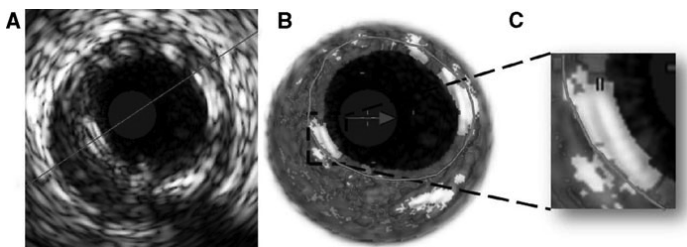


Fig. 1 Panel A: one frame of grey-scale IVUS indicating the appearance of the BVS's struts (double grey line). In Panel B the polymeric struts are recognized as dense calcium and

necrotic core by IVUS-VH and in (Panel C) a third contour (purple line) is drawn in a semi-automatic way by the dedicated software behind them

post-procedure and 6-month follow-up were done by the Wilcoxon signed rank test. Correlation between parameters was performed by Spearman test. A two-side P value of less than 0.05 indicated statistical significance. Intra-observer and inter-observer variabilities were measured by correlation test for IVUS data and by κ test of concordance for necrotic core in contact with the lumen. Statistical analyses were performed with use of SPSS 13.0 software.

Results

Baseline clinical and angiographic characteristics

Thirty-two patients in the ABSORB Cohort B study had paired post-implantation and 6-month IVUS-VH

Table 1 Clinical and angiographic characteristics of the patients

	Patients ($n = 15$) Lesions ($n = 15$)
Age (years)	
Mean \pm SD (n)	63.87 \pm 12.01
Men (%)	60.0
Smokers (%)	26.7
Diabetes (%)	13.3
Hypertension requiring medication (%)	66.7
Hyperlipidaemia requiring medication (%)	80.0
Previous target vessel intervention (%)	6.7
Previous myocardial infarction (%)	53.3
Stable angina (%)	53.3
Unstable angina (%)	33.3
Silent ischaemia (%)	6.7
Target vessel (%)	
Left anterior descending	33.3
Left circumflex	26.7
Right coronary artery	40.0
AHA/ACC lesion classification (%)	
A	6.7
B1	33.3
B2	53.3
C	6.7
Beta-blocker	93.3
ACEI/ARB	40.0
Calcium-channel blocker	40.0
Statin	100.0

SD standard deviation; ACEI angiotensin-converting enzyme inhibitor; ARB angiotensin receptor blocker

data. Out of these 32 patients, only 15 patients were imaged using the s5i system. Table 1 shows their clinical and angiographic data.

Grey-scale IVUS and IVUS-VH analyses (Table 2)

A significant increase in both EEM area and of PBS was observed with follow-up. A non significant 4% decrease in BVS area was observed at follow up ($P = 0.065$).

In the IVUS-VH analysis of the plaque behind the polymeric struts, there was a significant relative increase of 30% in fibrous tissue area (from $0.88 \pm 0.79 \text{ mm}^2$ to $1.15 \pm 1.05 \text{ mm}^2$; $P = 0.027$) and of 42% in necrotic core area (from $0.85 \pm 0.70 \text{ mm}^2$ to $1.21 \pm 0.92 \text{ mm}^2$; $P = 0.010$) at 6-month follow-up. There was a no significant increase of 3% in fibrofatty tissue area ($P = 0.286$) and 8% in dense calcium area ($P = 0.334$). However, the percentage weight of each plaque component did not change significantly.

There was a significant correlation between Δ plaque behind the polymeric struts and Δ mean EEM area ($r = 0.9$, $P < 0.001$; Fig. 2) There was no

Table 2 IVUS analysis in the treated segment at baseline and follow-up

	BVS 1.1 ($n = 15$)		P value
	Baseline	Follow-up	
Mean EEM area (mm^2)	13.76 \pm 4.07	14.76 \pm 4.56	0.006
PBS area (mm^2)	2.45 \pm 1.93	3.19 \pm 2.48	0.005
BVS area (mm^2)	6.51 \pm 1.38	6.25 \pm 1.14	0.065
Fibrous tissue (mm^2)	0.88 \pm 0.79	1.15 \pm 1.05	0.027
Fibrous tissue (%)	38.80 \pm 16.36	35.86 \pm 13.25	0.256
Fibro-fatty tissue (mm^2)	0.18 \pm 0.36	0.20 \pm 0.40	0.286
Fibro-fatty tissue (%)	5.31 \pm 7.82	4.43 \pm 6.70	0.532
Necrotic core (mm^2)	0.85 \pm 0.70	1.21 \pm 0.92	0.010
Necrotic core (%)	37.23 \pm 11.66	40.18 \pm 8.69	0.307
Dense calcium (mm^2)	0.54 \pm 0.85	0.62 \pm 0.72	0.334
Dense calcium (%)	18.66 \pm 14.06	19.52 \pm 12.77	0.691

Data are expressed as mean \pm SD

EEM external elastic membrane; PBS plaque behind struts; BVS bioresorbable vascular scaffold

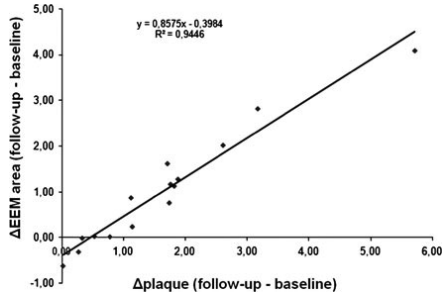


Fig. 2 Correlation between the temporal change of the plaque behind the polymeric struts and of EEM area. *EEM* external elastic membrane

correlation between Δ plaque behind the struts and the change in BVS area ($P = 0.9$).

Incidence of necrotic core in contact with the lumen

A representative IVUS image of necrotic core in contact with the lumen in the BVS treated segment is shown in Fig. 3. There was no significant change during follow-up in the content of the necrotic core in contact with the lumen in the treated segment (7.33 vs. 6.36%, $P = 0.256$; Fig. 4).

Intra-observer and inter-observer variabilities

Intra-observer and inter-observer variabilities yielded good concordance for IVUS data ($r^2 = 0.91$ and

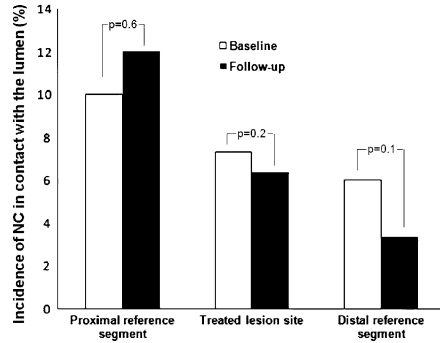


Fig. 4 Incidence of segments with necrotic core abutting the lumen at baseline and follow-up. Within the treated lesion site, proximal and distal reference segment necrotic core abutting the lumen did not significantly modify

$r^2 = 0.87$, respectively) and for necrotic core in contact with the lumen ($\kappa = 0.96$ and $\kappa = 0.90$, respectively)

Discussion

The major findings of our study are: (1) at 6 months follow-up, the increase in plaque area, and in particular the progression of necrotic core and fibrous tissue detected by IVUS-VH behind the polymeric struts, correlated to an increase in EEM area; (2) although there was an increase in necrotic core area behind the polymeric struts, there was not an increase in necrotic core in contact with the lumen in the treated segment.

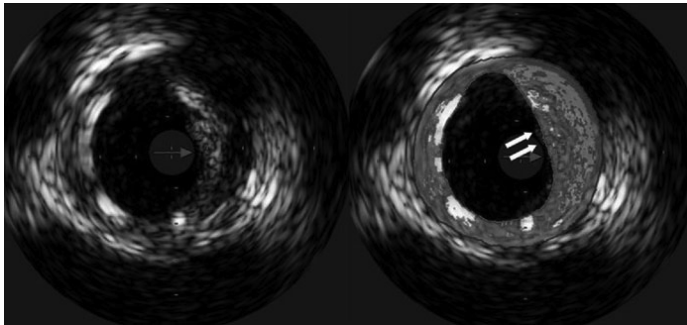


Fig. 3 Representative IVUS-VH image of necrotic core in contact with the lumen in the segment where a BVS has been implanted (white arrows). *BVS* bioresorbable polymeric scaffold

Similar to metallic stents, struts of the BVS are detected by IVUS-VH as dense calcium, surrounded by a “red halo” [5, 12]. This observation may be useful for the evaluation of the bioresorption process of the BVS, as temporal changes in dense calcium and necrotic core of coronary segments treated with a BVS appear to be a ‘surrogate’ of the bioresorption process [6, 12]. However, this misinterpretation of the polymeric struts by IVUS-VH prevents analysis of the actual amount of dense calcium and necrotic core within the plaque behind the struts. The semi-automatic introduction by the “Medis software” of a third contour, which represents the BVS, is a helpful tool to focus analysis on only the plaque behind the BVS. We acknowledge that this software has not previously validated for this use and in our analysis it has shown a good the inter- and intra-observers variabilities.

Previously Kubo et al. analyzed the long-term effects of drug-eluting stents (DES) and bare metal stents (BMS) on coronary arterial wall morphology using IVUS-VH, and demonstrated that DES-treated lesions had a greater frequency of “unstable lesion morphometry” at follow-up compared to BMS [7]. In particular assessing the total amount of the four IVUS-VH components, including also the contribution of the stent, it was found that DES-treated lesions showed a significantly higher incidence of necrotic core in contact with the lumen compared to BMS-treated lesions at follow up, although there was no significant difference in mean necrotic core area between both groups. This was due to a suppression of the protective neointimal hyperplasia layer with DES compared with BMS. In our study, focusing only on plaque burden behind the polymeric struts, we found a significant progression in necrotic core and fibrous tissue at 6 months follow-up. However, the incidence of necrotic core in contact with the lumen behind polymeric struts did not tend to increase during the same period. Histological validation studies have shown that necrotic core is a mainly highly lipid necrotic region with remnants of foam cells and some infiltration of inflammatory cells. It is unlikely that the changes described in the plaque behind the polymeric struts are influenced by changes in the BVS struts during the first 6 months: it has been, indeed, shown that the 100% of the boxes of the BVS, evaluated by optical coherence tomography, are preserved with completely absence of qualitative

alterations, whereas only 3% of the boxes of the first BVS generation appeared as “preserved” [13].

Recently concerns have been raised over the long-term biological reaction to metallic DES [14]. In rabbit iliac arteries, evidence of increased inflammation and delayed endothelialization was noted at 28 days in DES compared with polymer-coated inert stents or BMS [15]. In porcine coronary arteries treated with DES, arterial inflammation characterized by giant cells has been shown to gradually progress from 90 to 180 days with a corresponding increase in neointimal formation [16]. In humans, Aoki et al. have demonstrated in vivo that plaque volume behind a metallic stent eluting sirolimus increases slightly at 4 months follow-up, and then significantly decreases at 4 years follow-up compared to post-implantation, and that change in echogenicity is suggestive of a change in plaque composition [17]. The same phenomenon was observed following implantation of an everolimus-eluting metallic stent in the SPIRIT I study: slight increase of plaque behind the stent at 6 months, followed by a decrease at 1 year follow-up [18]. Aoki et al. also documented a significant increase in plaque area behind metallic stents eluting paclitaxel at 6 months, with subsequent regression at 2 years [19]. In the MAHOROBA study, that tested biodegradable polymer sustained release tacrolimus-eluting stent, Onuma et al. have shown that plaque volume increased significantly at 4-month angiographic follow-up [20]. In our study, at 6 months follow-up, we observed an increase of both plaque area and of necrotic core behind the polymeric struts of BVS.

Some preclinical studies in an atherosclerotic rabbit model have shown that the implantation of metallic everolimus eluting stents results in an autophagic process of macrophages through the inhibition of the mTOR pathway by everolimus [21, 22]. In a porcine model, Onuma et al. found inflammatory cells, in particular granuloma and giant cells, surrounding the polymeric struts of the BVS: the concentration of cells was highest 1 and 6 months after implantation, before decreasing over time [23]. In particular after 1 year there was a decrease in the inflammation score, granulomas and giant cells surrounding the polymeric struts. It is important to highlight that in the porcine coronary artery model, BVS associated inflammation is markedly less than with a sirolimus-eluting metallic stent. In humans at 6 months after BVS 1.0 implantation and with long-term follow-up Sarno et al. found

a similar increase of plaque area at 6-month, with a following decrease at 2 years, most likely due to the bioresorption of the polymeric struts [6].

It is also important to consider that the increase in plaque area, as a result mainly of necrotic core and fibrous tissue progression, did not translate into a decrease of a scaffold area of BVS, but only in a positive remodelling of the EEM [24]. Rodriguez-Granillo et al. have already shown how positive remodelling of the vessel may be related to plaque composition: in particular lipid core size was significantly larger in positively remodelled coronary lesions than in those with vessel shrinkage [24].

Limitations

The present study included a very small number of patients with a technique (VH) that has large variability. The use of the same patients at baseline and follow-up may reduce its variability. However, the intra- and inter-catheter variability of the VH previously shown supports longitudinal studies with the VH [25].

IVUS-VH data pre-BVS implantation were not available, therefore baseline characteristics of the artery have been evaluated in the presence of the BVS, and after pre-dilatation.

The interpretation of the backscattering signal from the plaque behind the polymeric struts by the IVUS-VH software may be influenced by the presence of the scaffold: analysis of the difference between 6-month follow-up and baseline may reduce this limitation.

Conclusions

In conclusion our study focusing on the IVUS-VH detection of plaque behind the BVS seems to show a progression in necrotic core and fibrous tissue components at 6 months. In particular, the progression in necrotic core confirms the histological data in animal models regarding an inflammatory microenvironment behind the polymeric struts, at least at 6-month follow-up.

References

- Moses JW, Leon MB, Popma JJ, Fitzgerald PJ, Holmes DR, O'Shaughnessy C, Caputo RP, Kereiakes DJ,

- Williams DO, Teirstein PS, Jaeger JL, Kuntz RE (2003) Sirolimus-eluting stents versus standard stents in patients with stenosis in a native coronary artery. *N Engl J Med* 349(14):1315–1323. doi:10.1056/NEJMoa035071349/14/1315[pii]
- Finn AV, Nakazawa G, Joner M, Kolodgie FD, Mont EK, Gold HK, Virmani R (2007) Vascular responses to drug eluting stents: importance of delayed healing. *Arterioscler Thromb Vasc Biol* 27(7):1500–1510. doi:ATVBAHA.107.144220[pii]10.1161/ATVBAHA.107.144220
- Joner M, Finn AV, Farb A, Mont EK, Kolodgie FD, Ladich E, Kutys R, Skorija K, Gold HK, Virmani R (2006) Pathology of drug-eluting stents in humans: delayed healing and late thrombotic risk. *J Am Coll Cardiol* 48(1):193–202. doi:S0735-1097(06)01109-0[pii]10.1016/j.jacc.2006.03.042
- Wilson GJ, Nakazawa G, Schwartz RS, Huibregtse B, Poff B, Herbst TJ, Baim DS, Virmani R (2009) Comparison of inflammatory response after implantation of sirolimus- and paclitaxel-eluting stents in porcine coronary arteries. *Circulation* 120(2):141–149, 141–142. doi:CIRCULATIONAHA.107.730010 [pii]10.1161/CIRCULATIONAHA.107.730010
- Kim SW, Mintz GS, Hong YJ, Pakala R, Park KS, Pichard AD, Satler LF, Kent KM, Suddath WO, Waksman R, Weissman NJ (2008) The virtual histology intravascular ultrasound appearance of newly placed drug-eluting stents. *Am J Cardiol* 102(9):1182–1186. doi:S0002-9149(08)00567-5[pii]10.1016/j.amjcard.2008.03.054
- Sarno G, Onuma Y, Garcia HM, Garg S, Regar E, Thuesen L, Dudek D, Veldhof S, Dorange C, Ormiston JA, Serruys PW (2010) Ivus radiofrequency analysis in the evaluation of the polymeric struts of the bioabsorbable everolimus-eluting device during the bioabsorption process. *Catheter Cardiovasc Interv* 5:627–632. doi:10.1002/ccd.22332
- Kubo T, Maehara A, Mintz GS, Garcia-Garcia HM, Serruys PW, Suzuki T, Klauss V, Sumitani S, Lerman A, Marso SP, Margolis MP, Margolis JR, Foster MC, De Bruyne B, Leon MB, Stone GW (2010) Analysis of the long-term effects of drug-eluting stents on coronary arterial wall morphology as assessed by virtual histology intravascular ultrasound. *Am Heart J* 159(2):271–277. doi:S0002-8703(09)00880-1 [pii]10.1016/j.ahj.2009.11.008
- Serruys PW, Ormiston JA, Onuma Y, Regar E, Gonzalo N, Garcia-Garcia HM, Nieman K, Bruining N, Dorange C, Miquel-Hebert K, Veldhof S, Webster M, Thuesen L, Dudek D (2009) A bioabsorbable everolimus-eluting coronary stent system (absorb): 2-year outcomes and results from multiple imaging methods. *Lancet* 373(9667):897–910. doi:S0140-6736(09)60325-1[pii]10.1016/S0140-6736(09)60325-1
- Ormiston JA, Serruys PW, Regar E, Dudek D, Thuesen L, Webster MW, Onuma Y, Garcia-Garcia HM, McGreevy R, Veldhof S (2008) A bioabsorbable everolimus-eluting coronary stent system for patients with single de novo coronary artery lesions (absorb): a prospective open-label trial. *Lancet* 371(9616):899–907. doi:S0140-6736(08)60415-8[pii]10.1016/S0140-6736(08)60415-8
- Hausmann D, Lundkvist AJ, Friedrich GJ, Mullen WL, Fitzgerald PJ, Yock PG (1994) Intracoronary ultrasound

- imaging: intraobserver and interobserver variability of morphometric measurements. *Am Heart J* 128(4):674–680
11. Nair A, Kuban BD, Tuzcu EM, Schoenhagen P, Nissen SE, Vince DG (2002) Coronary plaque classification with intravascular ultrasound radiofrequency data analysis. *Circulation* 106(17):2200–2206
 12. Garcia-Garcia HM, Gonzalo N, Pawar R, Kukreja N, Dudek D, Thuesen L, Ormiston JA, Regar E, Serruys PW (2009) Assessment of the absorption process following bioabsorbable everolimus-eluting stent implantation: temporal changes in strain values and tissue composition using intravascular ultrasound radiofrequency data analysis. A substudy of the absorb clinical trial. *EuroIntervention* 4(4):443–448
 13. Serruys PW, Onuma Y, Ormiston JA, De Bruyne B, Regar E, Dudek D, Thuesen L, Smith P, Chevalier B, McClean D, Koolen J, Windecker S, Whitbourn R, Meredith I, Dorange C, Veldhof S, Miquel-Hebert K, Rapoza R, Garcia Garcia HM (2010) Evaluation of the second generation of a bioresorbable everolimus drug-eluting vascular scaffold for treatment of de novo coronary artery stenosis: 6-month clinical and imaging outcomes. *Circulation* (in press)
 14. Virmani R, Liistro F, Stankovic G, Di Mario C, Montorfano M, Farb A, Kolodgie FD, Colombo A (2002) Mechanism of late in-stent restenosis after implantation of a paclitaxel derivate-eluting polymer stent system in humans. *Circulation* 106(21):2649–2651
 15. Klugherz BD, Llanos G, Lieuallen W, Kopia GA, Papandreou G, Narayan P, Sasseen B, Adelman SJ, Falotico R, Wilensky RL (2002) Twenty-eight-day efficacy and pharmacokinetics of the sirolimus-eluting stent. *Coron Artery Dis* 13(3):183–188
 16. Carter AJ, Aggarwal M, Kopia GA, Tio F, Tsao PS, Kolata R, Yeung AC, Llanos G, Dooley J, Falotico R (2004) Long-term effects of polymer-based, slow-release, sirolimus-eluting stents in a porcine coronary model. *Cardiovasc Res* 63(4):617–624. doi:10.1016/j.cardiores.2004.04.029 S0008636304002019[pii]
 17. Aoki J, Abizaid AC, Serruys PW, Ong AT, Boersma E, Sousa JE, Bruining N (2005) Evaluation of four-year coronary artery response after sirolimus-eluting stent implantation using serial quantitative intravascular ultrasound and computer-assisted grayscale value analysis for plaque composition in event-free patients. *J Am Coll Cardiol* 46(9):1670–1676. doi:S0735-1097(05)01846-2 [pii]10.1016/j.jacc.2005.06.076
 18. Tsuchida K, Piek JJ, Neumann FJ, van der Giessen WJ, Wiemer M, Zeiher AM, Grube E, Haase J, Thuesen L, Hamm CW, Veldhof S, Dorange C, Serruys PW (2005) One-year results of a durable polymer everolimus-eluting stent in de novo coronary narrowings (the spirit first trial). *EuroIntervention* 1(3):266–272. doi:EIJV113A44[pii]
 19. Aoki J, Colombo A, Dudek D, Banning AP, Drzewiecki J, Zmudka K, Schiele F, Russell ME, Koglin J, Serruys PW (2005) Persistent remodeling and neointimal suppression 2 years after polymer-based, paclitaxel-eluting stent implantation: insights from serial intravascular ultrasound analysis in the taxus ii study. *Circulation* 112(25):3876–3883. doi:CIRCULATIONAHA.105.558601 [pii]10.1161/CIRCULATIONAHA.105.558601
 20. Onuma Y, Serruys P, den Heijer P, Joeseof KS, Duckers H, Regar E, Kukreja N, Tanimoto S, Garcia-Garcia HM, van Beusekom H, van der Giessen W, Nishide T (2009) Mahoroba, first-in-man study: 6-month results of a biodegradable polymer sustained release tacrolimus-eluting stent in de novo coronary stenoses. *Eur Heart J* 30(12):1477–1485. doi:ehp127 [pii]10.1093/eurheartj/ehp127
 21. Verheye S, Martinet W, Kockx MM, Knaepen MW, Salu K, Timmermans JP, Ellis JT, Kilpatrick DL, De Meyer GR (2007) Selective clearance of macrophages in atherosclerotic plaques by autophagy. *J Am Coll Cardiol* 49(6):706–715. doi:S0735-1097(06)02888-9 [pii]10.1016/j.jacc.2006.09.047
 22. Martinet W, Verheye S, De Meyer GR (2007) Everolimus-induced mtor inhibition selectively depletes macrophages in atherosclerotic plaques by autophagy. *Autophagy* 3(3):241–244. doi:3711 [pii]
 23. Onuma Y, Serruys PW, Perkins L, Okamura T, Gonzalo N, Garcia HM, Regar E, Kamberi M, Powers JC, Rapoza R, van Beusekom H, van der Giessen W, Virmani R Intra-coronary optical coherence tomography (oct) and histology at 1 month, at 2, 3 and 4 years after implantation of everolimus-eluting bioresorbable vascular scaffolds in a porcine coronary artery model: an attempt to decipher the human oct images in the absorb trial. *Circulation* (in press)
 24. Rodriguez-Granillo GA, Serruys PW, Garcia-Garcia HM, Aoki J, Valgimigli M, van Mieghem CA, McFadden E, de Jaegere PP, de Feyter P (2006) Coronary artery remodeling is related to plaque composition. *Heart* 92(3):388–391. doi:hrt.2004.057810 [pii]10.1136/hrt.2004.057810
 25. Rodriguez-Granillo GA, Vaina S, Garcia-Garcia HM, Valgimigli M, Duckers E, van Geuns RJ, Regar E, van der Giessen WJ, Bressers M, Goedhart D, Morel MA, de Feyter PJ, Serruys PW (2006) Reproducibility of intravascular ultrasound radiofrequency data analysis: implications for the design of longitudinal studies. *Int J Cardiovasc Imaging* 22(5):621–631. doi:10.1007/s10554-006-9080-0

8.2

Analysis of one-year virtual histology changes in coronary plaque located behind the struts of the everolimus eluting bioresorbable vascular scaffold.

Salvatore Brugaletta, Josep Gomez-Lara, Hector M Garcia-Garcia, Jung Ho Heo, Vasim Farooq, Robert Jan van Geuns, Bernard Chevalier, Stephan Windecker, Dougal McClean, Leif Thuesen, Robert Whitbourn, Ian Meredith, Cecile Dorange, Susan Veldhof, Richard Rapoza, John A Ormiston, Patrick W Serruys

Int J Cardiovasc Imaging 2011, Epub ahead of print

Analysis of 1 year virtual histology changes in coronary plaque located behind the struts of the everolimus eluting bioresorbable vascular scaffold

Salvatore Brugaletta · Josep Gomez-Lara · Hector M. Garcia-Garcia · Jung Ho Heo · Vasim Farooq · Robert J. van Geuns · Bernard Chevalier · Stephan Windecker · Dougal McClean · Leif Thuesen · Robert Whitbourn · Ian Meredith · Cecile Dorange · Susan Veldhof · Richard Rapoza · John A. Ormiston · Patrick W. Serruys

Received: 4 July 2011 / Accepted: 14 November 2011

© The Author(s) 2011. This article is published with open access at Springerlink.com

Abstract Serial intravascular ultrasound virtual histology (IVUS-VH) after implantation of metallic stents has been unable to show any changes in the composition of the scaffolded plaque overtime. The everolimus-eluting ABSORB scaffold potentially allows for the formation of new fibrotic tissue on the scaffolded coronary plaque during bioresorption. We examined the 12 month IVUS-VH changes in composition of the plaque behind the struts (PBS) following the implantation of the ABSORB scaffold. Using IVUS-VH and

dedicated software, the composition of the PBS was analyzed in all patients from the ABSORB Cohort B2 trial, who were imaged with a commercially available IVUS-VH console (s5i system, Volcano Corporation, Rancho Cordova, CA, USA), immediately post-ABSORB implantation and at 12 month follow-up. Paired IVUS-VH data, recorded with s5i system, were available in 17 patients (18 lesions). The analysis demonstrated an increase in mean PBS area ($2.39 \pm 1.85 \text{ mm}^2$ vs. $2.76 \pm 1.79 \text{ mm}^2$, $P = 0.078$) and a

S. Brugaletta · J. Gomez-Lara · H. M. Garcia-Garcia · J. H. Heo · V. Farooq · R. J. van Geuns · P. W. Serruys (✉)
Department of Interventional Cardiology, Thoraxcenter, Erasmus MC, 's Gravendijkwal 230, 3015 Rotterdam, CE, The Netherlands
e-mail: p.w.j.c.serruys@erasmusmc.nl

S. Brugaletta
Department of Cardiology, Thorax Institute Hospital Clinic, Barcelona, Spain

H. M. Garcia-Garcia
Cardialysis B.V., Rotterdam, The Netherlands

B. Chevalier
Institut Cardiovasculaire Paris Sud, Massy, France

S. Windecker
Bern University Hospital, Bern, Switzerland

D. McClean
Christchurch Hospital, Christchurch, New Zealand

L. Thuesen
Skejby Sygehus, Aarhus University Hospital, Aarhus, Denmark

R. Whitbourn
St Vincents Hospital, Fitzroy, Australia

I. Meredith
Monash Cardiovascular Research Centre, Melbourne, Australia

C. Dorange · S. Veldhof
Abbott Vascular, Diegem, Belgium

R. Rapoza
Abbott Vascular, Santa Clara, CA, USA

J. A. Ormiston
Department of Cardiology, Auckland City Hospital, Auckland, New Zealand

reduction in the mean lumen area ($6.37 \pm 0.90 \text{ mm}^2$ vs. $5.98 \pm 0.97 \text{ mm}^2$, $P = 0.006$). Conversely, a significant decrease of 16 and 30% in necrotic core (NC) and dense calcium (DC) content, respectively, were evident (median % NC from 43.24 to 36.06%, $P = 0.016$; median % DC from 20.28 to 11.36%, $P = 0.002$). Serial IVUS-VH analyses of plaque located behind the ABSORB struts at 12-month demonstrated an increase in plaque area with a decrease in its NC and DC content. Larger studies are required to investigate the clinical impact of these findings.

Keywords Bioresorbable vascular scaffold · Coronary plaque · IVUS-VH · Everolimus · Necrotic core

Introduction

Percutaneous treatment of atherosclerotic lesions with use of metallic stents leads to a stretching of coronary plaques by baro-trauma [1]. The implantation of a foreign body, such as a metallic stent, is also known to induce an inflammatory response adjacent to the struts [2–4]. However, serial analyses by intravascular ultrasound virtual histology (IVUS-VH) have demonstrated no changes at 10 months in the VH components of coronary plaques after bare metal or drug eluting stent implantation [5, 6].

The new everolimus-eluting bioresorbable vascular scaffold (ABSORB, Abbott Vascular, Santa Clara, CA) has been developed with the intention to provide temporary lumen scaffolding and, in contrast to metallic platform stents, to allow late lumen enlargement and restoration of normal vasomotion post bioresorption [7]. In the ABSORB Cohort A trial a non significant reduction in the VH-derived necrotic core (NC) was demonstrated between 6 month and 2 year follow-up [7, 8]. However, as the polymeric struts are mistakenly recognized by IVUS-VH as dense calcium and necrotic core and are progressively bioresorbed, a concomitant result of scaffold bioresorption and plaque modification has to be taken into account for the correct interpretation of VH changes over time [9, 10].

Conversely, in the ABSORB Cohort B trial, a customized software, allowing for the exclusion of the

dense calcium and necrotic core due to the temporary presence of the scaffold from the quantification of the VH-plaque behind the polymeric struts, was used. At 6-month follow-up a slight increase in the plaque area, in particular in its relative NC content, was evident [11]. The 12 month follow-up of this trial recently demonstrated a further increase in the plaque size but with clear signs of pharmacologically induced vasomotion of the scaffolded segment, suggesting loss of the mechanical integrity and radial forces of the scaffold and favourable changes in the composition of the plaque [12].

The aim of this study was therefore to analyze the 12 month changes in the VH composition of only the plaque behind the polymeric struts.

Methods

Study population

The ABSORB Cohort B trial enrolled patients older than 18 years, with a diagnosis of stable, unstable or silent ischemia, subdivided in two subgroups: the first group (Cohort B1) underwent invasive imaging such as quantitative coronary angiography, IVUS, IVUS-VH and optical coherence tomography at 6 months whereas the second group (Cohort B2) underwent the same invasive imaging at 12 months. For the present analysis, we screened patients from ABSORB Cohort B2 with paired post-implantation and 12 month follow-up IVUS-VH.

Briefly, all lesions were de novo, in a native coronary artery with a reference vessel diameter of 3.0 mm, with a percentage diameter stenosis ≥ 50 and $< 100\%$ and a thrombolysis in myocardial infarction flow grade of ≥ 1 . All lesions were treated by implantation of the ABSORB scaffold 1.1 ($3.0 \times 18 \text{ mm}$) [7, 13]. Major exclusion criteria were: patients presenting with an acute myocardial infarction, unstable arrhythmias or patients who had left ventricular ejection fraction $\leq 30\%$, restenotic lesions, lesions located in the left main coronary artery, lesions involving a side branch $> 2 \text{ mm}$ in diameter, and the presence of thrombus or another clinically significant stenosis in the target vessel. The trial was approved by the ethics committee at each participating institution and each patient gave written informed consent before inclusion.

Imaging acquisition and analysis

IVUS-VH post-implantation and at 12 month follow-up were acquired with a phased array 20 MHz intravascular ultrasound catheter (EagleEye™, Volcano Corporation, Rancho Cordova, CA, USA) using an automated pullback of 0.5 mm per second. The baseline and one-year follow-up region of interest were matched by use of anatomical landmarks. The radiofrequency data, required for VH analysis, were acquired during the IVUS pullback and raw radiofrequency data capture gated to the R wave (In-Vision Gold, Volcano). These files were stored on DVD and sent to an independent core laboratory for analyses (Cardialysis, BV, Rotterdam, The Netherlands).

The data were analyzed by the QIVUs software (Medis, Leiden, The Netherlands). This allowed the user to draw, in a semi-automatic fashion, a third contour (i.e. the scaffold contour). One limitation of this software, however, is its ability to read only IVUS-VH data acquired using a specific commercially available IVUS-VH console (s5i system, Volcano Corporation, Rancho Cordova, CA, USA).

Three different contours were drawn (lumen, scaffold and external elastic membrane) by experienced IVUS analysts blinded to the time of acquisition (e.g. baseline or 12 month follow-up) [14]. Reproducibility of these measurements using this software has been previously demonstrated to be good [11]. Four tissue components (necrotic core NC—red; dense calcium DC—white; fibrous FT—green; and fibrofatty FF—light green) were identified with auto-regressive classification system. Each individual tissue component was quantified and colour coded in all IVUS cross sections [7, 15]. As previously described, the scaffold contour was drawn behind the polymeric struts of the ABSORB scaffold, excluding the polymeric struts and their ultrasonic signature from the quantification of the VH components of the plaque behind the struts (PBS). The PBS was calculated as the sum of all IVUS-VH components, excluding the grey media stripe seen with IVUS-VH.

In addition, we qualitatively evaluated the presence of necrotic core in contact with the lumen, defined as a confluent necrotic core >10% of plaque area without evidence of overlying non-necrotic core tissue in the treated segment and in the edges (5 mm length adjacent to each ABSORB scaffold edge), as previously reported [6, 11]. Importantly, as the polymeric

struts are recognized as dense calcium surrounded by necrotic core, this surrounding necrotic core, with the help of the corresponding grey-scale image, was not interpreted as necrotic core in contact with the lumen [5, 6, 9, 11].

Statistical analysis

Discrete variables are presented as counts and percentages. Continuous variables are presented as means \pm standard deviation (SD) or median and interquartile range, according to their normal or not normal distribution. Normal distribution of continuous variables was tested by the Kolmogorov-Smirnov test. The ratio between the number of frames with necrotic core in contact with the lumen and the total number of frames analyzed has been defined as the incidence of necrotic core in contact with the lumen for the treated segment and the edges. Paired comparisons between post-procedure and 12-month follow-up were done by paired t-test or Wilcoxon signed rank test, where appropriate. Correlation between parameters was performed by the Spearman test. A two-side *P* value of less than 0.05 indicated statistical significance. Statistical analyses were performed with the use of SPSS 16.0 software (SPSS Inc., Chicago IL, USA).

Results

Baseline clinical and angiographic characteristics

Overall, forty-six patients had paired post-ABSORB implantation and 12 month follow-up IVUS-VH data. Of these patients, only 17 patients (18 lesions) were imaged using the s5i system and therefore were included in the present study. Table 1 shows their clinical and angiographic data. No differences were found in the clinical and angiographic data between patients included and excluded from the analysis.

Grey-scale IVUS and IVUS-VH analyses (Table 2)

PBS tended to increase from baseline to 12 months follow-up (from 2.39 ± 1.85 to 2.76 ± 1.79 mm²; *P* = 0.078) with a significant reduction in lumen area (from 6.37 ± 0.90 to 5.98 ± 0.97 mm²; *P* = 0.006).

Table 1 Baseline clinical and angiographic characteristics

	Patients (n = 17) Lesions (n = 18)
Age (years)	
Mean \pm SD (n)	60.5 \pm 9.1
Men, n (%)	14 (82)
Smokers, n (%)	1 (6)
Diabetes, n (%)	2 (12)
Hypertension requiring medication, n (%)	11 (65)
Hyperlipidaemia requiring medication, n (%)	11 (65)
Previous PCI, n (%)	2 (11)
Previous myocardial infarction, n (%)	2 (13)
Stable angina, n (%)	11 (65)
Unstable angina, n (%)	4 (24)
Silent ischaemia, n (%)	2 (12)
Target vessel, n (%)	
Left anterior descending	11 (61)
Left circumflex	2 (11)
Right coronary artery	5 (28)
AHA/ACC lesion classification, n (%)	
A	0 (0)
B1	11 (65)
B2	5 (29)
Medical treatment, n (%)	
β -blockers	13 (80)
ACE-inhibitors	9 (55)
Statins	16 (94)

SD standard deviation, PCI percutaneous coronary intervention, AHA/ACC American Heart Association/American College of Cardiology

No changes were found in the EEM area (from 14.08 ± 3.14 to 14.32 ± 3.13 mm²; $P = 0.349$).

In the IVUS-VH analysis of the PBS, there was a significant increase in the absolute and relative content of fibrous and fibrofatty tissue. Conversely, there was a significant decrease in the relative content of necrotic core and dense calcium (Fig. 1).

Whilst there was no relationship between the changes in NC and DC areas and in the PBS area between baseline and follow-up (Spearman rho = 0.24, $P = 0.336$ for NC; Spearman rho = 0.15, $P = 0.553$ for DC), there was a significant relationship

between the changes in FT and FF area and in the PBS area (Spearman rho = 0.87, $P < 0.001$ for FT; Spearman rho = 0.78, $P < 0.001$ for FF).

Incidence of necrotic core in contact with the lumen

Overall there was a reduction in necrotic core in contact with the lumen not only at the scaffold site, but also at the proximal and distal reference segments (Fig. 2). In particular the reduction of NC in contact with the lumen approached a statistical significance in the proximal reference segment ($P = 0.09$) (Fig. 3).

Intra-observer and inter-observer variabilities yielded good concordance for necrotic core in contact with the lumen ($\kappa = 0.86$ and $\kappa = 0.80$, respectively).

Discussion

The major finding of our study is that at 12 month follow-up there is an increase of plaque located behind the polymeric struts of the ABSORB scaffold, mainly due to an increase in its fibrous and fibrofatty content. Conversely, there is a significant decrease in necrotic core and dense calcium tissue.

The use of IVUS-VH in the study of the coronary plaque after stent/scaffold implantation is challenging, as metallic and polymeric struts are detected as dense calcium, surrounded by necrotic core and are accounted for the quantification of the plaque VH component [6, 9]. In addition, with bioresorbable polymeric struts, the weight of the scaffold in the quantification of the VH plaque components changes at various time points according to the scaffold bioresorption. Consequently, a reduction in the dense calcium and necrotic core content of the plaque may be an artifactual result of this process [7–9]. The semi-automatic introduction of a third contour, excluding the scaffold from the analysis of the VH plaque, allows us to overcome these problems.

Using this methodology, at 6 month follow-up we demonstrated an increase in plaque area and in all the VH components, without an increase of the necrotic core in contact with the lumen [11]. At 12 months, we conversely found a significant decrease in necrotic core and dense calcium, despite an increase in plaque area. The reduction of necrotic core was also accompanied by a reduction in the necrotic core in contact with the lumen either in the scaffold region or within

Table 2 IVUS analysis in the scaffold segment at baseline and follow-up (n = 18 lesions)

	Baseline	Follow-up	Difference % based on individual data	P value
Mean EEM area (mm ²)	14.08 ± 3.14	14.32 ± 3.13	2.54 ± 12.77	0.349
PBS area (mm ²)	2.39 ± 1.85	2.76 ± 1.79	7.31 (-3.86 to 26.54)	0.078
Mean Lumen area (mm ²)	6.37 ± 0.90	5.98 ± 0.97	-6.19 ± 7.13	0.006
Fibrous tissue (mm ²)	0.59 (0.28–1.11)	1.01 (0.59–1.94)	42.76 (14.91–122.31)	0.004
Fibrous tissue (%)	28.10 (26.15–33.31)	43.90 (34.82–51.35)	45.02 (13.06–62.50)	0.001
Fibro-fatty tissue (mm ²)	0.04 (0.01–0.14)	0.12 (0.06–0.22)	200.14 (50.52–819.11)	0.011
Fibro-fatty tissue (%)	1.82 (0.83–4.08)	5.16 (3.85–6.86)	163.77 (56.34–513.07)	0.004
Necrotic core (mm ²)	0.89 (0.52–1.53)	0.81 (0.59–1.41)	-8.29 (-18.64–11.35)	0.369
Necrotic core (%)	43.24 (38.77–52.71)	36.06 (32.53–43.79)	-15.59 (-27.87–1.06)	0.016
Dense calcium (mm ²)	0.39 (0.08–0.55)	0.27 (0.15–0.46)	-20.94 (-42.72–14.30)	0.048
Dense calcium (%)	20.28 (11.95–27.04)	11.36 (8.59–18.78)	-30.16 (-50.71–20.20)	0.002

Data are expressed as mean ± SD or median and interquartile range, according to their normal or not normal distribution, respectively

EEM external elastic membrane, PBS plaque behind struts

the proximal/distal reference segments. Of note is that dense calcium is a frequent finding within the necrotic core region; in this case it is frequently “speckled” which can be due to calcification of a “nidus” of macrophages, a sign associated with plaque instability and rupture [16]. The reduction of dense calcium

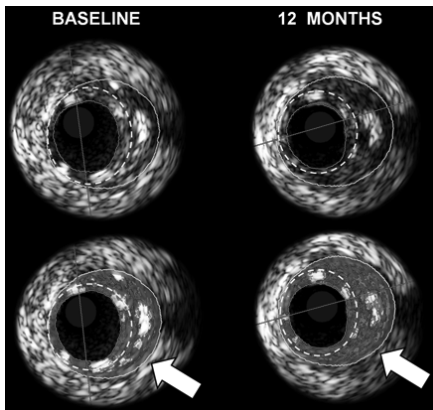


Fig. 1 Example of reduction of necrotic core and dense calcium in the plaque behind the polymeric struts (white arrows). Note also the increase of plaque size with predominant content of fibrous tissue. Yellow contour is drawn behind the ABSORB polymeric struts in a semi-automatic way by the dedicated software, excluding struts from the VH quantification of the plaque behind

found in our analysis was probably mainly due to the reduction of this type of dense calcium within the necrotic core area (Fig. 1). However, as calcium tends to be stable over short follow-up, another possible explanation could be that scaffold bioresorption influences the radiofrequency backscattering signal behind the scaffold, producing a reduction in dense calcium. At 12-month follow-up there was also an increase in fibrotic tissue content of the plaque. Previous optical coherence tomography studies have shown that polymeric struts apposed and embedded in the vessel wall become covered by neointima hyperplasia that also intersperses between the polymeric struts [17, 18].

Everolimus is probably the major component in the reduction of VH-derived necrotic core. Verheye et al.

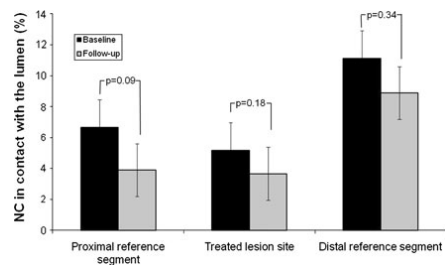


Fig. 2 Incidence of segments with necrotic core in contact with the lumen at baseline and follow-up

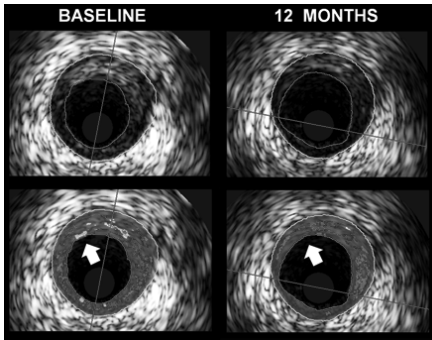


Fig. 3 Representative IVUS-VH image of necrotic core in contact with the lumen in the proximal reference segment at baseline and which has disappeared at follow-up

showed in rabbit atherosclerotic plaques that a stent-based delivery of everolimus leads to a marked reduction in macrophage content without altering the amount of smooth muscle cells, namely inducing autophagy by mTOR inhibition. [19, 20] This autophagy of macrophages is classically described as a process of vacuolization of the cytoplasm with formation of auto-phagosome, digesting the surrounding atherosclerotic debris. This observation is important in the context of plaque stabilization, as it is generally assumed that the presence of macrophages triggers plaque destabilization [21]. In addition, the 12 month inflammatory reaction after ABSORB implantation in a porcine model has been shown to be lower than for metallic stents, in which the inflammatory process is prolonged [22]. These pathological findings from animal studies are in line with the present reduction in the necrotic core content of the atherosclerotic plaque at 12 month follow-up after ABSORB implantation, where the favourable effects of everolimus are combined with a bioresorbable platform [2–4]. It is noteworthy that the lack of everolimus effect on the smooth muscle cells may be the basis of the preserved pharmacologically induced vasomotion of the scaffold segment, as highlighted at the 12-month follow-up [12].

Statin treatment, that was used in most of the patients, should be considered as another possible explanation of our findings, in particular of the reduction in necrotic core, as previously shown [23]. Statin therapy could also explain the reduction in the

necrotic core in contact with the lumen in the segment proximal to the device, as elution of everolimus is more frequent distal than proximal to the device [1].

Limitations

The present study included a small number of patients. IVUS-VH data pre-ABSORB implantation were not available. The interpretation of the backscattering signal from the plaque behind the polymeric struts by the IVUS-VH software may be influenced by the presence of the scaffold. IVUS-VH has not been validated to assess plaque composition behind scaffold struts and to identify bioresorbable struts. In addition struts bioresorption may account for the changes in the radiofrequency backscattering signal in the plaque behind.

Conclusions

At 12 months after ABSORB implantation, there was a slight increase in plaque area located behind the polymeric struts. Nevertheless, the necrotic core and dense calcium content of the plaque decreased significantly. These findings are compatible with the everolimus-induced autophagy of macrophages and subsequent reduction of inflammatory microenvironment of atherosclerotic plaque. The ability to decrease necrotic core content of coronary plaque without the permanent presence of metal may have important clinical implications in atherosclerosis treatment. Validation of the actual findings is needed and further studies with larger sample sizes and longer clinical follow-up are required before the impact of these observations can be fully understood.

Acknowledgments The ABSORB Trial is sponsored and funded by Abbott Vascular, Santa Clara, California, USA.

Conflicts of interest Cecile Dorange, Susan Veldhof and Richard Rapoza are employees of Abbott Vascular. There are no conflicts of interest regarding specific financial interests that there are relevant to the work conducted or reported in this manuscript.

Open Access This article is distributed under the terms of the Creative Commons Attribution Noncommercial License which permits any noncommercial use, distribution, and reproduction in any medium, provided the original author(s) and source are credited.

References

- Moses JW, Leon MB, Popma JJ, Fitzgerald PJ, Holmes DR, O'Shaughnessy C, Caputo RP, Kereiakes DJ, Williams DO, Teirstein PS, Jaeger JL, Kuntz RE (2003) Sirolimus-eluting stents versus standard stents in patients with stenosis in a native coronary artery. *N Engl J Med* 349(14):1315–1323. doi:10.1056/NEJMoa035071
- Finn AV, Nakazawa G, Joner M, Kolodgie FD, Mont EK, Gold HK, Virmani R (2007) Vascular responses to drug eluting stents: importance of delayed healing. *Arterioscler Thromb Vasc Biol* 27(7):1500–1510. doi:10.1161/ATVBAHA.107.144220
- Joner M, Finn AV, Farb A, Mont EK, Kolodgie FD, Ladich E, Kutys R, Skorija K, Gold HK, Virmani R (2006) Pathology of drug-eluting stents in humans: delayed healing and late thrombotic risk. *J Am Coll Cardiol* 48(1):193–202. doi:10.1016/j.jacc.2006.03.042
- Wilson GJ, Nakazawa G, Schwartz RS, Huijbregtse B, Poff B, Herbst TJ, Baim DS, Virmani R (2009) Comparison of inflammatory response after implantation of sirolimus- and paclitaxel-eluting stents in porcine coronary arteries. *Circulation* 120(2):141–149. doi:10.1161/CIRCULATIONAHA.107.730010 (141–142)
- Kubo T, Maehara A, Mintz GS, Garcia-Garcia HM, Serruys PW, Suzuki T, Klauss V, Sumitsuiji S, Lerman A, Marso SP, Margolis MP, Margolis JR, Foster MC, De Bruyne B, Leon MB, Stone GW (2010) Analysis of the long-term effects of drug-eluting stents on coronary arterial wall morphology as assessed by virtual histology intravascular ultrasound. *Am Heart J* 159(2):271–277. doi:10.1016/j.ahj.2009.11.008
- Kim SW, Mintz GS, Hong YJ, Pakala R, Park KS, Pichard AD, Satler LF, Kent KM, Suddath WO, Waksman R, Weissman NJ (2008) The virtual histology intravascular ultrasound appearance of newly placed drug-eluting stents. *Am J Cardiol* 102(9):1182–1186. doi:10.1016/j.amjcard.2008.03.054
- Serruys PW, Ormiston JA, Onuma Y, Regar E, Gonzalo N, Garcia-Garcia HM, Nieman K, Bruining N, Dorange C, Miquel-Hebert K, Veldhof S, Webster M, Thuesen L, Dudek D (2009) A bioabsorbable everolimus-eluting coronary stent system (ABSORB): 2-year outcomes and results from multiple imaging methods. *Lancet* 373(9667):897–910. doi:10.1016/S0140-6736(09)60325-1
- Sarno G, Onuma Y, Garcia-Garcia HM, Garg S, Regar E, Thuesen L, Dudek D, Veldhof S, Dorange C, Ormiston JA, Serruys PW (2010) IVUS radiofrequency analysis in the evaluation of the polymeric struts of the bioabsorbable everolimus-eluting device during the bioabsorption process. *Catheter Cardiovasc Interv* 75(6):914–918. doi:10.1002/ccd.22332
- Garcia-Garcia HM, Gonzalo N, Pawar R, Kukreja N, Dudek D, Thuesen L, Ormiston JA, Regar E, Serruys PW (2009) Assessment of the absorption process following bioabsorbable everolimus-eluting stent implantation: temporal changes in strain values and tissue composition using intravascular ultrasound radiofrequency data analysis. A substudy of the ABSORB clinical trial. *EuroIntervention* 4(4):443–448
- Brugaletta S, Garcia-Garcia HM, Diletti R, Gomez-Lara J, Garg S, Onuma Y, Shin ES, Van Geuns RJ, De Bruyne B, Dudek D, Thuesen L, Chevalier B, McClean D, Windecker S, Whitbourn R, Dorange C, Veldhof S, Rapoza R, Sudhir K, Bruining N, Ormiston J, Serruys P (2011) Comparison between the first and second generation bioresorbable vascular scaffolds: a six month virtual histology study. *Eurointervention* 6(9):1110–1116
- Brugaletta S, Garcia-Garcia HM, Garg S, Gomez-Lara J, Diletti R, Onuma Y, van Geuns RJ, McClean D, Dudek D, Thuesen L, Chevalier B, Windecker S, Whitbourn R, Dorange C, Miquel-Hebert K, Sudhir K, Ormiston JA, Serruys PW (2011) Temporal changes of coronary artery plaque located behind the struts of the everolimus eluting bioresorbable vascular scaffold. *Int J Cardiovasc Imaging* 27(6):859–866. doi:10.1007/s10554-010-9724-y
- Serruys PW, Onuma Y, Dudek D, Smits PC, Koolen J, Chevalier B, De Bruyne B, Thuesen L, McClean D, van Geuns RJ, Windecker S, Whitbourn R, Meredith C, Dorange C, Veldhof S, Miquel-Hebert K, Sudhir K, Garcia-Garcia HM, Ormiston JA (2011) Evaluation of the second generation of a bioresorbable everolimus-eluting vascular scaffold for the treatment of de novo coronary artery stenosis: 12-month clinical and imaging outcomes. *J Am Coll Cardiol* 58(15):1578–1588
- Ormiston JA, Serruys PW, Regar E, Dudek D, Thuesen L, Webster MW, Onuma Y, Garcia-Garcia HM, McGreevy R, Veldhof S (2008) A bioabsorbable everolimus-eluting coronary stent system for patients with single de novo coronary artery lesions (ABSORB): a prospective open-label trial. *Lancet* 371(9616):899–907. doi:10.1016/S0140-6736(08)60415-8
- Hausmann D, Lundkvist AJ, Friedrich GJ, Mullen WL, Fitzgerald PJ, Yock PG (1994) Intracoronary ultrasound imaging: intraobserver and interobserver variability of morphometric measurements. *Am Heart J* 128(4):674–680
- Nair A, Kuban BD, Tuzcu EM, Schoenhagen P, Nissen SE, Vince DG (2002) Coronary plaque classification with intravascular ultrasound radiofrequency data analysis. *Circulation* 106(17):2200–2206
- Garcia-Garcia HM, Mintz GS, Lerman A, Vince DG, Margolis MP, van Es GA, Morel MA, Nair A, Virmani R, Burke AP, Stone GW, Serruys PW (2009) Tissue characterisation using intravascular radiofrequency data analysis: recommendations for acquisition, analysis, interpretation and reporting. *EuroIntervention* 5(2):177–189
- Gomez-Lara J, Brugaletta S, Diletti R, Garg S, Onuma Y, Gogas BD, van Geuns RJ, Dorange C, Veldhof S, Rapoza R, Whitbourn R, Windecker S, Garcia-Garcia HM, Regar E, Serruys PW (2011) A comparative assessment by optical coherence tomography of the performance of the first and second generation of the everolimus-eluting bioresorbable vascular scaffolds. *Eur Heart J* 32(3):294–304. doi:10.1093/eurheartj/ehq458
- Serruys PW, Onuma Y, Ormiston JA, de Bruyne B, Regar E, Dudek D, Thuesen L, Smits PC, Chevalier B, McClean D, Koolen J, Windecker S, Whitbourn R, Meredith I, Dorange C, Veldhof S, Miquel-Hebert K, Rapoza R, Garcia-Garcia HM (2010) Evaluation of the second generation of a bioresorbable everolimus drug-eluting vascular scaffold for treatment of de novo coronary artery stenosis: six-month clinical and imaging outcomes. *Circulation* 122(22):2301–2312. doi:10.1161/CIRCULATIONAHA.110.970772

19. Verheye S, Martinet W, Kockx MM, Knaapen MW, Salu K, Timmermans JP, Ellis JT, Kilpatrick DL, De Meyer GR (2007) Selective clearance of macrophages in atherosclerotic plaques by autophagy. *J Am Coll Cardiol* 49(6): 706–715. doi:10.1016/j.jacc.2006.09.047
20. Martinet W, Verheye S, De Meyer GR (2007) Everolimus-induced mTOR inhibition selectively depletes macrophages in atherosclerotic plaques by autophagy. *Autophagy* 3(3): 241–244
21. Boyle JJ (2005) Macrophage activation in atherosclerosis: pathogenesis and pharmacology of plaque rupture. *Curr Vasc Pharmacol* 3(1):63–68
22. Onuma Y, Serruys PW, Perkins LE, Okamura T, Gonzalo N, Garcia-Garcia HM, Regar E, Kamberi M, Powers JC, Rapoza R, van Beusekom H, van der Giessen W, Virmani R (2010) Intracoronary optical coherence tomography and histology at 1 month and 2, 3, and 4 years after implantation of everolimus-eluting bioresorbable vascular scaffolds in a porcine coronary artery model: an attempt to decipher the human optical coherence tomography images in the ABSORB trial. *Circulation* 122(22):2288–2300. doi: 10.1161/CIRCULATIONAHA.109.921528
23. Hong MK, Park DW, Lee CW, Lee SW, Kim YH, Kang DH, Song JK, Kim JJ, Park SW, Park SJ (2009) Effects of statin treatments on coronary plaques assessed by volumetric virtual histology intravascular ultrasound analysis. *JACC Cardiovasc Interv* 2(7):679–688. doi:10.1016/j.jcin.2009.03.015

8.3

Endothelial-dependent vasomotion in a coronary segment treated by ABSORB everolimus-eluting bioresorbable vascular scaffold system is related to plaque composition at the time of bioresorption of the polymer: indirect finding of vascular reparative therapy?

Salvatore Brugaletta, Jung Ho Heo, Hector M Garcia-Garcia, Vasim Farooq, Robert Jan van Geuns, Bernard de Bruyne, Dariusz Dudek, Pieter C Smits, Jacques Koolen, Dougal McClean, Cecile Dorante, Susan Veldhof, Richard Rapoza, Yoshinobu Onuma, Nico Bruining, John A Ormiston, Patrick W Serruys

Eur Heart J 2012, Epub ahead of print

Endothelial-dependent vasomotion in a coronary segment treated by ABSORB everolimus-eluting bioresorbable vascular scaffold system is related to plaque composition at the time of bioresorption of the polymer: indirect finding of vascular reparative therapy?

Salvatore Brugaletta^{1,2†}, Jung Ho Heo^{1†}, Hector M. Garcia-Garcia^{1,3}, Vasim Farooq¹, Robert Jan van Geuns¹, Bernard de Bruyne⁴, Dariusz Dudek⁵, Pieter C. Smits⁶, Jacques Koolen⁷, Dougal McClean⁸, Cecile Dorange⁹, Susan Veldhof⁹, Richard Rapoza¹⁰, Yoshinobu Onuma¹, Nico Bruining¹, John A. Ormiston¹¹, and Patrick W. Serruys^{1*}

¹Interventional Cardiology Department, Thoraxcenter, Erasmus MC, 's Gravendijkwal 230, 3015 CE Rotterdam, The Netherlands; ²Department of Cardiology, Thorax Institute, Hospital Clinic, University of Barcelona, Barcelona, Spain; ³Cardialysis B.V., Rotterdam, The Netherlands; ⁴Cardiovascular Center Aalst, Aalst, Belgium; ⁵Jagiellonian University, Krakow, Poland; ⁶Maastad Hospital, Rotterdam, The Netherlands; ⁷Catharina Hospital, Eindhoven, The Netherlands; ⁸Christchurch Hospital, Christchurch, New Zealand; ⁹Abbott Vascular, Diegem, Belgium; ¹⁰Abbott Vascular, Santa Clara, CA, USA; and ¹¹Auckland City Hospital, Auckland, New Zealand

Received 17 August 2011; revised 19 November 2011; accepted 29 November 2011

Aims	To analyse the vasoreactivity of a coronary segment, previously scaffolded by the ABSORB bioresorbable vascular scaffold (BVS) device, in relationship to its intravascular ultrasound–virtual histology (IVUS–VH) composition and reduction in greyscale echogenicity of the struts. Coronary segments, transiently scaffolded by a polymeric device, may in the long-term recover a normal vasomotor tone. Recovery of a normal endothelial-dependent vasomotion may be enabled by scaffold bioresorption, composition of the underlying tissue, or a combination of both mechanisms.
Methods and results	All patients from the ABSORB Cohort A and B trials, who underwent a vasomotion test and IVUS–VH investigation at 12 and 24 months, were included. Acetylcholine (ACh) and nitroglycerin were used to test either the endothelial-dependent or -independent vasomotion of the treated segment. Changes in polymeric strut echogenicity—a surrogate for bioresorption—IVUS–VH composition of the tissue underneath the scaffold and their relationship with the pharmacologically induced vasomotion were all evaluated. Overall, 26 patients underwent the vasomotion test (18 at 12 and 8 at 24 months). Vasodilatory response to ACh was quantitatively associated with larger reductions over time in polymeric strut echogenicity ($y = -0.159x - 6.85$; $r = -0.781$, $P < 0.001$). Scaffolded segments with vasoconstriction to ACh had larger vessel areas (14.37 ± 2.50 vs. 11.85 ± 2.54 mm ² , $P = 0.030$), larger plaque burden (57.31 ± 5.96 vs. $49.09 \pm 9.10\%$, $P = 0.018$), and larger necrotic core (NC) areas [1.39 (+1.14, +1.74) vs. 0.78 mm ² (+0.20, +0.98), $P = 0.006$] compared with those with vasodilation.
Conclusion	Vasodilatory response to ACh, in coronary segments scaffolded by the ABSORB BVS device, is associated with a reduction in echogenicity of the scaffold over time, and a low amount of NC. In particular, the latter finding resembles the behaviour of a native coronary artery not caged by an intracoronary device.
Keywords	VH • ABSORB BVS • Echogenicity • Vasomotion

[†]These authors equally contributed to this work.

* Corresponding author. Tel: +31 10 4635260. Fax: +31 10 4369154. Email: p.w.j.c.serruys@erasmusmc.nl

Published on behalf of the European Society of Cardiology. All rights reserved. © The Author 2012. For permissions please email: journals.permissions@oup.com

Introduction

The ABSORB bioresorbable vascular scaffold (BVS; Abbott Vascular, Santa Clara, CA, USA) has been introduced in clinical trials with the aim to provide temporary vessel scaffolding and to be subsequently bioresorbed, thereby allowing the artery to respond to the shear stress and to have pharmacologically induced vasomotion, akin to a non-treated coronary segment.^{1,2} This entire process, making the coronary segment transiently scaffolded fully amenable to biological, pharmacological, and physiological stimuli, has recently been termed 'vascular reparative therapy'.³

Vasomotor testing, using nitroglycerin (NTG) and acetylcholine (ACh) as endothelial-independent or -dependent vasoactive drugs, were performed in the ABSORB trials at various time points. Clear signs of vasomotion in the scaffolded segment were demonstrated at 12 and 24 months in ABSORB Cohort B and ABSORB Cohort A trials, respectively, suggesting that the mechanical integrity and radial forces of the scaffold had substantially subsided at these time points.^{2,4} In addition, changes in the echogenicity of the polymeric struts appeared to be correlated to the recovery of vaso-reactivity in a small pilot study.⁵ Conversely, response to ACh demonstrated vasodilation in only half of the patients, suggesting that full coverage by endothelial cells and complete return of functional capacity of these cells are not achieved in the majority of the cases, and other factors should be considered to explain the vasomotor tone dysfunction.^{2,4}

In non-stented diseased coronary segments, Lavi *et al.*⁶ have previously demonstrated that local coronary endothelial dysfunction may be related to distinctive atherosclerotic characteristics, namely plaque burden and the presence of necrotic core (NC) or dense calcium, evaluated by intravascular ultrasound—virtual histology (IVUS—VH).

We sought to analyse: (i) the changes in the echogenicity of polymeric struts, a surrogate of bioresorption, and its relationship with the vasoreactivity in the scaffolded segment, and (ii) the IVUS—VH composition of the coronary segment scaffolded by an ABSORB BVS device at the time of the vasomotion test.

Methods

Study population

The ABSORB trial includes the ABSORB Cohort A and Cohort B trials. Briefly, in the ABSORB Cohort A trial (NCT00300131), 30 patients with a diagnosis of stable or unstable angina or silent ischaemia, were enrolled. All treated lesions were single and *de novo* in a native coronary artery of 3.0 mm diameter, shorter than 8 mm for the 12 mm scaffold and shorter than 14 mm for the 18 mm scaffold, with a diameter stenosis >50 and <100%, and with a thrombolysis in myocardial infarction (TIMI) flow grade more than 1. Major exclusion criteria were patients presenting with an acute myocardial infarction, unstable arrhythmias, or patients who had a left ventricular ejection fraction <30%, restenotic lesions, lesions located in the left main coronary artery, lesions involving an epicardial side branch ≥ 2 mm in diameter by visual assessment, and the presence of thrombus or another clinically significant stenosis in the target vessel. All lesions were treated by implantation of an ABSORB first-generation

scaffold (revision 1.0) (3.0 \times 12 mm and two lesions by 3.0 \times 18 mm) and invasively imaged at 6- and 24-month follow-up. The ABSORB Cohort B trial (NCT00856856) enrolled 101 patients with the same clinical profile and lesion type, divided into two groups according to the timeline of invasive follow-up: Cohort B1 with invasive imaging at 6 and 24 months; Cohort B2 with the same invasive imaging at 12 and 36 months. The 12-month follow-up has so far been performed. All lesions were treated by implantation of an ABSORB second-generation scaffold (revision 1.1) (3.0 \times 18 mm).⁷ The Ethics Committee at each participating institution approved the protocol and each patient gave written informed consent before inclusion.

As an optional investigation, vasomotion testing with ACh and NTG—according to local practice—was performed at 24-month follow-up in the ABSORB Cohort A trial and at 6- or 12-month follow-up in ABSORB Cohort B trial. As the integrity of the scaffold has been shown to be still present at 6-month follow-up, the present analysis only included patients with a 12- and 24-month follow-up.^{4,7}

Study device

The ABSORB BVS device consists of a polymer backbone of poly-L-lactide coated with a thin layer of a 1:1 mixture of poly-D,L-lactide polymer, and the anti-proliferative drug everolimus to form an amorphous drug-eluting coating matrix containing 100 μ g of everolimus/cm² of scaffold. The details of the device have been described previously.^{8–10} In brief, the ABSORB BVS revision 1.1 has a smaller maximum circular unsupported surface area compared with revision 1.0, with the struts arranged as in-phase zigzag hoops linked together by three longitudinal links, similar to the XIENCE V design.⁹

Study procedure and intravascular ultrasound acquisition/analysis

Target lesions were treated using standard interventional techniques, with mandatory pre-dilatation. Post-dilatation with a balloon shorter than the implanted scaffold was allowed at the operator's discretion, up to the prescribed maximal post-dilatation diameter.

The IVUS was performed using the Eagle Eye 20 MHz catheter (Volcano Corp., Rancho Cordova, CA, USA) with an automatic continuous pullback at a rate of 0.5 mm/s (30 frames/s) at the level of the scaffolded segment after ABSORB BVS implantation and at follow-up. Greyscale images and radiofrequency data, required for VH analysis, were acquired during the same pullback and raw radiofrequency data capture gated to the R-wave (In-Vision Gold, Volcano).

Quantitative IVUS measurements were performed within the scaffolded segment and 5 mm distal to the device, including vessel area, lumen area, plaque area (vessel area – minus lumen area), and plaque burden [(plaque area/vessel area) \times 100]. For the radiofrequency IVUS analyses, four tissue components [NC—red; dense calcium (DC)—white; fibrous (FT)—dark green; and fibrofatty (FF)—light green] were identified with autoregressive classification systems. All individual tissue components were quantified as area and percentage (per cross-section, NC + DC + FF + FF = 100%).^{2,11}

Echogenicity analysis

It has been previously shown that during *in vivo* ABSORB BVS degradation, a diminishing grey-level intensity of the struts over time can be detected by IVUS.^{2,12,13} A dedicated computer-aided greyscale value analysis program was used to assess the echogenicity of the polymeric struts after implantation and at the various follow-up time points.^{12,14} The applied algorithms of this software have been previously published

and validated.¹⁴ Briefly, the mean grey value of the adventitia is used to classify tissue components as either hypo-echogenic (e.g. grey values lower than the mean adventitia level) or as hyper-echogenic (e.g. grey values at higher levels than those of the adventitia). The polymeric struts of the ABSORB BVS are usually identified as hyper-echogenic tissue.¹² The difference between the follow-up and the post-procedural hyper-echogenicity was assessed in the treated segment and calculated as the following:

$$\frac{\% \text{hyper-echogenicity follow-up} - \% \text{hyper-echogenicity post-ABSORB implantation}}{\% \text{hyper-echogenicity post-ABSORB implantation}} \times 100$$

Quantitative coronary angiography and vasomotion test

β -Blockers, calcium channel blockers, and nitrates were withheld at least 48 h before the coronary angiogram. Quantitative coronary angiography (QCA) was performed with the CASS II analysis system (Pie Medical BV, Maastricht, The Netherlands) by an independent CoreLab (Cardialysis, Rotterdam BV, The Netherlands). The accuracy of this method has previously been reported in detail.¹⁵ The scaffolded segment was defined as the segment between the two radio-opaque platinum markers at both ends of the ABSORB BVS. The 5 mm edges distal to the device were also analysed.

The mean lumen diameter in the scaffolded and distal segments was measured by QCA after a baseline infusion of saline and subselective intracoronary administration of Ach, infused through a microcatheter at increasing doses up to a maximum of 10^{-6} M. In particular, a 2 min selective infusion of Ach (10^{-8} , 10^{-7} , and 10^{-6} mol/L) was administered with a washout period of at least 5 min between each dose.⁷ Nitrate (200 μ g) was administered following Ach. Vasoconstriction to Ach was defined as a 3% change of the mean lumen diameter, beyond the variability of the method of analysis, after infusion of the maximal dose of Ach (10^{-6} M), as previously shown.^{2,4,16}

Statistical analysis

The distribution normality of the variables was tested using the Kolmogorov–Smirnov test. Continuous variables are expressed as mean \pm standard deviation or median and inter-quartile range, according to their normal or not normal distribution. Dichotomous variables are reported as numbers and percentages. A comparison between categorical variables was performed by χ^2 or the Fisher tests, as appropriate. A comparison between groups was done by means of non-parametric tests for paired (Wilcoxon's signed-rank test) and not paired data (the Mann–Whitney test), as appropriate. A correlation between variables was performed by the Spearman test. A two-tailed value of $P < 0.05$ was considered statistically significant. Statistical analyses were performed with SPSS 17.0 software (SPSS Inc., Chicago, IL, USA).

Results

Patient population

A total of 26 patients with paired greyscale IVUS, VH, and vasomotion analyses were included (18 at 12- and 8 at 24-month follow-up). Table 1 shows their baseline and angiographic characteristics.

Acetylcholine and nitroglycerin test at the scaffold level

Overall, the change in the mean lumen diameter after Ach administration was -1.44% (-7.35 , $+2.56$; $P = 0.303$; Table 2). Patients

at 24 months exhibited a significant increase in the mean lumen diameter after Ach administration compared with patients at 12 months [$+2.14$ (-2.58 , $+8.80$) vs. -5.46% (-8.25 , $+1.86$); $P = 0.038$]. In particular, 11 patients (42.3%) exhibited a vasodilatory response to Ach (6/18 at 12 and 5/8 at 24 months; $P = 0.390$), whereas 14 patients (54.2%) had an abnormal response to Ach with vasoconstriction, with only 1 patient not exhibiting any changes in the mean lumen diameter.

Overall, the change in the mean lumen diameter after NTG administration compared with baseline was $+0.41\%$ (-3.77 , $+5.52$; $P = 0.494$). Patients at 24 months demonstrated a higher increase in the mean lumen diameter to nitrates compared with the 12-month group [$+5.79$ ($+1.41$, $+12.0$) vs. -0.60% (-5.46 , $+3.91$); $P = 0.032$]. The response to nitrates tended to be greater in patients with a normal response to Ach compared with those without [$+4.37$ (-1.77 , $+9.15$) vs. -0.39% (-5.58 , $+3.45$); $P = 0.093$].

Reduction in hyper-echogenicity in the scaffolded segment was larger at 24 than at 12 months [-66.76 (-91.15 , -50.45) vs. -18.73% (-30.56 , -0.74); $P < 0.001$]. Scaffolded segments with a vasodilatory response to Ach demonstrated a greater reduction in hyper-echogenicity, compared with those with a vasoconstrictive response to Ach [-54.75 (-78.95 , -41.51) vs. -16.34% (-30.56 , -0.74); $P = 0.009$]. A significant negative relationship between changes in the mean lumen diameter after Ach administration and in hyper-echogenicity was demonstrated ($r = -0.781$; $P < 0.001$) (Figure 1). A significant negative relationship was also found between changes in the mean lumen diameter after nitrates administration and hyper-echogenicity ($r = -0.511$; $P = 0.030$).

By greyscale IVUS and VH, scaffolded segments with a vasoconstriction response to Ach had larger mean vessel area, plaque burden, and NC content compared with those with a vasodilatory response to Ach (Table 3). A significant negative relationship was found between NC area and changes in mean lumen diameter after Ach administration ($r = -0.676$, $P = 0.001$) (Figure 2).

Response to acetylcholine and nitroglycerin at the distal edge of the scaffold

In 22 patients (14 at 12 and 8 at 24 months), both IVUS–VH analysis and an Ach test were available at the distal edge of the scaffold (Table 2).

Overall, no significant changes in the mean lumen diameter after Ach [-2.60% (-9.02 , $+4.38$); $P = 0.201$] were demonstrated. Patients at 24 months ($n = 8$) exhibited, on average, a significant increase in the mean lumen diameter after Ach administration compared with patients at 12 months [$+6.16$ (-1.07 , $+13.14$) vs. -6.41% (-11.74 , -1.17); $P = 0.006$]. Taken individually, 5 patients (22.7%) had a vasodilatory response to Ach (1/14 at 12 and 4/8 at 24 months; $P = 0.017$), whereas 14 (63.3%) exhibited a vasoconstriction response to Ach; the remaining 3 patients did not show changes in the mean lumen diameter.

After nitrate administration, a significant increase in the mean lumen diameter was found [$+9.45\%$ ($+1.01$, $+19.49$); $P = 0.006$], especially at 24-month follow-up when compared with 12 months [$+21.57$ ($+12.50$, $+27.26$) vs. $+7.91\%$ (-4.26 , $+10.50$);

Table 1 Clinical baseline characteristics

	All patients (26 patients)	12 months (18 patients)	24 months (8 patients)	P-value
Patient demographic and clinical data				
Age (years)	62.84 ± 9.08	60.66 ± 8.70	66.96 ± 8.78	0.146
Male, n (%)	16 (61.5)	11 (64.7)	5 (55.5)	0.692
Hypertension, n (%)	20 (76.9)	13 (76.5)	7 (77.8)	1.000
Hypercholesterolaemia, n (%)	19 (73.1)	13 (76.5)	6 (66.7)	0.661
Diabetes, n (%)	4 (15.4)	4 (23.5)	0 (0.0)	0.263
Current smoking, n (%)	6 (23.1)	5 (29.4)	1 (11.1)	0.380
Prior PCI, n (%)	3 (11.5)	3 (17.6)	0 (0.0)	0.529
Prior myocardial infarction, n (%)	7 (26.9)	6 (35.3)	1 (11.1)	0.357
Stable angina, n (%)	14 (53.8)	11 (64.7)	3 (33.3)	0.218
Unstable angina, n (%)	7 (26.9)	1 (5.9)	6 (66.7)	0.002
Silent ischaemia, n (%)	1 (3.8)	1 (5.9)	0 (0.0)	1.000
Lesion and angiographic characteristics				
Treated vessel, n (%)				
Left anterior descending artery	15 (57.7)	9 (52.9)	6 (66.7)	0.683
Left circumflex artery	6 (23.1)	5 (29.4)	1 (11.1)	0.380
Right coronary artery	5 (19.2)	3 (17.6)	2 (22.2)	1.000
ACC/AHA lesion type, n (%)				
Type A	0 (0)	0 (0)	0 (0)	NA
Type B1	21 (80.8)	14 (82.4)	7 (77.8)	1.000
Type B2	5 (19.2)	3 (17.6)	2 (22.2)	1.000
Type C	0 (0)	0 (0)	0 (0)	NA
QCA analysis pre-treatment				
RVD (mean ± SD, mm)	2.55 ± 0.19	2.57 ± 0.17	2.51 ± 0.22	0.335
MLD (mean ± SD, mm)	1.08 ± 0.24	1.12 ± 0.24	1.01 ± 0.23	0.307
Diameter stenosis (mean ± SD, %)	57.37 ± 9.73	56.23 ± 9.56	59.41 ± 10.25	0.349
Medical treatment, n (%)				
β-Blockers	21 (81)	15 (83)	6 (75)	0.657
ACE-inhibitors	13 (50)	9 (50)	4 (50)	1.000
Statins	25 (96)	17 (94)	8 (100)	0.833

Continuous variables are expressed as mean ± SD. Ach, acetylcholine; RVD, reference vessel diameter; MLD, minimum lumen diameter; SD, standard deviation.

Table 2 Mean lumen diameter at baseline and after acetylcholine and NTG administration in the 12- and 24-month groups

	Baseline	Ach	NTG	P-value, Ach vs. BL	P-value, NTG vs. BL
12-month group (n = 18 patients)					
Scaffold segment	2.50 ± 0.23	2.40 ± 0.23	2.47 ± 0.21	0.074	0.478
Distal segment	2.23 ± 0.26	2.03 ± 0.46	2.34 ± 0.30	0.011	0.148
24-month group (n = 8 patients)					
Scaffold segment	1.82 ± 0.35	1.89 ± 0.42	1.96 ± 0.41	0.262	0.035
Distal segment	1.76 ± 0.12	1.86 ± 0.20	2.12 ± 0.24	0.260	0.017

Data are presented as mean ± SD. SD, standard deviation; Ach, acetylcholine; NTG, nitroglycerin; BL, baseline.

$P = 0.009$]. The response to nitrates was greater in the presence of a normal response to Ach than in its absence [+12.99 (+12.85, +13.29) vs. -7.78% (-13.43, -3.90); $P < 0.001$].

By greyscale IVUS and VH, edge segments with a vasoconstrictive response to Ach had larger plaque burden, DC, FT, and NC area compared with those with a vasodilatory response to Ach

(Table 4). A significant negative relationship was found between NC area and changes in the mean lumen diameter after Ach administration ($r = -0.552$, $P = 0.011$).

Discussion

The major findings of the present study are: (i) the ability of a coronary segment scaffolded by an ABSORB BVS device to react

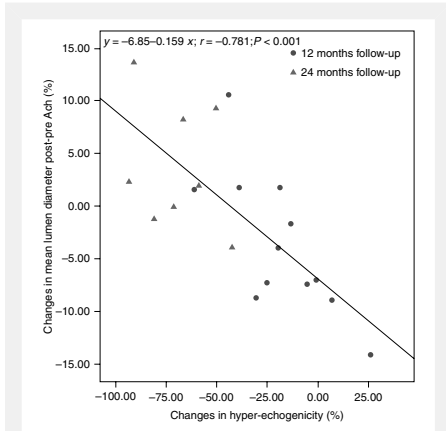


Figure 1 Correlation at the scaffolded segment between changes in hyper-echogenicity between post-implantation and follow-up and changes in the mean lumen diameter after administration of Ach.

to vasoactive drugs is related to the bioresorption of the polymeric struts, as indirectly evaluated by changes in their echogenicity; (ii) the presence of endothelial dysfunction in this segment is correlated to plaque burden and VH-NC, resembling the behaviour of a native diseased coronary vessel; moreover, recovery of a normal endothelial function was associated with a low plaque burden and VH-NC. (iii) The vasoactivity behaviour of the distal edge of the scaffold does not differ substantially from the physiological reaction observed in the scaffolded segment.

These findings suggest the return of a normal physiological reactivity to vasoactive drugs in the treated coronary segments—with a relative absence of NC—once the mechanical integrity of the device has disappeared.

Progressive return of vasoactivity as a function of polymeric bioresorption

Over the past 15 years, much attention has been focused on endothelial dysfunction in the segment distal to the implanted metallic drug-eluting stent (DES). Subsequently with the introduction of bioresorbable scaffolds, the interest about reactivity to vasoactive drugs has moved to the segment where the device was implanted. As the mechanical integrity of the ABSORB BVS is aimed *a priori* to disappear within 2 years, the scaffold's resistance to vasomotion induced by vasoactive drugs decreases over time, thereby allowing for the potential recovery of normal vasomotor tone. This is in contrast to a vascular structure permanently caged by a metallic prosthesis.²

The ABSORB Cohort A trial was the first study demonstrating some degree of return of vasoactivity in a coronary segment scaffolded by a polylactide device, after administration of Ach, methylergonovine, and nitrates at 2-year follow-up.² Recently, the ABSORB Cohort B trial demonstrated that the scaffolded segments react by vasomotion to Ach and methylergonovine as early at 12 months, due to the partial subsidence of the radial force of

Table 3 Intravascular ultrasound and virtual histology findings at follow-up in the scaffolded segment, according to the presence of vasoconstriction or vasodilation response to Ach. (12 and 24 months pooled)

	Scaffold vasoconstriction (n = 14)	Scaffold vasodilation (n = 11)	P-value
Mean vessel area (mm ²)	14.37 ± 2.50	11.85 ± 2.54	0.030
Mean lumen area (mm ²)	6.04 ± 0.71	5.89 ± 1.08	0.766
Mean plaque area (mm ²)	8.33 ± 2.07	5.96 ± 1.99	0.006
Mean plaque burden (%)	57.31 ± 5.96	49.09 ± 9.10	0.018
Dense calcium area (mm ²)	1.26 (0.98–1.48)	0.65 (0.20–1.31)	0.055
Dense calcium (%)	25.35 (17.47–34.88)	23.19 (16.46–27.85)	0.820
Fibrous tissue area (mm ²)	1.91 (1.02–2.99)	1.17 (0.43–1.90)	0.119
Fibrous tissue (%)	36.79 (32.78–46.92)	46.86 (36.31–52.22)	0.207
Fibrofatty tissue area (mm ²)	0.19 (0.09–0.29)	0.08 (0.03–0.15)	0.134
Fibrofatty tissue (%)	4.16 (2.97–6.02)	3.99 (2.70–5.05)	0.865
Necrotic core area (mm ²)	1.39 (1.14–1.74)	0.78 (0.20–0.98)	0.006
Necrotic core (%)	28.00 (24.32–31.63)	24.31 (23.18–26.61)	0.047

Data are expressed as mean ± SD or median (IQR), as appropriate. SD, standard deviation; IQR, interquartile range. One patient did not exhibit any changes in the mean lumen diameter after Ach administration and was excluded from the table.

the scaffolded vessel.⁴ Conversely, at 6 months, the scaffold is still able to counteract the pharmacologically induced vasoconstrictive effect of methylethergonovine⁴ (Figure 3). The differences in the degradation behaviour between the two revisions of the ABSORB device may be an explanation for the differing degree of vasomotion recovery.^{7,17}

Previous reports have described that degradation of the scaffold can be monitored *in vivo* by a reduction in hyper-echogenicity

tissue over time.^{4,12,13} It is also known from animal data that the scaffold polymer has a mass loss of 70 and 90% at 12 and 18 months, respectively, and becomes undetectable at 24 months.¹⁰ In the present analysis, a greater reduction in hyper-echogenicity of the scaffolded segment was associated with a normal vasodilatory response to Ach. These findings may support a link between the grade of scaffold degradation and the restoration of a normal vascular reactivity in the treated segment.

Influence of virtual histology composition of the underlying tissue on the vasoreactivity of the scaffolded coronary segment

In an untreated coronary artery segment, vasoconstriction to Ach has previously shown to be correlated to specific features of vulnerable plaque, in particular high content of DC and NC.⁶ These findings were in part confirmed in the present analysis at the level of the distal edge, where the presence of a vasoconstrictive response to Ach was related to high plaque burden, DC, and NC area. However, whereas the relative content (%) of DC was not different between the two groups, the relative content of NC tended to be higher in the edges with vasoconstriction to Ach ($P = 0.095$); the small number of patients or the short length of the segments analysed could explain the lack of statistical significance.^{6,16}

It was of note that in the scaffolded segment, the ability to recover a vasodilatory response to Ach appeared to be dependent on the plaque burden and NC content (Figure 4). The present study further supports the fact that NC, a proven site of active inflammation and oxidative stress, may constitute a pathophysiological link between plaque composition and endothelial dysfunction.^{18,19} Acetylcholine normally lowers the capillary resistance, thereby increasing flow and shear stress with stimulation of

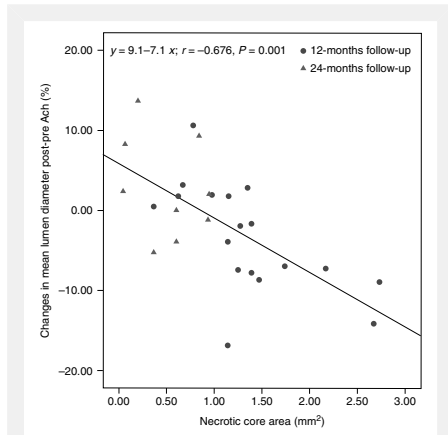


Figure 2 Correlation at the scaffold segment between necrotic core area and changes in the mean lumen diameter after administration of acetylcholine.

Table 4 Intravascular ultrasound and virtual histology findings at follow-up at the distal edge of the scaffold, according to the presence of vasoconstriction or vasodilation response to Ach (12 and 24 months pooled)

	Vasoconstriction of the distal edge (n = 14)	Vasodilation of the distal edge (n = 5)	P-value
Mean vessel area (mm ²)	12.58 ± 3.28	9.59 ± 1.76	0.173
Mean lumen area (mm ²)	6.81 ± 1.35	6.68 ± 1.34	0.924
Mean plaque area (mm ²)	5.76 ± 2.46	2.91 ± 0.51	0.004
Mean plaque burden (%)	44.51 ± 9.17	30.50 ± 2.58	0.001
Dense calcium area (mm ²)	0.23 (0.12–0.36)	0.01 (0.00–0.04)	<0.001
Dense calcium (%)	10.61 (6.88–27.51)	4.55 (0.00–22.71)	0.208
Fibrous tissue area (mm ²)	1.03 (0.43–2.62)	0.00 (0.00–0.20)	0.002
Fibrous tissue (%)	57.82 (44.36–61.51)	0.00 (0.00–56.38)	0.026
Fibrofatty tissue area (mm ²)	0.21 (0.03–0.43)	0.00 (0.00–0.03)	0.003
Fibrofatty tissue (%)	7.98 (4.15–14.65)	0.00 (0.00–8.35)	0.019
Necrotic core area (mm ²)	0.30 (0.18–0.64)	0.01 (0.00–0.05)	<0.001
Necrotic core (%)	18.81 (13.60–24.32)	6.28 (0.00–13.10)	0.095

Data are expressed as mean ± SD or median (IQR), as appropriate. SD, standard deviation; IQR, interquartile range. Three patients did not exhibit any changes in the mean lumen diameter after Ach administration and were excluded from the table.

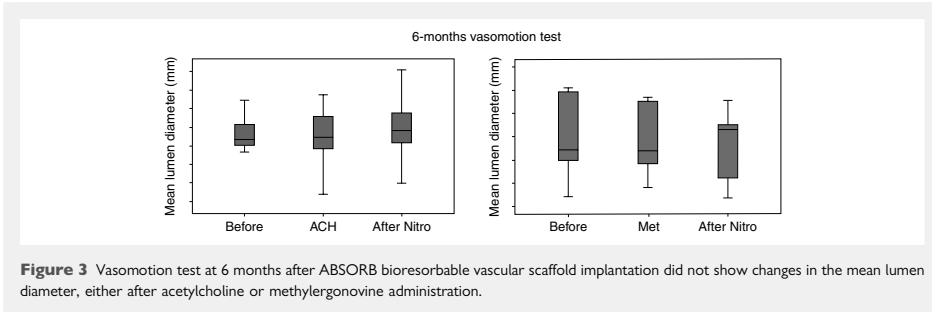


Figure 3 Vasomotion test at 6 months after ABSORB bioresorbable vascular scaffold implantation did not show changes in the mean lumen diameter, either after acetylcholine or methylergonovine administration.

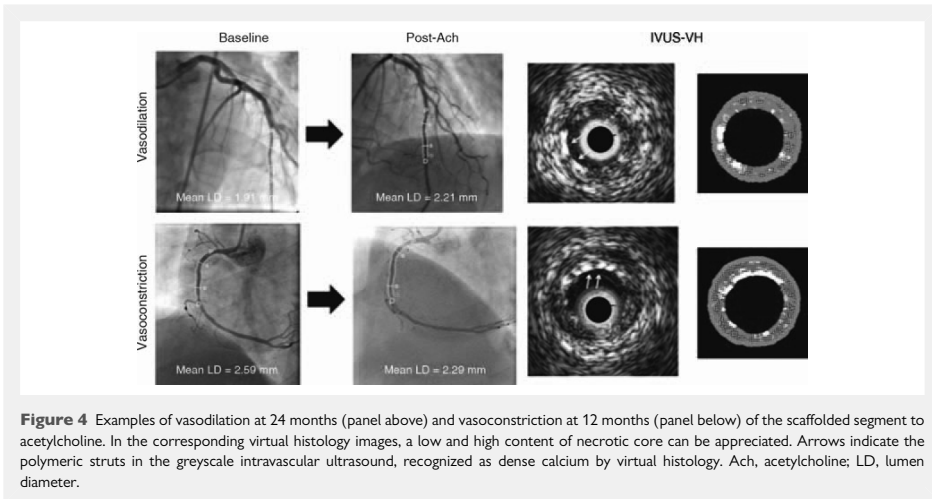


Figure 4 Examples of vasodilation at 24 months (panel above) and vasoconstriction at 12 months (panel below) of the scaffolded segment to acetylcholine. In the corresponding virtual histology images, a low and high content of necrotic core can be appreciated. Arrows indicate the polymeric struts in the greyscale intravascular ultrasound, recognized as dense calcium by virtual histology. Ach, acetylcholine; LD, lumen diameter.

endothelial receptors and eventual release of nitric oxide through endothelial nitric oxide synthesis activation. For this reason, the anatomical and functional integrity of coalescent endothelial cells is a *conditio sine qua non* for a vasodilatory reaction to Ach.

It is also important to highlight the analogy in response to Ach in relation to VH plaque composition between a coronary segment scaffolded by a bioresorbable device and previous findings in a native diseased coronary segment.⁶ The fact that they both exhibited the same dependence of the Ach response, to the presence of NC, may support the concept of recuperation of a normal reaction to shear stress and vasoactive drugs, in a coronary vessel, initially treated with a bioresorbable scaffold, once the scaffold is bioresorbed.

Previously, in a small series of patients investigated pre, post, 6, and 24 months after scaffold implantation (ABSORB Cohort A), it was demonstrated that the scaffold bioresorption process did not

globally affect the VH-NC content of the vessel wall.^{2,20} Everolimus has been shown to have some anti-inflammatory effects that can lead, in the long-term, to the VH-NC reduction in the plaque behind the polymeric scaffold.²¹

The vasoconstrictive reaction to Ach has to be therefore related to the pre-existing level of NC prior to the treatment with the scaffold. Further and novel strategies to halt or regress the NC need to be considered, in conjunction with the focal treatment with this transient scaffold. In particular, darapladib and lipid-lowering therapy, such as statins, have previously been shown to be promising drugs to reduce the NC content.^{22,23}

Eventually, it should be mentioned that two different versions of the ABSORB device have been therein analysed. Although both are made with the same polylactide material, a potentially different impact on coronary endothelium cannot be excluded.

Vasoreactivity of the coronary segments adjacent to a polymeric device

The coronary segment distal to a first-generation DES classically exhibits a paradoxical response to Ach, especially when compared with bare metal stent.^{16,24,25} The introduction of the second-generation DES has been shown to reduce this endothelial dysfunction. The present analysis investigating a new generation of the BVS device, made of polylactide that completely bioabsorbed in ~2 years, demonstrated that on average, the segment distal to the implanted scaffold did not have a significant vasoconstriction response to Ach administration. Four out of the eight cases tested at 24 months exhibited an intense endothelium-dependent vasodilatory response to Ach, while the majority of the cases tested at 12 months (12/14) had vasoconstriction.

It is widely known that the drug eluted during the first months after device implantation tends to reach the vessel wall distal to the device by elution, diffusion through the tissue, and the vasa vasorum.¹⁶ Clinical data support the hypothesis of drug impregnation distally but not proximally to the device, contributing to a lower restenosis rate at the distal compared with the proximal edge.²⁶ The present results may therefore be in favour of a more 'endothelium friendly impact' of the drug-eluting bioresorbable scaffold in minimizing the local device- and drug-specific response, affecting the endothelium-dependent vasomotion of the coronary segment distal to the device.²⁷ In particular, not only the presence of a non-metallic cage, but also the elution of everolimus should be considered as hypotheses to explain the present data. While sirolimus was suggested to have a direct detrimental effect on the endothelium and/or signalling pathway,^{16,28} everolimus was shown to cause a marked clearance of macrophages, by autophagy induced by mTOR inhibition, but without altering the endothelial or smooth muscle cell viability.^{29,30}

Limitations

The major limitation of the present analysis is the small number of patients. Nevertheless, this cohort of patients represents the largest series of patients receiving an ABSORB device studied by IVUS-VH and vasoreactivity testing. The second limitation is that the VH composition of the scaffolded plaque may be influenced by the presence of the scaffold; however, analysis of the plaque underlying the scaffold requires acquisition by a specific VH console, further limiting the number of the patients.²¹ Our analysis lacks of a control group, although the relationship between vasomotor response to Ach and VH composition of plaque in segments without scaffold has been reported previously.⁶

Conclusions

The present study demonstrated that endothelial dysfunction in a coronary segment scaffolded by an ABSORB BVS device is correlated to plaque burden and NC, resembling the behaviour of a native non-stented coronary segment. Reduction in hyper-echogenicity in the scaffolded segment over time appears to be also correlated to the recovery of normal vasoreactivity. The vasoreactive behaviour of the distal edge of the scaffold does not substantially differ from the physiological reaction observed in the

scaffolded segment. The clinical and prognostic implications of the present findings remain to be determined.

Conflict of interest: C.D., S.V., and R.R. are employees of Abbott Vascular. The ABSORB Trials are sponsored and funded by Abbott Vascular, Santa Clara, CA, USA.

References

- Ormiston JA, Serruys PW, Regar E, Dudek D, Thuesen L, Webster MW, Onuma Y, Garcia-Garcia HM, McGreevy R, Veldhof S. A bioabsorbable everolimus-eluting coronary stent system for patients with single de-novo coronary artery lesions (ABSORB): a prospective open-label trial. *Lancet* 2008;**371**: 899–907.
- Serruys PW, Ormiston JA, Onuma Y, Regar E, Gonzalo N, Garcia-Garcia HM, Nieman K, Bruining N, Dorange C, Miquel-Hebert K, Veldhof S, Webster M, Thuesen L, Dudek D. A bioabsorbable everolimus-eluting coronary stent system (ABSORB): 2-year outcomes and results from multiple imaging methods. *Lancet* 2009;**373**:897–910.
- Khattab A, Windecker S. Vascular restoration therapy: what should the clinical and angiographic measures for success be? *EuroIntervention* 2009;**5**(Suppl. F): F49–F57.
- Serruys PW, Onuma Y, Dudek D, Smits PC, Koolen J, Chevalier B, de Bruyne B, Thuesen L, McClean D, van Geuns RJ, Windecker S, Whitbourn R, Meredith I, Dorange C, Veldhof S, Hebert KM, Sudhir K, Garcia-Garcia HM, Ormiston JA. Evaluation of the second generation of a bioresorbable everolimus-eluting vascular scaffold for the treatment of de novo coronary artery stenosis 12-month clinical and imaging outcomes. *J Am Coll Cardiol* 2011;**58**:1578–1588.
- Sarno G, Bruining N, Onuma Y, Garg S, Brugaletta S, De Winter S, Regar E, Thuesen L, Dudek D, Veldhof S, Dorange C, Garcia-Garcia HM, Ormiston JA, Serruys PW. Morphological and functional evaluation of the bioresorption of the bioresorbable everolimus-eluting vascular scaffold using IVUS, echogenicity and vasomotion testing at two year follow-up: a patient level insight into the ABSORB A clinical trial. *Int J Cardiovasc Imaging* 2011. Published online ahead of print.
- Lavi S, Bae JH, Rihal CS, Prasad A, Barsness GW, Lennon RJ, Holmes DR Jr, Lerman A. Segmental coronary endothelial dysfunction in patients with minimal atherosclerosis is associated with necrotic core plaques. *Heart* 2009;**95**: 1525–1530.
- Serruys PW, Onuma Y, Ormiston JA, de Bruyne B, Regar E, Dudek D, Thuesen L, Smits PC, Chevalier B, McClean D, Koolen J, Windecker S, Whitbourn R, Meredith I, Dorange C, Veldhof S, Miquel-Hebert K, Rapoza R, Garcia-Garcia HM. Evaluation of the second generation of a bioresorbable everolimus drug-eluting vascular scaffold for treatment of de novo coronary artery stenosis: six-month clinical and imaging outcomes. *Circulation* 2010;**122**: 2301–2312.
- Ormiston JA, Webster MW, Armstrong G. First-in-human implantation of a fully bioabsorbable drug-eluting stent: the BVS poly-L-lactic acid everolimus-eluting coronary stent. *Catheter Cardiovasc Interv* 2007;**69**:128–131.
- Okamura T, Garg S, Gutierrez-Chico JL, Shin ES, Onuma Y, Garcia HM, Rapoza R, Sudhir K, Regar E, Serruys PW. In-vivo evaluation of stent strut distribution patterns in the bioabsorbable everolimus-eluting device: an OCT ad hoc analysis of the Revision 1.0 and Revision 1.1 stent design in the ABSORB clinical trial. *EuroIntervention* 2010;**5**:932–938.
- Onuma Y, Serruys PW, Perkins LE, Okamura T, Gonzalo N, Garcia-Garcia HM, Regar E, Kamberi M, Powers JC, Rapoza R, van Beusekom H, van der Giessen W, Virmani R. Intracoronary optical coherence tomography and histology at 1 month and 2, 3, and 4 years after implantation of everolimus-eluting bioresorbable vascular scaffolds in a porcine coronary artery model: an attempt to decipher the human optical coherence tomography images in the ABSORB trial. *Circulation* 2010;**122**:2288–2300.
- Nair A, Kuban BD, Tuzzu EM, Schoenhagen P, Nissen SE, Vince DG. Coronary plaque classification with intravascular ultrasound radiofrequency data analysis. *Circulation* 2002;**106**:2200–2206.
- Bruining N, de Winter S, Roelandt JR, Regar E, Heller I, van Domburg RT, Hamers R, Onuma Y, Dudek D, Webster MW, Thuesen L, Ormiston JA, Cheong WF, Miquel-Hebert K, Veldhof S, Serruys PW. Monitoring in vivo absorption of a drug-eluting bioabsorbable stent with intravascular ultrasound-derived parameters a feasibility study. *JACC Cardiovasc Interv* 2010;**3**:449–456.
- Brugaletta S, Gomez-Lara J, Serruys PW, Farooq V, van Geuns RJ, Thuesen L, Dudek D, Koolen J, Chevalier B, McClean D, Windecker S, Smits P, De Bruyne B, Whitbourn R, Meredith I, van Domburg R, Sihan K, de Winter S, Veldhof S, Miquel-Hebert K, Rapoza R, Garcia-Garcia HM, Ormiston J, Bruining N. Serial in vivo IVUS-based echogenicity changes of everolimus-eluting

- bioresorbable vascular scaffold during the first 12 months after implantation. Insights from ABSORB B trial. *JACC Cardiovasc Interv* 2011;**4**:1281–1289.
14. Bruining N, Verheye S, Knaapen M, Somers P, Roelandt JR, Regar E, Heller I, de Winter S, Ligthart J, Van Langenhove G, de Feijter PJ, Serruys PW, Hamers R. Three-dimensional and quantitative analysis of atherosclerotic plaque composition by automated differential echogenicity. *Catheter Cardiovasc Interv* 2007;**70**: 968–978.
 15. Reiber JH, Serruys PJ. Quantitative coronary angiography: methodologies. *Quantitative Coronary Angiography*. Dordrecht, The Netherlands: Kluwer Academic Publishers; 1996. p98–102.
 16. Hofma SH, van der Giessen WJ, van Dalen BM, Lemos PA, McFadden EP, Sianos G, Ligthart JM, van Essen D, de Feyter PJ, Serruys PW. Indication of long-term endothelial dysfunction after sirolimus-eluting stent implantation. *Eur Heart J* 2006;**27**:166–170.
 17. Brugaletta S, Garcia-Garcia HM, Diletti R, Gomez-Lara J, Garg S, Onuma Y, Shin ES, Van Geuns RJ, De Bruyne B, Dudek D, Thuesen L, Chevalier B, McClean D, Windecker S, Whitbourn R, Dorange C, Veldhof S, Rapoza R, Sudhir K, Bruining N, Ormiston J, Serruys P. Comparison between the first and second generation bioresorbable vascular scaffolds: a six month virtual histology study. *Eurointervention* 2011;**6**:1110–1116.
 18. Naghavi M, Libby P, Falk E, Casscells SW, Litovsky S, Rumberger J, Badimon JJ, Stefanadis C, Moreno P, Pasterkamp G, Fayad Z, Stone PH, Waxman S, Raggi P, Madjid M, Zarrabi A, Burke A, Yuan C, Fitzgerald PJ, Siscovick DS, de Korte CL, Aikawa M, Aikarsinen KE, Assmann G, Becker CR, Chesebro JH, Farb A, Galis ZS, Jackson C, Jang IK, Koenig W, Lodder RA, March K, Demirovic J, Navab M, Puri SG, Rekhker MD, Bahr R, Grundy SM, Mehran R, Colombo A, Boerwinkle E, Ballantyne C, Insull W Jr, Schwartz RS, Vogel R, Serruys PW, Hansson GK, Faxon DP, Kaul S, Drexler H, Greenland P, Muller JE, Virmani R, Ridker PM, Zipes DP, Shah PK, Willerson JT. From vulnerable plaque to vulnerable patient: a call for new definitions and risk assessment strategies: Part II. *Circulation* 2003;**108**:1772–1778.
 19. Pendyala LK, Li J, Shinke T, Geva S, Yin X, Chen JP, King SB 3rd, Robinson KA, Chronos NA, Hou D. Endothelium-dependent vasomotor dysfunction in pig coronary arteries with paclitaxel-eluting stents is associated with inflammation and oxidative stress. *JACC Cardiovasc Interv* 2009;**2**:253–262.
 20. Sarno G, Onuma Y, Garcia Garcia HM, Garg S, Regar E, Thuesen L, Dudek D, Veldhof S, Dorange C, Ormiston JA, Serruys PW. IVUS radiofrequency analysis in the evaluation of the polymeric struts of the bioabsorbable everolimus-eluting device during the bioabsorption process. *Catheter Cardiovasc Interv* 2010;**75**: 914–918.
 21. Brugaletta S, Garcia-Garcia HM, Garg S, Gomez-Lara J, Diletti R, Onuma Y, van Geuns RJ, McClean D, Dudek D, Thuesen L, Chevalier B, Windecker S, Whitbourn R, Dorange C, Miquel-Hebert K, Sudhir K, Ormiston JA, Serruys PW. Temporal changes of coronary artery plaque located behind the struts of the everolimus eluting bioresorbable vascular scaffold. *Int J Cardiovasc Imaging* 2011;**27**:859–866.
 22. Serruys PW, Garcia-Garcia HM, Buszman P, Erne P, Verheye S, Aschermann M, Duckers H, Bleie O, Dudek D, Botker HE, von Birgelen C, D'Amico D, Hutchinson T, Zambanini A, Mastik F, van Es GA, van der Steen AF, Vince DG, Ganz P, Hamm CW, Wijns W, Zalewski A. Effects of the direct lipoprotein-associated phospholipase A (2) inhibitor darapladib on human coronary atherosclerotic plaque. *Gratulation* 2008;**118**:1172–1182.
 23. Hong MK, Park DW, Lee CW, Lee SW, Kim YH, Kang DH, Song JK, Kim JJ, Park SW, Park SJ. Effects of statin treatments on coronary plaques assessed by volumetric virtual histology intravascular ultrasound analysis. *JACC Cardiovasc Interv* 2009;**2**:679–688.
 24. Togni M, Windecker S, Cocchia R, Wenaweser P, Cook S, Billinger M, Meier B, Hess OM. Sirolimus-eluting stents associated with paradoxical coronary vasoconstriction. *J Am Coll Cardiol* 2005;**46**:231–236.
 25. Shin DL, Kim PJ, Seung KB, Kim DB, Kim MJ, Chang K, Lim SM, Jeon DS, Chung WS, Baek SH, Lee MY. Drug-eluting stent implantation could be associated with long-term coronary endothelial dysfunction. *Int Heart J* 2007;**48**:553–567.
 26. Moses JW, Leon MB, Popma JJ, Fitzgerald PJ, Holmes DR, O'Shaughnessy C, Caputo RP, Kereiakes Dj, Williams DO, Teirstein PS, Jaeger JL, Kuntz RE. Sirolimus-eluting stents versus standard stents in patients with stenosis in a native coronary artery. *N Engl J Med* 2003;**349**:1315–1323.
 27. Hamilos M, Sarma J, Ostojic M, Cuisset T, Sarno G, Melikian N, Ntalianis A, Muller O, Barbato E, Beleslin B, Sagic D, De Bruyne B, Bartunek J, Wijns W. Interference of drug-eluting stents with endothelium-dependent coronary vasomotion: evidence for device-specific responses. *Circ Cardiovasc Interv* 2008;**1**:193–200.
 28. Guba M, von Breitenbuch P, Steinbauer M, Koehl G, Flegel S, Hornung M, Bruns CJ, Zuelke C, Farkas S, Anthuber M, Jauch KW, Geissler EK. Rapamycin inhibits primary and metastatic tumor growth by antiangiogenesis: involvement of vascular endothelial growth factor. *Nat Med* 2002;**8**:128–135.
 29. Verheye S, Martinet W, Kockx MM, Knaapen MW, Salu K, Timmermans JP, Ellis JT, Kilpatrick DL, De Meyer GR. Selective clearance of macrophages in atherosclerotic plaques by autophagy. *J Am Coll Cardiol* 2007;**49**:706–715.
 30. Martinet W, Verheye S, De Meyer GR. Everolimus-induced mTOR inhibition selectively depletes macrophages in atherosclerotic plaques by autophagy. *Autophagy* 2007;**3**:241–244.

8.4

Circumferential evaluation of the neointima by optical coherence tomography after ABSORB bioresorbable vascular scaffold implantation: can the scaffold cap the plaque?

Salvatore Brugaletta, Maria D Radu, Hector M Garcia-Garcia, Jung Ho Heo, Vasim Farooq, Crhysafios Girasis, Robert Jan van Geuns, Leif Thuesen, Dougal McClean, Bernard Chevalier, Stephan Windecker, Jacques Koolen, Richard Rapoza, Karine Miquel-Hebert, John Ormiston, Patrick W Serruys

Atherosclerosis 2012, 221:106-12

Circumferential evaluation of the neointima by optical coherence tomography after ABSORB bioresorbable vascular scaffold implantation: Can the scaffold cap the plaque?

Salvatore Brugaletta^{a,b}, Maria D. Radu^a, Hector M. Garcia-Garcia^{a,b,c}, Jung Ho Heo^a, Vasim Farooq^a, Chrysafios Girasis^a, Robert-Jan van Geuns^a, Leif Thuesen^d, Dougal McClean^e, Bernard Chevalier^f, Stephan Windecker^g, Jacques Koolen^h, Richard Rapozaⁱ, Karine Miquel-Hebert^j, John Ormiston^k, Patrick W. Serruys^{a,*}

^a Thoraxcenter, Erasmus MC, Rotterdam, The Netherlands

^b Department of Cardiology, Thorax Institute, Hospital Clinic, University of Barcelona, Barcelona, Spain

^c Cardialysis B.V., Rotterdam, The Netherlands

^d Skejby Sygehus, Aarhus University Hospital, Aarhus, Denmark

^e Christchurch Hospital, Christchurch, New Zealand

^f Institut Cardiovasculaire Paris Sud, Massy, France

^g Bern University Hospital, Bern, Switzerland

^h Catharina Hospital, Eindhoven, The Netherlands

ⁱ Abbott Vascular, Santa Clara, CA, USA

^j Abbott Vascular, Diegem, Belgium

^k Auckland City Hospital, Auckland, New Zealand

ARTICLE INFO

Article history:

Received 12 October 2011

Received in revised form 3 December 2011

Accepted 5 December 2011

Available online 13 December 2011

Keywords:

OCT

Neointima

Bioresorbable vascular scaffold

ABSTRACT

Objective: To quantify the circumferential healing process at 6 and 12 months following scaffold implantation.

Background: The healing process following stent implantation consists of tissue growing on the top of and in the space between each strut. With the ABSORB bioresorbable vascular scaffold (BVS), the outer circumference of the scaffold is detectable by optical coherence tomography (OCT), allowing a more accurate and complete evaluation of the intra-scaffold neointima.

Methods: A total of 58 patients (59 lesions), who received an ABSORB BVS 1.1 implantation and a subsequent OCT investigation at 6 ($n = 28$ patients/lesions) or 12 ($n = 30$ patients with 31 lesions) months follow-up were included in the analysis. The thickness of the neointima was calculated circumferentially in the area between the abluminal side of the scaffold and the lumen by means of an automated detection algorithm. The symmetry of the neointima thickness in each cross section was evaluated as the ratio between minimum and maximum thickness.

Results: The neointima area was not different between 6 and 12 months follow-up ($1.57 \pm 0.42 \text{ mm}^2$ vs. $1.64 \pm 0.77 \text{ mm}^2$; $p = 0.691$). No difference was also found in the mean thickness of the neointima (median [IQR]) between the two follow-up time points (210 μm [180–260]) vs. 220 μm [150–260]; $p = 0.904$). However, the symmetry of the neointima thickness was higher at 12 than at 6 months follow-up (0.23 [0.13–0.28] vs. 0.16 [0.08–0.21], $p = 0.019$).

Conclusions: A circumferential evaluation of the healing process following ABSORB implantation is feasible, showing the formation of a neointima layer, that resembles a thick fibrous cap, known for its contribution to plaque stability.

© 2011 Elsevier Ireland Ltd. All rights reserved.

* Corresponding author at: Interventional Cardiology Department Erasmus MC, Thoraxcenter, 's Gravendijkwal 230,3015 CE Rotterdam, The Netherlands.

Tel.: +31 10 4635260; fax: +31 10 4369154.

E-mail address: p.w.j.c.serruys@erasmusmc.nl (P.W. Serruys).

1. Introduction

The aim of percutaneous treatment of a coronary lesion with an intracoronary scaffolding device is to acutely restore the geometry of the coronary lumen, alleviating its flow-limiting character. Thereafter, the reaction of the vessel wall to the implanted stent initiates a healing process resulting in the growth of intra-scaffold

neointima [1,2]. Growth of this neo-tissue on top of a vulnerable thin-cap fibroatheroma may generate a new "fibrous cap" which may potentially increase the thickness of the cap [3–5]. This biological process may be of particular interest in cases where scaffolds have been implanted on top of a necrotic core, abutting the lumen.

Nevertheless, autopsy studies have suggested that metallic struts embedded in necrotic core may remain uncovered even at long-term, and thus be potentially a trigger for stent thrombosis [4].

The bioresorbable vascular scaffolds, which in the long-term are completely replaced by connective tissue and smooth muscle cells – overcoming the problem of metal persistence into the coronary vessel wall – can ensure the formation of a neointima layer [6,7]. In addition as the polymeric struts are translucent and do not create an optical shadow, an optical coherence tomography (OCT) evaluation of the neointima growth can be performed in a more refined way in the scaffold than in the metallic stents [8].

The aim of this analysis was to assess and to quantify the circumferential distribution of the intra-scaffold neo-intima tissue during the first year after ABSORB implantation.

2. Methods

2.1. Study population

The ABSORB Cohort B trial (NCT00856856) is a multicentre single-arm trial assessing the safety and performance of the ABSORB BVS (Abbott Vascular, Santa Clara, USA). The details of this trial have been previously reported [8,9].

In total, 101 patients were enrolled in the ABSORB Cohort B trial, subdivided in two subgroups of patients: the first group of 45 patients (Cohort B1) randomized to invasive imaging at 6 and 24 months; the second group of the remaining 56 patients (Cohort B2) randomized to the same invasive imaging at 12 and 36 months. OCT was realized as an optional investigation in some of these patients without any inclusion/exclusion criteria.

The present study is a post hoc analysis of the patients receiving an OCT investigation at the various follow-up time points.

2.2. ABSORB BVS

The ABSORB BVS is a fully bioresorbable intra-coronary device made of semi-crystalline poly (L-lactide) (PLLA) coated with an amorphous poly (D,L-lactide) (PDLLA) copolymer that contains and controls the release of the anti-proliferative drug everolimus. At the time of implantation, the total strut thickness is 156 μm . The primary mechanism for molecular weight degradation of both polylactide (PLA) materials is hydrolysis, a process in which the ester bonds between repeating lactide molecules are progressively cleaved by water. Ultimately, PLLA and PDLLA degrade into

lactic acid, which is readily converted to lactate and processed via both the Krebs's cycle (for L-lactate) and methylglyoxal metabolism (for D-lactate) [7,10,11]. Based on preclinical studies, the time for complete bioresorption is assumed to be approximately 2 years [6].

2.3. OCT acquisition and analysis

OCT imaging was performed as an optional investigation at selected centers, using either time domain [M3 system, Light Lab Imaging (LLI), Westford, MA, USA] or frequency domain OCT systems (C7XR system, LLI) at baseline and follow-up [12–17]. The OCT measurements were performed with proprietary software for off-line analysis (Light Lab Imaging, Westford, MA, USA). Adjusting for the pullback speed, the cross-sectional analysis was performed at 1 mm longitudinal intervals within the treated segment.

When imaged with OCT, the ABSORB BVS presents important differences compared to the metallic stents. The optically translucent polymeric struts appear as black boxes (strut core area) framed by light-scattering borders that do not produce dorsal shadows, thus allowing for a complete imaging of the strut thickness [8]. As the strut is entirely visible throughout its entire thickness, the main quantitative measurements (strut core area, strut area, lumen area, scaffold area, incomplete scaffold apposition area and neointima area) required different analysis rules than with the metallic stents, as previously described [8,9]. In particular, the neointima area has been previously calculated as [scaffold area – lumen area – strut core area] and the thickness of the coverage has been measured for every strut between the abluminal side of the strut core and the lumen [8,9].

At variance with this previous analysis, the strut core area is now included in the neointima area assessment, in order to perform a circumferential measurement of the neointima thickness by means of an automated contour detection algorithm available in the Light Lab proprietary software. The size and the thickness of the neo-intima area, delimited by the scaffold (as outer reference, drawn at the abluminal side of the struts) and the lumen contours (as inner reference), were measured in each frame (Fig. 1). Frames containing malapposed struts were excluded from the analysis, as the area included between the scaffold and the lumen does not contain in these cases any neointimal tissue, but represents incomplete scaffold apposition (ISA) area. The neointima area was estimated as scaffold area – lumen area. The neointima area was normalized per scaffold size as "in-scaffold area obstruction" and estimated as: [neointima area/scaffold area] \times 100. The symmetry of the neointima thickness in each cross-section was evaluated as a ratio between the minimum and the maximum thickness of neointima in that cross-section [18,19].

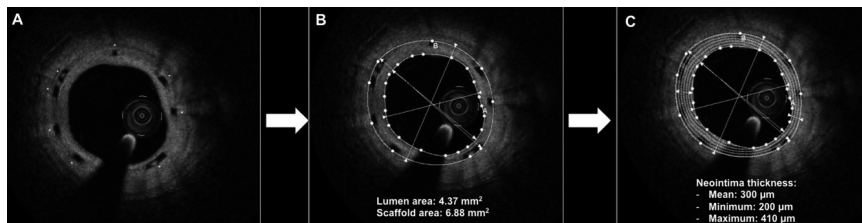


Fig. 1. Circumferential assessment of neointima for ABSORB BVS. Panel A shows the circumferential distribution of the polymeric struts (*) in a cross-section. After drawing the lumen and scaffold contours (Panel B), the neointima thickness is calculated (Panel C). The minimum and maximum diameters of lumen and scaffold areas are also drawn.

2.4. Statistical analysis

Continuous variables are expressed as mean \pm standard deviation (SD) or median and interquartile range, depending on their distribution. The distribution normality of the variables was tested using the Kolmogorov–Smirnov test. Dichotomous variables are reported as numbers and percentages. Comparison between groups was done by means of the non-parametric Mann–Whitney test. Adjustment for clustering data at cross section level was performed using a generalized estimating equations approach [20]. A two-tailed p -value < 0.05 was considered statistically significant. Statistical analyses were performed with SPSS statistical package, version 17.0 (SPSS Inc., Chicago IL, USA).

3. Results

3.1. Patient population

A total of 58 patients (59 lesions) received an OCT investigation at 6 ($n = 28$ patients/lesions) or 12 ($n = 30$ patients with 31 lesions) months follow-up after ABSORB BVS implantation, and all were included in the present analysis. (see Supplementary material for baseline clinical characteristics).

3.2. OCT analysis of neointimal area at 6 and 12 months follow-up

A total of 1083 cross sections were analyzed (531 and 552 at 6 and 12 months, respectively). Forty-nine cross sections were excluded from the analysis due to the presence of ISA (23 and 26 at 6 and 12 months follow-up, respectively).

At a cross-section level, lumen and scaffold areas tended to be smaller, while the minimum neointima thickness tended to be larger at 12 as compared to 6 months. However, the mean neointima area was not different between the two time points (Table 1). Fig. 2A shows the bimodal distribution histogram of the mean neointima thicknesses, pooling the 6 and the 12 months follow-up data. There was a significant relationship between the mean neointima thickness measured at the minimum lumen area frame and the angiographic late loss ($r = 0.624$, $p = 0.003$) (Fig. 2B).

At a lesion level, lumen and scaffold area also tended to be smaller at 12 months follow-up and the minimum neointima thickness tended to be larger at 12 than at 6 months follow-up (Table 1).

The symmetry of the neointima thickness (more homogeneous distribution of neointima) was significantly higher at 12 than at 6 months follow-up both at cross-section and at lesion level (Fig. 3).

4. Discussion

The main findings of the present analysis are: (1) the methodology for measuring the neointima thickness circumferentially by OCT is feasible with translucent bioresorbable scaffolds and allows for the measurement of the neointima on top and between the struts; (2) the neointima at 6 and 12 months does not differ in terms of thickness but appears to be more symmetric at 12 than at 6 months.

It is known that in the pathogenesis of acute coronary syndromes a major role is played by coronary plaque rupture and erosion with subsequent local thrombosis [21]. In particular, pathological studies have documented that these plaques are mostly represented by thin-cap fibroatheromas (TCFA), which are lipid core plaques covered by a thin fibrous cap ($< 65 \mu\text{m}$) [22,23]. The PROSPECT study has further demonstrated that IVUS-VH derived TCFA are independent predictors of coronary events in patients after an acute coronary syndrome at a median follow-up of 3.4

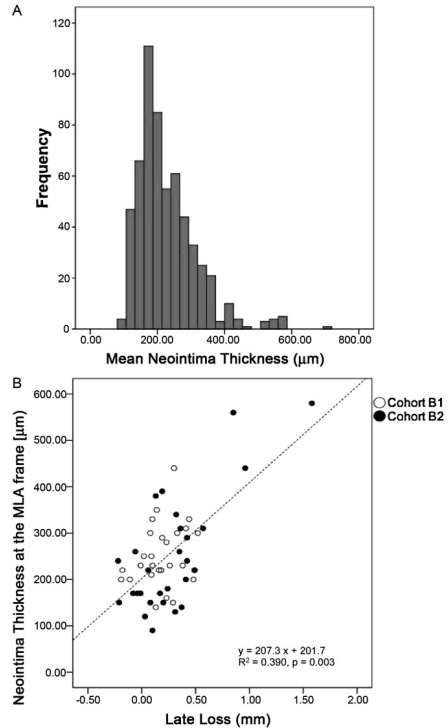


Fig. 2. Neointima thickness: histogram distribution and correlation with angiographic late loss. Panel A: Histogram distribution of the neointima thickness at cross-sectional level (1034 cross-section). The ABSORB BVS scaffold has a median (interquartile range) of $210 \mu\text{m}$ ($160\text{--}270 \mu\text{m}$) with a bimodal distribution. Panel B: the mean neointima thickness at the site of minimum lumen area (MLA) is significantly correlated with the angiographic late loss.

years [24]. Nevertheless, it has not been yet demonstrated which of these plaques are going to be the cause of events. Of note is that the majority of the events in the PROSPECT study were progressive angina, caused probably by plaque growth and not acute coronary syndromes that could be attributed to the rupture of a vulnerable plaque. In addition to this, TCFA were identified in the PROSPECT study by IVUS-VH, which has a limited resolution to measure the thickness of the cap. For these reasons, more natural history studies with more precise techniques for the detection of TCFA are needed before the interventional treatment of these lesions can be recommended.

Pharmacological and mechanical treatments aimed to stabilize TCFA are, however, a current topic of research. Takarada et al. [25] showed that pharmacological treatment, such as statins, enables to significantly increase the fibrous-cap thickness of coronary plaques. The pilot SECURIT trial attempted to address for the first time the question whether a mechanical preventive treatment of such kind of plaques by means of self-expandable metallic stent ("Shield") may be feasible and safe [3]. The percutaneous treatment of a TCFA by a metallic stent, especially bare-metal, triggers

Table 1
Neointima thickness analysis by OCT.

Cross section level			
	6 month (508 cross sections)	12 months (526 cross sections)	p-value
Mean lumen area (mm ²)	6.26 ± 1.72	5.63 ± 1.48	0.071
Mean scaffold area (mm ²)	7.86 ± 1.63	7.31 ± 1.38	0.095
Mean neointima thickness (μm)	230 [190–280]	190 [150–270]	0.410
Minimum neointima thickness (μm)	40 [10–105]	60 [30–120]	0.096
Maximum neointima thickness (μm)	330 [280–410]	310 [240–410]	0.648
Neointima area (mm ²)	1.60 ± 0.62	1.68 ± 0.77	0.517
In-scaffold area obstruction (%)	21.37 ± 9.44	23.46 ± 11.24	0.284
Symmetry of neointima thickness	0.10 [0.03–0.24]	0.20 [0.09–0.30]	0.005
Patient level			
	6 months (n = 28)	12 months (n = 31)	p-value
Mean lumen area (mm ²)	6.42 ± 1.40	5.64 ± 1.41	0.050
Mean scaffold area (mm ²)	7.98 ± 1.52	7.28 ± 1.08	0.031
Mean neointima thickness (μm)	210 [180–260]	220 [150–260]	0.904
Minimum neointima thickness (μm)	50 [30–80]	80 [40–120]	0.071
Maximum neointima thickness (μm)	335 [300–410]	340 [280–420]	0.912
Neointima area (mm ²)	1.57 ± 0.42	1.64 ± 0.77	0.691
In-scaffold area obstruction (%)	20.66 ± 7.47	23.38 ± 11.73	0.322
Symmetry of neointima thickness	0.16 [0.08–0.21]	0.23 [0.13–0.28]	0.019

Data are reported as median and interquartile range or mean ± standard deviation, according to their distribution.

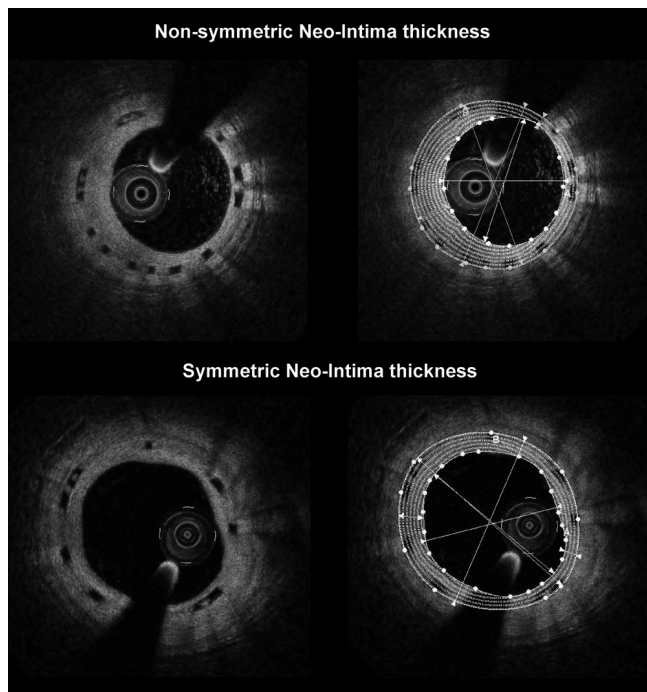


Fig. 3. Symmetry of the neointima. Examples of non-symmetric (6 months follow-up) and symmetric (12 months follow-up) neointima thickness. The minimum and maximum diameter of the lumen and scaffold contours are drawn.

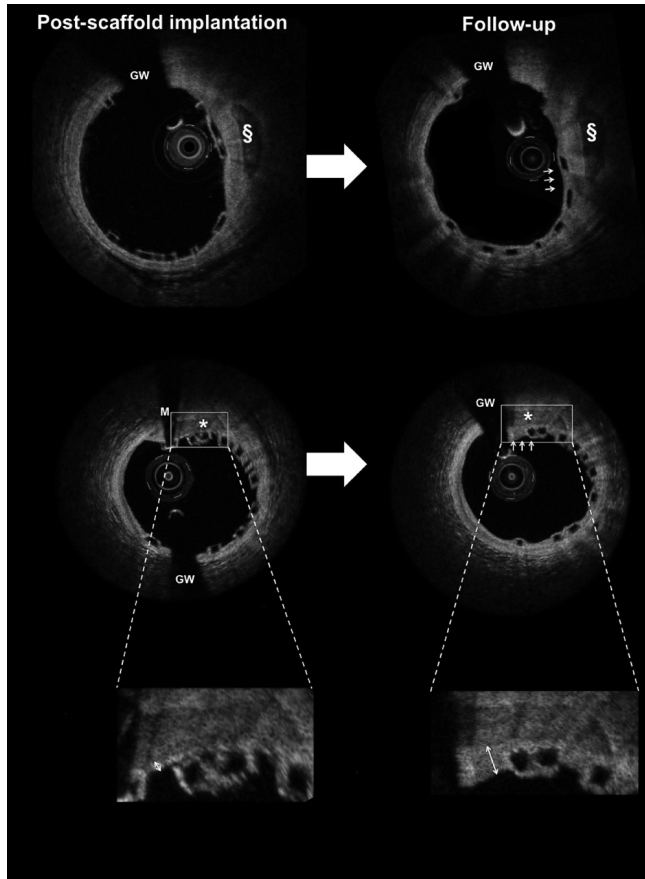


Fig. 4. Neointima layer covering coronary plaques. Examples of the formation of a neointima layer over two coronary plaques (indicated as § and *), scaffolded by an ABSORB BVS device. At follow-up a neo-tissue is visible not only on the top of the polymeric struts, but also in the space between two adjacent struts (white arrows), thickening the cap of the plaque originally treated (see the enlargement on the bottom). GW = shadow of the guidewire. M = shadow of the radio-opaque marker, present at the scaffold edge (note: the shadow of the marker at follow-up is hidden by the guidewire shadow).

the formation of a fibrotic layer (more or less thick) on the top of the thin cap covering the lipid pool, potentially reducing therefore the probability of plaque rupture/erosion. However, the persistence of metal and/or non-degradable polymers into the vessel wall can have some detrimental effects (e.g., permanent presence of foreign body, etc.) [26]. With regards to ABSORB bioresorbable vascular scaffold, it has been established that at approximately 2 years the polymeric material has been fully degraded and replaced by proteoglycans. At 4 years, the initial location of the struts in the vessel wall is no longer identifiable by histology or OCT and the neointimal layer built up on the scaffolding structure becomes thereby a “*de novo*” cap, which cannot be distinguished from a fibrotic cap, normally seen in fibroatheroma [6,10,27] (Fig. 4). The formation of

a symmetric neo-tissue with a mean thickness of 220 μm without remnants of polymeric struts, when the device is completely bioresorbed, may therefore favor the use of a bioresorbable device for the treatment of thin-cap fibroatheromas [10]. Based on the findings of our previous pre-clinical studies, we have established that the main component of the neointima following ABSORB BVS implantation is fibrous tissue, whereas fibrin and granulomatous cells are scarce at long-term follow-up [6].

Of note is that in our analysis the thickness of the neointima was on average not different between 6 and 12 months follow-up. Only the minimum neointima thickness exhibited some tendency to be larger at 12 than at 6 months follow-up. This observation suggests that the healing process following an ABSORB BVS implantation is

almost completed 6 months after the device implantation, without further increase of neointima overtime. Conversely, the symmetry of the neointima, although far away from the value of 1, which potentially represents a highly symmetric neointima, significantly increases from 6 to 12 months follow-up, reflecting a more circumferentially homogenous distribution of tissue capping the original plaque. A symmetric distribution of neointima thickness ensures more likely the presence of a "thick cap" on the top of the plaque originally treated, regardless of its circumferential location in the vessel wall.

It is noteworthy that the comparison between 6 and 12 months represents an unpaired comparison so that the tendency toward a reduction in lumen and scaffold areas should be carefully interpreted. In the paired comparison, previously reported, there was no reduction in scaffold area by OCT at 6 and 12 months [8,9]. The histogram distribution of the neointima thickness seems to have a bimodal distribution, which is consistent with the DES late loss distribution, previously observed [28]. Of note is that the angiographic late loss appeared to be significantly correlated with the thickness of the neointima at the site of MLA [29,30]. The difference in resolution between the two imaging techniques and other factors, such as remodeling of the vessel, should be taken into account for explaining this relationship. It is also known that the level of neointima proliferation may affect the correlation between late loss by QCA and neointima thickness by OCT that is high in presence of a high late loss [30]. The small number of patients did not allow us this kind of sub-analysis and will require further studies.

5. Limitations

Our analysis may have some limitations. The first is that the assessment of the intra-scaffold neointima area incorporates the area of the strut core in the quantification of the neointima area, at variance with the method previously described [8,9]. However, from animal studies, it may be argued that that each polymeric strut is ultimately replaced by proteoglycan and connective tissue: for this reason, the inclusion of the strut core area into the neointima area more correctly reflects the thickness of the tissue covering the plaque originally treated [6] (See Fig. 1 in Supplementary material).

Another important consideration is about the small sample size at the two time points. Nevertheless, these patients represent the unique cohort of patients received an ABSORB implantation and an OCT analysis.

The presence of ISA is another limitation of our methodology, as the automatic detection software algorithm of the software recognizes this area as neointima. However, the segments with ISA can be excluded and analyzed using conventional methodology.

6. Conclusions

An accurate and circumferential quantification of the healing process following implantation of bioresorbable scaffolds is allowed. The formation of a thick neointimal layer, without remnants of polymeric struts, creates a "de novo" cap, which may be used to seal a thin-cap fibroatheroma.

Acknowledgment

The ABSORB trial is sponsored and funded by Abbott Vascular, Santa Clara, California, USA.

Appendix A. Supplementary data

Supplementary data associated with this article can be found, in the online version, at doi:10.1016/j.atherosclerosis.2011.12.008.

References

- [1] Garg S, Serruys PW. Coronary stents: looking forward. *J Am Coll Cardiol* 2010;56:543–78.
- [2] Garg S, Serruys PW. Coronary stents: current status. *J Am Coll Cardiol* 2010;56:51–42.
- [3] Ramcharitar S, Gonzalo N, van Geuns RJ, Garcia-Garcia HM, Wyrzykowska J, Ligthart JM, et al. First case of stenting of a vulnerable plaque in the secret trial—the dawn of a new era? *Nat Rev Cardiol* 2009;5:374–8.
- [4] Joner M, Finn AV, Farb A, Mont EK, Kolodgie FD, Ladich E, et al. Pathology of drug-eluting stents in humans: delayed healing and late thrombotic risk. *J Am Coll Cardiol* 2006;48:193–202.
- [5] Finn AV, Joner M, Nakazawa G, Kolodgie F, Newell J, John MC, et al. Pathological correlates of late drug-eluting stent thrombosis: strut coverage as a marker of endothelialization. *Circulation* 2007;115:2435–41.
- [6] Onuma Y, Serruys PW, Perkins LE, Okamura T, Gonzalo N, Garcia-Garcia HM, et al. Intracoronary optical coherence tomography and histology at 1 month and 2, 3, and 4 years after implantation of everolimus-eluting bioresorbable vascular scaffolds in a porcine coronary artery model: an attempt to decipher the human optical coherence tomography images in the absorb trial. *Circulation* 2010;122:2288–300.
- [7] Serruys PW, Ormiston JA, Onuma Y, Regar E, Gonzalo N, Garcia-Garcia HM, et al. A bioabsorbable everolimus-eluting coronary stent system (absorb): 2-year outcomes and results from multiple imaging methods. *Lancet* 2009;373:897–910.
- [8] Serruys PW, Onuma Y, Ormiston JA, de Bruyne B, Regar E, Dudek D, et al. Evaluation of the second generation of a bioresorbable everolimus drug-eluting vascular scaffold for treatment of de novo coronary artery stenosis: six-month clinical and imaging outcomes. *Circulation* 2010;122:2301–12.
- [9] Serruys PW, Onuma Y, Dudek D, Smitz PC, Koolen J, Chevalier B, et al. Evaluation of the second generation of a bioresorbable everolimus-eluting vascular scaffold for the treatment of de novo coronary artery stenosis 12-month clinical and imaging outcomes. *J Am Coll Cardiol* 2011;58:1578–88.
- [10] Ormiston JA, Serruys PW, Regar E, Dudek D, Thuesen L, Webster MW, et al. A bioabsorbable everolimus-eluting coronary stent system for patients with single de-novo coronary artery lesions (absorb): a prospective open-label trial. *Lancet* 2008;371:899–907.
- [11] Ewaschuk JB, Naylor JM, Zello GA. D-lactate in human and ruminant metabolism. *J Nutr* 2005;135:1619–25.
- [12] Sihan K, Botha C, Post F, de Winter S, Gonzalo N, Regar E, et al. Fully automatic three-dimensional quantitative analysis of intracoronary optical coherence tomography: method and validation. *Catheter Cardiovasc Interv* 2009;74:1058–65.
- [13] Prati F, Regar E, Mintz GS, Arbustini E, Di Mario C, Jang IK, et al. Expert review document on methodology, terminology, and clinical applications of optical coherence tomography: physical principles, methodology of image acquisition, and clinical application for assessment of coronary arteries and atherosclerosis. *Eur Heart J* 2010;31:401–15.
- [14] Gonzalo N, Serruys PW, Okamura T, Shen ZJ, Onuma Y, Garcia-Garcia HM, et al. Optical coherence tomography assessment of the acute effects of stent implantation on the vessel wall: a systematic quantitative approach. *Heart* 2009;95:1913–9.
- [15] Okamura T, Garg S, Gutierrez-Chico JL, Shin ES, Onuma Y, Garcia HM, et al. In vivo evaluation of stent strut distribution patterns in the bioabsorbable everolimus-eluting device: an oct ad hoc analysis of the revision 1.0 and revision 1.1 stent design in the absorb clinical trial. *EuroIntervention* 2010;9:32–8.
- [16] Regar E, Leeuwen AMGJv, Serruys PW. Optical coherence tomography in cardiovascular research. *Informa Healthcare* 2007.
- [17] Gonzalo N, Serruys PW, Garcia-Garcia HM, van Soest G, Okamura T, Ligthart J, et al. Quantitative ex vivo and in vivo comparison of lumen dimensions measured by optical coherence tomography and intravascular ultrasound in human coronary arteries. *Rev Esp Cardiol* 2009;62:615–24.
- [18] Brugaletta S, Gomez-Lara J, Diletti R, Farooq V, Jan van Geuns R, de Bruyne B, et al. Comparison of in vivo eccentricity and symmetry indices between metallic stents and bioresorbable vascular scaffolds: Insights from the absorb and spirit trials. *Catheter Cardiovasc Interv* 2011. Epub ahead of print.
- [19] de Jaegere P, Mudra H, Figulla H, Almagor Y, Doucet S, Penn I, et al. Intravascular ultrasound-guided optimized stent deployment. Immediate and 6 months clinical and angiographic results from the multicenter ultrasound stenting in coronaries study (music study). *Eur Heart J* 1998;19:1214–23.
- [20] Guagliumi G, Costa MA, Sirbu V, Musumeci G, Bezerra HG, Suzuki N, et al. Strut coverage and late malapposition with paclitaxel-eluting stents compared with bare metal stents in acute myocardial infarction: optical coherence tomography substudy of the harmonizing outcomes with revascularization and stents in acute myocardial infarction (horizons-ami) trial. *Circulation* 2011;123:274–81.
- [21] Shah PK. Mechanisms of plaque vulnerability and rupture. *J Am Coll Cardiol* 2003;41:155–225.
- [22] Virmani R, Burke AP, Farb A, Kolodgie FD. Pathology of the vulnerable plaque. *J Am Coll Cardiol* 2006;47:C13–8.
- [23] Burke AP, Farb A, Malcom GT, Liang YH, Smialek J, Virmani R. Coronary risk factors and plaque morphology in men with coronary disease who died suddenly. *N Engl J Med* 1997;336:1276–82.
- [24] Stone GW, Maehara A, Lansky AJ, de Bruyne B, Cristea E, Mintz GS, et al. A prospective natural-history study of coronary atherosclerosis. *N Engl J Med* 2011;364:226–35.

- [25] Takarada S, Imanishi T, Kubo T, Tanimoto T, Kitabata H, Nakamura N, et al. Effect of statin therapy on coronary fibrous-cap thickness in patients with acute coronary syndrome: assessment by optical coherence tomography study. *Atherosclerosis* 2009;202:491–7.
- [26] Holmes Jr DR, Kereiakes DJ, Garg S, Serruys PW, Dehmer GJ, Ellis SG, et al. Stent thrombosis. *J Am Coll Cardiol* 2010;56:1357–65.
- [27] Khattab A, Windecker S. Vascular restoration therapy: what should the clinical and angiographic measures for success be? *EuroIntervention* 2009;5(Supplement F):F49–57.
- [28] Farooq V, Gogas BD, Serruys PW. Restenosis: delineating the numerous causes of drug-eluting stent restenosis. *Circ Cardiovasc Interv* 2011;4:195–205.
- [29] Kim BK, Kim JS, Ko YG, Choi D, Jang Y, Hong MK. Correlation of angiographic late loss with neointimal coverage of drug-eluting stent struts on follow-up optical coherence tomography. *Int J Cardiovasc Imaging* 2011.
- [30] Kim JS, Wallace-Bradley D, Alviar CL, Conditt G, Milewski K, Afari ME, et al. Correlation of angiographic late loss with neointimal proliferation in stents evaluated by oct and histology in porcine coronary arteries. *JACC Cardiovasc Imaging* 2011;4:1002–10.

Summary and Conclusions

SUMMARY AND CONCLUSIONS

Many intra-coronary imaging techniques are currently available and are highly accurate for the serial assessment of the natural history of coronary atherosclerosis, for the analysis of metallic/polymeric intracoronary devices and for the evaluation of the vessel wall response to these devices.

This thesis provides important data regarding the value of these techniques, validating in particular some potential imaging surrogates which can be used in future atherosclerosis and stent/scaffold trials to evaluate the performance of drug therapies or bioresorbable devices for atherosclerosis treatment.

VALIDATION

We described the various tissue characterization techniques (IVUS-VH and iMAP) based on ultrasound, highlighting their potential clinical applications for atherosclerosis and intra-coronary devices evaluation (chapter 1.1).

The reproducibility study of iMAP demonstrated that the geometrical and compositional output of iMAP has acceptable reproducibility, giving important information to perform power calculation for longitudinal studies using iMAP (chapter 1.2).

NEAR INFRA-RED SPECTROSCOPY

Near infra-red spectroscopy (NIRS), which is routinely used in science and industry to determine the chemical composition of substances, has the potential to identify lipid core plaques *in vivo*, possibly improving patient risk stratification and guiding therapy. Possible clinical applications of this technique are: 1) identification of large lipid core plaques, which are known to be at high risk of distal embolization and peri-procedural myocardial infarction. In this case pre-PCI identification of such

plaques can lead to the use of preventive strategies, employing distal embolic protection devices. 2) Delineation of length of vessel to stent with adequate lesion coverage and optimal stent expansion. 3) Identification of vulnerable plaques, which may lead to strategies to prevent future coronary events (chapter 2.1).

We showed that NIRS is able to study the longitudinal distribution of lipid core plaques, showing that such kind of plaques tend to cluster in the proximal segment of coronary arteries close to the ostium, in agreement with previous anatomic-pathological, clinical and IVUS studies (Chapter 2.2). Nevertheless, of note is that NIRS exhibits a weak correlation with intravascular ultrasound virtual histology (IVUS-VH) in detecting lipid core/necrotic core plaques. The fundamental differences in the principles of each technique - VH is based on pattern classification of backscattering ultrasound signal, while NIRS on near infrared spectral signals - and their respective limitations should be taken into account in the interpretation of this disagreement between NIRS and IVUS-VH (chapter 3.1).

COMBINED IMAGING APPROACHES FOR ATHEROSCLEROSIS EVALUATION

In chapter 3.2, the combined use of IVUS-VH and optical coherence tomography (OCT) for progression/regression assessment of atherosclerosis at coronary bifurcations is described. Greyscale intravascular ultrasound allows evaluation of coronary atherosclerosis, imaging the complete thickness of the plaque, but its limited resolution (axial 150–200 μm) precludes the visualization of certain microstructures (such as the thin fibrous cap or fine strut coverage). On the contrary OCT is a light-based imaging modality can be used to study tissues *in vivo* with near-histologic, ultrahigh resolution and may provide very valuable information for the detection of high-risk plaques *in vivo*,

especially by measuring the thickness of the fibrous cap. However due to its limited penetration OCT cannot provide a full analysis of large plaques. Thus, we showed that the combination of the IVUS-VH and OCT appears promising to better characterize progression/regression of coronary plaques at the level of coronary bifurcations.

The distribution and composition of atherosclerotic plaques at coronary bifurcations was further studied in chapter 3.3, using a combined approach with invasive (IVUS-VH) and non-invasive (MSCT) imaging techniques. The plaques with high-risk features on IVUS-VH and non-calcified type on MSCT show a differential distribution along the bifurcation being more frequent at the proximal segment.

In addition to this, we evaluated combination of IVUS-VH data with functional (e.g. FFR) or mechanical (e.g. strain value) characteristics of coronary plaques. Comparing FFR negative (≤ 0.80) and positive lesions, for example, the relative content of VH-necrotic core appeared to be higher in lesions with a FFR >0.80 . This could be a possible explanation of major adverse cardiac events for those patients with angiographically intermediate lesions, left untreated as no functionally significant by FFR (chapter 3.4). On the contrary, the combination of compositional (VH) and mechanical (palpography) characteristics of coronary plaques did not have any additional value for identifying those coronary plaques at high risk of events (chapter 3.5)

IN STENT RESTENOSIS AND STRUT COVERAGE EVALUATION

In chapter 4.1, IVUS analysis demonstrated no additional advantage of using rosiglitazone over glipizide in type 2 diabetic patients for the reduction of in-stent restenosis; however it did demonstrate that both drugs have comparable effect on neointimal growth up to 18-months after coronary stent implantation.

In chapter 4.2, we showed a wide inter- and intra-observer agreement for uncovered struts evaluated visually by OCT, which is highly dependent of the zoom setting used in the analysis. This finding may suggest that a new quantitative and automatic approach (e.g. light intensity) would be needed to enhance the clinical relevance of strut coverage assessment, which is used as imaging endpoint in many stent studies.

BIORESORBABLE VASCULAR SCAFFOLDS

Everolimus-eluting bioresorbable vascular scaffolds (BVS) are a promising alternative to conventional drug-eluting metallic stents for the treatment of coronary atherosclerosis. The aim of this device consists in providing temporary vessel scaffolding and subsequently be bioresorbed, thereby allowing the artery to respond to shear stress and exhibit pharmacologically-induced vasomotion, akin to a non-treated coronary segment. This entire process, making the transiently scaffolded coronary segment fully amenable to biological, pharmacological and physiological stimuli, has been recently termed “vascular reparative therapy”.

COMPARISON OF DIFFERENT BVS

Two different revisions (1.0 and 1.1) of BVS have been evaluated in the clinical arena and various imaging techniques have been extensively used in order to evaluate all the characteristics of these devices.

In chapter 5.1 and 5.2 the two revisions have been compared by IVUS-VH and OCT. Both imaging techniques agreed on the fact that the revision 1.1 exhibited a longer mechanical integrity than the revision 1.0. Of note is that qualitative assessment of BVS structures using IVUS 20 MHz should be avoided

due to its poor agreement and reproducibility when compared to OCT. Both IVUS and OCT have good reproducibility to assess lumen and scaffold areas but the margin of error with IVUS is larger than with OCT (Chapter 5.3).

MECHANICAL PROPERTIES OF BIORESORBABLE VASCULAR SCAFFOLDS

Imaging techniques have been used to study the mechanical properties of these devices. In particular we analyzed the conformability and the eccentricity/symmetry of the device by means of coronary angiography and IVUS, respectively. At mid-term follow-up, the BVS tended to allow restoration of the coronary geometry and systo-diastolic movements of the coronary arteries similar to that seen before implantation, in contrast with metallic stent, for which the coronary geometry and systo-diastolic movements of coronary arteries remained similar to that seen after implantation (chapter 6.1). In agreement with these findings, the bioresorbable vascular scaffold appeared also to have reduced eccentricity index and increased symmetry index, when compared to conventional metallic stents (chapter 6.2).

In chapter 6.3, we found that the vascular distensibility of the scaffolded segment, measured by palpography, is reduced by BVS implantation; however, in contrast to metallic stents, the created mismatch in compliance with the proximal and distal segments disappeared at mid term due to the bioresorption and disappearance of the scaffold with potential clinical benefits of these findings, related to restoration of vessel wall pulsatility and absence of mismatch.

STRUCTURAL CHANGES OF BIORESORBABLE VASCULAR SCAFFOLDS OVERTIME

It is interesting to note that in contrast with metallic devices, BVS structure changes overtime. These changes can be qualitatively and quantitative evaluated by IVUS-based-echogenicity, OCT and VH.

With IVUS-based echogenicity, we demonstrated that when the degradation process is imaged by IVUS, individual cross-sectional images show a diminishing grey-level intensity of the struts over time, that can be quantified by an automated and validated software. In particular the improvement in mechanical integrity of the revision 1.1 over the revision 1.0 resulted in a reduced amount of change in ultrasound-derived parameters (e.g., changes in hyper-echogenicity) at 6 and 12 months (15% and 20%, respectively), compared with its first generation (1.0) (chapter 7.1).

By OCT, BVS exhibited a low rate of acute, persistent, and late acquired incomplete strut/scaffold malapposition as well as uncovered struts overtime. Moreover, at baseline and follow-up, malapposed and side branch struts were related to a lack of tissue coverage at 6 months and scaffold pattern irregularities were the only cause of late acquired malapposed struts (chapter 7.2).

Although all these techniques are able to show a change in the various scaffold parameters analyzed during the bioresorption/degradation process, the correlation between them has shown to be very poor. This is not surprising, as each technique is based on ultrasound or light so that they analyze different phenomena and parameters during scaffold degradation (chapter 7.3).

MORPHOLOGICAL MODIFICATION IN THE CORONARY ARTERY AFTER BVS IMPLANTATION

IVUS-VH can analyze the changes in plaque composition of the plaque localized behind the polymeric struts. It is known that the presence of the scaffold in a coronary artery is recognized by VH as dense calcium. We showed that it is feasible to exclude this dense calcium related to the scaffold from the VH-analysis of the plaque located behind, finding a significant reduction in necrotic core up to 1 year follow-up (Chapter 8.1 and 8.2).

FUNCTIONAL MODIFICATION IN THE CORONARY ARTERY AFTER BVS IMPLANTATION

The main advantage of the bioresorbable devices consists on the so-called vascular reparative therapy. We explored two aspects of this therapy, related to the ability of the scaffolded segment to react to vasoactive drugs and to create a “thick cap” on the top of a thin-cap coronary plaque.

In chapter 8.3, we demonstrated that the ability of a coronary segment scaffolded by a BVS device to react to vasoactive drugs is related to the bioresorption of the polymeric struts, as indirectly evaluated by changes in their echogenicity; in addition recovery of a normal endothelial function was associated with a low plaque burden and VH-necrotic core, resembling the behavior of a native diseased coronary vessel.

Chapter 8.4 analyzes the feasibility of an accurate and circumferential quantification of the healing process following implantation of bioresorbable scaffolds, suggesting that the formation of a thick and symmetric neointimal layer, without remnants of polymeric struts, may create a “*de novo*” cap, which may be used to seal a thin-cap fibroatheroma.

CONCLUSION

I believe that this thesis is of value to better understand the clinical utility of intracoronary imaging techniques in studying the extent, distribution, morphology and composition of coronary atherosclerosis in our patients.

In particular, we have provided important data regarding NIRS and new combined approaches to better characterize high-risk plaques, suggesting possible imaging surrogates endpoints, that may be used in future trials.

In addition, this thesis has extensively studied the healing process following bioresorbable vascular scaffold implantation, highlighting the morphological and functional changes in the vessel wall that can be achieved with these devices.

SAMENVATTING EN CONCLUSIES

Er zijn momenteel vele nauwkeurige intra-coronaire beeldvormende technieken beschikbaar die voor de seriële beoordeling van de natuurlijke historie van coronaire atherosclerose ingezet kunnen worden. Ook voor de analyse van metalen en/of polymere intracoronaire implantaten en voor de evaluatie van de reactie van de vaatwand op deze implantaten.

Dit proefschrift bevat belangrijke gegevens over de eventuele toegevoegde waarde van het gebruik van deze technieken. Meer in het bijzonder de validatie van deze technieken als surrogaat eindpunt in studies die de prestaties van geneesmiddelen onderzoeken m.b.t. atherosclerose progressie-regressie en andere interventies, zoals bijvoorbeeld het gebruik van metalen en/of bioafbreekbare stents.

VALIDATIE

We beschrijven verschillende weefselkarakterisering technieken (IVUS-VH en IMAP) op basis van ultrageluid, de nadruk leggend op de evaluatie van de potentiële klinische toepassingen voor atherosclerose en intra-coronaire behandelingstechnieken (hoofdstuk 1.1).

De reproduceerbaarheids studie van het gebruik van de IMAP techniek heeft aangetoond dat de geometrische en compositorische output hiervan aanvaardbaar is. Het geeft belangrijke informatie om uit te kunnen rekenen hoeveel patiënten, statistisch gezien, in een studie moeten worden geïncludeerd, om een bepaalde evaluatie studie uit te kunnen voeren (hoofdstuk 1.2).

NABIJ-INFRARODE SPECTROSCOPIE

Nabij-infrarode spectroscopie (NIRS), welke routinematig wordt gebruikt in de wetenschap en de industrie om de chemische samenstelling van stoffen te bepalen, heeft de potentie om coronaire plaques die lipide bevatten te kunnen identificeren in vivo. Deze techniek biedt de mogelijkheid voor het verbeteren van de risicostratificatie van de patiënt en het optimaliseren van de toegepaste therapie. Mogelijke klinische toepassingen van deze techniek zijn: 1) identificatie van lipides in coronaire plaques, waarvan bekend is dat zij een hoog risico vormen van distale embolisatie en peri-procedurele myocardiinfarcten. In dit geval kan voordat een PCI wordt uitgevoerd preventieve strategieën worden ingezet zoals bijvoorbeeld het gebruik van distale embolusbeschermingssysteem. 2) Het zo correct mogelijk inschatten van de lengte van het coronaire vat dat beschermd, gestent, zou moeten worden tegen plaques die grote hoeveelheden lipiden bevatten. 3) Identificatie van kwetsbare plaques, wat kan leiden tot strategieën om toekomstige coronaire gebeurtenissen (hoofdstuk 2.1) te voorkomen.

We hebben aangetoond dat m.b.v. NIRS de longitudinale verdeling van lipides in plaques kan worden bestudeerd, waaruit gebleken is dat zulke plaques zich meestal in het proximale deel van de coronairen bevinden nabij het ostium, wat in overeenstemming is met eerdere anatomisch-pathologisch klinische studies en IVUS (hoofdstuk 2.2). Dit gezegd hebbende, is het van belang om nota te nemen van het feit dat deze bevindingen met NIRS niet correleren met die van de intravasculaire echografie virtuele histologie (IVUS-VH) techniek m.b.t. het opsporen van lipides en necrotische plaques. De fundamentele verschillen van beide technieken, waarbij IVUS-VH is gebaseerd op patroonherkenning van het ruwe ultrasone signaal, terwijl NIRS gebaseerd is op nabij-infrarode spectrale signalen,

met hun respectievelijke beperkingen, zou hieraan ten grondslag kunnen liggen (hoofdstuk 3.1).

GECOMBINEERDE BEELDVORMING VOOR DE EVALUATIE VAN ATHEROSCLEROSE

In hoofdstuk 3.2, wordt het gecombineerde gebruik van IVUS-VH en de optische coherentie tomografie (OCT) voor de progressie / regressie beoordeling van atherosclerose bij coronaire bifurcaties beschreven.

Grijswaarde intravasculaire echografie kan gebruikt worden voor de evaluatie van coronaire atherosclerose dit doordat de volledige dikte van de plaquekan worden gevisualiseerd. Echter door de beperkte resolutie (axiale 150-200 micrometer), kunnen bepaalde microstructuren (zoals de dunne fibreuze kap of de dekking met een dunne laag weefsel op coronaire stents) niet worden gevisualiseerd. Hierintegen een op licht gebaseerde beeldvormingstechniek, optische coherente tomografie (OCT), kan dit wel en kunnen weefsels in vivo op bijna histologische, ultrahoge resolutie bestudeerd worden. Hierdoor kan zeer waardevolle informatie van het atherosclerotische vat verkregen worden zoals de detectie van fibreuze kappen. Zo toonden we aan dat de combinatie van de IVUS-VH en de OCT veelbelovend lijkt te zijn voor progressie-regressie studies van coronaire plaques op het niveau van coronaire bifurcaties. Helaas is deze techniek beperkt voor de analyses van grote plaques (in diameter).

De verdeling en de samenstelling van atherosclerotische plaques op coronaire bifurcaties werd verder onderzocht in hoofdstuk 3.3, met behulp van een gecombineerde aanpak van invasieve (IVUS-VH) en niet-invasieve (MSCT) beeldvormende technieken. De plaques met een hoog risico geïdentificeerd met IVUS-VH en niet-verkalkte plaques op MSCT tonen een ongelijke verdeling over de bifurcaties

zijn frequenter aanwezig in het proximale segment. Daarnaast evalueerden we de combinatie van IVUS-VH metingen met die van functionele (FFR) en mechanische (Strain) metingen om de eigenschappen van coronaire plaques verder te bepalen. Hierbij werden negatieve FFR ($\leq 0,80$) waarden en positieve letsels, vergeleken met het relatieve gehalte van de VH-necrotische waarden in een plaque waarbij bleek dat deze hoger is in laesies met een FFR $>0,80$. Dit zou een mogelijke verklaring kunnen zijn om belangrijke cardiovasculaire gebeurtenissen toch te kunnen verklaren bij patiënten met een angiografisch niet significante stenose en die niet worden behandeld, omdat er geen functioneel belangrijke stenose door FFR (hoofdstuk 3.4) wordt geïdentificeerd. Aan de andere kant, de combinatie van compositorische (VH) en mechanische (palpography) kenmerken van coronaire plaques heeft geen enkele toegevoegde waarde voor het identificeren van die coronaire plaques met een hoog risico op negatieve cardiale gevolgen aangetoond (hoofdstuk 3.5).

IN-STENT RESTENOSE EN EVALUATIE VAN WEEFSELDEKKING VAN STENTS

In hoofdstuk 4.1, m.b.v. IVUS-analyse wordt aangetoond dat er geen bijkomend voordeel is van het gebruik van rosiglitazone in vergelijking met glipizide bij type-2 diabetes patiënten voor de vermindering van in-stent restenose, maar het toonde wel aan dat beide middelen resulteren in een vergelijkbaar effect op de neointima groei tot en met 18 maanden na een coronaire stent implantatie.

In hoofdstuk 4.2 laat zien dat er een relatief grote inter-en intra-observer spreiding is in de resultaten van niet bedekte stent struts als dit visueel wordt beoordeeld m.b.v. OCT welke sterk afhankelijk is van de beeldinstellingen zoals die worden gebruikt voor de analyse, meer in het bijzonder de vergrotingsfac-

tor. Deze bevindingen kunnen erop wijzen dat een kwantitatieve en automatische aanpak (de lichtsterkte) nodig is om de klinische relevantie van de stent bekleding met weefsel, die tegenwoordig vaak wordt ingezet als beeldvormings eindpunt in veel stent studies te verbeteren.

BIORESORBEERBARE STENTS

Everolimus-afscheidende bioresorbeerbare vasculaire stents (BVS) zijn een veelbelovend alternatief voor de conventionele metalen permanente geïmplanteerde drug-eluting stents voor de behandeling van coronaire atherosclerotische aandoeningen. Het doel van deze stents is het tijdelijk mechanisch ondersteunen van het behandelde vat, vervolgens verdwijnt, waardoor de coronair kan reageren op veranderde afschuifspanningen en farmacologisch geïnduceerde vasomotie, vergelijkbaar met een normale coronairen. Dit hele proces is onlangs aangeduid als “vasculaire herstellende therapie”.

VERGELIJKING VAN VERSCHILLENDE BVS

Twee verschillende revisies (1.0 en 1.1) van de BVS zijn geëvalueerd in de kliniek en verschillende beeldvormende technieken zijn uitgebreid gebruikt om alle kenmerken van deze stents te kunnen evalueren.

In hoofdstuk 5.1 en 5.2 zijn de twee revisies vergeleken m.b.v. IVUS-VH en OCT. Beide beeldvormende technieken zijn het eens over het feit dat de herziene versie 1.1 een langere mechanische integriteit vertoont in vergelijking met versie 1.0. Van belang is dat de kwalitatieve beoordeling van BVS structuren met behulp van IVUS 20 MHz dient vermeden te worden vanwege zijn slechtere reproduceerbaarheid in vergelijking met OCT. Zowel IVUS

als OCT hebben een goede reproduceerbaarheid om het lumen en stent oppervlak te meten, maar de foutmarge bij IVUS is veel groter als vergeleken met OCT (hoofdstuk 5.3).

MECHANISCHE EIGENSCHAPPEN VAN BIORESORBEERBAE STENTS

Beeldvormende technieken zijn gebruikt om de mechanische eigenschappen van deze stents te bestuderen. In het bijzonder hebben wij de vervormbaarheid en de excentriciteit /symmetrie van de BVS stent onderzocht m.b.v. respectievelijk coronaire angiografie en IVUS. De coronaire vaten die behandeld zijn met deze stents toonden na heronderzoek, 6 maanden tot 2 jaar later, de neiging tot herstel van de coronaire geometrie en staat systole-diaстole bewegingen van de coronairs toe, gelijk aan dat voor implantatie. Dit in tegenstelling tot permanente geïmplanteerde metalen stents, waarvan de coronaire geometrie en systole-diaстole bewegingen van de coronairs gelijk bleven aan die van net na implantatie (hoofdstuk 6.1). In overeenstemming met deze bevindingen heeft de bioresorbeerbare vasculaire stent een verminderde excentriciteits- en een toegenomen symmetrie index, in vergelijking met conventionele metalen stents (hoofdstuk 6.2).

In hoofdstuk 6.3, beschrijven we dat de vasculaire dissensibiliteit van deze gestente coronairen, gemeten door palpography, wordt vermindert. Daarentegen, in tegenstelling tot metalen stents, de gevonden mismatch met de proximale en distale segmenten verdween op termijn, waarschijnlijk veroorzaakt door de bioresorptie en het verdwijnen van de stent welke mogelijke positieve klinische voordelen heeft zoals herstel van de pulsatiliteit van de vaatwand.

STRUCTURELE VERANDERINGEN VAN BIORESORBEERBAAR VASCULAIRE STEIGERS OVERWERK

Het is interessant op te merken dat in tegenstelling tot metalen stents, de structuur van de BVS verandert door de tijd heen. Deze veranderingen kunnen kwalitatief en kwantitatief worden geëvalueerd door IVUS-based-echogeniciteit, OCT en VH.

Met de op IVUS-gebaseerde echogeniciteit metingen, hebben we aangetoond dat wanneer het afbraak proces in beeld wordt gebracht m.b.v. IVUS, individuele cross-sectionele beelden een afnemend grijs-waarde intensiteits niveau van de stent struts over de tijd laat zien, welke kan worden gekwantificeerd door een geautomatiseerde en gevalideerde software programma. Met name de verbeterde mechanische eigenschappen van de BVS versie 1,1 vergeleken met die van versie 1,0 liet een sterk verminderde hoeveelheid veranderingen in de ultrasoon afgeleide parameters zien (zoals bijvoorbeeld veranderingen in hyper-echogenesignalen) na 6 en 12 maanden (15% en 20% respectievelijk), in vergelijking met de eerste generatie BVS (1,0) (hoofdstuk 7.1).

M.b.v. OCT, is onderzocht of de stent goed geëxpandeerd tegen de vaatwand was aangebracht (e.g. geen struts die los in het lumen "hangen") en dat dit ook tijdens vervolgonderzoeken nog het geval was. Tevens is OCT gebruikt om te onderzoeken of de stent struts waren bekleed met nieuw weefsel. Struts die niet tegen de wand aan zaten na implantatie en/of die ter hoogte van de opening van een zijvat waren gepositioneerd, konden in verband worden gebracht met een gebrek aan weefsel dekking tijdens latere vervolgonderzoeken (hoofdstuk 7.2).

Hoewel al deze technieken in staat zijn om veranderingen tijdens het bioresorptie/afbraak proces te tonen, de correlatie tussen hen is slecht. Dit is niet

verwonderlijk, omdat elke techniek is gebaseerd op andere fysische eigenschappen zoals ultrageluid en licht, zodat ze in principe verschillende verschijnselen in beeld brengen (hoofdstuk 7.3).

MORFOLOGISCHE WIJZIGING IN DE CORONAIR NA BVS IMPLANTATIE

IVUS-VH kan worden toegepast voor het analyseren van de veranderingen in de plaque samenstelling van de plaque gelokaliseerd achter de polymere stent struts. Het is bekend dat de aanwezigheid van de stent op in de coronair wordt geïdentificeerd door VH als calcium. We hebben aangetoond dat het mogelijk is om de geïdentificeerde calcium van de stent te excluseren in de VH-analyse en dan de resterende plaque samenstelling te analyseren. Dit heeft geleid tot de bevinding dat de hoeveelheid necrotisch materiaal in de plaque achter de stent aanzienlijk vermindert bij vervolgonderzoeken na 1 jaar (hoofdstuk 8.1 en 8.2)

FUNCTIONELE WIJZIGINGEN IN DE CORONAIR NA BVS IMPLANTATIE

Het belangrijkste voordeel van de bioresorbeerbare stents bestaat uit het zogenoemde vasculaire herstel. Wij onderzochten twee aspecten van deze behandeling met betrekking tot het vermogen van deze stents gerelateerd tot het reageren op vasoactieve middelen en het creëren van een z.g. "dikke kap" op de bovenkant van een dunne kap coronaire plaque.

In hoofdstuk 8.3, tonen we aan dat het vermogen van een BVS gestent coronair segment om te reageren op vasoactieve medicatie, gerelateerd is tot de bioresorptie van de stent als indirect gemeten m.b.v. van veranderingen in het grijswaarde niveau van de stents m.b.v. IVUS (echogeniciteit). Bovendien

werd het herstel van de normale endotheelfunctie in verband gebracht met relatieve kleinere plaques en een kleine hoeveelheid necrotisch materiaal als gemeten bij VH, welke lijkt op het gedrag van een "normale" zieke coronair.

Hoofdstuk 8.4 analyseert de haalbaarheid van een nauwkeurige kwantificering van het genezingsproces na implantatie van de BSV stents, suggererend dat de vorming van een dikke en symmetrische neointima laag, zonder overblijfselen van polymere struts, een "de novo" cap maken die kan zou kunnen worden toegepast om een dunne-kap fibroathroma te verzegelen.

CONCLUSIE

Ik geloof dat dit proefschrift van waarde is om de klinische bruikbaarheid van intracoronaire beeldvormende technieken te begrijpen m.b.t. het bestuderen van de omvang, distributie, morfologie

en de samenstelling van coronaire atherosclerose bij onze patiënten.

Meer in het bijzonder hebben wij onderzocht de belangrijke toegevoegde waarde van NIRS en nieuwe gecombineerde methoden voor het beter te kunnen karakteriseren van hoog risicovolle plaques, waarin mogelijke beeldvormings surrogate eindpunten zouden kunnen worden gebruikt in toekomstige studies.

Daarnaast is in dit proefschrift het genezingsproces na implantatie van een bioresorbeerbare stent onderzocht, welke heeft laten zien dat er zowel morfologische als functionele veranderingen in de vaatwand kan worden bereikt door toepassing van deze stents.

ACKNOWLEDGEMENTS

To my opinion, this is the most important part of a thesis, because each single article would not have been published without the help of a lot of people. For this reason I would like to thank everyone who contributed and helped me in many ways during these last years and I hope I will not forget anyone.

This thesis is the result of a long trip, started in 2008 when I finished my residence in Cardiology. In that period I decided to move to Spain in order to do a fellowship in interventional cardiology, because there were no possibilities of work and research in a university Hospital in my own country. In this decision two persons played an important role: Dominick Angiolillo and Manel Sabaté.

Dear Dominick, since the beginning it was so easy to be friends, because both are from Sicily and both studied in the same university. I still remember the first time I asked you by email some advices about moving to another country and you called me by phone directly from USA, spending more than one hour of your time explaining me everything and introducing me to Manel Sabaté. I admire you as a friend and a scientist and I hope to visit you in USA and to know your beautiful family.

Dear Manel, since our first meeting in the kitchen of the cath lab, writing on napkins, you transferred me your enthusiasm for work and research. When you proposed me to work with you, I did not have any doubts to say yes. Thank you for supporting me continuously and thank you for giving me the great opportunity to work with you in Barcelona: you are the best chief of a Cardiology department whom a young interventional cardiologist, like me, can have. In 2009 you proposed me to complete my "learning curve" making a research fellowship in Rotterdam, under the supervision of professor Serruys, your mentor. After met him, I understood why you are a so incredible person.

Dear professor Serruys, it has been a real privilege and honor to work with you. I admire your outstanding intelligence and your incredible memory, which allows you to remember all your 1500 and more publications. To see you working and to be able to learn from you has been a great opportunity in my career. I feel proud to be your fellow. You have an incredible mind, projected already to the future, able to see possible problems and to solve them already. During my staying in Rotterdam, I appreciate a lot your philosophy of work: it is unbelievable to see how hard you work every day, more than every fellow. Thanks for all the days, nights, week-end spent in your attic, teaching me how to think from a scientific point of view and how to write a paper. I kept all the versions of the papers written in Rotterdam with your corrections and in the end they are more than 1500 pages! When I came the first time to Rotterdam to make the interview with you, you told me something that I will never forget. "To be successful you need three things: first intelligence, not so difficult, as most of the people have it; second to be a hard worker; third, the most important, to be collaborative and friendly with your colleagues". I remembered these words during all the two years of my fellowship and you were absolutely right: without my colleagues and friends I would not have reached any of the papers of this thesis. I would like also to thank your wife, Danielle, who has been always very kind with me.

Dear Hector, last but not least, there are no words to express to you my gratitude for the time spent together during the two years in Rotterdam. Since the beginning you have been more than a colleague. Thank you for all the time spent together working on a paper, but also drinking beers, talking about everything and having dinner with delicious Italian and Mexican dishes with your family. Thank also to your wife, Lulu, and your son, Andres, for

having given me always the feeling to be part of a family. You have been a real friend and you helped me more than you can imagine. I am very happy that you have been able to be my co-promotor: you deserve it for the all the help you gave me. I want to tell you that you can count on me for everything and I am waiting you in Barcelona.

Dear Josep, I consider you as one of my best friends. I have to thank you for the numerous afternoons spent together, trying to make a social life in Rotterdam, drinking a beer or watching the Barcelona football matches. I am happy that after Rotterdam we are now working in the same city and I am sure we will build up together beautiful projects. I am happy for you and Mercé for your coming baby.

Dr. Jung Ho, dear Dr. Heo, thank you for introducing me into the Korean culture and also for all the Photoshop tip & tricks. It was a real pleasure to work with you, sharing ideas, statistical analyses and papers. I hope we will meet each other over the world in future cardiology congresses.

Dear Yoshi, it was a pleasure to guide you in the south part of Italy, during the 1-day congress in Catanzaro, and to share with you some trips to Bruxelles. Do not forget your promise to come to Barcelona to visit me. I wish you the best for your decision to work in Europe: I am sure you will find a good place to work.

Dear Chris and Elina, it has been a pity that we started sharing time together only during my last months in Rotterdam, because I really enjoyed it. I am happy for your work in Greece and I hope to visit you in the future.

Dear Bill, many thanks for your patience. I never saw you angry and I think this is a very good quality. I wish you the best for your thesis and work.

Dear Vasim, many thanks for all your English lessons! I wish you will finish your thesis soon.

Dear Roberto, it was nice to share the flat with you and especially to have someone with whom

I could speak Italian at home. I wish you the best for your career.

Dear Maria, many thanks for introducing me to OCT analysis. I was impressed by your ability to organize everything in life. Let see if you will organize a trip to Spain.

Dear Lorenz, it was a pleasure to meet you in Rotterdam. Your wine is the best I ever drank! I am sure our collaboration will continue in future projects.

Dear Dr. Li, many thanks for your Buddhism lessons. I still have with me your paper saying "Compassion has no enemy". Barcelona is waiting for you.

I would like also to thank, among the fellows, Giovanna Sarno: thank you for your support during my first days in Rotterdam and for all the skype sessions! I am very happy for your work in Sweden and also for your coming baby.

Dear Paul, thank you for helping me to solve all the "Eurointervention" issues. You are a real nice person with a lot of interests out of work and I always enjoyed talking with you, despite your very difficult English! You are welcome for a Barca-Madrid

Dear Sylvie, you always made superb plans for Friday or Saturday evening either in Rotterdam or all over the world, such as San Francisco or Paris. Excellent! Many thanks for your friendship. I hope you will come soon to Barcelona in order that I can organize for you a beautiful visit of the city.

Dear Marie-Angele, a special thank for accepting to be my paranymph. I want also to thank you for helping me in Cardialysis and for introducing me to the Dutch life.

I would like also to thank Gerrit-Anne van Es for giving me the opportunity to stay in Cardialysis and all the people whom I met in Cardialysis, Ravindra, Jamal, Monique, Jeanette, Shiv, Marco, etcetc for helping me in many ways and for being always very kind with me.

I would like also to express my gratitude to all the interventional cardiologists from the Thoraxcenter, Robert Jan van Geuns, Evelyn Regar, Peter de Jaegere, Carl Schultz, Nicolas van Mieghem, Eric Duckers and Felix Zijlstra for helped me to develop and carry our my projects and to the committee members of my thesis. Thank also to Jurgen, the best technician I ever met, for all the coffee at 7.00 am talking about IVUS and OCT.

A special mention should be made to my dear friend Nico Bruining. Dear Nico, to work with you has been a great opportunity during my staying in Rotterdam. There are a lot of things for which I have to thank you. I enjoyed a lot working in your office on the echogenicity, talking about every thing and also eating your candies. I hope our collaboration and friendship will continue. A special thank also for the translation of the conclusion of my thesis. You are very welcome in Barcelona, together with Paul, for a Barca-Madrid.

Finally I should thank my Italian, Mexican and Spanish friends in Rotterdam, with whom I shared my few free time in Rotterdam. A special thanks to Alexia and Brunella, my closest Italian friends in Rotterdam: I hope we will keep in touch in the future. Thank also to Laura, Pierluigi, Antonio, Liz, Chuy, Dasha and I hope to not forget anyone.

I wish to thank Victoria Martin-Yuste, who really represents a person who supported me since my first day in Barcelona in 2008, during my staying in Rotterdam and still today. Dear Vicky, I think you

are one of the best interventional cardiologist I know, not only for your technical skills, but also for your ability to think about the best for patients. I consider a privilege to work now with you and to can still learn from you.

Another special person whom I have to thank is Gemma Berga. Dear Gemma, we both remember the first time we met: I was not talking Spanish yet, you were not talking Italian, nevertheless we started to be friends. There has not been a single day during my staying in Rotterdam in which we did not talk during the night. Thank also to your family, Jose Luis, Aina and the "new entry" Pau to be always very kind with me.

Dear Luis, thank you for being the only friend coming to visit me in Rotterdam. I know that you still remember your first time biking in the Netherlands under the rain and freezing. I wish you and your girlfriend Irma the best for your life together.

I wish also to thank Monica Masotti and all the nurse staff of the Hospital Clinic in Barcelona to have welcomed me in the best way possible.

Finally I have to thank my family, my father Nunzio, my mother Anna Maria and my sister Rita for continuously supporting me in every decision. Sapete meglio di me quanto è stato difficile andare a vivere in un altro paese; nonostante tutto, mi avete sempre dato un appoggio incondizionato nel lasciarmi fare quello che io volevo. Anche se può sembrare banale, voglio dirvi che siete le persone che più voglio bene al mondo. Grazie!

CURRICULUM VITAE

NAME BRUGALETTA, Salvatore
DATE OF BIRTH 24/02/1979
PLACE OF BIRTH Ragusa, Italy
CITIZENSHIP Italian
EMAIL: sabrugaletta@gmail.com
LANGUAGES Italian (fluent), Spanish (fluent), English (fluent), Catalan (Intermediate)

EDUCATION AND DEGREES

- 1997-2003: Catholic University of the Sacred Heart
Faculty of Medicine
Degree in Medicine and Surgery
Rome, Italy
- 2003-2007: Catholic University of the Sacred Heart
Faculty of Medicine
Degree in Cardiology
Rome, Italy
- 2008-2009: Clinical and Research Fellowship in Interventional Cardiology
Hospital de Sant Pau
Barcelona, Spain
- 2009-2011 PhD Research Fellowship in "Molecular and Cellular Cardiology"
Catholic University of the Sacred Heart
Promotor: prof. Filippo Crea
Rome, Italy
- 2010-2011 PhD Research Fellowship
Erasmus Medical Center, COEUR PhD program
Promotor: prof. Patrick W. Serruys
Rotterdam, The Netherlands

LIST OF PUBLICATIONS

1. "C-reactive protein and other anti-inflammatory biomarkers as predictors of outcome following acute coronary syndromes". Abbate A, Biondi-Zoccai GGL, **Brugaletta S**, Liuzzo G, Biasucci LM. *Seminars in Vascular Medicine* 2003;3:375-84
2. "Novel anti-inflammatory effect of statins: reduction of CD4⁺CD28^{null} T lymphocytes frequency in patients with unstable angina". **Brugaletta S**, Biasucci LM, Pinnelli M, Biondi-Zoccai G, Digiannuario G, Trotta G, Liuzzo G, Crea F. *Heart* 2006;92:249-250
3. "Modulation of CD4⁺CD28^{null} T Lymphocytes by Tumor Necrosis Factor- α Blockade in Patients with Unstable Angina". Rizzello V, Liuzzo G, **Brugaletta S**, Rebuzzi AG, Biasucci LM, Crea F. *Circulation* 2006;113:2272-2277
4. "Safety of colony stimulating factor in acute myocardial infarction (the RIGENERA study)". Leone AM, Galiuto L, Giannico MB, **Brugaletta S**, Garramone B, De Stefano V, Liuzzo G, Calcagni ML, Cirillo F, Giordano A, Niccoli G, Biasucci LM, Crea F. *Heart* 2006;92:249-250
5. "Persistent Activation of Nuclear Factor Kappa-B Signaling Pathway in Patients With Unstable Angina and Elevated Levels of C-Reactive Protein: Evidence for a Direct Proinflammatory Effect of Azide and Lipopolysaccharide-Free C-Reactive Protein on Human Monocytes Via Nuclear Factor Kappa-B Activation". Liuzzo G, Santamaria M, Biasucci LM, Narducci M, Colafrancesco V, Porto A, **Brugaletta S**, Pinnelli M, Rizzello V, Maseri A, Crea F. *J Am Coll Cardiol* 2007;49:185-194
6. "Usefulness of granulocyte-colony-stimulating factor in patients with a large anterior wall acute myocardial infarction to prevent left ventricular remodelling (the rigenera study)". Leone AM, Galiuto L, Garramone B, Rutella S, Giannico MB, **Brugaletta S**, Perfetti M, Liuzzo G, Porto I, Burzotta F, Niccoli G, Biasucci LM, Leone G, Rebuzzi AG, Crea F. *Am J Cardiol* 2007;100:397-403
7. "1059G/C Polymorphism within the exon 2 of the C-reactive protein gene: relation to C-reactive protein levels and prognosis in unstable angina". Rizzello V, Liuzzo G, Di Giannuario G, Trabetti E, **Brugaletta S**, Santamaria M, Piro M, Pignatti PF, Maseri A, Biasucci LM, Crea F. *Coronary Artery Disease*. 2007;18:533-8
8. "Unusual CD4⁺CD28^{null} T Lymphocytes and Recurrence of Acute Coronary Events." Liuzzo G, Biasucci LM, Trotta G, **Brugaletta S**, Pinnelli M, Digiannuario G, Rizzello V, Rebuzzi AG, Rumi C, Maseri A, Crea F. *J Am Coll Cardiol* 2007;50:1450-8
9. "Cystatin C is associated with an increased coronary atherosclerotic burden and a stable plaque phenotype in patients with ischemic heart disease and normal glomerular filtration rate". Niccoli G, Conte M, Bona RD, Altamura L, Siviglia M, Dato I, Ferrante G, Leone AM, Porto I, Burzotta F, **Brugaletta S**, Biasucci LM, Crea F. *Atherosclerosis*. 2008;198:373-80
10. "Sirolimus, Paclitaxel and Zotarolimus eluting stents to treat bifurcated lesions: a 7-month clinical outcome comparison". **Brugaletta S**, Burzotta F, Trani C, Todaro D, Talarico G, Porto

- I, Leone AM, Niccoli G, Mazzari MA, Mongiardo R, Schiavoni G, Crea F. *Minerva Cardioangiol.* 2008;56:35-42
11. "Prediction of functional capacity by low-dose dobutamine stress echocardiography in chronic heart failure". Natali R, Lotrionte M, Marchese N, DiGiannuario G, **Brugaletta S**, Pisanello C, Commerci G, Savino M, Lombardo A, Forni F, Vigna C, Loperfido F. *Minerva Cardioangiol* 2008;56:277-85
 12. "Effect of intensive vs standard statin therapy on endothelial progenitor cells and left ventricular function in patients with acute myocardial infarction: statins for re generation after acute myocardial infarction and PCI (STRAP) trial". Leone AM, Rutella S, Giannico MB, Perfetti M, Zaccone V, **Brugaletta S**, Garamone B, Niccoli G, Porto I, Liuzzo G, Biasucci LM, Bellesi S, Galiuto L, Leone G, Rebuzzi AG, Crea F. *Int J Cardiol* 2008;130:457-62.
 13. "Pharmacogenetic modulation of platelet inhibition". **Brugaletta S**, Porto I. *Current Pharmacogenomics & Personalized Medicine* 2008;6(3):171-184
 14. "Outcome of patients treated by a novel thin-strut cobalt-chromium stent in the drug-eluting stent era: Results of the SKICE (Skylor in real world practice) registry". Burzotta F, Trani C, Todaro D, Mazzari MA, Porto I, De Vita M, **Brugaletta S**, Coroleu SF, Niccoli G, Leone AM, Giammarinaro M, Mongiardo R, Schiavoni G, Crea F. *Catheter Cardiovasc Interv* 2009;73:457-65
 15. "Drug eluting stent and endothelial dysfunction: what to measure, how to measure it and when to measure it". **Brugaletta S**, Martin-Yuste V, Sabaté M. *Circulation Cardiovascular Interventions.* 2009;2:e1
 16. "Zotarolimus for the treatment of coronary artery disease : pathophysiology, drug-eluting stent design, clinical evaluation and future perspective". **Brugaletta S**, Burzotta F, Sabaté M. *Expert Opinion of Pharmacotherapy. Expert Opin Pharmacother* 2009;10:1047-58
 17. "Diabetes mellitus : a prothrombotic state implications for outcome after coronary revascularization". Cola C, **Brugaletta S**, Yuste VM, Campos B, Angiolillo DJ, Sabaté M. *Vasc Health Risk Manag* 2009;5:101-19
 18. "Evaluation of a strategy for treating bifurcated lesions by single or double stenting based on the Medina Classification". Todaro D, Burzotta F, Trani C, **Brugaletta S**, De Vita M, Talarico GP, Giammarinaro M, Porto I, Leone AM, Niccoli G, Mongiardo R, Mazzari MA, Schiavoni G, Crea F. *Rev Esp Cardiol* 2009;62:606-614
 19. "Intensifying platelet inhibition with tirofiban in poor responders to aspirin, clopidogrel, or both agents undergoing elective coronary intervention. Results from the double-blind, prospective, randomized tailoring treatment with tirofiban in patients showing resistance to aspirin and/or resistance to clopidogrel study". Valgimigli M, Campo G, De Cesare N, Meliga E, Vranckx P, Furgieri A, Angiolillo DJ, Sabaté M, Hamon M, Repetto A, Colangelo S, **Brugaletta S**, Parriniello G, Percoco G, Ferrari R. *Circulation* 2009;119:3215-22
 20. "Delayed neutrophil apoptosis in patients with unstable angina : relation to C-reactive protein and recurrence of instability". Biasucci LM, Liuzzo G, Giubilato S, Della Bona R, Leo M, Pinnelli M, Severino A, Gabriele M, **Brugaletta S**, Piro M, Crea F. *Eur Heart J* 2009;30:2220-5

21. "Immunomodulator Activity of 3-hydroxy-3-methylglutaryl-CoA inhibitors". Smaldone C, **Brugaletta S**, Pazzano V, Liuzzo G. *Cardiovasc hematomol Agents Med Chem* 2009;7:279-94
22. "Role of the CD14 C(-260)T promoter polymorphism in determining the first clinical manifestation of coronary artery disease". Rizzello V, Liuzzo G, Trabetti E, Di Giannuario G, **Brugaletta S**, Santamaria M, Piro M, Boccanelli A, Pignatti PF, Biasucci LM, Crea F. *J Cardiovasc Med (Hagerstown)* 2010;11:20-5
23. "Long-term clinical outcome based on aspirin and clopidogrel responsiveness status after elective percutaneous coronary intervention". A 3T/2R Trial substudy. Campo G, Fileti L, de Cesare N, Meliga E, Fugieri A, Russo F, Colangelo S, **Brugaletta S**, Ferrari R, Valgimigli M. *J Am Coll Cardiol* 2010;56:1447-55.
24. "Background, incidence and predictors of antiplatelet therapy discontinuation during the first year after drug eluting stent implantation". I Ferreira-Gonzalez, J Marsal, A Ribera, G Permanyer-Miralda, B Garcia-del-blanco, G Martí, P Cascant, V Martín-Yuste, **S Brugaletta**, M Sabaté, F Alfonso, M Capote, JM De-la-torre, M Ruiz-Lera, D Sanmiguel, M Cardens, B Pujol, J A Baz, A Iniguez, R Trillo, O Gonzalez-Bejar, J Casanova, J Sanchez-Gila, D Garcia-Dorado. *Circulation* 2010;122:1017-1025.
25. "Paradoxical preservation of vascular function in severe obesity". Biasucci LM, Graziani F, Rizzello V, Liuzzo G, Guidone C, De Caterina AR, **Brugaletta S**, Mingrone G, Crea F. *Am J Med* 2010;123:727-734
26. "Endothelial progenitor cell capturing stent and short dual antiplatelet therapy in patients on chronic anti-vitamin k regimen undergoing percutaneous coronary interventions : long-term outcomes of a single centre registry". Martín-Yuste V, **Brugaletta S**, Ferreira-Gonzalez I, Cola C, Alvarez-Contreras L, De antonio M, Martí V, Garcia-Picart J, Sabate M. *Eurointervention* 2011;6:831-7
27. "Ethica award 2010: Antonio Colombo". Serruys PW, **Brugaletta S**. *Eurointervention* 2010;6:431
28. "Temporal changes of coronary artery plaque located behind the struts of the everolimus eluting bioresorbable vascular scaffold". **S Brugaletta**, HM Garcia-Garcia, S Garg, J Gomez-Lara, R Diletti, Y Onuma, RJ van Geuns, D McClean, D Dudek, L Thuesen, B Chevalier, S. Windecker, R Whitbourn, C Dorange, K Miquel-Herbert, K Sudhir, JA Ormiston, PW Serruys. *International Journal of cardiovascular imaging* 2010 Epub ahead of print.
29. "Relationship between palpography and virtual histology in patients with acute coronary syndromes: a sub-analysis from the PROSPECT trial". **Brugaletta S**, Garcia-Garcia HM, Serruys PW, Maehara A, Farooq V, Mintz GS, de Bruyne B, Marso SP, Verheye S, Dudek D, Hamm CW, Farhat N, Schiele F, McPherson H, Lerman A, Moreno PR, Grip L, Templin B, Morel MA, van Es GA, Stone GW. *J Am Coll Card Imaging* 2012;5:519-27
30. "CROSSER As First choice for crossing Totally occluded coronary arteries (CRAFT Registry): Focus on conventional angiography and computer tomography angiography predictors of success". HM Garcia-Garcia, **S Brugaletta**, CAG van Mieghem, N Gonzalo, R Diletti, J Gomez-Lara, F Airoldi, M Carlino, DTavano, A Chieffo, M Montorfano, I Michev, A Colombo,

- M van der Ent, PW Serruys. *Eurointervention* 2011;7:480-6.
31. "Morphology of coronary artery lesions assessed by virtual histology intravascular ultrasound tissue characterization and fractional flow reserve". **S Brugaletta**, HM Garcia-Garcia, ZJ Shen, J Gomez-Lara, R Diletti, G Sarno, N Gonzalo, W Wijns, F Alfonso, PW Serruys. *Int J Cardiovasc Imaging* 2011;28:221-8
32. "Letter to the editor regarding the article "Vascular reactivity and flow characteristics of radial artery and long saphenous vein coronary bypass grafts: a 5-year follow-up". S Brugaletta, V Martin-Yuste, M Sabaté. *Circulation* 2011;123:e421
33. "Comparison of plaque prolapse in consecutive patients treated with Xience V and Taxus Liberté stents". ZJ Shen, **S Brugaletta**, HM Garcia-Garcia, J Lighthart, J Gomez-Lara, R Diletti, G Sarno, K Witberg, PW Serruys. *Int J Cardiovasc Imaging* 2012;28:23-31
34. "Morphological and functional evaluation of the bioresorption of the bioresorbable everolimus vascular scaffold using IVUS, echogenicity and vasomotion testing at two year follow-up: a patient level insight into the ABSORB A clinical trial. G Sarno, N Bruining, Y Onuma, S Garg, **S Brugaletta**, S de Winter, E Regar, L Thuesen, D Dudek, S Veldohf, C Dorange, HM Garcia-Garcia, JA Ormiston, PW Serruys. *Int J Cardiovasc Imaging* 2012;28:51-8
35. "Baseline C-Reactive protein serum levels and in-stent restenosis pattern after m-TOR inhibitors drug-eluting stent implantation" G Niccoli, M Conte, N Cosentino, D Todaro, **S Brugaletta**, RA Montone, S Minelli, F Fracassi, V Galiffa, AM Leone, F Burzotta, I Porto, C Trani, F Crea. *J Invasive Cardiol* 2011;23:16-20
36. "Assessment of drug-eluting stents and bioresorbable stents by grayscale IVUS and IVUS-based imaging modalities". **S Brugaletta**, J Ribamar Costa Jr, HM Garcia-Garcia. *Int J Cardiovasc Imaging* 2011;27:239-48
37. "Comparison between the first and second generation bioresorbable vascular scaffolds: a six month virtual histology study". **S Brugaletta**, HM Garcia-Garcia, R Diletti, J Gomez-Lara, Y Onuma, E Shin, RJ van Geuns, B de Bruyne, D Dudek, L Thuesen, B Chevalier, D McClean, S Windecker, R Whitbourn, C Dorange, S Veldhof, R Rapoza, K Sudhir, N Bruining, J Ormiston, PW Serruys. *Eurointervention* 2011;6:1110-6
38. "Optical coherence tomography (OCT) of overlapping bioresorbable scaffolds: from bench-work to clinical application". V Farooq, Y Onuma, M Radu, T Okamura, J Gomez-Lara, **S Brugaletta**, B Gogas, RJ van Geuns, E Regar, C Schultz, S Windecker, T Lefevre, B Brueren, J Powers, L Perkins, R Rapoza, R Virmani, H Garcia-Garcia, PW Serruys. *Eurointervention* 2011;7:386-399.
39. "Assessment of coronary atherosclerosis progression and regression at bifurcations using combined IVUS and OCT". R Diletti, HM Garcia-Garcia, J Gomez-Lara, **S Brugaletta**, JJ Wyrzykowska, N van Ditzhuijzen, R van Geuns, E Regar, G Ambrosio, PW Serruys. *J Am Coll Cardiol imaging* 2011;4:774-80
40. "Serial analysis of the malapposed and uncovered struts of the new generation of everolimus-eluting bioresorbable scaffold using optical coherence tomography". J

- Gomez-Lara, M Radu, **S Brugaletta**, V Farooq, R Diletti, S Windecker, L Thuesen, D McClean, J Koolen, R Whitbourn, D Dudek, PC Smits, E Regar, S Veldhof, R Rapoza, JA Ormiston, HM Garcia-Garcia, PW Serruys. *J Am Coll Cardiol Intervention* 2011;4:992-1001
41. "Differences in neointimal thickness between the adluminal and the abluminal sides of malapposed struts in a bioresorbable vascular scaffold at 6 months follow-up: indirect evidence about the role of shear stress in healing after stenting". JL Gutierrez-Chico, F Gijssen, E Regar, L Thuesen, D McClaen, S Windecker, D Dudek, R Whitbourn, **S Brugaletta**, JA Ormiston, PW Serruys. *J Am Coll Cardiol Intervention* In press
42. "Comparison of in vivo eccentricity and symmetry indices between metallic stents and bioresorbable vascular scaffolds: insights from the ABSORB and SPIRIT trials". **S Brugaletta**, J Gomez-Lara, R Diletti, V Farooq, RJ van Geuns, B de Bruyne, D Dudek, HM Garcia-Garcia, JA Ormiston, PW Serruys. *Catheter Cardiovasc Interv* 2012;79:219-28
43. "Near-infrared spectroscopy, virtual histology and grayscale IVUS for characterization of atherosclerosis in patients undergoing coronary angiography". **S Brugaletta**, HM Garcia-Garcia, PW Serruys, S de Boer, J Ligthart, J Gomez-Lara, K Witberg, R Diletti, J Wykzykowska, RJ van Geuns, C Schultz, E Regar, HJ Duckers, N van Mieghem, P de Jaeger, SP Madden, JE Muller, AFW van der Steen, W van der Giessen, E Boersma. *J Am Coll Cardiol Imaging* 2011;4:647-55.
44. "A comparative assessment by optical coherence tomography of the performance of the first and second generation of the everolimus-eluting bioresorbable vascular scaffolds". J Gomez-Lara, S Brugaletta, R Diletti, S Garg, Y Onuma, B Gogas, RJ van Geuns, C Dorange, S Veldhof, R Rapoza, R Whitbourn, S Windecker, HM Garcia-Garcia, E Regar, PW Serruys. *Eur Hear J* 2011;32:294-304
45. "Expansion of CD4+CD28null T-lymphocytes in diabetic patients: exploring new pathogenetic mechanisms of increased cardiovascular risk in diabetes mellitus". S Giubilato, G Liuzzo, **S Brugaletta**, D Pitocco, F Graziani, C Smaldone, RA Montone, V Pazzano, D Pedicino, LM Biasucci, G Ghirlands, F Crea. *Eur Hear J* Epub ahead of print
46. "A guide to interpreting and assessing the performance of prediction models". V Farooq, **S Brugaletta**, P Vrancks, PW Serruys. *Eurointervention* 2011;6:909-912
47. "Quantitative multi-modality imaging analysis of a fully bioresorbable stent: a head-to-head comparison between QCA, IVUS and OCT". JL Gutierrez-Chico, PW Serruys, C Girasis, S Garg, Y Onuma, **S Brugaletta**, H Garcia-Garcia, GA van Es, E Regar. *Int J Cardiovasc Imaging* 2011 [epub ahead of print]
48. "Evaluation of in-stent restenosis in the APPROACH trial (assessment on the prevention of progression by Rosiglitazone on atherosclerosis in diabetes patients with cardiovascular history)". HM Garcia-Garcia, S Garg, S Brugaletta, G Morocutti, RE Ratner, NS Kolatkar, BG Kravitz, DM Miller, C Huang, RW Nesto, PW Serruys; The APPROACH study group. *Int J Cardiovasc Imaging* 2011 epub ahead of print
49. "Agreement and reproducibility of grey-scale intravascular ultrasound and optical

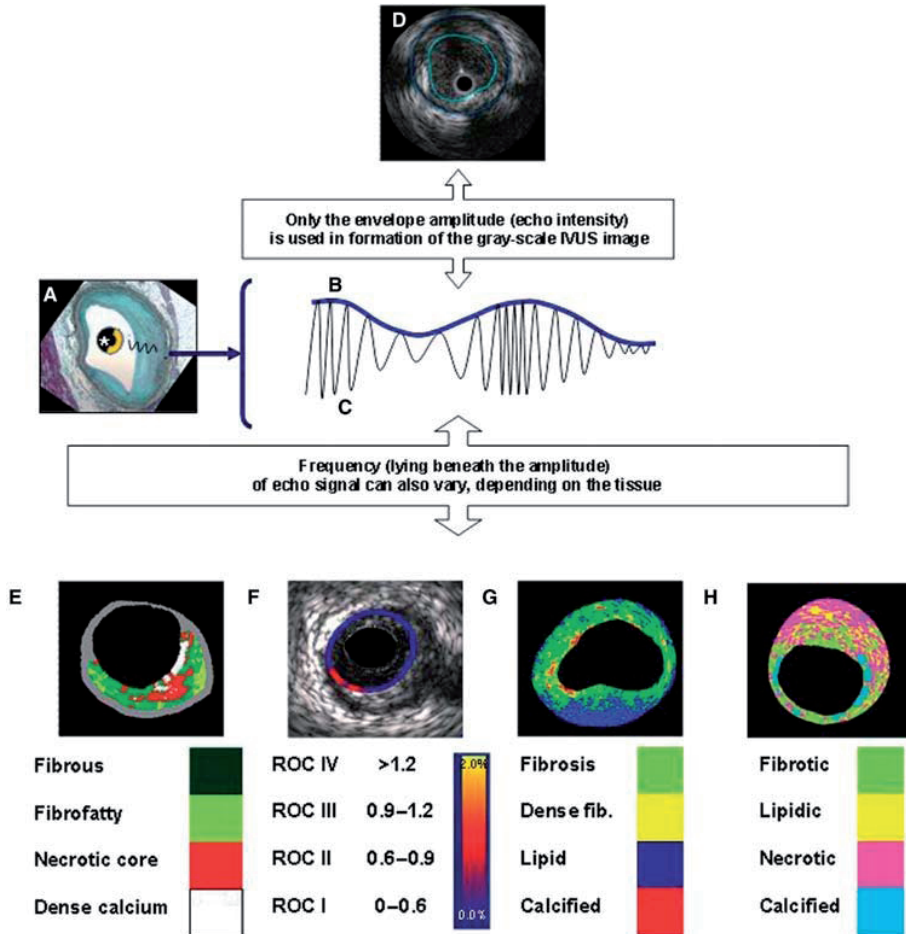
- coherence tomography for the analysis of the bioresorbable vascular scaffold" Gomez-Lara J, **Brugaletta S**, Diletti R, Gogas BD, Farooq V, Onuma Y, Gobbens P, van Es GA, Garcia-Garcia HM, Serruys PW. *Catheter Cardiovasc Interv* 2011. Epub ahead of print
50. "Impact of body mass index on the five-year outcome of patients having percutaneous coronary interventions with drug-eluting stents". Sarno G, Raber L, Onuma Y, Garg S, **Brugaletta S**, van Domburg RT, Pilgrim T, Pfaffli N, Wenaweser P, Windecker S, Serruys PW. *Am J Cardiol* 2011;108:195-201
51. "Usefulness of the Tornus Catheter in non-dilatable coronary chronic total occlusion" Martin-Yuste V, Alvarez-Contreras L, Cola C, **Brugaletta S**, Garcia-Picart J, Marti-Claramunt V, Masotti M, Sabate M. *Rev Esp Cardiol* 2011;64:935-8
52. "Healing of a coronary artery dissection detected by intravascular ultrasound and optical coherence tomography". Diletti R, Garcia-Garcia HM, **Brugaletta S**, Gomez-Lara J, Serruys PW, Regar E. *Eurointervention* 2011;7:288-9
53. "Cardiovascular risk in obesity: different activation of inflammation and immune system between obese and morbidly obese subjects" Graziani F, Cialdella P, Liuzzo G, Basile E, **Brugaletta S**, Pedicino D, Leccesi L, Guidone C, Iaconelli A, Mingrone G, Biasucci LM, Crea F. *Eur J Intern Med* 2011;22:418-23
54. "Angiographic geometric changes of the lumen arterial wall after bioresorbable vascular scaffold and metallic platform stents at 1-year follow-up". Gomez-Lara J, **Brugaletta S**, Farooq V, van Geuns RJ, De Bruyne B, Windecker S, McClean D, Thuesen L, Dudek D, Koolen J, Whitbourn R, Smits PC, Chevalier B, Morel MA, Dorange C, Veldhof S, Rapoza R, Garcia-Garcia HM, Ormiston JA, Serruys PW. *J Am Coll Cardiol Interv* 2011;4:789-99 IF
55. "Utilizing risk scores in determining the optimal revascularization strategy for complex coronary artery disease". Farooq V, **Brugaletta S**, Serruys PW. *Curr Cardiol Rep* 2011;13:415-23
56. "New insights into the coronary artery bifurcation hypothesis-generating concepts utilizing 3-dimensional optical frequency domain imaging". Farooq V, Serruys PW, Heo JH, Gogas BD, Okamura T, Gomez-Lara, **Brugaletta S**, Garcia-Garcia HM, van Geuns RJ. *JACC Cardiovasc Interv* 2011;4:921-31
57. "3D reconstructions of optical frequency domain imaging to improve understanding of conventional PCI". Farooq V, Okamura T, Gogas BD, Heo JH, Magro M, Gomez-Lara J, **Brugaletta S**, Onuma Y, Radu M, Garcia-Garcia HM, Serruys PW. *JACC Cardiovasc Imaging* 2011;4:1044-6
58. "Emergent versus elective percutaneous stent implantation in the unprotected left main: long-term outcomes from a single-center registry". Martin-Yuste V, Alvarez-Contreras L, Brugaletta S, Ferreira-Gonzalez I, Cola C, Garcia-Picart J, Marti V, Sabate M. *J Invasive Cardiol* 2011;23:392-7
59. "Tools & Techniques: risk stratification and diagnostic tools in left main stem intervention" Farooq V, Heo JH, Raber L, **Brugaletta S**, Radu M, Gogas BD, Diletti R, Onuma Y, Garcia-Garcia HM, Serruys PW. *Eurointervention* 2011;7:747-53

60. "Angiographic maximal lumen diameter and appropriate deployment of the everolimus-eluting bioresorbable vascular scaffold as assessed by optical coherence tomography: an ABSORB cohort B trial substudy". Gomez-Lara J, Diletti R, **Brugaletta S**, Onuma Y, Farooq V, Thuesen L, McClean D, Koolen J, Ormiston JA, Windecker S, Whitbourn R, Dudek D, Dorange C, Veldhof S, Rapoza R, Regar E, Garcia-Garcia HM, Serruys PW. *Eurointervention* 2011; Epub ahead of print.
61. "The SYNTAX Score and SYNTAX-based Clinical risk scores" Farooq V, **Brugaletta S**, Serruys PW. *Semin Thorac Cardiovasc Surg* 2011;23:99-105
62. "Analysis of 1 year virtual histology changes in coronary plaque located behind the struts of the everolimus eluting bioresorbable vascular scaffold". **Brugaletta S**, Gomez-Lara J, Garcia-Garcia HM, Heo JH, Farooq V, van Geuns RJ, Chevalier B, Windecker S, McClean D, Thuesen L, Whitbourn R, Meredith I, Dorange C, Veldhof S, Rapoza R, Ormiston JA, Serruys PW. *Int J Cardiovasc Imaging* 2011, epub ahead of print.
63. "Rationale and design of the EXAMINATION trial: a randomized comparison between everolimus-eluting stents and cobalt-chromium bare metal stents in ST-elevation myocardial infarction" Sabate M, Cequier A, Iniguez A, Serra A, Hernandez-Antolin R, Mainar V, Valgimigli M, Tsepili M, den Heijer P, Benthécourt A, Vazquez N, **Brugaletta S**, Backx B, Serruys PW. *Eurointervention* 2011;7:977-84
64. "Adequate antiplatelet regimen in patients on chronic anti-vitamin K treatment undergoing percutaneous coronary intervention" **Brugaletta S**, Martin-Yuste V, Ferreria-Gonzalez I, Cola C, Alvarez-Contrearras L, Antonio MD, Garcia-Moll X, Garcia-Picart J, Marti V, Ballcells-Iranzo J, Sabate M. *World J Cardiol* 2011;3:367-73
65. "Head to head comparison of optical coherence tomography, intravascular ultrasound echogenicity and virtual histology for the detection of changes in polymeric struts over time: insights from the ABSORB trial". **Brugaletta S**, Gomez-Lara J, Bruining N, Radu MD, van Geuns RJ, Thuesen L, McClean D, Koolen J, Windecker S, Whitbourn R, Oberhauser J, Rapoza R, Ormiston JA, Garcia-Garcia HM, Serruys PW. *Eurointervention* 2011. Epub ahead of print.
66. "Risk of target lesion failure in relationship to vessel angiographic geometry and stent conformability using the second generation of drug-eluting stents". Gomez-Lara J, Heo JH, **Brugaletta S**, Garg S, Garcia-Garcia HM, van Geuns RJ, Silber S, Windecker S, Serruys PW. *Am Heart J* 2011;162:1069-79
67. "Head-to-head comparison of the neointimal response between metallic and bioresorbable everolimus eluting scaffolds using optical coherence tomography". Gomez-Lara J, **Brugaletta S**, Farooq V, Onuma Y, Diletti R, Windecker S, Thuesen L, McClean D, Koolen J, Whitbourn R, Dudek D, Smits PC, Chevalier B, Regar E, Veldhof S, Rapoza R, Ormiston JA, Garcia-Garcia HM, Serruys PW. *JACC Cardiovasc Interv.* 2011;4:1271-80
68. "Serial In vivo Intravascular ultrasound-based Echogenicity changes of everolimus-eluting bioresorbable vascular scaffold during the first 12 months after implantation. Insights from the ABSORB B trial." **Brugaletta S**,

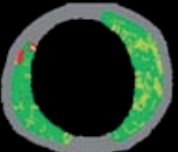
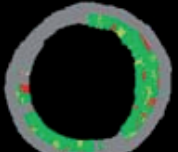
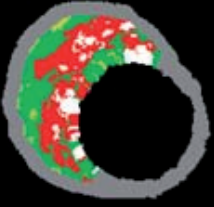
- Gomez-Lara J, Serruys PW, Farooq V, van Geuns RJ, Thuesen L, Dudek D, Koolen J, Chevalier B, McClean D, Windecker S, Smits PC, de Bruyne B, Whitbourn R, Meredith I, van Domburg RT, Sihan K, de Winter S, Veldhof S, Miquel-Hebert K, Rapoza R; Garcia-Garcia HM, Ormiston JA, Bruining N. *JACC Cardiovasc Interv* 2011;4:1281-9
69. "Factors determining success in percutaneous revascularization of chronic total coronary occlusion: multidetector computer tomography analysis". Martin-Yuste V, Barros A, Leta R, Ferreira I, **Brugaletta S**, Pujadas S, Carreras F, Pons G, Cinca J, Sabate M. *Rev Esp Cardiol* 2012 Epub ahead of print
70. "Endothelial and smooth muscle cells dysfunction distal to recanalized chronic total coronary occlusions and the relationship with the collateral connection grade". **Brugaletta S**, Martin-Yuste V, Padro T, Alvarez-Contreras L, Gomez-Lara J, Garcia-Garcia HM, Cola C, Liuzzo G, Masotti M, Crea F, Badimon L, Serruys PW, Sabate M. *J Am Coll Cardiol Intervention* 2012;5:170-8
71. "Lipid core burden index and Framingham score: can a systemic risk score predict lipid core burden in non-culprit coronary artery?" Heo JH, Garcia-Garcia HM, **Brugaletta S**, de Boer S, Simsek C, Farooq V, Boersma E, Serruys PW. *Int J Cardiol* 2012. Epub ahead of print.
72. "Correlation between kidney function and near-infrared spectroscopy derived lipid-core burden index score of a non-intervened coronary artery segment". Simsek C, Garcia-Garcia HM, **Brugaletta S**, de Boer SP, Magro M, Duckers HJ, van Geuns RJ, Boersma E, Serruys PW. *Int J Cardiol* 2012 Epub ahead of print.
73. "Circumferential evaluation of the neointima by optical coherence tomography after ABSORB bioresorbable vascular scaffold implantation: can the scaffold cap the plaque?" **Brugaletta S**, Radu MD, Garcia-Garcia HM, Heo JH, Farooq V, Girasis C, van Geuns RJ, Thuesen L, McClean D, Chevalier B, Windecker S, Koolen J, Rapoza R, Miquel-Hebert K, Ormiston J, Serruys PW. *Atherosclerosis* 2012;221:106-12
74. "Reproducibility of intravascular ultrasound iMAP for radiofrequency data analysis: implications for design of longitudinal studies". Heo JH, **Brugaletta S**, Garcia-Garcia HM, Gomez-Lara J, Ligthart JM, Witberg K, Magro M, Shin ES, Serruys PW. *Catheter Cardiovasc Interv* 2011 Epub ahead of print.
75. "Three-dimensional optical frequency domain imaging in conventional percutaneous coronary intervention: the potential for clinical application". Farooq V, Gogas BD, Okamura T, Heo JH, Magro M, Gomez-Lara J, Onuma Y, Radu MD, **Brugaletta S**, van Bochove G, van Geuns RJ, Garcia-Garcia HM, Serruys PW. *Eur Heart J* 2011 Epub ahead of print.
76. "Contemporary and evolving risk scoring algorithms for percutaneous coronary intervention". Farooq V, **Brugaletta S**, Serruys PW. *Heart* 2011;97:1902-13
77. "Plaque compositional syntax score: combining angiography and lipid burden in coronary artery disease". **Brugaletta S**, Magro M, Simsek C, Heo JH, de Boer S, Ligthart J, Witberg K, Farooq V, van Geuns RJ, Schultz C, van Mieghem N, Regar E, Zijlstra F; Duckers HJ, de Jaegere P, Muller JE, van der Steen AF; Boersma E, Garcia-Garcia HM, Serruys PW. *JACC Cardiovasc Imaging* 2012;5:S119-21

-
78. "Distance of Lipid-core rich plaques from the ostium by NIRS in nonculprit coronary arteries". **Brugaletta S**, Garcia-Garcia HM, Serruys PW, Gomez-Lara J, de Boer S, Ligthart J, Witberg K, Simsek C, van Geuns RJ, Schultz C, Duckers HJ, van Mieghem N, de Jaegere P, Madden SP, Muller JE, van der Steen AF, Boersma E, van der Giessen WJ, Zijlstra F, Regar E. *JACC Cardiovasc Imaging* 2012;5:297-9
79. "Everolimus-eluting ABSORB bioresorbable vascular scaffold: present and future perspectives". **Brugaletta S**, Garcia-Garcia HM, Onuma Y, Serruys PW. *Expert Rev Med Devices* 2012. Epub ahead of print.
80. "Reproducibility of qualitative assessment of stent struts coverage by optical coherence tomography". **Brugaletta S**, Garcia-Garcia HM, Gomez-Lara J, Radu MD, Pawar R, Khachabi J, Bruining N, Sabaté M, Serruys PW. *Int J Cardiovasc Imaging* 2012 epub ahead of print.

Color section



Chapter 1.1 Figure 1. Intravascular ultrasound signal is obtained from the vessel wall (A). Grayscale intravascular ultrasound imaging is formed by the envelope (amplitude) (B) of the radiofrequency signal (C). By grayscale, atherosclerotic plaque can be classified into four categories: soft, fibrotic, calcified and mixed plaques. (D) shows a cross-sectional view of a grayscale image. The blue lines limit the actual atheroma. The frequency and power of the signal commonly differ between tissues, regardless of similarities in the amplitude. From the backscatter radiofrequency data different types of information can be retrieved: virtual histology (E), palpography (F), integrated backscattered intravascular ultrasound (G) and iMAP (H). Virtual histology is able to detect four tissue types: necrotic core, fibrous, fibrofatty and dense calcium. Plaque deformability at palpography is reported in strain values, which are subsequently categorized into four grades according to the Rotterdam Classification (ROC). The tissues characterized by integrated backscattered intravascular ultrasound are lipidic, fibrous and calcified; iMAP detects fibrotic, lipidic, necrotic and calcified. (from *Eur Heart J* 2010;31:2456-69)

Lesion Type	
<p>Adaptative Intimal Thickening (AIT) <600 μm of intima thickness for <20% of the circumference</p>	
<p>Pathological Intimal Thickening (PIT) \geq600 μm thickness for >20% of the circumference with FF >15%, and no confluent NC or DC</p>	
<p>Fibrotic Plaque (FT) Dominant FT and no confluent NC or DC</p>	
<p>Fibrocalcific Plaque (FC) >10% Confluent DC with no confluent NC</p>	
<p>Fibroatheroma (FA) >10% Confluent NC not at the lumen on three consecutive frames</p>	
<p>Thin Cap Fibroatheroma (TCFA) >10% Confluent NC at the lumen on three consecutive frames</p>	

Chapter 1.1 Figure 2. Virtual histology plaque types. (from Eur Heart J 2010;31:2456-69).

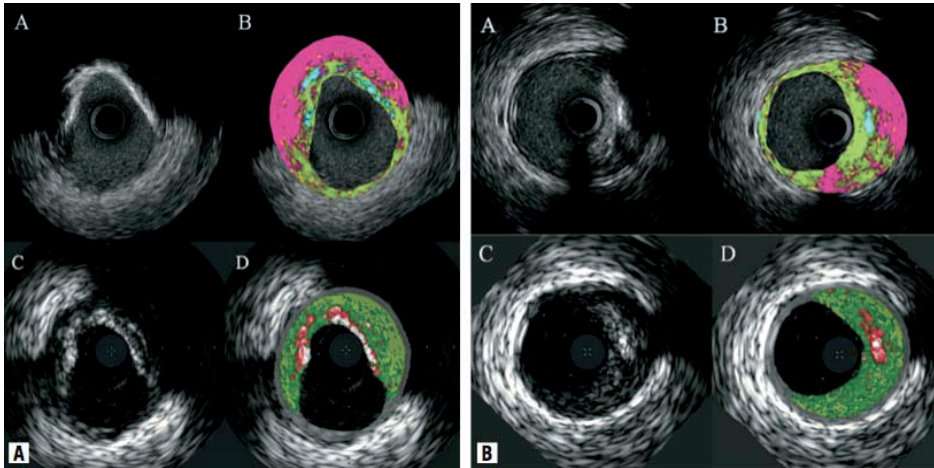
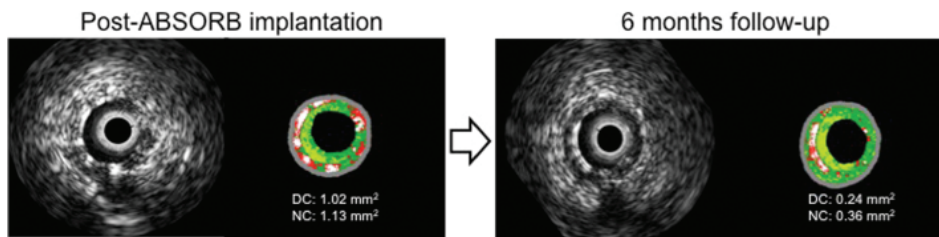
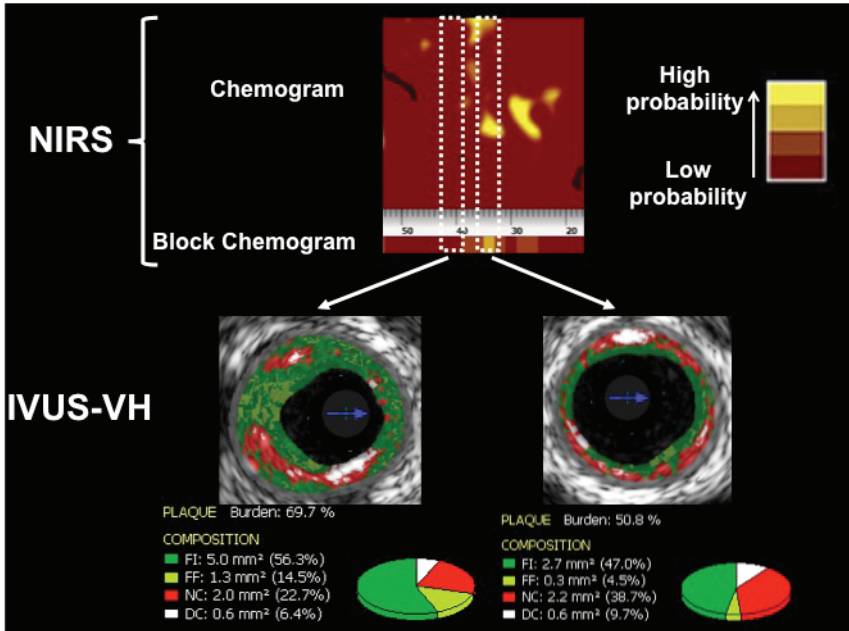


Figure 4. Corresponding cross-section of iMap (top) and VH images (bottom). iMap shows large amounts of necrotic tissue behind calcium, while with VH the same area is reported as fibrous or fibrofatty tissue. In panel B, iMAP shows necrotic tissue because also of the wire artifact. (from Eurointervention 2011;6:1017-1019).

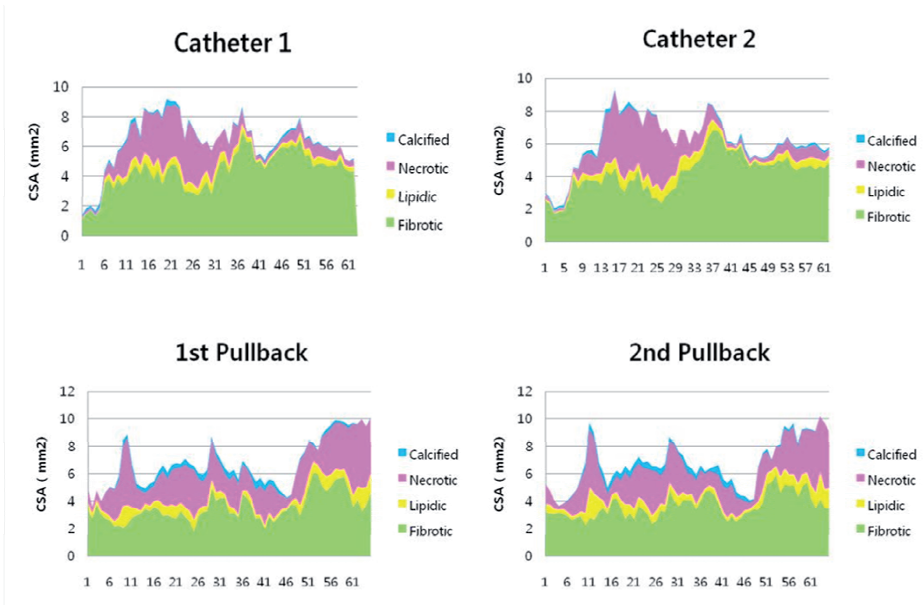


Chapter 1.1 Figure 5. IVUS-VH recognizes the polymeric struts of the ABSORB scaffold as dense calcium (DC), surrounded by a read halo of necrotic core (NC). At follow-up, a reduction in DC and NC can be appreciated. In order to pick up all the struts, the lumen contour has been drawn surrounding the catheter, according to the Shin's method.

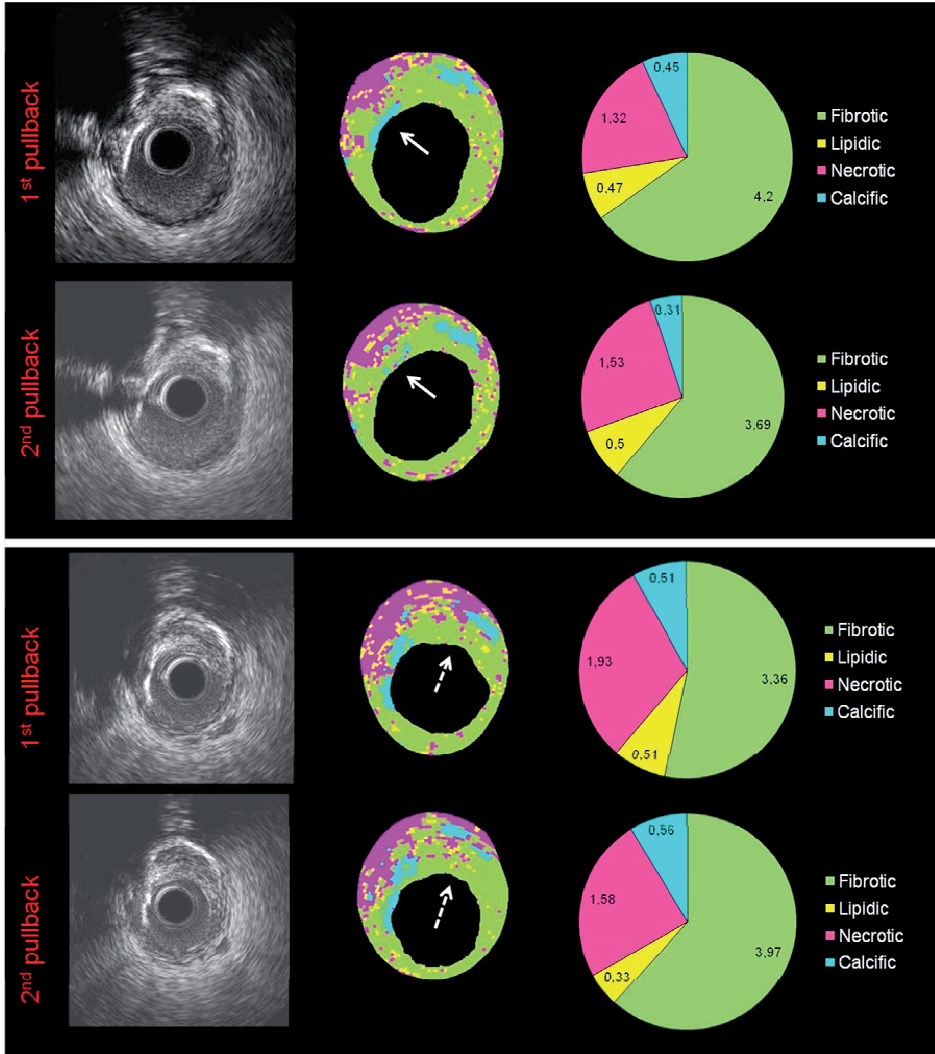


Chapter 1.1 Figure 7. Near infra-red spectroscopy displays the probability of lipid core plaque in a false color scale from red (low probability) to yellow (high probability). In this example, two VH-necrotic core rich plaques are displayed with two different colors on the NIRS output.

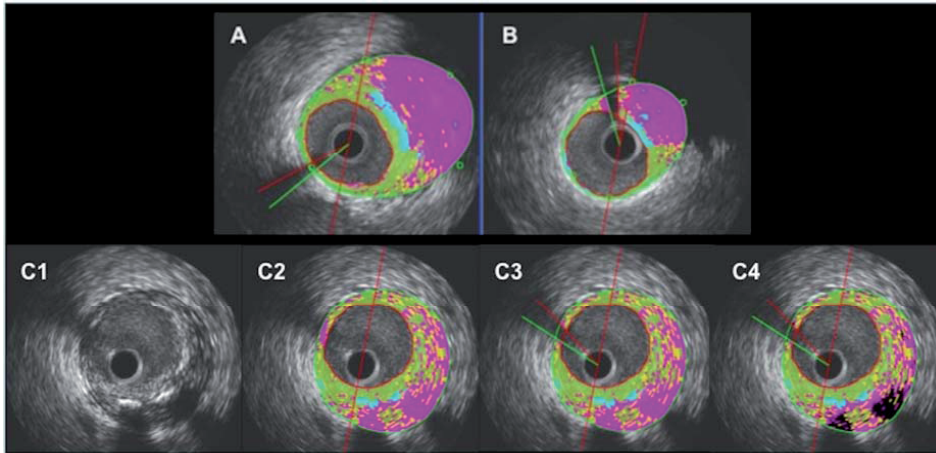
mal thickening; TCFA = thin-cap fibroatheroma.



Chapter 1.2 Figure 4. Sequential plotting of a matched ROI interrogated with two different catheters (on the top) or with two different pullbacks (on the bottom). The mean Cross Sectional area(y axis) of each plaque component is color-coded (calcium: blue, necrotic: pink, lipidic: yellow, and fibrotic: green). These figures show examples of the impact of different catheters of pullbacks on compositional measurements. ROI = region of interest.



Chapter 1.2 Figure 5. Examples of the impact of two different pullbacks acquired with the same catheter on the calcium (white continuous arrows on the top panel) and necrotic core (white dotted arrows on the bottom panel) detection. Note the difference in terms of brightness between the two pullbacks.

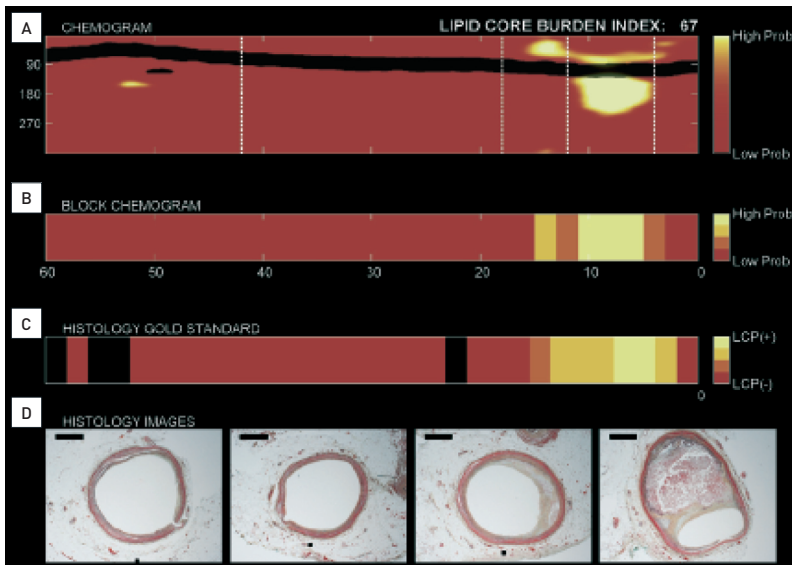


Chapter 1.2 Figure 6. The information lost due to the wire shadow is depending on where the shadow is located. If the shadow is projected on the coronary plaque, a bigger part of the plaque is excluded from the analysis (**B**), as compared if the shadow is projected on a part of the vessel wall without plaque (**A**). The software used for the analysis allows the exclusion of the wire shadow from the tissue characterization (**C1-C3**) and/or the exclusion of the tissue underneath calcification, where an adequate spectral analysis is not possible due to the drop of the signal (**C4**).

FIGURE 2

A NIRS scan correlates well to histologic findings in coronary artery from a 65-year-old male with a history of MI

(A) Chemogram image indicating artery wall lipid content (x axis – pullback in millimetres; y axis – rotation in degrees). Each pixel is marked with red for low probability and yellow for high probability of lipid core plaque of interest (LCP). The lipid core burden index (top right) indicates amount of lipid in scanned artery on a 0-1,000 scale. **(B)** Summary (block chemogram) of LCP presence at 2 mm intervals in 4 probability categories. **(C)** Map of histologic classifications (yellow – LCP; light orange – small or thick-capped fibroatheroma; dark orange – intimal xanthoma and pathologic intimal thickening; red – all other types). **(D)** Movat cross-sections from locations along the artery (dotted lines). Black bars denote 1 mm. Image interpretation: The chemogram shows prominent lipid core signal at 2 to 6 mm, occupying 180°. The block chemogram shows that the strongest LCP signals extend 5 to 11 mm. The NIRS signals at 18 and 42 mm correctly indicate absence of LCP.

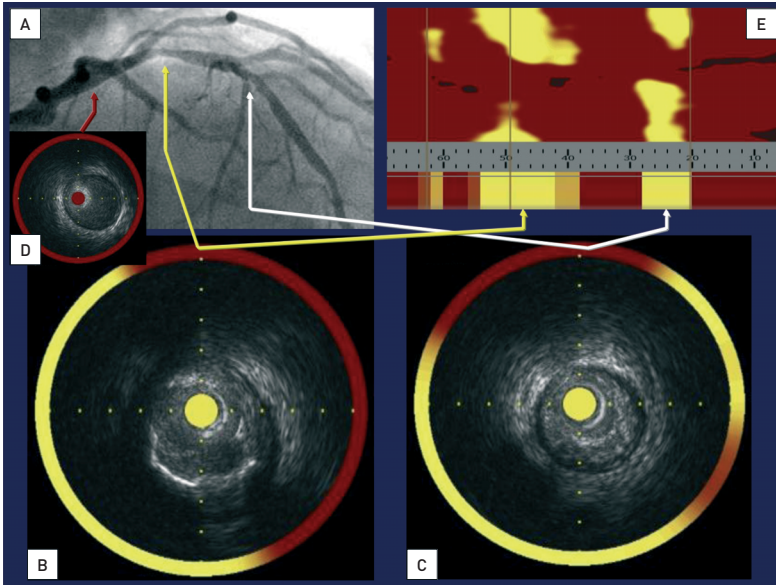


Chapter 2.1

FIGURE 3

Correlation between angiography, IVUS and chemogram obtained with the NIRS-IVUS catheter

Simultaneously obtained co-registered NIRS-IVUS images demonstrating angiographically "mild" disease in the proximal LAD (A, yellow arrow), with a more severe stenosis in the mid-LAD (A, white arrow). In the NIRS-IVUS chemogram, a 2nd block chemogram (E, top) documents that both lesions contain large LCP. Cross-sectional IVUS views (B, C, D), with the chemogram data overlaid in a halo while the block chemogram colour value is portrayed in the central catheter artifact (bottom). IVUS reveals the proximal LAD lesion (B) is a LCP with ulceration and the mid-lesions is a bulky LCP with tight stenosis.

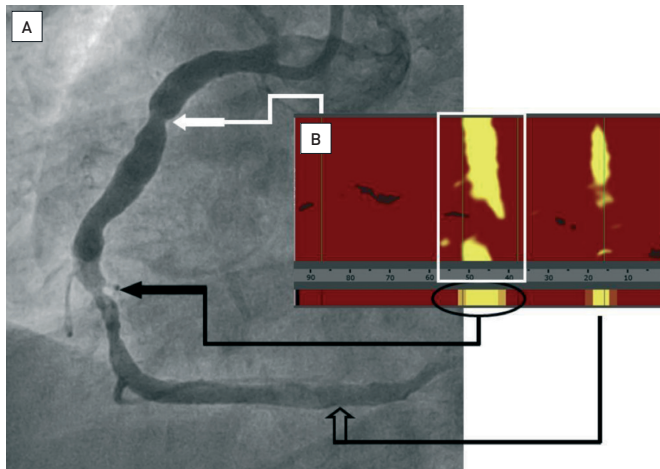


Chapter 2.1

FIGURE 4

Correlation angiogram and chemogram

Angiogram (A) and chemogram (B) showing no LCP in a proximal moderate stenosis (solid white arrow), a large, extensive LCP at the stenotic culprit plaque (solid black arrow), and a small LCP in a distal non-stenotic location (open arrow). PCI resulted in abrupt no-reflow associated

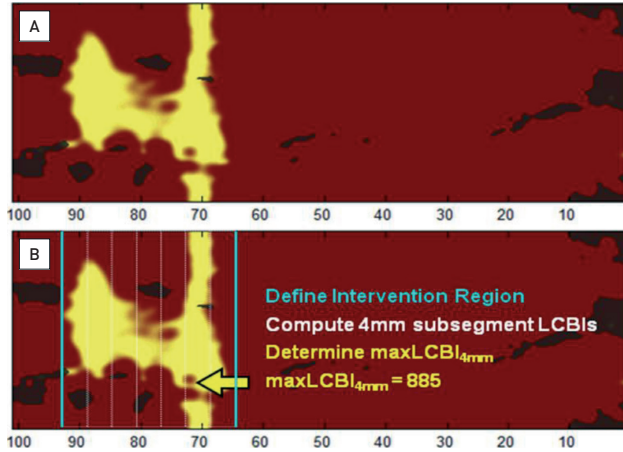


Chapter 2.1

FIGURE 5

Illustration of methodology for determination of the maximum 4 mm sub-segment LCBI ($\text{maxLCBI}_{4\text{mm}}$)

(A) The chemogram displays the NIRS findings obtained during rotation and pullback of the imaging element within the coronary artery of a patient. The x-axis represents mm of pullback, and the y-axis represents degrees of rotation from zero to 360. Yellow indicates a high probability that LCP is present at the interrogated site. **(B)** $\text{maxLCBI}_{4\text{mm}}$ is determined by defining the intervention region, computing LCBI for all 4 mm sub-segments within the intervention region, and identifying the maximum LCBI sub-segment. [Goldstein et al. *Cir Cardiovasc Intervent* in press]

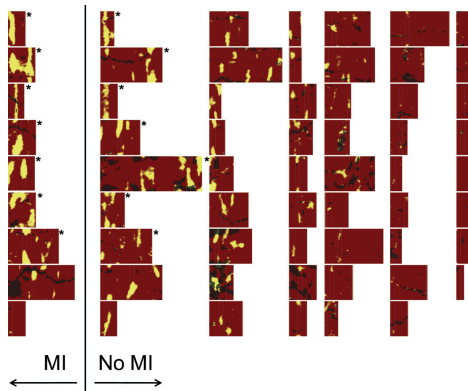


Chapter 2.1

FIGURE 6

A mosaic of the 62 study chemogram intervention zones

All patients had a coronary stenosis requiring stenting. Chemograms from patients experiencing a periprocedural myocardial infarction (MI) are shown on the left and those without on the right. Chemograms with $\text{maxLCBI}_{4\text{mm}} \geq 500$ are indicated with an asterisk.

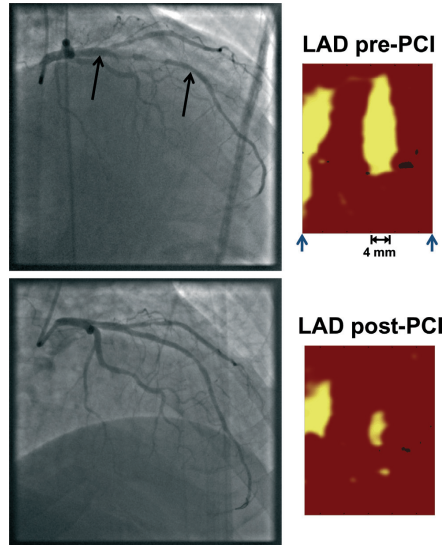


Chapter 2.1

FIGURE 7

Pre and post percutaneous coronary intervention (PCI) angiogram frames and chemograms for a patient experiencing a periprocedural myocardial infarction (MI)

The black arrows indicate the location on the angiogram of the proximal and distal boundaries of the PCI location and correspond to the boundaries of the chemogram segment. Pre-PCI $\text{maxLCBI}_{4\text{mm}}$ was 591 at the region indicated by the 4 mm mark. The post-PCI chemogram shows substantial reduction in LCP ($\text{maxLCBI}_{4\text{mm}}$ reduced to 189 in the matched region). [Goldstein et al. *Circ Cardiovasc Intervent* in press].



Chapter 2.1

FIGURE 8

Acute stent thrombosis of a DES edge implanted in a not fully covered LCP. [Jang Circ Img]

Acute Stent Thrombosis

63 y.o. male with MI

Recurrent pain eight hours post stenting

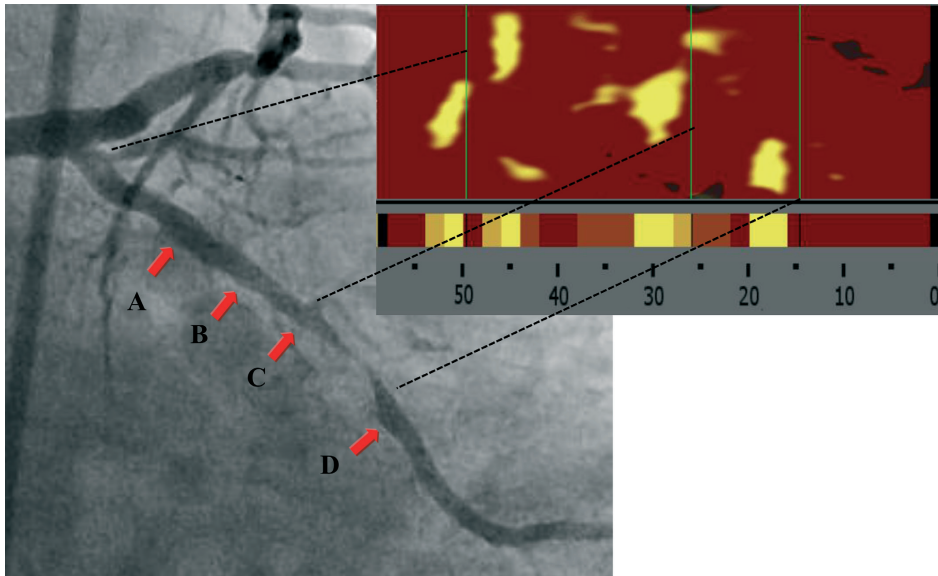
The proximal end of the stent that thrombosed is located in a lipid-core plaque.

Proximal

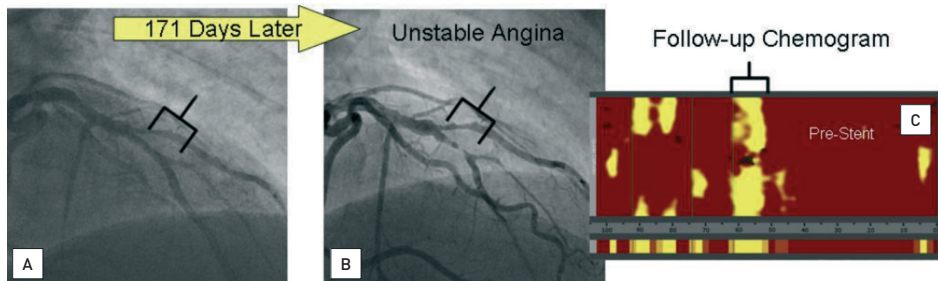
Data courtesy of Dr. I.K. Jang Massachusetts General Hospital

FIGURE 9**Use of NIRS to determine length of vessel to stent**

Severe circumflex stenosis between C and D with corresponding chemogram documenting LCP. Contiguous proximal plaque, though not severely narrowed, also contains LCP [A-B-C].

**Chapter 2.1****FIGURE 10****Chemogram of a lesion that has progressed in a patient with unstable angina**

(A) Baseline angiogram from a 59 year old male undergoing PCI in the RCA showing little to no angiographic evidence of disease in the LAD. (B) 171 day follow-up angiogram after presentation with unstable angina showing progression to near total occlusion. (C) Pre-stent chemogram showing high longitudinal and angular extent LCP very likely to also have been present at baseline.

**Chapter 2.1**

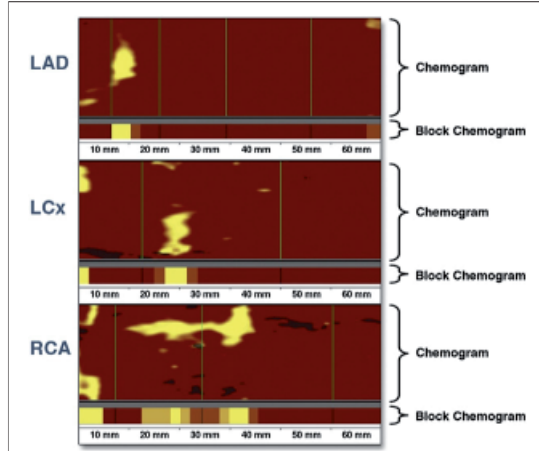


Figure 2. Examples of Distribution of LCP

The presence of LCP is indicated as yellow, 2-mm-long block chemograms, in the 3 coronary arteries, from the coronary ostium (left) up to 60 mm distally. Abbreviations as in Figure 1.

Chapter 2.2

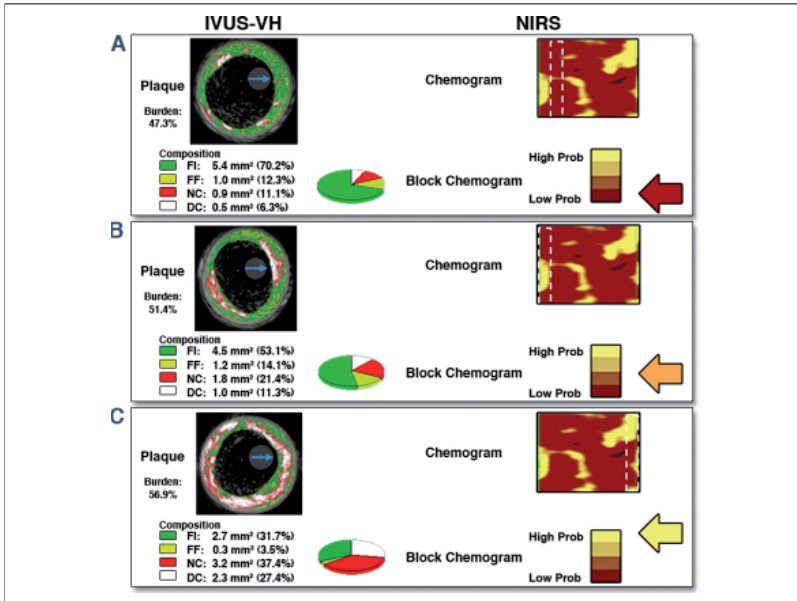
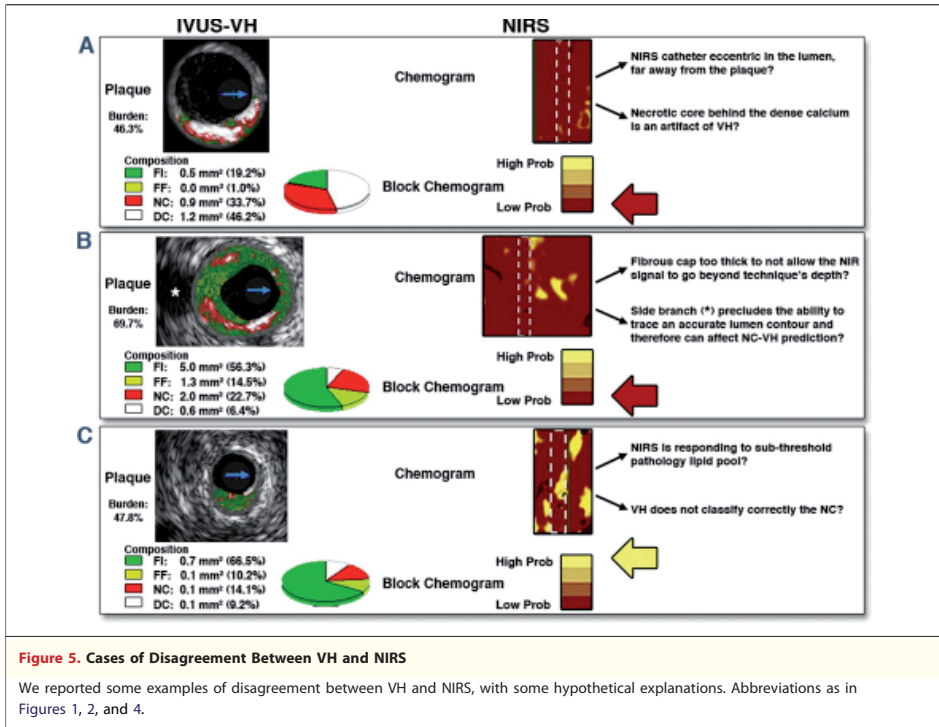


Figure 4. Cases of Agreement Between VH and NIRS

(A) There is no confluent NC in the VH that correlates with a low probability of lipid content by near-infrared spectroscopy (NIRS). (B) A VH plaque with moderate amount of NC (from 7 to 9 o'clock) that is confluent in close proximity to the lumen. This correlates with intermediate probability of lipid by NIRS. (C) Large confluent area of VH-NC from 7 to 9 o'clock next to a severe calcified region that correlates with a "yellow" NIRS plaque representing high probability for lipid content. DC = dense calcium; FF = fibrofatty tissue; FI = fibrous tissue; other abbreviations as in Figures 1 and 2.

Chapter 3.1



Chapter 3.1

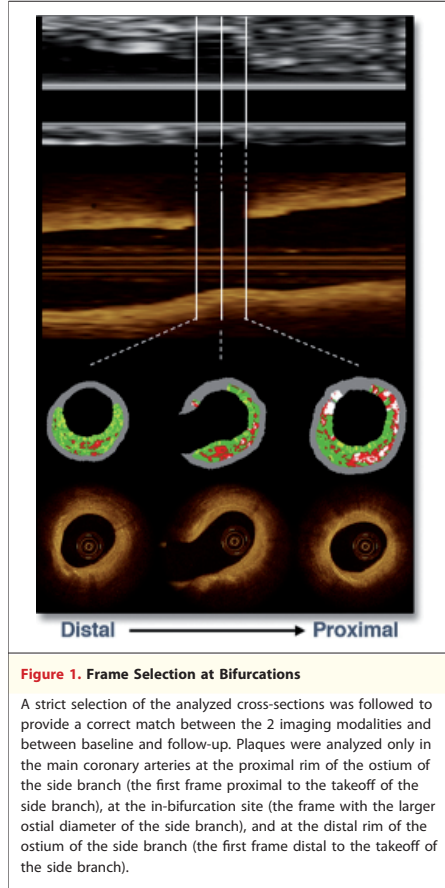


Figure 1. Frame Selection at Bifurcations

A strict selection of the analyzed cross-sections was followed to provide a correct match between the 2 imaging modalities and between baseline and follow-up. Plaques were analyzed only in the main coronary arteries at the proximal rim of the ostium of the side branch (the first frame proximal to the takeoff of the side branch), at the in-bifurcation site (the frame with the larger ostial diameter of the side branch), and at the distal rim of the ostium of the side branch (the first frame distal to the takeoff of the side branch).

Chapter 3.2

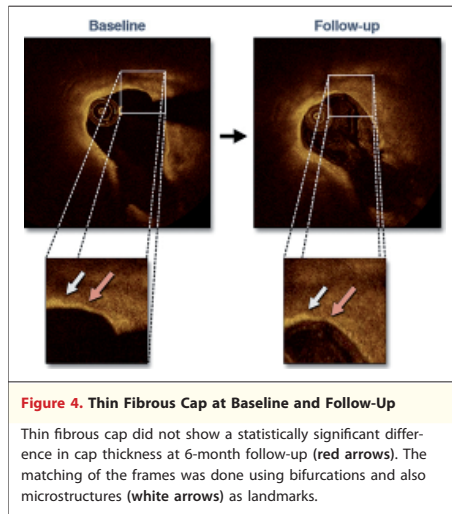
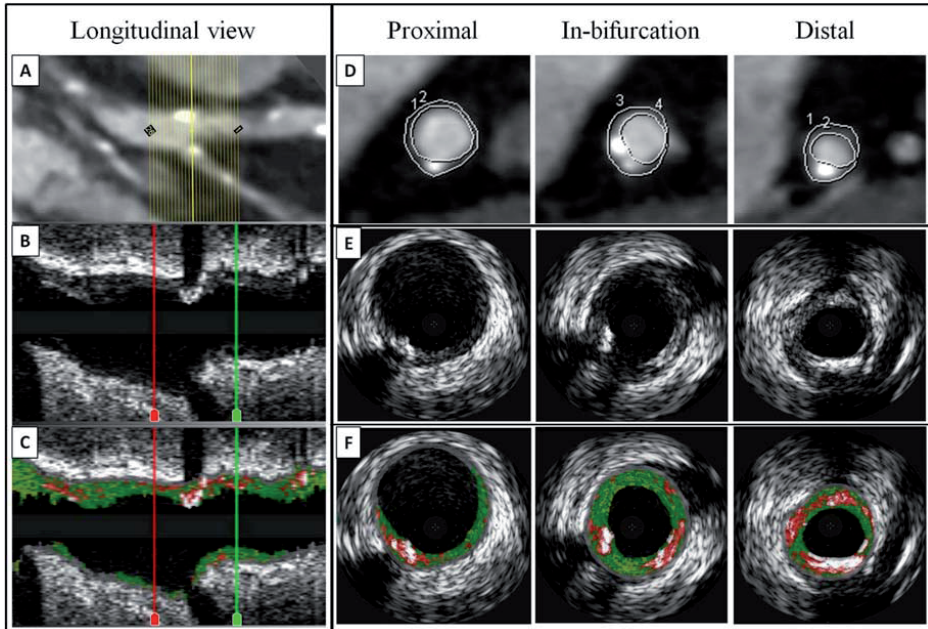


Figure 4. Thin Fibrous Cap at Baseline and Follow-Up

Thin fibrous cap did not show a statistically significant difference in cap thickness at 6-month follow-up (red arrows). The matching of the frames was done using bifurcations and also microstructures (white arrows) as landmarks.

Chapter 3.2



Chapter 3.3 Figure 2. Bifurcation matching and analysis by MDCT and IVUS-VH.

To ensure correct matching of the bifurcations with the 2 techniques, anatomic landmarks and characteristic calcifications were used. Longitudinal vessel view by MDCT (A), grayscale IVUS (B) and virtual histology (C). Examples of corresponding analyzed cross-sections (panels D-F) in the proximal, in-bifurcation and distal segment. IVUS-VH, intravascular ultrasound-virtual histology; MDCT, multidetector computed tomography.

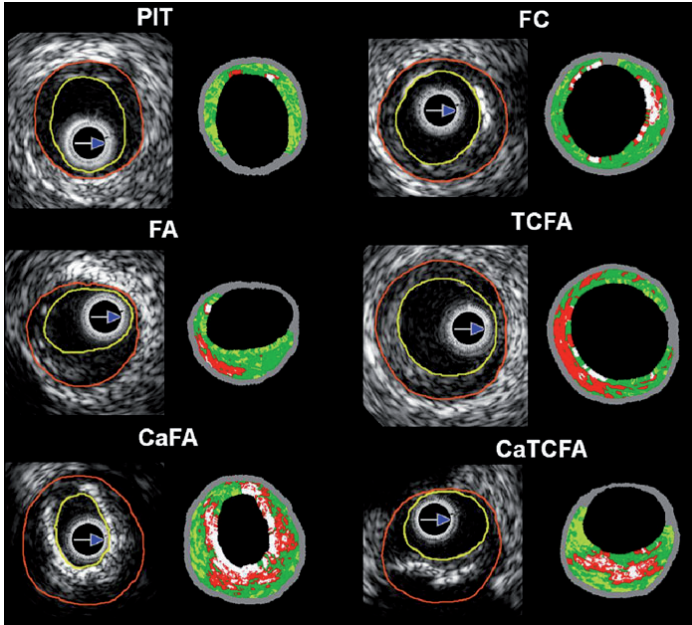


Fig. 1 Examples of various type of VH-plaque found in the analysis with the corresponding IVUS appearance. Lumen contour (yellow line) and vessel contour (red line) are shown. In the VH images, necrotic core is coded as red, dense calcium as white, fibrous tissue as dark green and fibrofatty tissue as

light green. PIT pathological intimal thickening, FC fibrocalcific plaque, FA fibroatheroma, TCFA thin-cap fibroatheroma, CaFA calcified fibroatheroma, CaTCFA calcified thin-cap fibroatheroma

Chapter 3.4

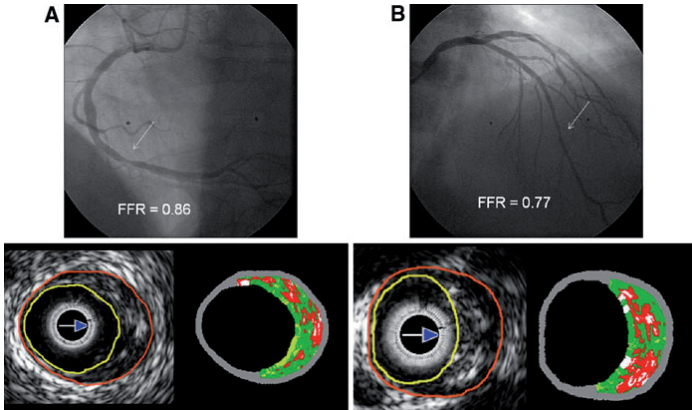


Fig. 2 Examples of two different lesions (white arrows) with a FFR > 0.80 (panel A) and ≤ 0.80 (panel B), both showing a FA VH-plaque type. In the IVUS images red and yellow contours indicate vessel and lumen contours, respectively

Chapter 3.4

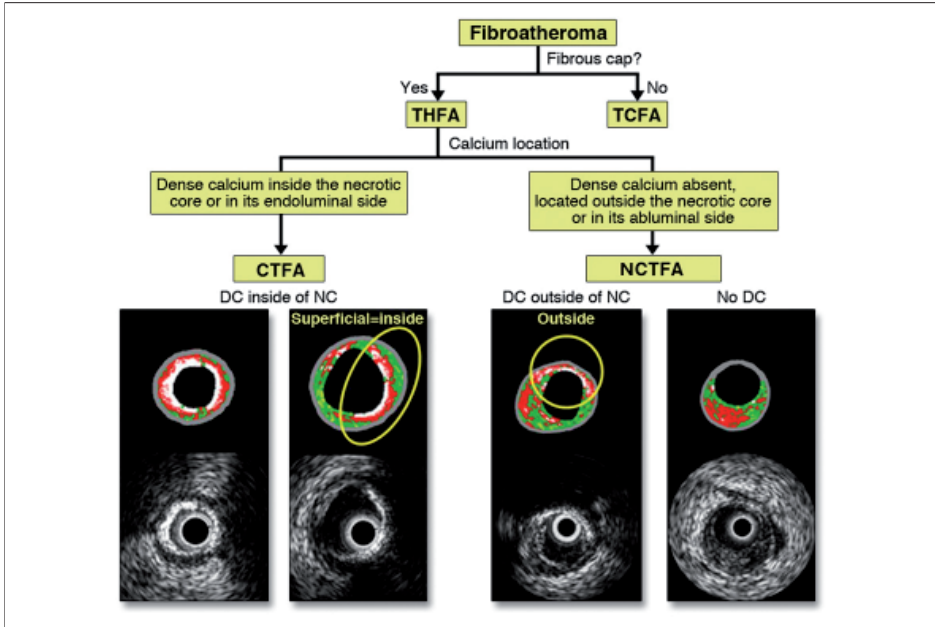


Figure 1. Subclassification of Fibroatheromas

Subclassification of fibroatheromas according to the presence of a fibrous cap and the topographic distribution of the dense calcium respect to the necrotic core. CTFA = calcified thick-cap fibroatheroma; DC = dense calcium; NC = necrotic core; NCTFA = noncalcified thick-cap fibroatheroma; TCFA = thin-cap fibroatheroma; THFA = thick-cap fibroatheroma.

Chapter 3.5

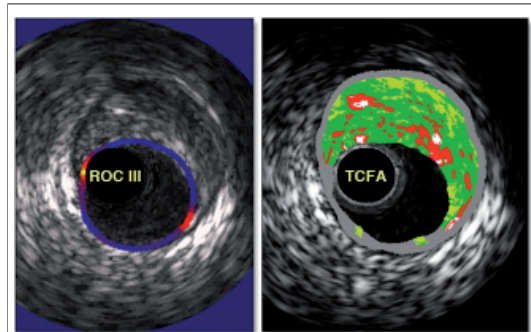


Figure 2. Palpography and IVUS-VH

Side-by-side view of palpography (left) and IVUS-VH (right) for a TCFA. High-strain spots on palpography are present at the edges of the plaque. Note that the time of acquisition of the images for both techniques is the same. IVUS-VH = intravascular ultrasound virtual histology; TCFA = thin-cap fibroatheroma.

Chapter 3.5

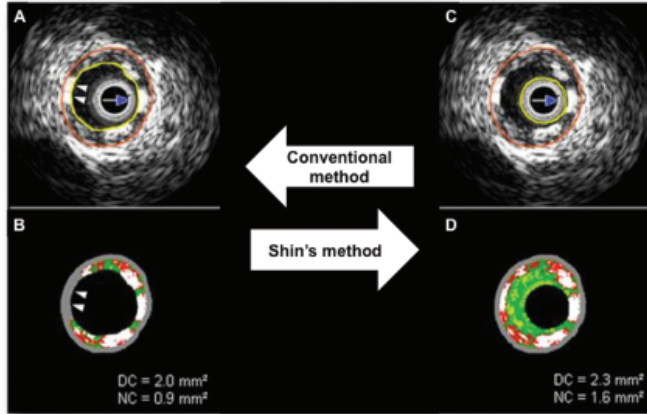


Figure 2. The conventional method (A and B) does not show some necrotic core and dense calcium (two white arrow heads), hidden by the grey medial stripe (two white arrow heads), that are showed by the Shin's method (C and D). DC: dense calcium, NC: necrotic core

Chapter 5.1

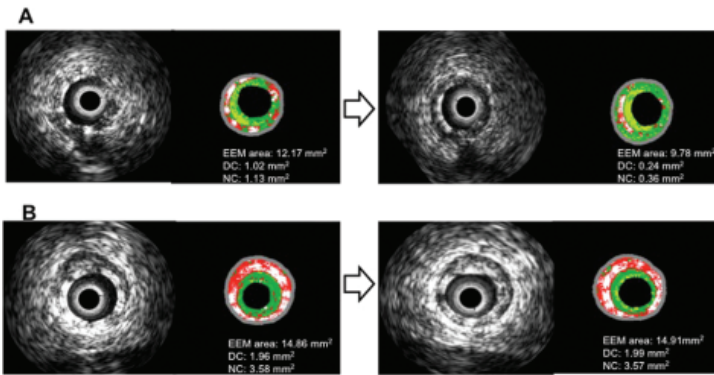
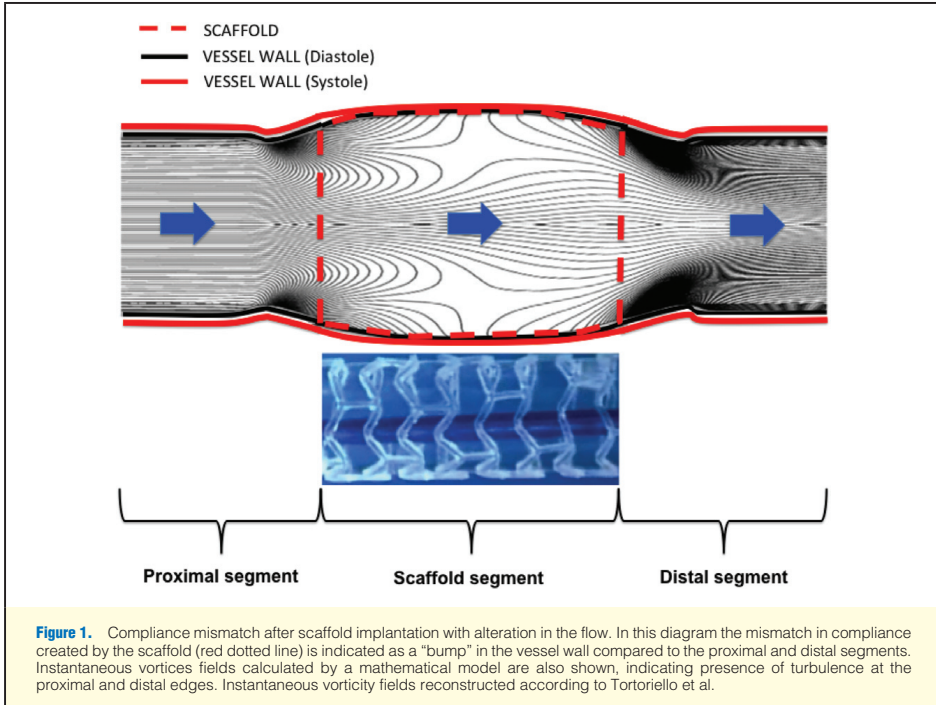
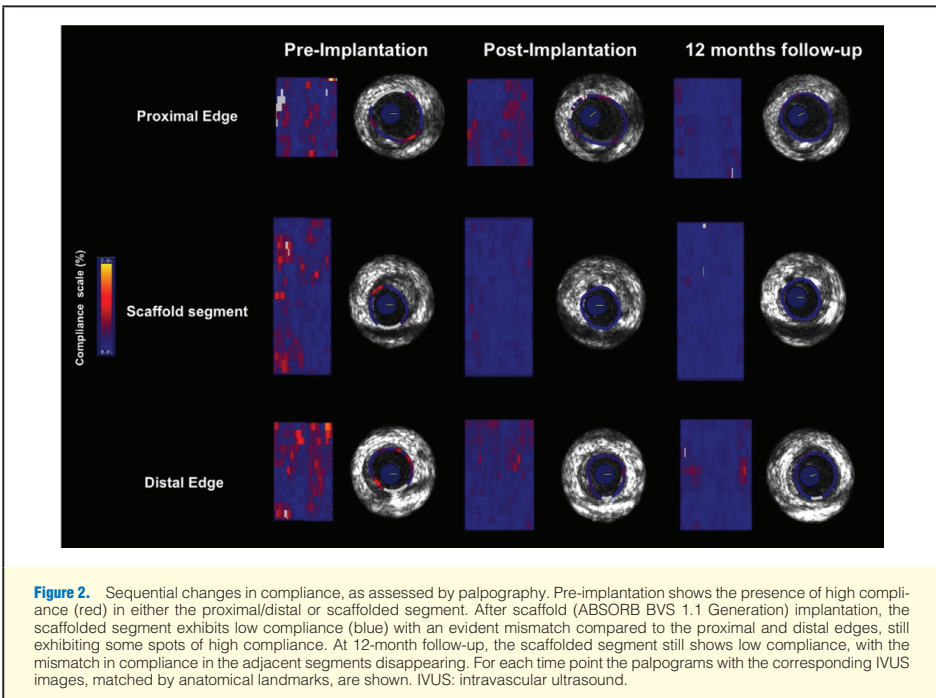


Figure 5. In the A panels, an extreme example of bioresorption at 6-months correlated with EEM area reduction. In the B panels, the persistence of the stent at six months is not associated with EEM area reduction. With the Shin method, blood surrounding ultrasound catheter is detected as fibrous and fibrous-fatty tissues. The boundaries of the lumen area are not depicted or superimposed on the figures. EEM: external elastic membrane; DC: dense calcium; NC: necrotic core

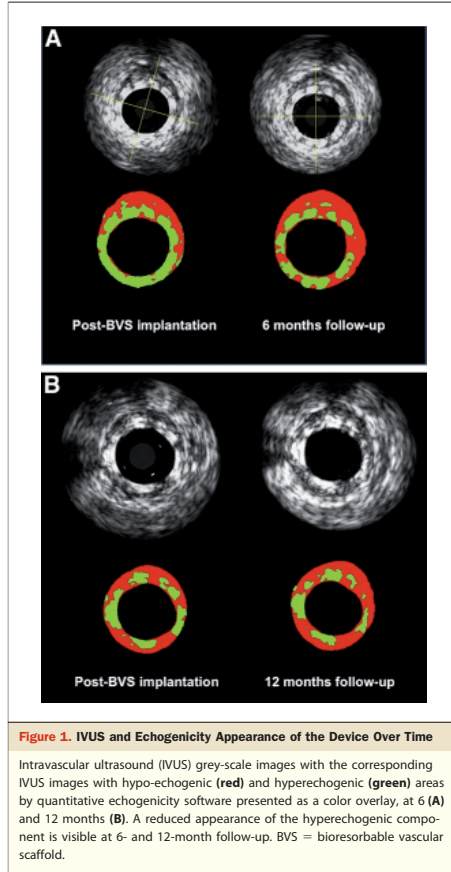
Chapter 5.1



Chapter 6.2



Chapter 6.2



Chapter 7.1

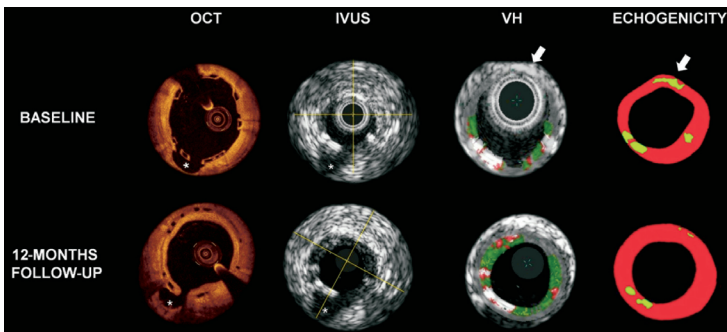


Figure 2. Examples of OCT, IVUS, VH and echogenicity findings of corresponding cross-sectional images with a side branch (*) selected as an anatomical landmark. The white arrows indicate a hyper-echogenic tissue in echogenicity analysis, hidden by the grey media stripe in the VH analysis; OCT: optical coherence tomography; IVUS: intravascular ultrasound; VH: virtual histology

Chapter 7.2

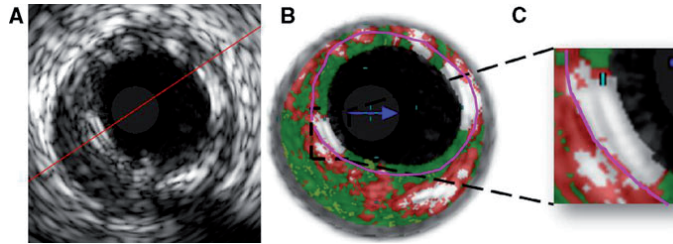


Fig. 1 *Panel A*: one frame of *grey-scale* IVUS indicating the appearance of the BVS's struts (*double grey line*). In *Panel B* the polymeric struts are recognized as dense calcium and

necrotic core by IVUS-VH and in (*Panel C*) a third contour (*purple line*) is drawn in a semi-automatic way by the dedicated software behind them

Chapter 8.1

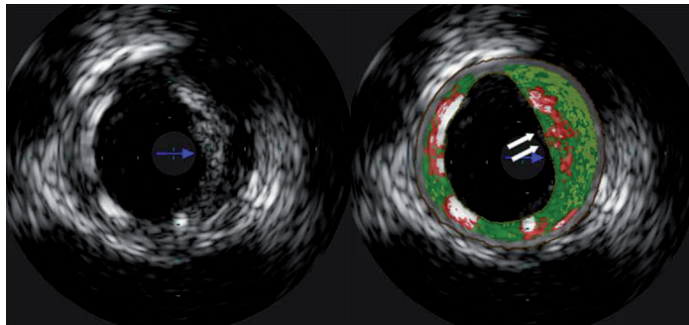


Fig. 3 Representative IVUS-VH image of necrotic core in contact with the lumen in the segment where a BVS has been implanted (*white arrows*). BVS bioresorbable polymeric scaffold

Chapter 8.1

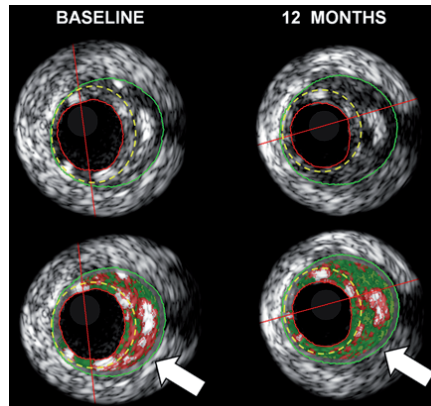


Fig. 1 Example of reduction of necrotic core and dense calcium in the plaque behind the polymeric struts (*white arrows*). Note also the increase of plaque size with predominant content of fibrous tissue. Yellow contour is drawn behind the ABSORB polymeric struts in a semi-automatic way by the dedicated software, excluding struts from the VH quantification of the plaque behind

Chapter 8.2

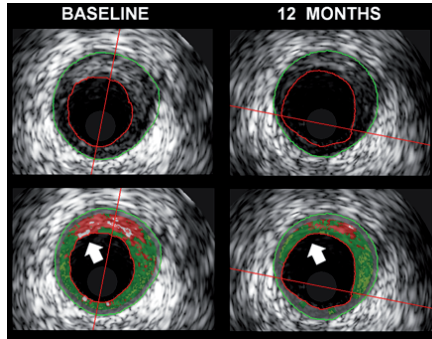


Fig. 3 Representative IVUS-VH image of necrotic core in contact with the lumen in the proximal reference segment at baseline and which has disappeared at follow-up

Chapter 8.2

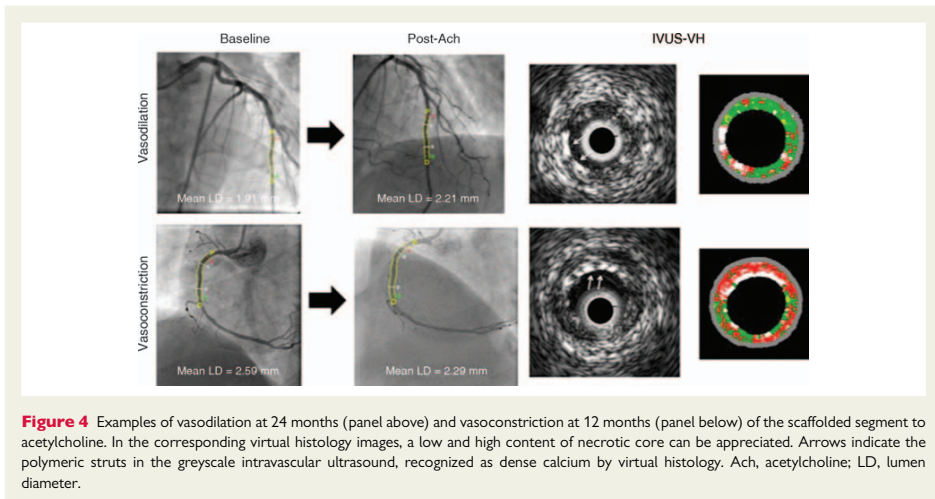


Figure 4 Examples of vasodilation at 24 months (panel above) and vasoconstriction at 12 months (panel below) of the scaffolded segment to acetylcholine. In the corresponding virtual histology images, a low and high content of necrotic core can be appreciated. Arrows indicate the polymeric struts in the greyscale intravascular ultrasound, recognized as dense calcium by virtual histology. Ach, acetylcholine; LD, lumen diameter.

Chapter 8.3